UNIVERSITY OF OKLAHOMA

GRADUATE COLLEGE

ITERATIVE MODEL-GUIDED POST STACK SEISMIC IMAGING AND INTERPRETATION OF HALOKINETIC STRUCTURES: RAS BANAS AREA, OFFSHORE NORTHERN RED SEA

A Dissertation

SUBMITTED TO THE GRADUATE FACULTY

in partial fulfillment of the requirements for the

Degree of

Doctor of Philosophy

By

ABDELAZIM A. IBRAHIM

Norman, Oklahoma

1998

ITERATIVE MODEL-GUIDED POST STACK SEISMIC IMAGING

AND INTERPRETATION OF HALOKINETIC STRUCTURES:

RAS BANAS AREA, OFFSHORE NORTHERN RED SEA

Dissertation APPROVED FOR THE

SCHOOL OF GEOLOGY AND GEOPHYSICS

BY

Acknowledgements

I thank my advisor, Dr. John D. Pigott for his advice. I am very grateful for his encouragement, and support. I extended my thanks to my committee members, Dr. James M. Forgotson, Dr. Roger Young for serving on my committee. I deeply appreciate their suggestions and comments. I am very grateful to my other committee members, Dr. Colin Barker, Dr. Roy Knapp for their contribution and comments. I thank Unocal Corporation for kindly providing the seismic data for this study. I also would like to thank the Society of Exploration Geophysicists (SEG), the Geophysical Society of Oklahoma City, the American Association of Petroleum geologists (AAPG), and Geological Society of America (GSA) for their financial assistance in funding this investigation.

To: Eisar, Alaa, and Sufyan.

TABLE OF CONTENTS

LIST OF FIGURES

Figure Page

ABSTRACT

Offshore northern Red Sea salt basins are dominated by complex halokinetic features and variable seafloor topography. The resulting severe imaging distortions observed on seismic profiles from these basins mask the salt and subsalt structures and create uncertainty in structural interpretation and definition of hydrocarbon prospects in this region. 2-D seismic models are used to investigate the causes and effects of image distortions observed on seismic lines from the study area. The modeling reveals five discrete causes: rugged seafloor topography, thick salt bodies varying in lateral geometry and exhibiting complex boundaries, rapid lateral velocity variations, intensive diffractions from faults and faulted block edges, and discrete lateral velocity anomalies from shallow reefal limestone and evaporite bodies. Through iteratively integrating both geological and geophysical data, an economic only feasible solution is presented to minimize these distortions and improve the imaging and structural interpretation of subsalt seismic events. The 2-D seismic modeling provides constraints in a form of raypath analyses, anticipates imaging problems, and narrowly constrains the range of acceptable interpretation. Post stack signal enhancement techniques are implemented to remove random noise, suppress water-related multiples, and reduce the deleterious effects of varying seafloor topography on the underlying reflections. Post stack migrations performed after using signal enhancement techniques significantly improve the seismic imaging and interpretation of salt and subsalt reflections.

CHAPTER I

INTRODUCTION

The Red Sea is a long narrow depression extending nearly 1932 km in a northwesterly direction from the Strait of Bab el Mandeb at its southern end to the tip of the Sinai Peninsula to the north (Fig. 1.1). The width increases from north to south averaging about 280 km, reaching a maximum of 306 km near Masawa and narrowing to a minimum of 26 km at the Strait of Bab el Mandeb. The study area (Fig. 1.2) is located between latitudes 23°N and 25° 24' N and comprises an offshore zone in the southern Egyptian Red Sea. The area extends landward to the Red Sea shoreline and seaward to a water depth in excess of 1000 m. The area is dominated by structurally complex halokinetic features which contribute to a variable seafloor bathymetry. The uneven water-bottom topography in this area is additionally caused by organic reef buildups, erosion during past sea level falls, and localized tectonics. Consequently, the bathymetry varies greatly, ranging mostly from few meters in the shallow parts to over a km in the deeper areas. The study is based on a grid of offshore two-dimensional seismic profiles with approximately 5-km spacing and oriented perpendicular to the present Red Sea shoreline. The seismic lines are constrained by data from two wells drilled in the central and southern parts of the study area. All of the seismic profiles used in this study were acquired, in 1975, by Western Geophysical for Union Oil Company of Egypt, and were made available through the OU Red Sea Project.

I.1. DEFINITION OF the problem

The complex halokinetic features and irregular seafloor topography caused severe imaging distortions that mask the salt and subsalt structures and create uncertainty in

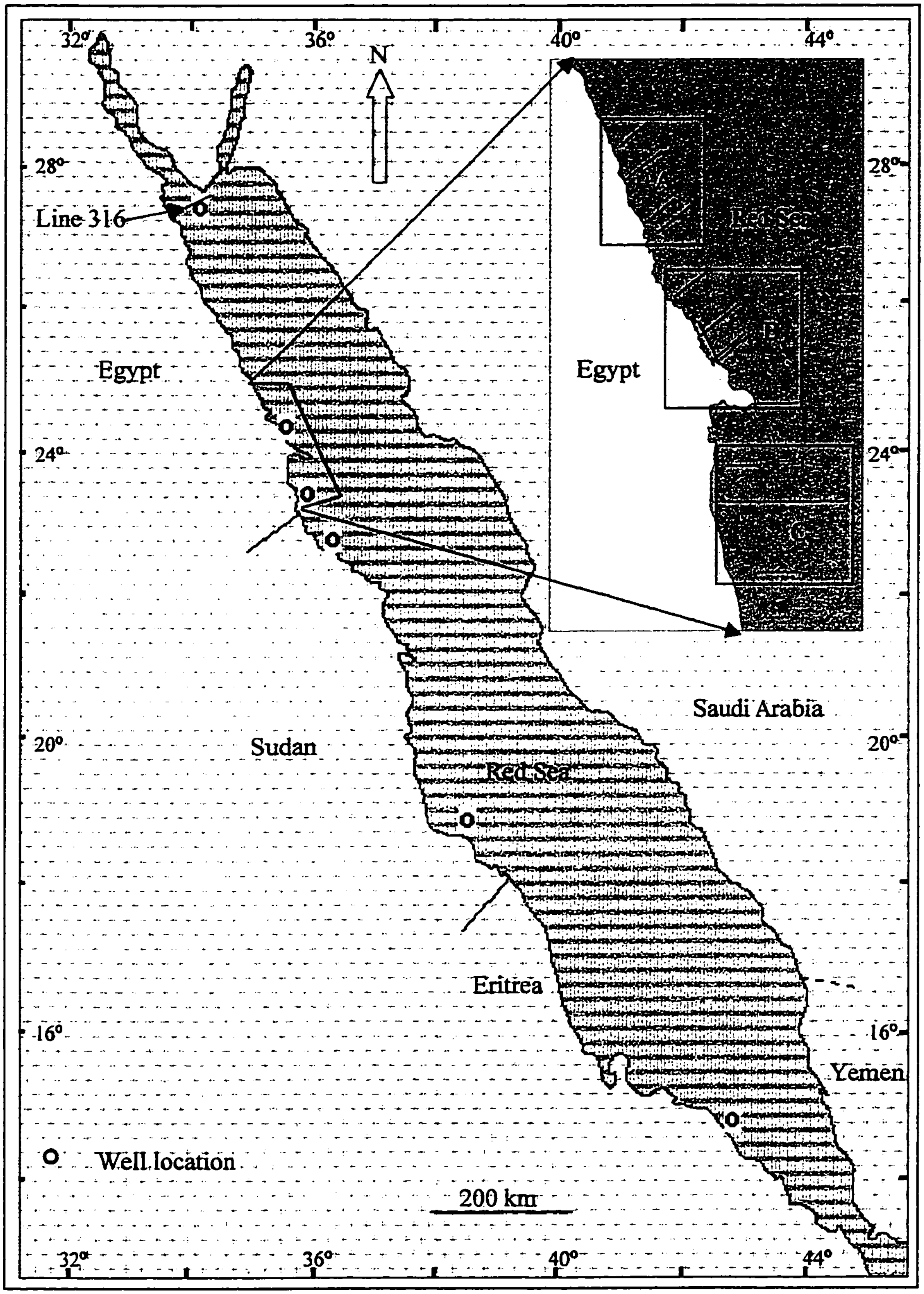

Figure 1.1 Location map showing the northern (A), central (B), and southern (C) parts of the study area in the offshore of southern Egyptian Red Sea.

structural interpretation and definition of hydrocarbon prospects in this region. Specific factors which contribute to these imaging distortions are: (a). Rugged water-bottom topography and the strong velocity contrast between water layer and underlying higher-velocity material (carbonates) which cause severe ray bending and sharp refraction. These in turn induce distortion and disruptions of reflections from salt and subsalt structures below. (b). Thick salt bodies varying in lateral geometry and exhibiting complex boundaries cause complicated ray-bending, resulting in insufficient downgoing energy for illuminating the subsalt structures. (c). Commingled diffraction and reflections from faults and faulted block edges adversely affect subsalt sections and further complicate the imaging problem. (d). Discrete lateral velocity anomalies from shallow reefal limestone and evaporite bodies lead to velocity pull-up of the underlying structures and thus degrade the subsalt image quality. (f). Water bottom related multiples and salt boundaries multiples further contaminate the subsalt images. These raypath distortions produce a poor quality image of subsalt seismic events. Thus, the delineation of subsalt structural traps and reservoir geometry, which is critical for accurate subsalt prospect evaluation, remains a challenge.

I.2. <u>Objectives:</u>

The imaging distortions observed on the seismic profiles from this area indicate that routine seismic acquisition and processing methods previously performed in this area do not adequately account for the ray bending effects associated with structurally complicated salt basins. The traditional methods commonly result in misinterpretation and in inaccurate mapping of salt and subsalt structures. Not surprisingly, such misinterpretations have contributed to unsuccessful exploration wells drilled in this region.

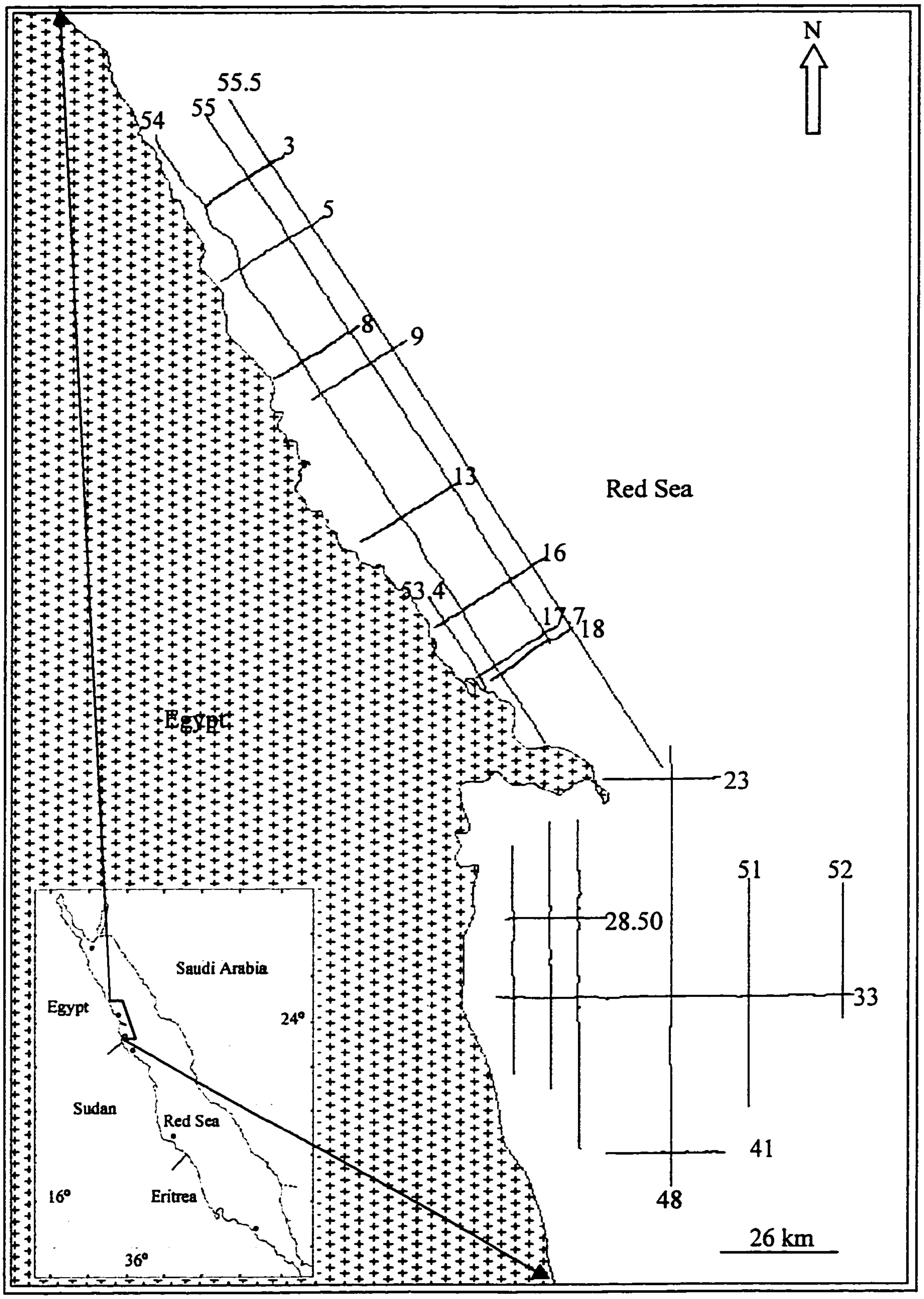

Figure 1.2. Location of seismic lines in the study area: Dip and strike lines are high-lighted in red and blue, respectively. The Red Sea coast-line is high-lighted in green.

An integrated approach which combines both geological and geophysical data is required to provide adequate seismic imaging and accurate geologic interpretation.

I.3. Methods and research tools:

Through iteratively integrating both geological and geophysical data, an economic post-stack solution to the minimization of these distortions is conducted in order to improve the imaging and structural interpretation of subsalt seismic events. These objectives are met by implementing proper signal enhancement techniques, and a systematic application of integrated, iterative model-guided seismic migration and interpretation.

First, 2-D seismic modeling performed on GXII software is used to identify the raypath distortions, anticipate imaging problems, and constrain the structural interpretation of seismic profiles from the study area. Second, to improve post-stack migration results, the following techniques are incorporated: wave equation multiple suppression to estimate and remove the water-related multiples, F-X trace interpolation to overcome the effect of spatial aliasing associated with large spatial sampling (Spitz, 1991), F-X deconvolution to remove the random noise (Canales, 1984), and wave equation datuming to remove the deleterious effects of the irregular water-bottom on underlying reflections (Berryhill, 1979, Bec, 1997). Iterative post-stack migrations performed after signal enhancement, significantly remove the distortions and improve the imaging and structural interpretation of subsalt seismic events.

CHAPTER II

OVERVIEW OF TECTONIC SETTING

The Red Sea was formed by rifting of the Arabian plate away from northeast Africa. The time of rift initiation is dated as late Oligocene to early Miocene. (Fichera et al., 1992, Cochran and Martiez, 1988, Salah, 1994, and Moretti et al, 1986). The Afro-Arabian Shield was formed in the Late Precambrian Pan-African tectonic cycle, (Kroner et al., 1987; Stoeser and Camp, 1985, Vail, 1985). During most the Paleozoic and Mesozoic, the Shield formed relatively high region and was onlapped by marine transgressions from the Indian Ocean to the east and Tethys to the north. Although recent published studies on the Red Sea agree on Neogene evolution, controversy remains regarding the mechanism of extension and the nature of resulting crust below the continental shelf. One group of authors propose that the shelves are underlain by a thinned continental crust (e.g., Cochran 1983, Davison ET aL., 1994a). Other group suggest oceanic crust beneath the shelves (e.g., Girdler and Underwood, 1985; Sultan et al, 1992). A number of models have been developed for the evolution of the Red Sea. The proposed rifting mechanisms include: (a) Simple shear model (with low-angle detachment fault) involving extension along crustal or lithospheric-scale detachment horizons (Bohannon, 1989; Voggenreiter and Hotzl, 1989; Voggenreiter et al., 1988; Wernicke, 1985). (b) Pure shear models involving uniform extension and thinning of the continental crust (Berhe, 1986; Cochran and Martinez, 1988; Lowell and Genik, 1972, Martinez and Cochran, 1988). (c) Sea floor spreading (Pull-apart) models involving the development of oceanic crust across a wider portion of the Red Sea (e.g. Gaulier et al.' 1988; Girdler and Styles, 1974; Izzeldin, 1987; Makris and Rihm, 1985).

The earliest rift-related sequence are of Oligocene to earliest Miocene age and rest unconformably upon Eocene to Precambrian rocks throughout most of the onshore Red Sea region. This regional unconformity implies a period of pre-rift arching (doming), uplifting and erosion during middle Miocene to Oligocene time. However, recent studies in The Gulf of Suez (Evans, 1998; Garfunkel, 1988; Purser and Hötzl, 19988) suggest that a hiatus in sedimentation during that time is possibly due to a worldwide lowstand in sea level.

Further phase of rifting occurred in the early to early middle Miocene. During this period, The Gulf of Suez and the Red Sea formed a single elongated basin. Development of the Aqaba-Levant fault zone 14 m.y. (Bayer et al., 1988) together with the onset of sea floor spreading in the Gulf of Aden 12 m.y. (Cochran, 1982), accommodated the northeastward movement of Arabian plate away from northeastern Africa. Subsequent to this time, the Gulf of Suez experienced limited extension and was dominated by thermally driven subsidence. Large extension continued, however, in the Red Sea to the south (Sikander A.H., 1990).

II.1. **Stratigraphy:**

The stratigraphic succession of this region is generally divided, relative to the rifting stages (Sikander A. H., 1990), into three depositional megasequences: Pre-rift (Pre-Miocene, 570-23 Ma), syn-rift (Miocene, 23-5), and post-rift (Pliocene-Recent, 5-0 Ma) (Fig. 2.1).

II.1.1 Pre-rift Megasequence (Nubian, Quseir, Duwi, Esna, and Thebes formations):

The pre-rift sedimentary rocks consist of Paleozoic, Lower and Upper Cretaceous, Paleocene, and Lower Eocene units. The Pre-rift rocks have not been encountered in any of the offshore wells drilled in Red Sea. In the study area, the Miocene units rest uncomfortably on crystalline basement. However, the pre-rift Paleozoic and Lower Cretaceous units found in the Gulf of Suez and northernmost part of the Red Sea consist of continental to shallow marine non fossiliferous sandstone know as the Nubian Formation. The Upper Cretaceous, Paleocene and Eocene pre-rift rocks have also been found in onshore wells of northwest Red Sea part and in half-grabens in onshore outcrops in Safaga-Quser area to the west of the central Egyptian Red Sea. In Safaga-Quseir area, the Upper Cretaceous Nubian consists of non-marine sandstone with excellent reservoir quality and rests unconformably on crystalline basement. These sandstones are conformably overlain by the Paleocene Esna Shale formation. The fact that the few wells drilled to the basement were located on structural high indicate that the Nubian Formation and uncomfortably overlying Upper Cretaceous-Eocene marine units may be preserved offshore in untested structurally low areas. Because seismic resolution below thick Miocene evaporite sequence is very poor, subsurface data, critical to identification of the underlying pre-rift rocks, are currently very limited.

II.1.2. <u>Syn-rift (Miocene, 23-5)</u>:

The syn-rift megasequence is further divided, from base to top, into: Lower syn-rift sequence (pre-evaporite) and an Upper syn-rift sequence (evaporite).

II.1.2.a. <u>Lower syn-rift megasequence</u> :

The Lower syn-rift sedimentary succession consists largely of a clastic unit known in the Egyptian Red Sea as the Gharandal Group. This group was deposited on the tilted and rotated block unconformity surfaces of the pre-rift and comprises, from the base to

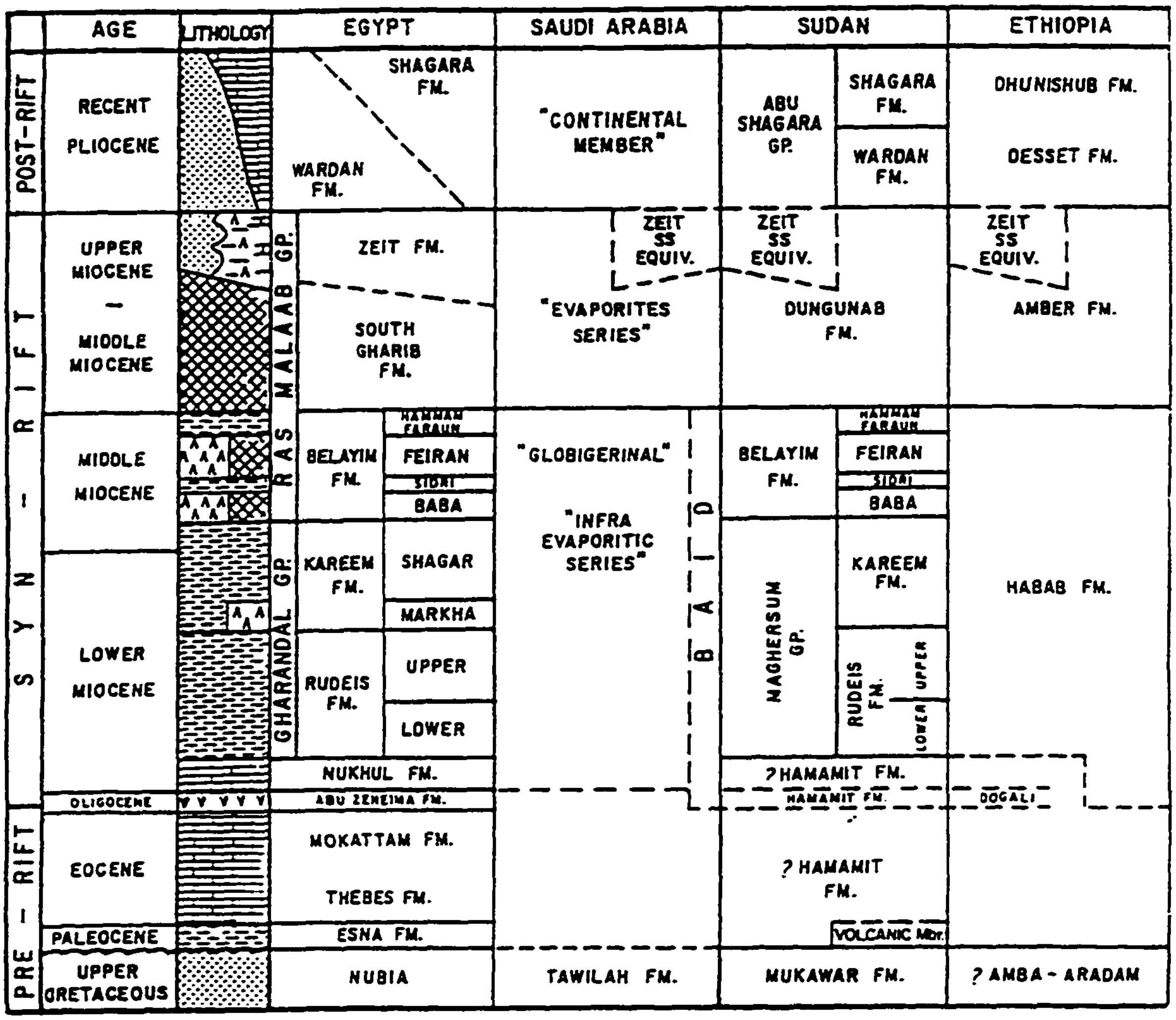

Figure .2.1. Stratigraphy of the Red Sea (after Robertson, 1991).

top: the Lower to Middle Miocene Nukhul, Rudeis, Kareem, and Belayim formations. The Nukhul Formation consists largely of clastics, chiefly sandstone and shale, representing an initial marine transgression. The overlying Rudeis formation consists of clastic lithologies, chiefly shales, sandstones, marls, and siltstones and represents dominantly an open marine environment. Kareem and Belayim consist of mixed evaporites, mainly anhydrite and halite, carbonates and minor clastics, and mark transition from open marine to restricted environment as marine circulation from the north into the Red Sea became restricted (Salah and Alsharhan, 1996).

II.1.2.b <u>Upper syn-rift megasequence:</u>

This megasequence comprise the Middle South Gharib Formation and overlying Middle-Upper Miocene evaporitic clastic units of Zeit Formation. The thick South Gharib formation typically consists of a thick crystalline halite with thin intercalated anhydrite and shale interbeds and minor carbonates and sand. The South Gharib salt indicate highly restricted, hypersaline water condition with the deposition of halite in the depocenters and anhydrite and thin shale on the basin margins. The factors that restricted the circulation into the Red Sea at that time are not fully understood. The restriction was probably related to a worldwide drop in sea level at 10.5 Ma (Evans, 1988).

Middle-upper Miocene evaporitic clastic units of the Zeit Formation represent a return to an alternating restricted and open marine environment. The Zeit Formation was encountered in five wells in offshore Egyptian Red Sea with thickness ranging from 195 ft to 848 ft. The lithology of the Zeit Formation consists largely of evaporites, mainly anhydrite and clastic rocks in varying proportion. The thickest (1813m) sections were found in the offshore Toker Delta and Halaib areas of Sudanese Red Sea. The presence of thick Zeit Formation in these areas indicates the development of two depocentres, which continued during the post-rift megasequence of Pliocene to Recent age. These depocentres are located at the mouths of drainage basins, which extend across the Red Sea rift shoulder into the Red Sea Hills. These drainage basins developed as early as the Middle-Upper Miocene.

II.1.3. Post –rift Megasequence (Pliocene to Recent):

Uplift at the end of the Miocene resulted in major erosional unconformity, and a return to the normal marine conditions as connection with the Indian Ocean was established. Renewed rifting and subsidence was followed by deposition of the Pliocene to Recent post-rift clastic and carbonates on top of the Zeit unconformity surface. The post-rift consists of lower the Wardan and upper Shagara formations. The post-rift depositional patterns reflect present drainage system along the Red Sea margins. The post-rift section is poorly defined and generally thin in the offshore Egyptian Red Sea. In this region, the section generally thins from west to east consistent with sediment supply from the Red Sea Hills to the west. The thinning is attributed to a lack of structural topographic breaks or conduits through which drainage from the Red Sea Hills to the west enters the basin. However, in the southern part of the study area, seismic data have indicated a pronounced thickening, just east of the basin margins, in channels between salt bodies, and into inter-diapir lows. The Pliocene Wardan Formation consists of mixed clastic facies transitional between the Upper Miocene evaporite basin and open marine environment of today. The Shagara formation is primarily a shelf carbonate and more sandy toward the coast. It consists predominately of coraline limestone with sandstones and claystones.

II.2. Hydrocarbon potential:

The offshore northern Red Sea contains all the necessary ingredients, which are responsible for hydrocarbon generation and entrapment in the productive Gulf of Suez to the north. These include similar pre-evaporite source and reservoir rocks and the overlying evaporite seal. The structural style and possible pre-rift source and reservoir rocks in the northern Red Sea are also similar to those in the Gulf of Suez. Geochemical results (BEICIP, 1990) indicate that pre-evaporite source rocks are currently within the oil window.

II.2.1. Pre-rift:

Pre-rift sedimentary rocks have not been encountered in the wells drilled in the offshore Egyptian area of the Red Sea. However, these wells were drilled on structural highs and the pre-rift rocks possibly are preserved in structural lows, which have not been tested by drilling. The Upper Cretaceous Duwi (TOC= 1.1-1.6%), the overlying part of Dakhla (TOC= 1.9-6.4 %) and Matulla (Average TOC=3.13%) Formations, found in onshore wells and in adjacent Red Sea Hills, are considered excellent potential source rocks (Ganz 1986; Ganz and Kalkreuth, 1987; Ganz et al, 1987). The pre-rift Nubian sandstones are important reservoirs in a number of producing fields in the Gulf of Suez (e.g., Hurghada oil field). The interbedded shales are likely to provide an effective seal for possible pre-rift reservoirs.

II.2.2 Syn-Rift:

Geochemical studies (Barakat, 1982) have indicated that the lower syn-rift Rudeis, Kareem and Belayim formations contain good oil-prone source rocks. Sandstone intervals of upper Kareem and Rudeis Formations have been encountered in offshore wells of the

Egyptian Red Sea, including the study area. These sandstones have good reservoir characteristics and form important reservoir rocks in the productive Gulf of Suez. Reefal carbonate intervals of the Belayim Formation, encountered in RA West-1 well drilled in the central part of study area, show good reservoir quality with an average porosity of 14% (Tewfik and Ayyad, 1982). The intercalated mudstone beds and anhydrites of Kareem and Belayim Formations and Rudeis shales would make good seal rocks for syn-rift reservoirs. Rich source rocks have been found in thin beds within the upper syn-rift South Gharib and Zeit evaporites sequence (Robertson Group, 1991). Sandstone lenses within evaporites offer good quality reservoir potential. The halite and anhydrite of South Gharinb and Zeit formations offer potentially effective seals.

II.2.3 Post-Rift:

Interdiapir lows, distal from clastic sources, are likely to provide source kitchens. In the Gulf of Suez, the lower part of Wardan Formation contains oil-prone source rock and is situated within the oil window in this area (Robertson Group, 1 991). The anhydrite and mudstones in transgressive cycles may provide adequate seal.

CHAPTER III

TECHNIQUES

III.1. Strategy:

This interdisciplinary investigation integrates geology and geophysics. 2-D seismic models are used to identify raypath distortions, anticipate imaging problems, and verify and constrain the seismic interpretation. To improve the migration results: the following signal enhancement techniques were applied: wave equation multiple suppression to estimate and remove water-related multiples, F-X (frequency, distance) trace interpolation to overcome the effect of spatial aliasing associated with large spatial sampling, and F-X deconvolution to remove the random noise. Post-stack wave equation datuming was used to remove the distortion of underlying reflections by the rugged water-bottom. Time migrations performed after wave equation datuming produce results, which are nearly identical to more costly, full depth migration.

Residual migrations improve the finite difference performance in the presence of steep dips. A constant-velocity Stolt F-K in the first pass is followed by FD (finite difference) time migration in the second pass. The first pass F-K migrates the steep dips that the second-pass FD cannot handle. The second pass FD residual migration handles lateral velocity changes, hence, correcting for the constant velocity prerequisite for F-K (frequency-wave number) migration. FD depth migration, better suited to dealing with strong lateral velocity variations, is implemented to eliminate the distortion caused by ray bending associated with irregular salt geometry.

III.2. 2-D SEISMIC MODELING:

Basic Concept

GXII 2-D seismic modeling software is used to simulate and analyze seismic energy as it propagates through the subsurface and to show how this energy reflects, transmits, refracts, and diffracts in the subsurface at various layer boundaries. Each seismic model created in this study represents 2-D cross-sectional views of the subsurface that shows the relative positions of horizons, geological layers, faults, and wells. Layers are the regions of the model through which energy is transmitted and are defined by specifying their material properties such as lithology, velocity, and density. GXII modeling program shows the path of reflected and transmitted seismic wave in a form of rays that reflects at or transmits across the horizons defined in the model. The material properties of each layer determine how fast the seismic waves can propagate through it. This in effect determines the travel time of each ray at each horizon in the 2-D model. The difference in material properties between layers is used to compute acoustic impedance, a factor that controls reflection coefficients, energy transmission, and refraction angle. The reflection coefficients (spike traces) show the arrival times and reflection strength of each ray. By applying a filter and its corresponding wavelet to the spike traces, GXII calculates the amplitudes needed to generate synthetic seismic section

III.2.1. Modeling Approaches:

Two modeling approaches are used to produce final acceptable velocity-depth model. These are forward and inversion modeling (Fig. 3.1).

III.2.1.a. Inversion:

Inversion modeling begins by building a time model from a time interpretation of unmigrated seismic section as shown in Figure 3.2. The time model is then converted to depth using a normal incidence rays time-to-depth conversion method. The output from inversion is an initial depth model. Forward zero offset ray tracing is then performed on the initial depth model to create synthetic seismic section (Fagin S. W., 1992). The synthetic section is compared with the original unmigrated seismic section to verify the interpretation. If the synthetic and the original seismic section do not match, the interpretation of the original section is iteratively modified until an acceptable match is obtained. If the synthetic and the original seismic sections match, the depth model that produced the synthetic is considered the final acceptable one.

III.2.1.b. Forward Modeling:

Forward modeling begins with an initial guess of a velocity-depth model (Fig. 3.3). The initial guess depth-velocity model is built from an interpretation of seismic reflections and estimate of layer velocities from sonic logs and seismic data. Zero offset raytracing is then applied to the depth-velocity model followed by synthetic trace generation. If the synthetic and the original seismic section do not match, the initial velocity-depth model is modified until an acceptable match is obtained. The output from forward modeling approach is a final depth model.

III.2.2. **Procedure:**

Three steps are required for 2-D seismic modeling: model building, ray tracing, and synthetic trace generation as illustrated in Figure 3.4.

III.2.2.1. Modeling Building:

As pointed out previously, the initial model is built from an interpretation of seismic reflections and the construction of an estimate of layer velocities from sonic logs

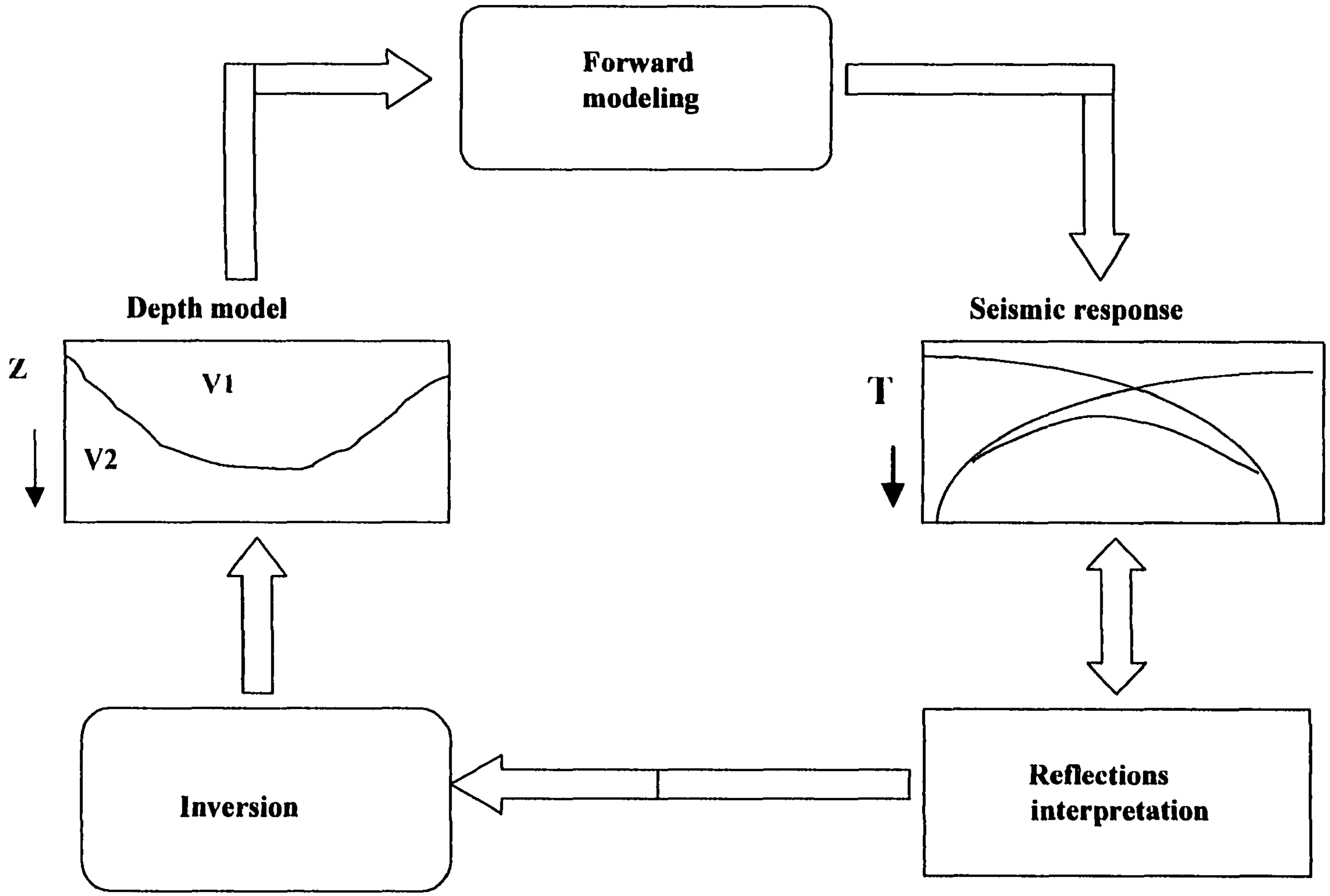

Figure 3.1. Forward- inverse 2-D seismic modeling loop.

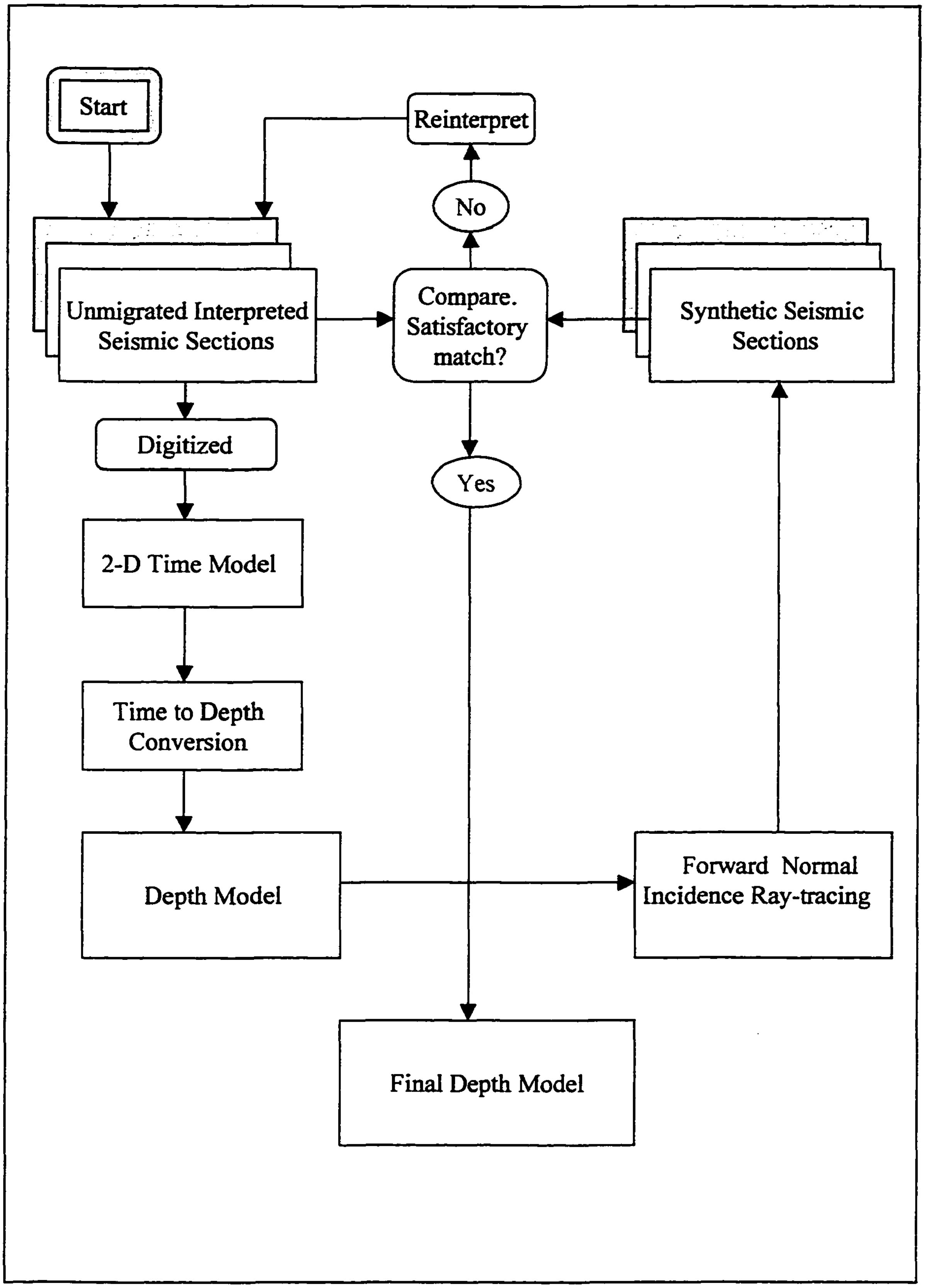

Figure 3.2. Schematic diagram illustrating 2-D seismic inversion approach.

and seismic data. Each seismic model created represents 2-D cross-sectional views of the subsurface that shows the relative positions of horizons, faults, and geological layers. Layers are the regions of the model through which energy is transmitted and are defined by specifying their material properties such as velocity and density.

III.2.2.2. Ray-Tracing:

Definition and basic concepts:

Seismic waves propagating through a homogeneous medium can be predicted by Huygen's Principle. This principle states that, every point on a wavefront can be regarded as the source of entirely new wavefront. Lines perpendicular to the wavefronts are known as wave paths or raypaths. Although raypaths do not in reality exist, thinking of seismic waves in term of raypaths to describe the propagation of seismic waves can be simpler and convenient than using the full wavefront (Dobrin M. B., and Savit C. H., 1988). Therefore, rayapaths are conceptual tools which allow us to describe the geometry of the path of transmitted and reflected seismic waves as they propagate between the source, reflecting interfaces, and receivers (Evans B. J., 1997). The point of origin on the recording surface, the material properties of each layer, and the angle of reflecting interface determine the path, speed, and arrival time of each ray. Hence, the concept of ray-tracing is that, given a velocity-depth model, a source and receiver locations, the raypath reflected from a particular model interface to the source and receiver can be found.

III.2.2.2.a. Raypath characteristics:

Seismic wave propagation and raypath trajectories are determined by three rules: A raypath is unbent in a constant velocity medium, a raypath bends across velocity

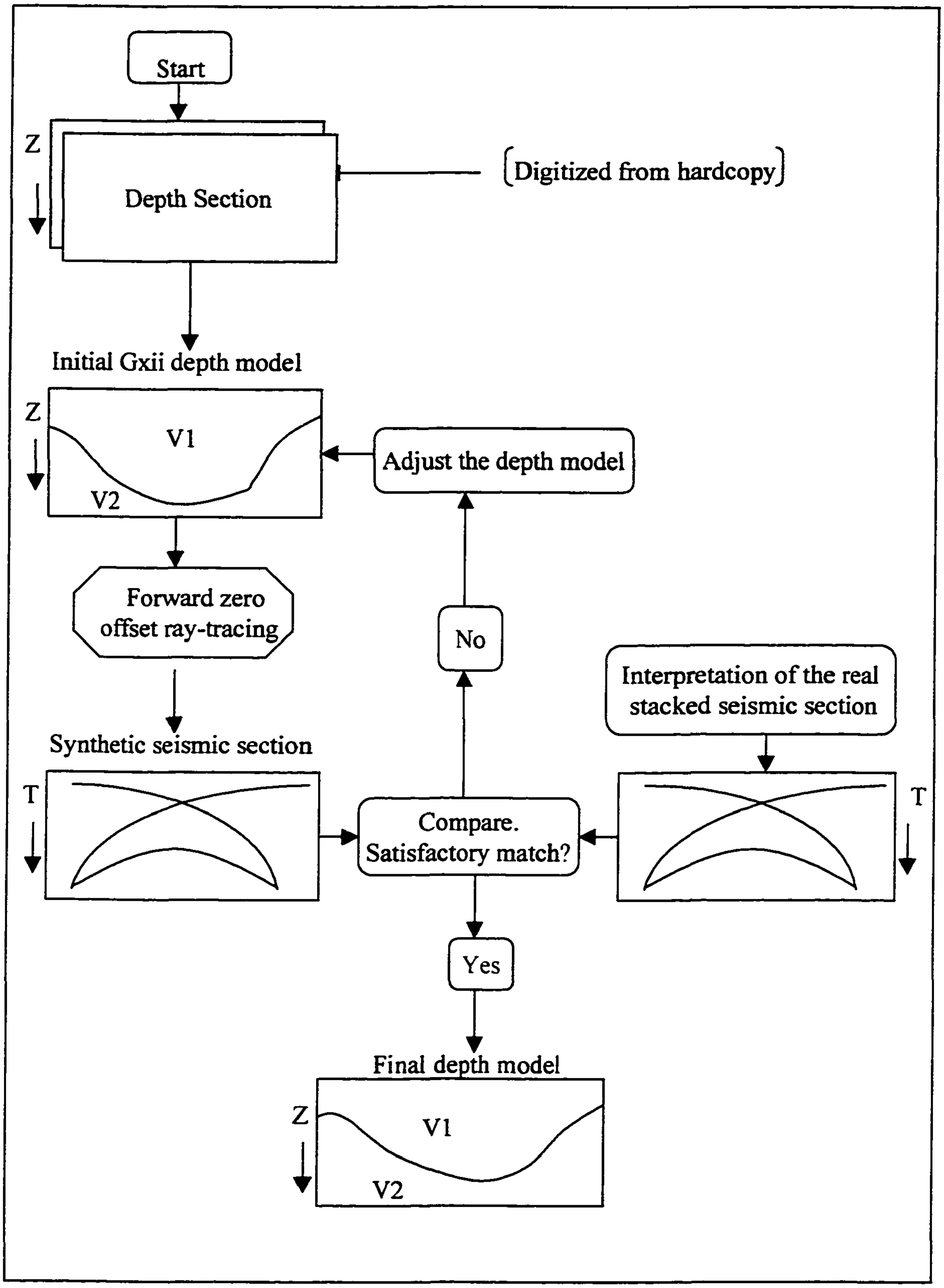

Figure 3.3. Schematic diagram illustrating forward 2-D seismic modeling approach.

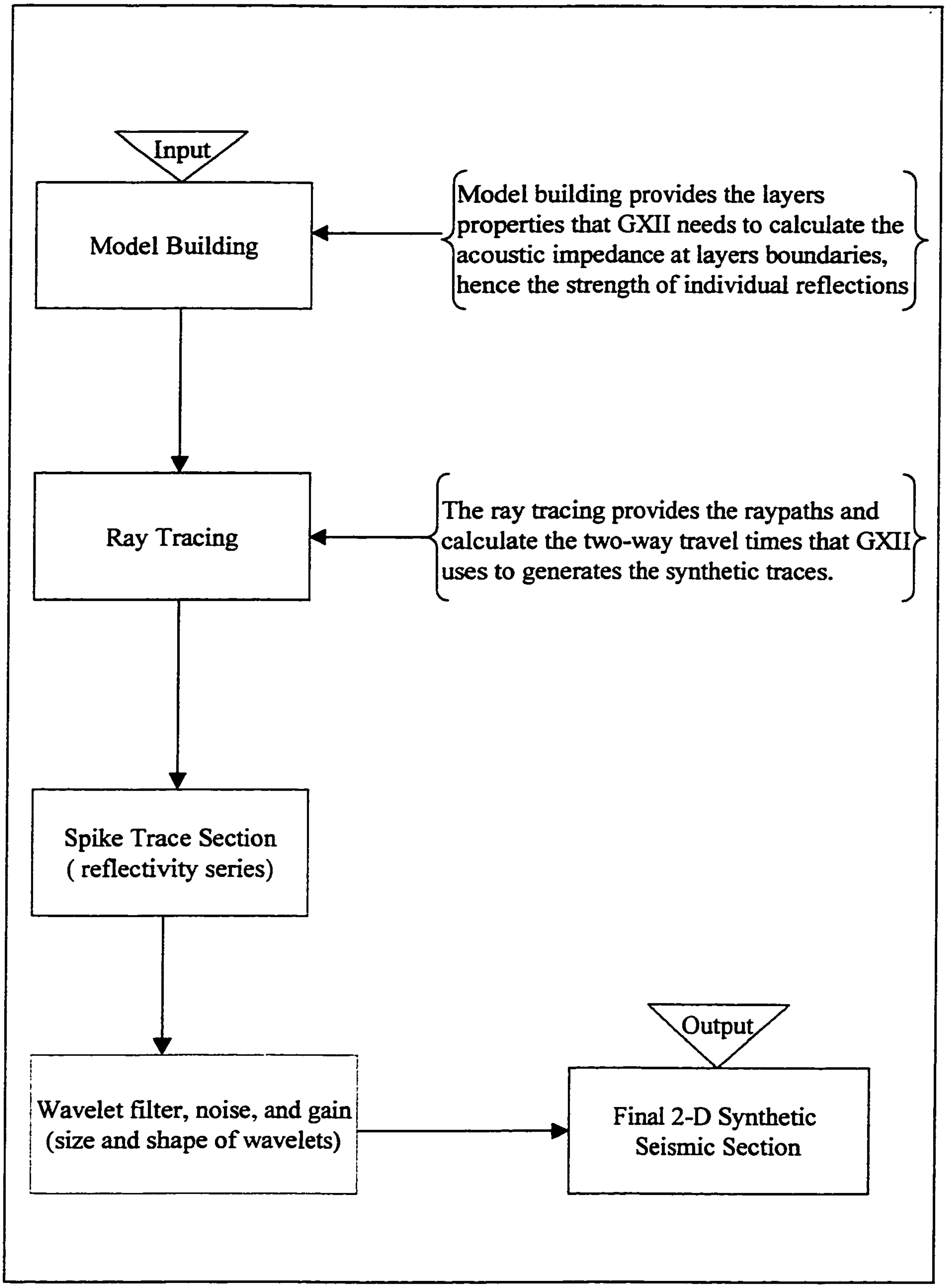

Figure 3.4. Flowchart illustrating the steps needed to generate a 2-D synthetic seismic section on GXII modeling software.

interfaces according to Snell's Law, and a ray reflects at an angle equal to the incidence angle when it encounters impedance contrast at interfaces. Let us examine these in more detail.

(a) In a constant velocity layer, the wavefronts are concentric and raypaths are normal to the wavefronts. In other words, raypaths are radii, which connect successive wavefronts with their source points on the proceeding wavefronts; thus the raypaths are unbent in a constant velocity medium.

(b). A raypath bends across velocity interfaces according to Snell's Law, which states that the sine of the incidence angle sin i, divided by the upper medium velocity V_1 equals the sine of refracted angle, sin r, divided by the lower medium velocity V_2. That is: $\sin(i)/V_1 = \sin(r)/V_2$, where i and r are the angles of incidence and of reflectance, respectively. V_1 and V_2 are the velocities of the upper and lower media, respectively. Thus when a seismic wave strikes an interface separating layers with different velocities, part of the seismic energy is reflected and part of the energy is refracted or transmitted with the direction of propagation changing at the interface. The geometry and the derivation of Snell's Law are illustrated in Figure 3.5. When the raypath is normal to an interface, (i = zero, r = zero), no raypath bending occurs in the transmitted seismic wave. The amount of raypath bending is proportional to the velocity contrast across the interface. Ray bending increases raypath length in the higher velocity medium and thus, shortens traveltime. Raypath bending complicates and distorts the seismic imaging particularly in areas with steep interfaces separating layers with strong contrasting velocities.

(c) A ray reflects at an angle equal to the incidence angle when it encounters impedance contrast at interfaces. The impedance is the product of a medium velocity and density.

Assuming normal incidence, the relationship between incident amplitude (A_i), reflected amplitude (A_r), and the reflection coefficient (R_c) is:

$$A_r = R_C * A_i \qquad \text{(III.1)}$$

Where,

$$R_C = (\rho_2 V_2 - \rho_1 V_1)/(\rho_2 V_2 + \rho_1 V_1) \qquad \text{(III.2)}$$

Rc can be positive or negative in polarity depending on whether the lower layer has higher or lower velocity-density product (ρv) than the upper layer, respectively. Hence, the amplitude and polarity of reflection depends on the difference in acoustic impedance between layers.

III.2.2.2.b. Ray tracing types:

The three ray tracing methods are used to simulate the stacked and migrated seismic profiles are normal incidence, image ray, and vertical ray tracing. Figure 3.6 shows the geometry and characteristics of these rays.

<u>Normal incidence rays:</u>

These are zero offset rays that reflect at right angle from the reflectors and simulate the unmigrated stacked seismic section. In other words, these rays leave the source and hit the reflecting interfaces in the subsurface at right angles, and return to the surface along the same path (angle of incidence is zero). Thus for a common midpoint stacked section, CMP, the time to particular events can be associated with a normal-incidence raypath. Normal incidence rays are commonly used in areas with complex structures and have been conducted in this investigation. Figure 3.7 shows how normal incidence rays are used in this study to convert the unmigrated sections to depth during the inversion process.

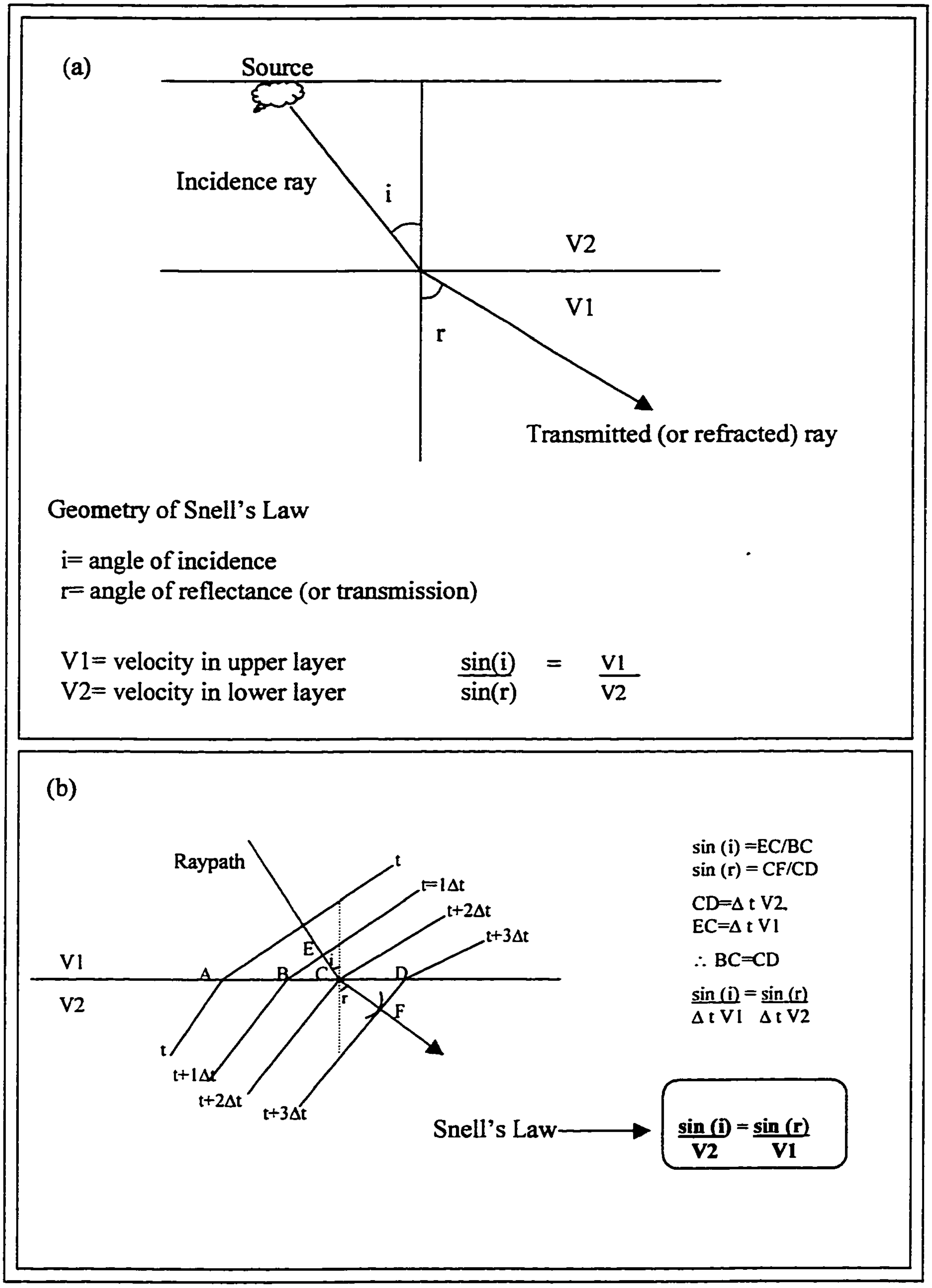

Figure 3.5. The geometry (a) and derivation (b) of Snell's law.

Image ray:

The concept of image ray was first introduced by Hubral, (1977). Although image rays curve in areas with lateral velocity changes, they arrive at the recording surface in a vertical direction (Fig. 3.6). Image rays represent the least travel time from a given subsurface point to any position on the recording surface. The apex of a diffraction hyperbola also represents the shortest travel time from point diffraction to the surface. Time migration algorithms collapse the seismic energy to the apex of a diffraction hyperbola. Hence, image rays represent the imaging result of time migration and are often used to convert the time migrated seismic section to depth migrated structures.

Vertical rays:

Vertical rays do not bend across horizontal interfaces in the subsurface and therefore represent the outcome of a proper depth migration.

III.2.2.3. Synthetic Trace Generation:

Following ray tracing, an appropriate wavelet is determined from phase and frequency analysis of seismic line relative to the well control. The wavelet is then convolved with the spike section resulting from ray tracing to generate a synthetic seismic section.

III.3. Post stack signal enhancement techniques:

III.3.1. **Wave equation datuming**:

The nature of the problem:

As pointed out previously, the bathymetry of the study area varies greatly, ranging from few meters in the shallow part to over a kilometer m in the deeper areas. The irregular water-bottom topography and the velocity contrast across the sea floor causes

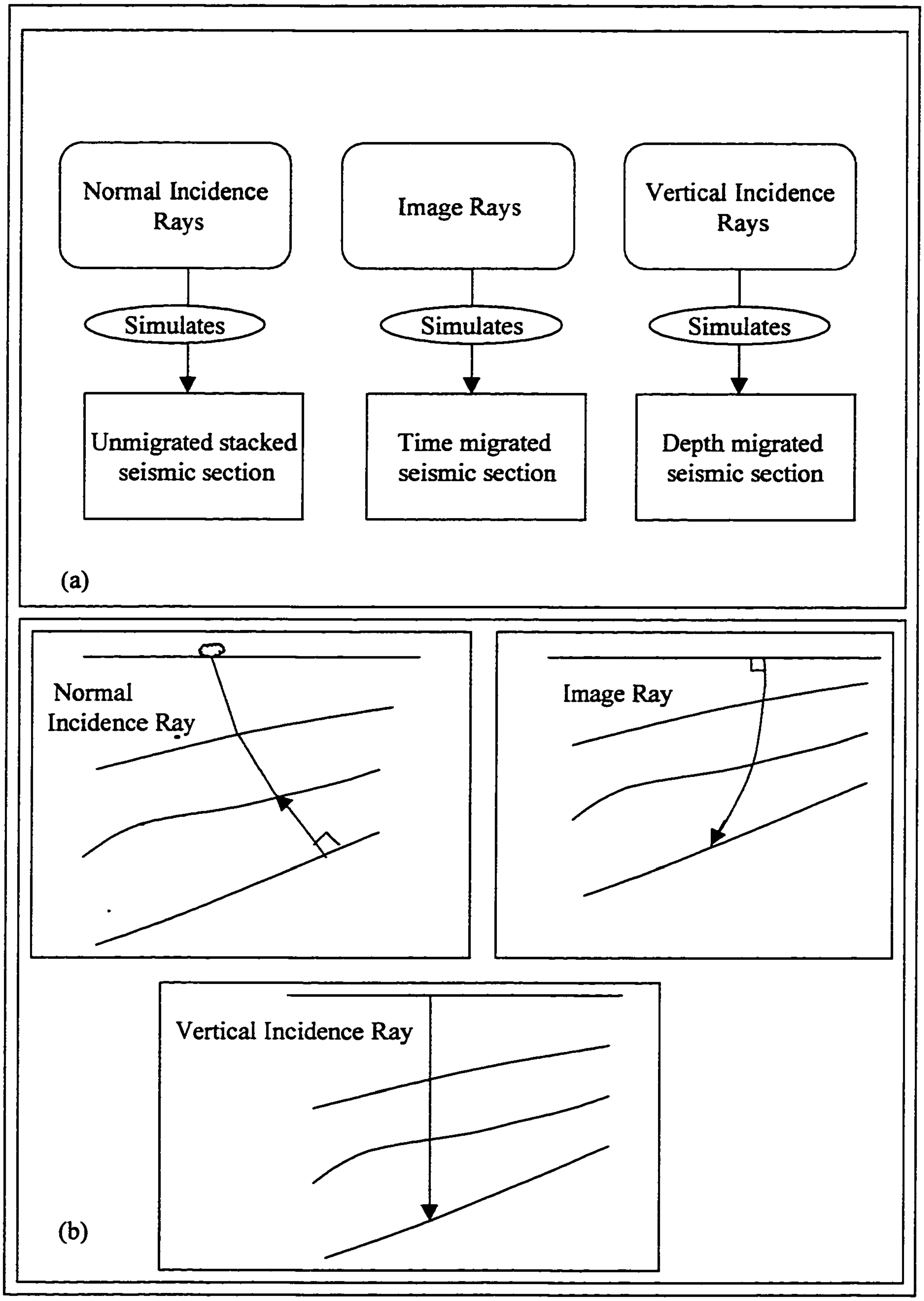

Figure 3.6. Ray-tracing types (a) and their geometry (b).

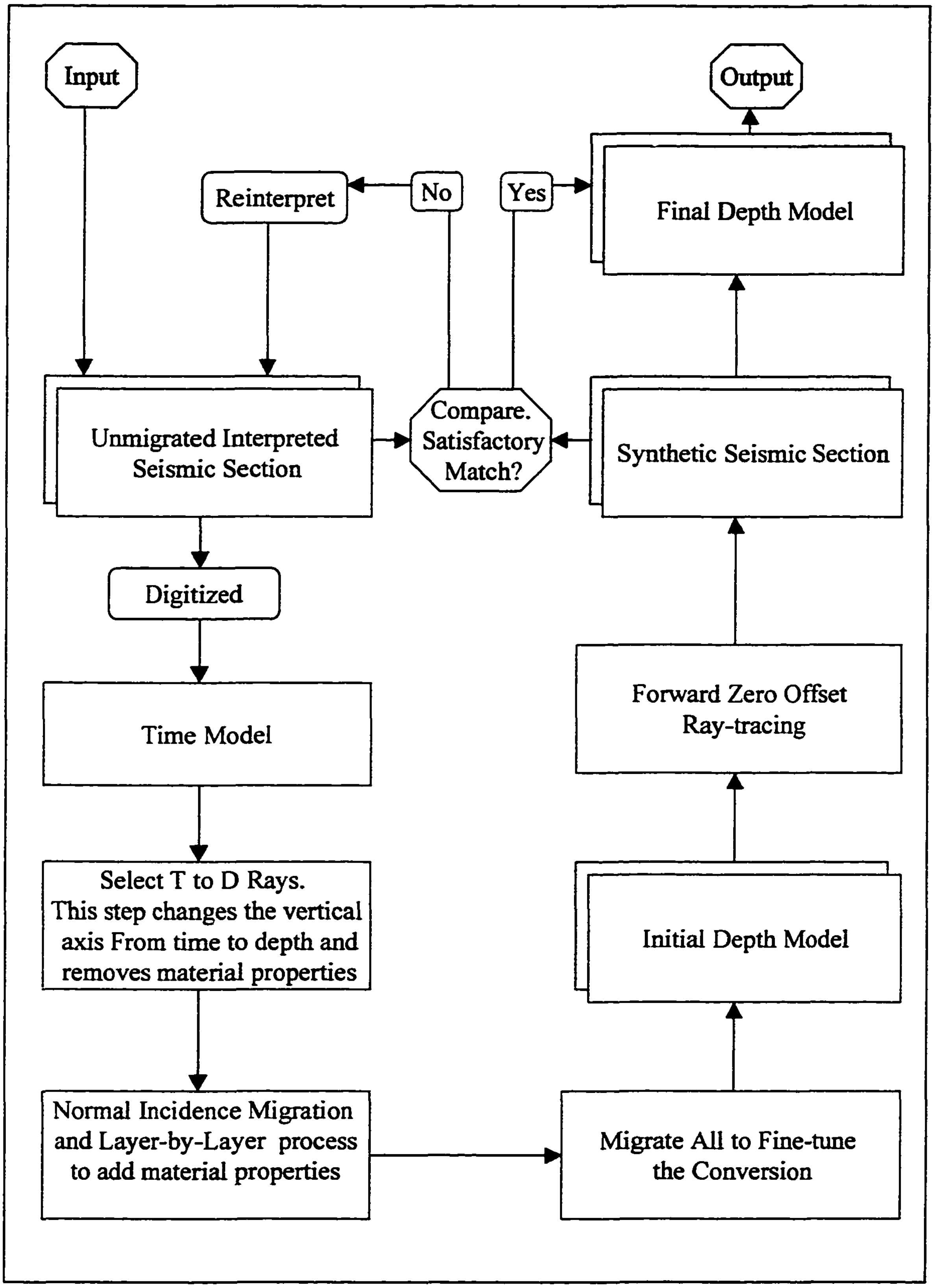

Figure 3.7. Flowchart showing how inversion and forward modeling approaches were combined to construct an acceptable depth model. The normal incidence rays method was used to convert the unmigrated stacked sections to depth during inversion process.

significant raypath bending and sharp refractions at the sea floor, which induced distortions and disruptions on reflections below. These distortions are (a). Variation in arrival times (false time pull-ups and sags). (b). Drastic reduction of the amplitudes of reflections from below a variable seafloor. (c). Linear and hyperbolic coherent noise due to in-line and out-of-section scattering of reflections off the sides of sea floor irregularities, (valleys and ridges). These distortions create uncertainty in structural interpretation, lead to inaccurate mapping of subsalt structures, and to making poor definitions of seismic sequences.

Because seismic imaging algorithms conventionally assume data are recorded on a planar datum, the migration of seismic profiles from this area without an adequate datuming method applied, can be severely affected by the distortions associated with topographic variations of the water-bottom. The conventional static correction is adequate in areas with mild topography where the near surface raypaths are close to vertical (Bevc, 1997). However, in area with significant sea floor variations, such as the offshore northern Red Sea, assumptions of a vertical raypath are not valid. In addition, the time changes from a rapidly varying water depth introduce changes in arrival times that are not static, but dynamic, since they differ for different events of a single seismic trace (Dent, 1983). Therefore, applying the conventional static correction under such conditions can substantially distort the data and compromise the migration results. However, a post stack, non-static shift wave equation datuming (Berryhill, 1997, 1986) can account for ray bending associated with irregular topography, in a manner consistent with wavefield propagation, and moreover, can provide an effective method of extrapolating distorted wavefields to a planar datum.

Basic Concept of Wave Equation Datuming

The concept of post-stack wave-equation datuming process was first proposed by Berryhill (1979). This technique involves two passes. In the first pass the seismic data are extrapolated downward from the surface to the water bottom using both water and substratum velocities. In the second pass, the seismic data are extrapolated upward to the surface replacing the water velocity with substratum velocity. Post stack wave equation datuming technique can be performed by any extrapolation method, such as finite difference, phase shift, or Kirchhoff summation (Yilmaz, 1991). The wave equation datuming performed in this investigation uses explicit finite different (FD) extrapolation which is available on the Promax processing software.

Parameters

The parameters utilized in wave –equation datuming are:

1. CMP spacing (ft or m)
2. Maximum frequency (in Hz). Frequencies higher than this value will not be datumized
3. Depth step size for datuming. These are depth increments for downward and upward continuation of the seismic data.
4. Elevation: An elevation (ft or m) of the flat datum to which the seismic data will be downward or upward continued.
5. Maximum dip:
6. Interval velocities

Advantages

For wave-equation datuming, the wavefield must propagate only a short distance rather than through the entire subsurface data volume. Therefore, one only requires an accurate representation of water-bottom profile (migrated and scaled to depth) and a proper replacement velocity. The propagation does not require the knowledge of the geology or velocities at depth greater than the sea floor.

Test of wave equation datuming technique:

In order to evaluate wave equation datuming as an effective solution for the Red Sea, the technique is first tested on synthetic seismic sections before applying it to the real seismic data. The three experiments discussed below are conducted using GXII modeling program and Promax processing software.

Experiment 1: The effect of varying water-bottom on imaging of underlying reflections:

This experiment is designed to demonstrate how seismic reflections could be severely distorted by overlying variable seafloor. Consider the simple depth model illustrated in Figure 3.8a. The model has four layers with constant velocities. It consists of variable water-bottom topography underlain by a shallow flat horizon and deep dipping planar one. Figure 3.8b shows the zero offset rays traced through the model. The raypaths from the underlying planar horizons undergo considerable bending across the water bottom. The bending is more significant at the irregular parts of the water bottom. Note that the raypaths within the water layer are not vertical but exhibit a wide range of dip angles. The normal incidence seismic response of the model reveals false bowties and time sags in the two horizons below irregular water bottom (Fig. 3.9b). In effect, the two horizons represent a mirror image of the water bottom. The disruptions and distortions of the underlying planar reflectors are caused by raypaths bending associated with the velocity contrast across the varying water bottom.

To further demonstrate this point, consider the raypaths to the two planar

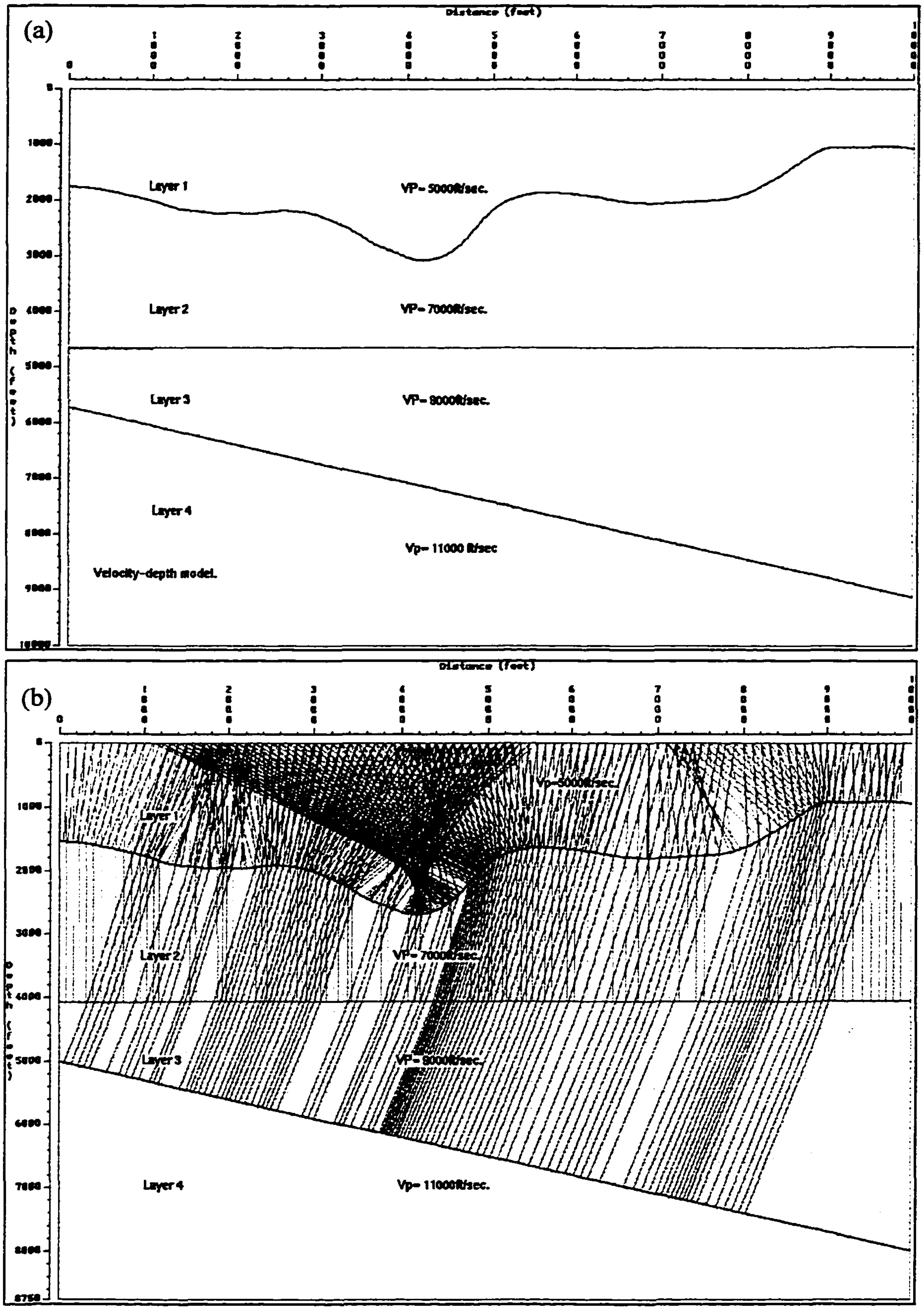

Figure 3.8. Velocity-depth model (a) and zero offset raypaths (b).

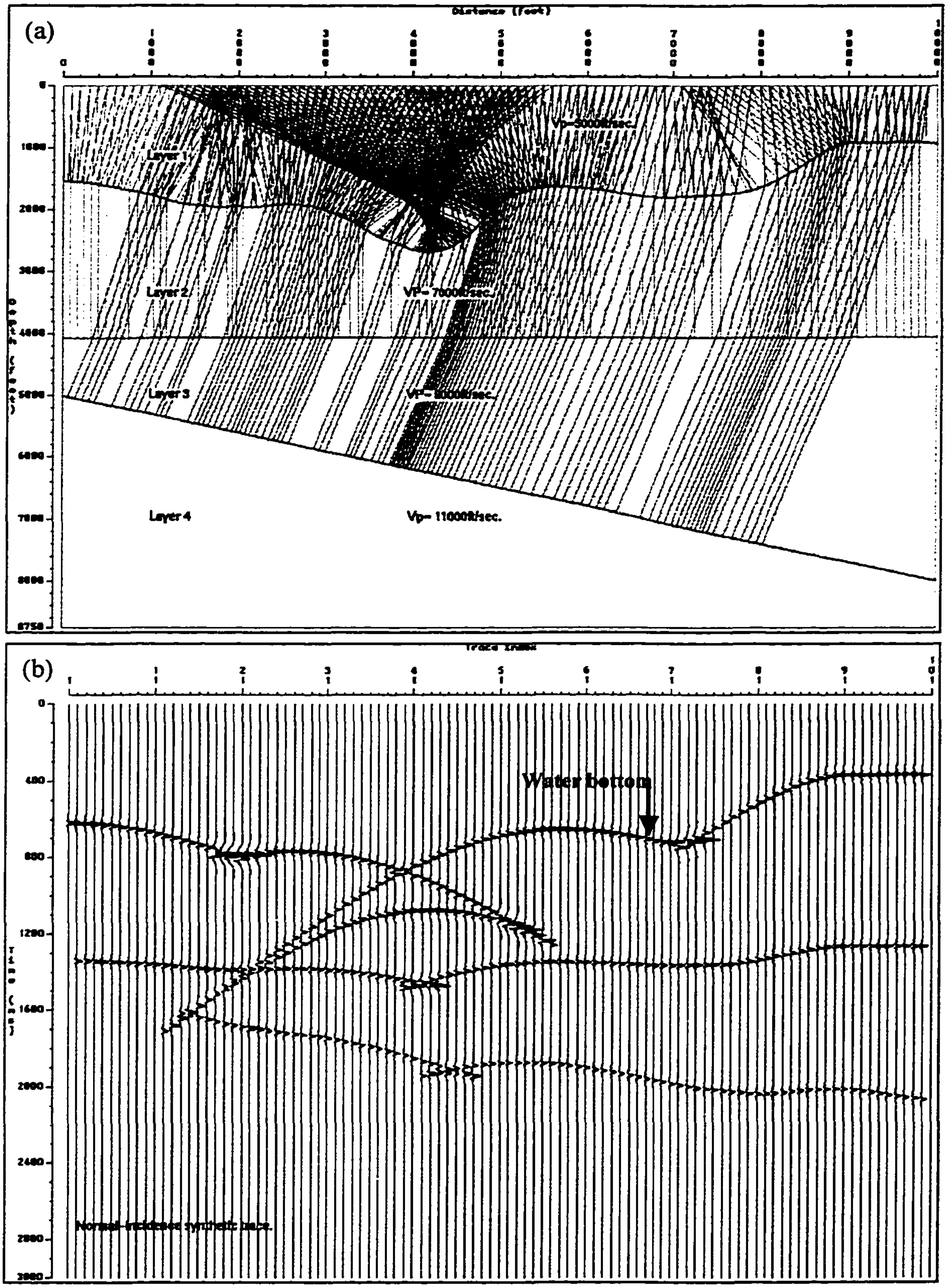

Figure 3.9. Zero offset raypaths (a) and normal incidence synthetic section (b). The synthetic section (b) was used as an input to post stack wave equation datuming as well as to time migration before stack.

reflectors below the water bottom and the corresponding seismic response (Fig. 3.10). Owing to the velocity contrast, raypaths from the underlying horizons undergo significant bending across the water bottom (a). The time distortions associated with ray bending are quite obvious on the synthetic section (b). Now observe Figure 3.11, which illustrates the ray diagram (a) and the seismic seismic response (b) when the water layer velocity is replaced with substratum velocity. Because there is no velocity contrast, hence no ray bending across the water bottom, the two planar reflectors are not distorted

Experiment 2: How effectively can wave equation datuming technique remove the distortions associated with variable water bottom?

The input to this experiment is the synthetic section of Figure 3.9b. This experiment consists of two passes: datuming up and datuming down.

Datuming down

In the first pass, the zero offset synthetic section (Fig. 3.9b) is downward continued from the surface to a flat datum just below the lowest point of the water bottom. Both water velocity (5000 ft/sec) and the substratum (sediment between the water bottom and flat datum) velocity (7000 ft/sec) are used in the extrapolation. Figure 3.12a illustrates the result of the first pass. Note that when datuming down, the data (sample values) that are pushed upward into negative times are wrapped around to the bottom of the trace. After the second pass, these data will unwarp from the bottom of the trace and are placed back to their original time at the top of the trace.

Datuming up

In the second pass, the synthetic section is extrapolated upward back to the surface replacing the water velocity with the substratum velocity. This step removes the

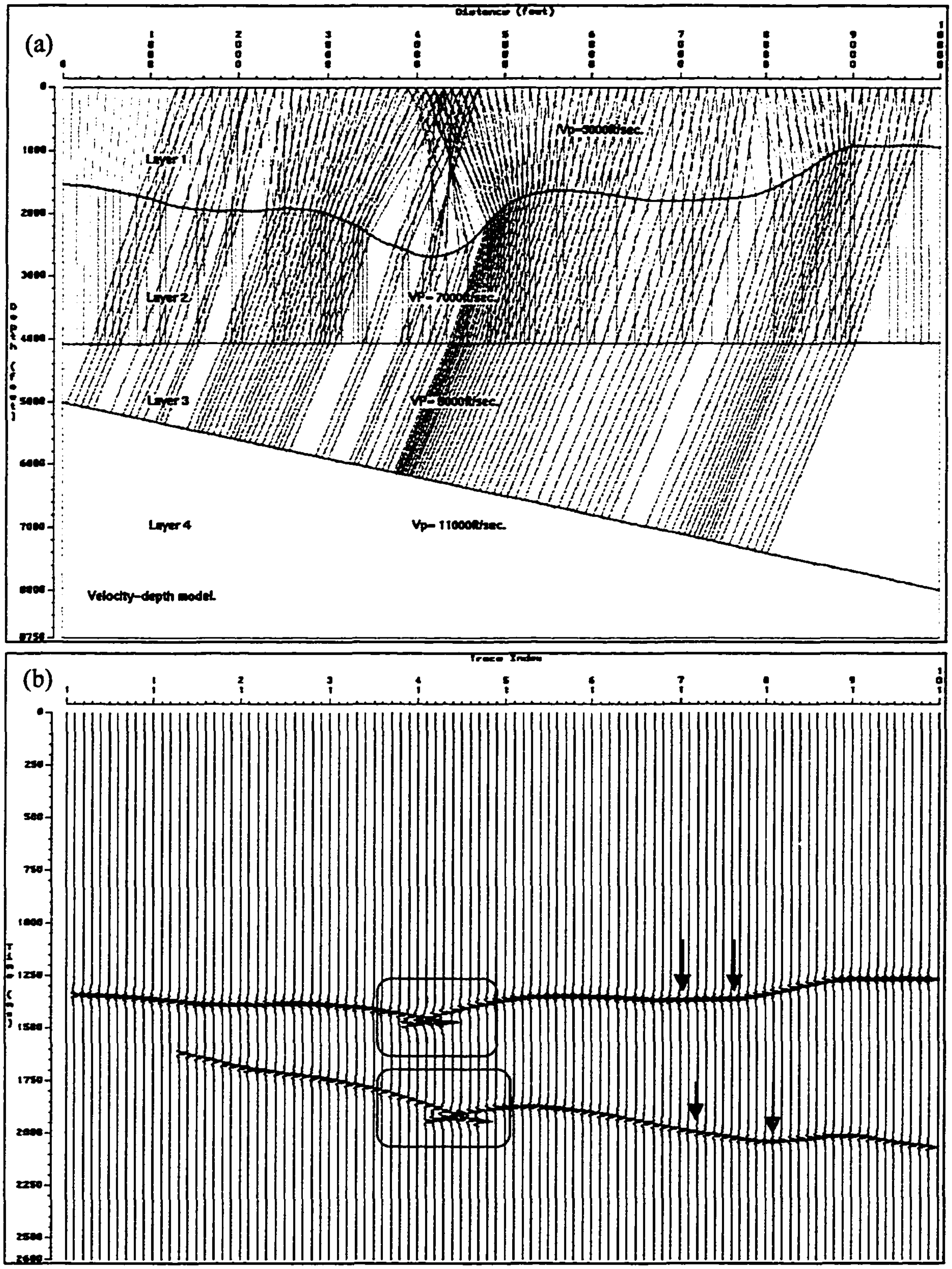

Figure 3.10. Zero offset raypaths (a) and synthetic section (b) of the two planar horizons with velocity contrast across the water bottom. Note how the raypaths from the horizons undergo significant bending at the water bottom (a) and the resulting time distortions on the synthetic section (b).

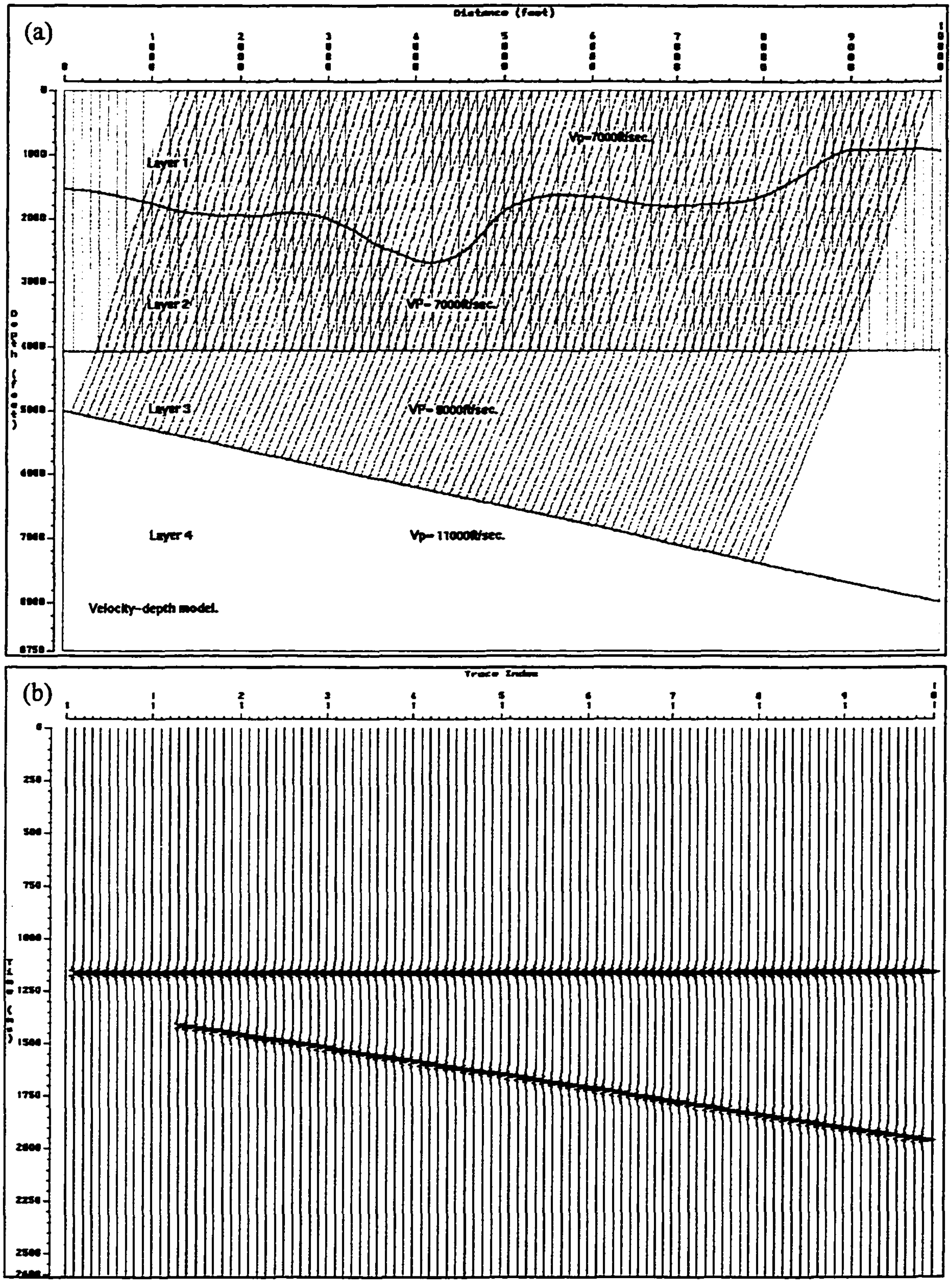

Figure 3.11. Zero offset raypaths (a) and synthetic section (b) for the two planar horizons with no velocity contrast across the water bottom. Because the raypaths from the horizons do not bend at the water bottom, the reflectors are not distorted (b).

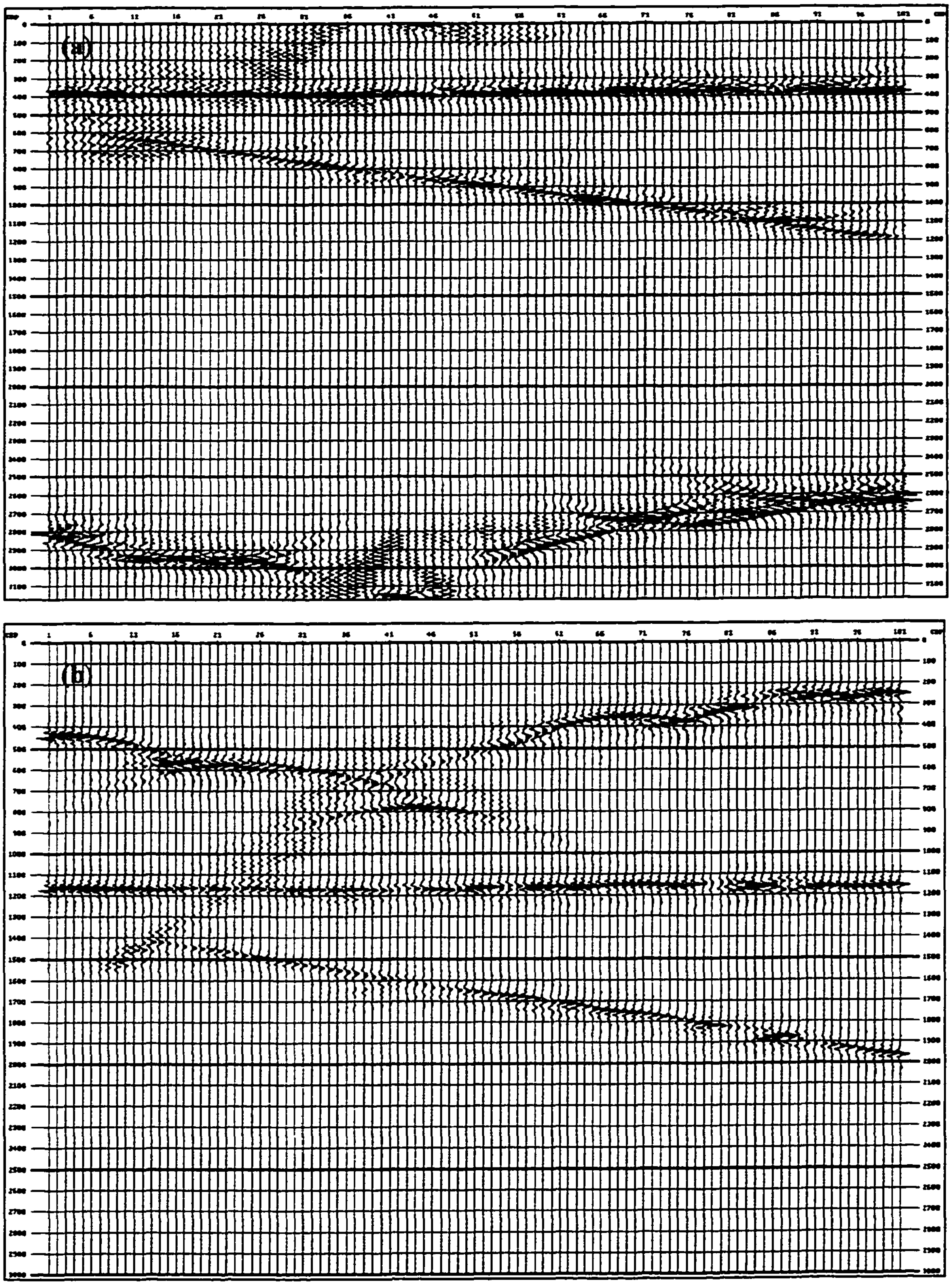

Figure 3.12. (a) Zero offset synthetic section after extrapolating the seismic data from the surface to a flat datum just below the lowest point of the water bottom (First pass). (b) After extrapolating the data from the flat datum back to the surface (Second pass).

velocity contrast across the water bottom, hence eliminates the ray bending problems. The result of the second pass (Fig. 3.12b) demonstrates that the degrading effect of variable water bottom on underlying planar reflectors has been removed and the reflectors are now properly positioned. Figure 3.13 compares the synthetic section before and after post stack wave equation datuming. The reflectors beneath the varying water bottom clearly exhibit good lateral continuity after wave equation datuming.

Experiment 3: Time migration before and after wave equation datuming.

This experiment is conducted to reveal the improvement of the results of time migrations performed after wave equation datuming. Using Promax processing software, three principal time migration algorithms are performed: FK, Kirchhoff, and steep dip explicit FD time migrations. The input to these migrations are the synthetic seismic sections before (Fig. 3.9b) and after (Fig. 3.12b) wave equation datuming. Figures 3.14, 3.15, and 3.16 display the results of F-K, Kirchhoff, and steep dip finite difference time migrations before (Figs. 3.14a, 3.15a, and 3.16a) and after (Figs. 3.14b, 3.15b, and 3.16b) post stack wave equation datuming, respectively. When performed before wave equation datuming, these three time migration methods produce severely distorted images. Where as when these methods are applied after wave equation datuming, the migration algorithms more accurately approach the true structural image.

Results:

The results from post-stack wave equation datuming are unmigrated time sections with deleterious effects of irregular water-bottom on the underlying reflections removed. The topographic variations of the water-bottom remain the same but it no longer causes time distortions. Hence, the ray bending problems have been effectively removed. The

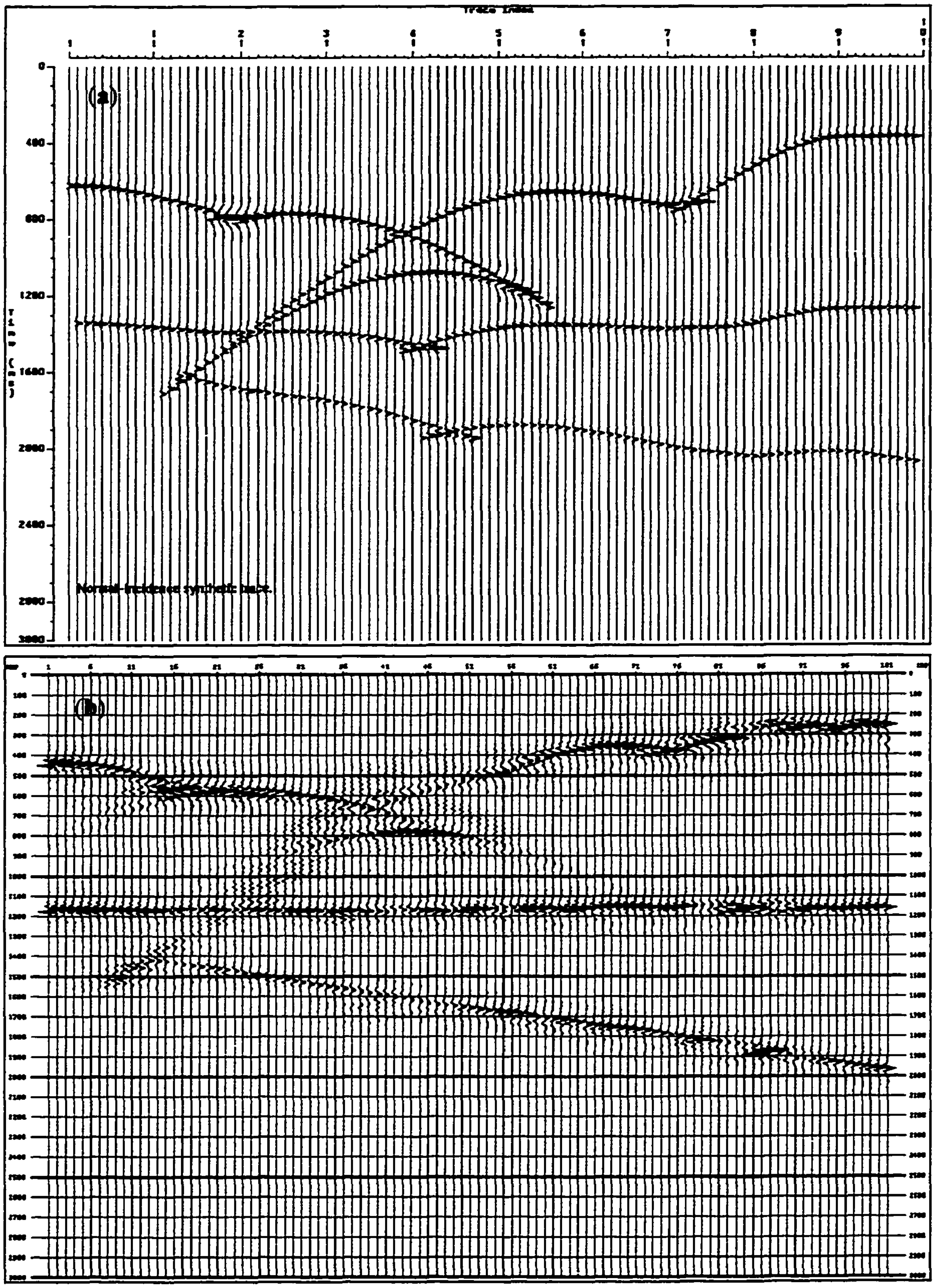

Figure 3.13. Normal incidence synthetic trace. Before (a) and after (b) post-stack wave equation datuming.

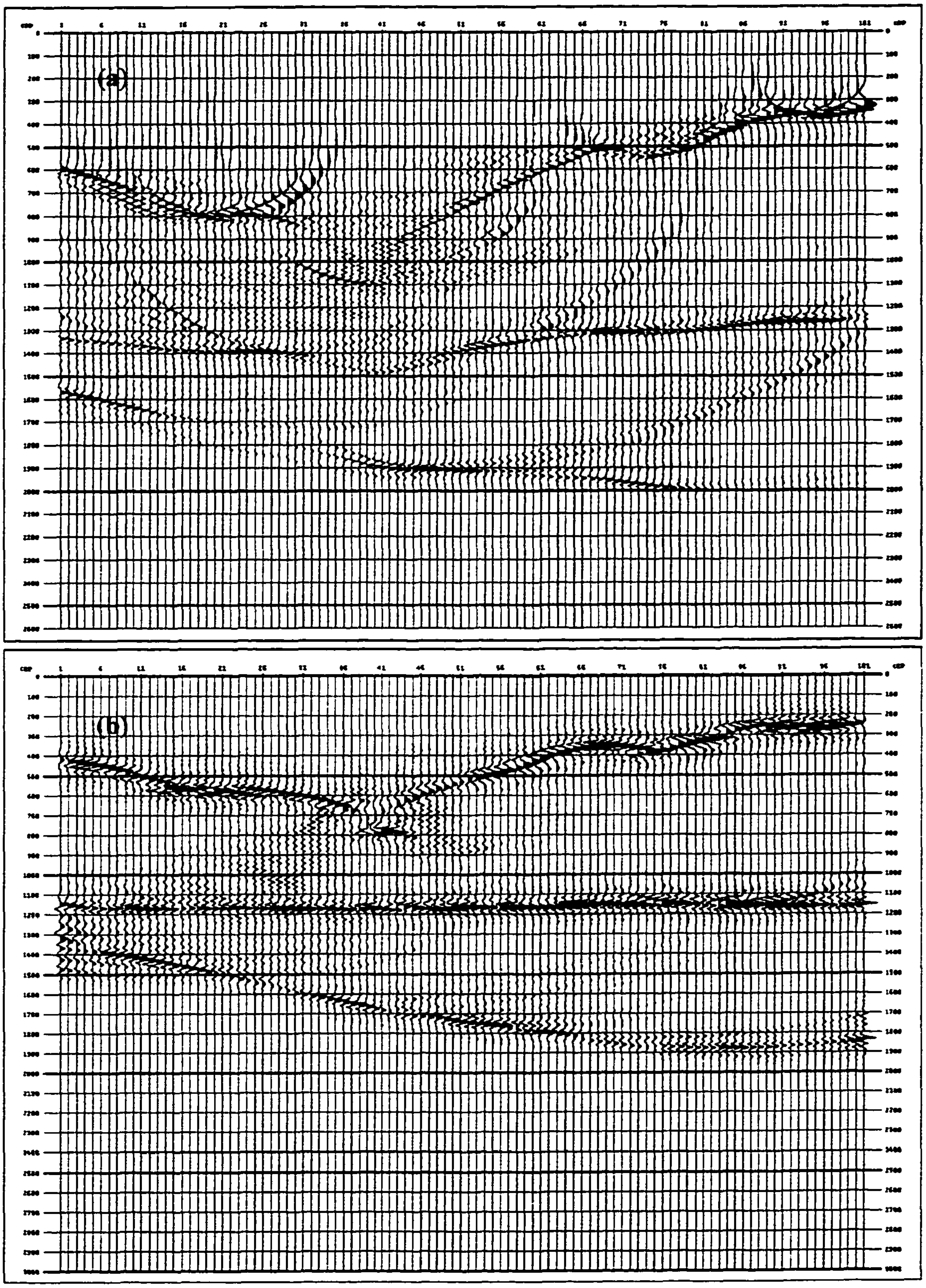

Figure 3.14. Stolt F-K time migration. Before (a) and after (b) post-stack wave equation datuming.

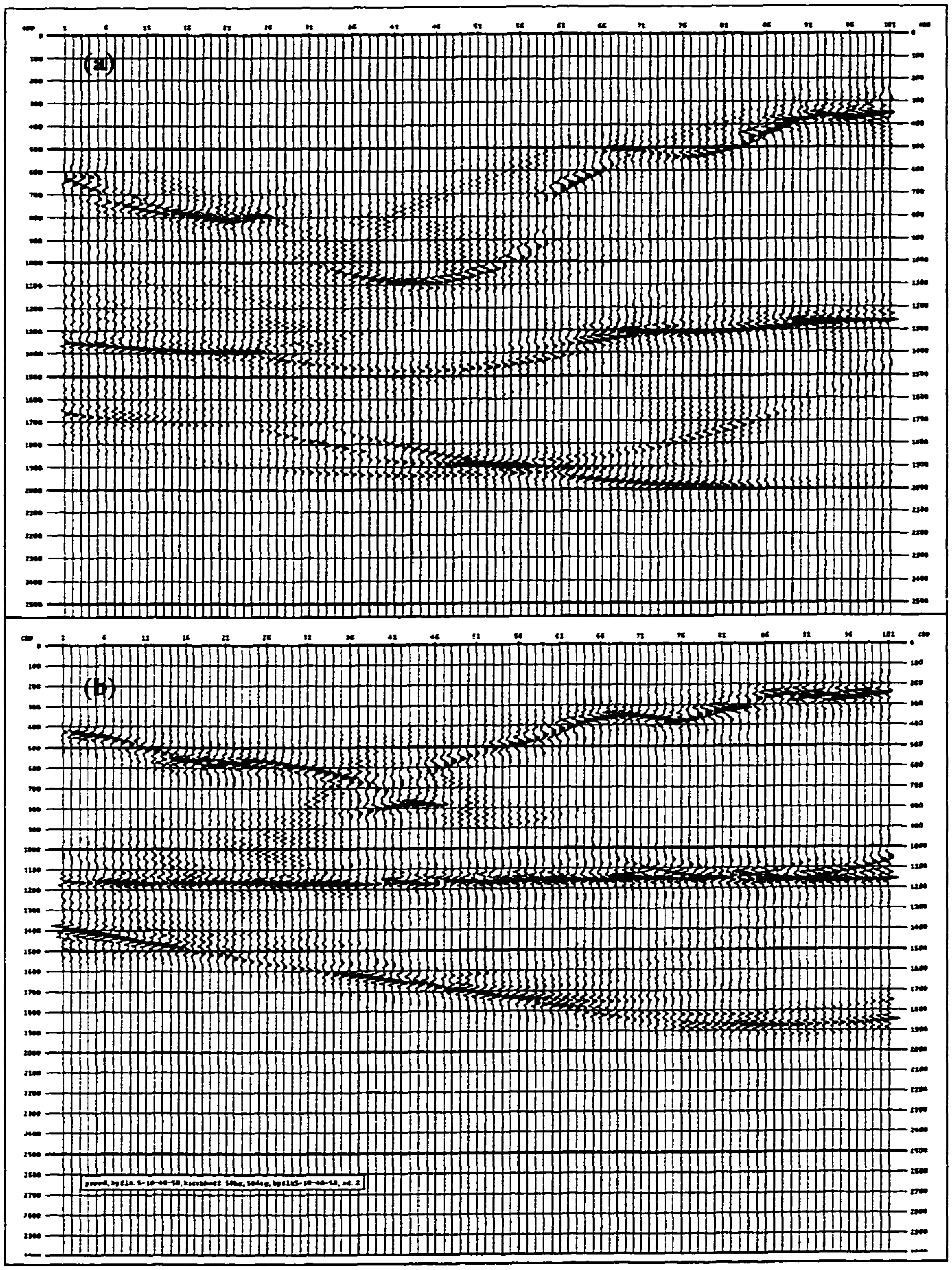

Figure 3.15. Kirchhoff time migration. Before (a) and after (b) post-stack wave equation datuming.

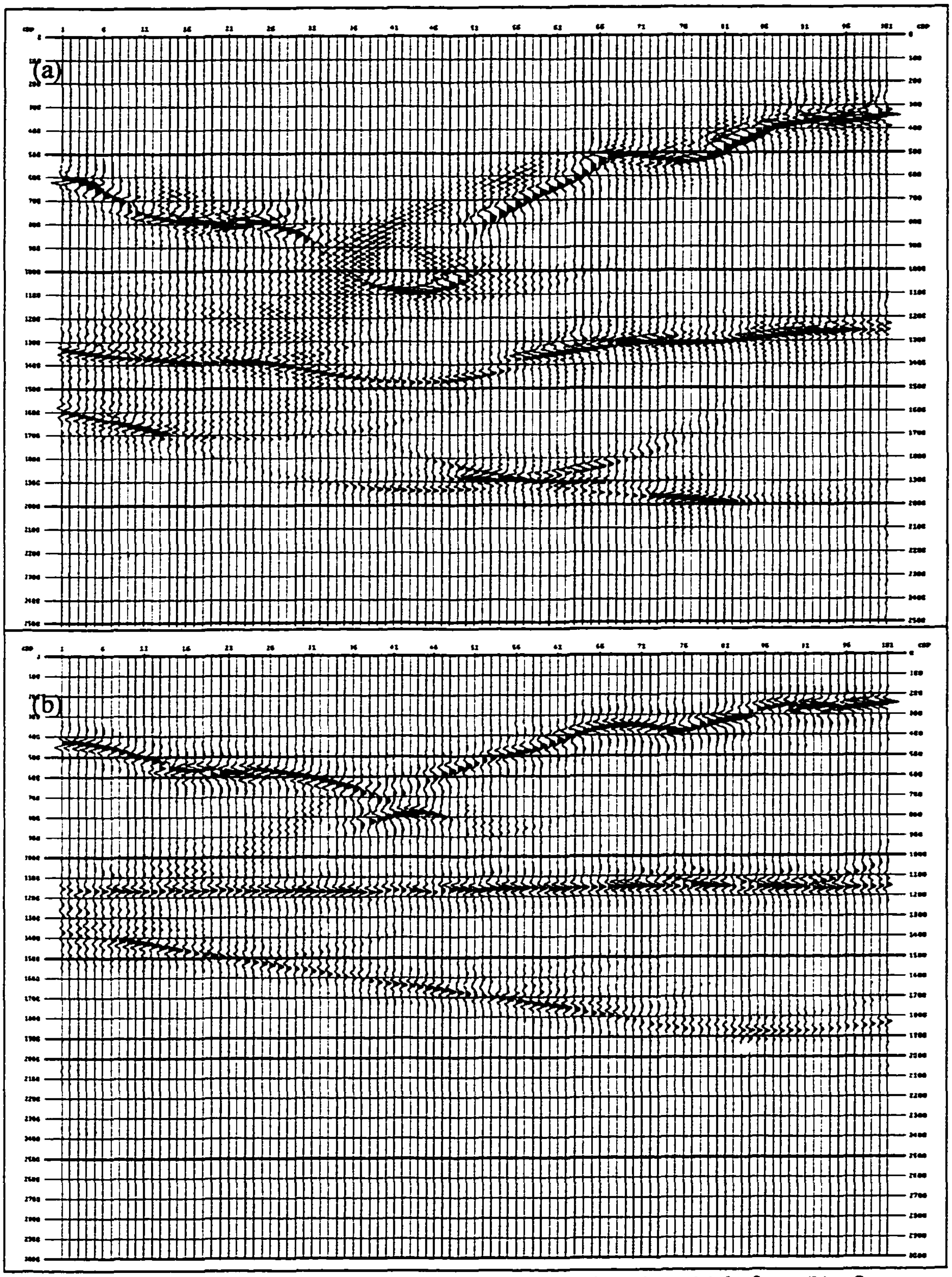

Figure 3.16. Steep dip explicit finite difference time migration, (a) before, (b) after post-stack wave equation datuming.

improvement in reflector continuity below variable water depth is the result of higher amplitude and increased coherence after wave equation datuming. The post-stack datuming followed by time migration produces results that are nearly identical to more costly full post-stack FD depth migration.

III.3.2. **F-X deconvolution**:

The F-X deconvolution (Canales, 1984) is used to reduce the random noise and spurious events from the unmigrated stacked seismic sections. This technique improves the continuity of reflection events without distorting the wavefield or causing lateral smearing.

The Procedure:

The stacked section is divided into small windows of constant linear dip. Each trace of an input stacked section is then transformed from the time and distance domain (t-x) to the frequency and distance domain (f-x). Each horizontal time slice is transformed to a complex frequency slice. Any sample in the transformed data has both an imaginary and real components. Events that have similar dips appear as a sinusoidal complex signal along given frequency slice. Thus, these events can be described in the form (cos wt + i sin wt). Thus, the signal is predictable in a Fourier sense. A complex, Weiner unit prediction filter is used to predict the signal one trace ahead, across the frequency slice. The difference between the actual waveform and the predicted one is considered noise and therefore removed. Inverse Fourier results in transferring the frequency information back in to time domain and provides output traces with less random noise.

Important parameters

The important parameters that must be selected for F-X deconvolution are:

1. Type of filter: One must specify the prediction filter to use (e.g., complex Wiener)
2. Horizontal window length: This parameter specifies the number of traces in the horizontal (F-X prediction window).
3. Number of filter samples: specifies the number of samples in the complex prediction filter. Recommended minimum value is 4 samples. A larger number must be used if there are no conflicting dips in the section. However, the choice must be smaller than the horizontal window length.
4. Time window length: This parameter controls the time gate length (in ms) of the prediction filter windows. If the input data have event curvature and conflicting dips, this parameter must be small (300ms smallest). If both the event curvature is negligible and the event dips have the same slope, the time window length can be the full length of the section.
5. Time window overlap: The window extension to be added to both the top and bottom of each time window, for vertical blending.
6. (f) F-X filter start frequency: This initiating frequency is the minimum frequency in the seismic data. Frequencies below the start frequency will be attenuated.
7. (k) F-X filter frequency. This filter frequency must be the maximum frequency observed in the data. Frequencies higher than this will be attenuated.

III.4. **Post stack time migrations:**

Post stack migration algorithms assume the data have been accurately processed to the final stack, and all that remains is the datum correction and migration.

IV.4.1. Basic principles:

Zero-offset section:

Using the simple basic concept of the exploding reflector model, (Lowental et al., 1976)), one can think of the subsurface reflectors as being the sources of their own energies (Fig. 3.17b). That is, each reflecting interface is regarded to consist of continuous distribution of sources. All the sources are assumed to explode at the same time (t=0) and emit up-going waves that propagate to the surface (z=0) where they are received as a seismic section. Thus, given the initial source distribution along the subsurface structure one can compute the wavefield as it appears on the surface. This computational process is termed wavefield construction (Robertson, E. A., 1983).

Now recall that the normal moveout (NMO) correction which is applied to CMP records prior to stacking converts the records to the forms they would have had at coincident source-receiver (zero offset). Therefore, CMP stacking process produces a seismic section that is conceptually equivalent to a zero offset section (Fig. 3.17a), which involves the two-way travetime. So, we can divide the stacked section time scale by two and regard it as being generated by an exploding reflector model. That is, the stack section is equivalent to recordings from hypothetical sources distributed along reflecting interfaces.

Migration after stack:

Post-stack migration is an inverse process. It depropagates the wavefield recorded at the surface backward in time to their positions on the subsurface reflectors. The value of the depropagated wavefield computed at zero time represents the distributed sources which rest on the reflecting interface and thus reveals the subsurface structure. This

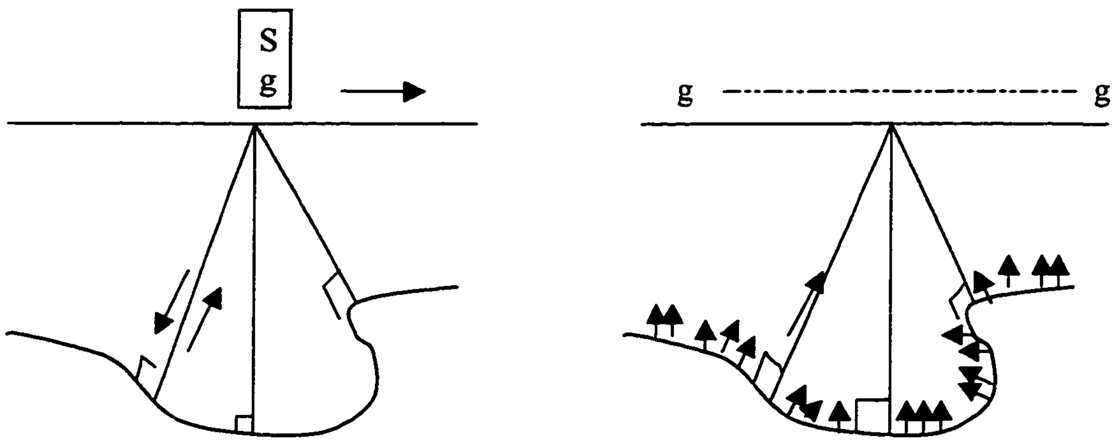

(a) Zero-offset section.

(b) Exploding reflector.

Figure 3.17. (a) Sketch showing how Zero-offset section can be obtained by coincident source-receiver geometry. (b) The mathematical model that approximates the zero-offset section is referred to as exploding reflector model (Claerbout, 1985).

depropagation of surface recorded section to zero time can be considered as a progressive lowering of the receivers into the subsurface. This process is referred to as downward extrapolation.

On a zero-offset stacked section, reflections from a subsurface reflector are plotted vertically beneath the source-receiver points. Hence, flat horizontal plane reflectors appearing on the stacked section are in their true subsurface positions and the seismic section represents the true image of the subsurface structure. However, the problem is that for dipping interfaces, the reflected raypath (at zero offset) is plotted vertically below the source-receiver points, whereas in reality, the raypath is normal to the dipping reflectors. Thus, in areas with steep slopes, dipping reflectors appear on stacked seismic sections considerably removed from their true subsurface positions. The stacked section, in this case, represents a distorted image of the subsurface structures.

Migration Principles:

Post stack migration is a process, which removes the distortions by depropagating the seismic wave backward to the sources distributed on subsurface reflectors. Migration repositions dipping reflectors, both spatially and in time, at their true subsurface locations and collapses (focuses) diffracted energy. The dipping events move up dip, steepen, and become shorter after migration. The greater the dip, the greater the distance the events move during migration. The goal of migration, therefore, is to construct a geologic cross section that represents the true subsurface structure along a stack seismic line.

Basic Assumptions:

There are three fundamental assumptions to performing an accurate post-stack migration:

1. The CMP stack is equivalent to a zero offset section (coincident source-receiver).
2. The stack section does not contain energy from outside the plane of recording.
3. Only primary reflections exist. If multiples do exist, they will be migrated with the primaries.
4. A high signal to noise (S/N) ratio must exist.

The Wave Equation:

Introduction:

The wave equation is a partial differential equation that is solved with mathematical principles (Bancroft B. C., 1997). Differential equation relates distance, velocity, and acceleration and other things such as time, or the rate of change of temperature. Note: Velocity is the rate of change of distance and is defined as dx/dt, where dx is a small portion of distance x and dt is a small portion of time t. Now recall that acceleration is the rate of change of velocity. That is: v= dv/dt, where dv means a small change in velocity v, and dt is a small change in time t. Therefore, one may write:

$$\text{Acceleration} = dv/dt = (d/dt)(dx/dt) = (d^2x/dt^2) \tag{III.3}$$

Wave propagation can be described as a solution of the wave equation. There are many forms of the wave equation and several assumptions are required to derive these forms. The principal assumption is that the medium is acoustic and that only p-waves exist. These equations describe the wave motion by relating the time and spatial dependence of a disturbance, which can propagate as a wave. For example, a wavefield P (x, t) produces the disturbance P as a function of position x and time t. At any point the disturbance has a slope in the t direction and x direction, as computed by the first partial derivatives. The rate of change of this slope is measured by the second partial derivative.

derivative.The wave equation states that the rate of change of the slope in t direction is proportional to the rate of change of the slope in x direction. The one-way (up-going energy only) wave equation is: $\partial^2 P/\partial t^2 = (1/v^2)(\partial^2 P/\partial x^2)$. (III.4)

This is a second order partial differential equation. When two dimensions spatial coordinates (x, z) are considered, the two-dimensional wave equation becomes:

$$\partial^2 P/\partial t^2 = v^2 (\partial^2 P/\partial x^2 + \partial^2 P/\partial z^2). \quad \text{(III.5)}$$

Where P is the wavefield and is a function of x, y, z, and t. t is time, and x, y, and z are distance and v is velocity. This equation describes propagation of compressional wave field P (x, z, t) in a medium with constant density and compressional wave velocity v (x, z). P (x, 0,t) represents normal incidence wavefield recorded at the surface (Yilmaz, 1991). By solving the wave equation, we can downward extrapolate the wavefield P (x, 0,t) and predict a normal incidence reflection field at any recording plane in subsurface P(x, z, t). At any value of z, a migrated sample occurs at t=0, this because there is no migration at the outcrop of reflectors. So if we downward extrapolate the surface wavefield P (x, 0,t) then collecting it at t=0 (invoking imaging principles) we conveniently obtain P (x, z, 0) which represents the migrated section (or subsurface structure).

III.4.2. Migration methods:

The three major migration methods (Fig. 3.18) are Kirchhoff Summation, Downward continuation (e.g., Finite difference), and Frequency-wavenumber (F-K) migrations. Kirchhoff migration (Schneider, 1978) is accomplished by an integral solution (by integration along diffraction curves) of the scalar wave equation whereas Finite difference (Claerbout and Doherty, 1972) is based on the differential solution to this equation. F-K migration, on the other hand, (Stolt, 1978) is performed by a solution in the

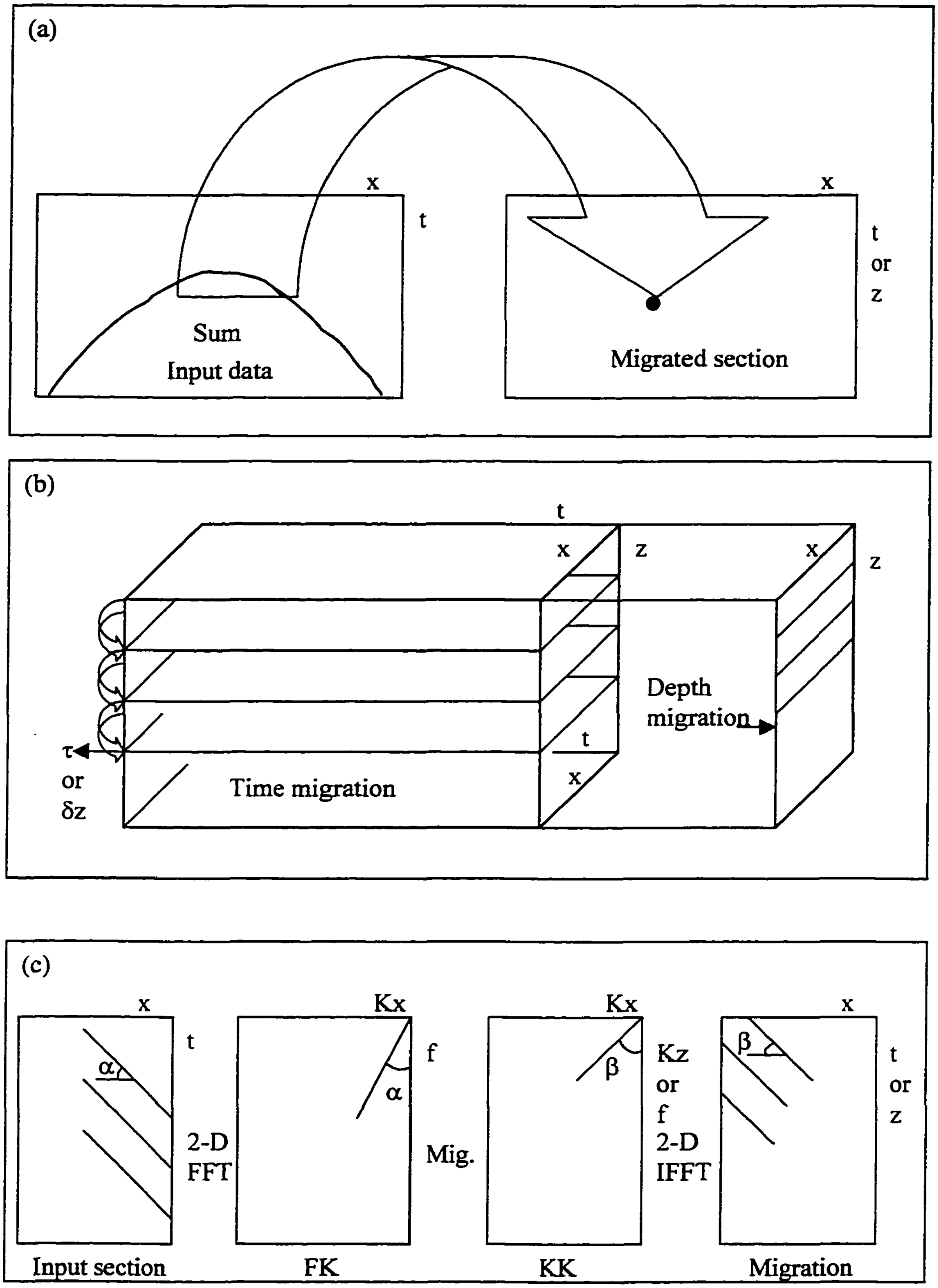

Figure 3.18. Sketches of the three principal post-stack migration methods (a) Kirchhoff, (b) Downward continuation, and (c) FK. Modified from Bancroft J. C., 1997.

frequency-wavenumber domain. Each technique has its own advantage, however, no current time migration method can handle all the problems of steep dip, noise, and rapidly changing velocities. In fact, these migration methods vary in performance relative to these problems. For example, Finite difference migration can handle dips up to 35 degrees and with mild to moderate lateral velocity variations. By comparison, the Kirchhoff algorithm is restricted to best handling lateral velocity changes but can handle higher dips. The frequency-domain methods are limited in handling velocity variations, but have no dip limitation.

III.4.2.1. Kirchhoff Migration:

Kirchhoff migration is the oldest, but still one of the most robust and heavily utilized algorithms. It is powerful owing to its ability to vary from a simple algorithm, such as diffraction summation, to a more complex one. In principle, this method is based on the summation of amplitudes along a diffraction hyperbola. That is, it defines the diffraction curve, weighs and sums the amplitudes value along that curve, and inserts the summed value at the migrated position. This process is repeated for each migrated sample (Fig. 3.19). The diffraction shape is defined by the hyperbolic traveltime equation:

$$t^2_{(x)} = t^2_{(o)} + (4x^2/v^2_{rms}). \quad \text{(III.6)}$$

Where t $(_o)$ is the one-way time at zero offset, x is the half offset, and v_{rms} is the RMS velocity at the apex of the hyperbola at time (t_0).

Important parameters for Kirchhoff migration:

1. <u>Aperture width</u> (i.e., the lateral extent of the diffraction hyperbola).

An excessively small aperture width causes suppression (dip filtering) of steeply dipping events (excludes steeper flanks of the diffraction hyperbola from the summation)

(a)

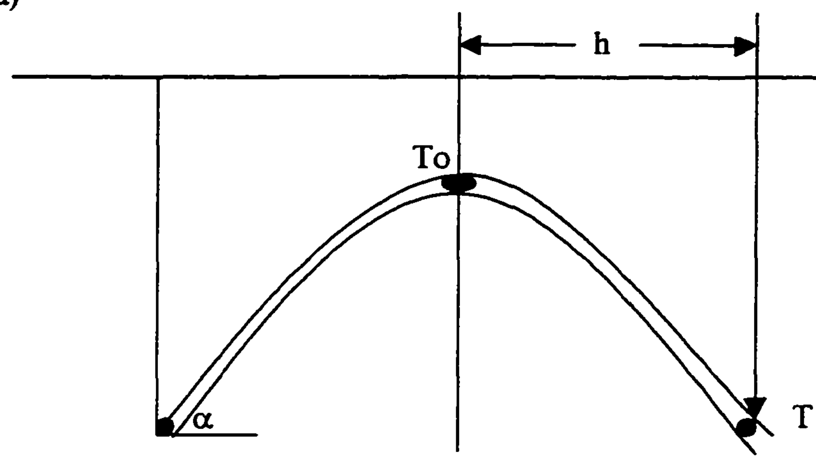

Where h is the half offset, To the one-way time at zero offset, T the travel time at each offset and α is the pre-migration dip.

Diffraction hyperbola for Kirchhoff migration.

(b)

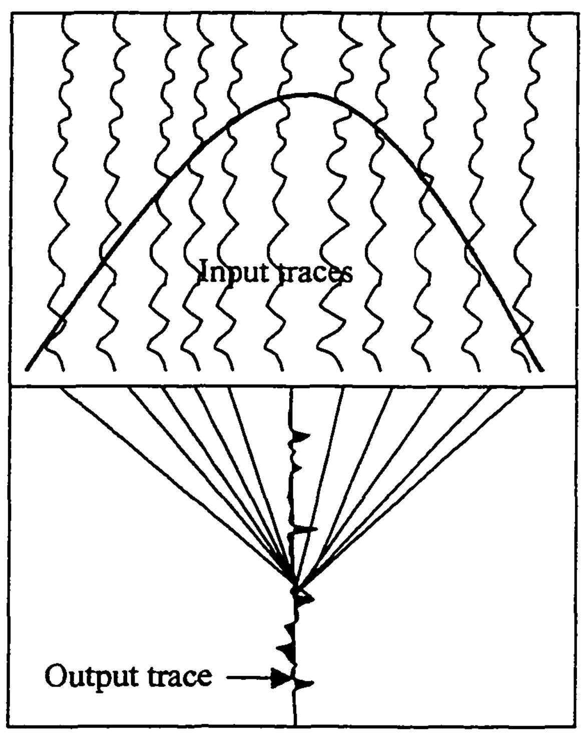

Figure 3.19. (a). Diffraction hyperbola for Kirchhoff migration. (b) Schematic diagram showing how each amplitude at (x, z) is obtained by summing the input amplitudes along the travel-time curve.

and rapidly varying amplitude changes. It also organizes random noise particularly in the deeper part of the section, as horizontally dominant spurious events. A large aperture degrades the migration quality in poor S/N ratio conditions (the noise in the deeper part of the section creep into the good data). It is recommended that the maximum dip, the regional velocity function and the noise condition of the data be used to compute the optimum aperture width.

2. Maximum dip to migrate (ms/trace).

Events with dips greater than this value are suppressed. The maximum dip must be chosen carefully so that the steep dips of interest in the input section are preserved. Limiting dip is a way to reduce the computational cost because the dip is related to aperture width, which determines the cost. The smaller the maximum allowable dip required the smaller aperture width. The combination of maximum dip and maximum aperture determine the effective aperture width.

3. Velocity function.

Diffractions and dipping events are undermigrated if incorrect low velocities are used for migration. Likewise, using incorrect high velocities causes overmigration.

III.4.2.2. Downward Continuation Migration:

The downward continuation is a powerful method that enables simple migration of data with complex velocity distribution. This migration method works on a volume of data and not on two planes of section as in the Kirchhoff and FK migrations. Downward continuation migration includes finite difference and phase shift.

III.4.2.2.a. Finite Difference Migration.

Finite difference (Claerbout and Doherty 1972) is based on the principle of downward continuation and uses differential solution to scalar wave equation.

Imaging Procedure:

1. Start with the wavefield at the surface (P (x, z=0,t) CMP stack section

2. Downward continue to z=dz to approximate the zero-offset data that would have been recorded at this depth.

3. Reflection energy moves updip in time because receivers are closer to the reflectors.

4. Any reflections at the receiver depth will arrive at zero time

5. Take energy at zero time and place it in the migrated section at the current depth.

Parameters that governed the F-D migration Performance:

1. Depth step size. 2. Velocity function. 3. maximum dip to migrate. 4. Wavelet period.

1. Depth step size:

Downward continuation of wave field recorded at the surface is performed at discrete depth point spacing called depth step size. Incorrect specification of this parameter causes migration artifacts. Large depth step size, at steep dips, can cause:

a. Undermigration

b. Dispersion of the waveform along reflectors.

c. Kinks along reflectors at discrete intervals.

These effects are more pronouced at increasing steeper dips. The dispersive noise, which accompanies undermigration, increases at large frequencies and wavenumbers. It can be reduced significantly by taking smaller trace spacing and sampling in time and depth (Claerbout, 1985). Kinks that accompany undermigration can be suppressed by:

a. Adjustment of migration velocities.

b. Using smaller depth step sizes.

Selection of appropriate depth size that minimizes undermigration and despersive noise depend on the interaction between temporal and spatial sampling intervals, velocity function, dips in the subsurface, and the frequency content of the data. Steep dips require small depth step size. Optimal depth step size should be between one-half and one-full dominant period of the seismic line to be migrated depending on the steepness of the dips.

2. Velocity function:

As in Kirchhoff and F-K migration method, using velocity values higher or lower than the medium velocity cause over-and undermigration steep events, respectively. However, using large velocity errors in Finite difference method cause less mispositioning of steep dips than Kirchhoff summation.

3. Maximum dip to migrate

This is the steepest dip (in time units per trace) we wish to preserve. Using too large value increases execution time. Too small value reverses the direction of some dips.

4. Wavelet period

This parameter value is the time measured (from trough to trough or from peak to peak) at the location where the maximum dip occurs.

III.4.2.3. FK Migration.

FK migration was first introduced by Stolt in 1978 and is considered by many to be the fastest and most economical algorithms. The original Stolt's algorithm is strictly valid only for constant velocity medium but can be modified to handle velocity changes.

<u>Basic concepts</u>:

The Fourier transform (FT) is a mathematical operation that converts data in one domain (e.g., time) to a different domain (e.g., frequency). Although the different domains contain the same data, they present it differently. For example, the FT takes a series of numbers and calculates another series of numbers that has a different arrangement of the same information (Bancroft B. C., 1997). Fourier transform converts time series of samples and distance series into a series that represent frequency (F) and wave numbers (K), respectively along with phase.

The FK migration method uses 2-D Fourier transform to convert an unmigrated seismic section in 2-D Fourier domain where it is conveniently migrated. The inverse of the Fourier transform provides the migrated section. The term FK denotes the Fourier transform of time to frequency (F) and the Fourier transform from distance to wave-number (k). The technique involves a direct mapping in 2-D Fourier transform domain from temporal frequency w to the vertical wave-number k_z while keeping the horizontal wavenumber k_x unchanged. The vertical wavenumber (K_z) can be expressed as:

$$K_z = 2w/v\ [1-(vk_y/2w)^2]^{½} \qquad \text{(III. 7)}$$

By rewriting equation (III.7) we get:

$$W = v/2(k_y^2+k_z^2)^{½} \qquad \text{(III. 8)}$$

Procedure:

1. Start with the stack time section P (x, z=0,t)

2. 2-D forward Fourier transform P (K_x, z=0,w)

3. Map the temporal frequency (w) and vertical wave-number (kz) via equation 6.

4. Apply the scaling factor using equation:

$$W =(v/2)\ k_z/(k_y^2+k_z^2)^{1/2} \qquad \text{(III.9)}$$

P (kx, kz, t=0)

5. 2-D inverse Fourier Transform

P (x, z, t=0)

6. Final migrated section

Stolt constant velocity migration yields acceptable result in presence of moderate dips or mild vertical velocity changes. However, in areas involving steep dips and significant vertical velocity changes required generalized Stolt migration.

Generalized Stolt Method:

Stolt modified his original constant-velocity algorithm to account for significant vertical velocity variations by applying a dynamic time shift to the vertical time axis of the input time stacked section (Stolt, 1978). The goal of a time stretch is to make the input stacked line appear as though it has a constant velocity so that the Stolk migration yields an accurate result (Yilmaz, 1991).

The migration results depend on dip, time, the W-factor and input velocity. No one value of the stretch factor is optimal for all dips, times, and vertically changing velocity field. Therefore, using single W-factor value in presence of significant vertical velocity changes and steep slopes result in undermigration at some depths and overmigration at other depths and, thereby compromise the migration result.

The modified Stolt method overcomes the restrictions on temporal velocity changes by applying cascading F-K migration. The input stacked section is migrated several times. The output from preceding stage is used as input for the next stage. The changes in velocity function for each migration stage is small, hence approximating the Stolt' constant velocity algorithm. Each single stage performs a portion of the total migration. After any stage, m, the data migrated with a cumulative interval velocity:

$$V^2_m(t)=\sum_{j=1} V^2{}_j(t) \qquad \text{(III.10)}$$

Where $v_m(t)$ is the migration interval velocity for the final cascade Vj is interval velocity for nth stage.

For each stage, the velocity is constant with depth till the final stage. The accuracy of the extended Stolt method depends on the value of the interval velocity for each stage. Also, the accuracy increases or decreases with increasing and decreasing the number of migration stages, respectively.

The Stolt stretch migration is sensitive to lateral changes in velocity. Thus, in cases involving lateral velocity variations, the velocities are smoothed over half the migration aperture (500 traces or more). W-factor ranges between 0.0 to 2.0. A value of 1(W=1) corresponds to Stolt constant-velocity method. The value is less or greater than 1.0 when the velocity increases or decrease with depth, respectively.

F-K migration parameters are: maximum dip, depth step size, and velocity Function

III.4.2.4. Finite difference depth migration:

The disadvantages of time migration schemes are their inability to image reflections with complex velocity distributions. For example, when conventional time migrations are performed in areas with strong lateral velocity variations the diffraction hyperbola is skewed with its apex shift laterally away from the diffraction source.

Finite difference depth migration is better suited to dealing with significant lateral velocity variations. The factor that is of particular significant in finite difference depth migration is small additional time-shift or "thin-lens term" (Claerbout, 1976, and Larner et al 1978) which is incorporated with diffraction term:

$$\partial Q/\partial z = (ivk^2_y)/(4w/Q) + i2w\,[1/v_{(z)} - 1/v_{(y,\,z)}]\,Q. \qquad \text{(III.11)}$$

Where $(ivk^2_y)/(4w/Q)$ is diffraction term and $i2w\,[1/v_{(z)} - 1/v_{(y,\,z)}]]\,Q$ represents thin-lens term. $V_{(y,z)}$ is a laterally varying velocity and $v_{(z)}$ is horizontal average of $v_{(y,z)}$. Therefore in case there is no lateral velocity change ($v_{(z)} = v_{(y,z)}$), thin-lens equal zero and only diffraction term remains: $\partial Q/\partial z = (ivk^2_y/4w)\, Q$ (III.12)

FD depth migration solves the two terms sequentially: The diffraction term is first applied on the upcoming wavefield (Q). Then, the thin-lens term is applied on each individual trace for each downward extrapolation step Δz. The time shift term applies small relative correction to the data in area with lateral velocity variations.

Procedure:

The stacked section, which represents the initial downward extrapolation step ($z=0$), will be downward extrapolated in small depth increment instead of traveltime increments used in time migration. The lateral velocity variation along a layer causes changes in transmission time, which is corrected by small laterally varying static time-shift applied to each trace. Downward extrapolate the surface recorded wavefield to depth Δz. the data down to Δz are fully migrated. The deeper part of the data represents a wavefield (a time section) recorded at depth Δz. the process is repeated until the volume is complete.

To demonstrate the main difference between finite difference time and depth migration, consider a layer that extends horizontally a distance y (Fig. 3.20). We assume the interval velocity ($V_{(y)}$) over the interval (Δz) changes with horizontal location y along the section (Judson et al, 1985). Two diffracting sources exist at the same depth ($=\Delta z$) but at different lateral positions with high and low interval velocities. Figure 3.20a illustrates the hyperbolic seismic response of the two diffracting points. Conventional time migrations will focus (collapse) the hyperbolas at their apices with time $2\Delta z/V_{(y)\,high}$ and $2\Delta z/V_{(y)low}$, and position the two diffracting sources at different depths (Fig. 3.20b). This

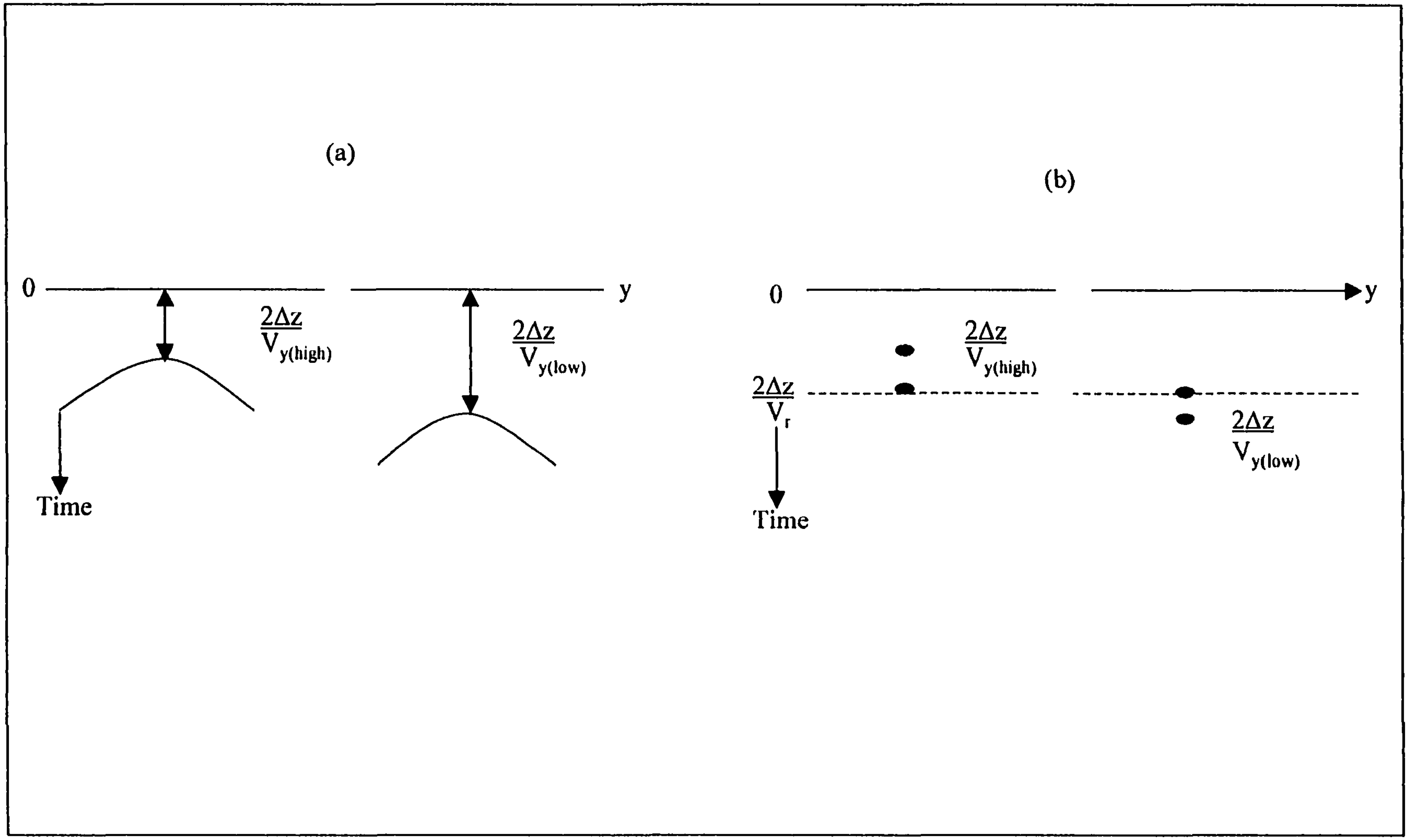

Figure 3.20. (a) Zero-offset seismic response to two diffracting points (●) at the same depth Δz. (b) Time migration of the two diffraction curves (●). Where Δz is depth, y is horizontal distance, V_y is laterally varying velocity, and V_r is laterally invariant velocity that may changes with depth. Modified from Judson et al, 1985.

error is due to changes in transmission time caused by the lateral velocity variations along the layer (Judson et al, 1985). Depth migration corrects the error and images the two points at the same depth by applying the small laterally varying time-shift to each trace. For example consider a stack section (zero offsets) recorded at the surface $z=0$. We wish to extrapolate the stack section downward to Δz, so that the section down to Δz is fully migrated. Finite difference depth migration relocates the two diffracting points during each downward extrapolation step by small lateral static time shift of: $2\Delta z\ [(1/V_r)-(1/V_y)]$ for each individual trace for output times greater than $2\Delta z/V_r$. Where V_r is a replacement velocity and may change with depth. The final output is a depth section converted to time section by the laterally invariant replacement velocity $V_r(z)$. The laterally varying static time-shifts will change the apparent dips of the deeper seismic events.

CHAPTER IV

IMAGE DISTORTIONS ASSOCIATED WITH RUGGED SEAFLOOR TOPOGRAPHY CASE HISTORY: SOUTHERN RAS BANAS AREA

The most obvious, major image problem observed on seismic lines from Southern Ras Banas area (Fig. 1.1) is attributed to highly variable water bottom topography. The rugged seafloor is caused by organic reef buildups, complex halokinetic features, and localized tectonics. The irregular water-bottom topography and the velocity contrast across the seafloor causes severe raypath distortion, which induced disruptions and degradation of reflections below. The variable water depth not only produces coherent noise (due to in-line and out-of-section scattering of reflections off the sides of sea floor irregularities), but also causes travetime errors, and reduces the amplitudes of the underlying reflections. These distortions create uncertainty in structural interpretation, lead to inaccurate mapping of salt and subsalt seismic events.

The dip lines 33, and 28.50 have been selected because they best reflect the imaging distortions caused by rugged sea topography. The locations of these lines are shown in Figure 1.2. The main objective here is to identify and reduce the deleterious effect of variable seafloor on the underlying reflections and improve the imaging of salt and subsalt structures. This objective is met by performing post stack wave equation datuming followed by time migration.

IV.1. Seismic Line 33:

Seismic line 33 is perpendicular to the shoreline. This dip line runs from west to east across the shelf, slope and passes into deep water (Fig. 4.1). It appears, at first glance,

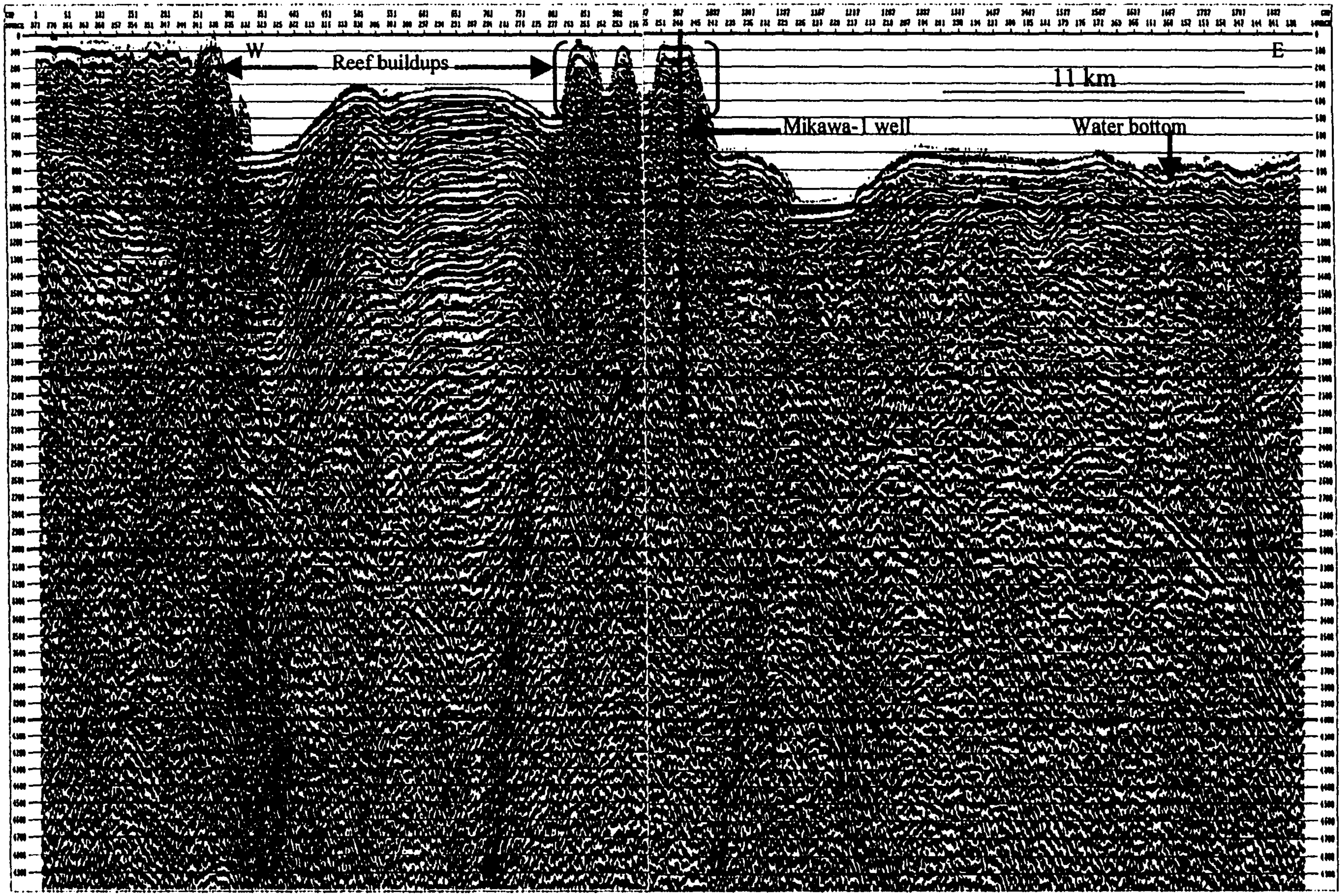

Figure 4.1. Seismic line 33 before signal enhancement and migration. Mikawa-1 well, located at shotpoint 248, bottomed at 3360 m in the basement.

that the most prominent features of seafloor topography are the three reef build-ups in the middle of the line and what appears to be a major depocentre just east of the basin margin. The water depth varies considerably, from about 180 feet in the shallower parts to 2675 feet in the deepest parts. The areas of seismic line 33 that are significantly affected by the damaging effects of varying seafloor are those underneath the interpreted reef buildups in the middle of the line and below shotpoints 373 to 310 to the west. Post stack wave equation datuming is performed on line 33 to reduce the deleterious effects of variable water bottom on underlying reflection events.

Well data:

Mikawa-1 well located at shotpoint 248 on line 33 and encountered the tops of salt, basesalt, and the basement at 860m, 1850, 3334m, respectively and bottomed in the basement at 3360m. The basement is unconformably overlain by the Lower Miocene syn-rift subsalt megasequence which comprises sedimentary succession that consists, from bottom to top, of Rudies (2430m to 3334m), Kareem (1985m to 2430m), and Belayim (1850-1985m) Formations. Belayim Formation is overlain by the Middle Miocene South Gharib Formation (860? –1850m). Data on the Middle to Upper Miocene Zeit Formation and the overlying Pliocene to Recent Wardan and Shagara Formation are not available, as these Formations were not recovered.

Lithological description

The basement rocks encountered in this well consist of generally fine grained, pink commonly weathered granitic igneous rocks. The lower unit of Rudies formation consists mostly of dolomite with interbeds of sandstone in the lower parts and modstone in the upper parts. The upper Rudies unit consists of mudstone with thin interbeds of limestone and sandstone. Kareem Formation comprise of locally sandy mudstone and siltstone with thin interbeds of sandstone and minor thin beds of limestone, dolomite, and anhydrite occur towards the top of the interval. Belayim Formation consists of silty and sandy mudstone interbedded with anhydritic sandstone and thin interbed of dolomite and anhydrite. South Gharib Formation consists mainly of halite with minor interbeds of anhydrite. The base of South Gharib is made of finely crystalline anhydrite with minor interbeds of dolomitic sandstone and minor mudstone. Data are not available on Zeit Formation and the overlying supra-salt megasequence at this location.

IV.1.1. Initial seismic interpretation.

Several basement-related major normal faults cut through and affect the deeper parts of the sedimentary section. Most of these faults do not cut through the overlying, shallow post-rift megasequence but terminate at the base of salt. Definition of these fault planes was accomplished by identifying offset reflectors in some parts of the section and by joining successive diffraction apexes in other parts.

Calibration of seismic line with the well data:

Following the initial definition and tracing of major faults, the synthetic seismogram generated from the sonic log of Mikawa-1 well, is then used to geologically constrain the interpretation. The synthetic seismogram is compared to line 33 at shotpoint 248 until sufficient tie is obtained (Figs. 4.2a, 4.2b). Three key horizons: Blue, green and red representing topsalt, basesalt, and top of basement, respectively, are then extrapolated to the western and eastern part of the line. However, the continuity of these horizons is disrupted and severely distorted in some parts of the line, such as underneath the reef build-ups in the middle of the line or to the east in areas that are heavily faulted.

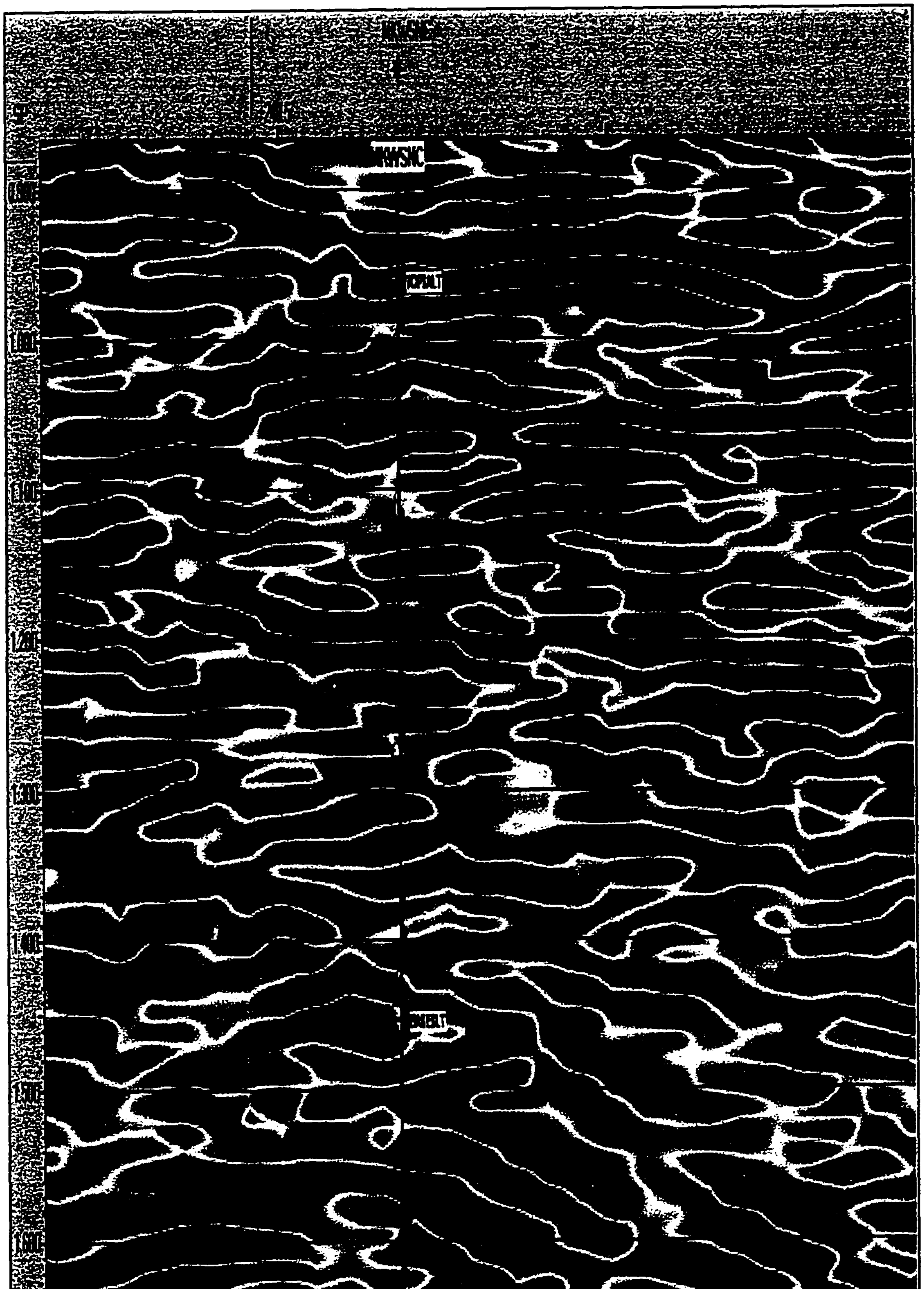

Figure 4.2a. Matching (topsalt and basesalt) of the synthetic seismogram with seismic line 33 at the well location.

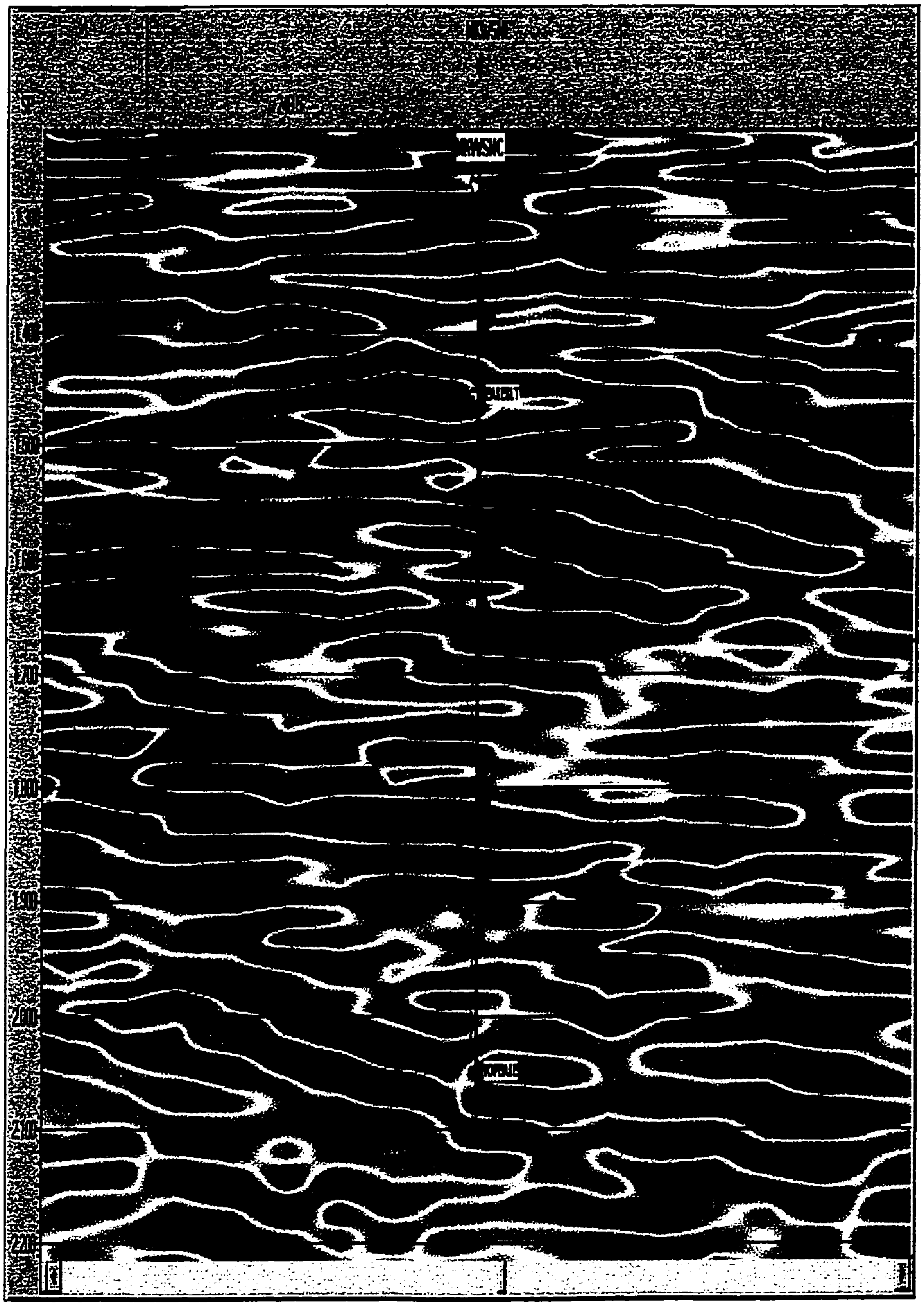

Figure 4.2b. Matching (basesalt and top of basement) of the synthetic seismogram with seismic line 33 at the well location.

At such locations, the objective horizons were matched (on either side of the structural feature causing the disruption) by using reflection character (Jump correlation) and sequence boundaries as a guide to correlation. The seismic line in Figure 4.3 shows the interpreted faults, horizons, and three major sequences referred to as supra-salt, salt, subsalt, and basement. This initial seismic interpretation constitutes a time section that, more or less, reflects the subsurface structures.

IV.1.2. Imaging problems:

The initial seismic interpretation suggests that the magnitude and significance of the distortions of the subsalt seismic events vary along the line. However, the most serious image distortions are observed below the reef build-ups in the middle of the seismic line. The development of thick depocentre just east of the shelf edge, and the very thick salt section in the eastern part of the seismic line also contribute to the image problem.

The western part (SP: 373 to 297):

This part extends from shotpoint 373 at the beginning of the line to the west to shotpoint 297 to the east. What is significant about this part of the line is the presence of a fan-shaped depocentre caused by pronounced thickening of the post-rift section just east of the shelf edge. This depocentre can be attributed to sufficient drainage in the basin from the Red Sea Hills to the west. The significant sediments loading associated with the depocentre led to salt withdrawal as indicated by thin salt and detachment fault just east of the shelf edge (Fig. 4.3). The thick post-rift section appears to have been detached, rotated ,and glided down slope on the detachment fault. On the shelf area towards the basin margin, the salt sequence possesses simple internal configuration. The reflection events show high amplitude, low frequency, and good continuity. This facies corresponds

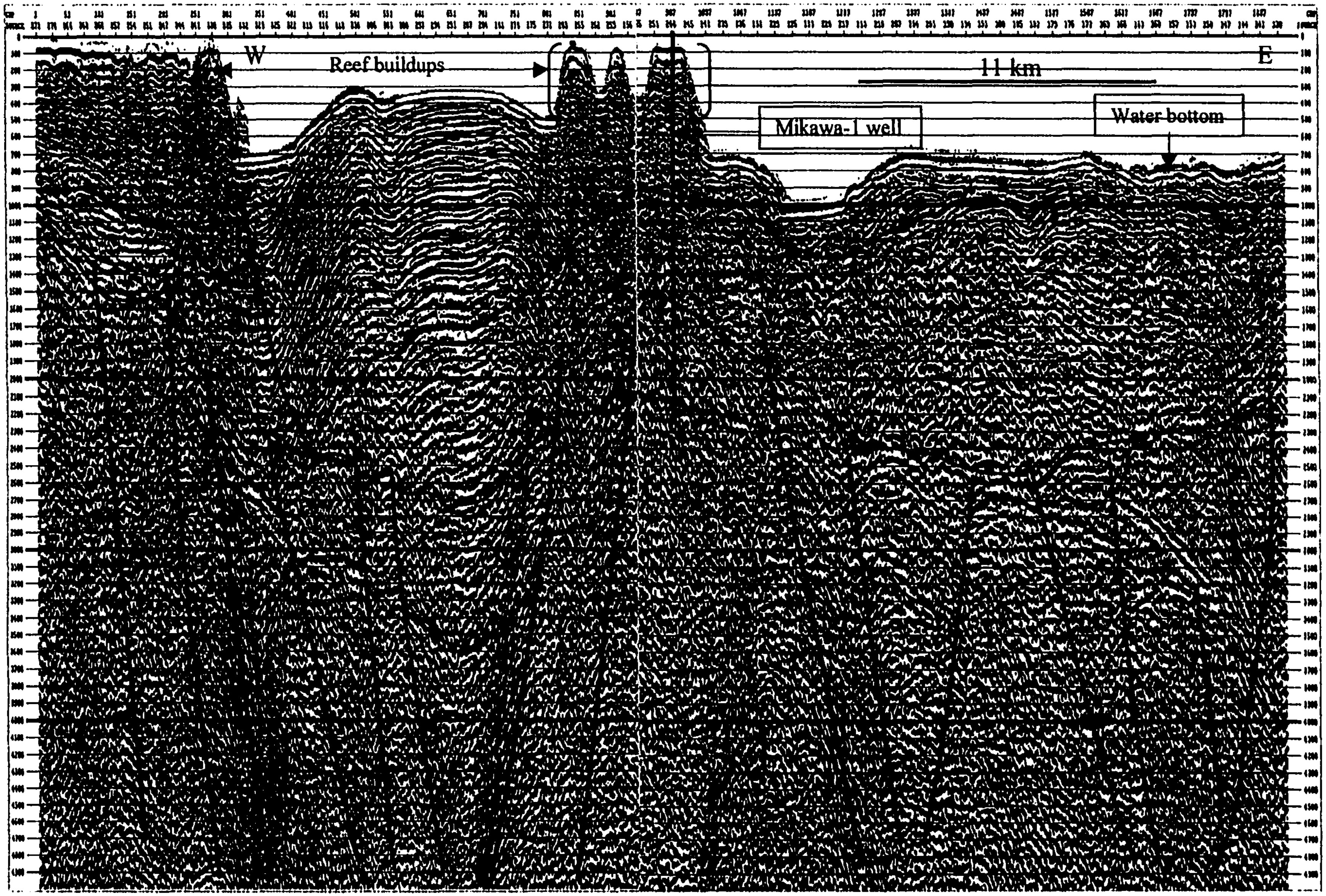

Figure 4.3. Unmigrated, interpreted line 33. Mikawa-1 well, encountered the topsalt (blue), basesalt (green), and bottomed in the basement (red) at 3360m.

to layers mainly consisting of anhydrite. The internal reflection pattern of the salt sequence between shotpoints 272 and 332 exhibits parallel reflections with moderate continuity, low amplitude and frequency. This reflection pattern implies the salt sequence consists of halite and shale interbeds. This is consistent with the fact that top of basement can be easily observed in this part of the line suggesting the salt section is seismically not opaque.

Figures 4.4 and 4.5 illustrate image distortions observed on this part of the seismic line. These distortions include diffraction, coherent, linear events, out-off-plane reflections, and water-related multiples. What is unusual about some of these reflections is that they crosscut and interfere laterally with adjacent and underlying subsalt and basement reflectors. The questions that remain are: could these events be reflections from outside the plane of the section (sideswipe) or just water-related multiples and top of salt multiples?

<u>Middle part of line 33</u>:

The intensive hyperbolic and steeply dipping linear events overwhelm this part ofthe line and severely distorted the salt and subsalt seismic events. Figures 4.6 and 4.7 illustrate some of the distortions observed on this part of the line These distortions include: Intensive diffractions, steeply dipping, linear, coherent events, drastic reduction of the amplitudes of reflections from below the reef buildups, false time pull-ups and sags, and sideswipe. These distortions masked the salt and subsalt seismic events. According, horizons corresponding to the top and base of salt and top of basement cannot accurately be defined. These disruptions can be attributed to the overlying rugged seafloor, heavy faulting, and complex salt boundaries. Fortunately, the Mikawa-1 well penetrated this section and bottomed in the basement. The well indicated that the salt section is relatively

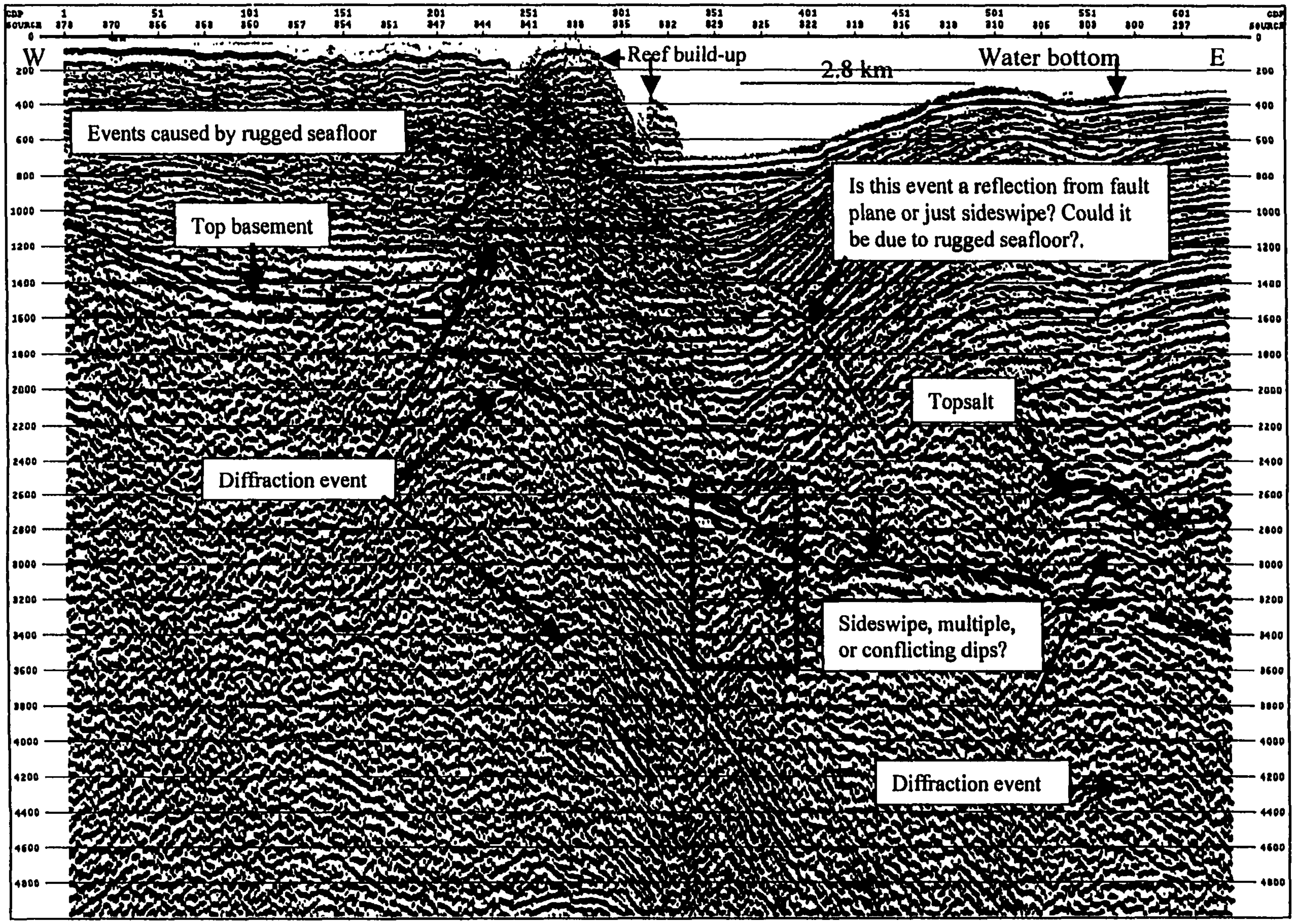

Figure 4.4 . Image distortions observed on the western part (SP: 373 to 297) of seismic line 33.

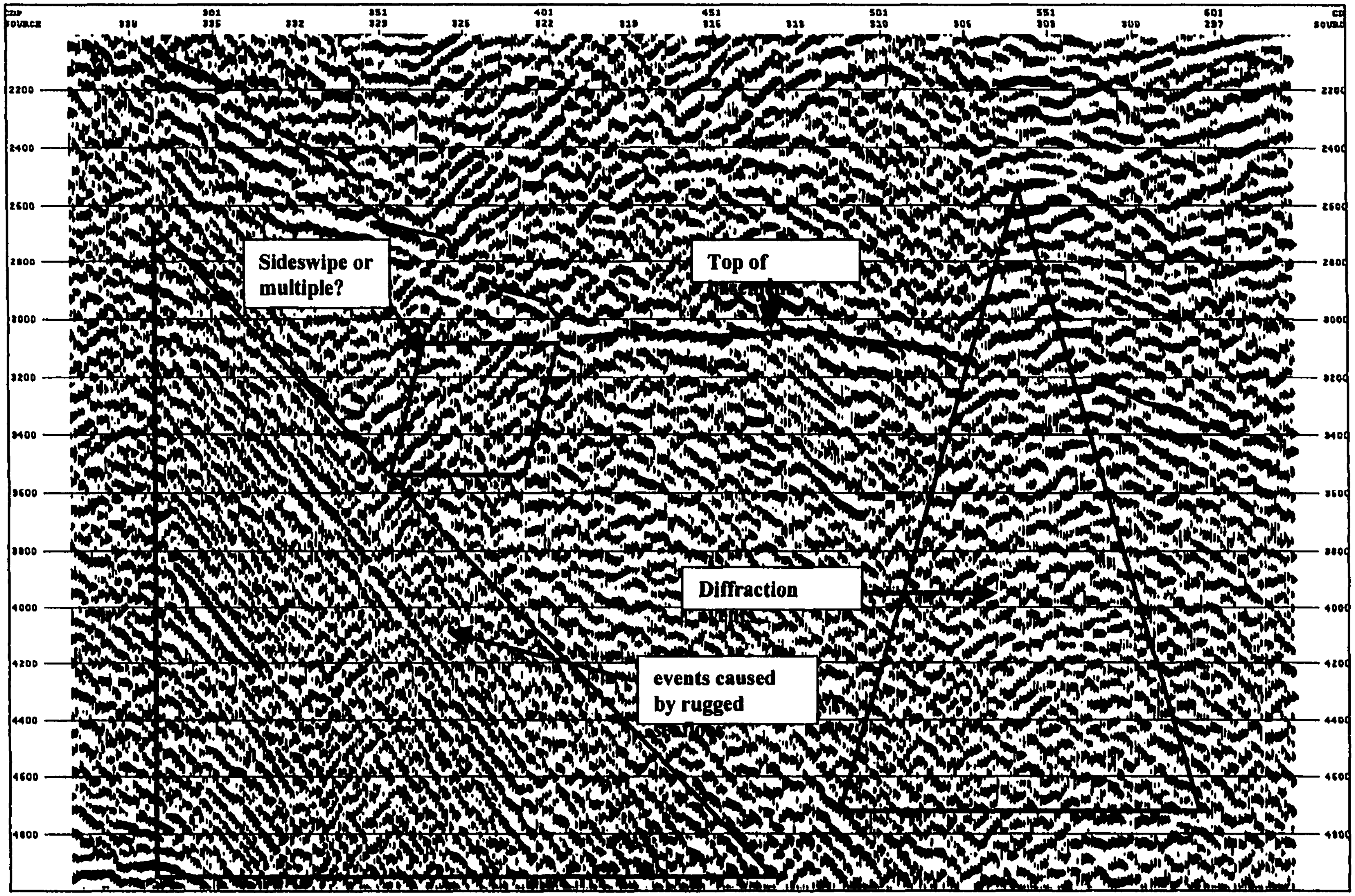

Figure 4.5. The image distortions observed (below 2.0 seconds) on the western part of the unmigrated seismic line 33.

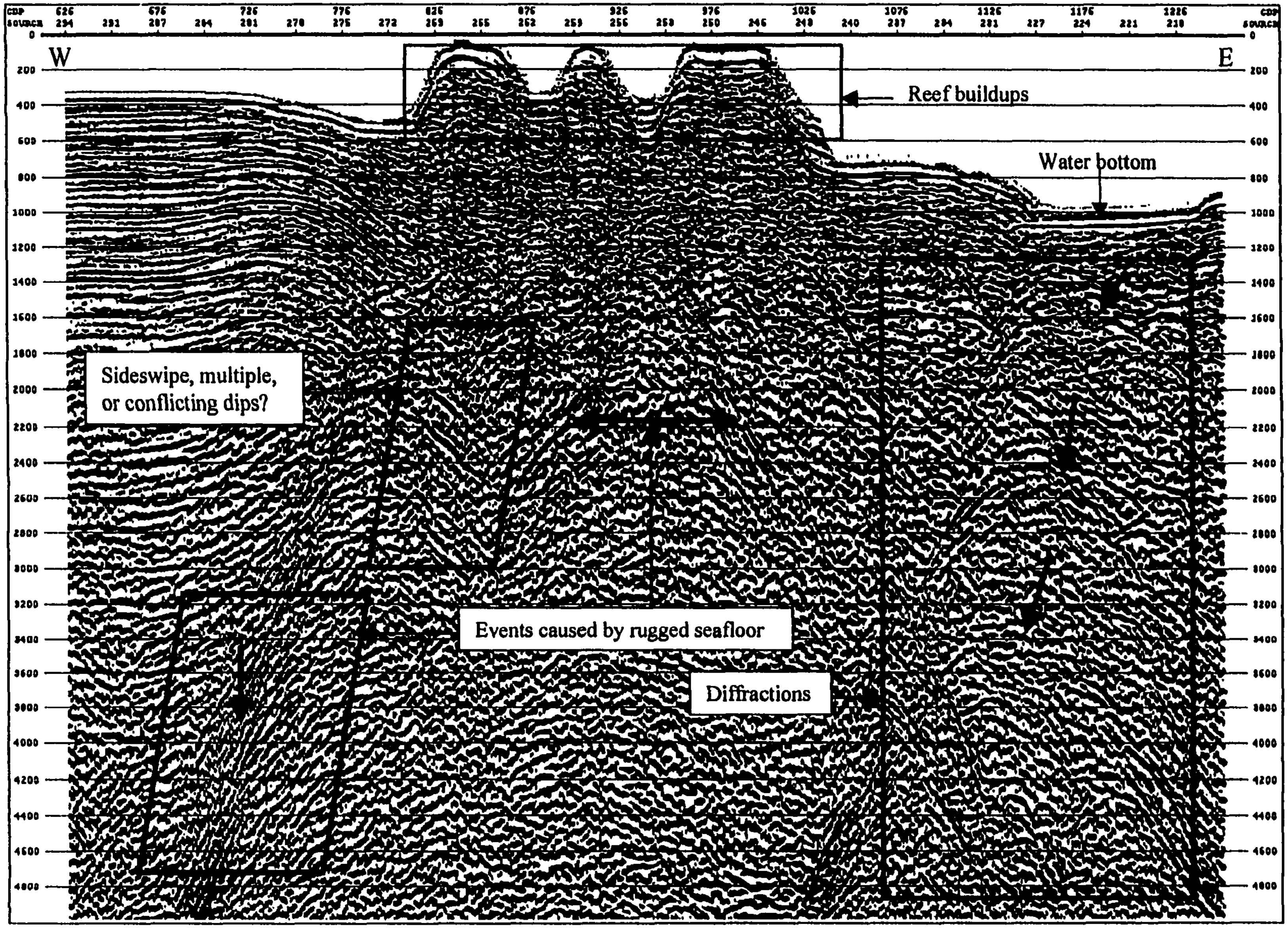

Figure 4.6. The middle part of line33 beforesignal enhancement and migration. Note the severe image distortion of salt and subsalt seismic events.

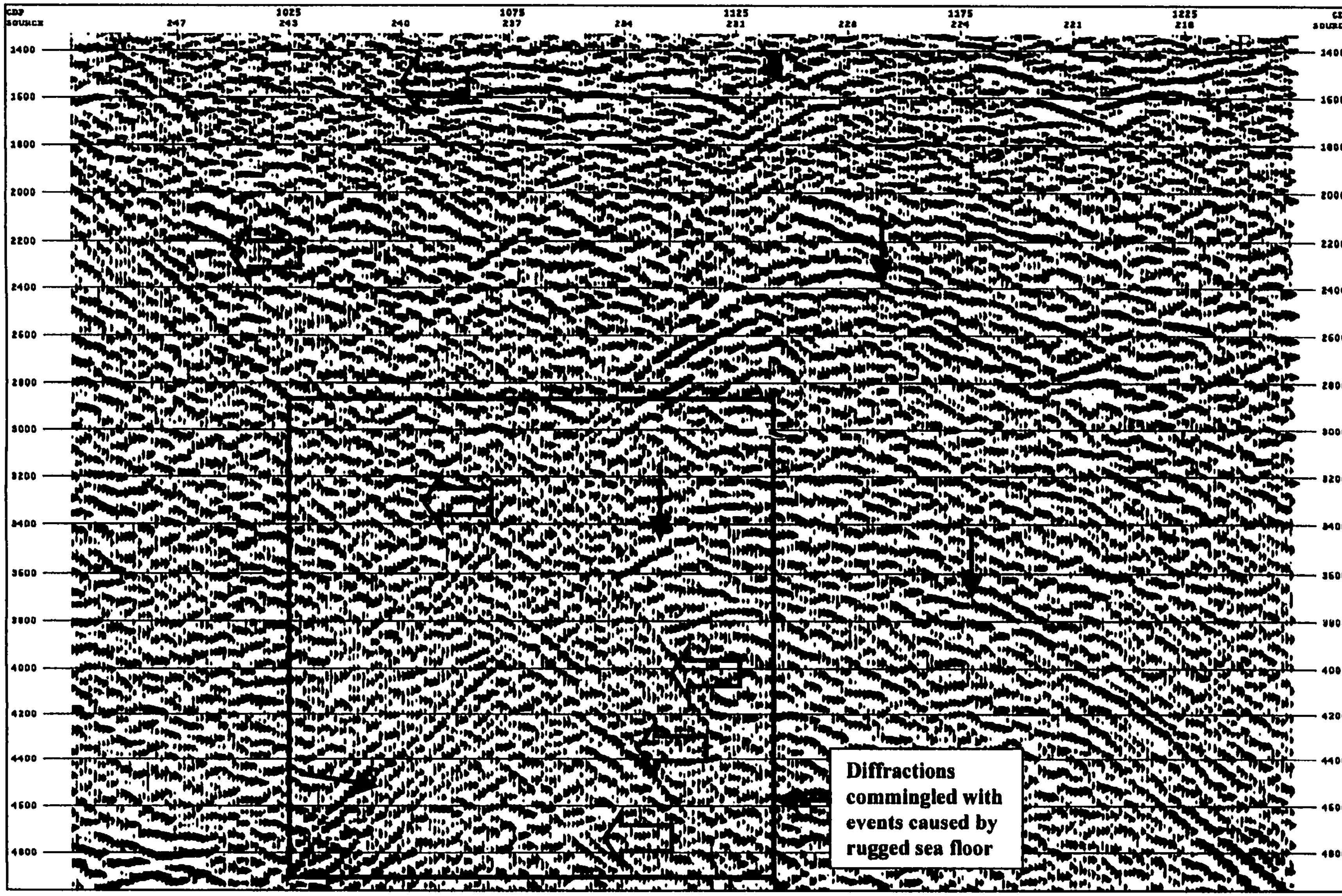

Figure 4.7. The middle part of line 33 below 2400 ms (magnified) just east of the reef buildups in the middle of the line. Note how diffractions (red arrows) and reflections from rugged seafloor (block arrows) have complicated the imaging of the subsalt events.

thin and mainly consists of halite with minor anhydrite interbeds.

The eastern part of line 33 (SP: 215 to 136):

This part of the line extends west to east from shotpoints 215 to 136 and is shown in Figure 4.8. The seafloor topography varies mildly along the line, ranging from 1875 to 2178 feet. The water bottom reflector possesses a high amplitude and excellent continuity and represents the coraline limestone of the Upper Pleistocene Shagara Formation .The initial interpretation revealed that the post-rift sedimentary section overlying the salt is very thin and exhibits relatively high amplitude, parallel reflections and moderate continuity. The thinning of the post-rift sedimentary section is consistent with an insufficient sediment supply from the Red Sea Hills to the west. The salt sequence varies in lateral geometry and exhibits complex boundaries. The salt sequence is very thick and shows complex internal configuration. West of shotpoint 179, the sequence has no correlatable internal reflection events and consist mostly of chaotic and reflection free facies. These reflection pattern suggests that the sequence can be identified as mainly consisting of halite. It is also possible that the deformations of salt, in response to the underlying faults movement, are the cause of this reflection pattern. East of shotpoint 179, the internal reflections show low amplitude, low frequency, subparallel, and moderate continuity. This implies the salt consists of halite with anhydrite or carbonate interbeds. These reflections may also be salt boundaries or water bottom multiples. The top of basement reflectors is not easily observed. The overlying thick salt section which varies in lateral geometry and exhibiting complex boundaries may cause complicated ray-bending, and refraction resulting in insufficient downing energy for illuminating the subsalt structures. Another imaging problem observed in this part is the diffraction phenomena,

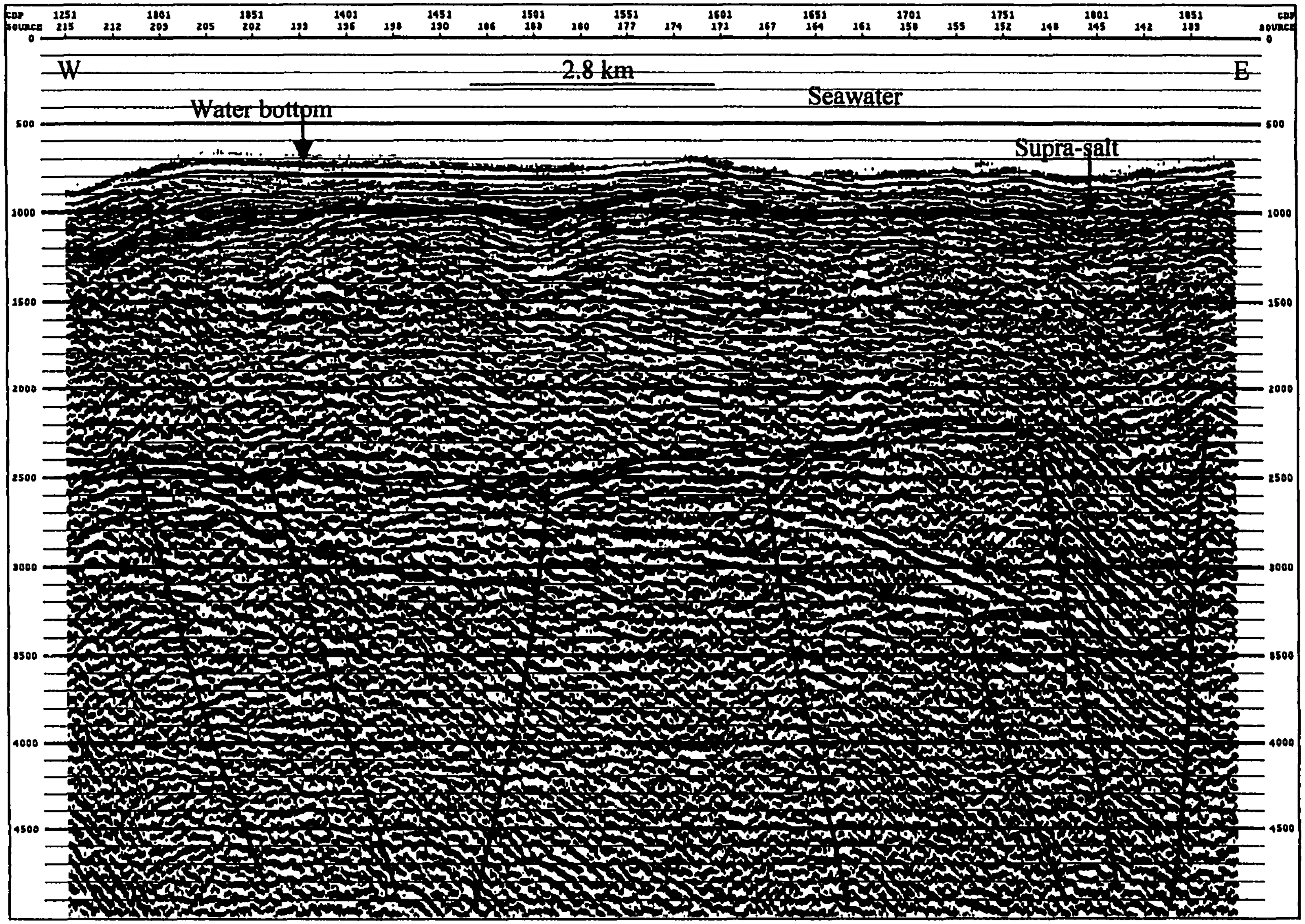

Figure 4.8. Unmigrated, interpreted eastern part of line33. Topsalt, basesalt and top basement are high-lighted in blue, green, and red, respectively.

which appears as strong hyperbolic events, masking subsalt structures. The diffractions may be associated with the basement involved, steeply dipping normal faults, which divided the subsalt section into a series of horsts and grabens. Other possible sources of diffraction include, faulted block edges, unconformity at the top of basement. Other distinct features of this part of the line are the two broad hyperbolic events with their peaks below shotpoints 207 and172 at 2600 ms beneath the salt section (Fig. 4.8). These observations lead to the following questions. Are these diffraction hyperbolas associated with deep, high velocity diffracting sources. Note (1/velocity) gives the slope of asymptote of diffraction curve, hence the hyperbola widens with increase in depth and velocity of a diffracting source)? Or, they could instead be two anticlines with a companion syncline in between? Could these be sideswipe or just simply tilted or rotated fault blocks on tops of the underlying two horsts? It is also possible that these events represent just velocity pull-ups of subsalt reflectors caused by overlying the fast salt. Certainly one cannot unequivocally answer, at this stage of interpretation, as to what caused these hyperbolic events.

IV.1.3. 2-D seismic modeling results and analysis:

Our specific goal of using 2-D seismic model construction is to provide a detailed forward-modeled description of the causes of the image distortions observed on the seismic sections, and verify and constrain the structural interpretation of this line. A combination of 2-D seismic inversion and forward modeling approaches are implemented to produce an acceptable velocity-depth model for line 33. The interpretation progressively develops through an iterative process, which consists of modifying the interpretation of unmigrated stacked section and comparing it to the synthetic section generated through forward modeling. The initial seismic interpretation (Fig. 4.3) is used as an input to the inversion process. The faults and the horizons corresponding to water-bottom, topsalt, basesalt, and the top of basement defined in the initial seismic interpretation of line 33 are then digitized into GXII modeling program. Layers correpondsing to water bottom, supra-salt, salt, subsalt, and the basement are then created. The material properties of these layers are defined using the velocity from the seismic line and well information. Figure 4.9a shows the time model constructed. The time model is converted to depth using normal incidence rays process, which migrate the horizons defined in the time model to their proper positions while converting to depth. The output from inversion is an initial depth model. The objective here is to see if the forward ray-tracing of the initial depth model, constructed through inversion, will recreate the real unmigrated seismic section. The normal incidence synthetic section generated by forward ray tracing the depth model was then compared to the real seismic section. If the two fit satisfactory, then the depth model is considered acceptable. If no match was obtained, the interpretation of the seismic section is modified until acceptable depth model is produced. The modifications that were used to improve the match between the real section and the synthetic include the geometry of the layer boundaries, the faults, and the interval velocity. Figure 4.9b show the initial velocity-depth model built through inversion process. The normal incidence synthetic section displayed with arrival times for water bottom, topsalt, basesalt, and top basement is shown in Figure 4.10. Close inspection of the synthetic indicated that the arrival times of top basement, basesalt, and topsalt west of the three reef buildups do not match those of the real seismic section. The synthetic also has not recreated the same features observed close to the end of line 33 to the east. Based

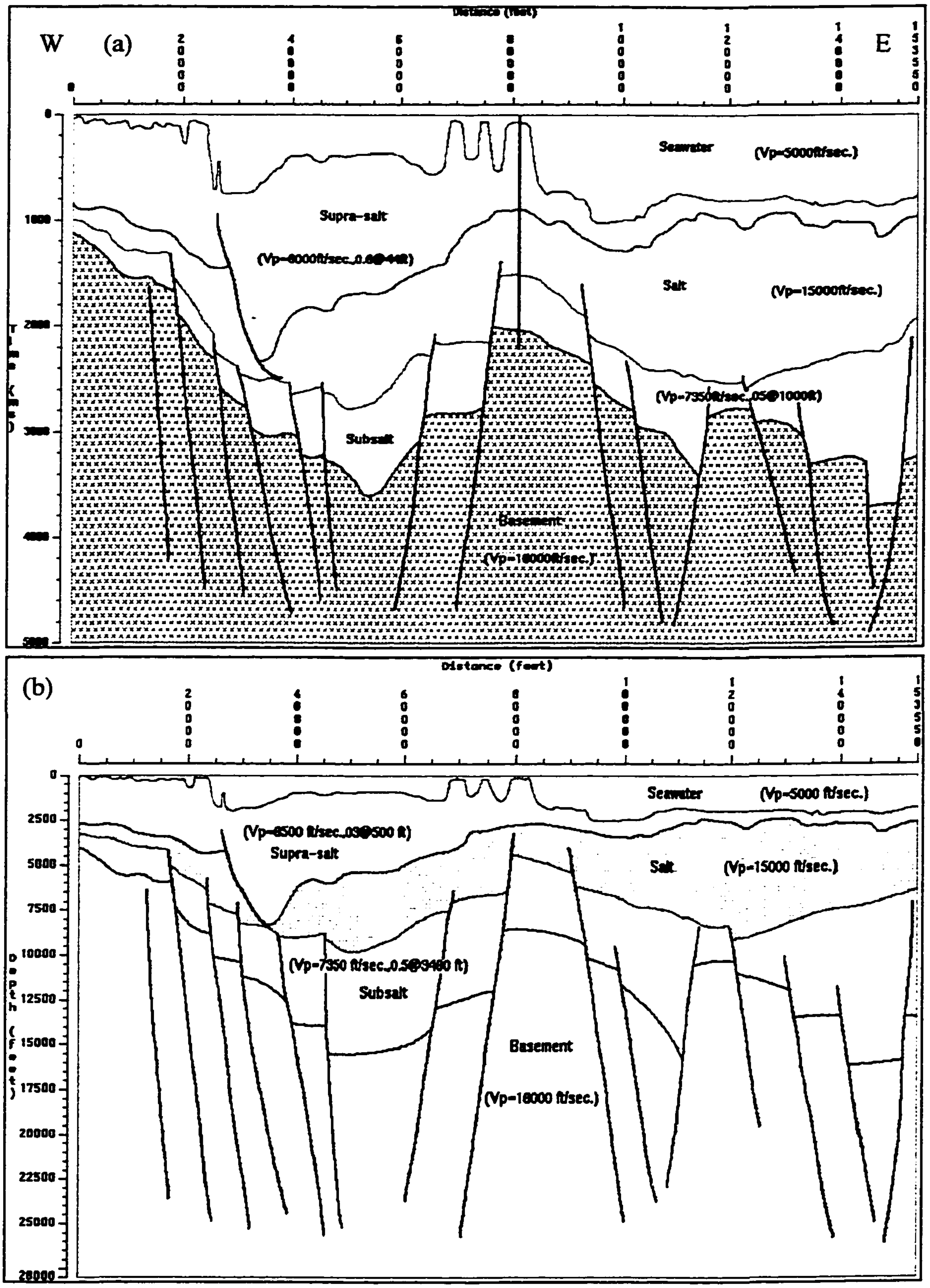

Figure 4.9. (a) Input time model built from initial seismic interpretation of line 33.
(b) Initial velocity- depth model resulting from conversion of the time model.

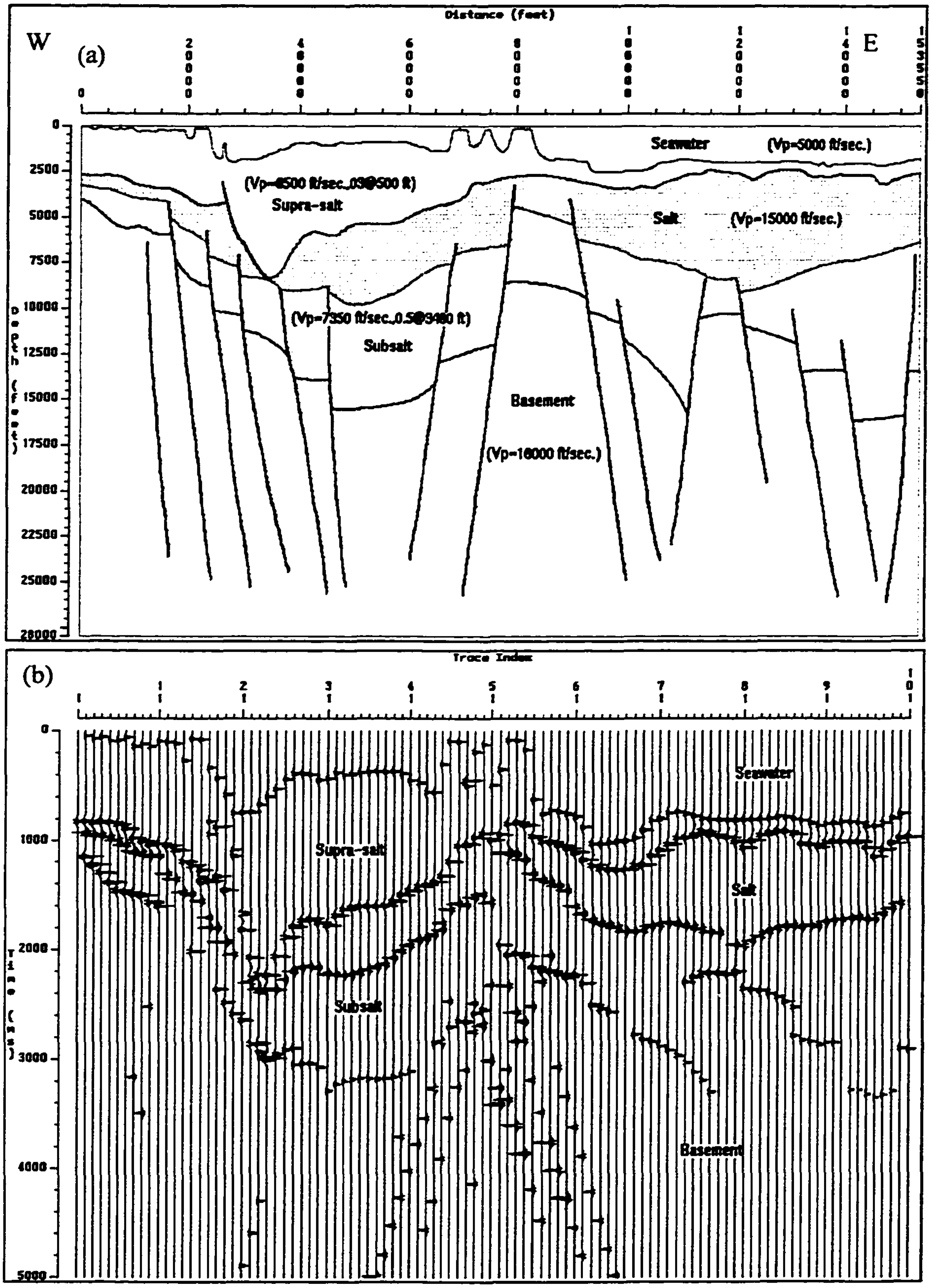

Figure 4.10. Velocity-depth model (a) and normal incidence synthetic seismic section (b) for line 33.

on these observations, the interpretation of line 33 and accordingly, the depth model is now modified. The modification is performed through an iterative procedure, which involves several alterations of seismic interpretation, inversion of the time model to depth, and forward ray-tracing the depth model. The modifications include: changes in the positions and geometry of faults and fault blocks, thinning of subsalt section and a significant thickening of post-rift sequence west of the three reef buildups. Close to the end of the line to the east, the base of salt horizon is moved to a deeper position resulting in substantial thickening of salt section. The velocity of supra-salt, subsalt, and the basement are also modified. The time and depth models after modification are shown in Figure 4.11. The synthetic section produced from the model is shown in Figure 4.12. The synthetic section displays several aspects of the real seismic section, which would not be easily recognized without the benefit of 2-D modeling. The arrival times corresponding to water bottom, top and base of salt and top of basement match those of the interpreted real section. The geometry of supra-salt, salt, and subsalt depict those observed on line 33.

Image distortion observed on the synthetic section:

The top of the basement reflector is significantly disrupted below the thick salt on the eastern part of the synthetic but is quite visible below the thin salt section on the west part of the synthetic. The salt and subsalt seismic events are severely distorted underneath the reef buildups in the middle of the synthetic section. The synthetic produced steeply dipping linear events below the irregular parts of water bottom. Diffraction events that obscured the salt and subset reflection structures on the line 33 were also recreated in the synthetic section.

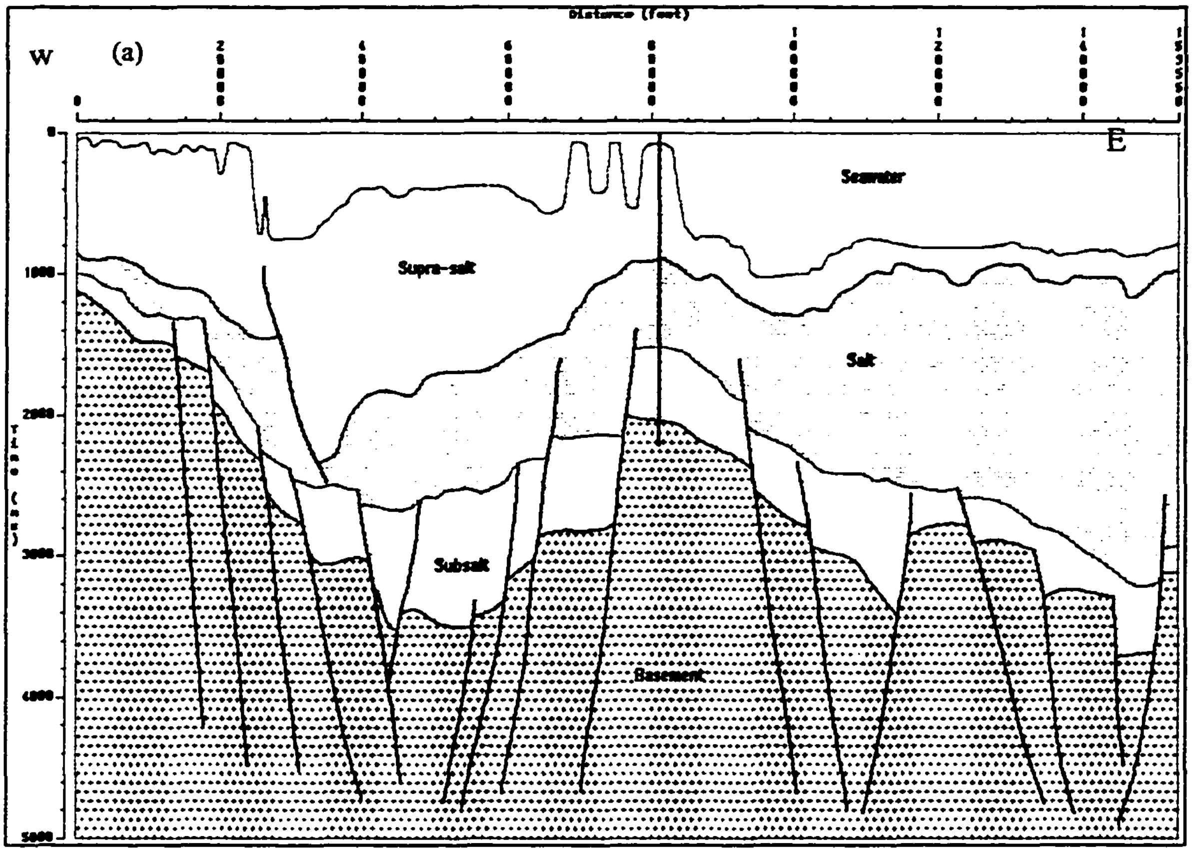

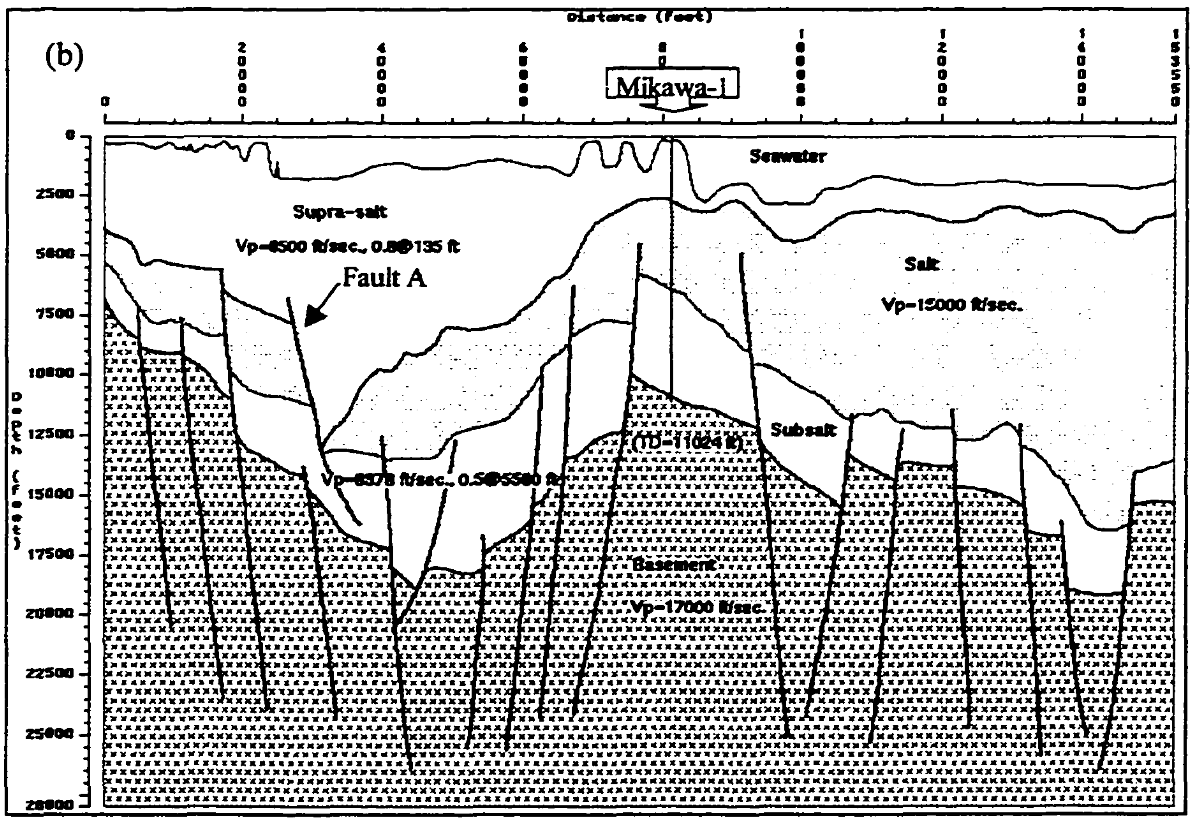

Figure 4.11. (a) Input time model constructed from seismic interpretation of line 33. (b) Velocity-depth model resulting from conversion of the time model.

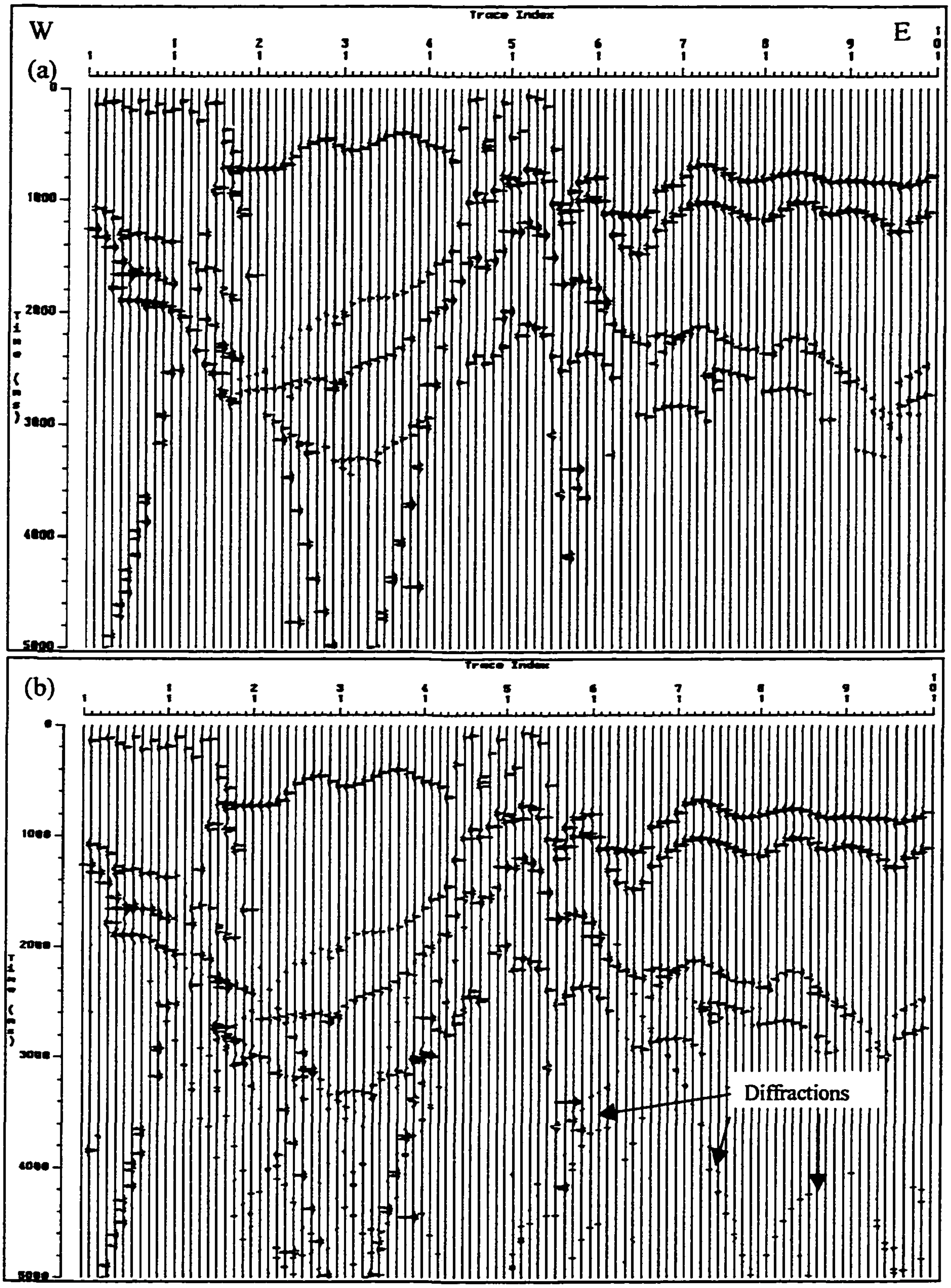

Figure 4.12. Synthetic section displayed with arrival times. (a) For reflections from water bottom (sky-blue), topsalt (blue), basesalt (green), and top basement (red). (b) For reflections from all layers and diffractions from faults and faulted block edges.

Raypath characteristics:

To investigate the possible causes of imaging distortions, the raypaths and synthetic trace were generated, separately, for water bottom, diffractions, basesalt and top of basement. Figure 4.13 shows the zero offset raypaths and synthetic trace for water bottom. Examination of these displays revealed that the severe raypath distortions observed on this Figure are caused by complex ray bending at the irregular parts of the water bottom and refraction at the top of the salt. Raypath deviation within supra-salt section, due to lateral velocity variation of supra-salt layer, further complicated the problem. The synthetic trace and arrival time for water bottom indicates steeply dipping, coherent, linear events underneath the rugged parts of the seafloor topography (Fig. 4.13b). These events bear a remarkable similarity to those observed underneath the edges of the reef buildups on the shelf area and the middle of seismic line 33 as shown on Figures 4.4 and 4.6. To examine the possible cause of diffraction events observed on seismic section 33, consider Figure 4.14 which displays the raypaths for diffraction from a single fault and synthetic trace for diffractions from all faults an faulted block edges. Note how some of the up-going rays deviated sharply at the top of high-velocity salt and changed direction with supra-salt. The ray bending is due to the high velocity contrast at the top of salt and lateral velocity change within supra-salt. The diffractions (Fig. 4.14b) closely resemble those exist on the real seismic section.

Figure 4.15 show normal incidence raypaths for the base of salt and top of basement. The raypaths undergo significant deviation at the water bottom and at top and base of salt. As described previously, zero offset ray tracing is normal to the reflecting interface and the reflections generated from these rays are plotted directly below the source receiver

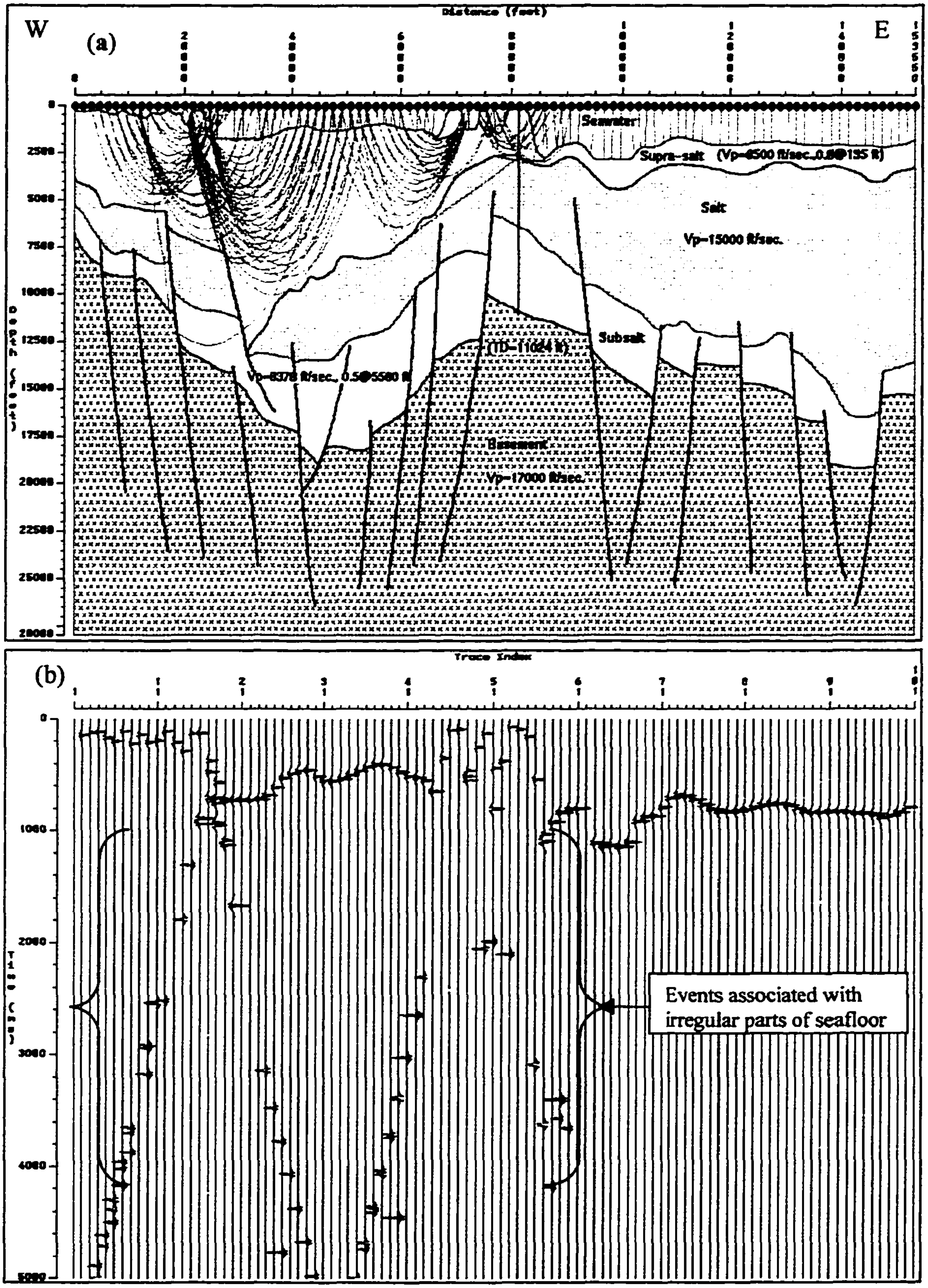

Figure 4.13. Zero offset raypaths (a) and normal incidence synthetic trace (b) for water bottom.

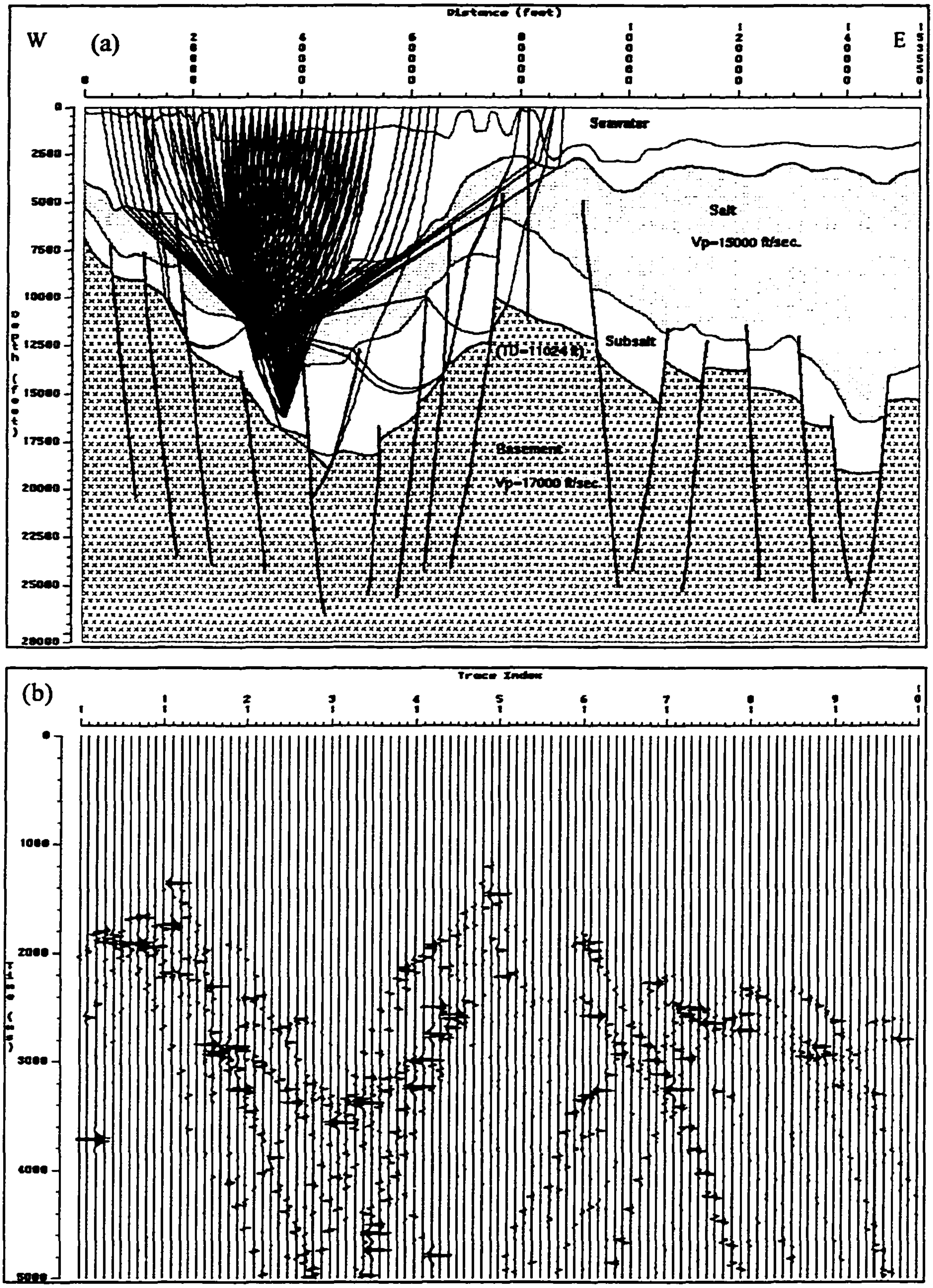

Figure 4.14. (a) Raypaths for diffraction from fault A. (b) Synthetic section for diffraction from all faults and faulted block edges.

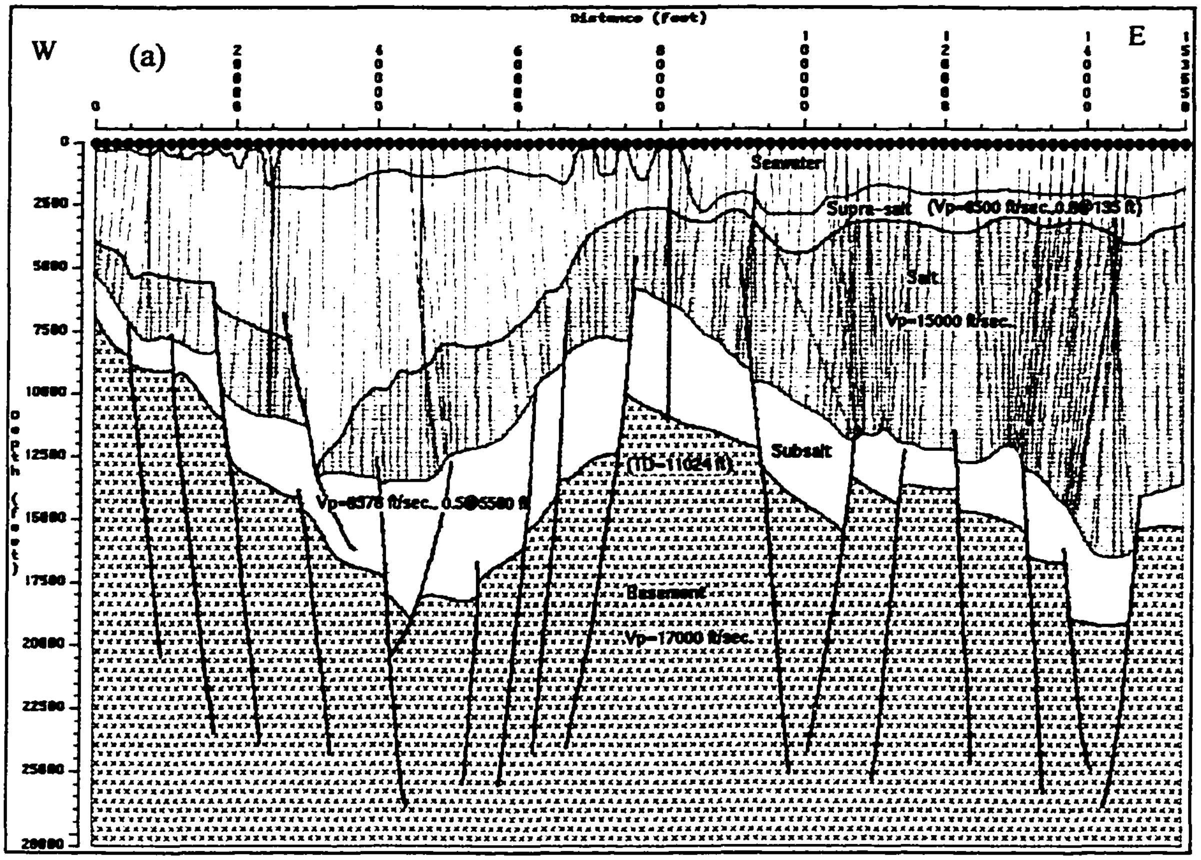

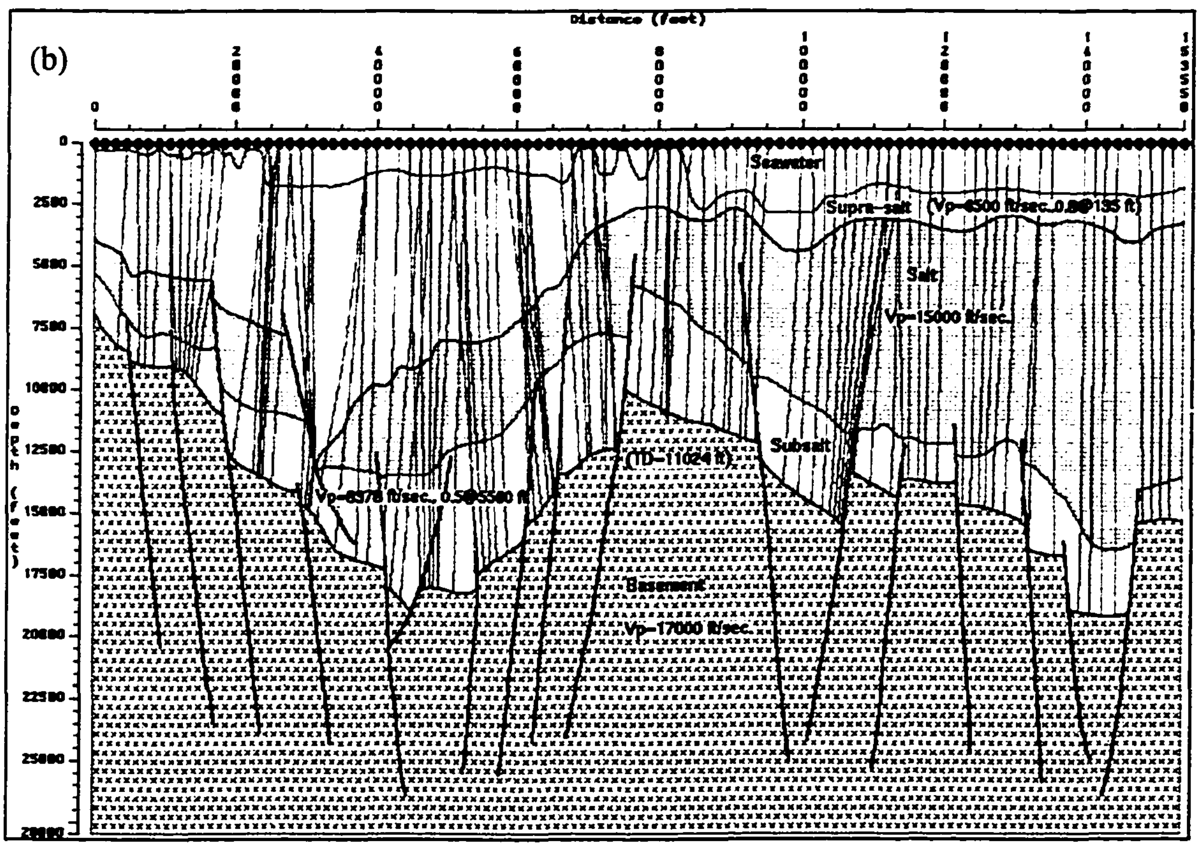

Figure 4.15. Zero offset raypaths for topsalt (a) and top of the basement (b) of line 33.

location. The ray bending is attributed to irregular geometry of layers boundaries and the impedance contrast across these layers. As shown on these Figures, the ray bending caused considerable gaps at base of the salt and top of basement, which resulted in poor imaging of subsalt structures. Although the depth model constructed through inversion and forward modeling recreated the real seismic section, however, many interpretational questions still remain regarding those parts of the seismic line that are not constrained by well data, such as the position and geometry of faults underneath the depocentre on the west part. The difficulty of interpreting underneath the depocentre is caused by the significant image distortions of reflection structures. These distortions are caused by raypath bending associated with the overlying rugged sea floor, diffractions from faults and faulted block edges, out off plane reflections, and the deformation caused by salt withdrawal.

In the velocity-depth model discussed above (Fig 4.11b.), the fault system beneath the post-rift depocentre consist of basement involved normal faults and salt related fault. The basement related faults cut through the subsalt and terminated at or offset the base of the salt. The faults divided the subsalt section into a series of tilted and rotated fault blocks. The salt related growth fault is interpreted to be the product of seaward gravity sliding and detaching of the post-rift section on underlying salt. This fault only affects the post-rift section and became inactive before it reached the top of the subsalt section. The fault provided a conduit for the salt withdrawal from beneath the thick overburden to structurally high area on its footwall. The greater thickness of the post-rift section on the down thrown side indicates that the sedimentation was coeval with fault movement.

An alternative possibility could be that the salt is syn-rift and was controlled by the geometry of basement-involved fault. The salt was later mobilized, by differential loading of the overburden into the footwalls of the basement faults. To include this possibility, the interpretation of faults underneath the post-rift depocentre is modified. The salt-related fault is replaced with a major basement involved fault. Figure 4.16 shows the modified depth model and the synthetic section derived from it. As shown on this Figure, the modifications do affect the match that has been achieved between the synthetic section and line 33.

Another alternative interpretation of this part of line 33 is that, the three basement related faults and the salt related fault are replaced with one major, down to the east listric normal fault and antithetic faults. The depth model constructed from this interpretation and the synthetic section derived from it are shown in Figures 4.17. Figure illustrates the synthetic section displayed with arrival times. The arrival times of water bottom, top and base of salt and top of the basement match those interpreted on the real seismic line 33. Again, the synthetic also reveals the imaging distortions associated with rugged seafloor, intense faulting, rapid lateral velocity variation, and high velocity salt. Figure 4.18 displays (after enlargement) the raypaths and normal incidence synthetic trace for water bottom. The raypaths demonstrate severe bending at the rugged seafloor and within supra-salt, and refraction at the top of salt layer. To demonstrate that the significant ray bending in supra-salt is due to lateral velocity variation, compare the two zero offset raypaths displays in Figure 4.19. These displays show significant ray bending, below water bottom, when supra-salt has variable velocity (Fig. .19a). There is no raypaths bending in constant velocity supra-salt (Fig. 4.19b).

The modeling results reveal that the imaging distortions observed on seismic line

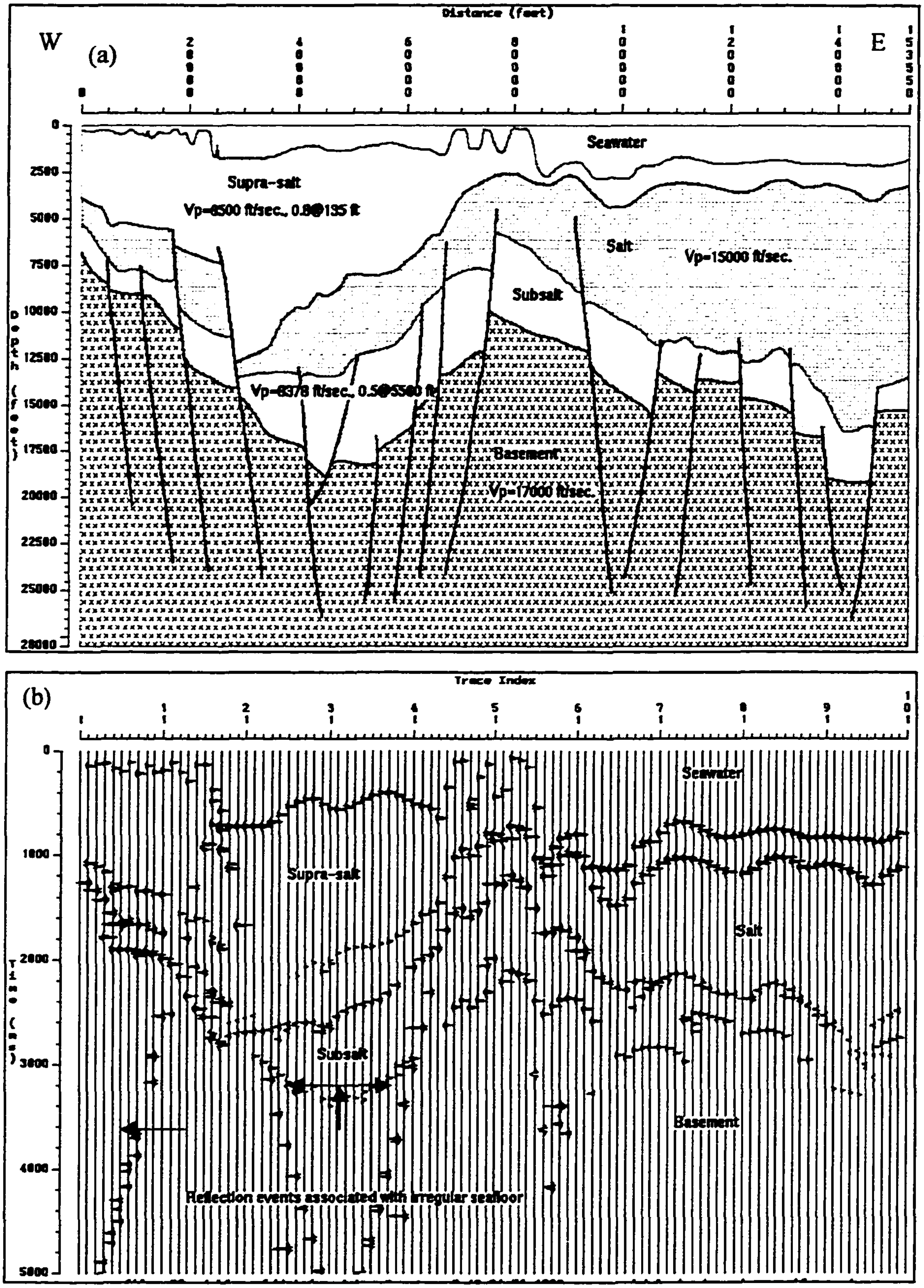

Figure 4.16. Velocity-depth model (a) and normal incidence synthetic section (b) for seismic line 33.

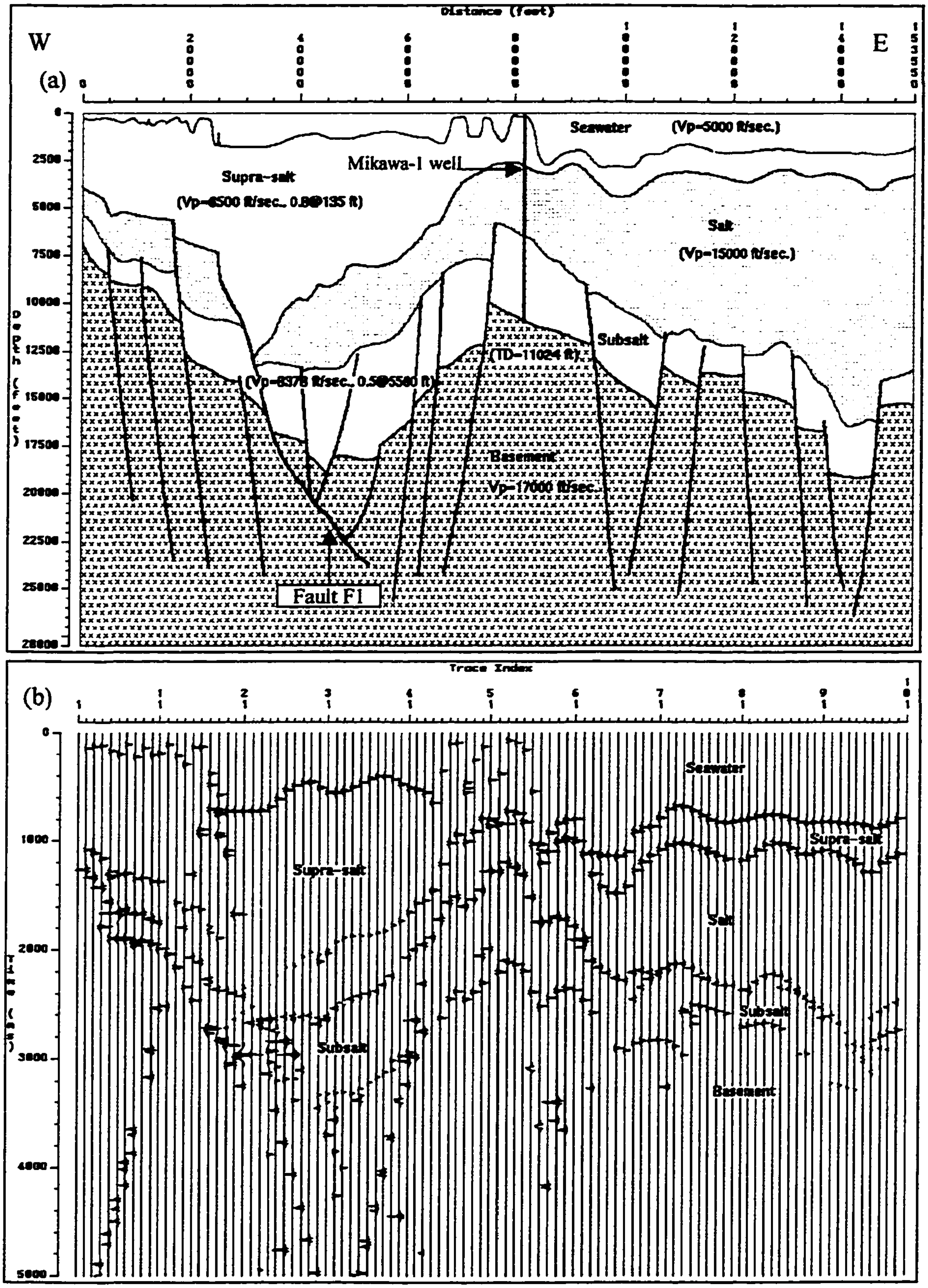

Figure 4.17. Velocity-depth model for seismic line 33 (a) and the synthetic seismic section (b) derived from it. Mikawa-1well bottomed at 11024 ft in the basement.

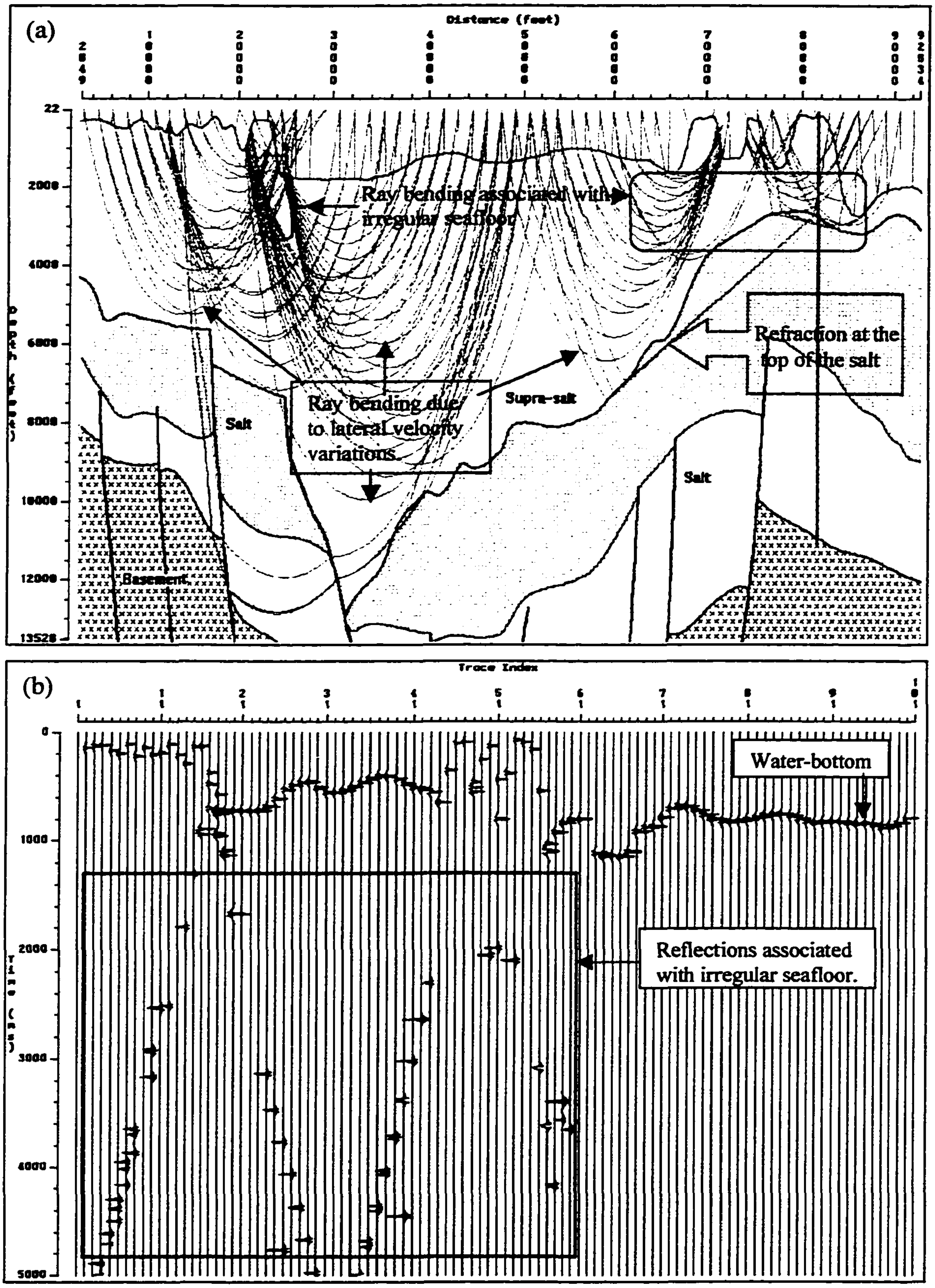

Figure 4.18. Zero offset raypaths (magnified) (a) and normal incidence synthetic trace (b) for water-bottom of seismic line 33.

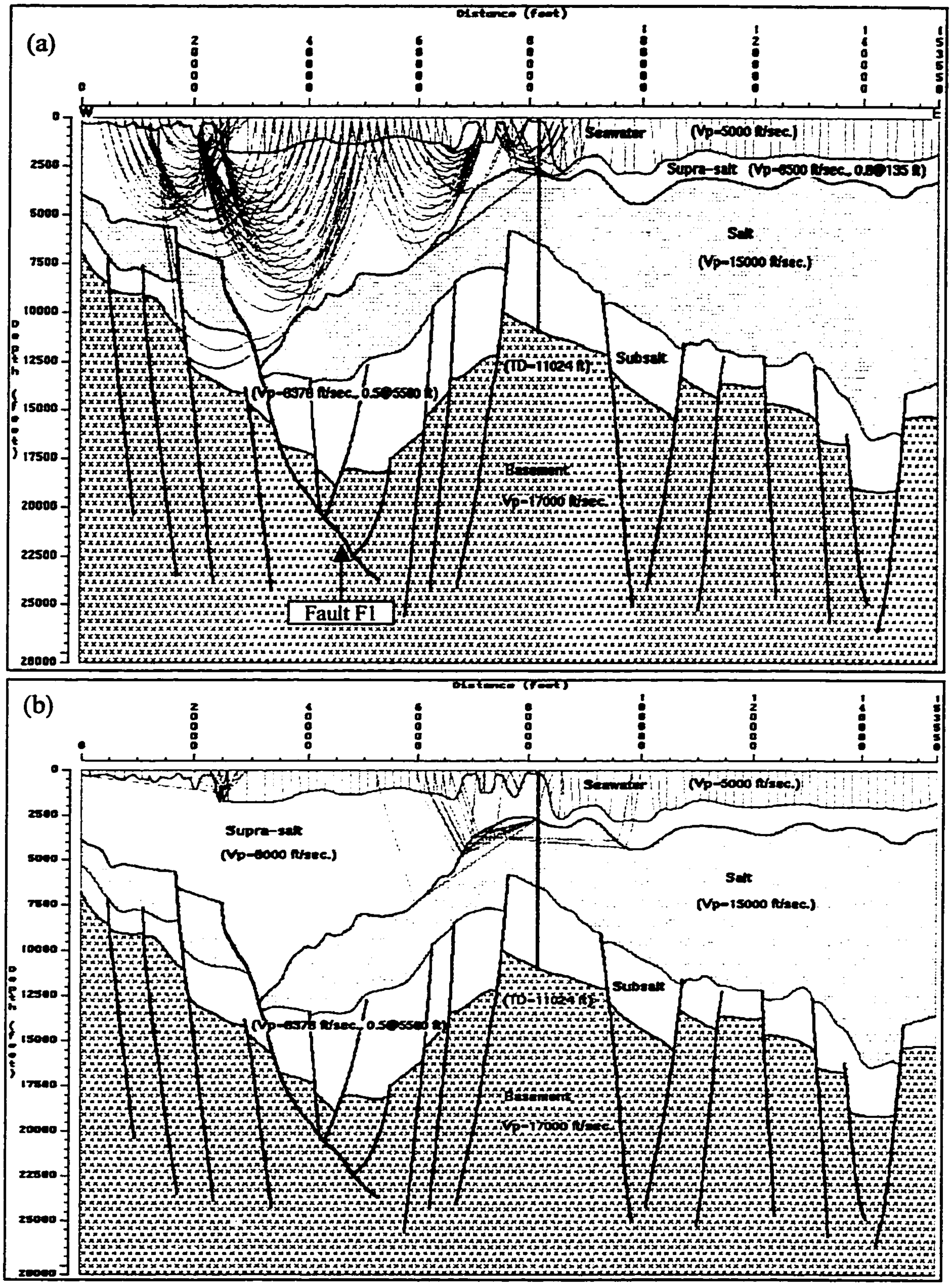

Figure 4.19. Zero offset raypaths for water-bottom with supra-salt having variable (a) and constant (b) velocity. Note the significant ray bending (top) associated with variable velocity.

33 can be attributed to servere ray bending caused by rugged seafloor, sharp refraction and severe raypath distortion at the top of irregular salt. These distortions result in serious travel time errors and considerable amplitude reduction of the underlying reflection events. The presence of thick salt on the eastern part of line 33 resulted in insufficient illumination of the underlying basesalt and top of basement reflectors. Additionally, the intense diffractions from faults and faulted block edges and raypaths distortion due to lateral velocity variations farther complicated the imaging of subsalt section.

IV.1.4. Post stack signal enhancement.

IV.1.4.a. The results of the wave equation multiple rejection:

Wave equation multiple rejection program is performed on line 33 to attenuate the water bottom multiple and reduce peg leg multiple. Figure 4.20 and 4.21 show the western, middle, and eastern parts of line 33 after wave equation multiple attenuation process was performed. The wave equation multiple rejection process does not suppress the crossing events (indicated by a box) that overlap with the subsalt and basement reflections. This suggests that these events are not water-related multiples. The estimated water bottom multiples removed from line 33 are insignificant and only from the shallow part of the line.

IV.1.4.b. The results of F-X deconvolution:

F-X deconvolution (Canales, 1984) was performed to reduce the random noise and spurious events from unmigrated line 33. Figures 4.22, 2.23, and 4.24 show the western, middle, and eastern parts of line 33 after F-X deconvolution. The steeply dipping linear events, intensive diffractions, and crossing events can be observed clearly after FX decon. There is also a significant improvement in reflection continuity particularly of western and

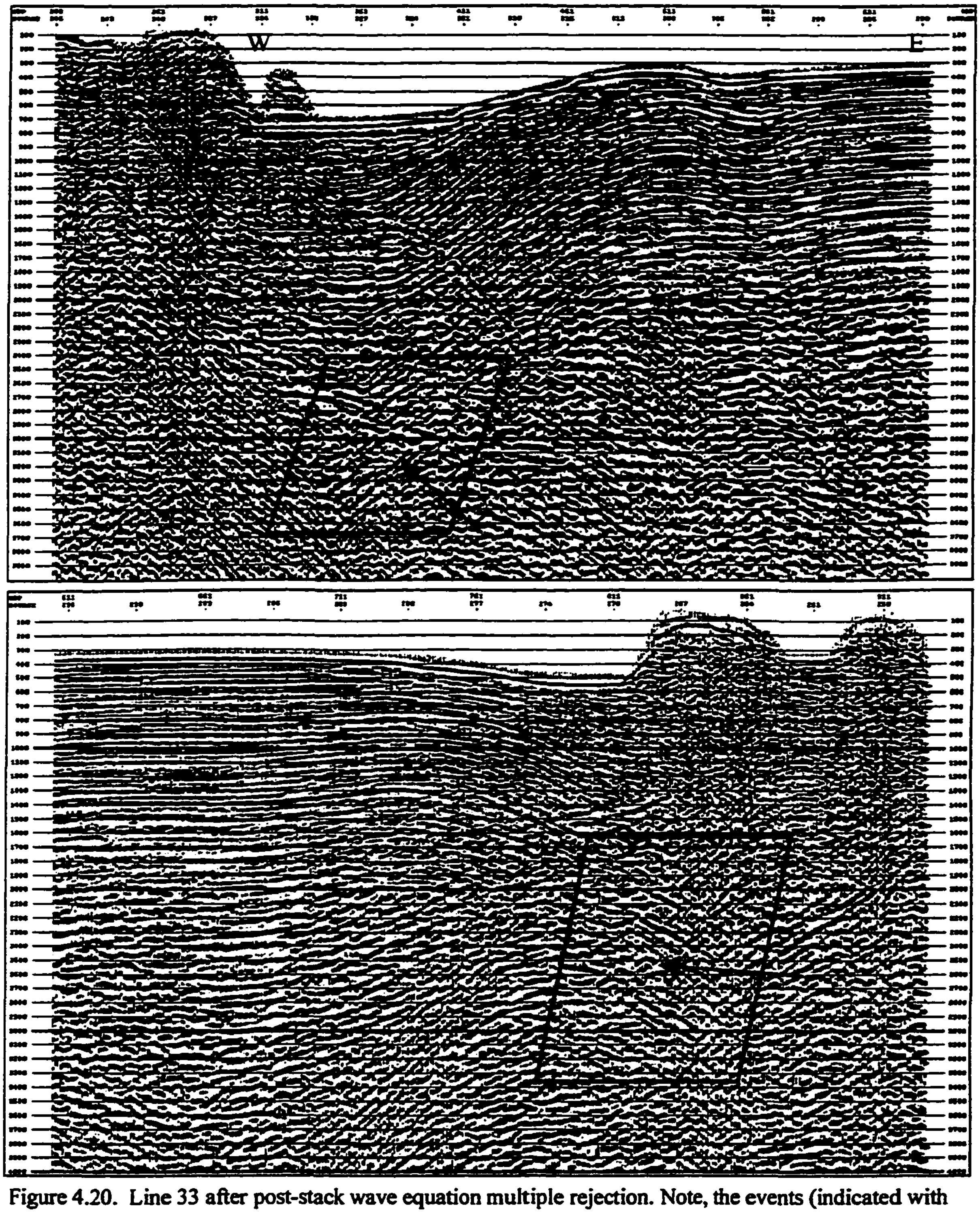

Figure 4.20. Line 33 after post-stack wave equation multiple rejection. Note, the events (indicated with arrows) overlapping with subsalt and basement reflections still exist. This suggests that they are not water-bottom multiples.

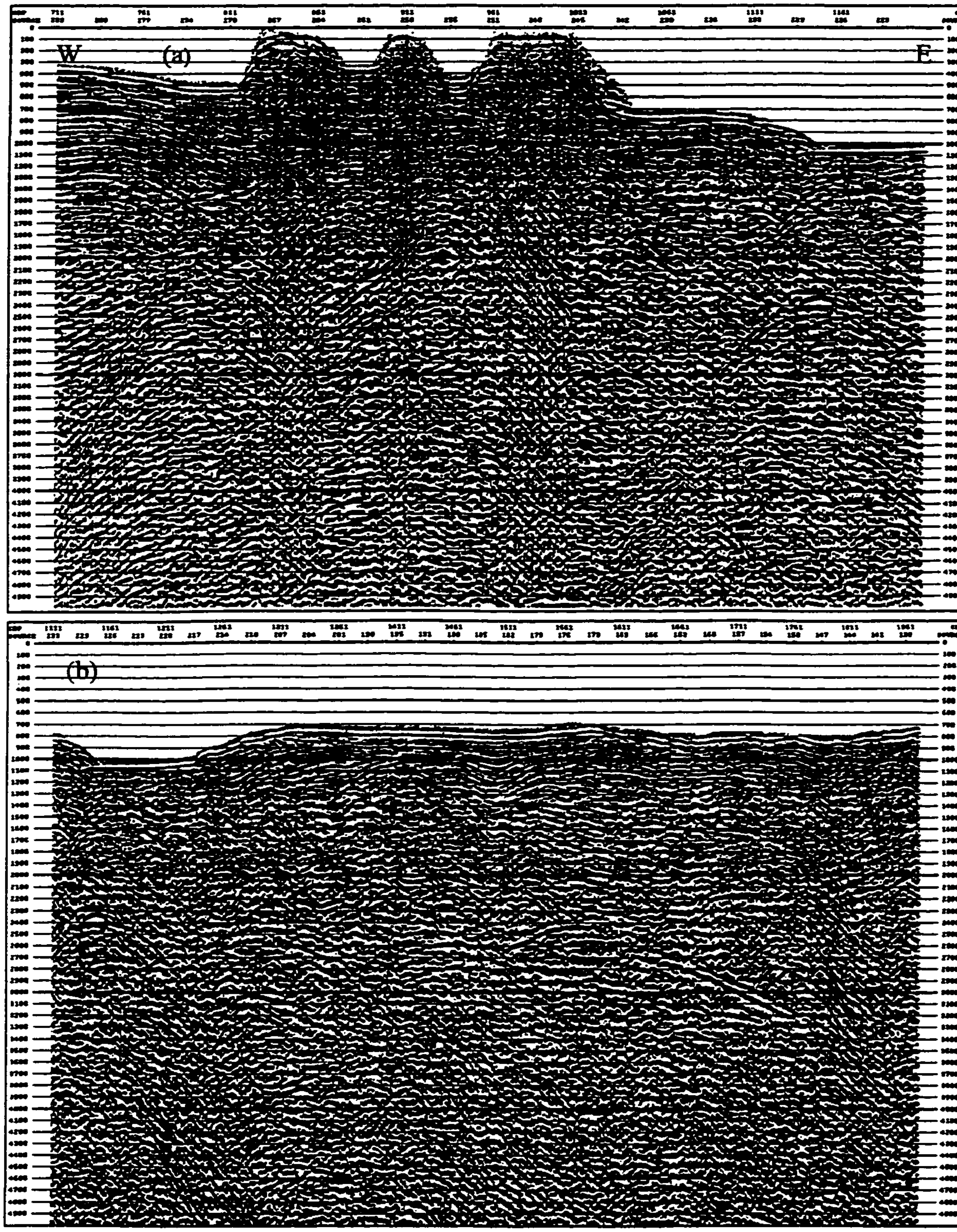

Figure 4.21. The middle(a) and eastern parts of line 33 after wave equation multiple rejection.

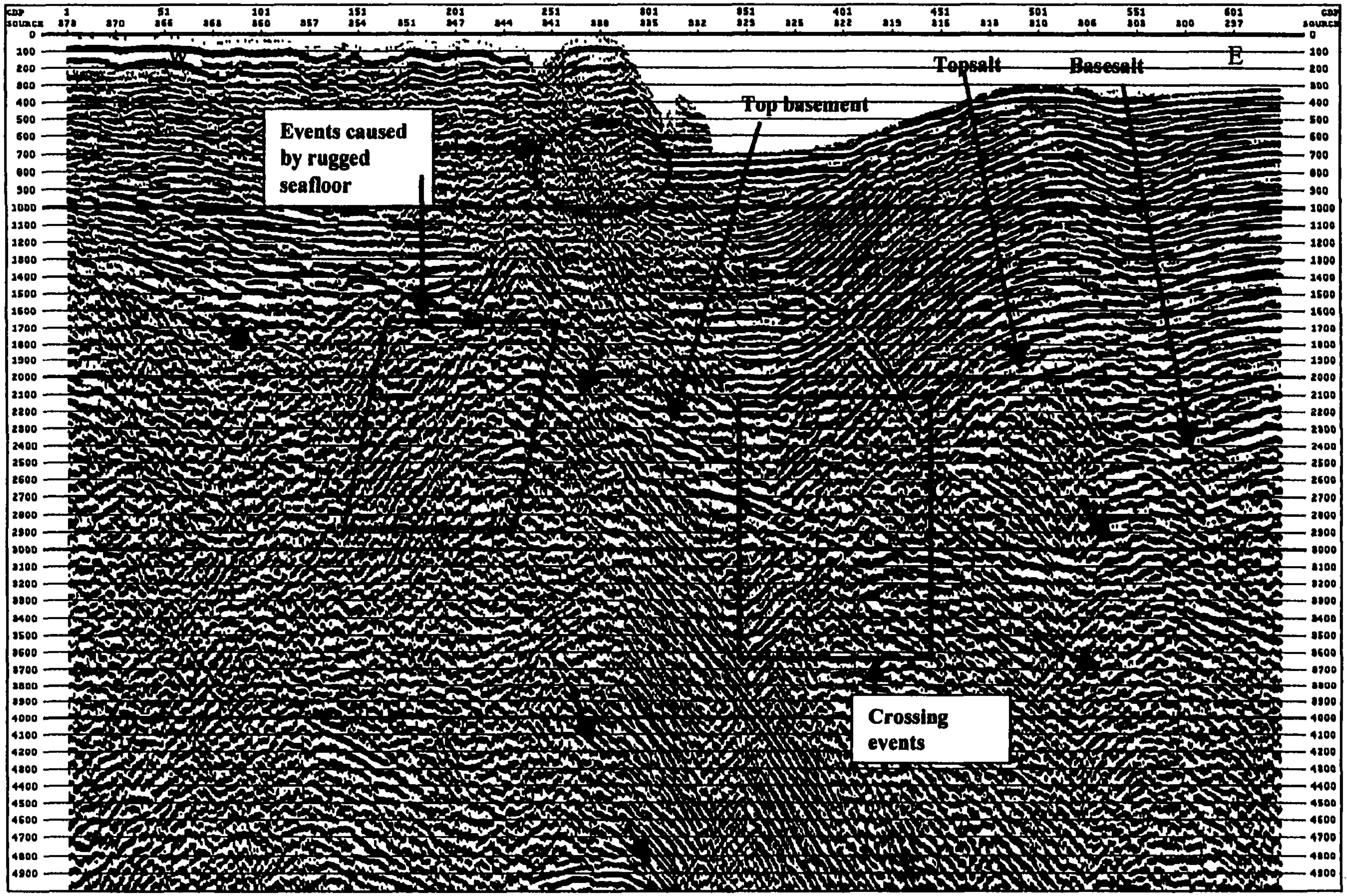

Figure 4.22. The western part of line 33 after FX deconvolution. Diffractions (indicated by arrows), linear events, and crossing events are now more visible than before F-X decon.

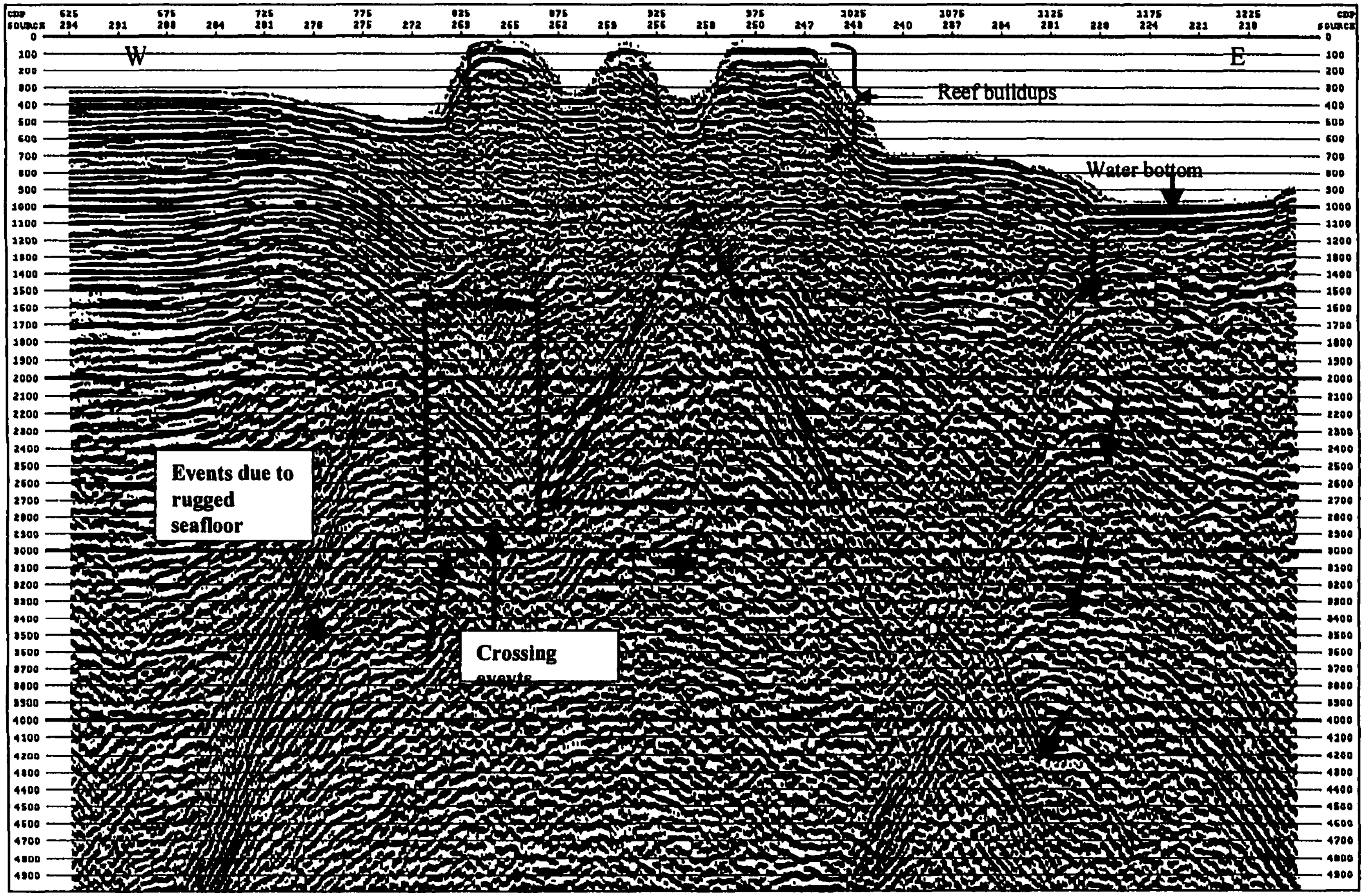

Figure 4.23. The middle part of line 33 after FX deconvolution. The severe distortions of salt and subsal t reflectors underneath the reef buildups are very obvious than before FX decon. The intensive diffractions are indicated with arrows. Steeply dipping linear events are indicated with a triangle.

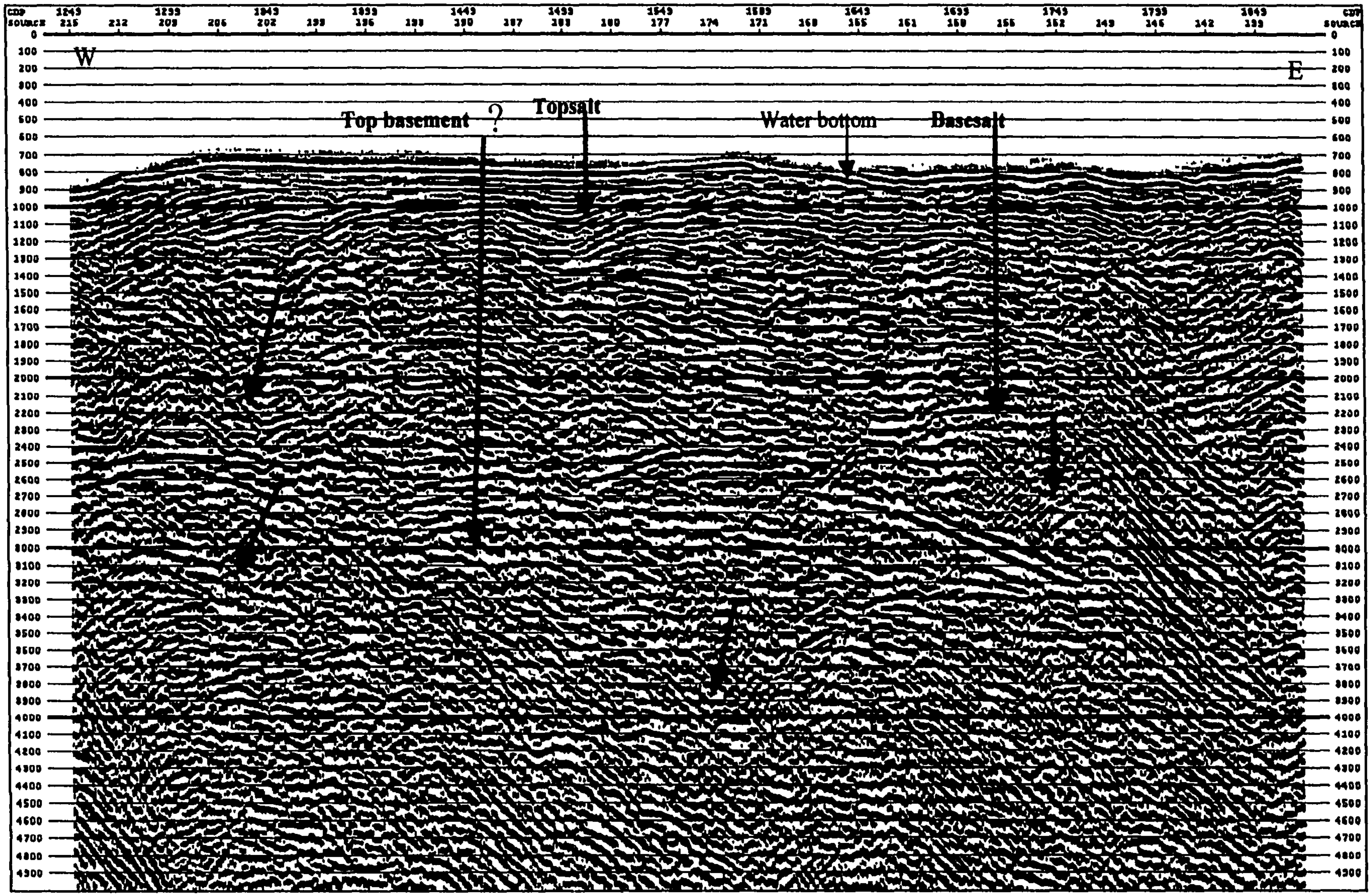

Figure 4.24. The eastern part of line 33 after FX deconvolution. Note how the top of the basement reflector is poorly imaged. Diffraction hyperbolas are indicated with arrows.

eastern parts of line 33.

IV.1.4.c.The results of post stack wave equation datuming:

Post stack wave equation datuming is performed on line 33 to reduce the deleterious effects of variable water bottom on underlying reflection events. Figure 4.25 shows the western part of line 33 after wave equation datuming. There is a considerable improvement in reflection continuity of subsalt, salt, and supra-salt seismic events of this part of line 33. The improvement in reflection continuity is the result of higher amplitude and increase in coherence after wave equation datuming. The curved event that crosses supra-salt depocentre is almost removed and no fault offset is observed. Therefore, this event is not reflection or diffraction from a fault plane. The enhancement obtained by wave equation datuming, reveals significant offsets in reflection continuity, which marks the position of salt-related seaward-dipping listric normal fault. Figure 4.26 shows one possible interpretation of position and shape of this fault. The improvement in the middle part of line 33, below the reef buildups, is not as good as had been hoped. It is likely that the severe image distortions in this area obscure the enhancement in reflection continuity obtained by wave equation datuming, or the distortion is so severe that wave equation datuming technique can not performed optimally.

IV.1.5. Post stack migration results and analysis:

The goal of post stack migration is to reveal the true subsurface structures and improve the lateral resolution of seismic data by moving the dipping reflectors to their correct subsurface positions and collapsing diffraction hyperbolas. The post stack migration algorithms performed on seismic line 33 are Iterative FK time migration, steep dip explicit finite difference time migration, residual migration (FK plus FD), and finite

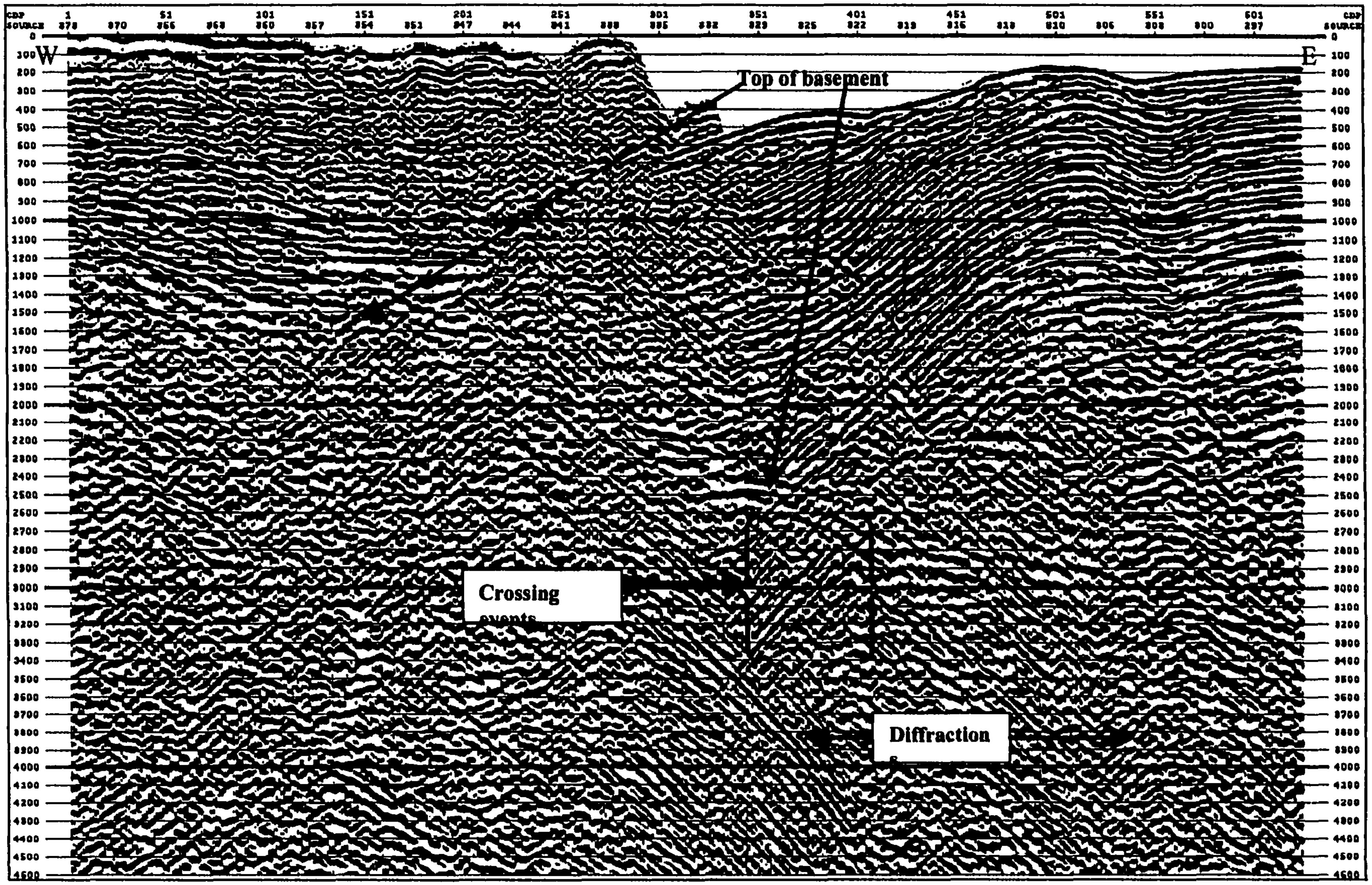

Figure 4.25. The western part of line 33, after post-stack wave equation datuming.

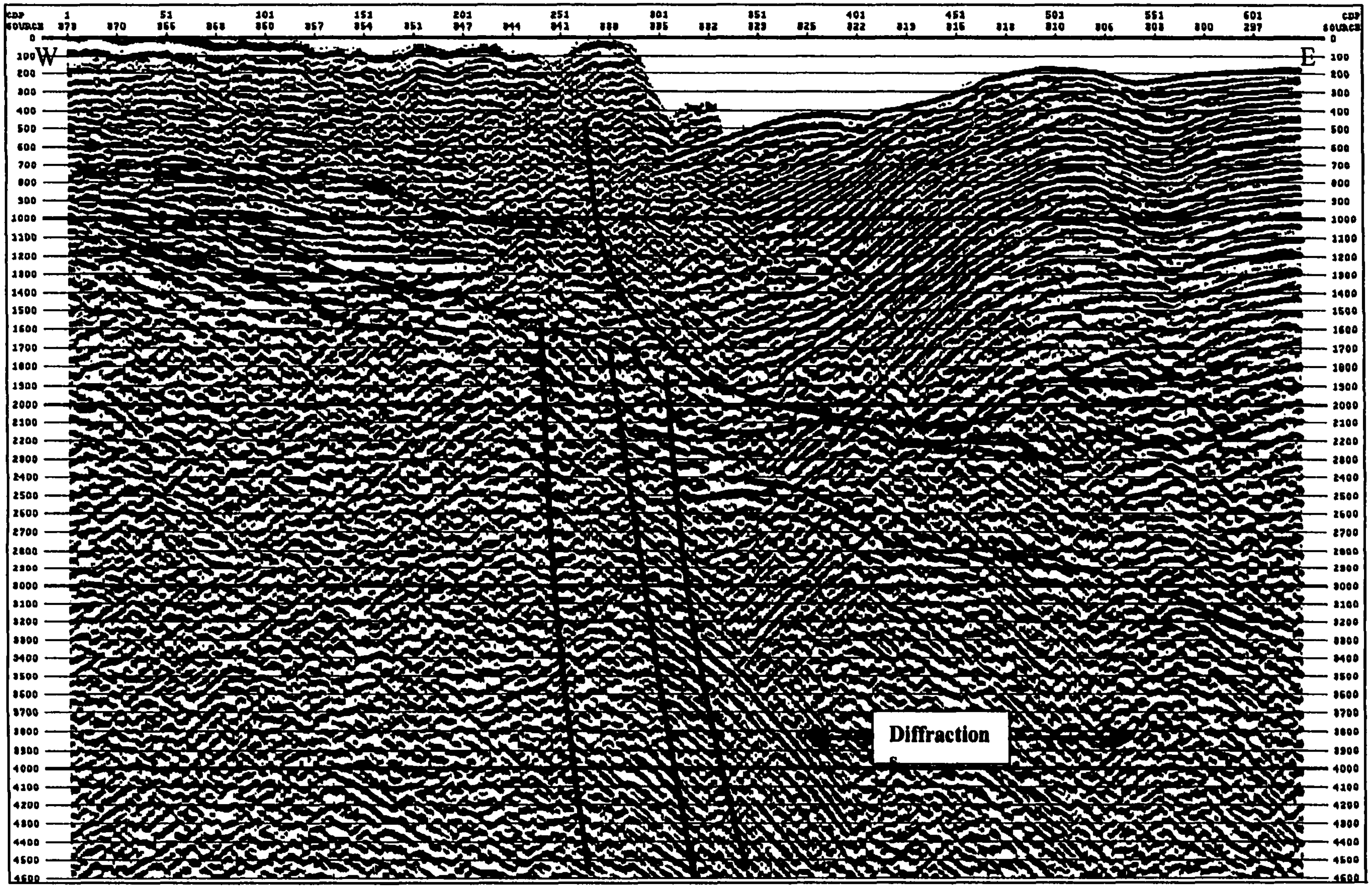

Figure 4.26. The western part of line 33, after post-stack wave equation datuming, showing salt-related seaward-dipping listric normal fault. Topsalt, basesalt, and top of basement are high-lighted in blue, green, and red, respectively.

difference depth migration. The primary objective here is to investigate, compare, and evaluate the results obtained from these methods and draw conclusion as to which method yields much better image of salt and subsalt reflection structures in this area.

IV.1.5.a. Iterative Stolt FK time Migration:

Iterative FK migration overcomes the restrictions, of Stolt constant velocity algorithm, on temporal velocity changes by applying cascading F-K migration in time. The input stacked section is migrated several times in constant velocity stages. The changes in velocity function for each migration stage is small, hence approximating the Stolt's constant velocity algorithm. After each single stage is performed, the migration is completed down to the time corresponding to that stage while the rest of stacked section is partially migrated. The results of iterative FK time migration performed after post-stack wave equation datuming are shown in Figures 4.27, 4.28, and 4.29 as shown on these Figures, iterative FK migration produced poor and uninterpretable image for topsalt, basesalt and top of basement reflectors. Considerable distortion of these reflectors and migration artifacts can be observed on the middle part of line 33 (shotpoints 278 to 218) underneath the reef buildups (Fig. 4.28) and below shotpoints 344 to 325 at the shelf area (Fig. 4.27). The distortions include significant pull-up and mispositioning of base of salt and top of subsalt reflectors, and dispersion of their amplitudes. Edge effects and spurious events observed in the deeper part of the section further complicate the problem. The lateral velocity changes associated with irregular geometry of salt and steeply dipping boundaries of subsalt section in these parts of line 33 suggest that the poor imaging is caused by laterally invariant velocity assumption inherited in iterative FK migration algorithm. Iterative FK migration, however, made a modest improvement in subsalt

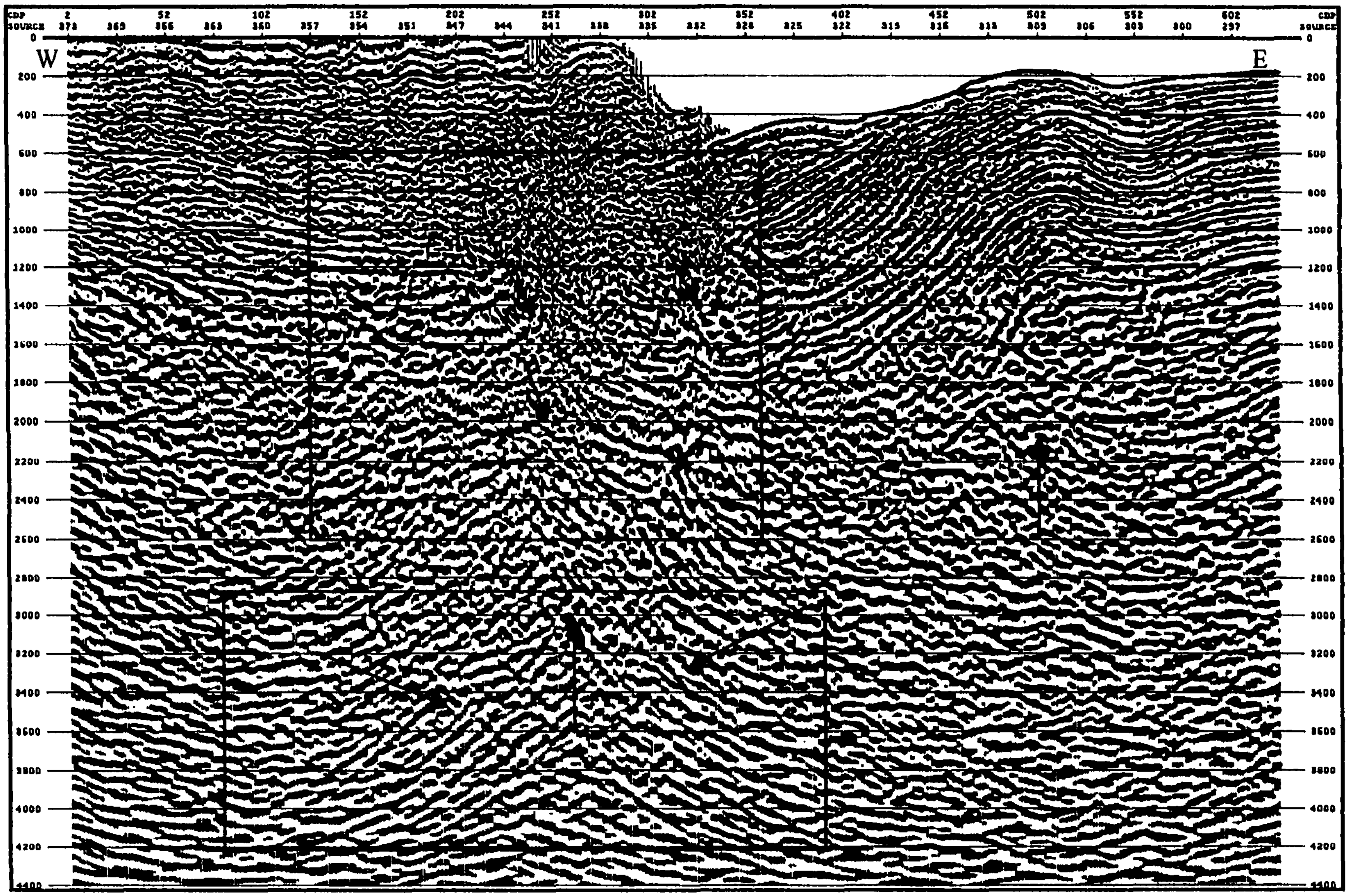

Figure 4.27. The western part of seismicline 33 after iterative F-K time migration. Note the distortion of salt and subsalt seismic events (red arrows) and the spurious events (blue arrows) in the deeper part of the line.

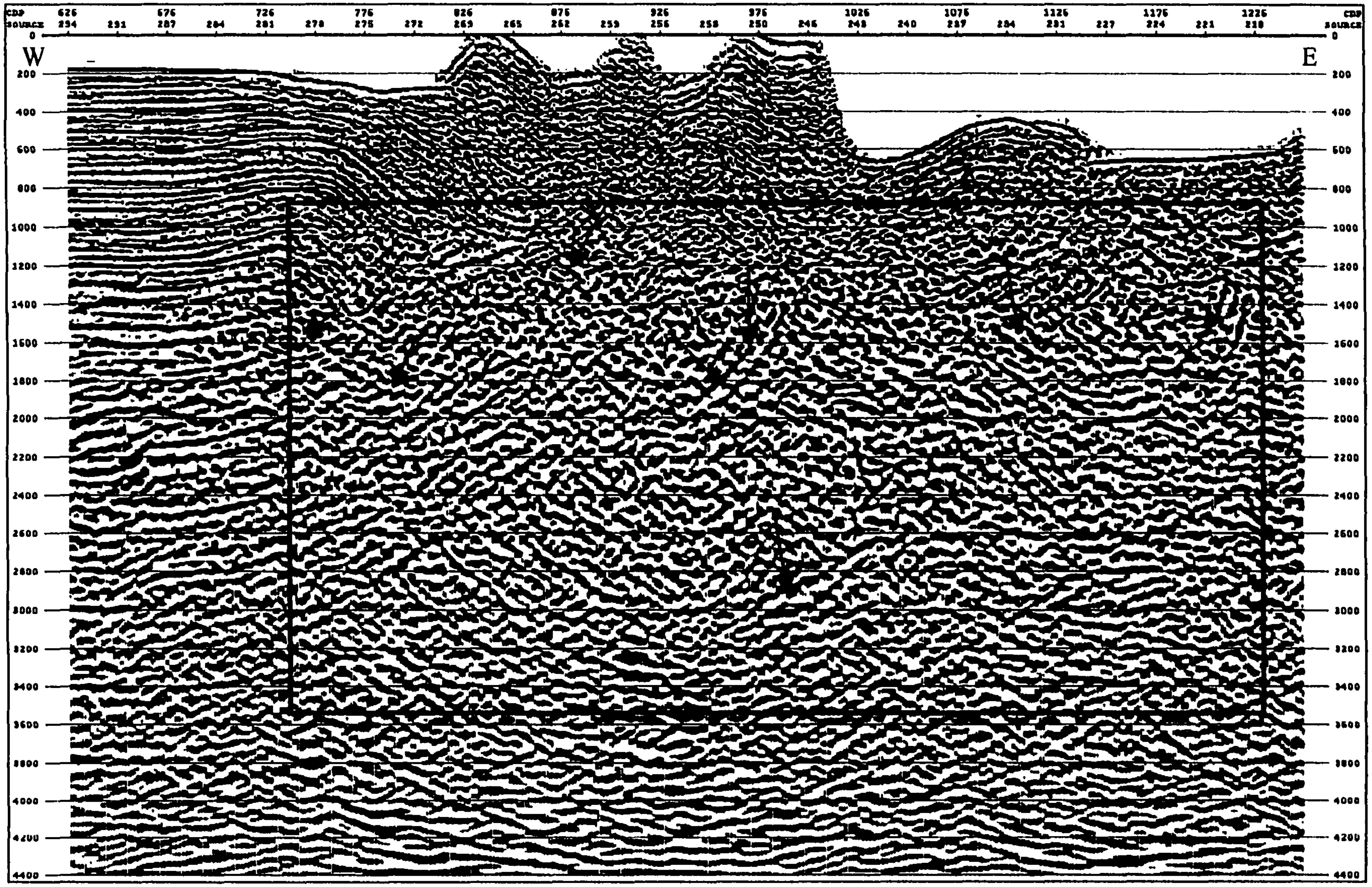

Figure 4.28. The middle part of line 33 after iterative F-K time migration. The top and base of salt and top of basement reflectors are very poorly imaged and uninterpretable. Note the distortion of subsalt reflection amplitudes, pull up of base of salt reflector, and the spurious events in the deeper part of the section.

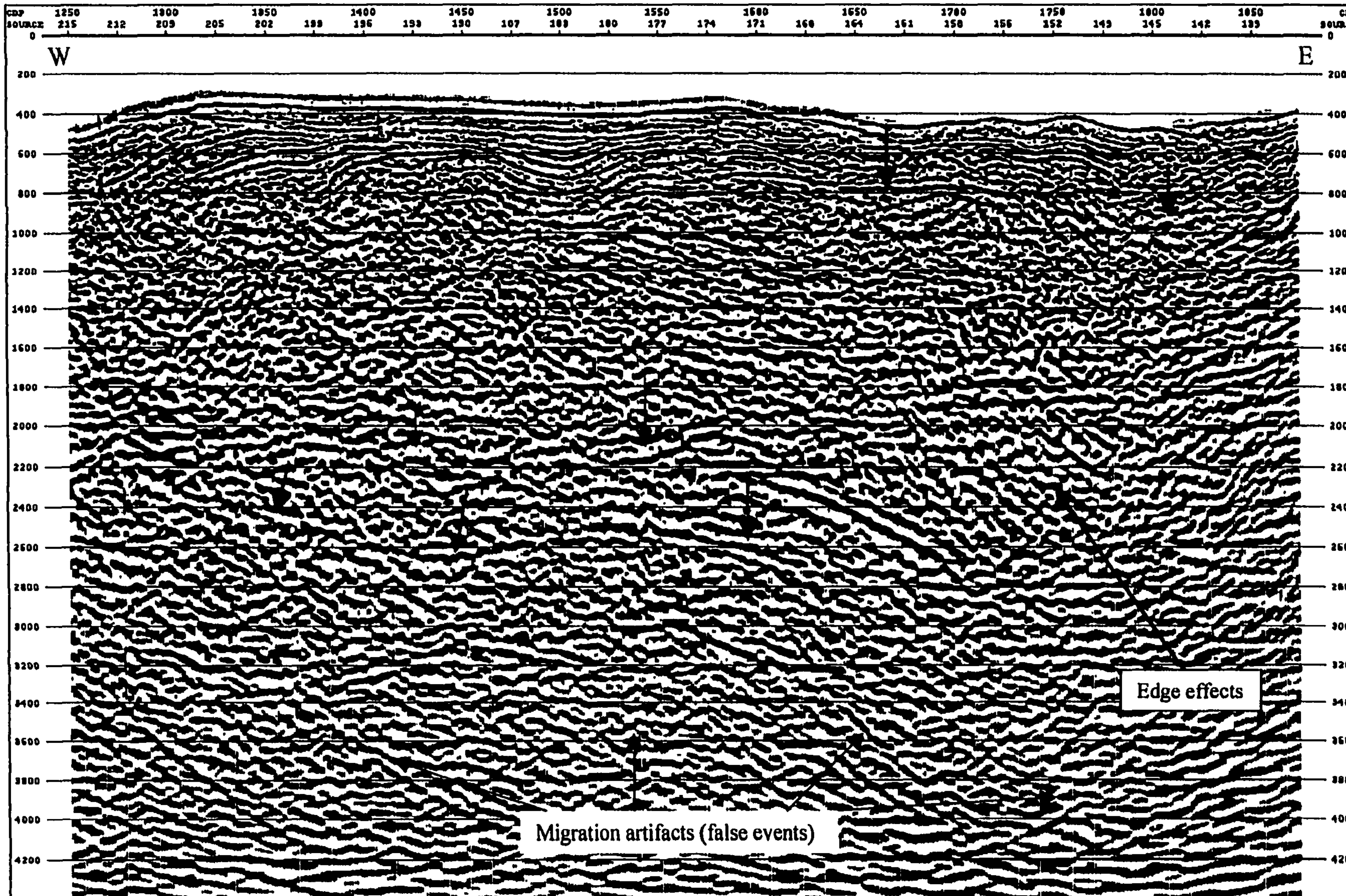

Figure 4.29. The eastern part of line 33 after iterative F-K time migration. Topsalt, basesalt and top of basement are high-lighted in blue, green, and red arrows, respectively.

(a)

```
FLOW - WEQDatum  Mon Aug  5 16:32:32 1996
  Output - line33 Add 1873 Over 0
 SEG-Y Input

FLOW - WEQDatum  Mon Dec 23 14:51:54 1996
  Output - 33wbdtm2750ftDN Add 1873 Over 0
 Disk Data Input
  Read data from other lines/surveys?          No
  Select dataset                               line33
  Trace read option                            Sort
    Select primary trace header entry          CDP bin number
    Select secondary trace header entry        No trace header entry selec
    Sort order for dataset
    */
    Presort in memory or on disk?              Memory
  Read the data multiple times?                No
  Process trace headers only?                  No
  Override input data's sample interval?       No
 Post Stack Wave Eq. Datuming★
  CDP spacing (feet or meters)                 82.
  Maximum frequency (in Hz)                    50.
  Depth step size for datuming                 0.
  Elevation to datumize to                     -2750.
  What maximum dip would you like to           50 degrees
  handle?
  Datumize through a constant velocity?        No
  Get interval velocities from database?       Yes
    Select interval vs. depth velocity         Vintindpthshift100msffordtr
  file
  Get velocity reference datum from the        No
  database?
     Reference datum for the velocity          0.
  field.
  Change maximum memory usage?                 No
  Taper the edges?                             No
  Re-kill dead traces?                         No
 Disk Data Output
  Output Dataset Filename                      33wbdtm2750ftDN
  New, or Existing, File?                      New
  Record length to output                      0.
  Trace sample format                          16 bit
```

(b)

```
  Skip primary disk storage?                   No

FLOW - WEQDatum  Mon Dec 23 15:25:11 1996
  Output - 33wb02dtm0000fsUP Add 1873 Over 0
 Disk Data Input
  Read data from other lines/surveys?          No
  Select dataset                               33wb02dtm2750ftDN
  Trace read option                            Get All
  Read the data multiple times?                No
  Process trace headers only?                  No
  Override input data's sample interval?       No
 Post Stack Wave Eq. Datuming★
  CDP spacing (feet or meters)                 82.
  Maximum frequency (in Hz)                    50.
  Depth step size for datuming                 0.
  Elevation to datumize to                     0.
  What maximum dip would you like to           50 degrees
  handle?
  Datumize through a constant velocity?        Yes
  Velocity to use for datuming                 8000.
  Change maximum memory usage?                 No
  Taper the edges?                             No
  Re-kill dead traces?                         No
 Disk Data Output
  Output Dataset Filename                      33wb02dtm0000fsUP
  New, or Existing, File?                      New
  Record length to output                      0.
  Trace sample format                          16 bit
  Skip primary disk storage?                   No

FLOW - WEQDatum  Mon Dec 23 15:35:06 1996
  Output - 33wb02dtm0000fsUPtrclngth Add 1073 Over 0
 Bandpass Filter★
  TYPE of filter                               Time and Space-Variant Filt
  Type of filter specification                 Ormsby bandpass
  PHASE of filter                              Zero
  Apply a notch filter?                        No
  Space-variant filter parameters
    1:0:8-16-44-66,5-10-36-54,4-8-24-36/
  Get time gates from the DATABASE?            No
    SELECT Primary time gate header word       CDP bin number
    SELECT Secondary time gate header          No trace header entry selec
  word
    SPECIFY filter time gate parameters
    1:0:0-600,600-1300,1300-5000/
 Trace Length
  New trace length                             4600.

FLOW - WEQDatum  Mon Dec 23 16:02:54 1996
  Output - 33wb02dtmIterFKMIG Add 1872 Over 0
 Iterative Stolt Migration★
  Maximum frequency to migrate (in Hz)         50.
  Get RMS velocities from DATABASE?            Yes
    SELECT RMS Velocity Parameter File         33RMSVEL
  Percent velocity scale factor                95.
  Specify migration stage  times and        Stolt stretch factors
    1000,1/2000,1/3000,1/4600,0.9,/
  Re-apply trace mutes?                        Yes
  Re-kill dead traces ?                        Yes
```

The processing sequence and parameters used in post-stack signal enhancement and iterative FK time migration performed on seismic line 33.

reflections continuity and definition of faults in areas with mild lateral velocity variation such as on the eastern part of line 33 (Fig. 4.29).

IV.1.5.b. The result of steep dip explicit finite difference migration:

The steep dip explicit finite difference time migration is performed after post-stack wave equation datuming to improve the imaging of salt and subsalt events in areas where iterative FK algorithm has not succeeded. Steep dip explicit FD time migration yielded a better result than iterative FK migration. Figures 4.30, 4.31 and, 4.32 compare the western, middle, and eastern parts of line 33 before and after post stack signal enhancement and steep dip explicit FD time migration. Close inspection of these Figures indicates a reasonable improvement in imaging of the topsalt, basesalt, and top of basement reflectors particularly in the western and eastern parts of the line. The improvement can be attributed to the fact that steep dip explicit FD time migration is better suited to dealing with moderate lateral velocity variations. However, the method does not yield an accurate result in areas with steep dip such as beneath the reefs in the middle of the section. In this area, the salt and subsalt reflections are poorly focused and show significant dispersion, which makes identification of faults and picking of topsalt, basesalt, and top basement reflectors very difficult. The poor performance of the steep dip explicit FD time migration in this case can be attributed the steep dip and strong lateral velocity variations exist in these areas.

IV.1.5.c. The result of residual migration:

Residual migration (Rothman, et al., 1985) is performed on line 33 to improve the finite difference performance in areas of steep dips. The result of one-pass of Stolt F-K migration followed by three passes of steep dip explicit FD time migration is shown in

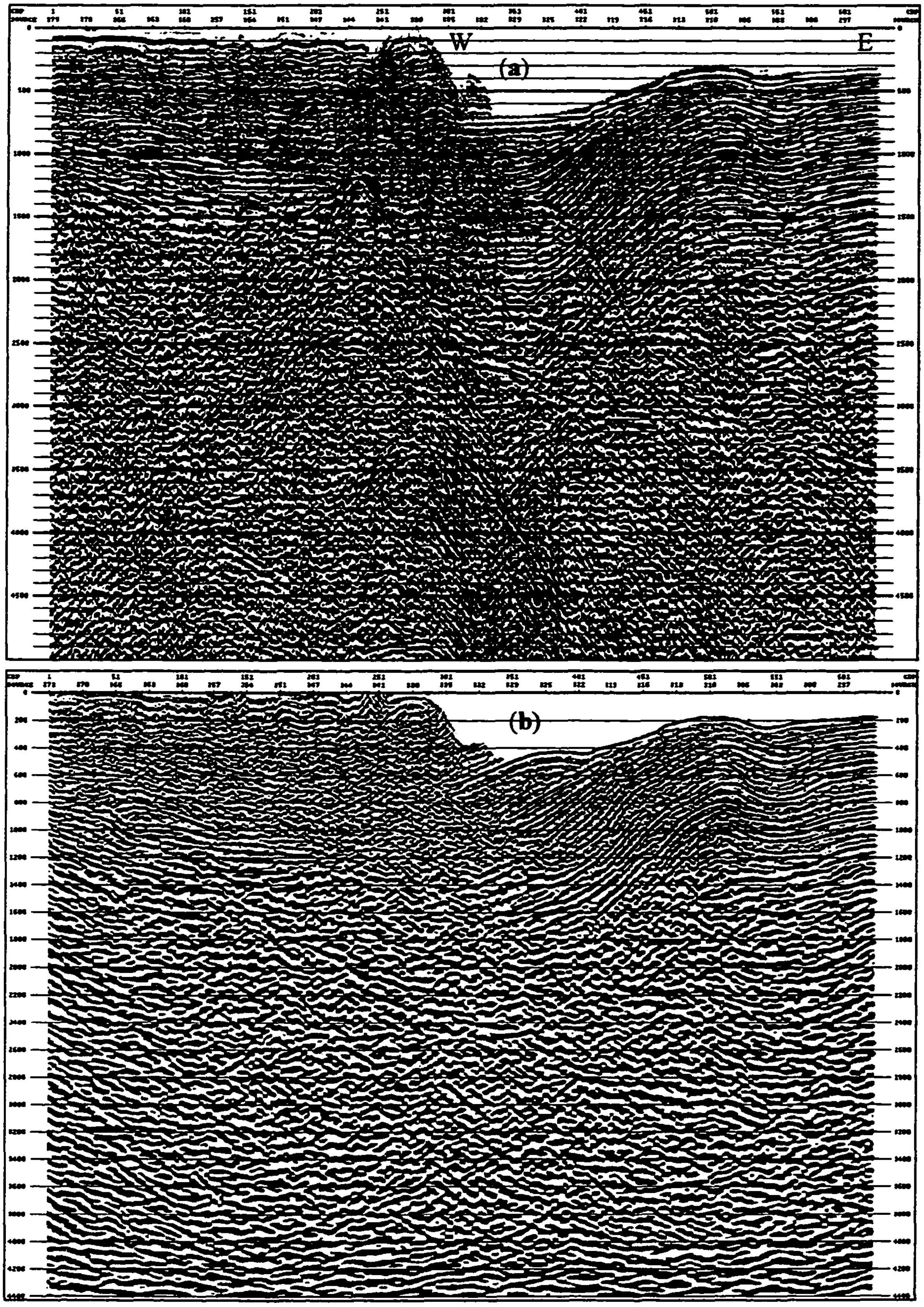

Figure 4.30. The western part of seismic line 33 before (a) and after (b) signal enhancement and steep dip explicit finite difference time migration.

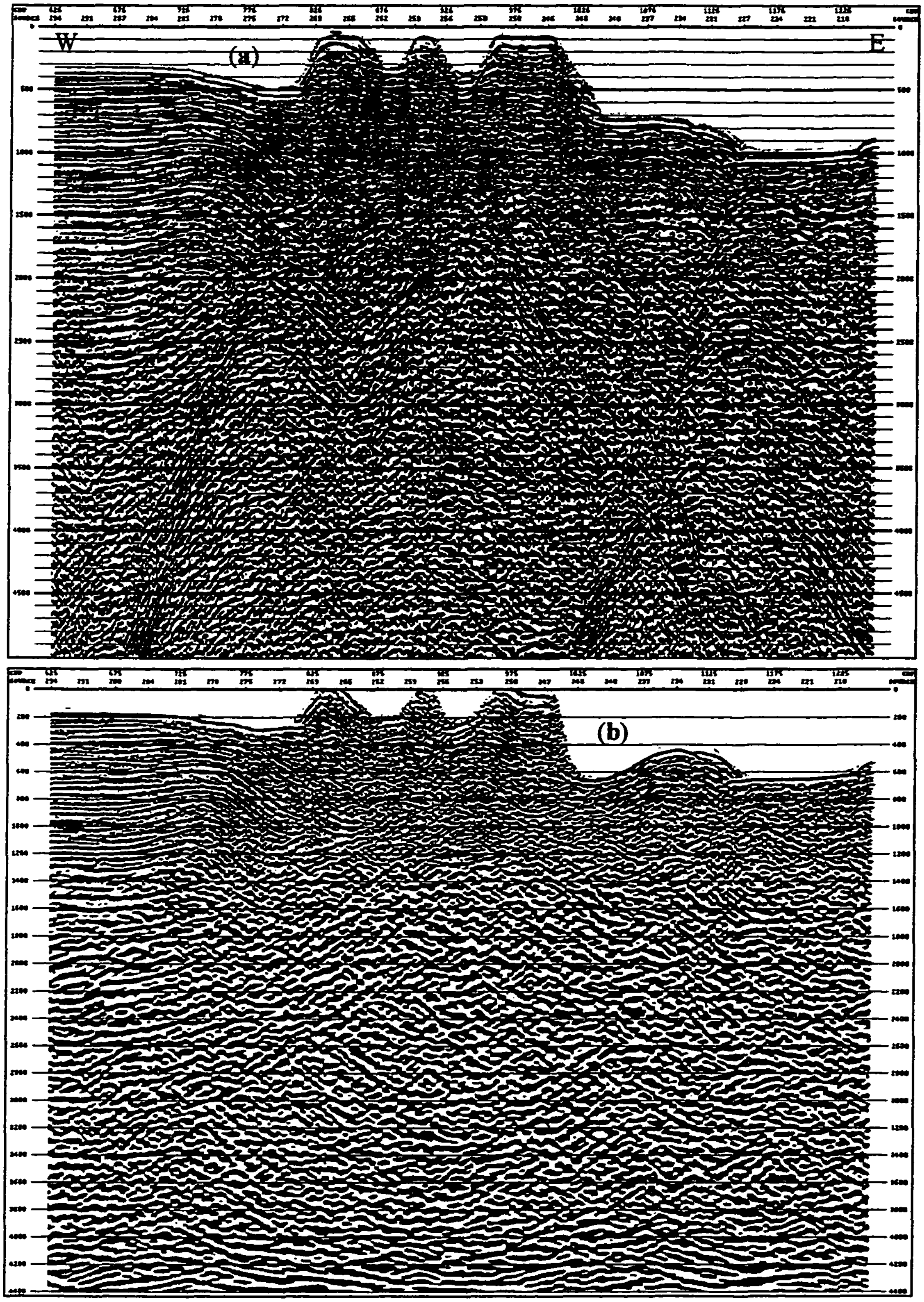

Figure 4.31. The middle part of seismic line 33 before (a) and after (b) signal enhancement and steep dip explicit finite difference time migration.

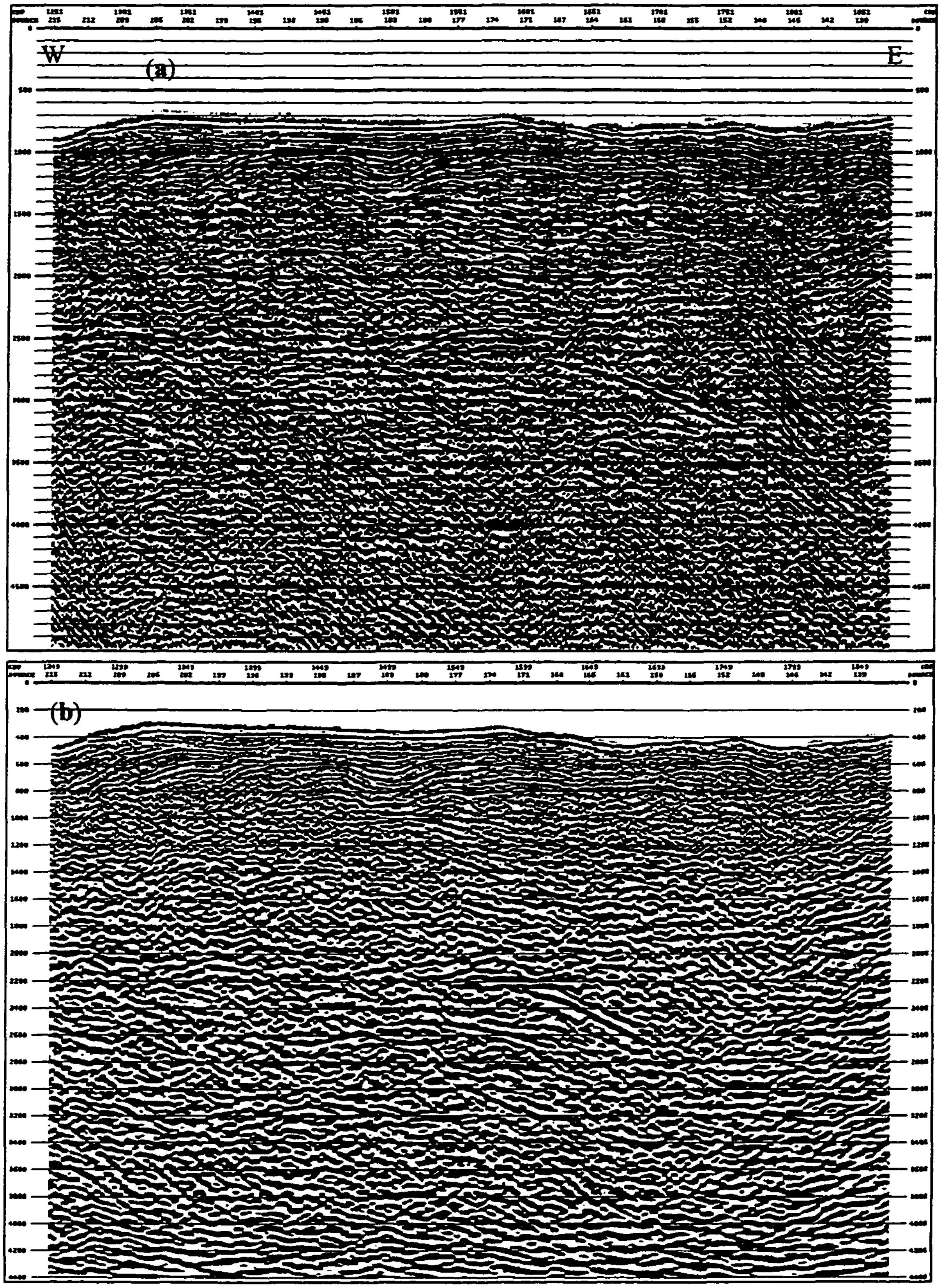

Figure 4.32. The eastern part of seismic line 33 before (a) and after (b) signal enhancement and steep dip explicit finite difference time migration.

FLOW - WEQDatum Mon Aug 5 16:32:32 1996	
Output - Line33 Add 1873 Over 0	
SEG-Y Input	
FLOW - WEQDatum Mon Dec 23 14:51:54 1996	
Output - 33wbdtm2750ftUN Add 1873 Over 0	
Post Stack Wave Eq. Datuming★	
Maximum frequency (in Hz)	50.
Datumize through a constant velocity?	No
Get interval velocities from database?	Yes
Select interval vs. depth velocity file	Vintindpthshift100msffordtm
FLOW - WEQDatum Mon Dec 23 15:25:11 1996	
Output - 33wb82dtm8000fsUP Add 1873 Over 0	
Post Stack Wave Eq. Datuming★	
Maximum frequency (in Hz)	50.
Datumize through a constant velocity?	Yes
FLOW - WEQDatum Mon Dec 23 15:35:06 1996	
Output - 33wb82dtm8000fsUPtrclngth Add 1873 Over 0	
Bandpass Filter★	
TYPE of filter	Time and Space-Variant Filt
Type of filter specification	Ormsby bandpass
PHASE of filter	Zero
Apply a notch filter?	No
Space-variant filter parameters	
1:0:8-16-44-66,5-10-36-54,4-8-24-36/	
Get time gates from the DATABASE?	No
SELECT Primary time gate header word	CDP bin number
SELECT Secondary time gate header word	No trace header entry selec
SPECIFY filter time gate parameters	
1:0:0-600,600-1300,1300-5000/	
Trace Length	
New trace length	4600.
FLOW - WEQDatum Mon Dec 23 18:52:17 1996	
Output - 33wb82dtmexfdtmig Add 1873 Over 0	
Steep Dip Explicit FD Time Mig★	
Maximum frequency (in Hz)	50.
Get interval velocities from database?	Yes
Select interval vs. time velocity file	Vintimeshiftmims300ms
Re-apply trace mutes?	Yes
FLOW - WEQDatum Sat Jan 11 15:13:53 1997	
Output - 33wb82dtmexfdtmigTVF Add 1873 Over 0	
Bandpass Filter★	
TYPE of filter	Time and Space-Variant Filt
Type of filter specification	Ormsby bandpass
PHASE of filter	Zero
Apply a notch filter?	No
Space-variant filter parameters	
1:8-16-44-66,5-10-36-54,4-8-24-36/	
Get time gates from the DATABASE?	No
SELECT Primary time gate header word	CDP bin number
SELECT Secondary time gate header word	No trace header entry selec
SPECIFY filter time gate parameters	
1:0-1300,1300-2000,2000-5000/	
FLOW - WEQDatum Fri Jul 10 16:54:52 1998	
Output - 33wb82dtmexfdtmigTVFmut Add 1873 Over 0	
Trace Muting★	
Re-apply previous mutes	No
TYPE of mute	Top
Starting ramp	30.
SELECT mute parameter file	tpaftersdexfdtmig

The Processing sequence and parameters used in post-stack signal enhancement and steep dip explicit finite difference time migration performed on seismic line 33.

Figures 4.33, 4.34, and 4.35. It is obvious from these Figures that this method yielded much better results on the western part of the line than the steep dip explicit FD time migration discussed above. A modest improvement was also observed on the middle part of the seismic section. However, the eastern part of the line is degraded by what appear to be side boundary effects and spurious events that obscured reflection events (Fig. 4.35) and caused lateral smearing.

The results of time migration discussed above reveals significant improvement in spatial resolution, which enhanced our ability to define faults and pick topsalt, basesalt and top of basement reflectors in western and eastern part of line 33. However, the improvement in the middle part of line 33 and below shotpoints 344-319 of the western part is not as great as had been hope for. It appears that the situation is more complicated in these areas. As already pointed out, these areas are dominated by irregular salt geometry, tilted fault blocks, significant lateral velocity changes, and rugged seafloor. These led to significant distortion of salt and subsalt reflection structures as revealed by 2-D seismic modeling discussed previously. The inadequate performance of time migrations, in this area, can be attributed to their inability to accurately image reflections with complex velocity distributions.

IV.1.5.d. <u>The results of steep dip finite difference depth migration</u>:

The steep dip finite difference depth migration is better suited to dealing with lateral velocity changes. It corrects the error associated with changes in transmission time by applying laterally varying time shift to each trace. Compared to the result of migration methods discussed above, steep dip finite difference depth migration yields reasonably good result without distorting the wavefield (Figs. 4.36, 4.37, 4.38). The analysis of these

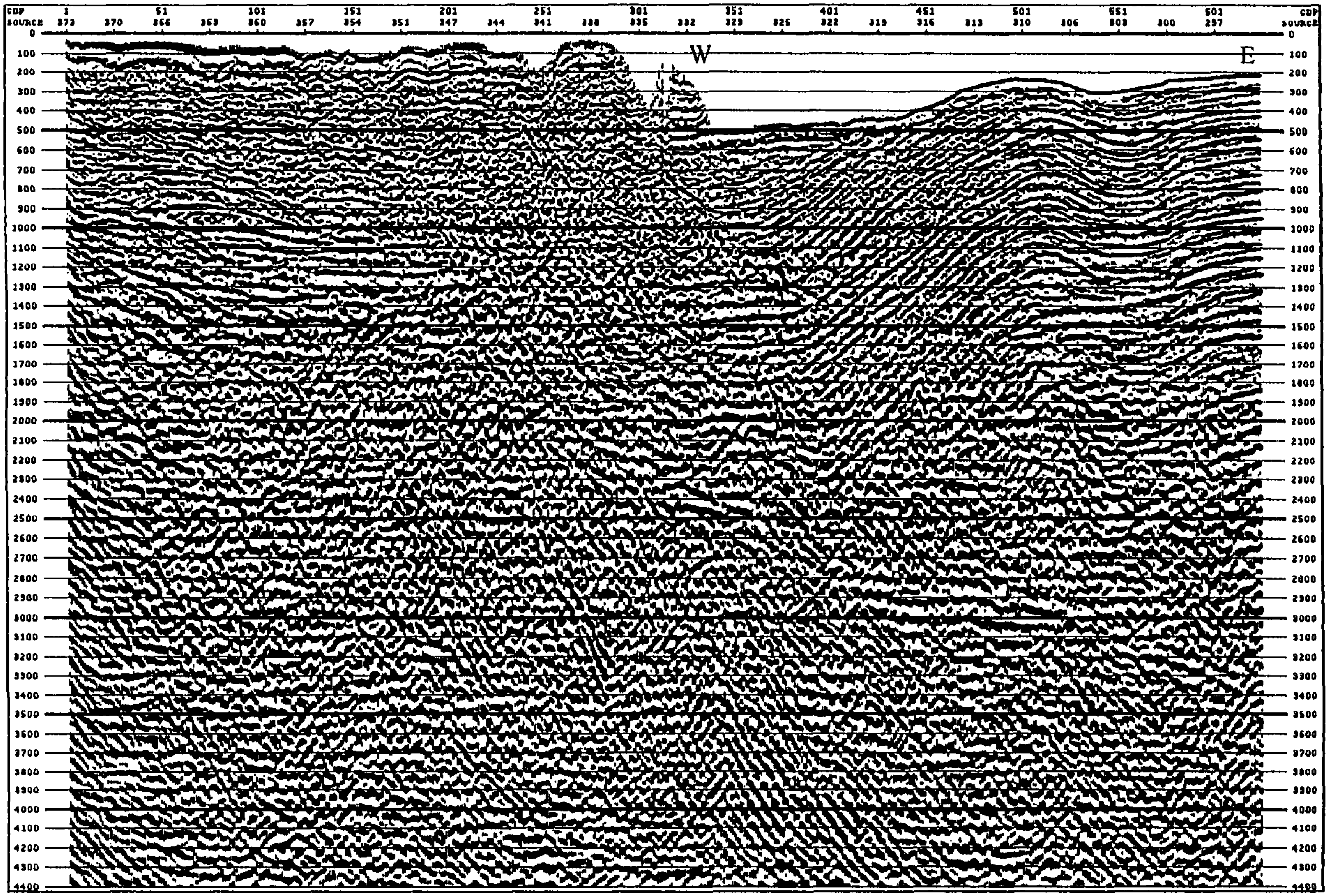

Figure 4.33. The western part of line 33 after F-K time migration followed by three passes of steep dip explicit FD time migration.

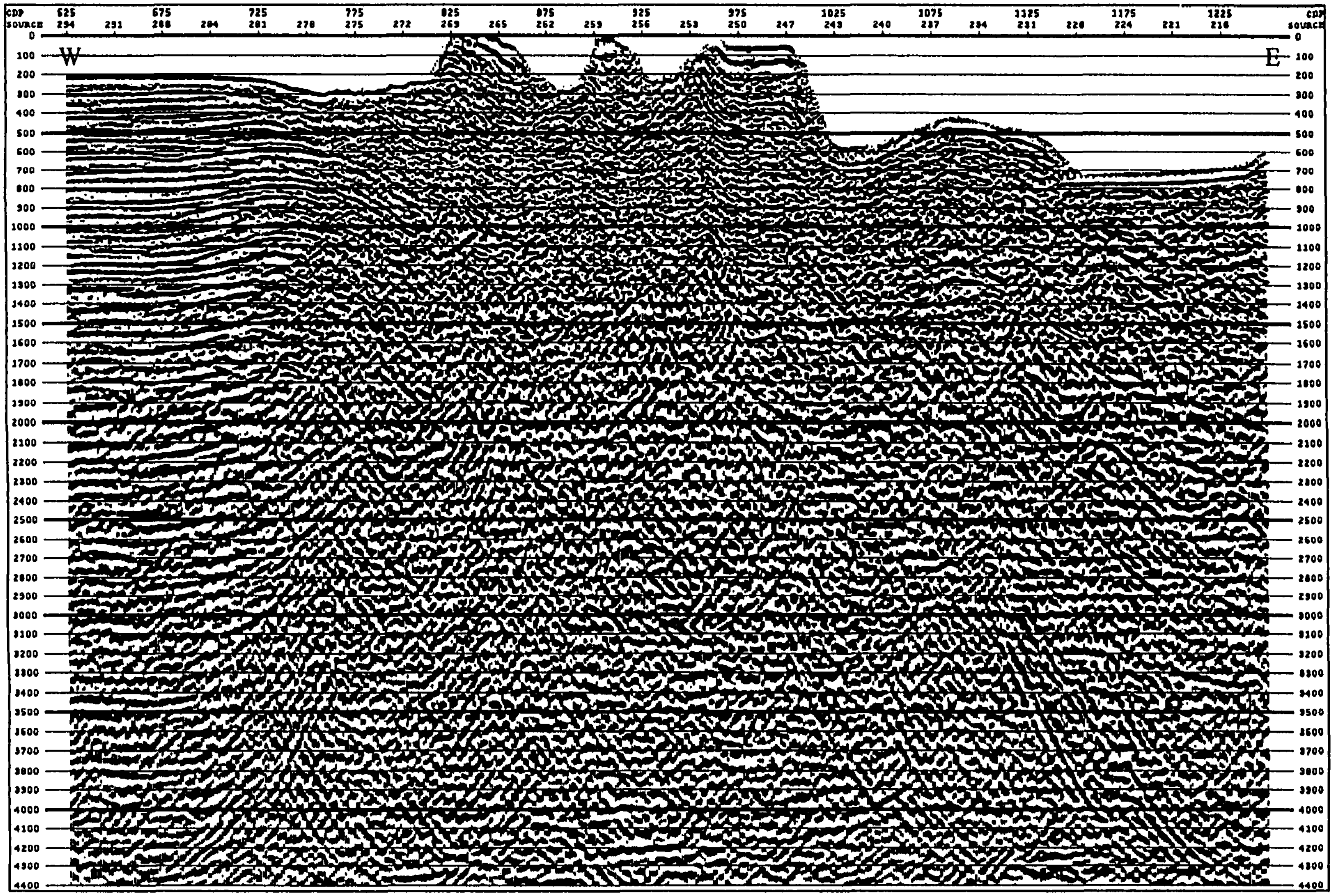

Figure 4.34. The middle part of line 33 after F-K time migration followed by three passes of steep explicit FD time migration.

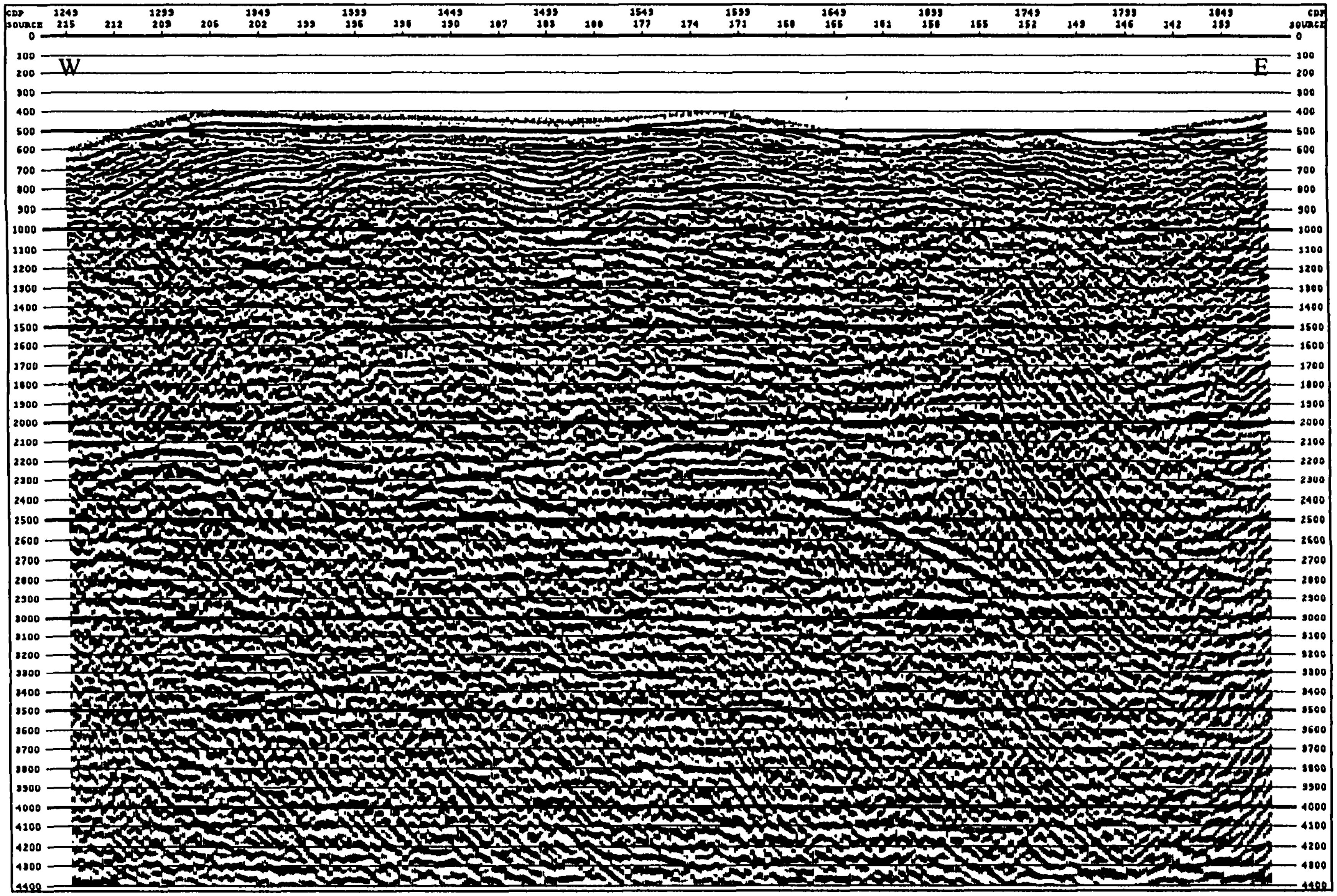

Figure 4.35. The eastern part of line 33 after F-K time migration followed by three passes of steep dip explicit FD time migration.

```
FLOW - WEQDatum  Mon Aug  5 16:32:32 1996
  Output - line33 Add 1873 Over 0
 SEG-Y Input

FLOW - WEQDatum  Tue Oct 29 23:07:32 1996
  Output - 33WBDTUMTO-2700ftDN Add 1873 Over 0
 Post Stack Wave Eq. Datuming
  Maximum frequency (in Hz)                          50.
  Datumize through a constant velocity?              No
  Get interval velocities from database?             Yes
    Select interval vs. depth velocity               33ViDfrmViTIVEFORDATUM
  file

FLOW - WEQDatum  Tue Oct 29 23:30:17 1996
  Output - 33WBDTMTOZEROWITH9500f/sUP Add 1873 Over 0
 Post Stack Wave Eq. Datuming
  Maximum frequency (in Hz)                          50.
  Datumize through a constant velocity?              Yes

FLOW - WEQDatum  Tue Oct 29 23:37:13 1996
  Output - 33WBDTUMTOZEROTRCELENGUP Add 1873 Over 0
 Trace Length
  New trace length                                   5000.

FLOW - WEQDatum  Tue Oct 29 23:56:38 1996
  Output - 33MFKMINISINGLEPASS5000f/s Add 1873 Over 0
 Memory Stolt F-K Migration
  Maximum frequency  to migrate (in Hz)              50.
    Select velocity file                             RMSVELATCDPMODTOWBDTM
  Number of traces to smooth velocity                0
  field over
  Percent velocity scale factor                      100.
  Stolt stretch factor                               0.6
  Re-apply trace mutes?                              Yes
  Re-kill dead traces?                               Yes

FLOW - WEQDatum  Sat Nov  2 13:29:35 1996
  Output - 332ndpassEXFDTIMEMIG Add 1873 Over 0
 Steep Dip Explicit FD Time Mig.
  Maximum frequency (in Hz)                          50.
  Get interval velocities from database?             Yes
```

(Continue on next page)

Post-stack processing sequence performed on line 33. Memory F-K followed by three passes of steep dip explicit FD time mig.

```
    Select interval vs. time velocity          33CDPVitfor2nDFDCASCADE
  file
  Re-apply trace mutes?                        Yes

FLOW - WEQDatum  Sat Nov  2 23:54:45 1996
  Output - 333ndpassEXFDTMIG Add 1873 Over 0
 Steep Dip Explicit FD Time Mig.
  Maximum frequency (in Hz)                    50.
  Get interval velocities from database?       Yes
    Select interval vs. time velocity          33CDPVitfor3rdFDCASCADE
  file
  Re-apply trace mutes?                        Yes

FLOW - WEQDatum  Sun Nov  3 00:58:03 1996
  Output - 334THpassEXFDTM Add 1873 Over 0
 Steep Dip Explicit FD Time Mig.
  Maximum frequency (in Hz)                    50.
  Get interval velocities from database?       Yes
    Select interval vs. time velocity          33Vint4thpass
  file
  Re-apply trace mutes?                        Yes

FLOW - WEQDatum  Mon Jul 20 17:48:32 1998
  Output - 334ThpassEXFDTMmut Add 1873 Over 0
 Trace Muting
  Re-apply previous mutes                      No
  TYPE of mute                                 Top
    Starting ramp                              30.
    SELECT mute parameter file                 after4pathsdfdtmig
```

Post-stack processing sequence performed on line 33. Memory F-K and 3passes of steep dip explicit FD time migration.

results reveals significant imaging improvement particularly in the areas that time migrations are unable to handle such as the middle part of the seismic section.

First of all, the diffractions are well focused and basement-involved normal faults as well as the salt-related listric faults are better defined. In addition to delineation of faults, the overall spatial resolution, within the sequences and at their boundaries, has improved significantly. The continuity of topsalt, basesalt, and top of basement reflectors are well-imaged. The steeping dipping, the linear events associated with rugged water bottom, the curved event observed on the depocentre, and the diffractions all disappeared. Even the events that overlapped with subsalt and basement below shotpoints 329 and 269 are no longer visible. The migration artifacts include false 'smiling', spurious events in deeper part of the section, and side boundary effect at the end of the line to the east.

IV.1.5.e. Comparison of migration results:

Compare to the three other methods, finite difference depth migration yielded a reasonably well-imaged salt and subsalt reflection events, on all three parts of line 33, with minimum amount of distortions. Residual time migration produced better results on the western and the middle portions of the line than steep dip explicit finite difference time migration. However, steep dip explicit FD time migration yields better image on the eastern part of the line than residual time migration. Compare to the other three algorithms, iterative FK time migration produced least accurate and distorted image particularly on the western and middle parts of line 33.

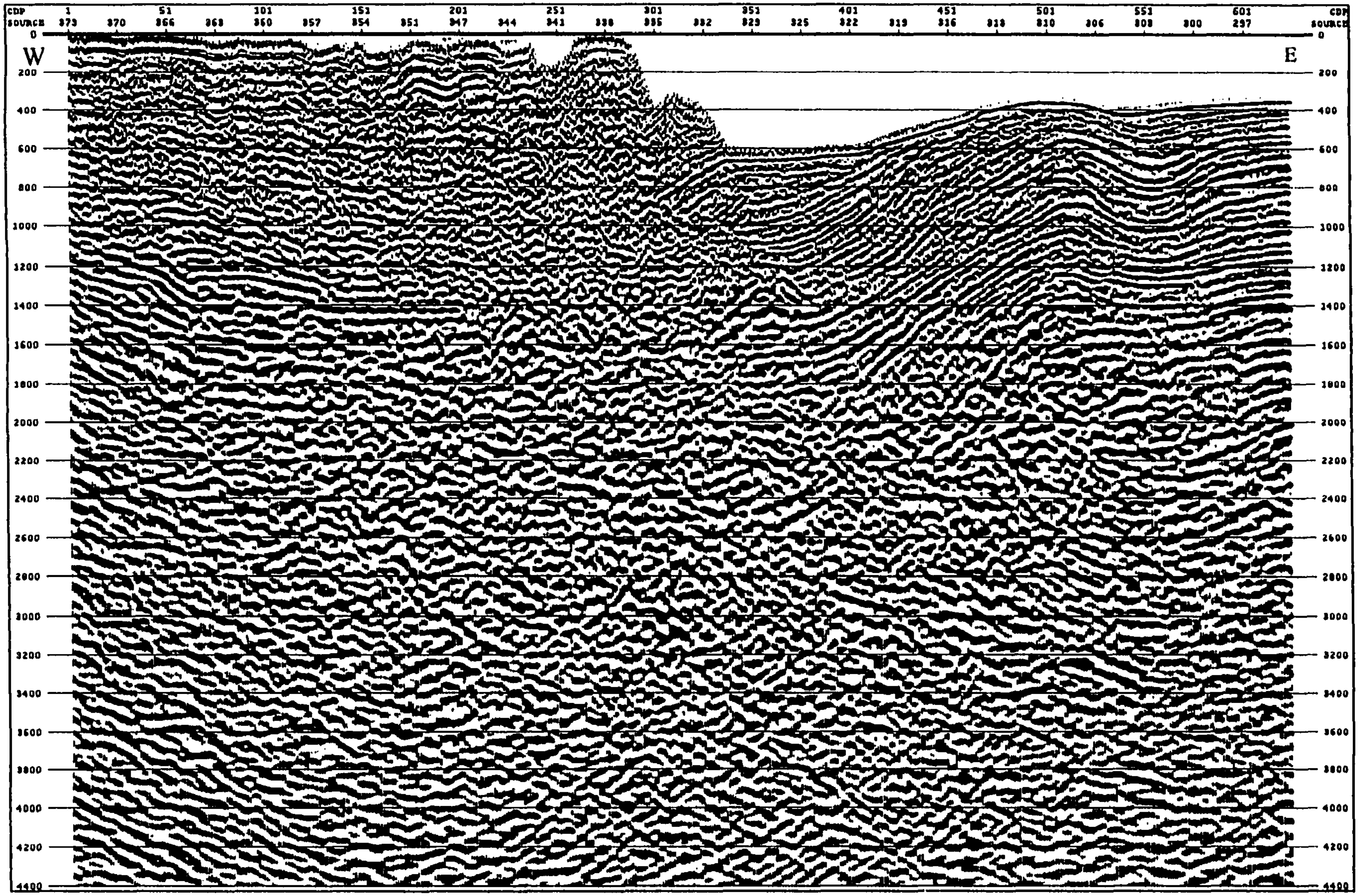

Figure 4.36. The western part of seismic line33 after post-stack steep dip finite difference depth migration.

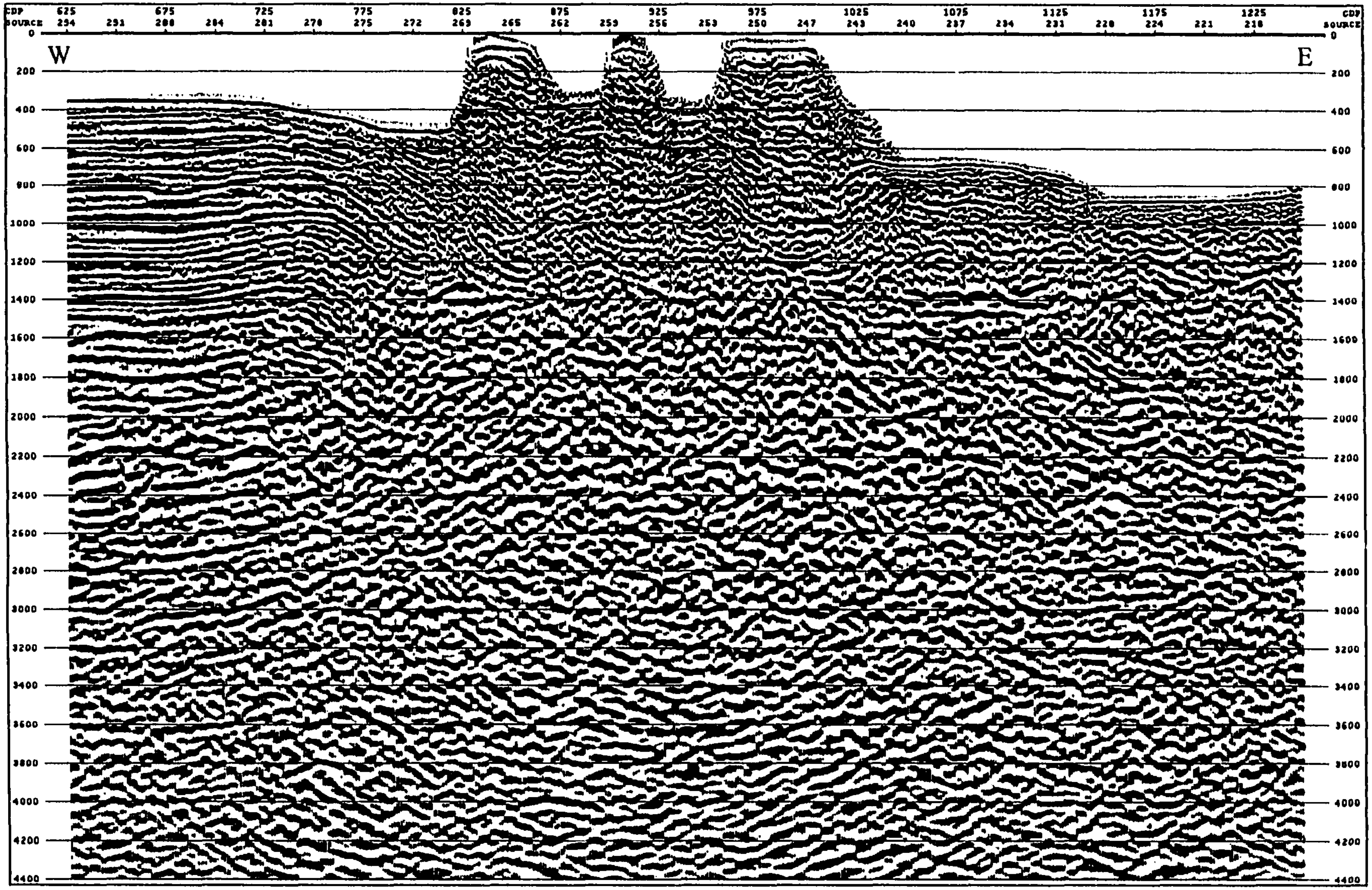

Figure 4.37. The middle part of seismic line 33 after post-stack steep dip FD depth migration.

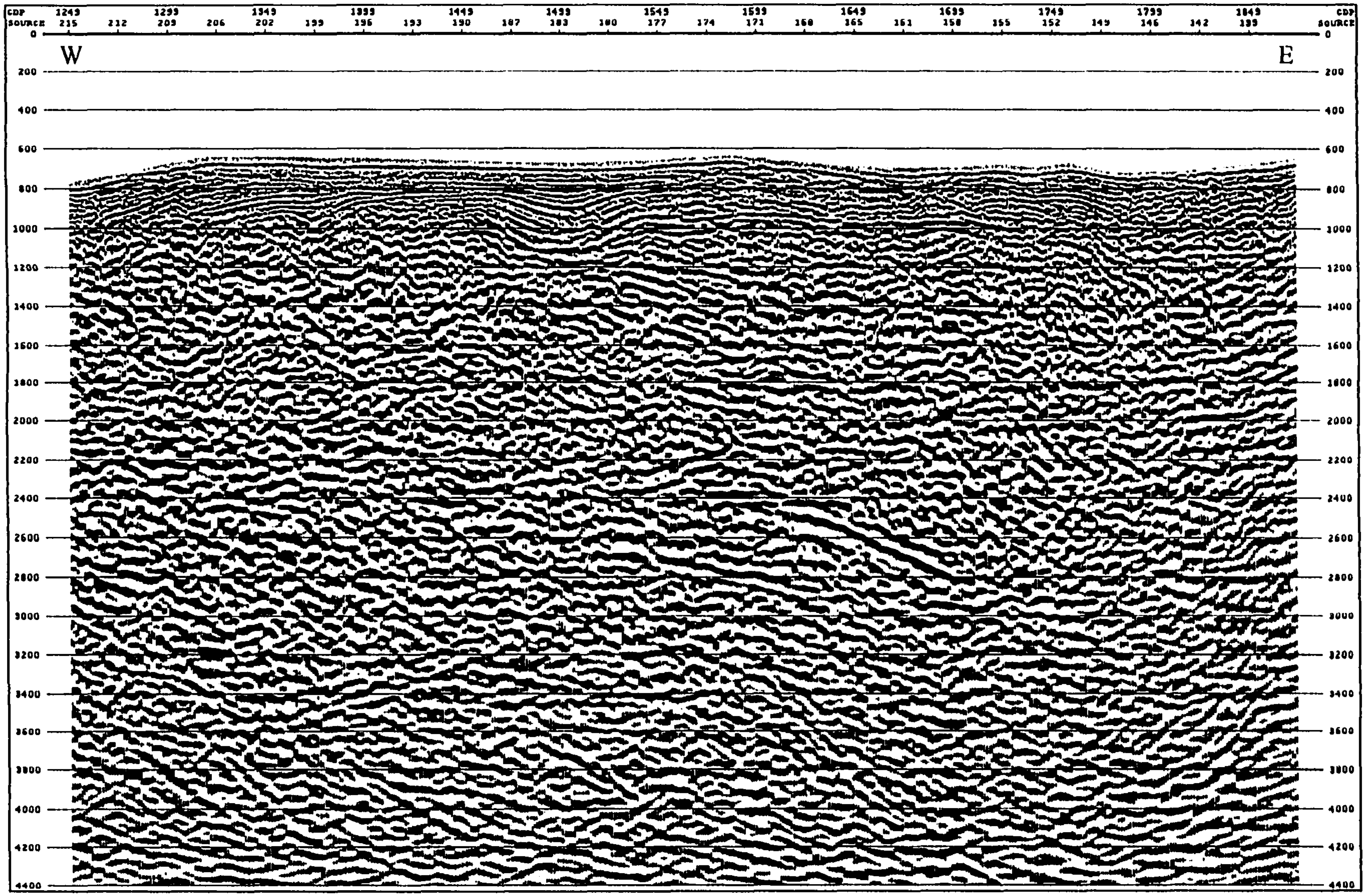

Figure 4.38. The eastern part of seismic line 33 after steep dip finite difference depth migration.

```
FLOW - WEQDatum  Mon Aug  5 16:32:32 1996
  Output - line33 Add 1873 Over 0
 SEG-Y Input

FLOW - WEQDatum  Tue Dec 24 17:00:45 1996
  Output - 33UNdtm82FLTRSDFDDMIG Add 1873 Over 0
 Bandpass Filter ★
  TYPE of filter                                Time and Space-Variant Filt
  Type of filter specification                  Ormsby bandpass
  PHASE of filter                               Zero
  Apply a notch filter?                         No
  Space-variant filter parameters
    1:8-16-44-66,5-10-36-54,4-8-24-36/
  Get time gates from the DATABASE?             No
    SELECT Primary time gate header word        CDP bin number
    SELECT Secondary time gate header           No trace header entry selec
  word
    SPECIFY filter time gate parameters
    1:0-1300,1300-2000,2000-5000/
 Steep Dip FD Depth Migr.★
  Maximum frequency vs depth to migrate
    0-50,1300-50,2000-36,5000-24/
  Get interval vs depth velocities from         Yes
  DATABASE?
    SELECT Interval vs depth Velocity           VintsmthforEXFDDMIG
  File
  Percent velocity scale factor                 95.
  Defines the largest angle to properly         45
  migrate.
  Output the migration in Depth or Time?        TIME
  Re-kill dead traces ?                         Yes

FLOW - WEQDatum  Sat Jan 11 00:05:36 1997
  Output - 33undtm82fltrSDFDDMIGFLTR Add 1873 Over 0
 Bandpass Filter ★
  TYPE of filter                                Time and Space-Variant Filt
  Type of filter specification                  Ormsby bandpass
  PHASE of filter                               Zero
  Apply a notch filter?                         No
  Space-variant filter parameters
    1:8-16-44-66,5-10-36-54,4-8-24-36/
  Get time gates from the DATABASE?             No
    SELECT Primary time gate header word        CDP bin number
    SELECT Secondary time gate header           No trace header entry selec
  word
    SPECIFY filter time gate parameters
    1:0-1300,1300-2000,2000-5000/

FLOW - WEQDatum  Mon Jul 13 01:03:40 1998
  Output - 33undtm82fltrsdfddmiffltrmut Add 1873 Over 0
 Trace Muting★
  Re-apply previous mutes                       No
  TYPE of mute                                  Top
    Starting ramp                               30.
    SELECT mute parameter file                  aftersdfddmig
```

Processing sequence and parameters used in post-stack signal enhancement and steep dip finite depth migration performed on line 33.

IV.2. **Seismic Line 28-50**

Seismic line 28-50 runs from west to east and is located about 19 km north of line 33. This dip line begins 7 km east of the shoreline and extends 21-km seaward (Fig. 1.2). The water depth varies from 200 feet over the shelf area and the reef buildups to 1625 feet in the deeper parts. Between shotpoints 326 and 306, the water bottom is almost flat. Figure 4.39 shows the major features observed on line 28-50. These features include: Possible reef buildups on and just east of the shelf edge, a magnificent one close to the end of the line to the east, an anticlinal feature between shotpoint 306 and 279, and a depocenter between the shelf edge and the anticline. The line is also dominated by diffractions and steeply dipping linear events.

Initial interpretation

Because no well has been drilled on this line, the horizons corresponding to topsalt, basesalt, and top basement picked on line 33 are transferred to the strike lines and then carried to the dip line 28-50. Generally, the supra-salt, salt, and subsalt seismic events are poorly imaged on line 28-50. The two locations where sedimentary section is well developed and not significantly distorted are in the folded area underneath shotpoint 290 and in the depocenter below shotpoint 320. The strike lines are chosen such that they intersect line 28-50 at these locations. The picking and extrapolation of topsalt, and basesalt reflectors is rather speculative in areas that are poorly imaged such as underneath irregular seafloor.

IV.2.1. Imaging problems:

The most obvious imaging problems observed on this line are the areas below the irregular water bottom. In these areas, the reflection continuity of top and base of the salt

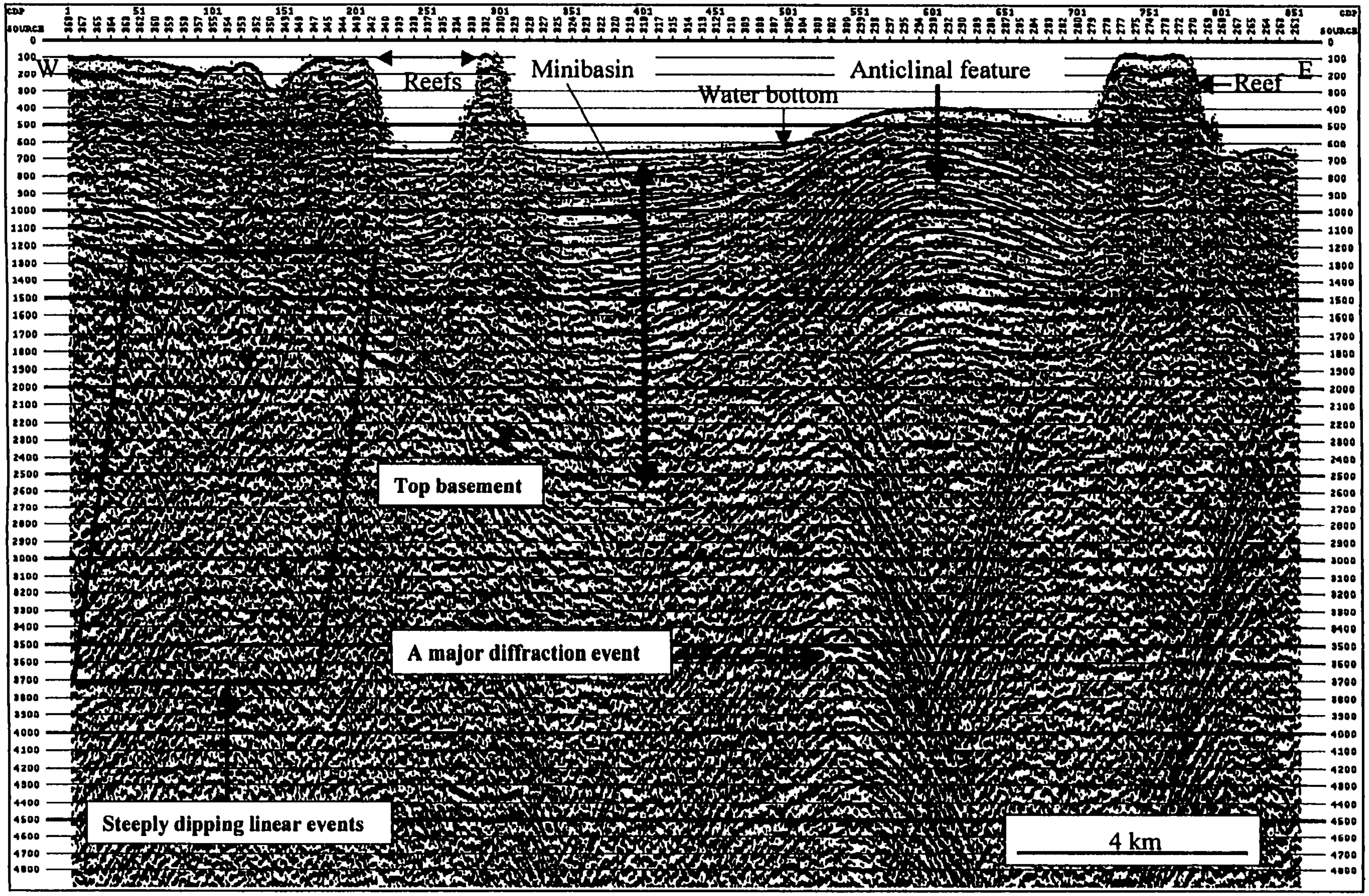

Figure 4.39. The major features observed on seismic line 28-50 before signal enhancement and migration.

and top basement reflectors are severely disrupted. The area underneath the reef buildup near the end of the line to the east (Fig. 4.40) is dominated by linear and diffraction events and severe reduction of amplitudes of desirable reflections. This resulted in disruption of the sequence boundaries and the internal reflections of salt and subsalt sections. The area beneath the shelf (Fig. 4.41) is overwhelmed with criss-cross pattern of steeply dipping linear events, which extend deep into the basement. A considerable amount of diffractions are also observed in this area. In the poorly imaged areas, the diffractions and linear events overlap with each other and commingle with salt and subsalt seismic events which makes the picking very difficult in the areas. The top and base of salt reflectors are significantly pulled up beneath the reef buildup just east of the shelf edge. The subsalt in the middle part of the line (between shotpoints: 315 to 299) is obscured by what appears to be a major diffraction event (Fig. 4.42) that extends to the bottom of the line. 2-D seismic modeling discussed below is used to investigate the causes of the imaging distortions observed on line 82-50.

IV.2.2. 2-D seismic modeling results and analysis:

Velocity-depth model 1

Figure 4.43a show the initial depth model constructed through forward modeling, using the initial interpretation and seismic derived velocity. The normal incidence synthetic section (Fig. 4.43b), resulting from zero offset ray-tracing performed on the initial depth model, simulates the main features observed on seismic line 28-50, such as the anticlinal structure, the minibasin, reef buildups, and the steeply dipping linear events beneath the reefs. Although this depth model recreates the major features observed on the real line, the

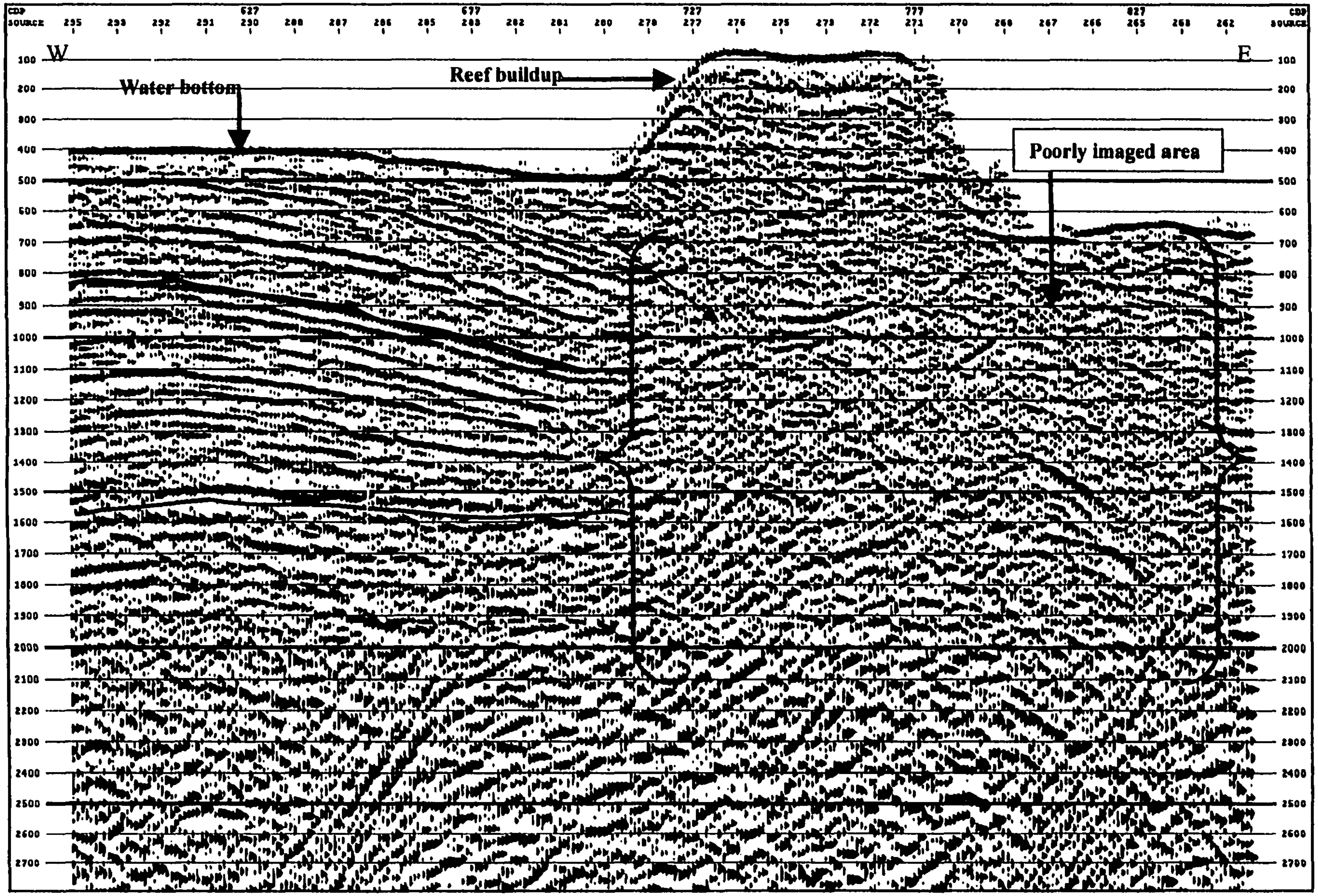

Figure 4.40. Line28-50 (enlarged) displaying the severe distortion of topsalt (blue), basesalt (green), and top of basement (red) reflectors below the reef buildup.

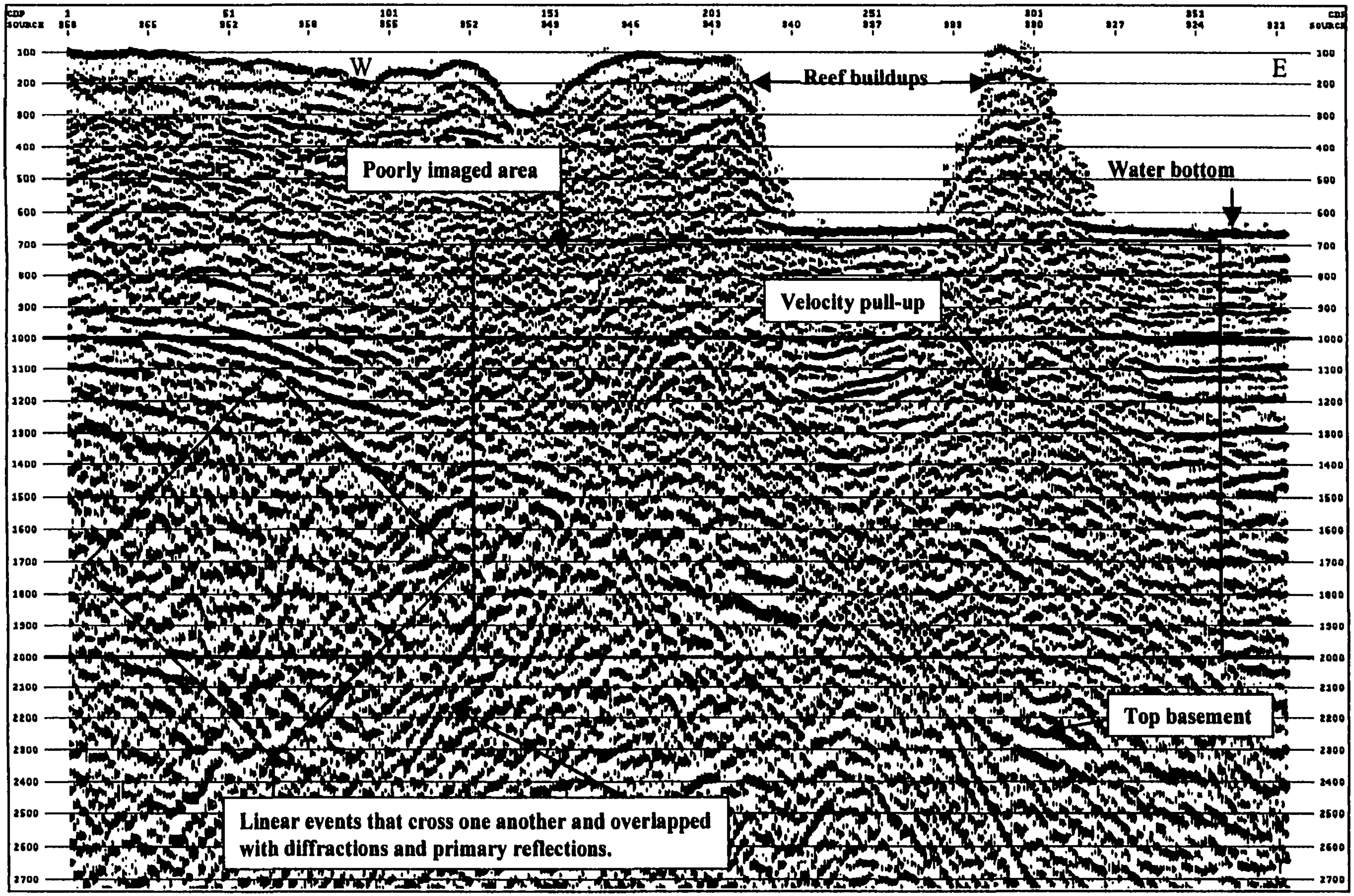

Figure 4.41. The image distortions observed on the western part of seismic line 28-50 before signal enhancement and migration.

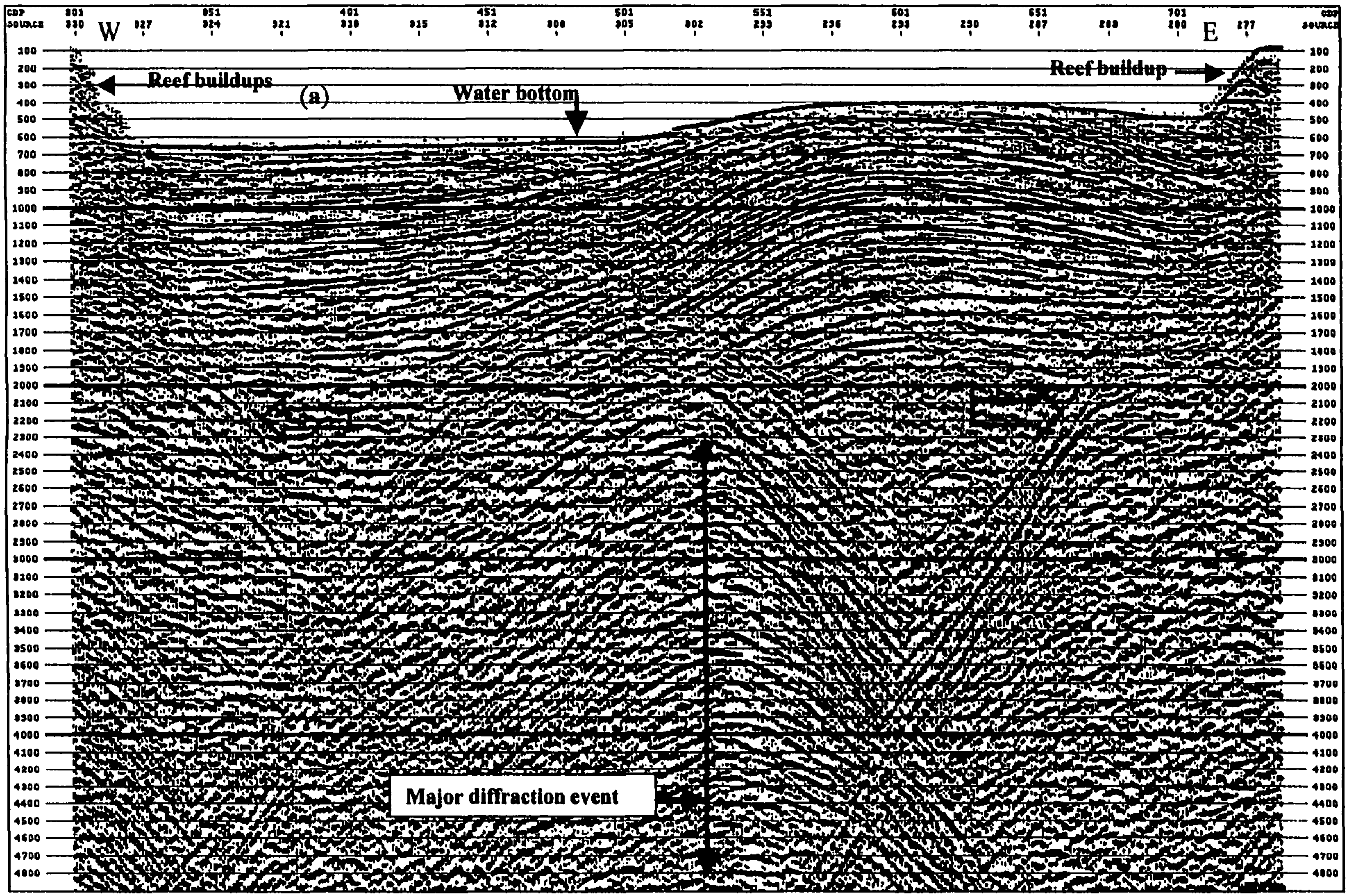

Figure 4.42. The image distortions observed on the middle part of line 28-50 before signal enhancement and migration. Steeply dipping, linear events associated with rugged seafloor are indicated by block arrows.

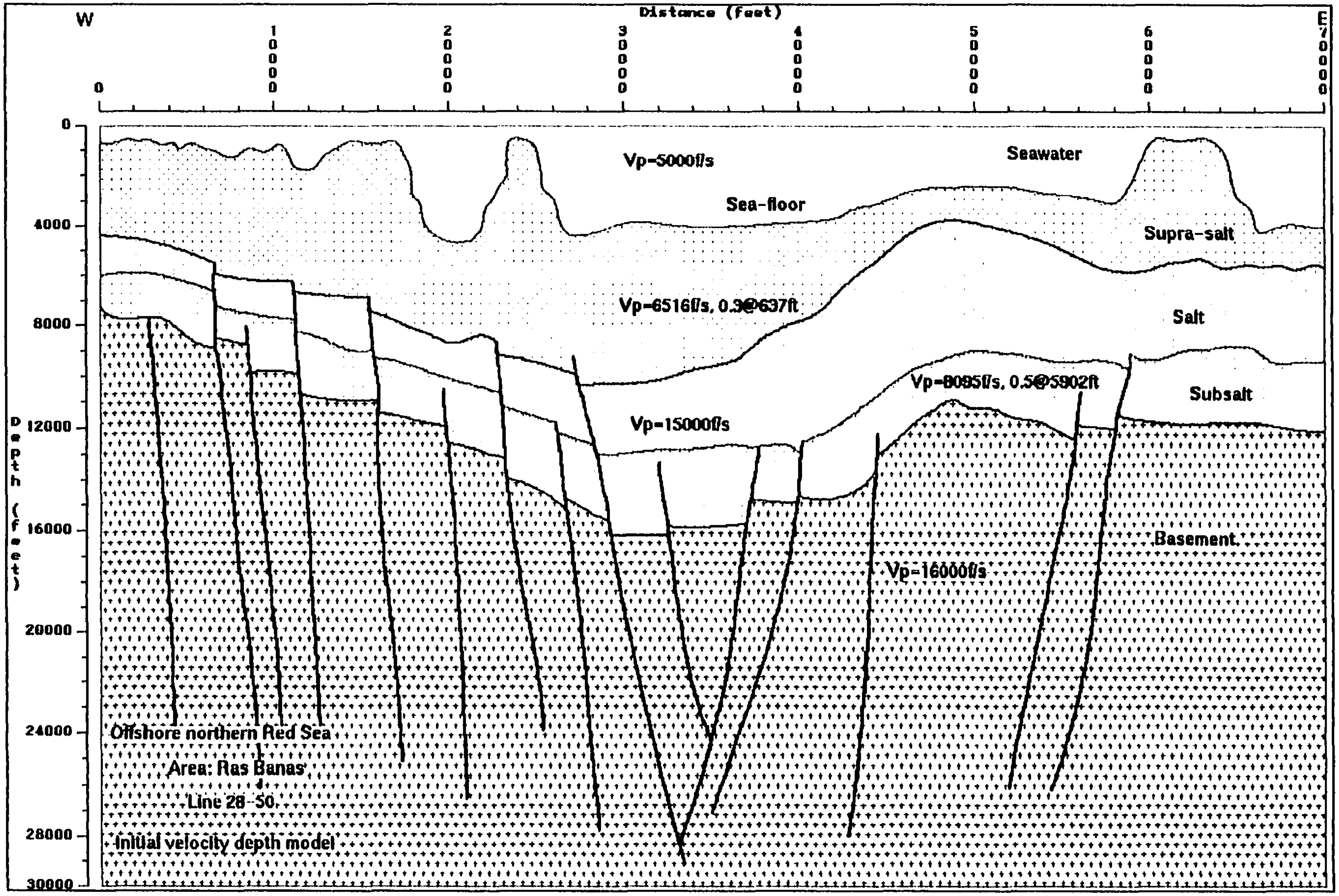

Figure 4.43a. Initial velocity-depth model for seismic line 28-50.

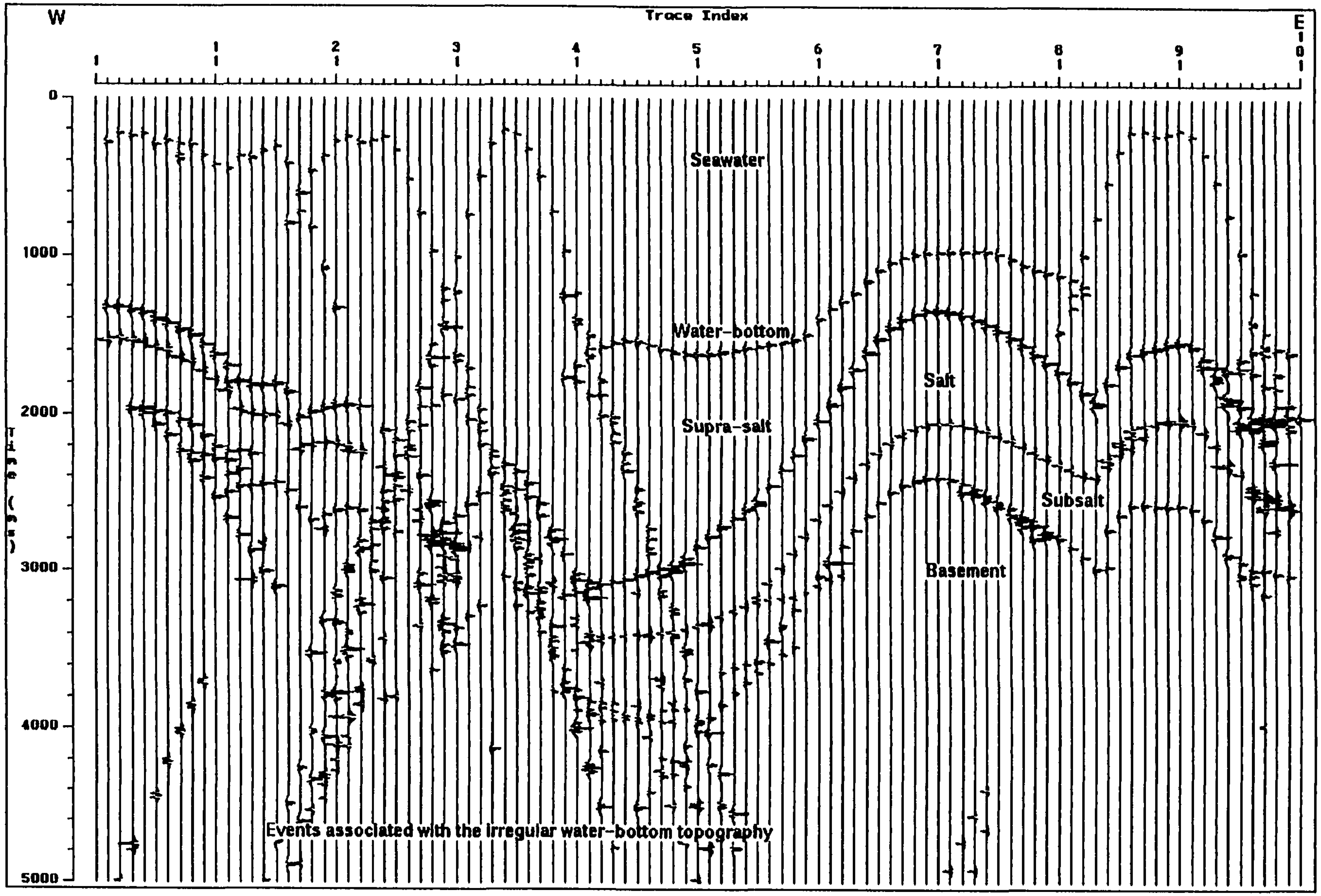

Figure 4.43b. The synthetic section resulting from zero offset ray-tracing performed on the initial velocity-depth model of Figure 4.43a.

arrival times corresponding to water bottom, topsalt, basesalt, and top of basement do not match those of the line 28-50.

Velocity depth model 2

Using the initial interpretation of line 28-50 and seismic velocity, the time model is constructed (Fig. 4.44a). The velocity depth model resulting from conversion of the time model is shown in Figure 4.44b. The differences between this depth model and the one constructed through forward modeling (Fig. 4.43a), are the geometry and the thickness of supra-salt, salt, and subsalt. The velocities of supra-salt, and subsalt sections also differ. The depth model constructed through a combination of inversion and forwarding model approach yields a synthetic section (Fig. 4.45b) that displays many attributes of the real section. The arrival times of the water bottom, topsalt, basesalt, and top of basement horizons of the synthetic match those on the real seismic section 28-50. The synthetic also simulates some of the distortions of salt and subsalt reflections below the irregular portions of seafloor of line 28-50, such as undesirable linear events and velocity pull-ups underneath the reef buildups. Figure 5.46 shows zero offset raypaths for water bottom and top of basement. The complex raypaths deviation caused by the reefs is quite obvious. Note how the raypath for top basement is affected by the reef buildup and curvature of the salt layer boundaries.

The complex raypath bending and amplitude distortions caused by rugged seafloor and lateral velocity changes degrades the desirable underlying reflection events and make identification of topsalt and basesalt reflectors beneath the reef buildups difficult. Accordingly, extrapolation of topsalt and basesalt, from where they are well developed (shotpoints: 290 to 320) landward to the areas beneath the reef buildups (Shotpoints: 324

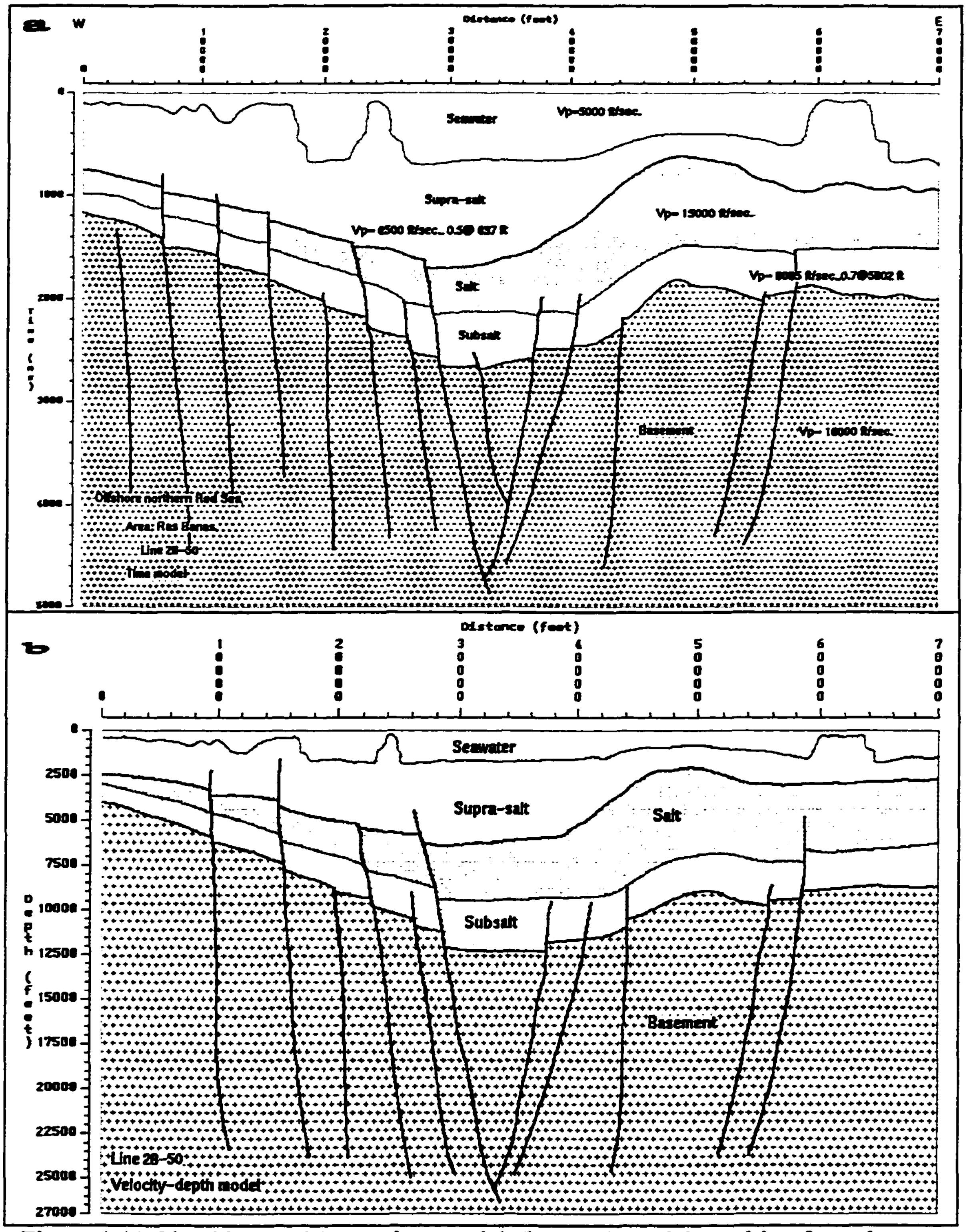

Figure 4.44. Line 28-50. (a) Input time model. (b) Depth model resulting from the conversion of the time model, using seismic derived velocities.

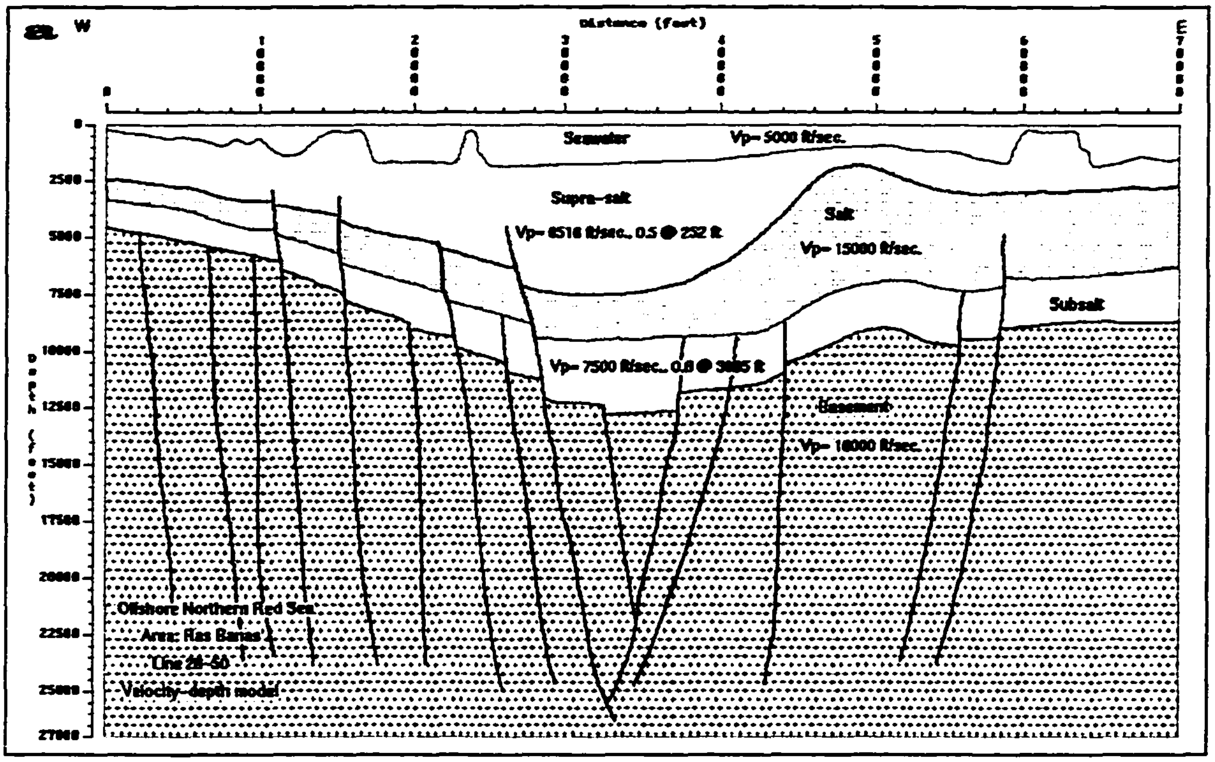

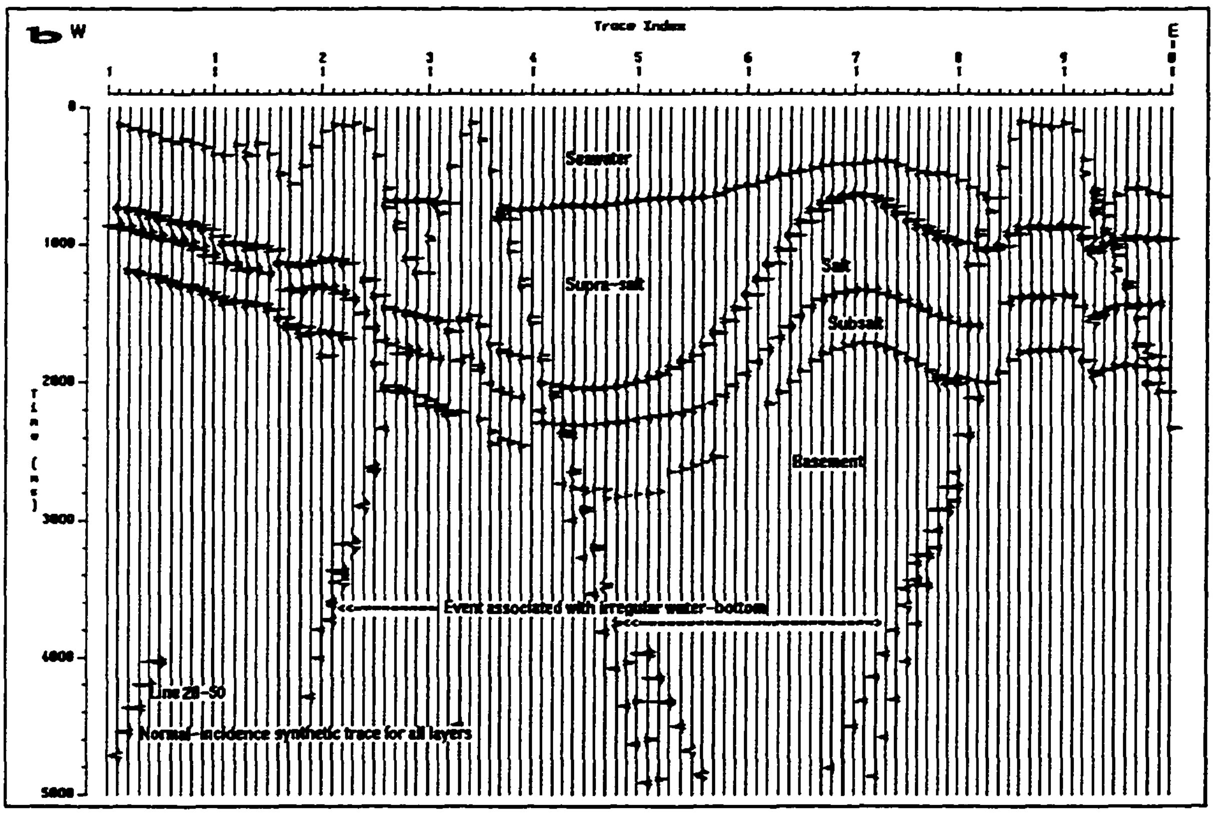

Figure 4.45. Line 28-50. (a) Velocity-depth model. (b) Normal incidence synthetic trace.

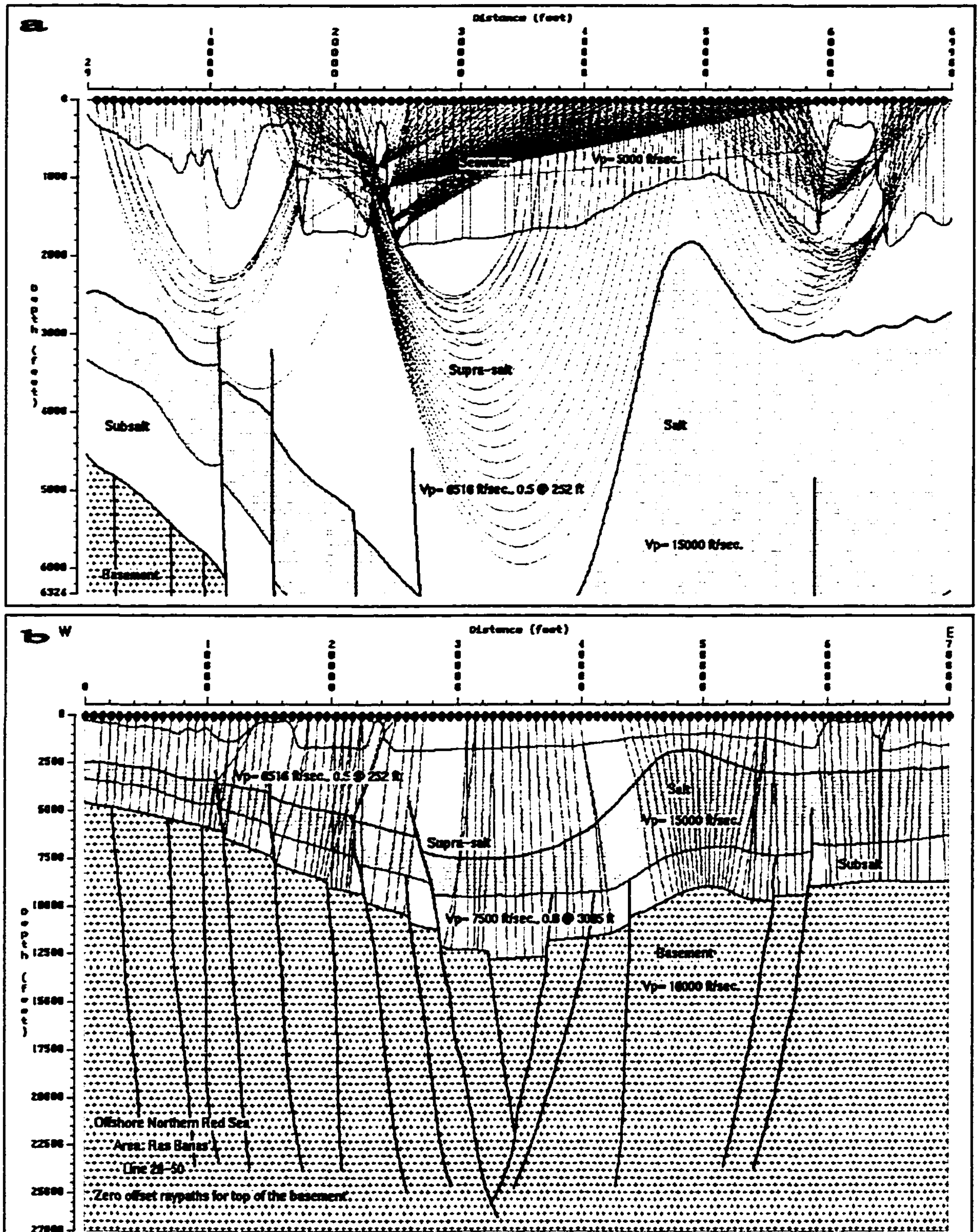

Figure 4.46. Line 28-50. (a) Zero offset raypaths for water-bottom (magnified). (b) Zero offset raypaths for the top of basement.

to 368), is hard to accomplish. The initial seismic interpretation and the 2-D modeling discussed above indicate that the salt layer does exist beneath the shelf area west of shotpoint 338. The other possibility may be that the salt has not been originally deposited in this area or is evacuated (due the differential loading of the overburden) seaward towards structurally high area. To investigate this possibility two alternative model-guided seismic interpretations are developed:

Velocity-depth model 3

This model is based on the idea that, due to differential loading, the salt is completely evacuated from beneath the syncline and folded area and moved seaward to the area below the reef at the end of line 28-50. The final velocity-depth model constructed from this interpretation and its seismic response are shown in Figure 4.47. The zero offset raypaths for water bottom (Fig. 4.48) shows a complex geometry. Note how some downward traveling rays bend at the seafloor, deviate or curve in supra-salt, and then refract at top of salt. However, the synthetic section generated from this depth model does not simulate major anticline feature observed on the real seismic section 28-50.

Velocity-depth model 4.

The final velocity depth model constructed from this interpretation and the synthetic section derived from it are shown in Figure 4.49. As shown on this model, the geometry of salt and the thickness of supra-salt have been modified. The velocity gradient of supra-salt and subsalt section has also changed. Comparison of the arrival times of seafloor, topsalt, basesalt, and top of basement of the synthetic to those picked on the real line (Fig. 4.50) reveals a reasonable match. In fact, the synthetic displays most of the features and distortions seen on the line 28-50. However, what significant about this

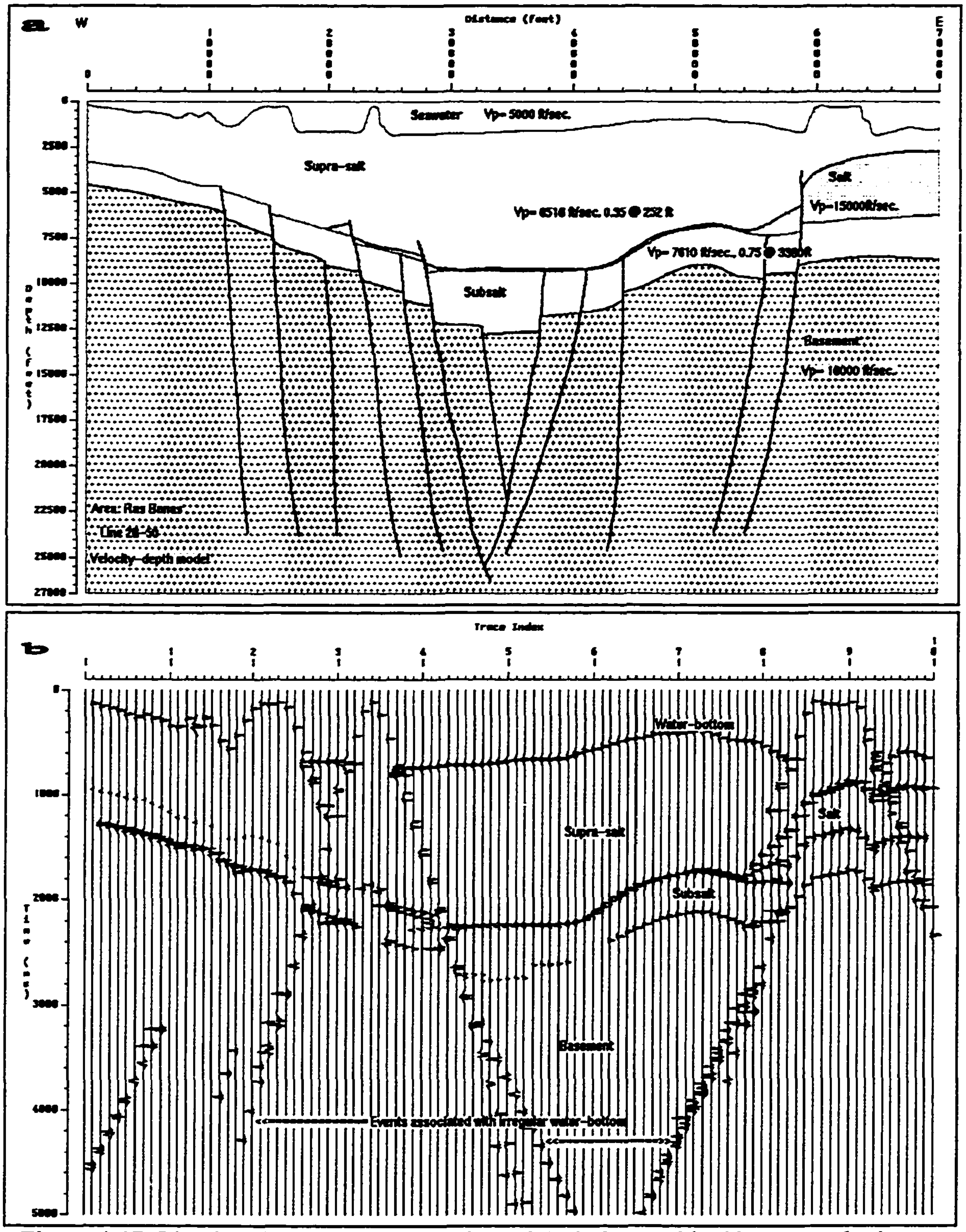

Figure 4.47. Line 28-50. (a) Velocity-depth model. (b) Normal incidence synthetic trace dispalyed with arrival time.

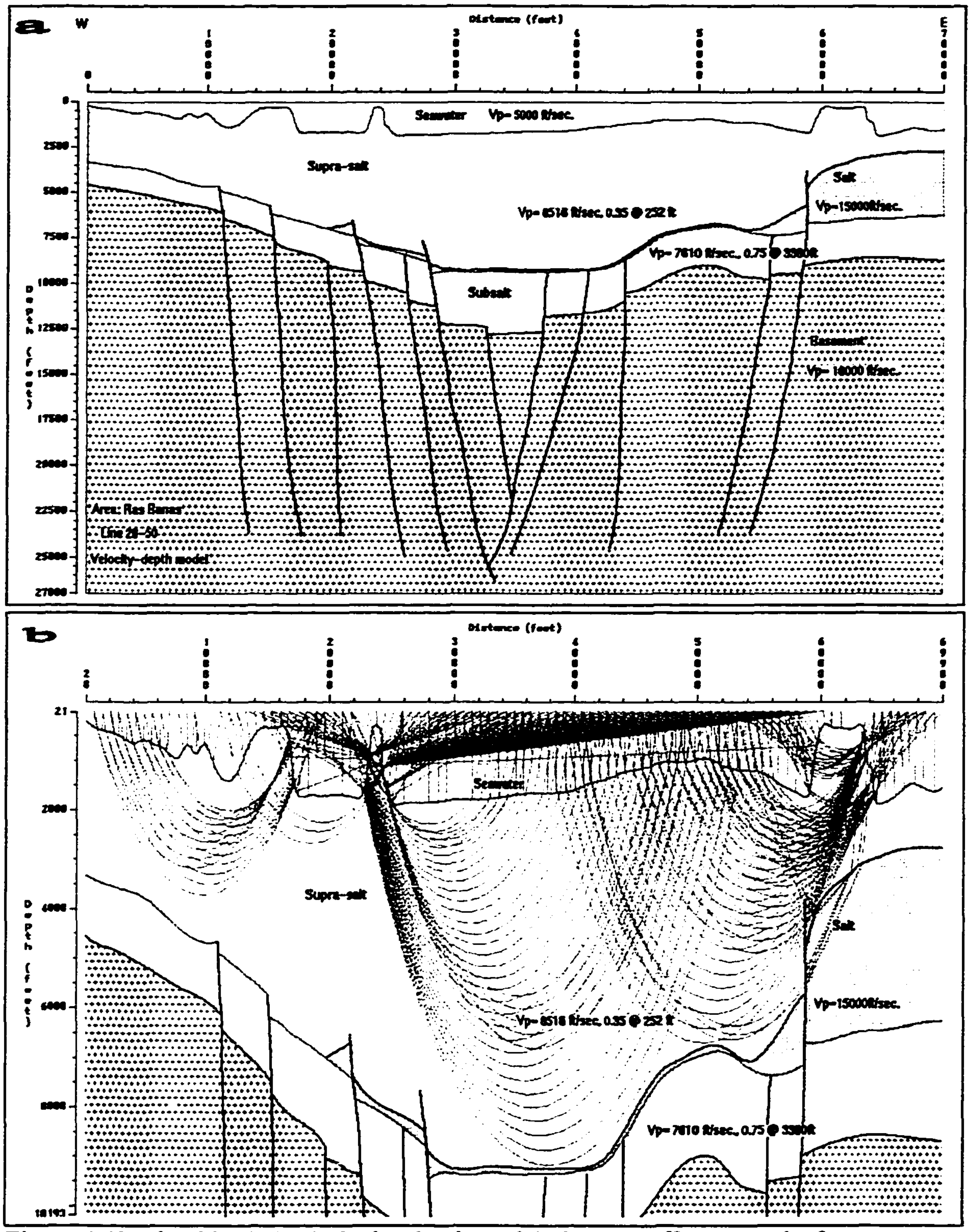

Figure 4.48. Line 28-50. (a) Velocity-depth model. (b) Zero offset raypaths for water-bottom.

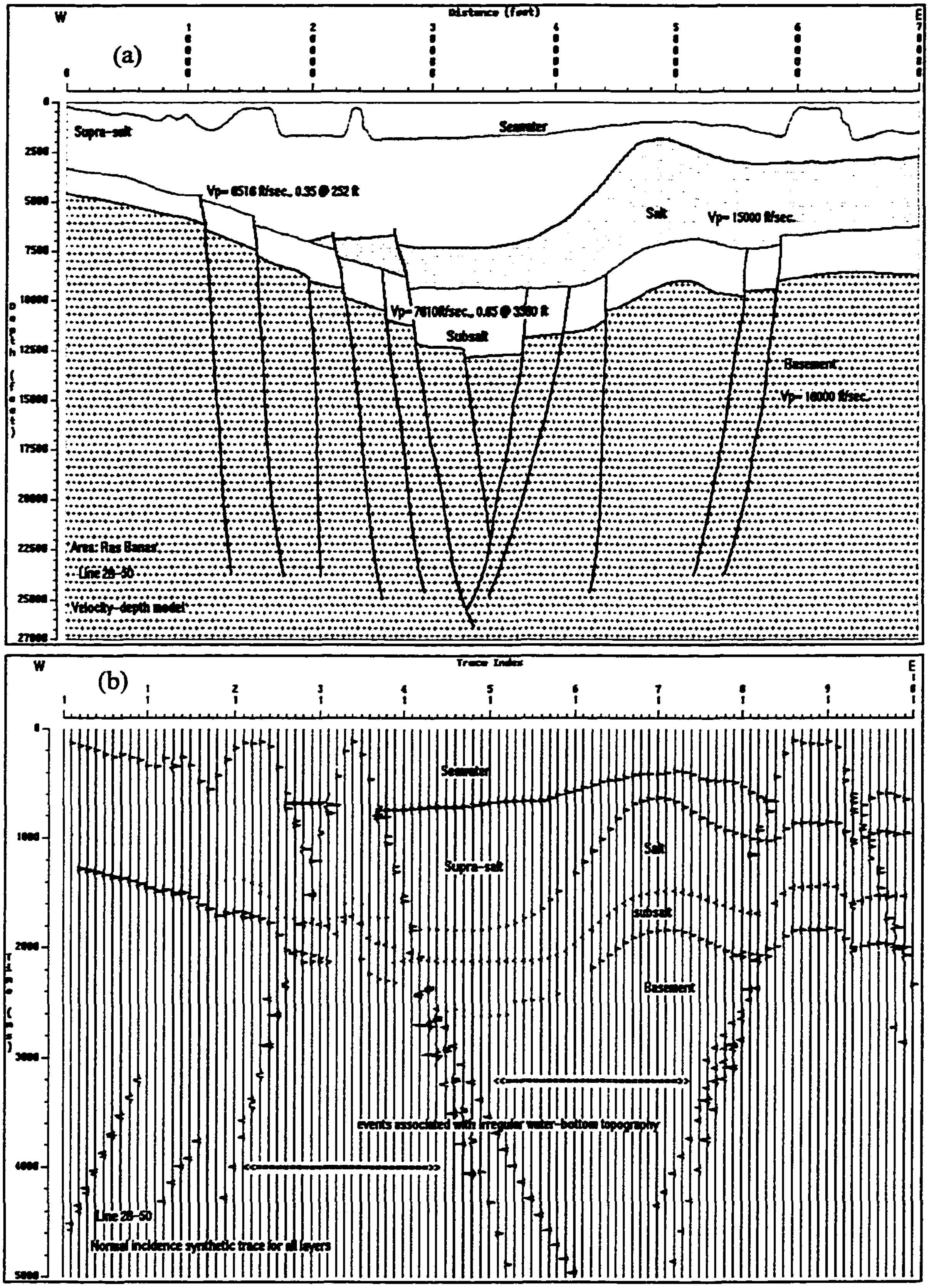

Figure 4.49. Velocity-depth model (a) and normal incidence synthetic section for line28-05.

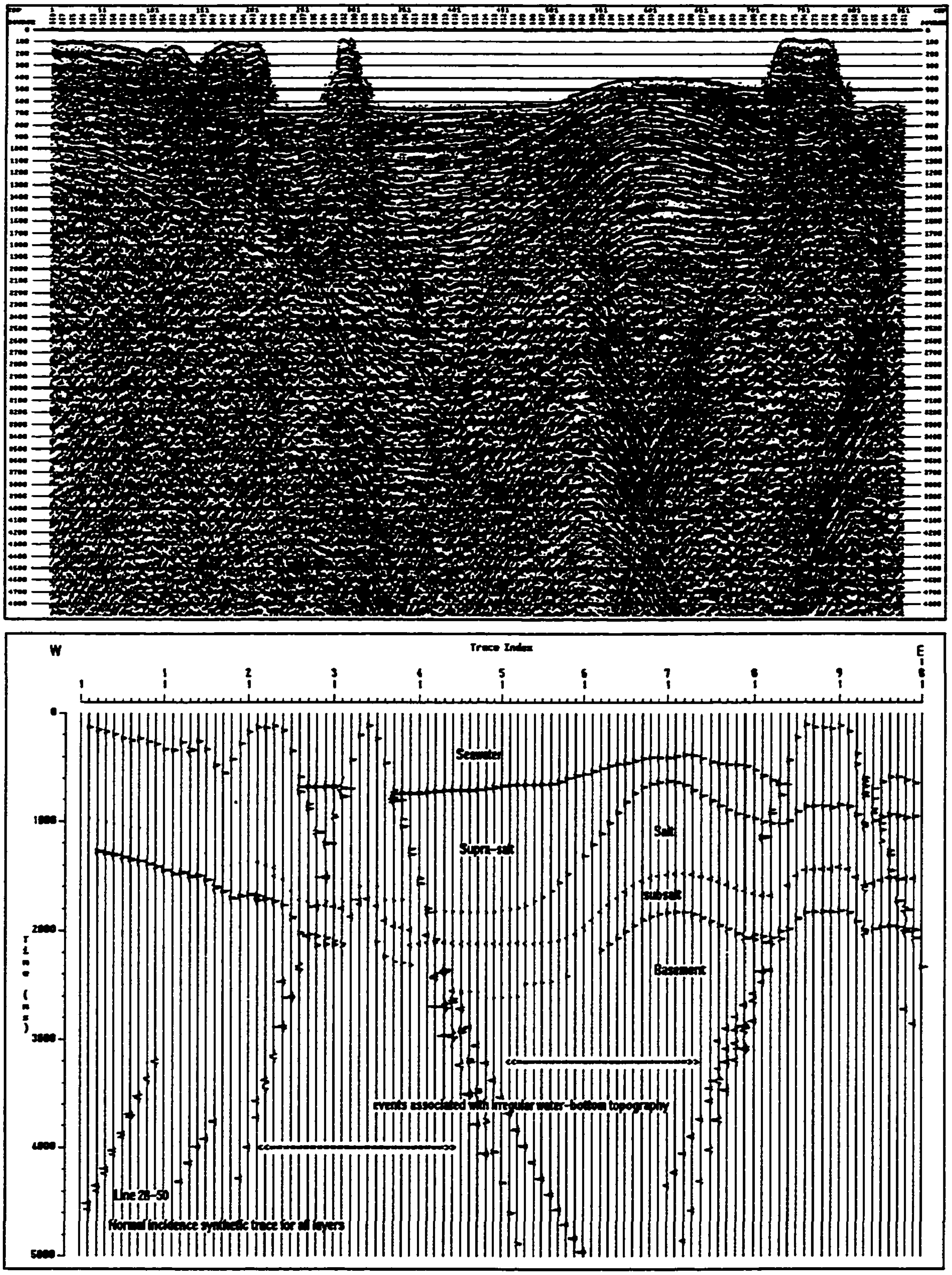

Figure 4.50. Line 28-50 before signal enhancement and migration (top) and normal-incidence synthetic section (bottom).

synthetic, is that it simulates the poorly imaged area observed below the rugged seafloor west of the shotpoint 326 of line 28-50. The subsalt reflections, in this area, are weak and disrupted. The top of basement reflector observed on line 28-50 is comparable to the one simulated by the synthetic section. The top of basement reflector is continuous and has high amplitude in the area west of shotpoint 339 on seismic line 28-50 and in the same area on the synthetic section. However, it is relatively weak and hard to pick east of shotpoint 339. This is consistent with the absence and presence of overlying high velocity salt in these areas, respectively. That is, the absence of salt west of shotpoint 339 resulted in sufficient down-going energy for illuminating the top of basement. Zero offset raypaths from tops of basement and subsalt (Fig. 4.51) illustrate the ray bending caused by irregular salt geometry and seafloor irregularities. Note that the rays travel vertically unbent over the flat portions of water bottom and top of salt.

<u>Image distortion associated with irregular seafloor</u>:

On the synthetic section, the image problems caused by irregularities in water bottom include velocity pull-ups below reef buildups, reduction of the amplitudes of the underlying reflections, and generation of strong, coherent, linear noise. Figure 4.52 shows the complex raypaths distortion associated with varying sea floor and their seismic response.

<u>Distortions caused by faults and faulted block edges</u>:

The synthetic discussed so far does not include diffractions. In fact, the basement involved faults and the tilted faulted block edges observed on line 28-50 cause considerable diffraction events, which further complicate the imaging problem. Figure 4.53 displays the normal incidence synthetic and diffractions from faults and faulted block

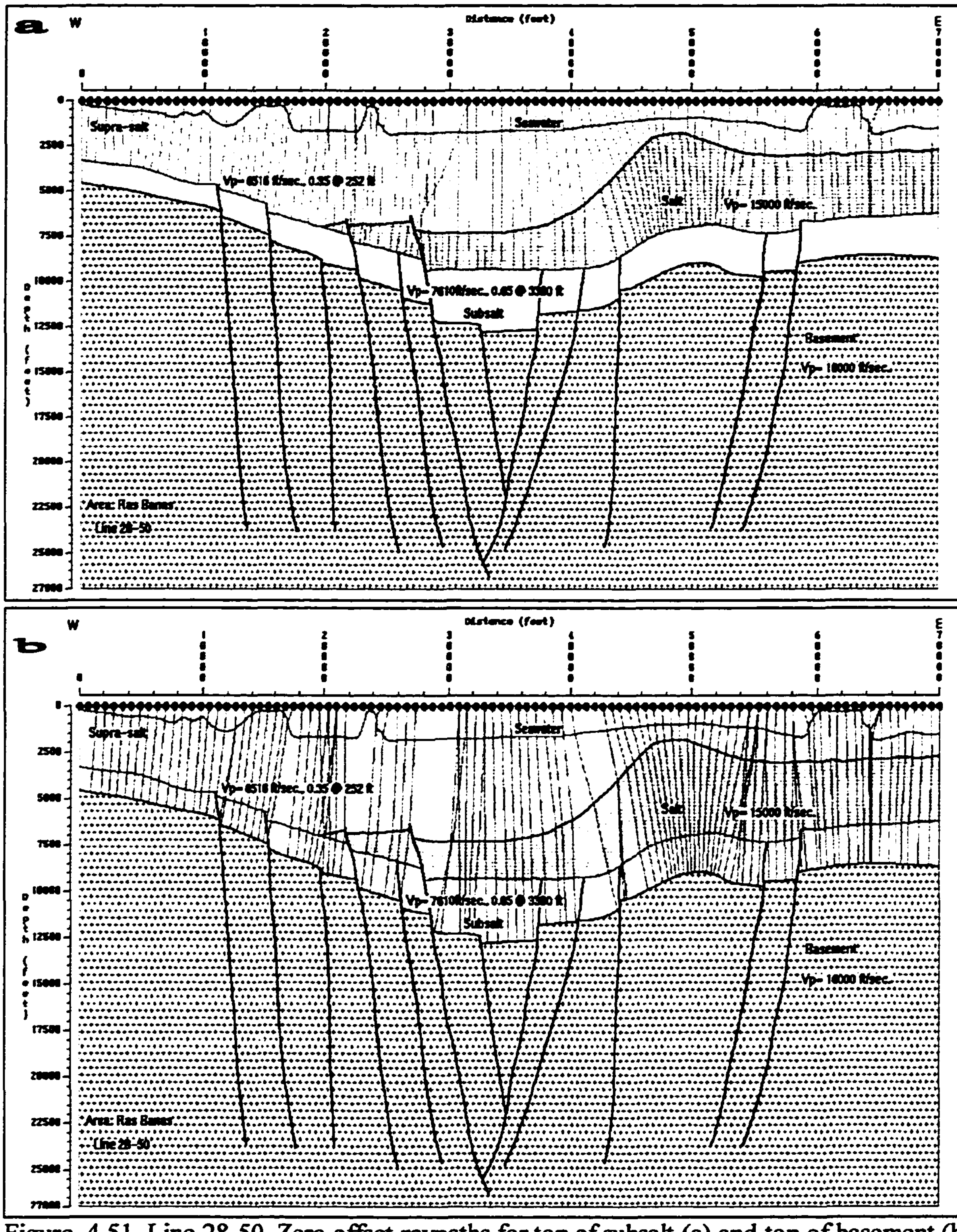

Figure .4.51. Line 28-50. Zero offset raypaths for top of subsalt (a) and top of basement (b).

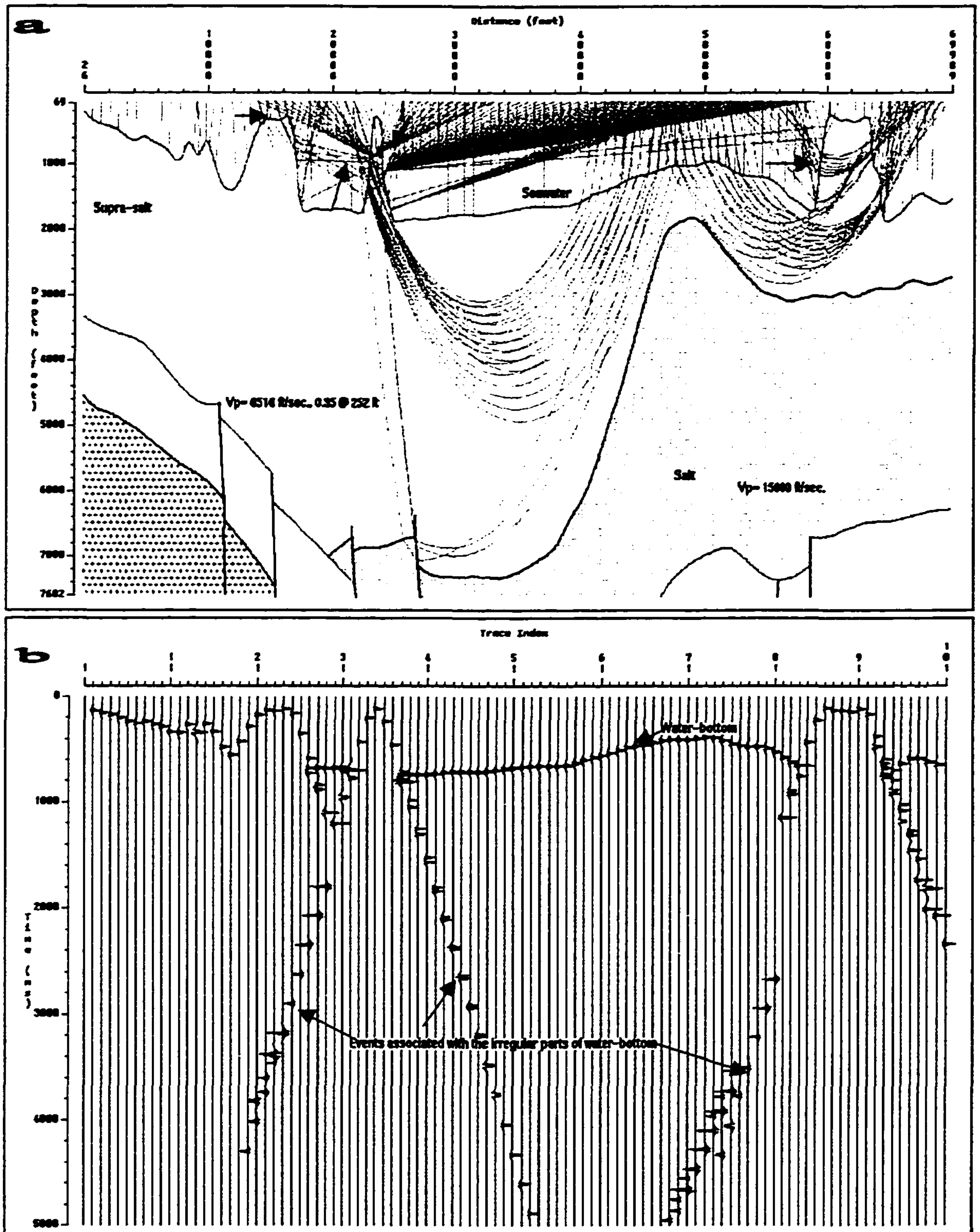

Figure 4.52. Line 28-50. (a) Zero offset raypaths for water-bottom only (magnified). Note the severe ray bending (red arrows) at the irregular parts of sea-floor.(b) The resulting synthetic trace. Events associated with the rugged sea-floor are highlighted with blue arrows.

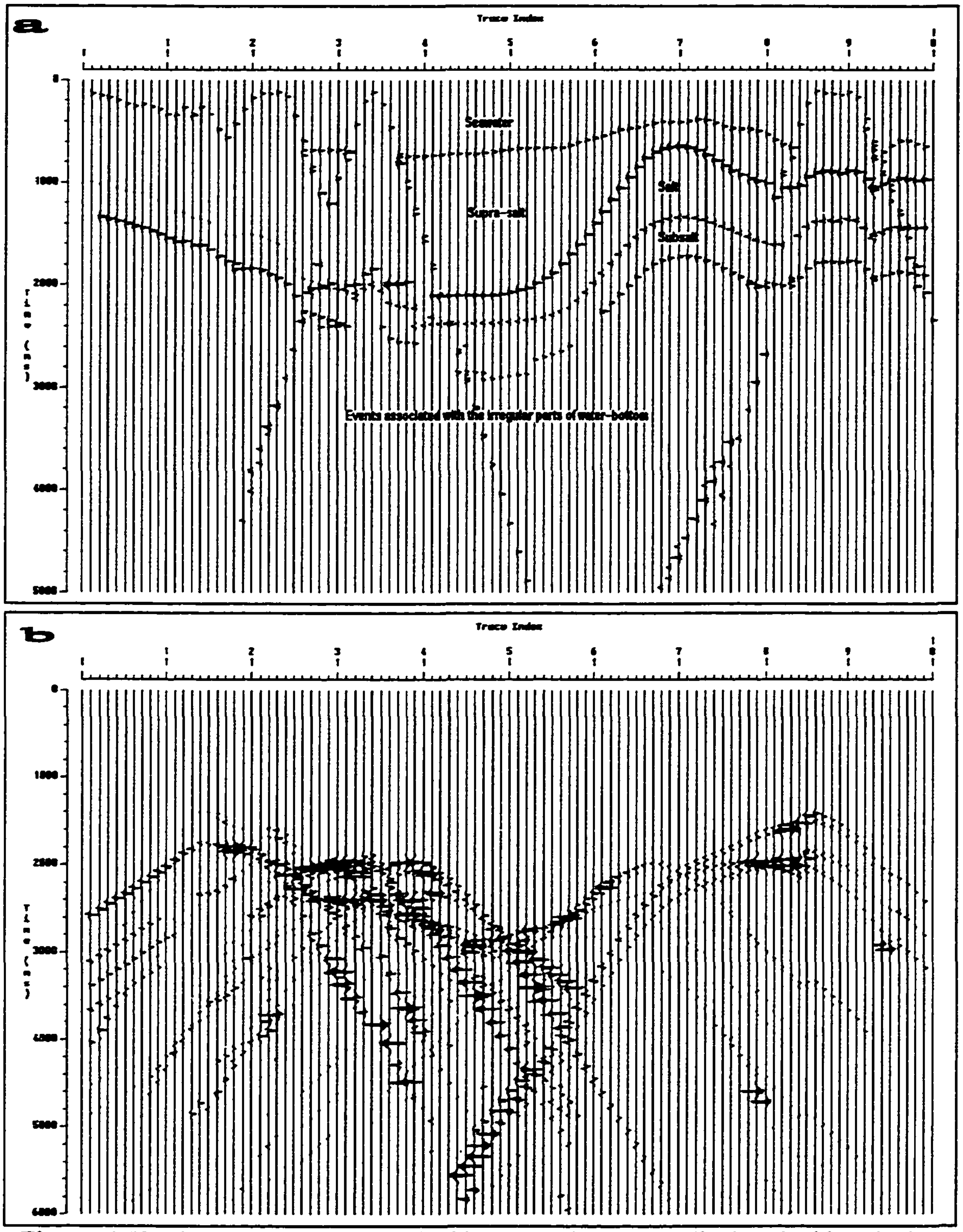

Figure 4.53. Line 28-50. (a) Normal incidence synthetic trace displayed with arrival times. (b) Diffractions associated with faults and faulted block edges.

edges. The diffraction events are displayed here separately so that their contribution to the imaging problem can be observed and not confused with distortions caused by other factors.

Distortions due velocity variations:

To investigate the effects of vertical and lateral velocity variations on raypaths distortion, consider Figures 4.54a and 4.54b. Both Figures display zero offset raypaths for water bottom. The only difference is that the velocity gradient of supra-salt is 0.35 for model (a) and 0.9 for model (b). The model with high velocity gradient shows considerable raypaths bending than the one with low gradient. Note the relatively gentle curvature of the ray bending in model (a) and the sharp one in model (b). Now compare the zero offset raypaths of Figure 4.55. The supra salt has velocity gradient of 0.35 in model (a) constant velocity (Gradient =0.0) in model (b). None of the rays has transmitted or refracted in constant velocity supra-salt layer. In all the models discussed above, the salt has constant velocity (15000 fps). Now compare the raypaths for water bottom of Figure 4.56. The only difference between the two models is that the salt has constant velocity in model (a) and variable velocity in model (b). Note the refraction at the top of the salt in model (b). It is worth noting that in the entire zero offset raypaths discussed above, the raypaths travel vertically, unbent, and unrefracted over the flat portions of seafloor.

Summary:

The complex ray bending caused by vertical and lateral velocity variations and irregular geometry of supra-salt, salt, subsalt sections, and seafloor topography result in the considerable image distortions observed on line 28-50. These distortions are: reduction

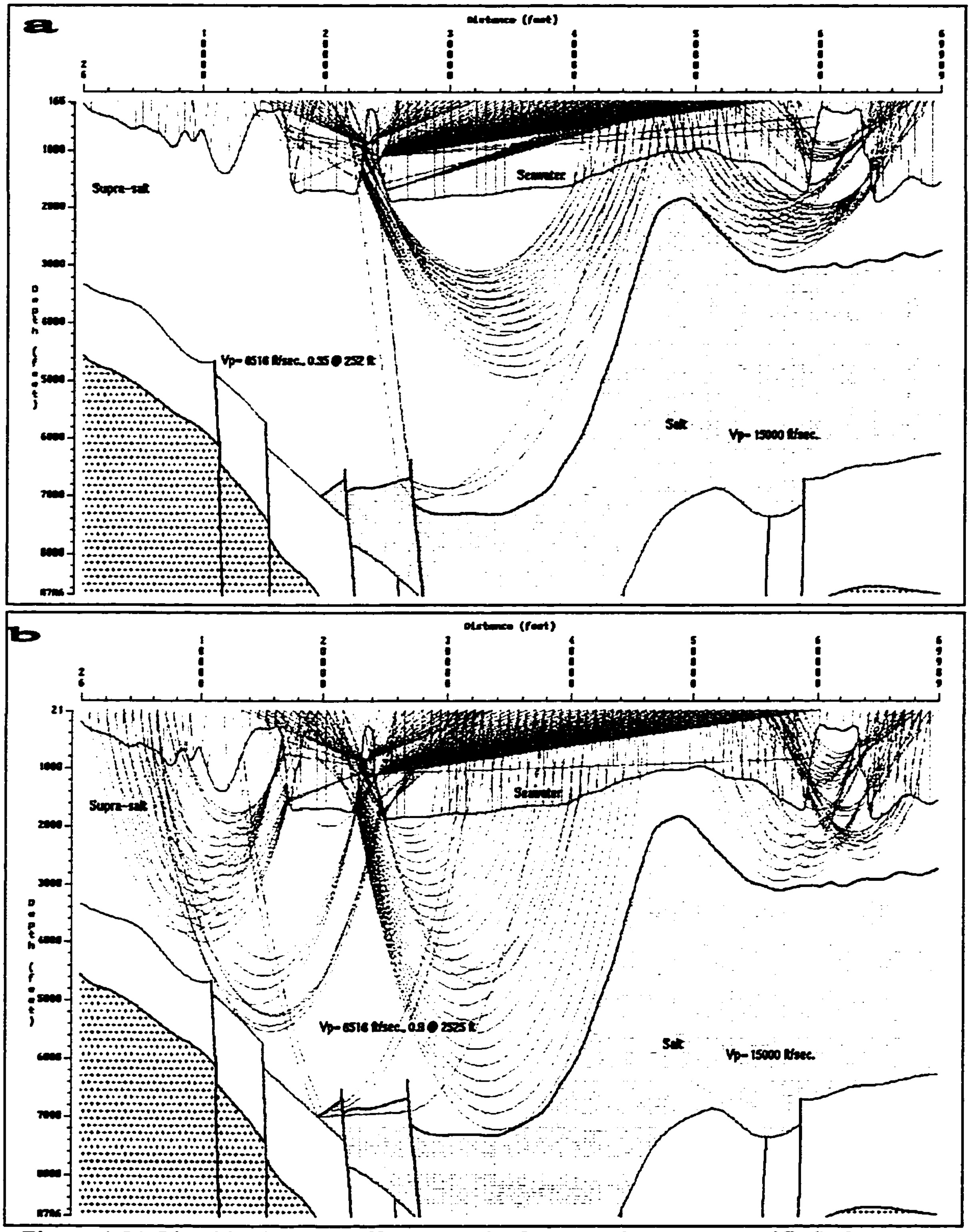

Figure 4.54 Line 28-50. Zero offset raypaths for water-bottom (magnified). Supra-salt velocity gradient is (a) 0.35 and (b) 0.9. Note how the velocity gradient influences the ray bending in the supra-salt.

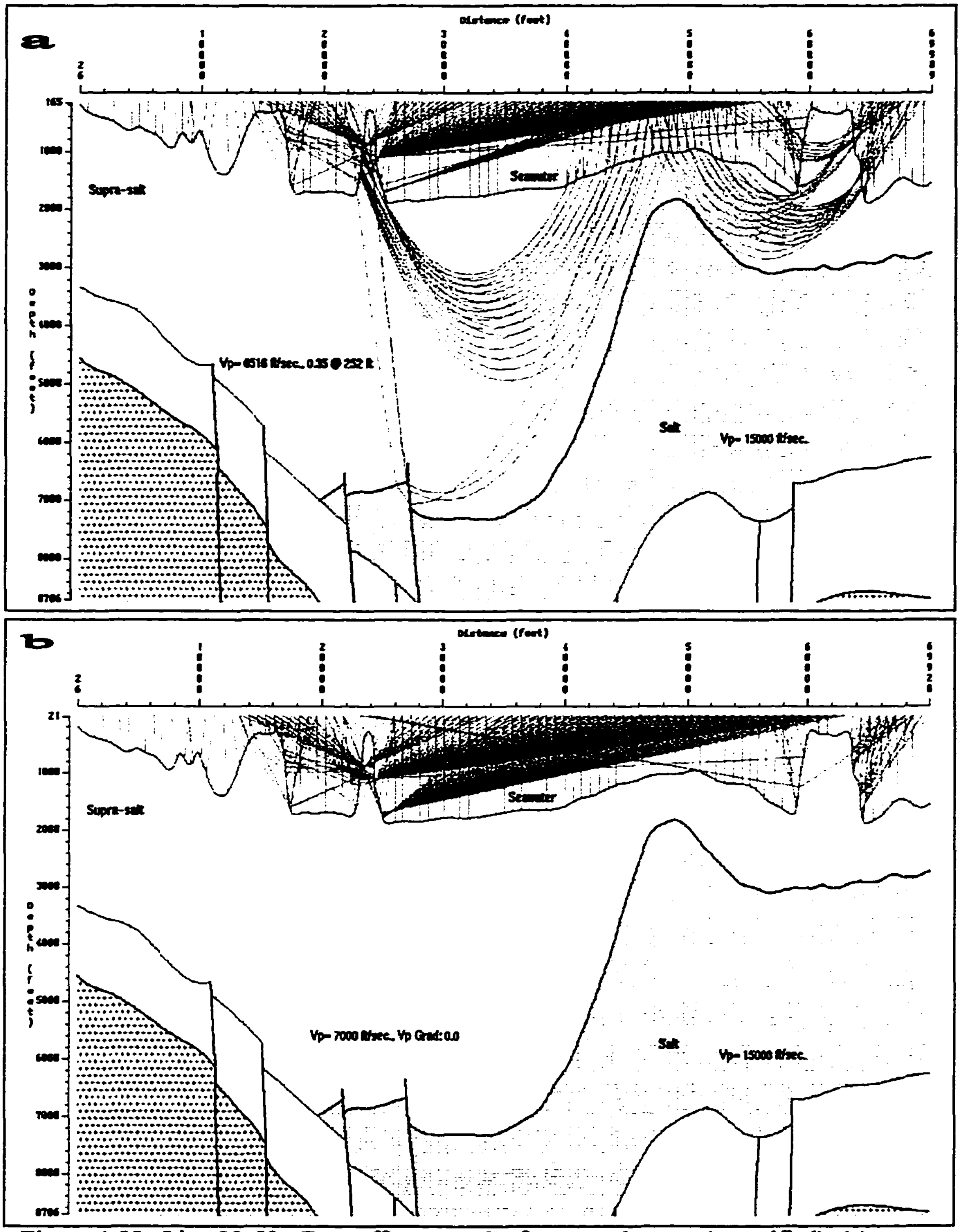

Figure 4.55. Line 28-50. Zero offset raypaths for water-bottom (magnified). (a) Supra-salt with variable velocity (6516 ft/sec., 0.35 @ 252 ft). (b) Supra-salt velocity is constant (7000 ft/sec.).

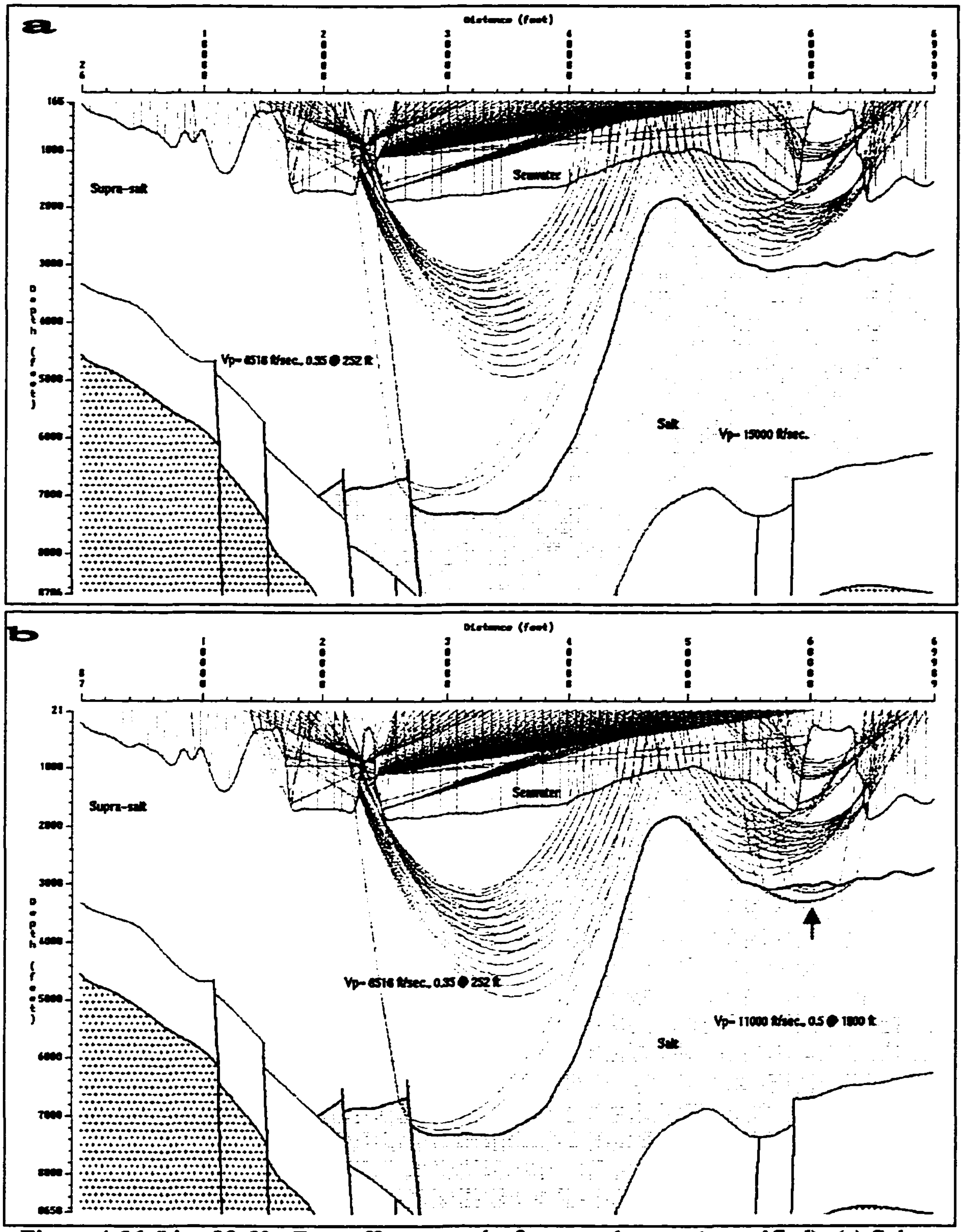

Figure 4.56. Line 28-50. Zero offset raypaths for water-bottom (magnified). (a) Salt with constant velocity (15000 ft/sec.). (b) Salt velocity varies vertically and laterally (11000 ft/sec., 0.5 @ 1900 ft). Note the refraction at the top of salt (red arrow).

of reflection amplitudes, travel times anomalies that disrupt the continuity of desirable reflections, a strong, steeply dipping, coherent noise which obscures the salt and subsalt seismic events, velocity pull-up of underlying reflections due to shallow reef buildups, and intense diffractions from faults and tilted block edges. Image distortions that are not simulated on the synthetic include sideswipe and multiples. Based on the analysis of inversion and forward modeling results discussed above, the velocity-depth model 4 (Fig. 4.49a) is considered final acceptable depth model.

IV.2.3.The results of post stack signal enhancement:

IV.2.3.1. F-X deconvolution:

The F-X deconvolution is used to reduce the random noise and spurious events from unmigrated seismic section 28-50. The results indicate a very significant improvement in continuity of top of basement and overlying subsalt, salt, and supra-salt reflection events (Fig. 4.57). The process not only enhances the lateral coherence of the seismic section, but also makes the image distortions very clear. As shown on this figure, one can easily distinguish, for example, between diffraction events and steeply dipping, linear events. This is particularly important as the diffractions from faults and linear events associated with rugged seafloor overlap with one another and with primary reflections which makes it very hard to distinguish between them.

IV.2.4. Post stack migrations results and analysis.

IV.2.4.1. Stolt FK time migration:

The Stolt FK migration handles steep dips, but is very sensitive to lateral velocity variations. This fast and most economical algorithm is performed on Line 28-50 in order

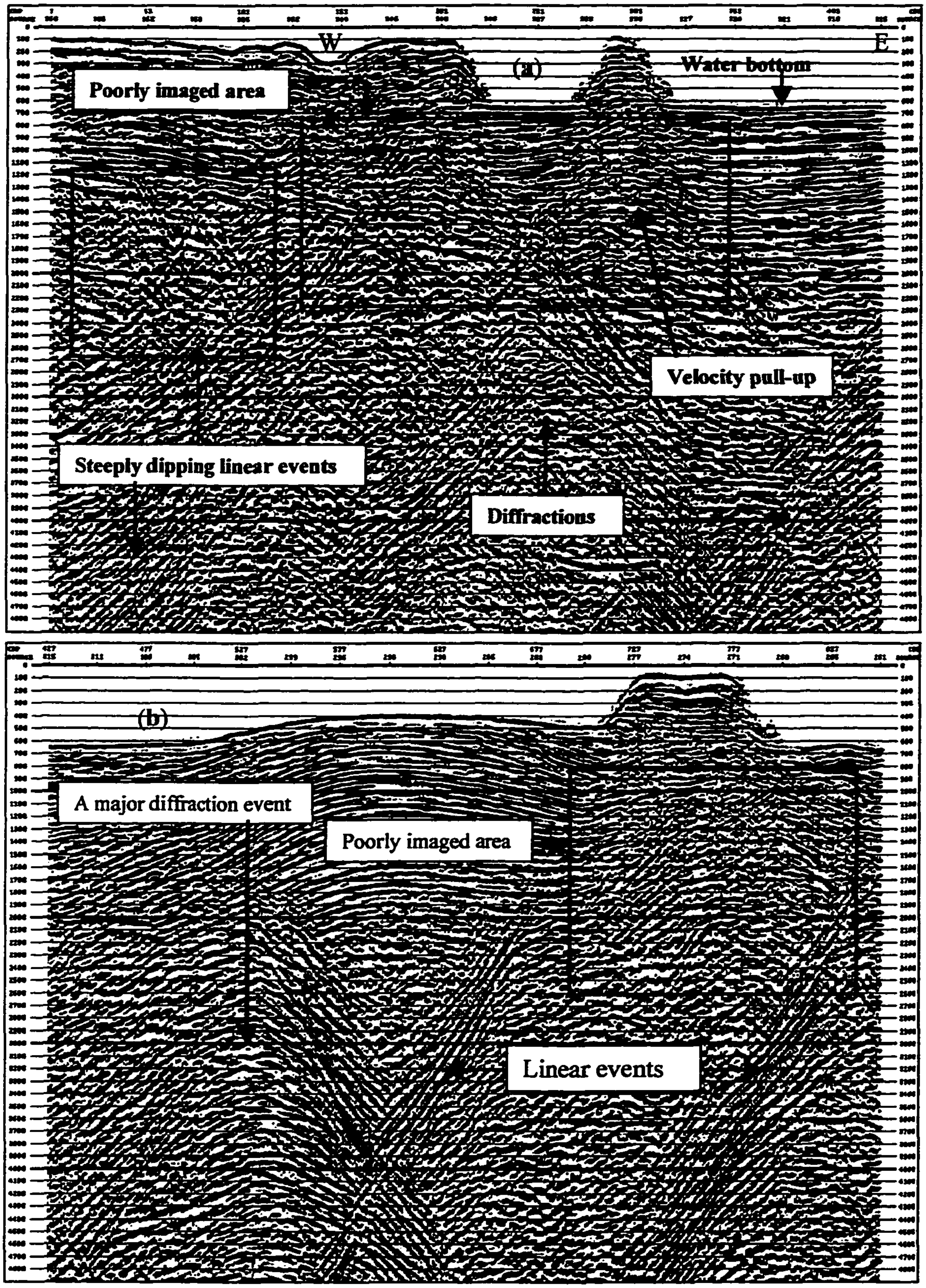

Figure 4.57. The eastern part of line 28-50 before (a) and after (b) F-X deconvolution. The image distortions become very clear after F-X deconvolution.

to obtain an initial idea of possible imaging problem caused by lateral velocity changes. Stolt FK migration produces unsatisfactory result (Fig. 4.58) particularly in the areas underneath the varying sea floor. Stolt FK migration also yields considerable migration artifacts and spurious events.

IV.2.4.2. Steep dip explicit finite difference time migration:

Steep dip Explicit FD time migration performed on line 28-50, after post stack signal enhancement, produce migrated section (Fig. 4.59) with a lateral resolution that is far better than the one obtained by Stolt FK migration. Steep dip explicit FD time migration focuses all the diffraction hyperbolas, corrects the velocity pull-ups, and removes steeply dipping events. The continuity of topsalt, basesalt, and top of basement reflectors has improved considerably and many major faults can be easily traced. However, steep dip explicit FD time migration yields strong migration artifacts in the deeper potions of the shelf area and the eastern part of line 28-05. The imaging of salt and subsalt section below the reef at the east end of the section is not as satisfactory as in the other parts of the section. There is also an image disruption or migration artifacts below the eastern edge of the reef. As already pointed out, steep dip explicit FD time migration handles mild to moderate lateral velocity changes and dip up to 50 degrees. It is likely that the migration artifacts yielded by this method are due to abrupt lateral velocity variation.

IV.2.4.3. Kirchhoff time migration:

Kirchhoff time migration yields a reasonable result that is much better than both Stolt FK and steep dip explicit FD time algorithms. Kirchhoff time migrated section does not contain the migration artifacts produced by Stolt FK and steep dip FD time migrations in the shallow part of line 28-50. Comparison of the western and eastern portions of line

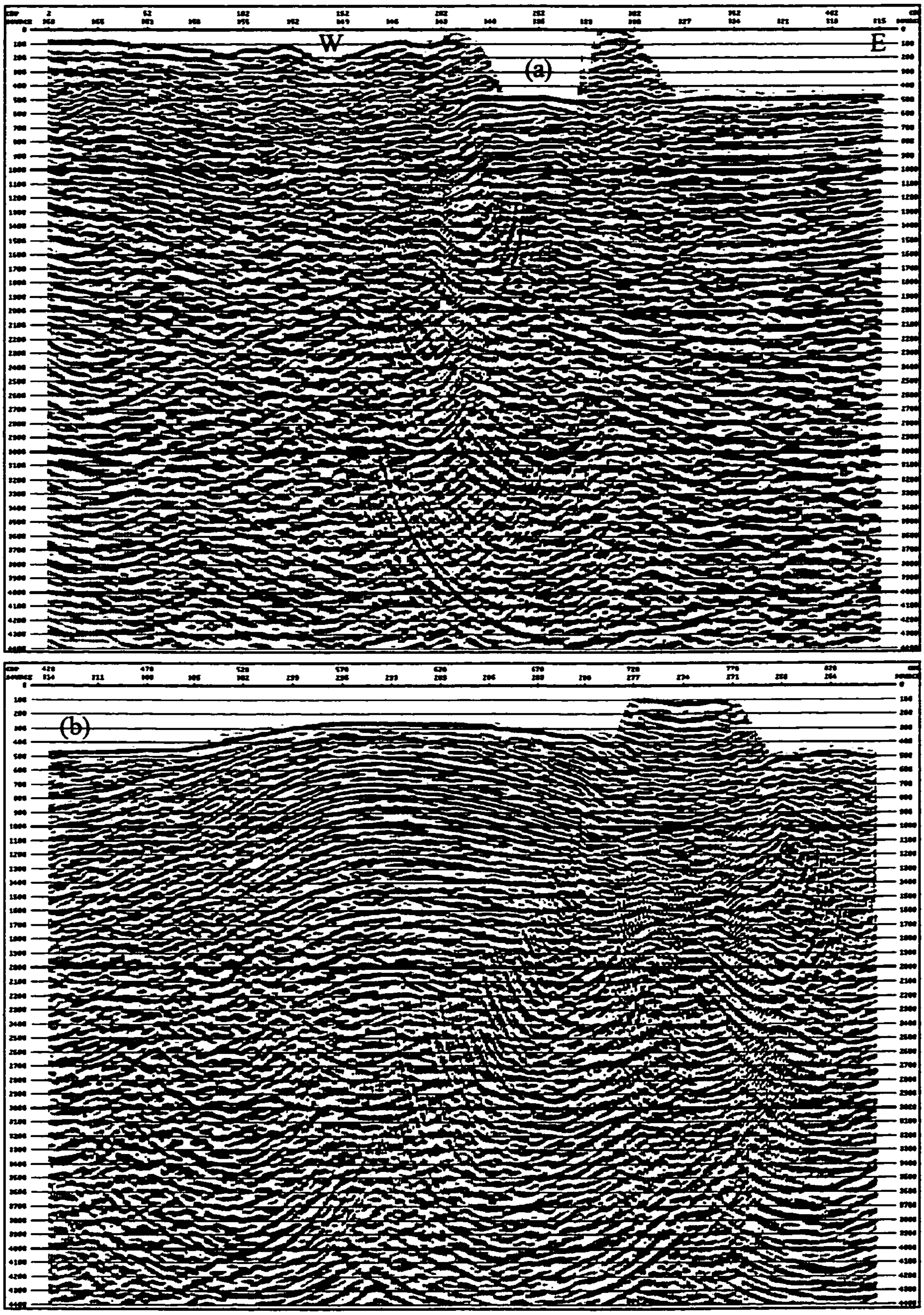

Figure 4.58. The western (a) and eastern (b) parts of line 28-50 after FK time migration

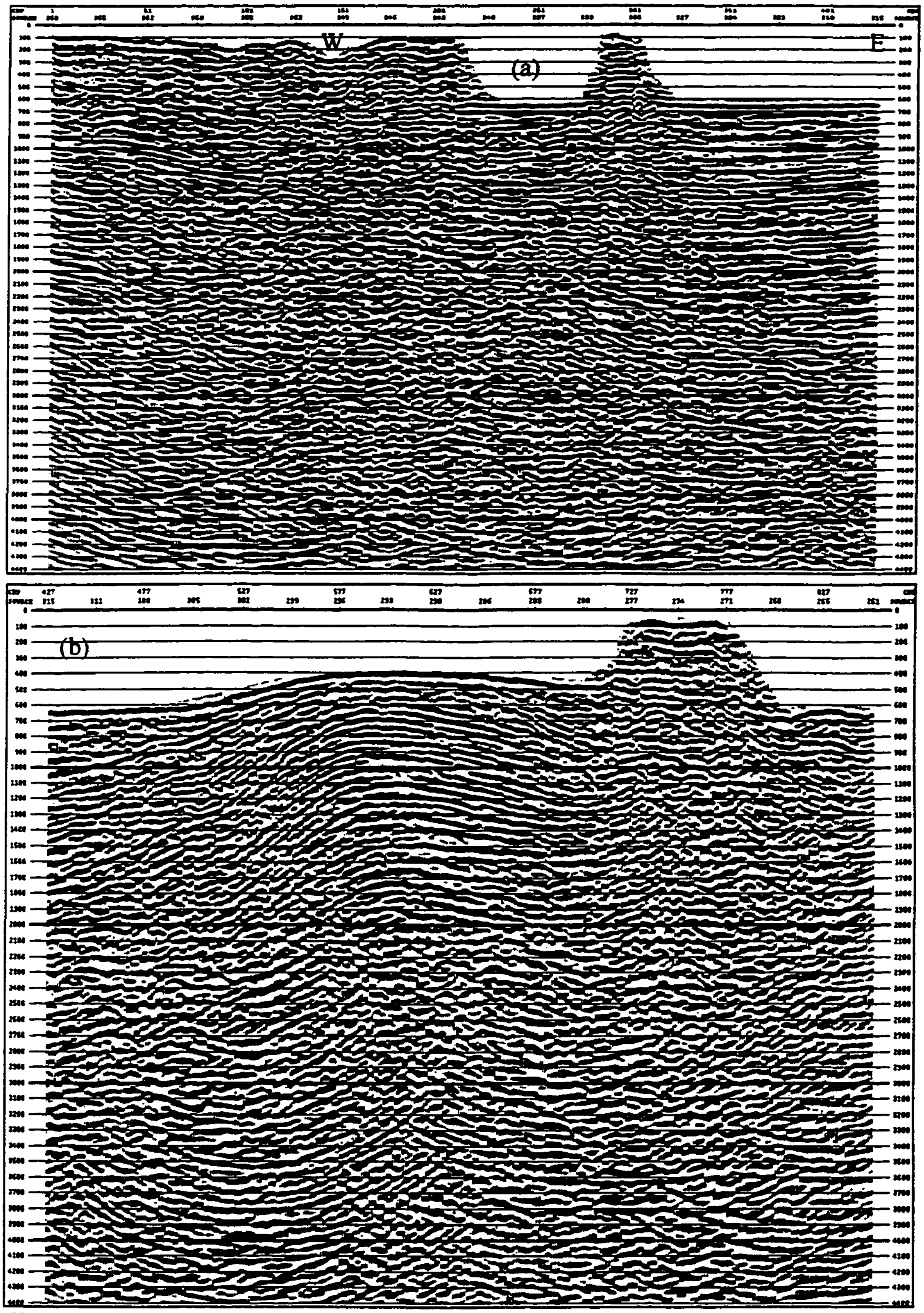

Figure 4.59. The western (a) and eastern (b) parts of line 28-50 after wave equation multiple rejection, dynamicS/N filtering, and steep dip explicit finite difference time migration.

28-50 before and after Kirchhoff time migration (Figs. 4.60, 4.61) indicates a significant improvement in spatial resolution of the sedimentary section overlying the basement. First, there is a significant improvement in reflection continuity of poorly imaged areas below the reefs. The diffractions are well focussed and the major faults can be easily identified. The criss-cross, steeply dipping, linear events below the shelf and the velocity pull-up beneath the shallow reef have also been removed. The coherence of subsalt, salt, and supra-salt reflection events has been enhanced considerably. However, Kirchhoff migration result does contains false horizontal events in the deep noisy portion of the section and significant smearing caused by side boundary effect at the ends of the line. Although these migration artifacts occurs below the zone of interest (subsalt section), they contributes to obscuring the structural details (e.g., the geometry and shape) of basement-involved faults in the deeper part of the section. Imaging of these structural details is essential, as they may have controlled the development of deformation observed in the overlying sedimentary section such as the major anticline on the eastern part of the line and the depocenter in the middle of the section. Knowledge of deep structures will also help distinguish their contribution to the imaging problems observed on this line.

IV.2.4.4. Finite difference depth migration:

Compared to the results of all the migration methods discussed above, finite difference depth migration yields reasonably accurate subsurface structures. Comparison of Kirchhoff and FD depth migrations results (Figs. 4.62, 4.63) indicates that steep dip FD depth migration does perform very well. Figures 4.64, 4.65 compare the western and eastern parts of line 28-50 before and after steep dip FD depth migration. It is evident from these Figures that the diffractions are well focussed and the faults are clearly defined.

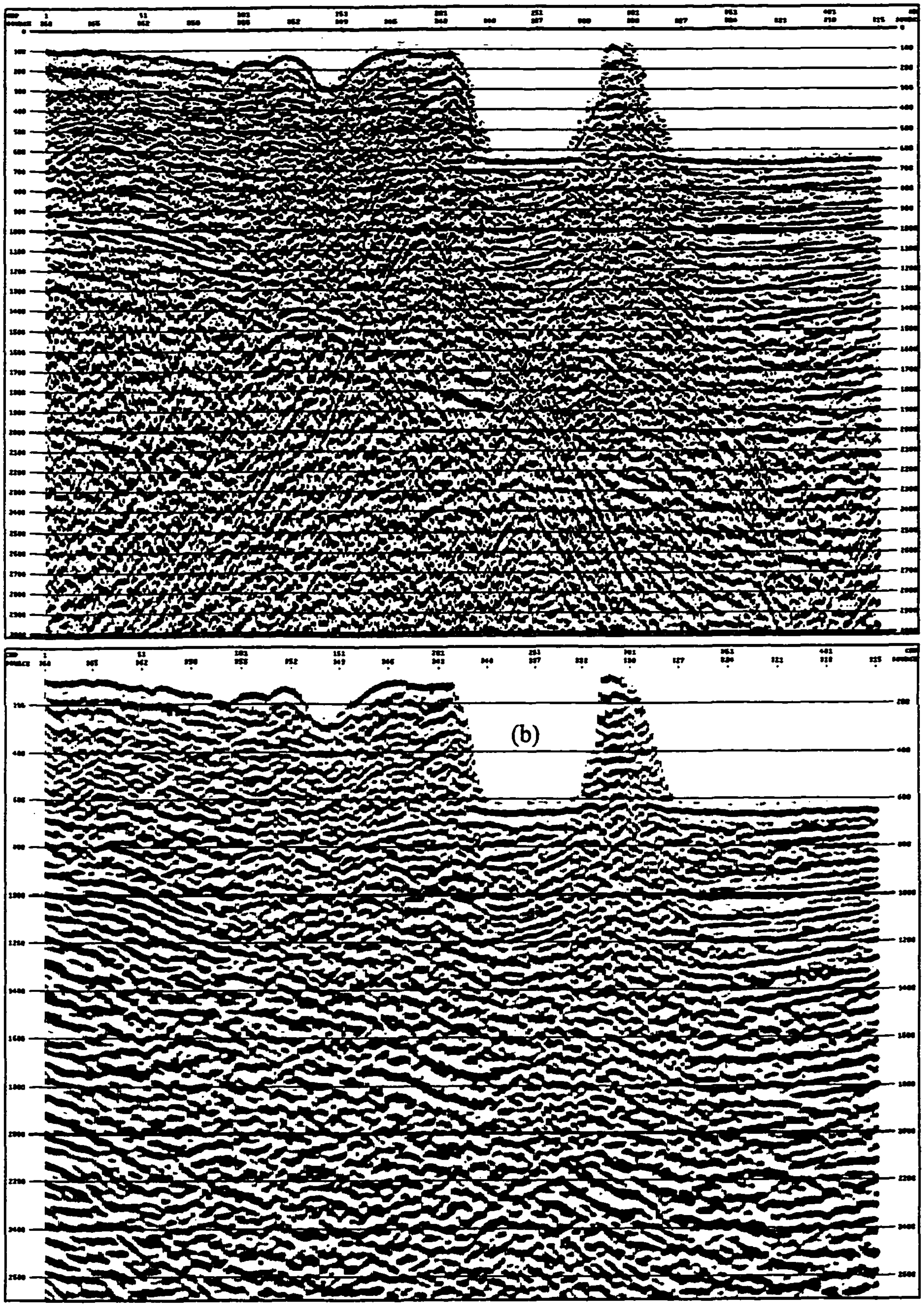

Figure 4.60. The western part of line 28-50 (indicated by a box) before (a) and after (b) signal enhancement and Kirchhoff time migration.

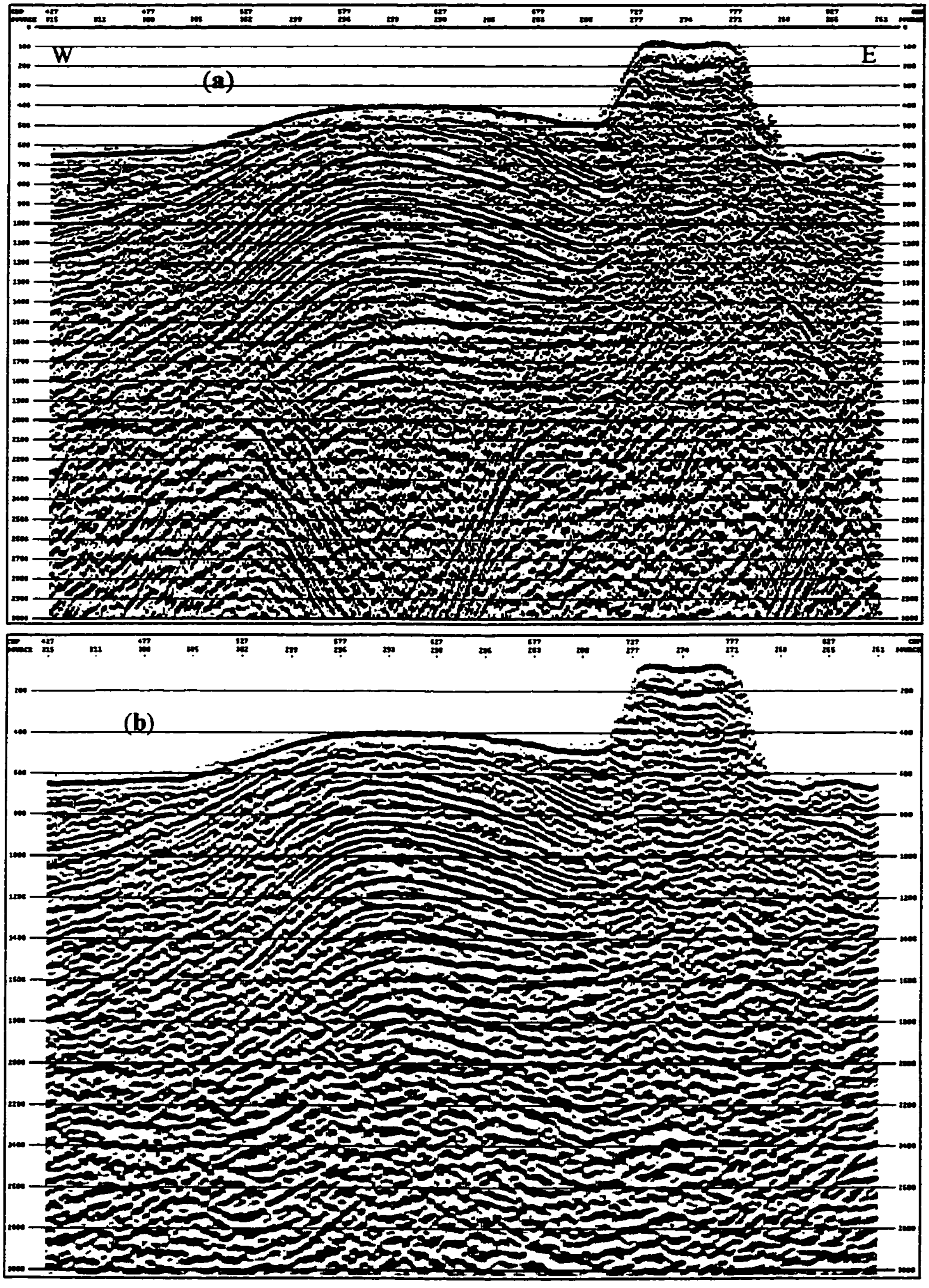

Figure 4.61. The eastern part of line 28-50 before (a) and after (b) wave equation multiple rejection, dynamic S/N filtering and Kirchhoff time migration.

The velocity pull-up below the reef buildup is corrected and criss-cross, linear events no longer exist. No significant migration artifacts are observed on FD depth migrated section except one high amplitude spurious horizontal event observed deep in the section below the shelf area and minor edge effect at the end of the section to the east. Steep dip FD depth migration performs well because it handles the strong lateral velocity variations that are beyond the capability of the time migration methods discussed above. It is obvious that steep dip FD depth migration not only improves the lateral resolution of salt and subsalt reflections and delineated the fault planes but also reveals the details of deep and shallow structures. First and most importantly, FD depth migration reveals that the anticline (which is not observed below 2.0 second on the unmigrated section) becomes progressively tighter with depth and extends deep into the section. The crest of the anticline is more localized and can be clearly observed between 2.2 to 3.7 seconds on the migrated section. The anticline is bounded to the east by landward dipping basement involved normal fault which extends upward into supra-salt section. The western part of the anticline in the sedimentary section is bounded by seaward-dipping normal listric fault. A faint hint of what appear to be a thrust fault is observed west of the anticline (Fig 4.66). This fault extends deep into the basement down to the bottom of the section and terminates upward at the top of basement. The structurally low area (below 2.5 second) between the thrust fault and the anticline can be interpreted as a small syncline. The presence of a half graben beneath the western limb of the anticline is a possible alternative interpretation. Steep dip FD depth migration also reveals a major graben underneath the depocenter in the middle of line 28-50 and major seaward-dipping basement-involved normal faults. These faults cut through the overlying subsalt section resulting in the tilted

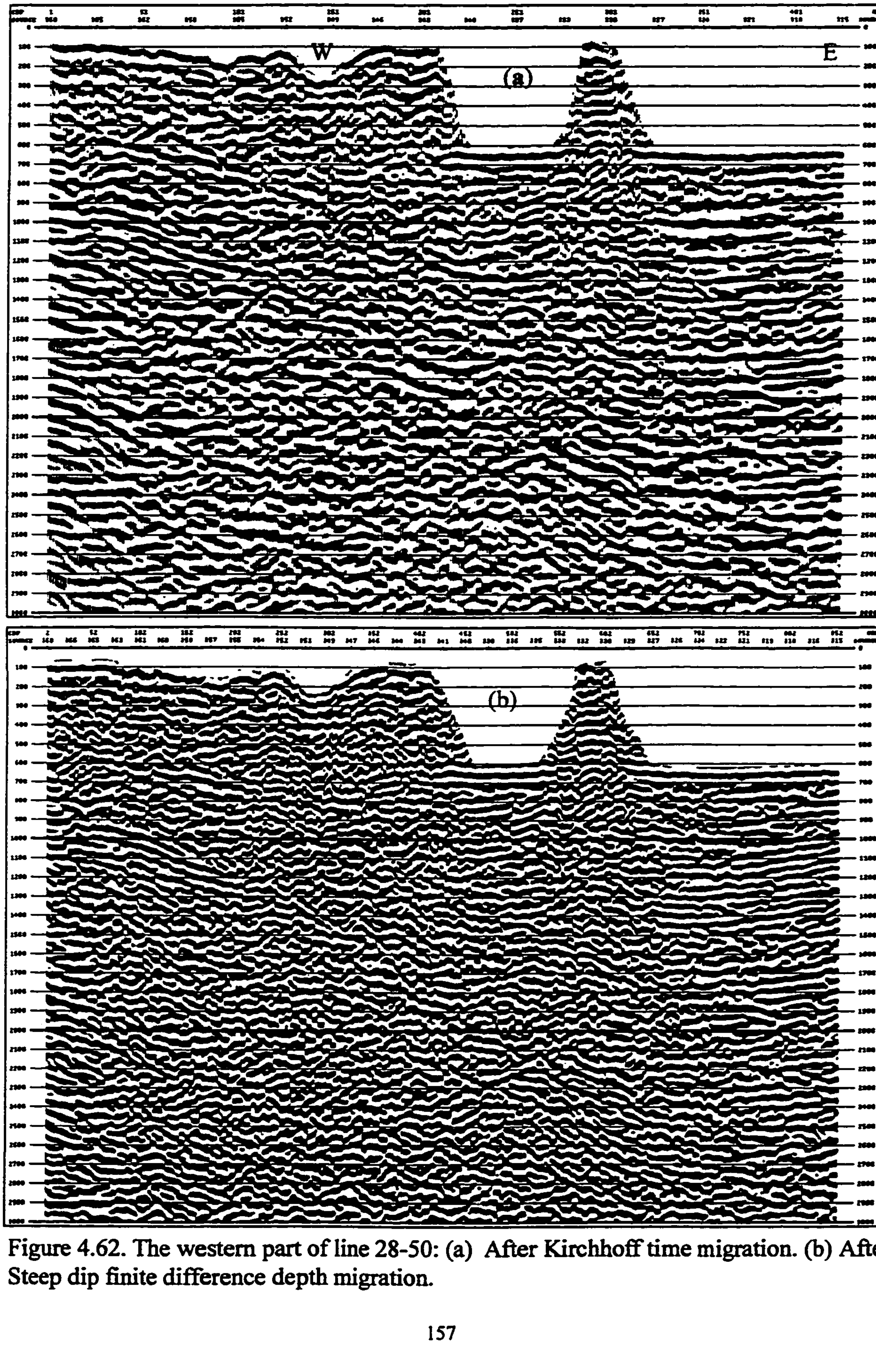

Figure 4.62. The western part of line 28-50: (a) After Kirchhoff time migration. (b) After Steep dip finite difference depth migration.

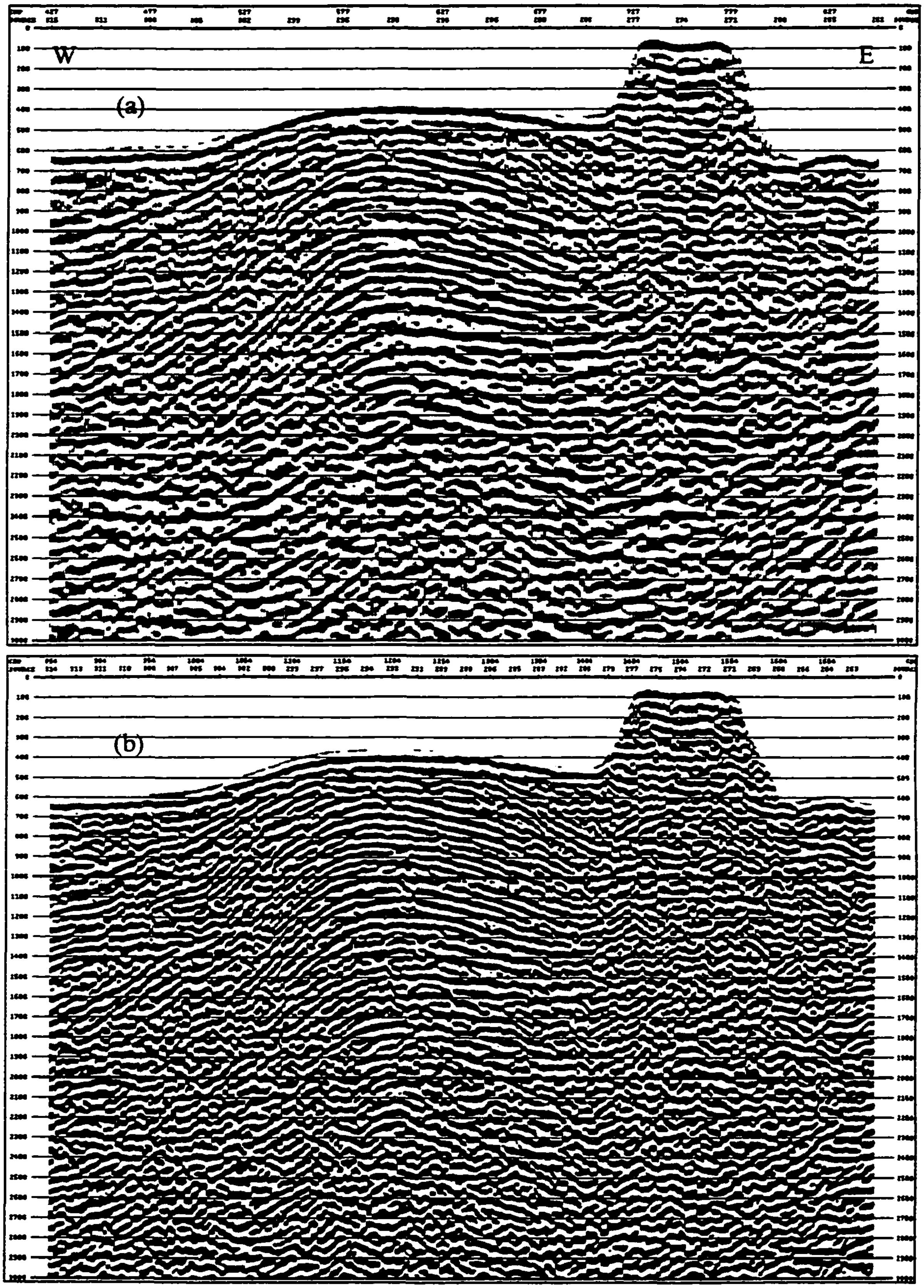

Figure 4.63. The eastern part of line 82-50. (a) After Kirchhoff time migration. (b) After steep dip finite difference depth migration.

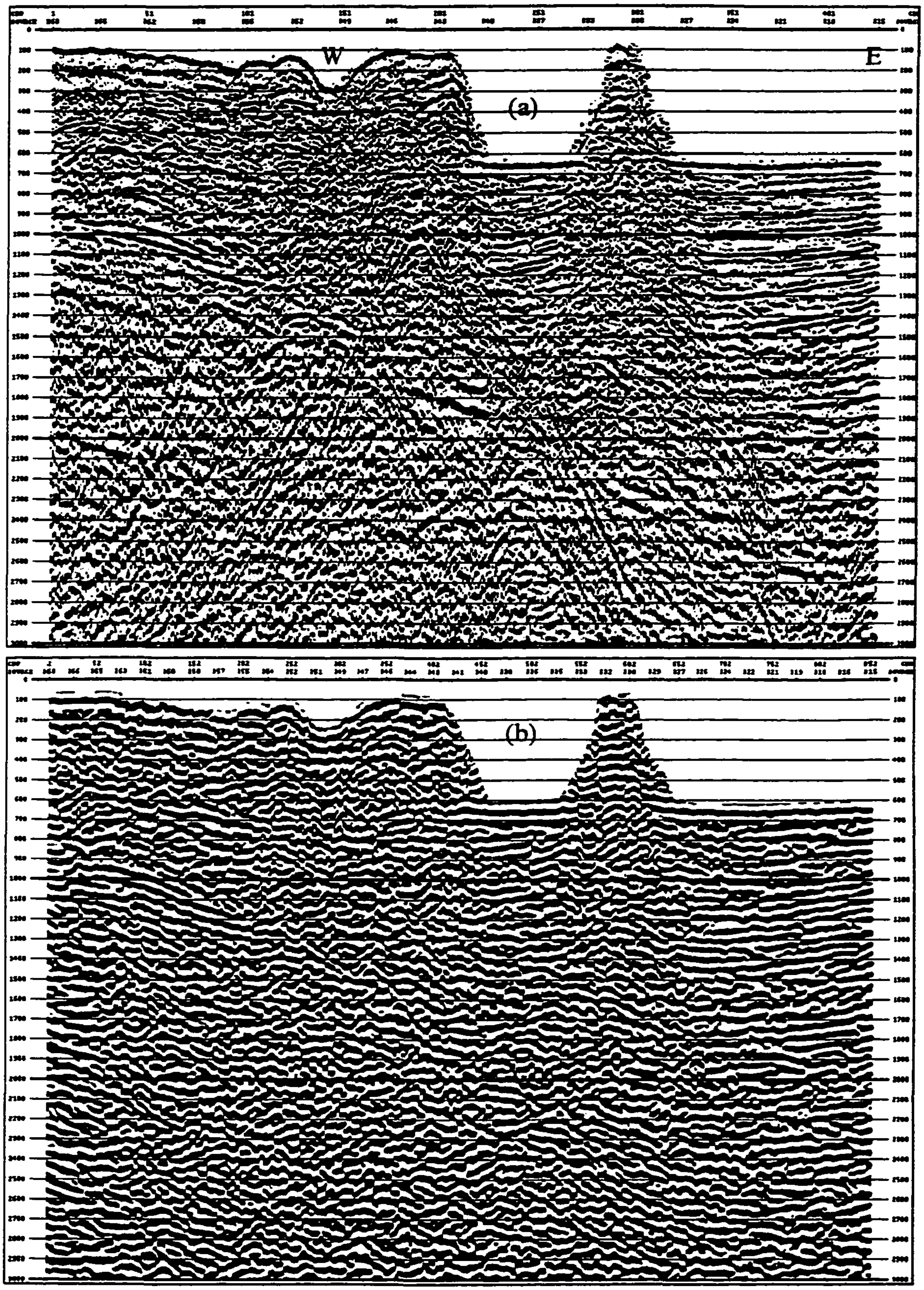

Figure 4.64. The western part of line 28-50 before (a) and after (b) post-stack signal enhancement and steep dip finite difference depth migration.

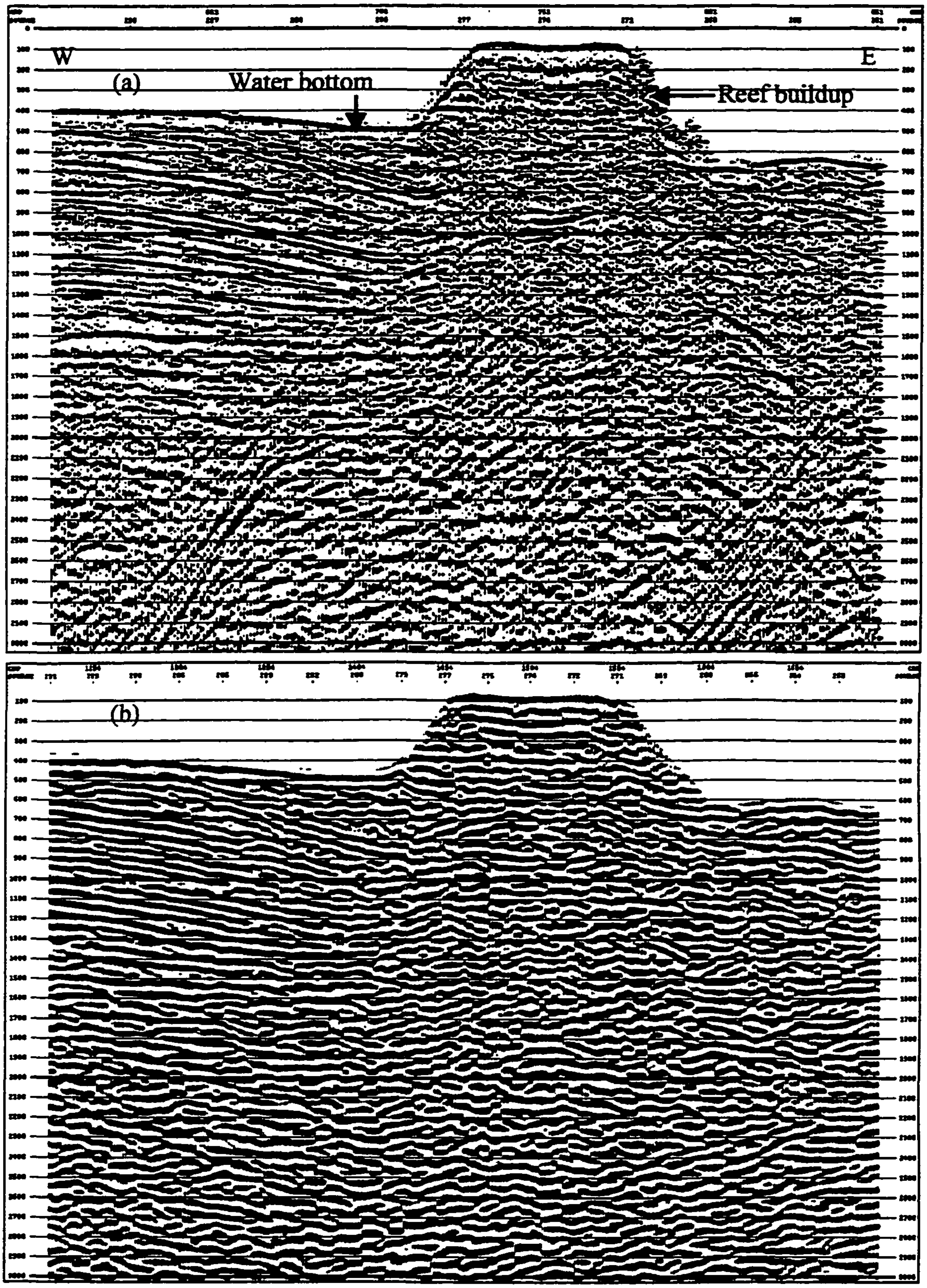

Figure 4.65. The eastern part of line 28-50 before (a) and after (b) post-stack signal enhancement and steep dip finite difference depth migration.

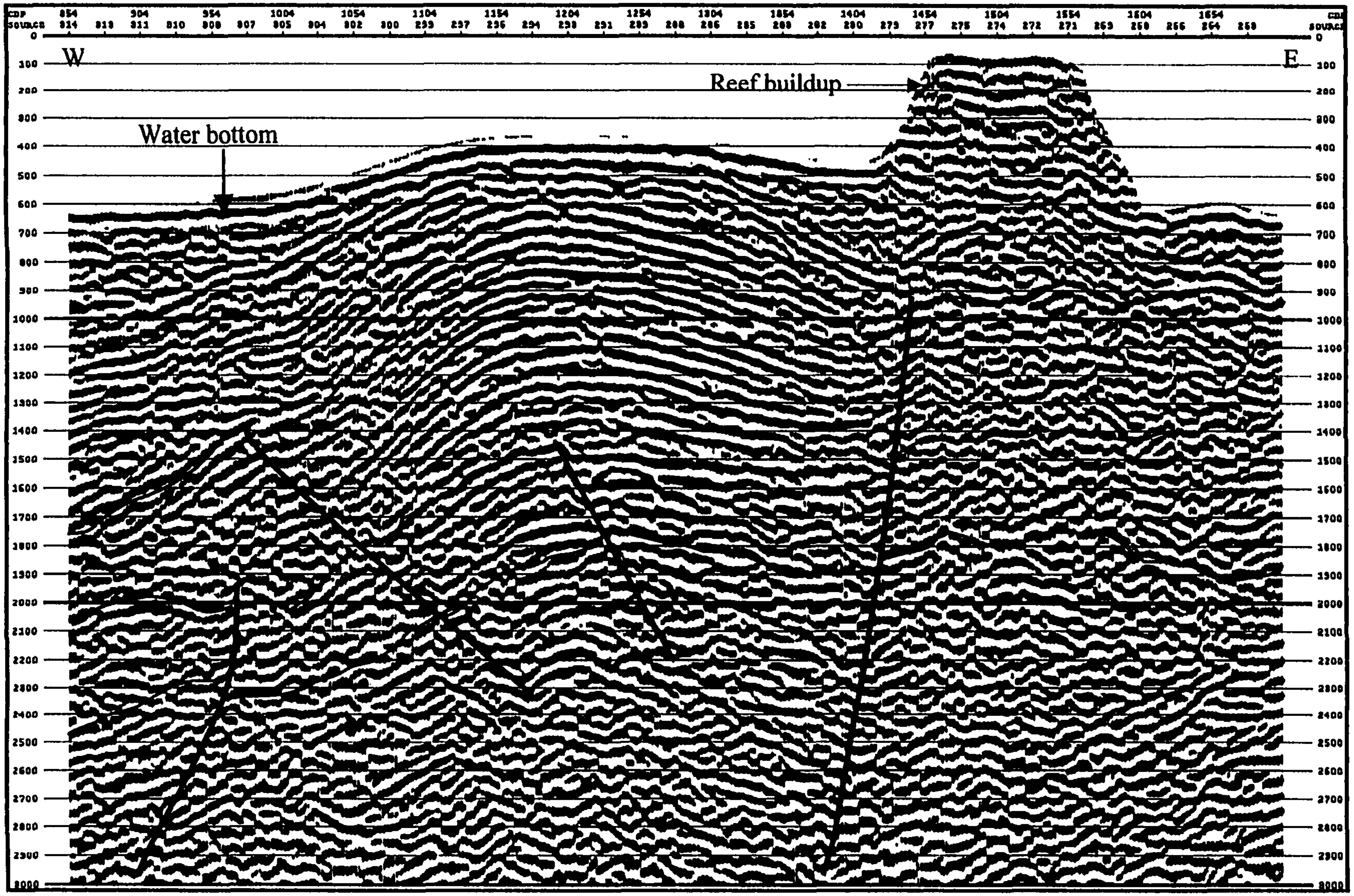

Figure 4.66. The eastern part of line 28-50 after steep dip finite difference depth migration and interpretation. Topsalt, basesalt, and top basement horizons are high-lighted in blue, green, and red, respectively.

fault blocks observed on this part of the line.

Summary:

The 2-D seismic modeling reveals that the highly irregular water bottom topography and the velocity contrast across the seafloor causes severe raypath bending, which induces disruption and distortion of the underlying subsalt reflection events. These distortions are: Coherent noise due to in-line and out-of-section scattering of reflections off the sides of sea floor irregularities, significant travel time errors, and drastic reduction of the amplitudes of the underlying reflections. Wave equation datuming reduces the damaging effects of variable seafloor on the underlying reflections and improves time migration results. The improvement in reflection continuity below variable water depth is the result of higher amplitude and increased coherence after wave equation datuming. The results from post stack wave equation datuming are unmigrated time sections with deleterious effects of irregular water-bottom on the underlying reflection removed. Time migrations performed after wave equation datuming produce results nearly identical to more costly full depth migration methods. Steep dip Finite difference depth migration eliminates the distortions caused by strong lateral velocity changes. It effectively collapses the diffractions, improves the resolution of subsalt seismic events.

CHAPTER V

IMAGE DISTORTIONS ASSOCIATED WITH SALT BODIES VARYING IN LATERAL GEOMETRY AND EXHIBITING COMPLEX BOUNDARIES CASE HISTORIES: CENTRAL AND SOUTHERN RAS BANAS AREA

The severe ray bending and sharp refraction caused by the irregular geometry and complex boundaries of salt result in insufficient down-going energy for illuminating the subsalt reflection events. The loss of transmission energy due to reflection at top of thick, high velocity salt also contributes to the image distortion of the underlying reflections. Velocity pull-ups due to high-velocity salt and deformation and rupturing associated with salt-sediments interaction further complicated the imaging problem in these areas.

V.1. Seismic line 41

Seismic line 41 runs from west to east and is located about 34 km south of line 33 and 6.5 km from Sudan border. This dip line begins 20 km east of the shoreline and extends 26-km seaward (Fig. 1.2). The water depth on the western part (between shotpoints 113 and 56) of the line is flat reaching 2500 ft. It varies from 2500 ft at shotpoint 113 to 1600 ft at the beginning of the line to the west. On the eastern portion (east of shotpoint 56), water depth varies mildly averaging about 1875 ft. The most important, major features observed on line 41 are highlighted in Figure 5.1. These features include: A bowl-shaped mini-basin on the western part of the line with its deepest part at about 3.5 seconds below shotpoint 76 and diffraction events (indicated by a box) on the eastern part of the seismic section. Steep dipping, coherent events crosscut and mask the

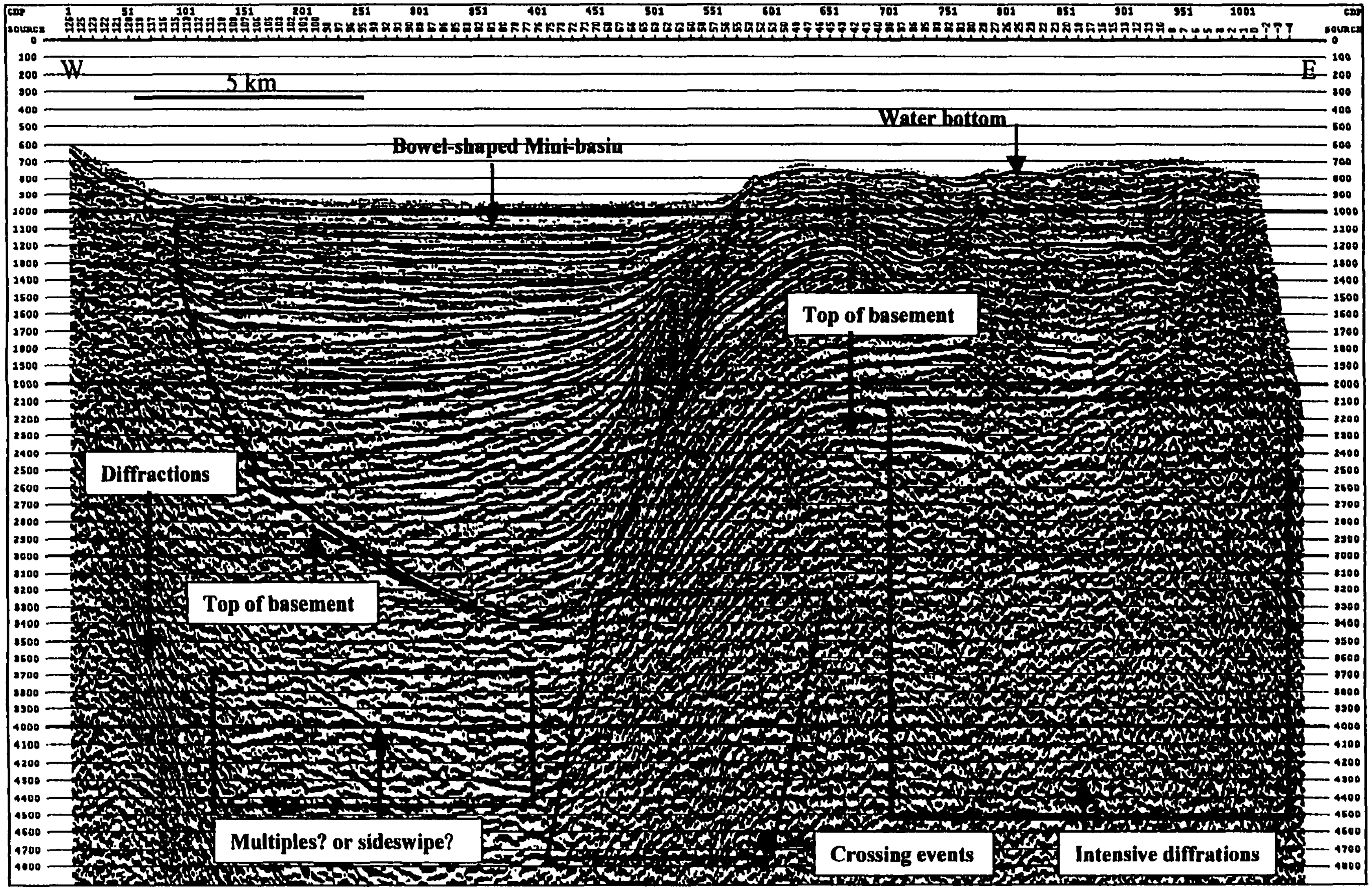

Figure 5.1. The major features and image distortions observed on seismic line 41 before signal enhancement and migration.

subsalt and top of basement reflections in the middle part of the seismic line. These coherent events also obscure the basement structures underneath the deeper part of the mini-basin. The high amplitude, seaward dipping, linear events that crosscut the basement reflections on the western part of the line are likely to be multiples. High amplitude hyperbolic events are also observed in this part of the line. These hyperbolic events are possibly reflections from outside the 2D plane of line 41 or diffractions from deep-seated, high velocity diffractors.

Initial interpretation

No well has been drilled on seismic line 41. The topsalt, basesalt, and top basement reflectors picked on line 33 to the north are transferred to the strike lines 46-75, 47-50, 48, and 49 and then carried to the dip line 41. The initial interpretation indicates seaward-dipping basement-involved major normal faults on the western part of the line. These faults offset the subsalt section and appear to cut deep into the basement. Down-to-the-mini-basin listric growth fault and associated antithetic faults are observed within the overlying supra-salt sequences. On the eastern part of the line, major horst and graben are observed between shotpoint 43 to 29 and 29 to 13, respectively. The major normal faults that formed these horst and graben structures offset the subsalt section and terminate at the base of salt. The intensive diffractions east of the graben on the western part of the section and the crossing events observed on and beneath the deeper part of the mini-basin obscure the structures and make the identification of faults in these areas very difficult. The initial interpretation confirms the presence of the bowl-shaped mini-basin and reveals that it mainly consists of very thick post-rift supra-salt section.

Based on the internal reflection pattern and the sequence boundaries, the supra-salt section is further divided, from bottom to top, into three facies referred to as supra-salt 1,2, and 3. Supra-salt 1 consists of relatively low amplitude reflections and low to moderate continuity. This unit is underlain by relatively thin salt and subsalt rocks in the deepest part of the mini-basin. To the west, supra-salt is separated from the underlying subsalt by what seems to be a residual salt or salt weld. The overlying supra-salt 2 is characterized by high amplitude, parallel reflection pattern with excellent continuity in the middle portion of the mini-basin. On the basin margin (west of shotpoint 101), supra-salt 2 consists of low amplitude, discontinuous reflections and underlain by thin subsalt section. On the western part of the line and the eastern flank of the mini-basin, the salt section is relatively thick (averaging about 0.8 seconds). In this area, The salt section consists of high amplitude, continuos reflection pattern in the lower part and low amplitude, discontinuous reflections in the upper part. It is not known, at this stage of interpretation, whether the high amplitude, continuous events are water bottom multiples, anhydrite, or shale interbeds. Subsalt and supra-salt sections are relatively thin. The salt rapidly thins in the deeper part of the mini-basin and pinches out below shotpoint 82. No salt is observed on the western flank of the mini-basin. The structural discordance relation observed at this location suggests the presence of salt weld.

V.1.1. <u>Imaging problem</u>:

The most obvious imaging problems on the eastern part of seismic line are the intensive diffractions which commingle with one another and with reflection events resulting in disruption of the subsalt, salt, and basement reflection structures east of shotpoint 26 (Fig. 5.2). On the western part of the line, the details of basement structures are masked by coherent, high amplitude, linear reflections and hyperbolic events (Fig. 5.3)

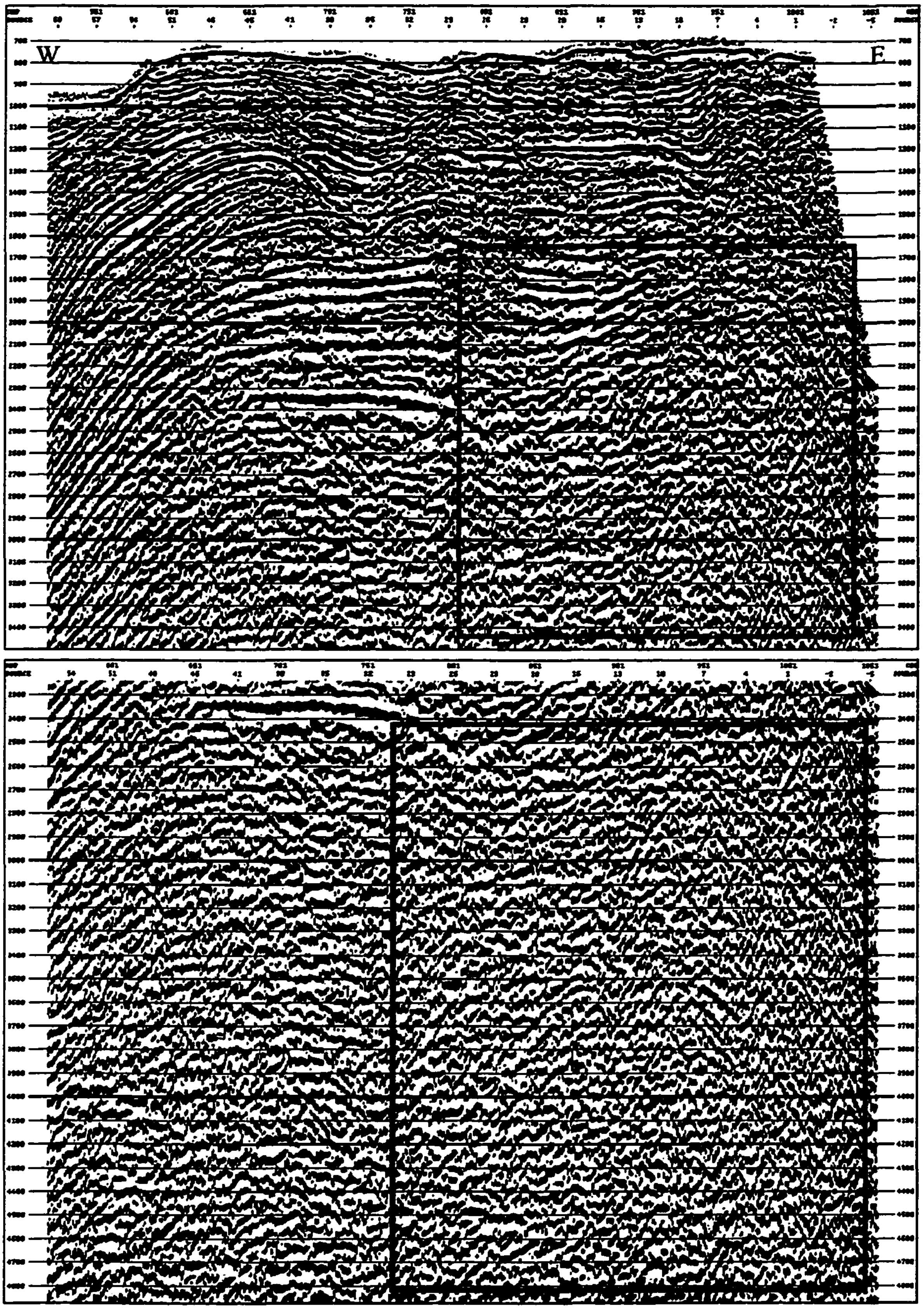

Figure 5.2. The intensive diffraction events (indicated by boxes)observed on the upper (top) and deeper (bottom) portions (enlarged) of the eastern part of seismic line 41.

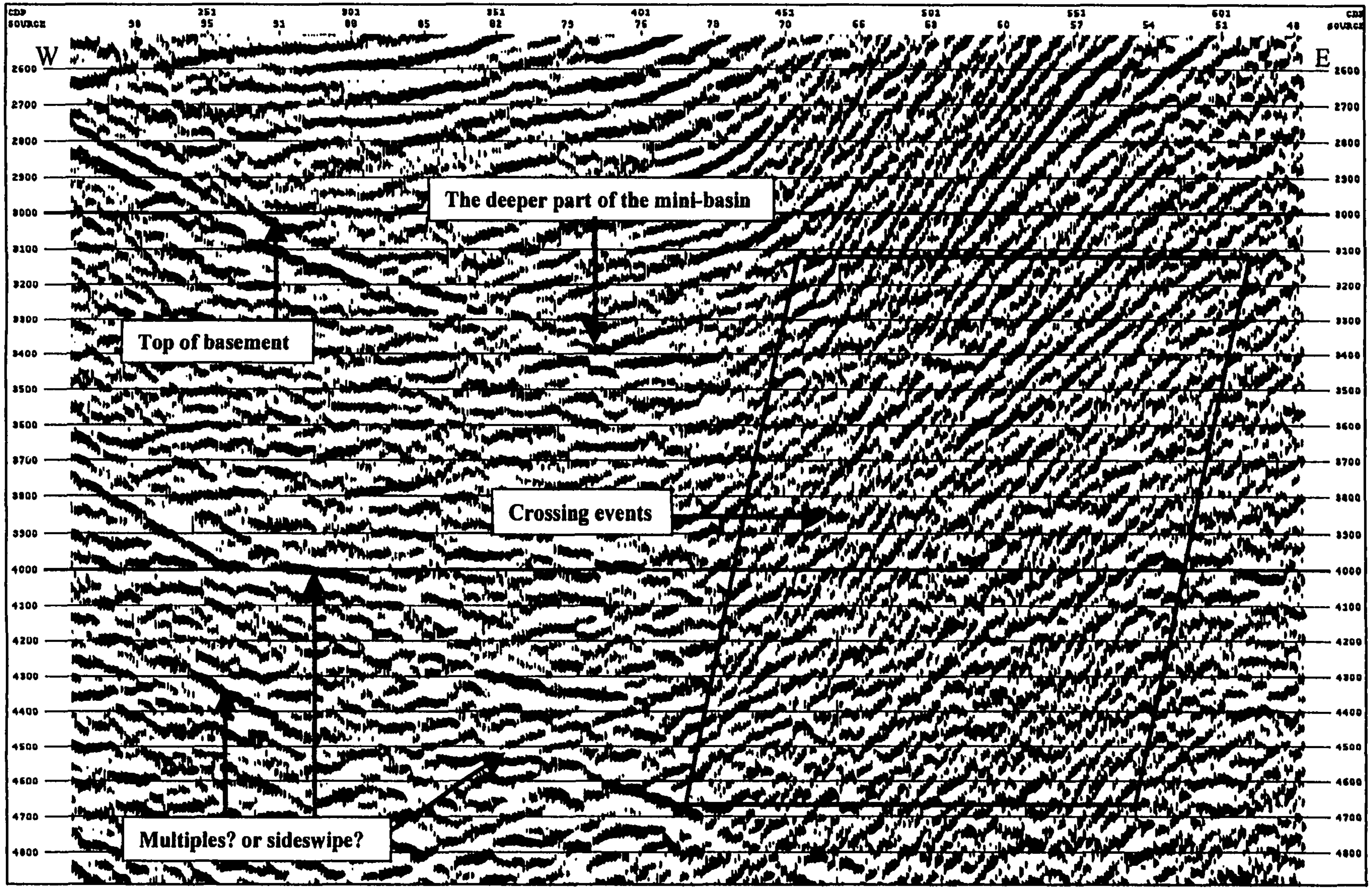

Figure 5.3. Magnified portion of seismic line 41 displaying the linear events that crossed and obscured the salt, subsalt, and top of basement reflections. The crossing events also masked the basement structures below the deeper part of the mini-basin.

which are interpreted to be multiples and sideswipe, respectively. The continuity of top of basement reflector, possible subsalt, and supra-salt 2 reflections on the western part of the line (west of shotpoint 108) is also disrupted by diffraction.

The most significant interpretation question is whether the subsalt and salt sections exist west of shotpoint 82 on the western part of the seismic line. Although topsalt, basesalt, and top of basement reflectors are well defined on the eastern part of the seismic line, their extrapolation to the western part of the seismic section is difficult due to the presence of the crossing events in the deeper part of the mini-basin. The crossing events cause a serious imaging problem on this line. These events overwhelm the eastern flank and deeper part of the mini-basin, crosscut and mask the underling salt and subsalt seismic events (Fig 5.3). The apparent spatial aliasing associated with these events complicates the identification of dipping events in this part of the section. The low amplitude, weak reflections of the deeper and western portions of the mini-basin further complicate the problem of defining the salt and subsalt sequences on this part of the line. The most significant structural features that can be used to investigate this problem are the apparent structural discordance or unconformity above the basement on the western flank of the mini-basin and the pronounced thickening of salt over its eastern flank. The very steep dip and irregular geometry of high velocity salt may have also contributed to this problem. These observations are discussed in 2-D seismic modeling.

V.1.2. 2-D seismic modeling:

<u>Velocity-depth model 1</u>

In this velocity-depth model (Fig. 5.4), a thin salt layer exists on the upper part of the western flank of the mini-basin. No subsalt layer exists in this area and the thin salt

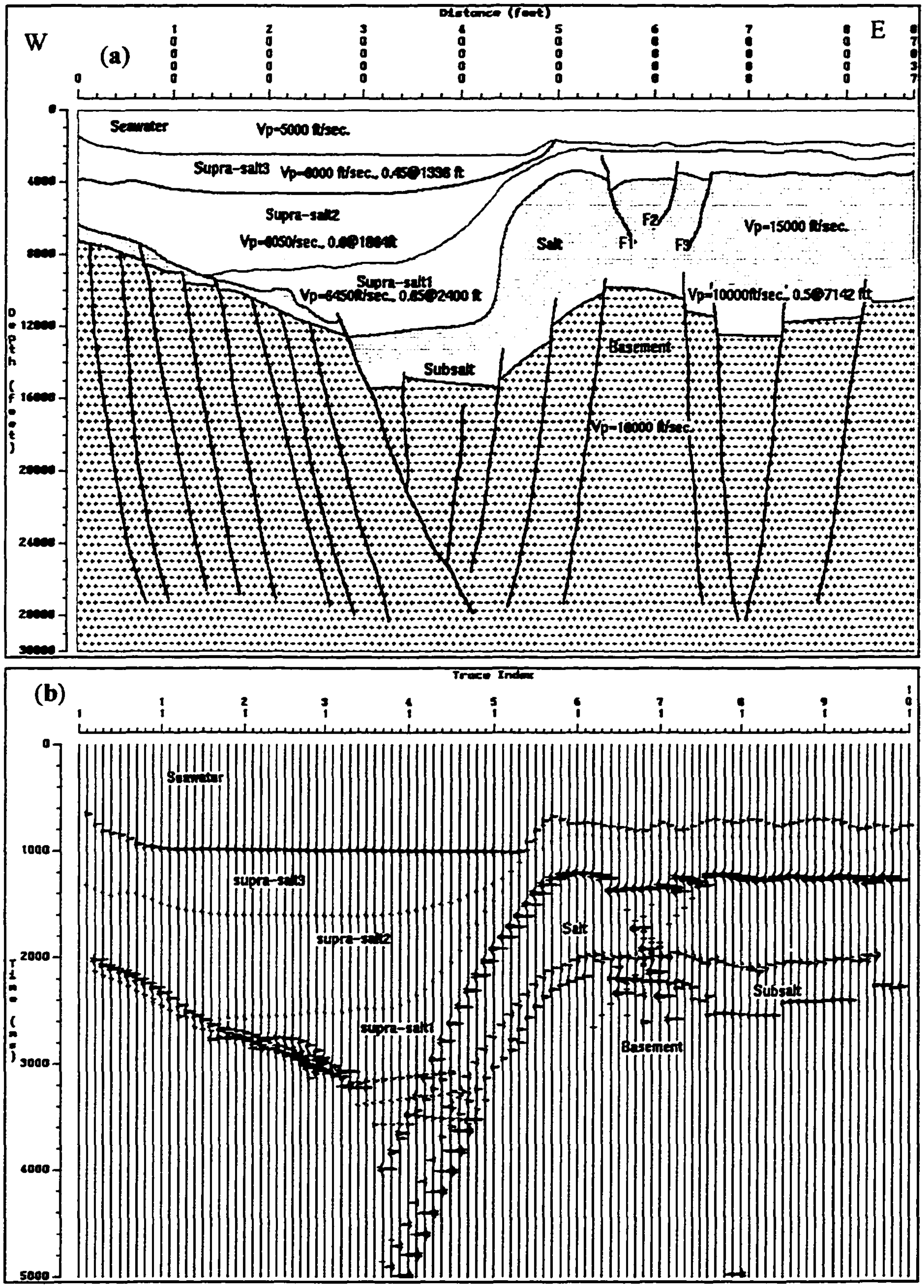

Figure 5.4. Velocity-depth model (a) and normal incidence synthetic section (b)for all layers of seismic line 41.

rests directly on the basement and is overlain by supra-salt 2 facies. Beneath the supra-salt 1, down the slope, the basement is overlain by a very thin subsalt layer. A residual salt separates the supra-salt 1 and subsalt layer. The apparent unconformity, inferred from the discordance relationship between the top of basement and the overlying sedimentary section, suggests that the absence of subsalt layer in this part of the line is likely to due erosion.

The salt layer is very thin in the deepest part of the mini-basin but shows a pronounced thickening and a very steep upper boundary on the east part of the basin. The thinning and thickening of salt is possibly due to salt withdrawal, (caused by differential loading) from below the deeper part of the mini-basin to structurally high, low pressure area on the east side of the basin. The residual salt overlying the subsalt layer, to the west of mini-basin, suggests that the salt, which originally separated supra-salt from the underlying subsalt, have been evacuated from this position and moved updip to the west.

The normal incidence synthetic section resulting from zero offset ray tracing performed on the velocity-depth model is shown in Figure 5.4b. Comparison of synthetic section and real seismic line indicates a good match in arrival times of water bottom, topsalt, basesalt, and top of basement. The synthetic section has also some characteristic of the real data. However, the most significant feature that the model has recreated is the steeply dipping coherent events (highlighted with arrows) which crosscut the subsalt and the basement reflection structures in the deeper part of the mini-basin. The colors of the arrows indicate the horizons that produce these events.

Although the depth model reproduces several features observed on the real line, the high amplitude, continuos top of salt reflector has no match on real seismic line 41.

Therefore, before investigating in the details the causes of the raypaths distortions, the western part of line 41 is reinterpreted and the depth model is modified.

Velocity model 2

The modified depth model is shown in Figure 5.5. Note there is no salt on the western part of this model (east of the garben), only salt weld exists between supra-salt 1 and the thin underlying subsalt layer. The geometry of the shallow normal faults offsetting the upper boundary of salt on the eastern part of the depth model is modified. The salt within the deeper part of the mini-basin is relatively thinner in the modified depth model.

The normal incidence synthetic section (Fig. 5.5b) produced from the modified model provides a much better match with seismic line 41 especially on the western part of the line. It also recreates the crossing events below the deeper part of the mini-basin and simulates the major horst and graben structures observed on the eastern part of line 41.

Raypath characteristics

The zero offset ray tracing performed on the modified model reveals a complex raypaths distortions. The raypaths for the basesalt and top of basement (Fig. 5.6) show considerable ray bending at the very steep portion of the upper boundary of salt body. It worth noting that some rays are missing on the base of subsalt section underneath this area creating what appear to be a "shadow zone" below this location (Fig. 5.6b). These rays are missing because they impinge upon the steeper part of topsalt at or above the critical angle and therefore are not transmitted through high-velocity salt. Note how even mild irregularities in salt boundaries result is a significant raypaths deviation. The raypaths geometry for supra-salt layers, shallow faults, water bottom, and topsalt (Fig. 5.7) confirm the severe raypaths distortion at the steepest portion of the upper boundary of salt. Note

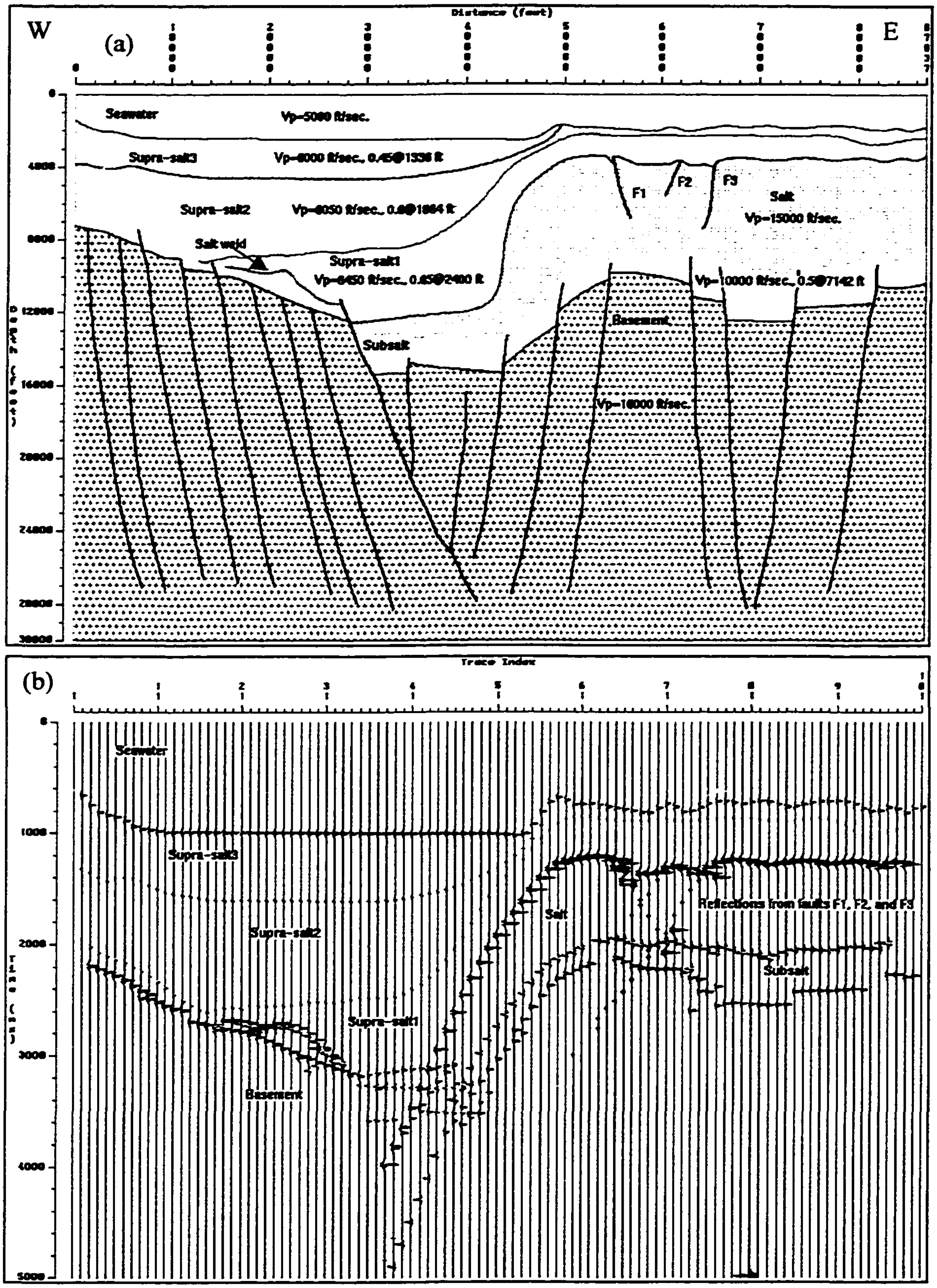

Figure 5.5. Velocity-depth model (a) and normal incidence synthetic section (b) displayed with arrival times for all layers of seismic line 41.

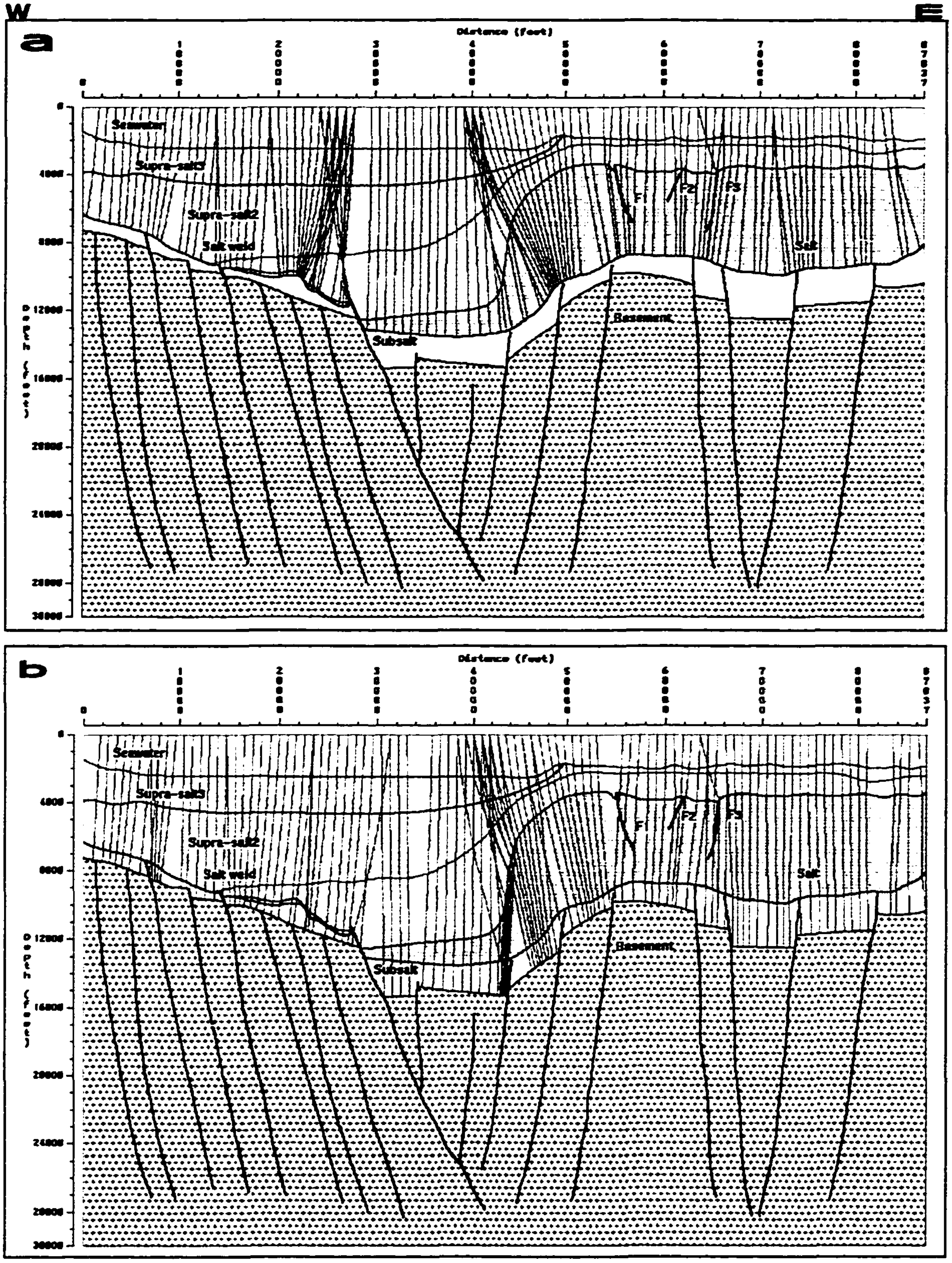

Figure 5.6. Zero offset raypaths for basesalt (a) and top of the basement (b). Salt velocity = 15000 ft/sec.

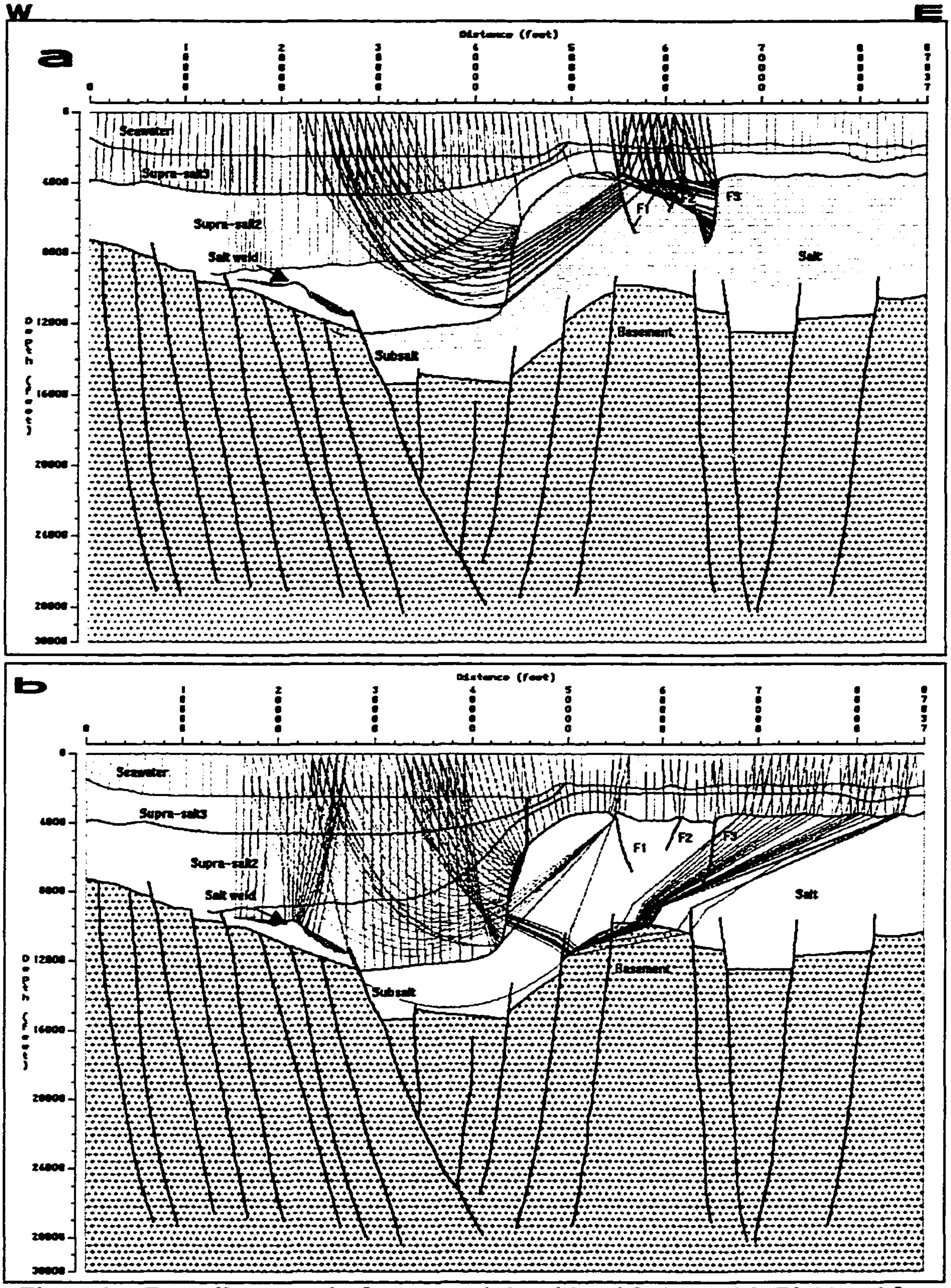

Figure 5.7. Zero offset raypaths for supra-salt 2 and 3 and faults F1, F2, F3 (a) and for water-bottom and topsalt (b). Salt velocity = 15000 ft/sec.

how some rays are transmitted in the salt, refracted at top of basement, and then bent at the base and top of salt. As indicated on the depth model discussed above, the salt body is considered to consist mainly of halite and is thus given a constant velocity of 15,000 ft/sec.

To investigate effects of vertical or lateral velocity changes within the salt, the salt layer is given a velocity gradient to account for velocity variations associated with possible anhydrite and shale interbeds within the lower and upper part of salt body, respectively (Fig. 5.8). The normal incidence synthetic reflections and diffraction events yielded by this depth model are shown in Figure 5.9. Figure 5.10 compares the raypaths for water bottom and topsalt of the two depth models. The raypaths shows curved and straight paths within the varying and constant velocity salt, respectively. A similar comparison between raypaths of supra-salt layers and shallow faults (Fig. 5.11) indicates serious raypaths distortion within varying velocity salt. Figure 5.12 compares the synthetic sections produced by the depth models with salt having variable and constant velocity. The synthetic section, generated by the depth model with salt having variable velocity, has thicker salt layer and shows steeply dipping events within the basement on the eastern part of the model.

<u>Summary:</u>

It is evident, from the analysis of the 2-D seismic modeling results presented above, that the imaging distortions seen on line 41, are caused by the following factors: the steepest portion of the upper boundary of salt on the eastern flank of the mini-basin resulted in severe rayapaths distortions, which obscure the underlying salt, subsalt, and basement reflection structures, the high velocity of salt and lateral velocity variations

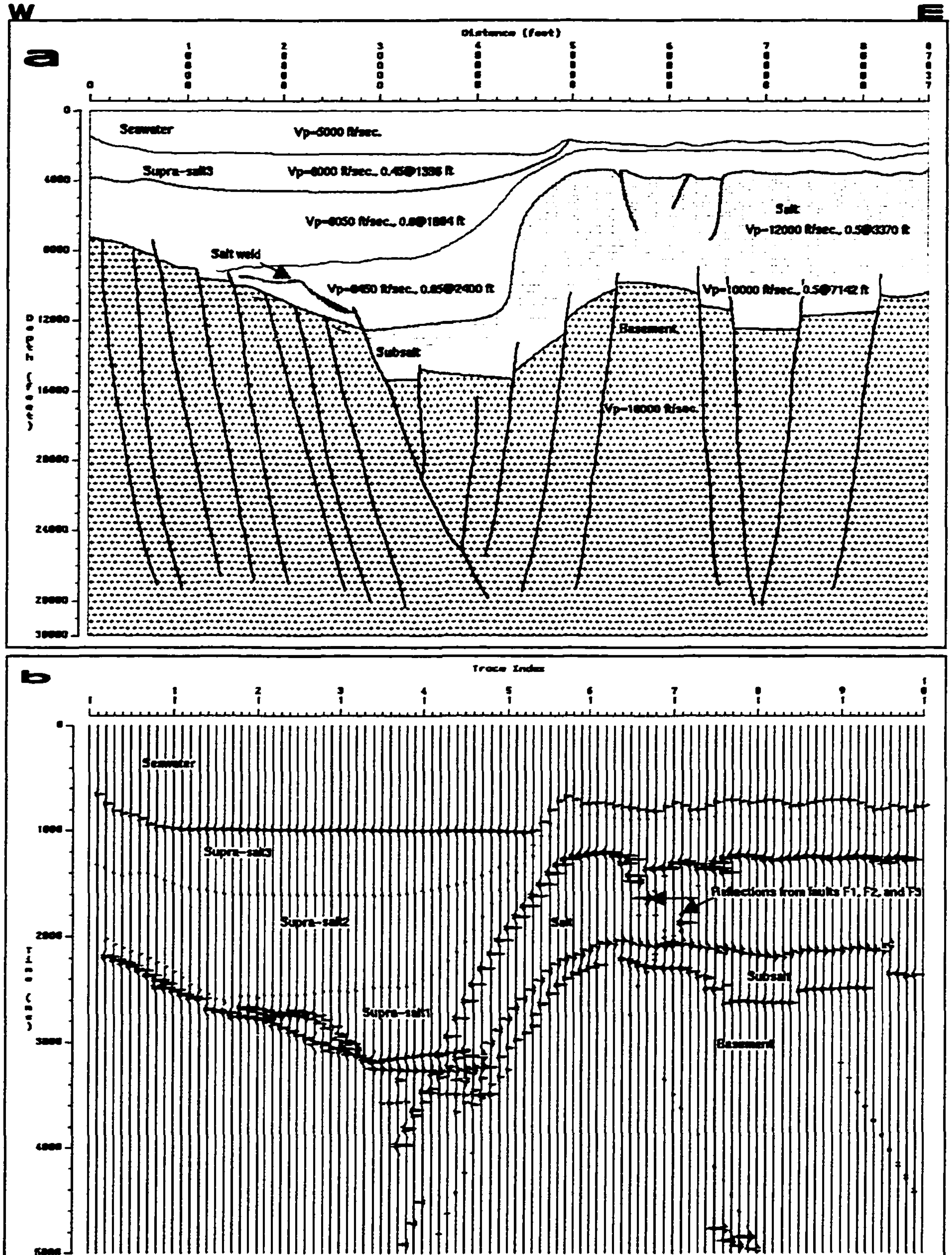

Figure 5.8 . (a) Velocity-depth model for seismic line 41. (b) Normal incidence synthetic trace displayed with arrival times for all layers.

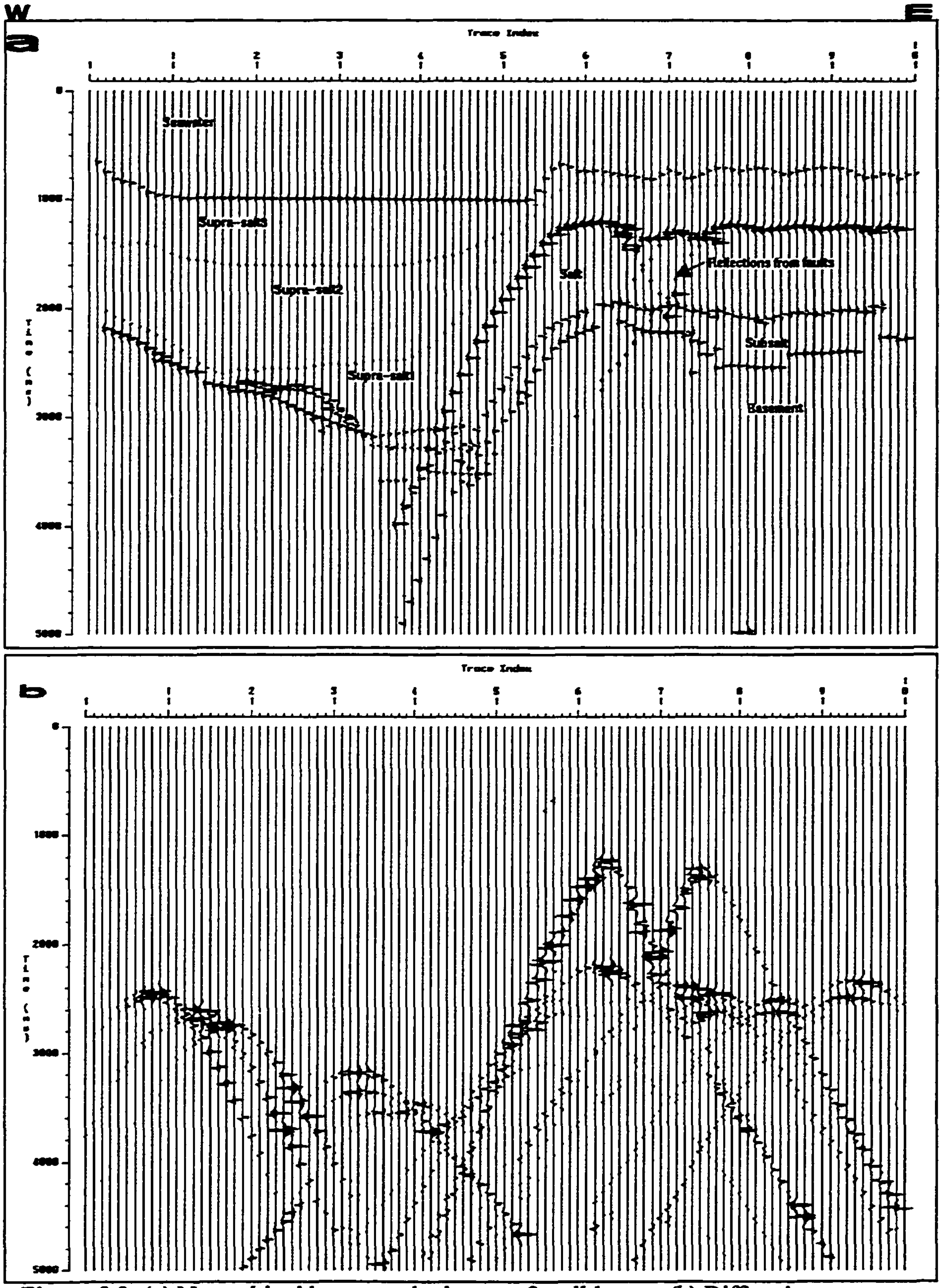

Figure 5.9. (a) Normal incidence synthetic trace for all layers. (b) Diffractions associated with faults and faulted block edges.

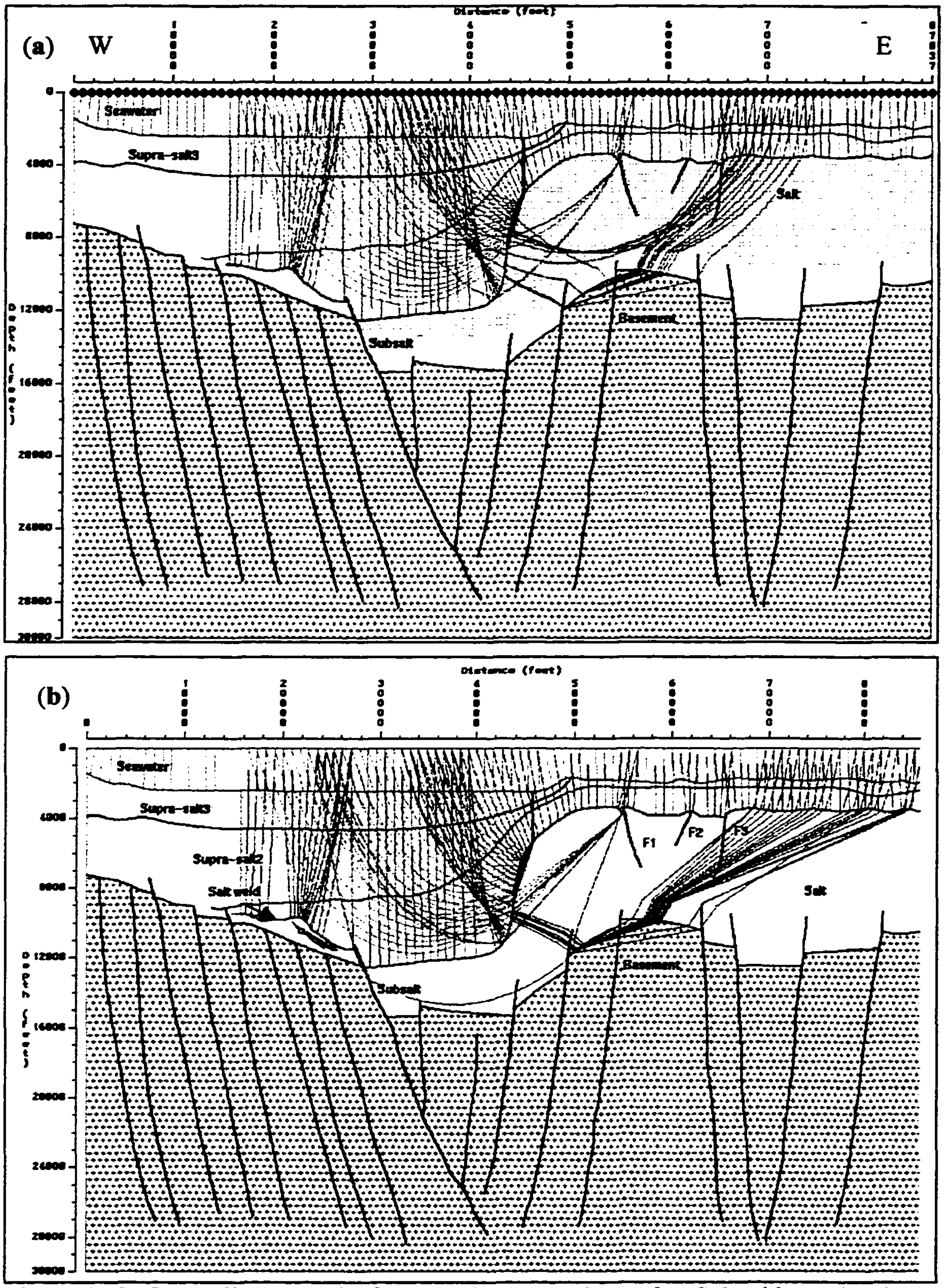

Figure 5.10. Zero offset raypaths for water-bottom and topsalt. Salt with varying (a) and constant (15000 ft/sec.) velocity (b).

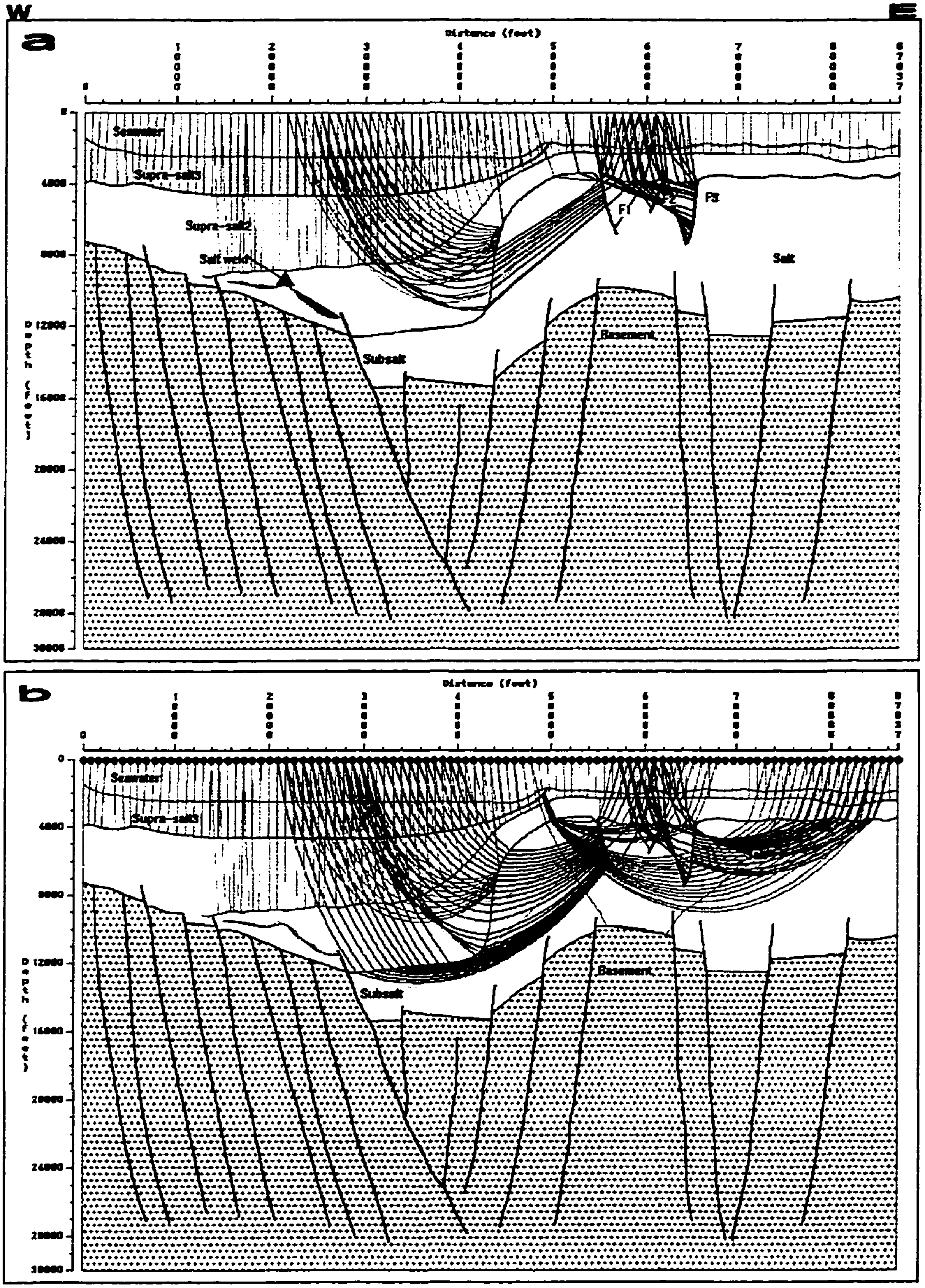

Figure 5.11. Zero offset raypaths for supra-salt 2, 3, and faults F1, F2, and F3. Salt with constant (a) (15000 ft/sec.) and varying velocity (b).

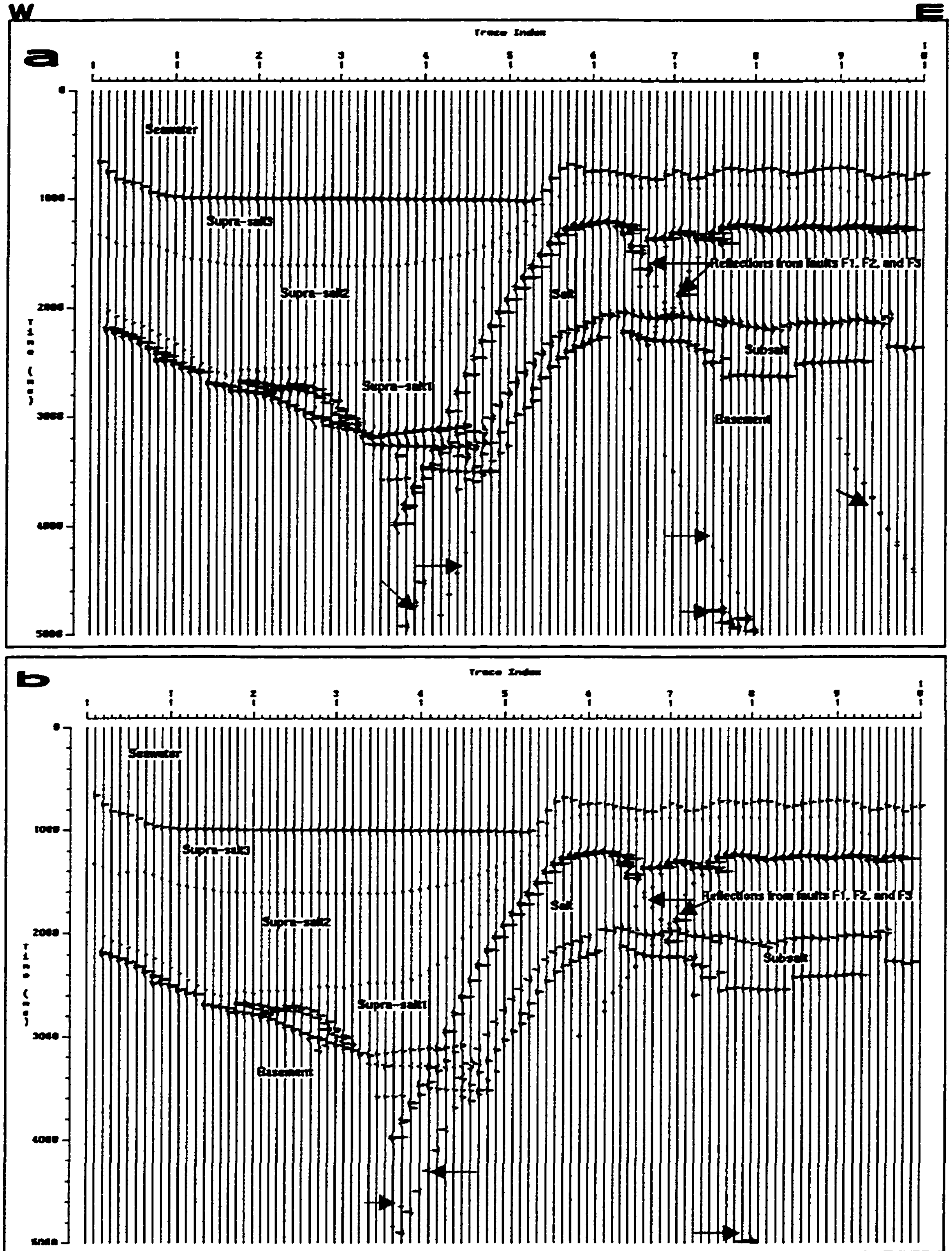

Figure 5.12. Normal incidence synthetic trace displayed with arrival times for all layers. Salt with varying (a) and constant (15000 ft/sec.) velocity (b).

within supra-salt further complicate the imaging problem in this part of the line, the basement involved normal faults and tilted fault block edges on the eastern and western parts of the line cause considerable diffractions, which disrupt the subsalt and top of basement seismic events, the linear and hyperbolic events within the basement on the western part of the seismic section interfere with the primary reflections and complicate the picking and definition of faults in this area.

V.1.3. Post-stack signal enhancement.

Wave equation multiple suppression, F-X trace interpolation, and F-X deconvolution are implemented on line 41 to suppress water bottom multiple, overcome adverse effect of possible spatial aliasing associated with steep dip, and remove random noise, respectively. Wave equation multiple rejection process does not suppress the linear events that are thought to be water bottom multiples within the basement on the western part of the line. The process does suppress some water-related multiples in the upper part of the bowl-shaped mini-basin. The wave equation multiple suppression also does not remove the crossing events that overwhelm the western side of the mini-basin and underlying basement. This suggests that the linear and crossing events are not water bottom multiple. Random noise reduction by F-X deoconvoltion (Fig. 5.13) improves the reflection continuity and enables us to observe the diffraction events more clearly on the eastern and western parts of the line.

V.1.4. Post-stack migration results:

Time migrations performed on seismic section 41 include Steep dip explicit finite difference, Kirchhoff, FK Stolt, and residual time migrations. Steep dip finite difference depth migration is also performed. Although time migrations collapse most of the

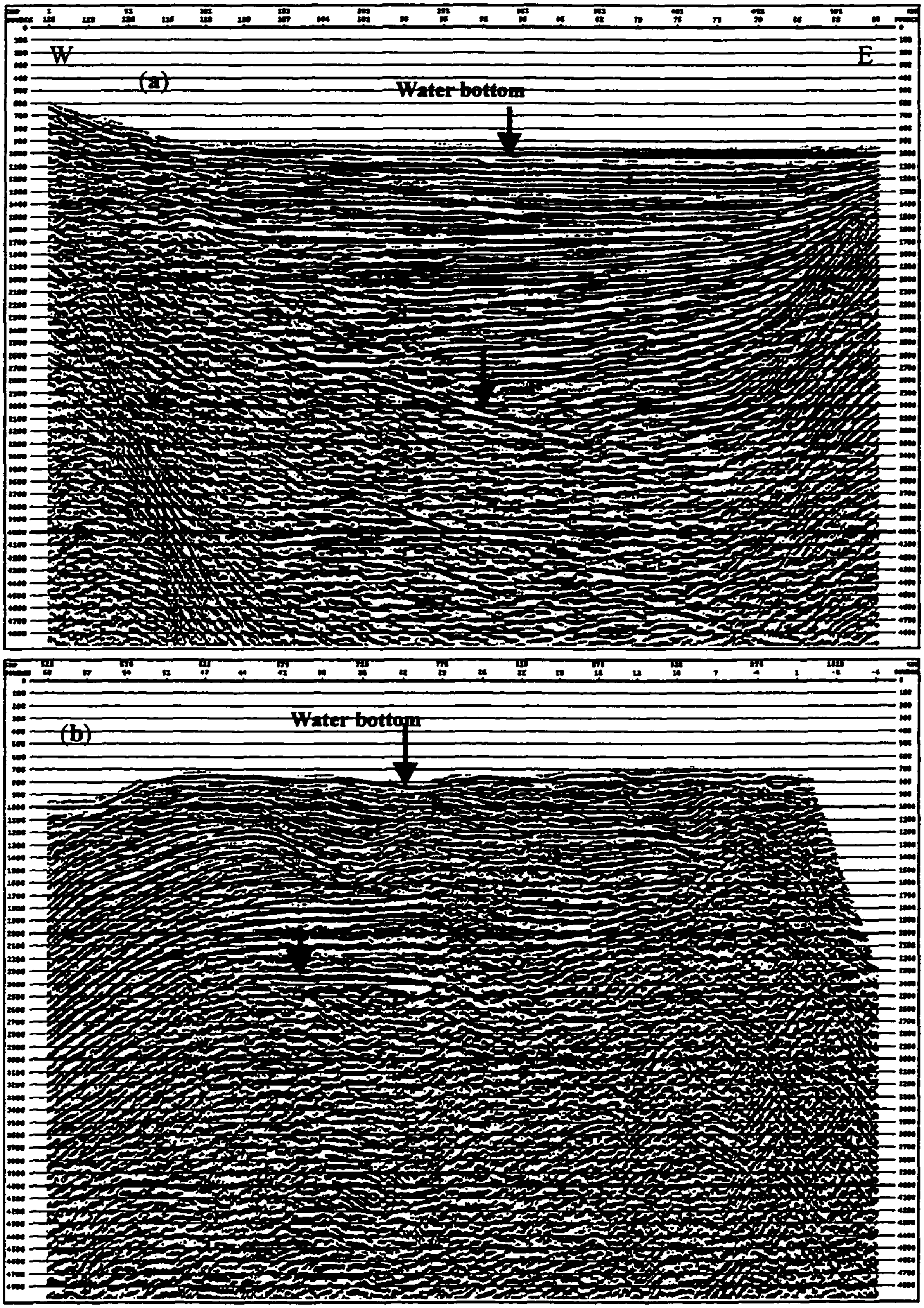

Figure 5.13. The western (a) and eastern (b) parts of line 41 before (a) and after (b) F-X deconvolution. The diffractions became very obvious after F-X deconvolution. Arrows indicate the top of basement.

diffractions observed on line 14, they all fail to accurately image the salt and subsalt reflection events below steep flank of the bowl-shaped mini-basin. Comparison of the migrated seismic section 41 produced by each of migration method reveals that steep dip finite difference depth migration yields a reasonably accurate result.

V.1.4.a. Steep dip finite difference depth migration result:

The choice of steep dip finite difference depth migration method is motivated by its capability to handle strong lateral velocity variation. The method yields reasonably accurate results on most parts of seismic line 41. Comparison of the western and eastern parts of the line before and after steep dip FD depth migration indicates a significant improvement in lateral resolution on the migrated section (Figs. 5.14, 5.15). It is evident from these figures that the migration collapses the diffraction events, resulting in a much better subsalt and basement reflection structures. The fault planes are very clear and easy to pick on the migrated section (Fig. 5.16). Figure 5.17 also shows that the linear events (indicated by a box on sections) within the basement on the western part of the line still exist on the migrated section. The hyperbolic or curved events are also not focussed and remain in this area after migration. This implies that these events are likely to be due to a reflection from outside the 2-D plane of line 41. Figure 5.18 compares the bowl-shaped mini-basin before (a) and after (b) steep dip FD depth migration. The considerable enhancement in resolution, particularly within the deeper potion of the mini-basin, is very obvious on the migrated section. Most of the crossing events are removed. The primary reflections become apparent on the eastern part of the mini-basin. It evident from this result, that some of these events can be attributed to lateral velocity variations. This is consistent with the modeling results discussed previously. However, some of the

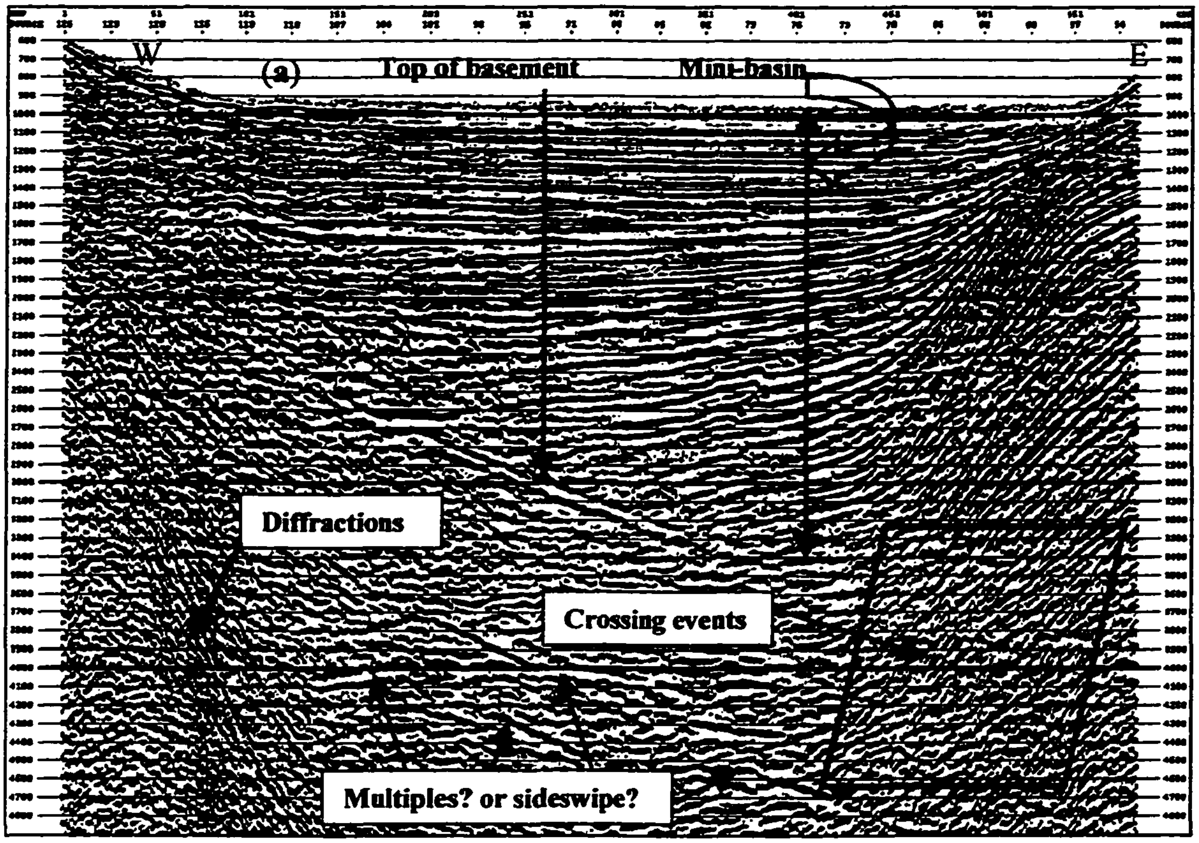

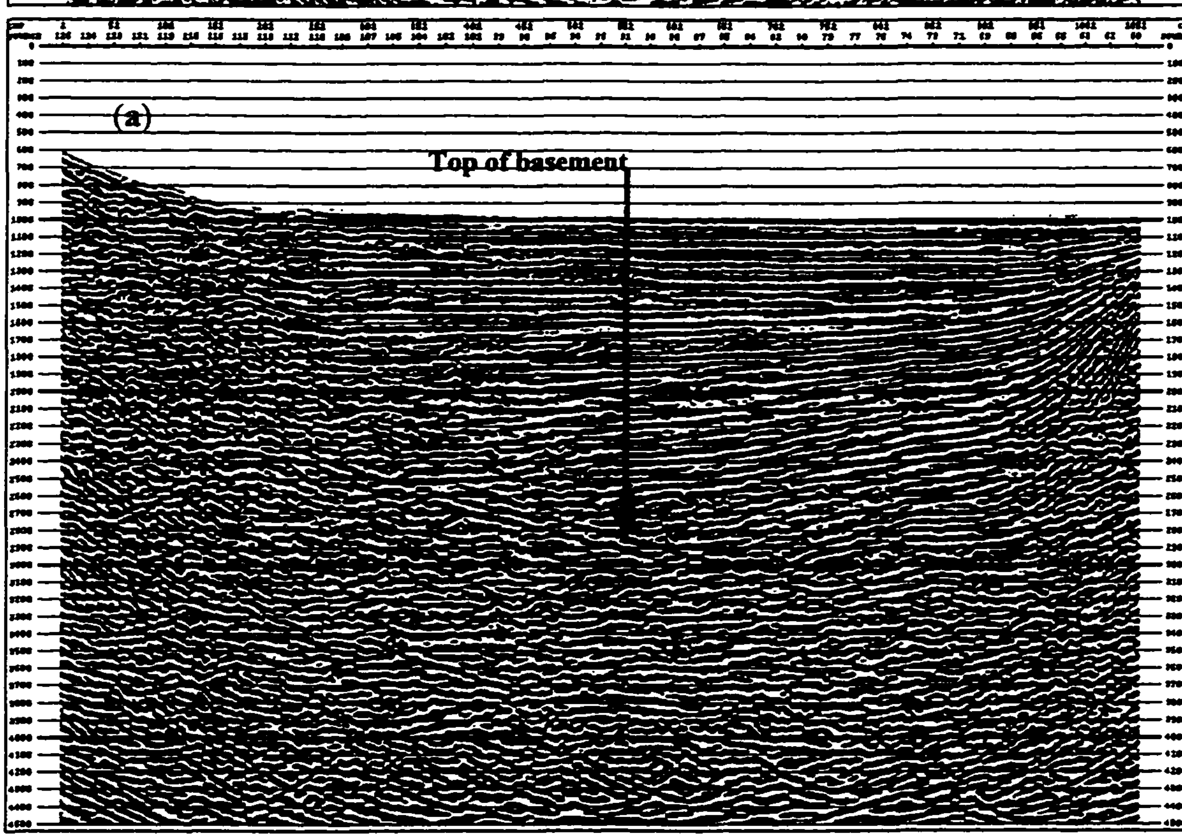

Figure 5.14. The western part of line 41 before (a) and after (b) post-stack signal enhancement and steep dip finite difference depth migration.

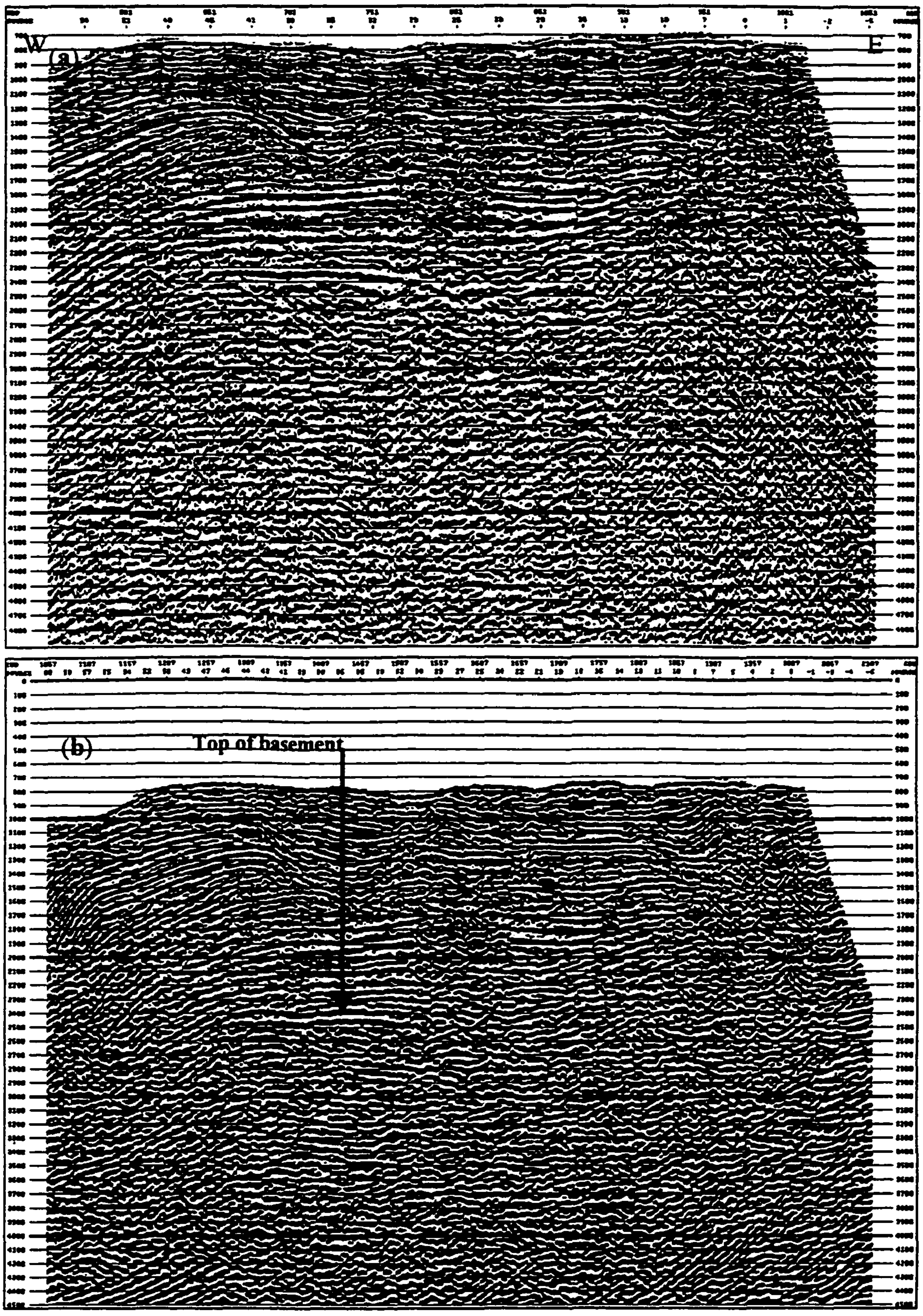

Figure 5.15. The eastern part of line 41 before (a) and after (b) post-stack signal enhancement and steep dip finite difference depth.

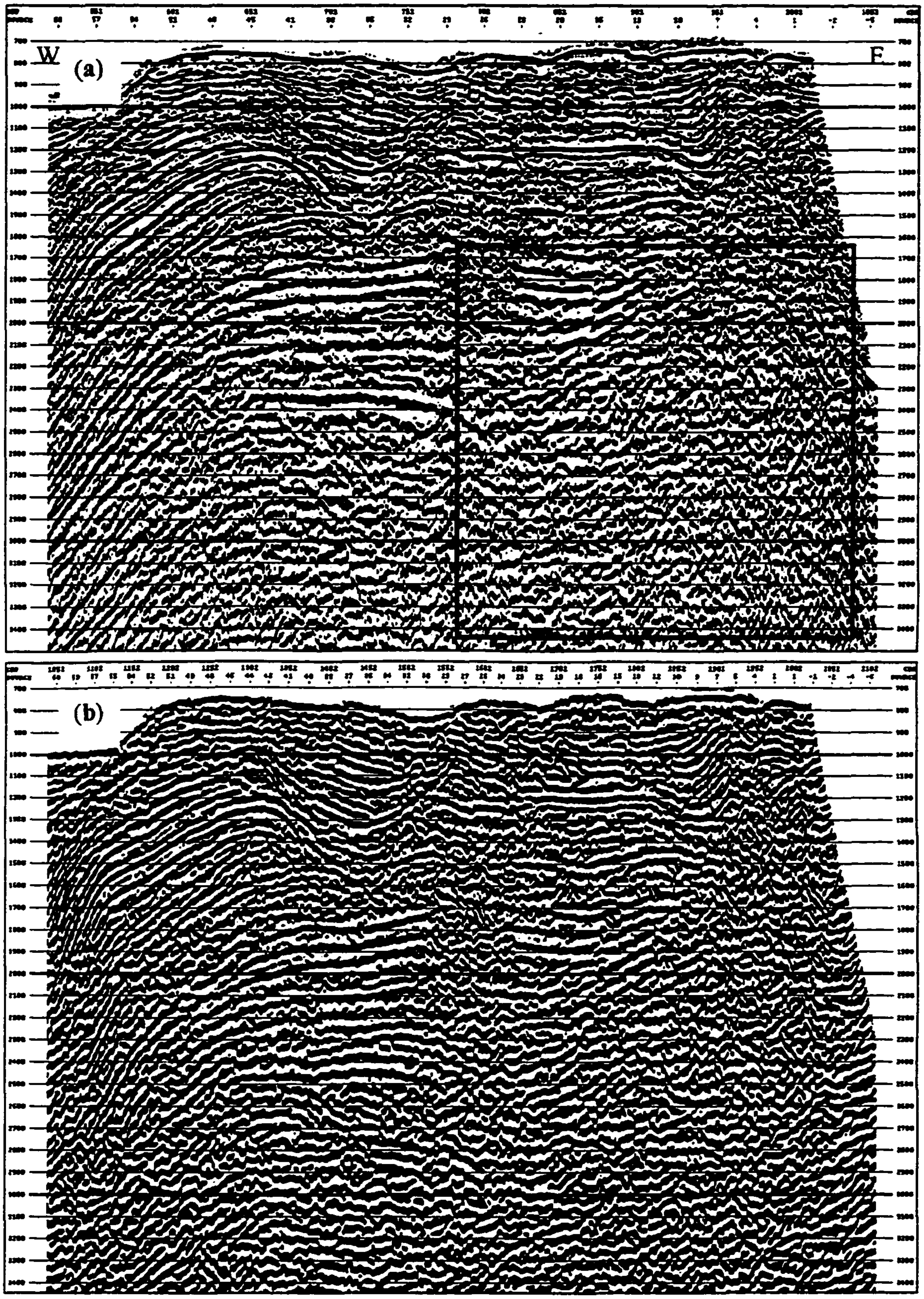

Figure 5.16. The eastern part of line 41 before (a) and after (b) signal enhancement and steep dip finite different depth migration. The migration collapsed diffractions and made the definition of faults easier.

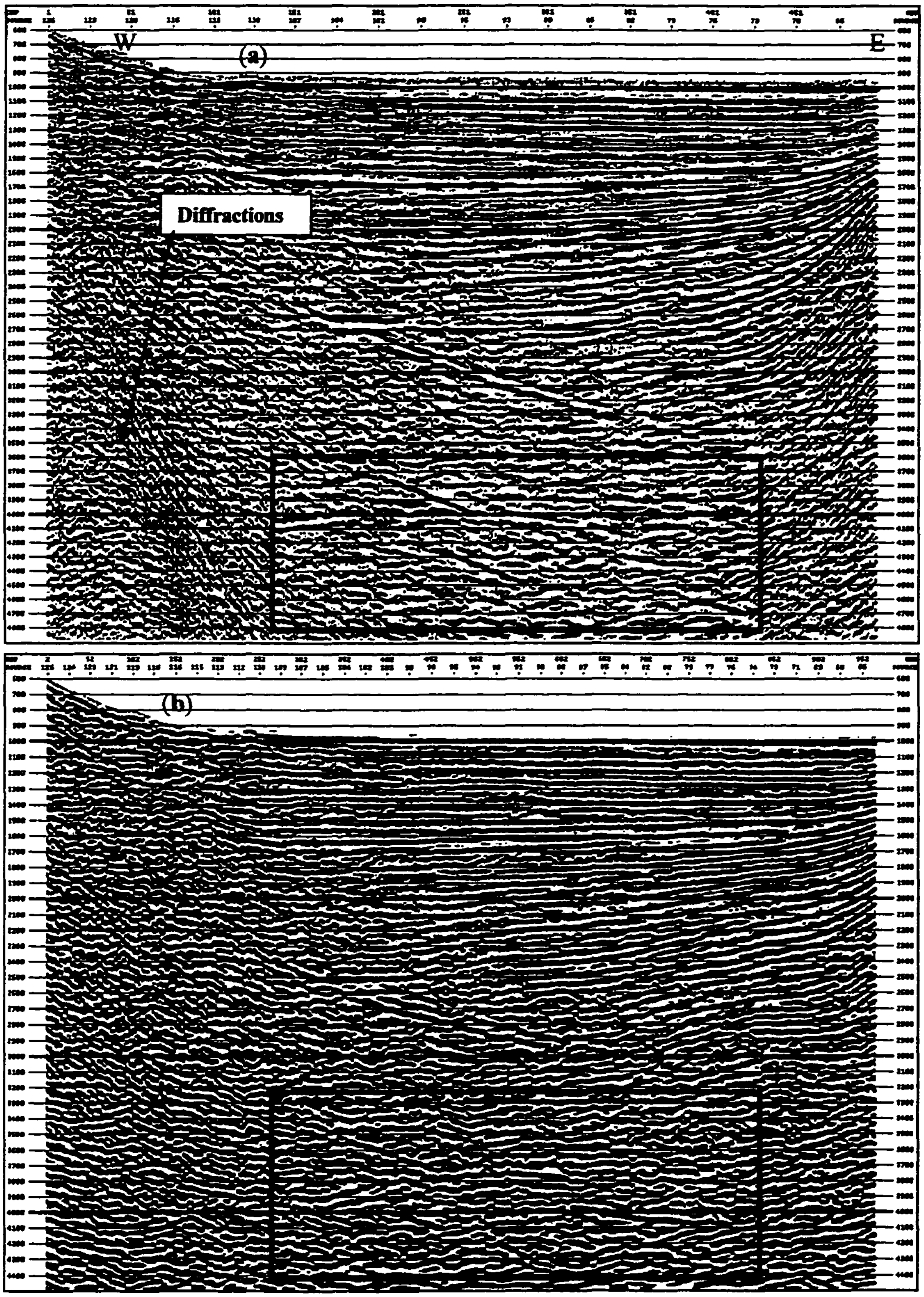

Figure 5.17. The western part of line 41 before (a) and after (b) steep dip finite difference depth migration. The linear and hyperbolic events (indicated by a box) exist on the migrated section.

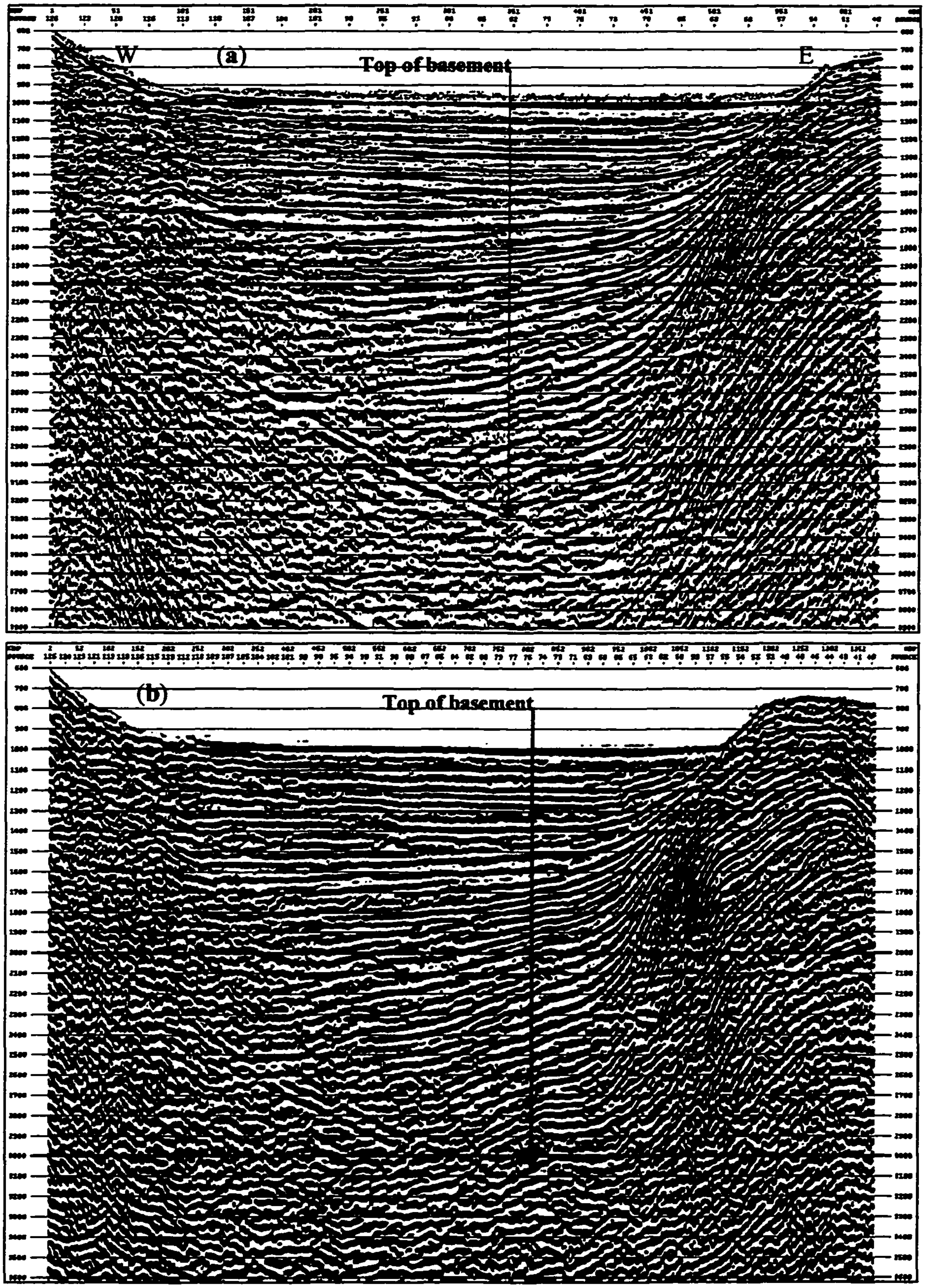

Figure 5.18. The western part of line 41 showing the bowel-shaped mini-basin before (a) and after (b) steep dip finite difference depth migration. Significant improvement in lateral resolution after migration.

crossing events still remain on the migrated section on and below the steeper side of the mini-basin and obscure salt and subsalt reflection events in this areas. This implied that some of the distortions that remain on the migrated section are more complex and beyond the capability of post-stack steep dip FD depth migration. It worth is noting, that the previous processing performed on line 41 does not include DMO process. This suggests that the steep boundary of salt on the eastern side of the mini-basin may have resulted in reflection point smearing. The solution to this problem is to perform DMO process before stack. It is also possible that the severe ray distortions due to irregular geometry of salt and the strong lateral velocity variations at steep dips have resulted in non-hyperbolic travel times and thus degraded the stacking quality in this part of the section. Pre-stack depth migration is optimal imaging tool to consider in such complex area. Unfortunately, the field records required for these processes are not available to us.

V.2. **Seismic Line 16**

This dip line runs from southwest to northeast (Fig.1.2). It begins 1.5 km east of the shoreline and extends 30 km seaward. The shallow carbonate reefs on the southeast part (SW of shotpoint 65) of the line cause considerable changes in seafloor topography (Fig. 5.19). Consequently, the bathymetry varies greatly, ranging from 250 ft in the shallow parts to 2125 ft in the deeper areas. The water depth of the northeast part (NE of shotpoint 56) of the line varies mildly, ranging from 1775 to 2188 ft. Ra West-1 well is located at shotpoint 135 on the southwestern part of line 16. The well encountered the tops of salt, basesalt, and the basement at 2832, 3523, and 4550ft respectively, and bottomed in Pre-Cambrian basement at total depth of 5275ft.

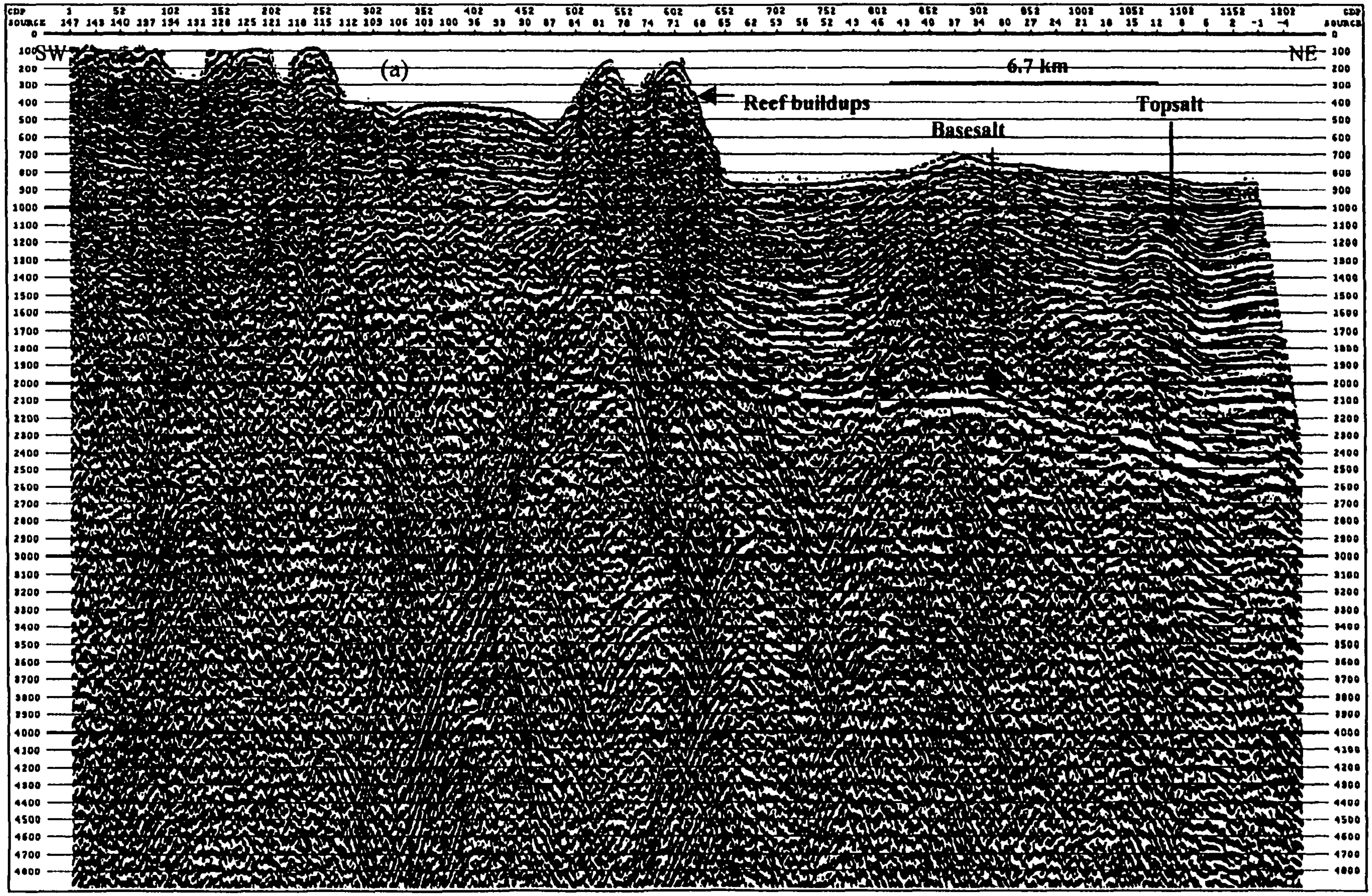

Figure 5.19. Seismic line 16 before signal enhancement and migration.

Well data:

The basement is umconformably overlain by the Lower Miocene lower syn-rift megasequence which consist, at this location, from bottom to top, of Nukhl (3760-4550 ft) and Belayim (3523-3760 ft) Formations. Belayim Formation is overlain by the Middle Miocene South Gharib Formation (2832-3523 ft). The post-rift Pliocene to Recent mega-sequence overlying South Gharib FM consists of Wardan (1,921-2,832 ft) and Shagara (642-1,921 ft) Formations.

Lithological description:

The basement rocks encountered in this well consist of coarse-grained granodioritic igneous rocks in the lower part (4550- 5275 ft) and weathered granitic igneous rocks in the upper part (3760-4550 ft). Nukhl formation consists mostly of medium to coarse-grained sandstone interbedded with granitic clasts. Thin interbeds and anhydrite and mudstone are locally common. Belayim Fm consists of locally argillaceous and anhydritic dolomite. Dolomitic limestone occurs locally.

South Gharib Formation consists mainly of fine to coarsely crystalline anhydrite interbedded with locally argillaceous and anhydritic dolomite. Halite interbed (2930-3020ft) occurs in the upper part. Wardan Fm consists of fine to very coarse-grained sandstone interbedded with mudstone in the lower part and medium to very coarse-grained sandstone and conglomarate in the upper part. Shagara Fm consists of poorly consolidated, vugy, finely crystalline and limestone with minor interbeds of sand and conglomerate. The limestone is locally rich in reefal and skeletal debris.

Initial interpretation:

Following the definition of major faults, the three objective horizons (defined at the well location) representing topsalt, basesalt, and top of basement are extrapolated to the northeast part of the line (Fig. 5.20). The well was drilled closed to the southwestern end of the line in the coastal area, which is dominated by varying seafloor topography and complex basement structures. The resulting image distortions disrupt the continuity of topsalt, basesalt, and top basement reflectors hence their extrapolation to the northeast portion of the line is rather difficult. The interpretation reveals several basement-involved major normal faults offsetting overlying subsalt section and resulting in a series of horsts and half grabens structures. The faults terminate at the base of salt on the northeast part of the section and cut through the entire sedimentary section on the southeast part. Thick salt with undulating upper boundary shows gradual thinning beneath a small depocenter just northeast of the two carbonate reefs in the middle of the seismic line. The salt section is relatively thin and is offset by the basement-related faults on the northeast part of the line. The internal reflection pattern of salt on the northeast part of the line

varies from high amplitude continuous reflection to low amplitude chaotic pattern. Underneath and to the southwest of the reefs in the middle of the section, the salt shows discontinuous, relative low amplitude reflection pattern. The tops of basement and subsalt seismic events are generally weak and significantly disrupted on the southwest portion of the line.

V.2.1. Imaging problems:

Close inspection of line 16 indicates that complexity and origin of imaging problems vary along this line. The imaging distortions observed on seismic line 16 are illustrated in Figures 5.21, 5.22, 5.23, and 5.24. On the southwest portion of the line, beneath the carbonate reefs; the salt and subsalt show a weak reflection pattern with low

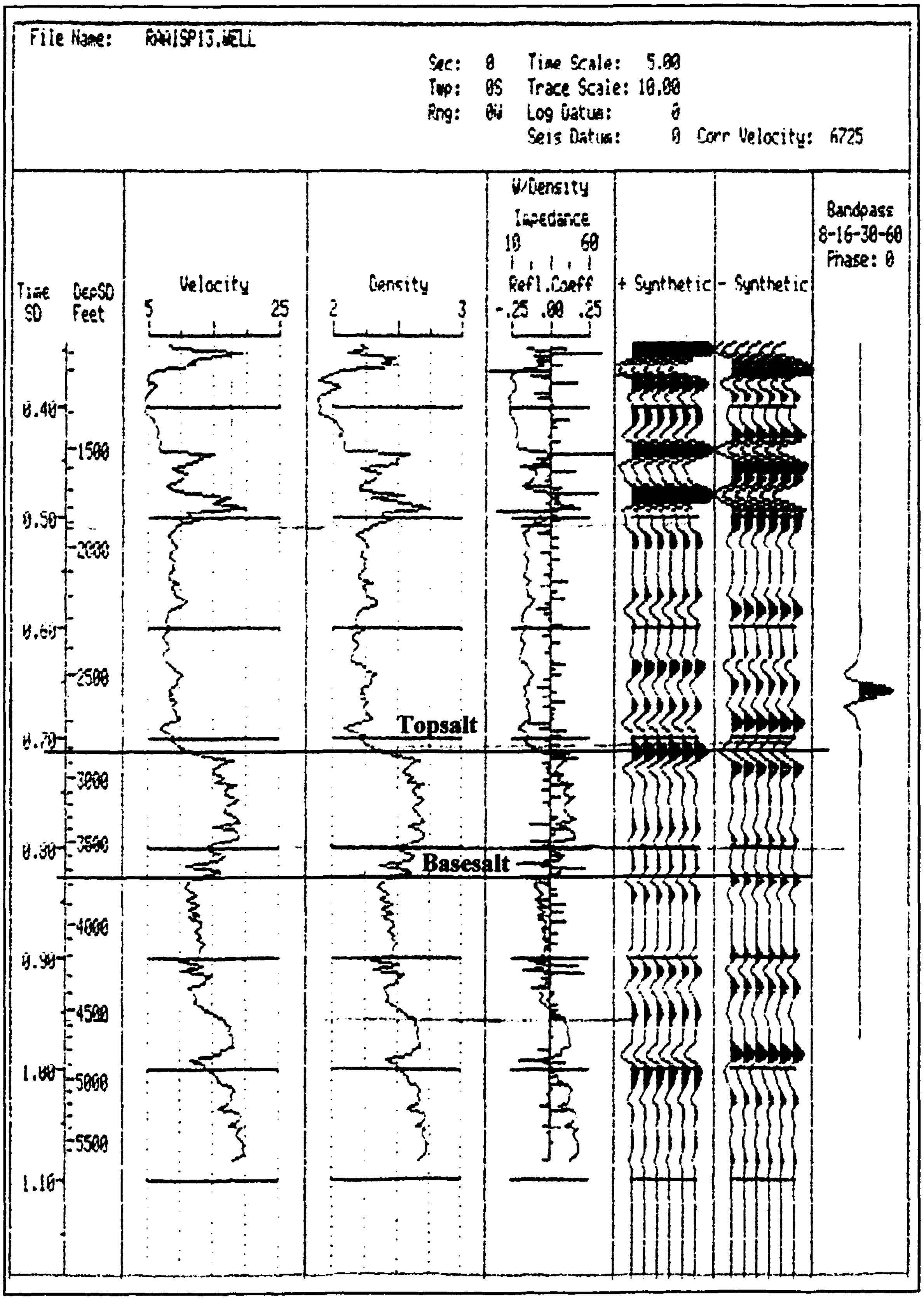

Figure 5.20. Synthetic seismogram for RA West-1 well with stratigraphic interpretation.

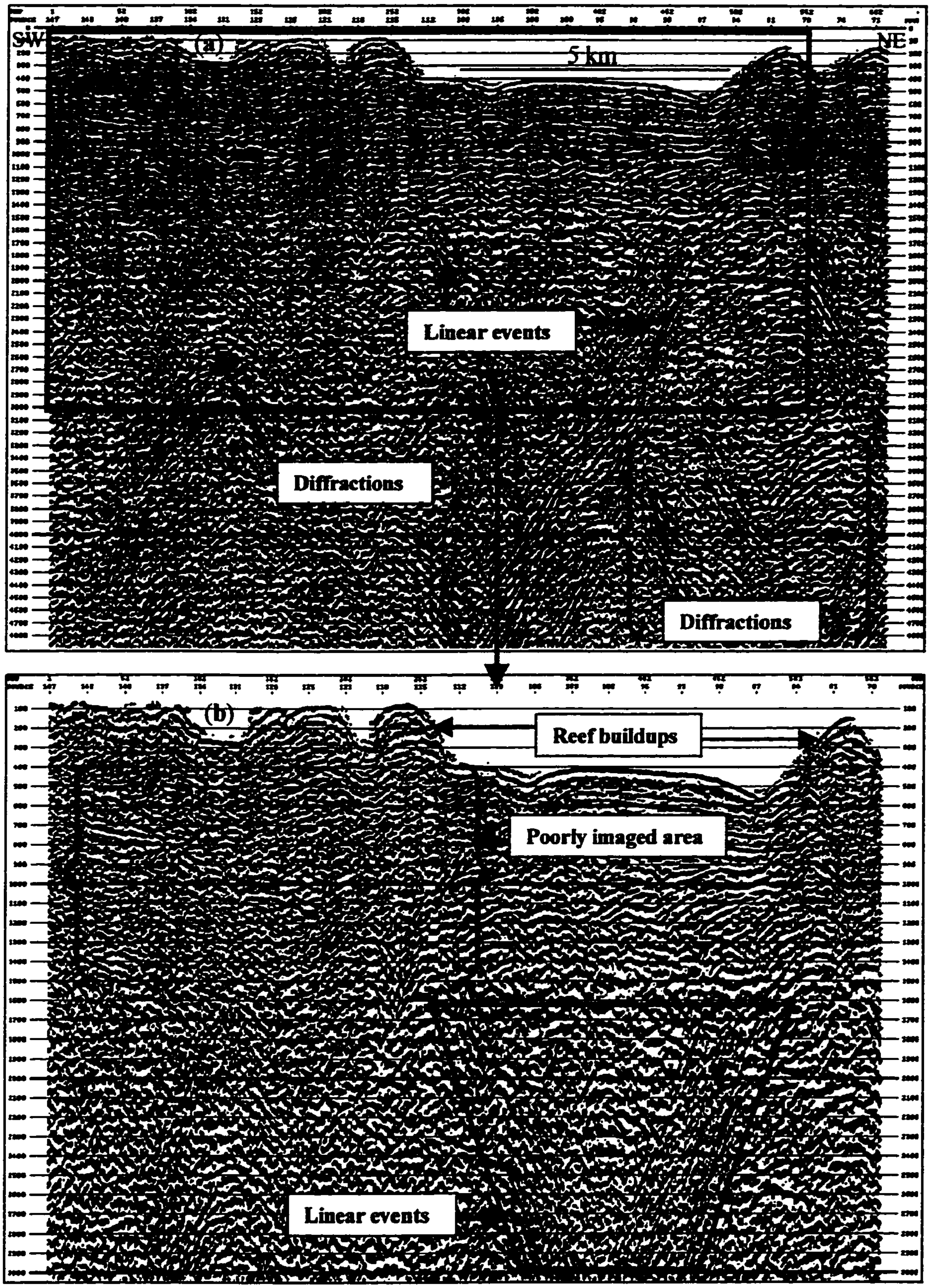

Figure 5.21. (a) The southwest part of line 16 indicating the image disruption due to rugged seafloor and basement-involved normal faults. (b) Salt and subsalt reflection events are poorly image beneath the reefs.

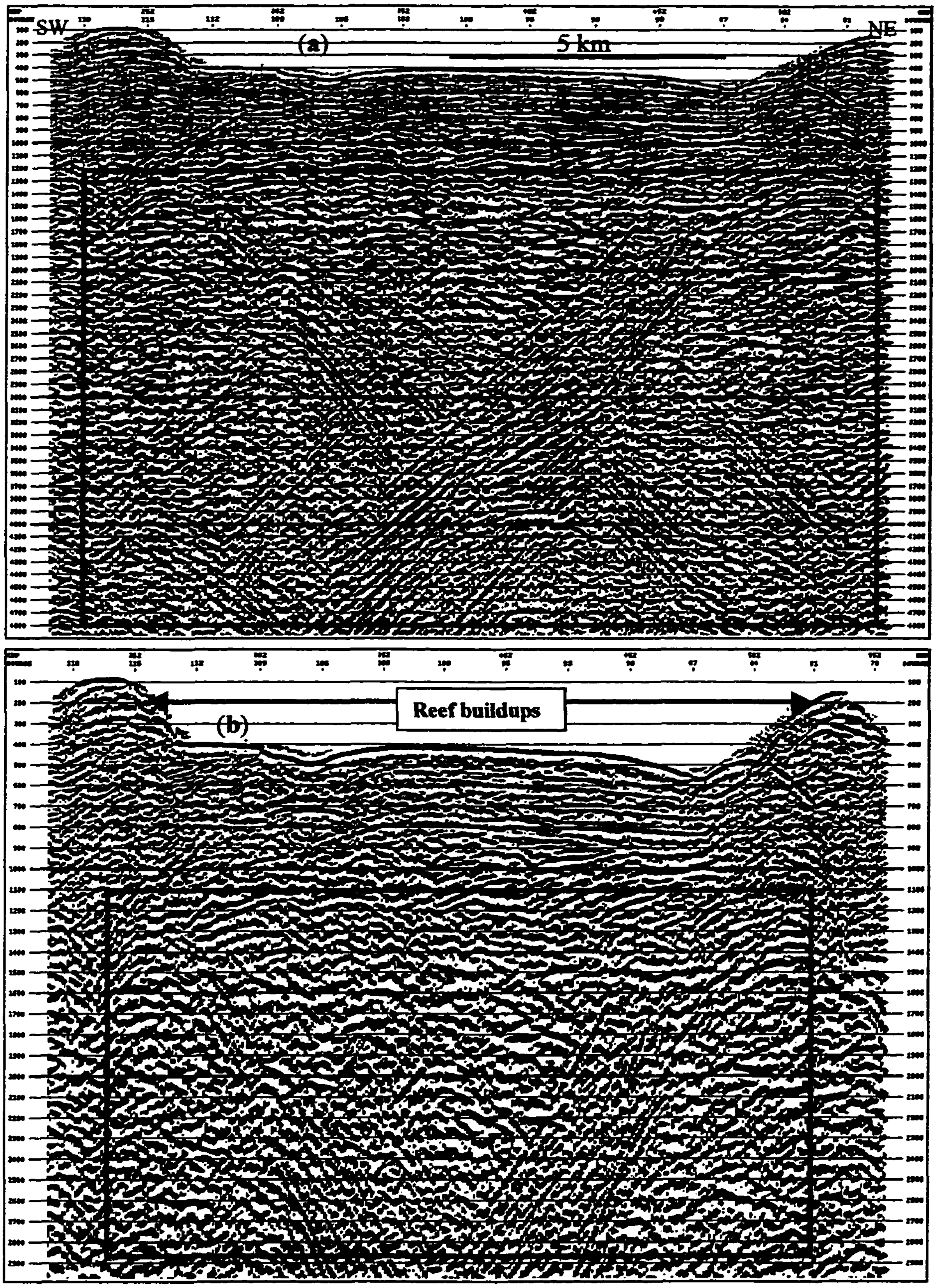

Figure 5.22. (a) The image distortions observed between the reefs in the middle of the section and the ones to the southwest. Note how diffractions and linear events interfered with each other and with primary reflections. (b)The salt, subsalt, and basement reflections structures are poorly imaged.

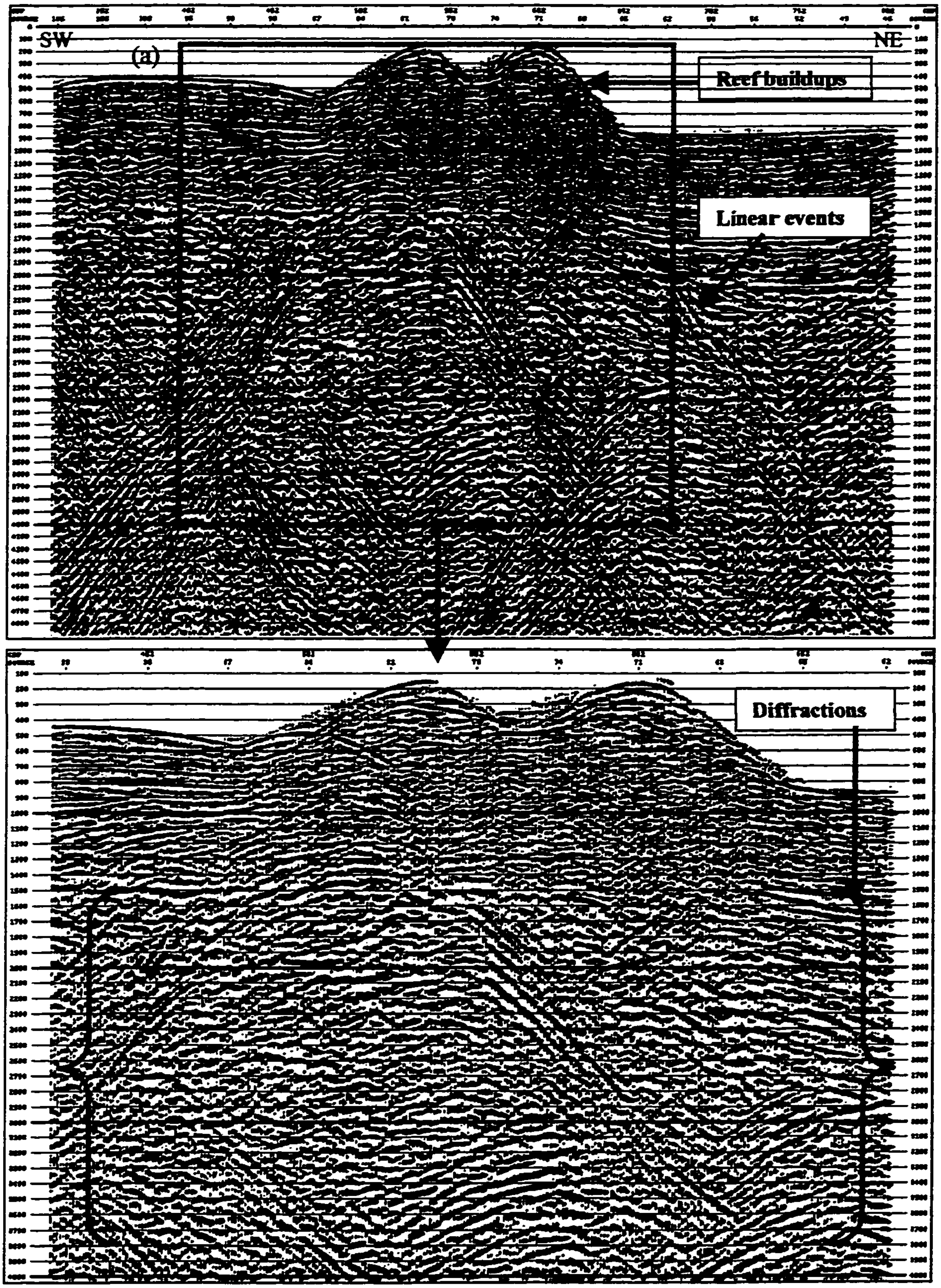

Figure 5.23. The image distortions observed on the middle part of line 16. Note how diffractions and linear events commingled with each other and with genuine reflection.

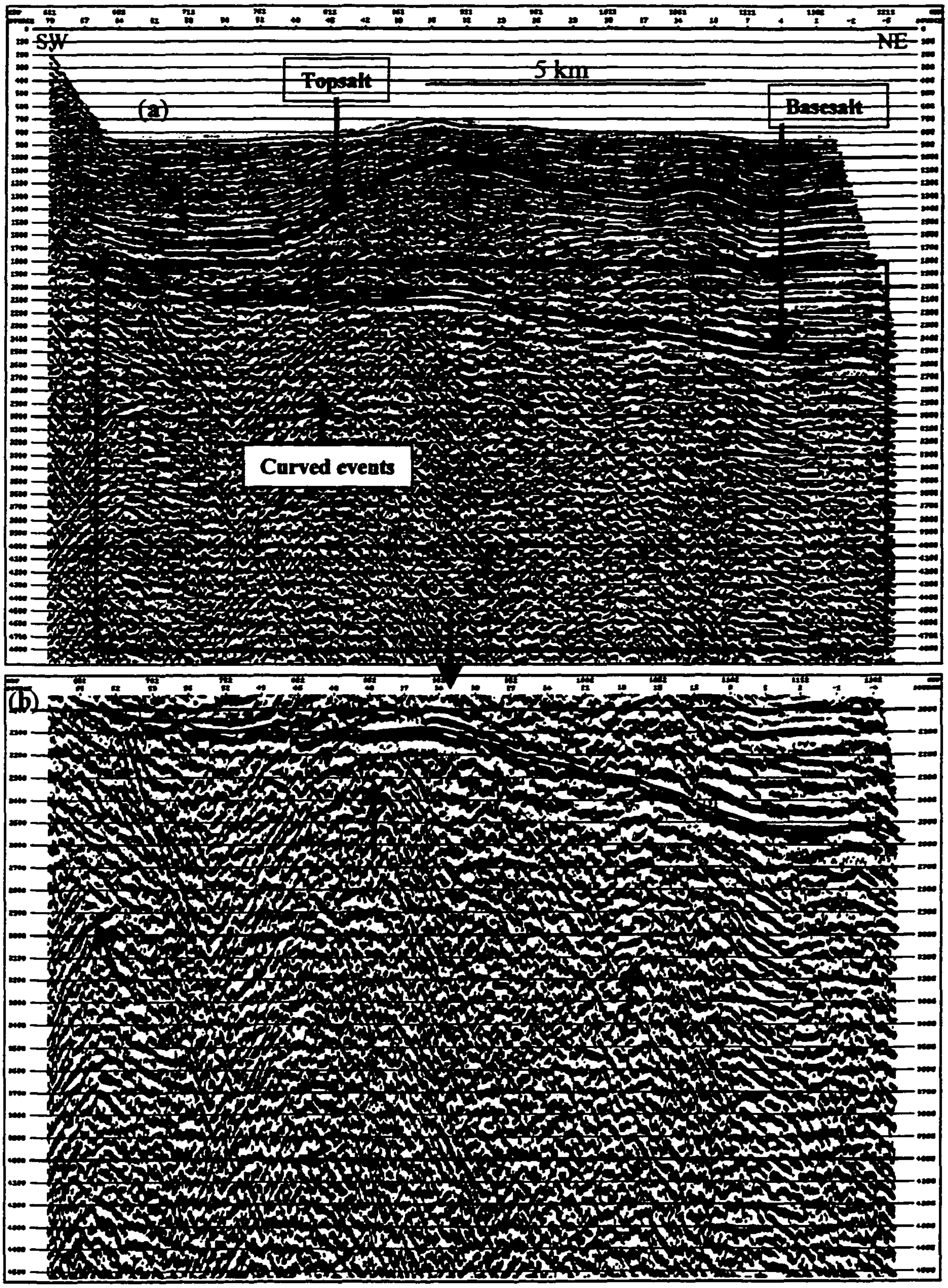

Figure 5.24. (a)The image distortions observed on the northeast part of line 16. (b) Poorly imaged area below thick, high-velocity salt. Diffractions (indicated by arrows) also dominated this area and masked the the underlying subsalt seismic events.

amplitude and continuity. The reflection events are further disrupted by considerable diffractions and steeply dipping linear events resulting in the poorly imaged area beneath the rugged water bottom as shown in Figure 5.21.

In the area between the reefs in the middle of the section and those to the southwest, the diffraction and linear events commingle with each other and with genuine reflections (Fig. 5.22). This complicates the picking of topsalt, basesalt seismic events and makes the definition of basement-related faults more difficult. The most severe image distortions observed on this line occur in the area underneath the two reef buildups in the middle of the section (Fig. 5.23). This part of the section is overwhelmed by diffractions, which severely distort the reflection events of the entire sedimentary section and obscure the underlying basement structures. In northeast part of the line (SP: 65 to –5), the top and base of salt are very visible (Fig. 5.24). The salt sequences is very thick between shotpoints 38 and –5, but exhibits gradual thinning beneath the structurally low area just northeast of the reefs in the middle of the line. The area beneath the thick salt is poorly focussed. It shows low amplitude, discontinuous reflection pattern disrupted by diffraction events. The presence of curved events that appear to crosscut the primary reflections adds to the confusion of picking subsalt reflection events and top of basement reflector. The origin of these events is not known. They are likely multiples or sideswipe.

The origin of the imaging distortions discussed above and their likely effects must be understood in order to image and interpret the data properly. 2-D seismic modeling is used to investigate the causes and effects of these distortions, anticipates imaging problems and verifies the interpretation.

V.2.2. 2-D Seismic modeling results.

Figure 5.25 shows the final velocity-depth model and zero offset raypaths for water bottom. In this model, the salt is considered consisting mainly of halite, hence is given a constant velocity of 15000 ft/sec. Subsalt and supra-salt layers are given a velocity gradients to account for their dipping interfaces and changes in their thickness. Figure 5.26 displays (after enlargement) the raypaths for water bottom and their seismic response. It is evidence from this Figure that the rugged portion of seafloor has caused severe distortion of the reflected and transmitted raypaths. The reflected raypaths undergo severe bending and scattering at the boundaries of the reefs and at the sides of the small valleys that separate them. The transmitted rays undergo serious bending (due to lateral velocity changes) within the supra-salt layer and sharp refraction at the top of the salt. The seismic response shows some of the distortions associated with these complex raypaths. Note how the steeply dipping, linear events on this synthetic section are similar to those observed at the edges of the reefs on the original seismic section. Figure 5.27 illustrates the zero offset raypaths and synthetic section for water bottom and top of basement. The raypaths for the top of basement suffer from serious bending, not only at the rugged seafloor but also at the top and base of salt. The key factors responsible for these raypaths deviation are the velocity of the layers and geometry of the interfaces that separate them. The distortions caused by the complex raypaths are very obvious on the synthetic section (Fig. 5.27b). The top of basement reflector shows low continuity and amplitude beneath thick salt and contains a relatively broad, gentle hyperbolic feature. Is this feature a velocity pull-up due to the overlaying high-velocity salt? Or just a response to the geometry of seafloor above this location? The features observed below thick salt body on the synthetic simulate those

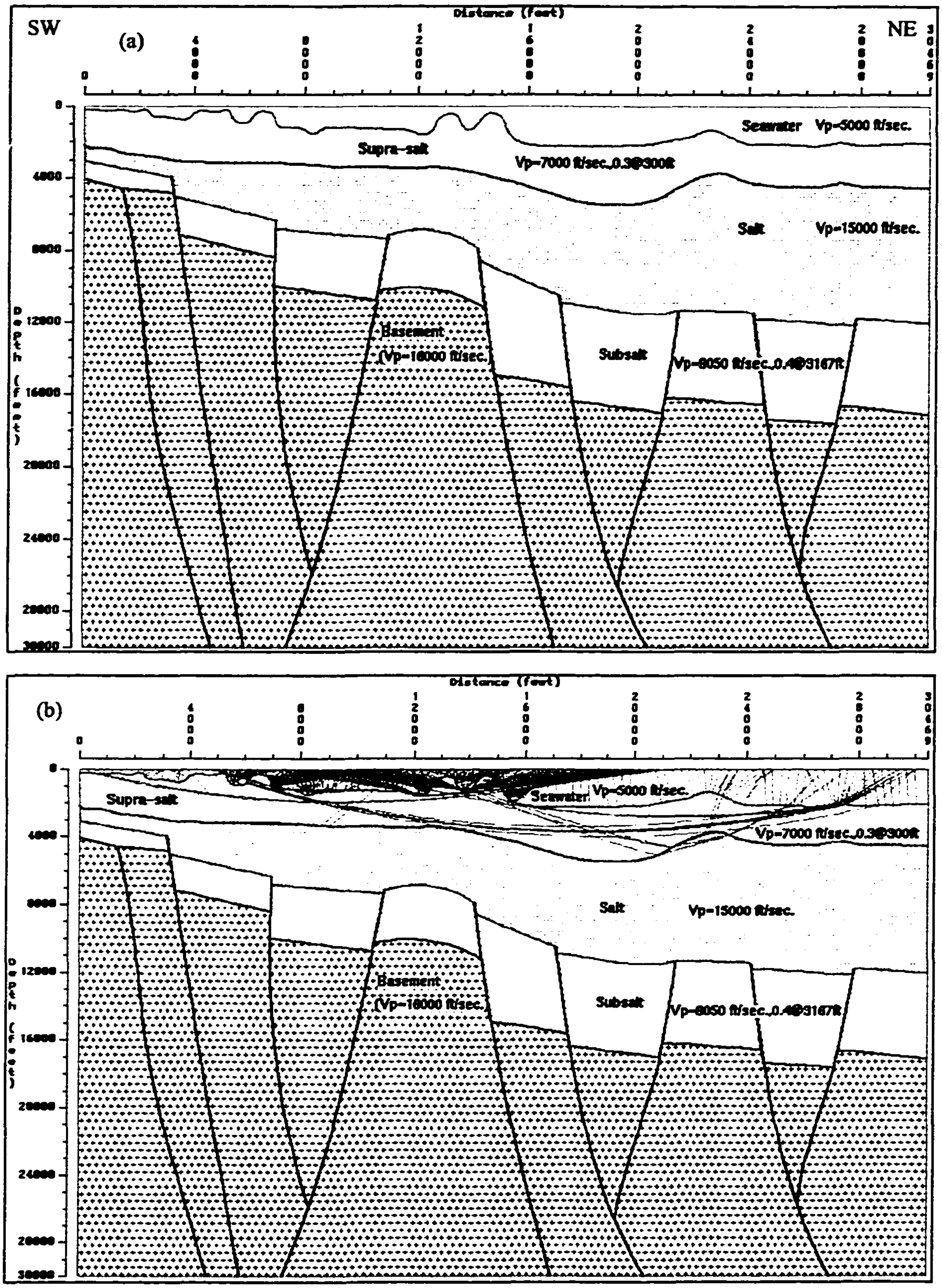

Figure 5.25. Velocity-depth model (a) and zero offset raypaths (b) for water-bottom of seismic line 16.

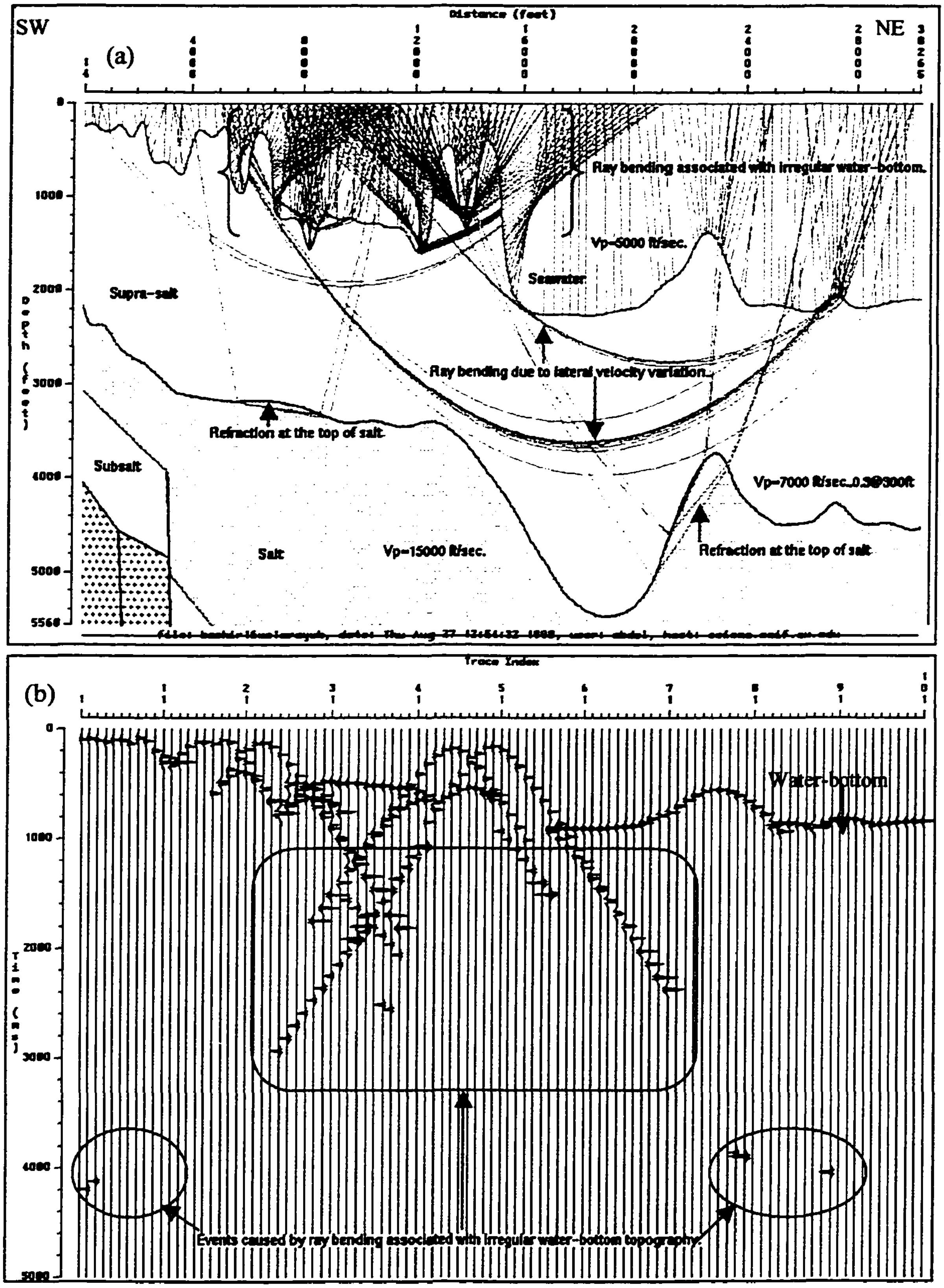

Figure 5.26. Zero offset raypaths (a) and normal incidence synthetic trace for water-bottom of seismic line 16.

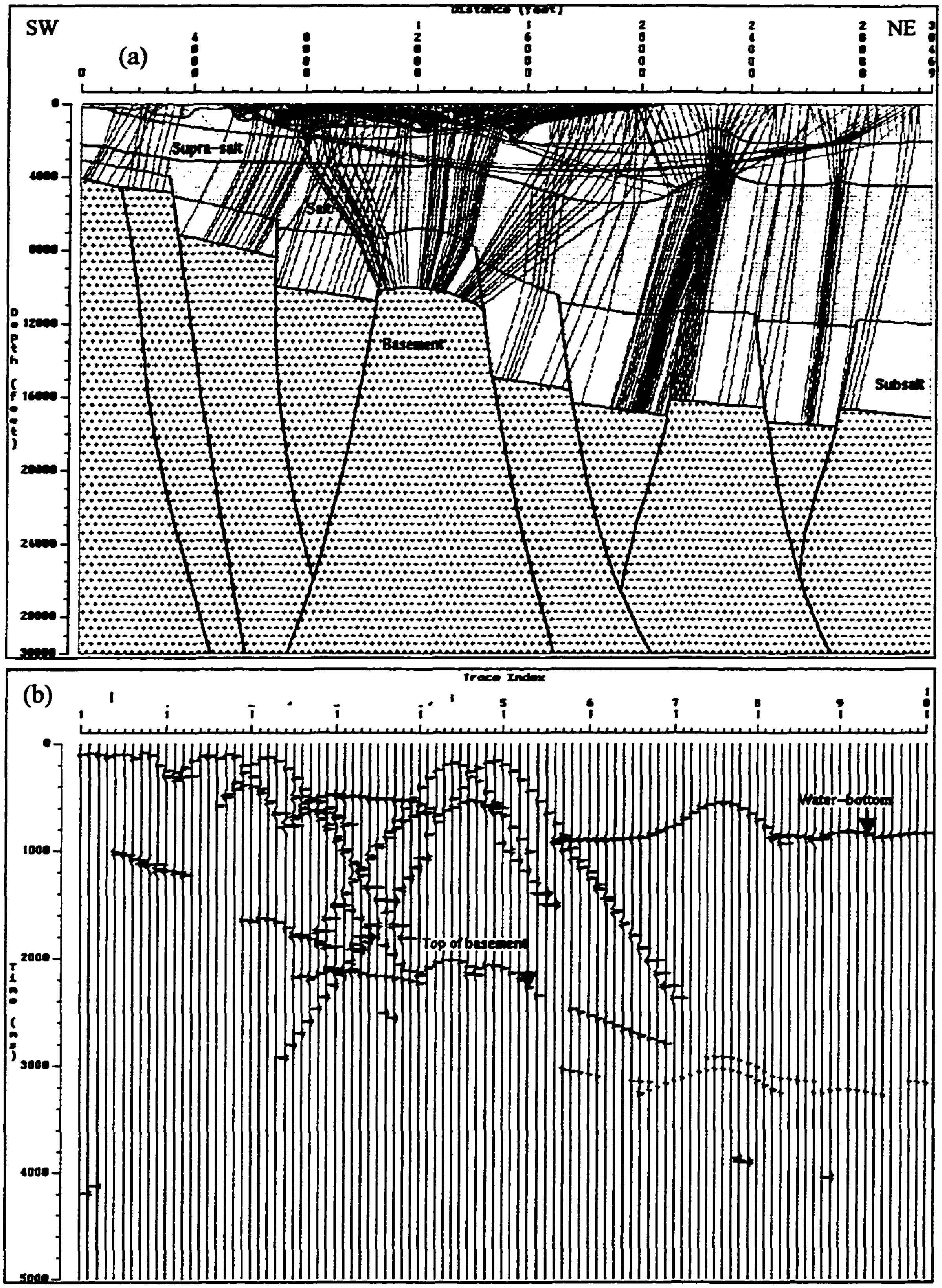

Figure 5.27. Zero offset raypaths (a) and normal incidence synthetic trace (b) for water-bottom (sky-blue) and the top of basement (red) of seismic line 16.

observed on the same area on the real section. In area beneath the two reefs in the middle of the synthetic, the top of basement reflector represents a mirror image of the overlying seafloor. To the southwest of the reefs in the middle of the section, the top of basement reflector has low continuity and is crosscut by linear events associated with the rugged seafloor. Beneath the irregular water bottom of the first portion of the line to the southwest, the top of the basement reflector is seriously distorted.

The zero offset raypaths for top and base of salt are shown in Figure 5.28. It is clear that the raypaths undergo significant bending at irregular parts of the seafloor and top of the salt. Note how the high and low curvatures of the undulating top salt focus and defocus the rayapths, respectively. On the synthetic section (Fig.5.28b), the smooth undulating top and the underlying base of salt on the depth model bear a distinct expression of water bottom. Note how the top and base of salt and the top of basement reflectors are pulled up beneath the reefs in the middle of the line. A false bow-tie is also very obvious below the low area just to the northeast of these reefs (Fig. 5.29). The normal incidence synthetic section for all layers and diffractions from faults and tilted block edges are displayed, separately, in Figure 5.30. When combined together, the synthetic diffractions and reflection structures simulate very much the distortion observed on the real seismic section.

<u>Image distortions due to velocity variations</u>:

As pointed out previously the South Gharip Formation encountered in Ra west-1 well, consists mainly of anhydrite interbedded with argillaceous and anhydritic dolomite. On the northeast part of the line, South Gharip Formation exhibits a high amplitude, continuous to chaotic internal reflection pattern. Based on these observations, the salt

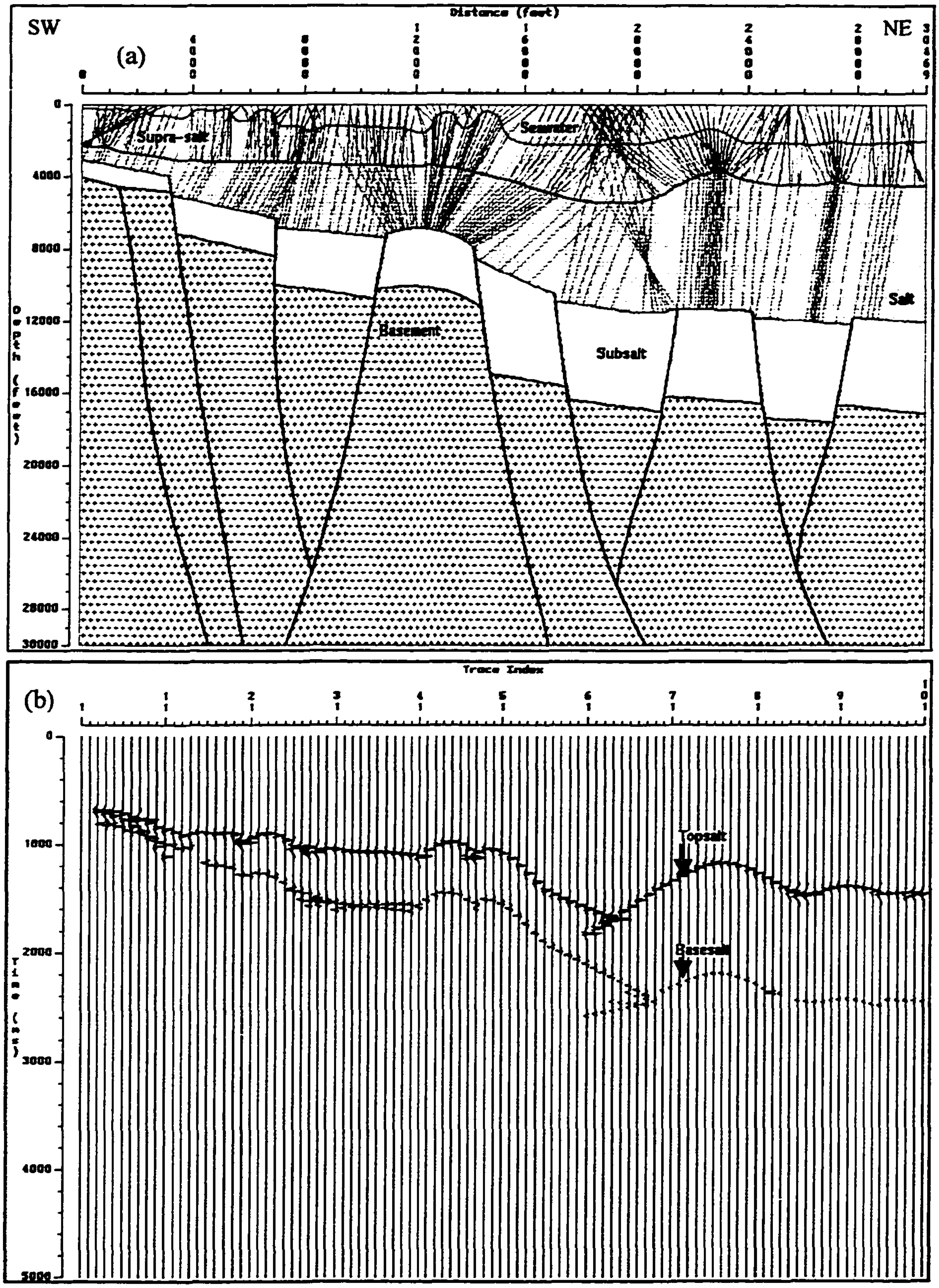

Figure 5.28. Zero offset raypaths (a) and normal incidence synthetic trace (b) for the top and base of salt of seismic line 16.

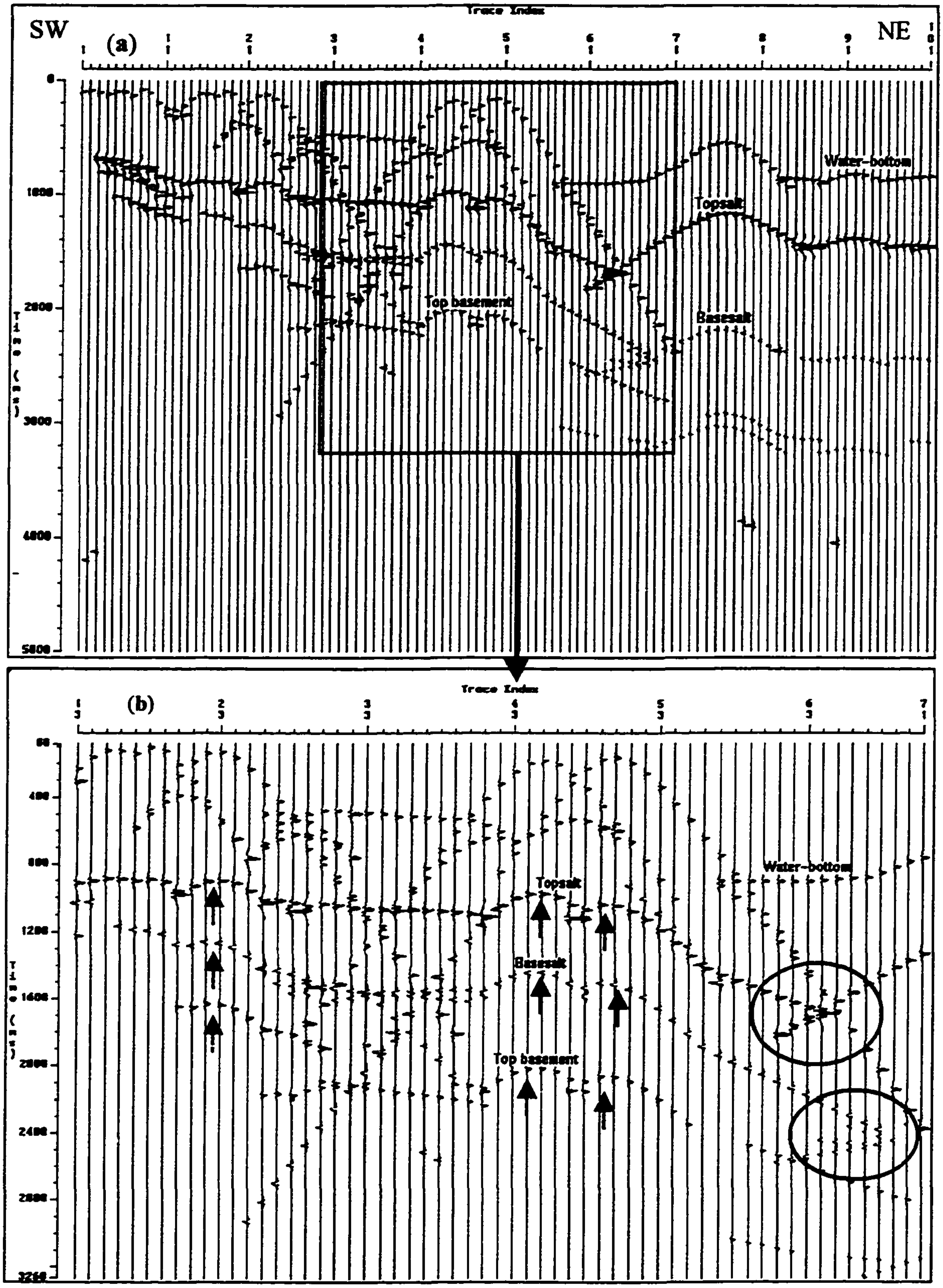

Figure 5.29. (a) Normal incidence synthetic trace displayed with arrival times for all layers of line 16. (b) The topsalt, basesalt, and top of basement reflectors are pulled up below the reefs as shown by arrows. note the bow-ties (indicated by circles) in top and base of salt beneath the deep portion of seafloor.

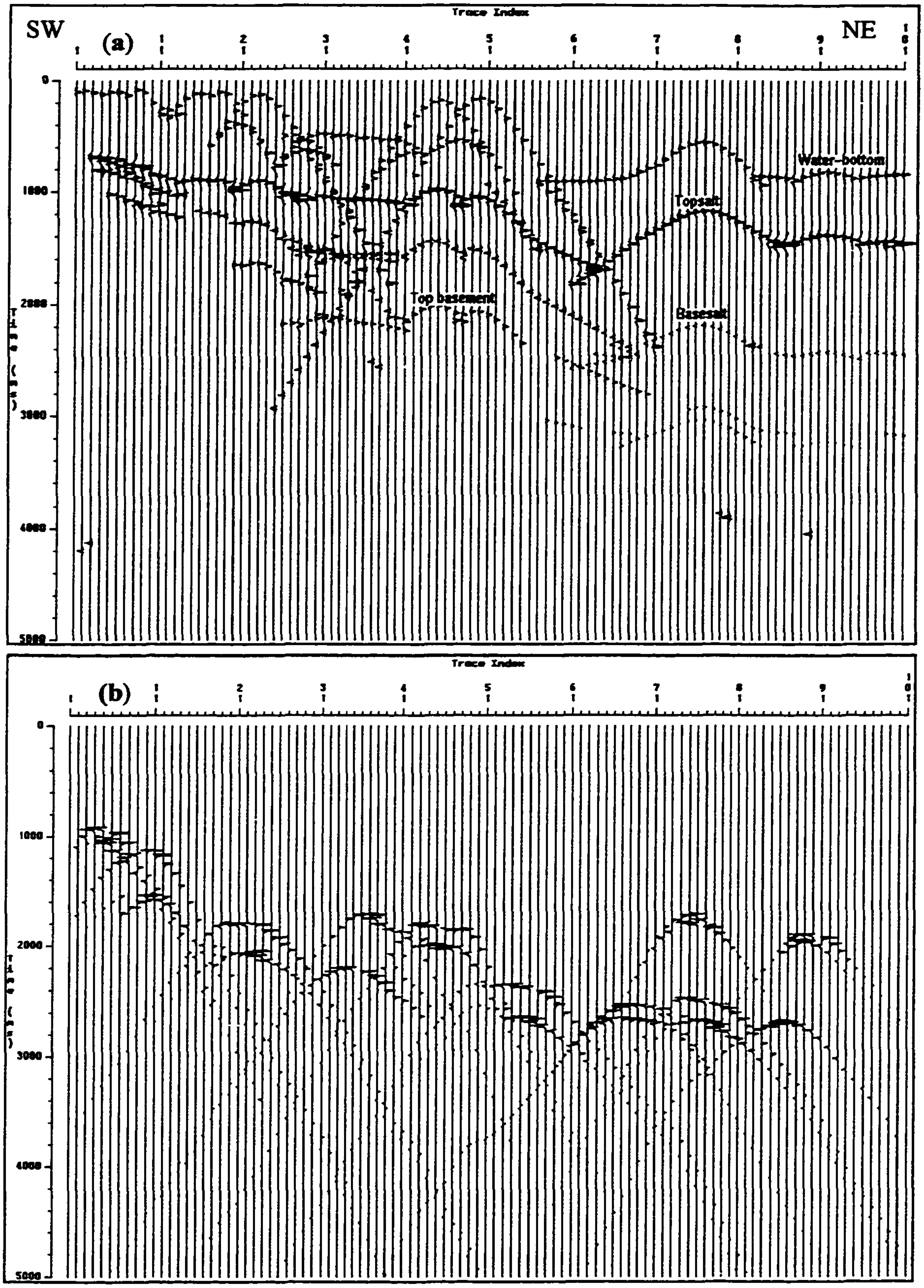

Figure 5.30. Normal incidence synthetic section for all layers (a) and diffractions from faults and faulted block edges (b) of seismic line 16.

layer is given a velocity gradient to account for possible lateral velocity variations. To investigate the image distortions that may result from velocity changes within the salt layer, consider Figure 5.31. This Figure compares zero offset raypaths of water bottom with the salt layer having constant and varying velocity. The result is very clear; the rays transmitted below seafloor undergo more refraction (due to the critical angle effect) when the salt has a velocity gradient. This is because these rays obey Snell's Law (Fig 3.5), hence, the amount of ray bending and refraction is proportional to velocity contrast across interface and the angle of incidence and refraction. The additional ray bending and refraction associated with lateral velocity variations within the salt layer introduce travel time errors, complicate, and distort the seismic image. To further demonstrate this point, compare the zero offset raypaths in Figure 5.32. Due to relatively high impedance contrast between constant velocity (7000 ft/sec) supra-salt layer and the water bottom (5000 ft/sec), very few rays are transmitted in supra-salt (Fig. 5.32a). These few rays are unbent and follow straight paths. This is because, in constant velocity medium, wavefronts are concentric. Since the raypaths are normal to wavefronts, they follow straight paths. On the other hand, more rays are transmitted and bended below water bottom when supra-salt layer has a lower velocity (6000 ft/sec) and with a gradient of 0.3 (Fig. 5.32b).

<u>Summary of 2-D seismic modeling</u>:

The 2-D seismic modeling reveals that image distortions observed on line16 are attributed to diffractions from basement-related faults. Severe ray bending and scattering due to irregular seafloor cause travel time errors, distort the amplitude, and yield steeply dipping, linear events that interfere with guenuine reflections and diffractions. Thick, high-velocity salt, varying in lateral geometry results in severe ray bending and sharp

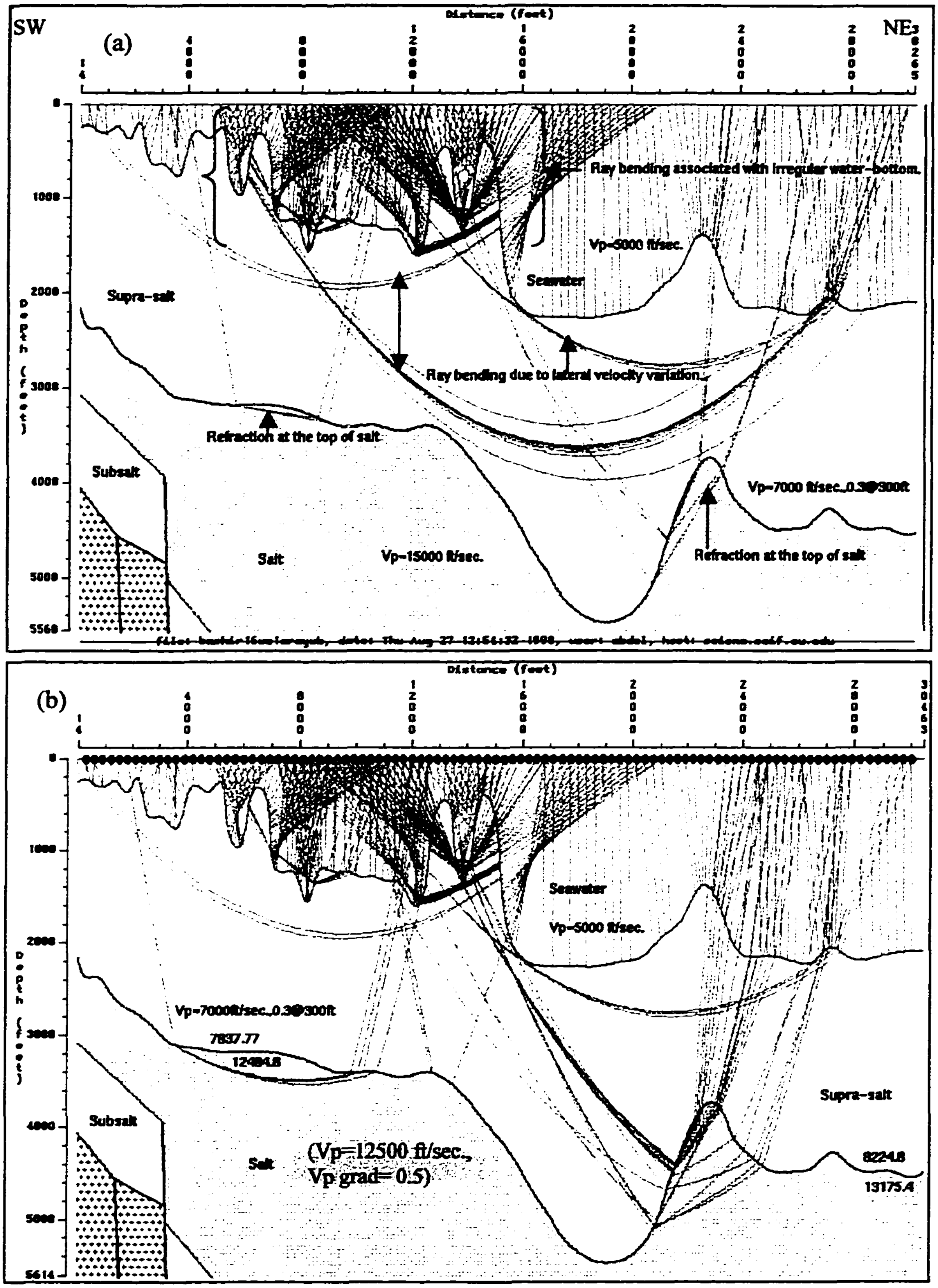

Figure 5.31. Zero offset raypaths for water-bottom of seismic line 16. The salt has constant (a) and variable (b) velocity field.

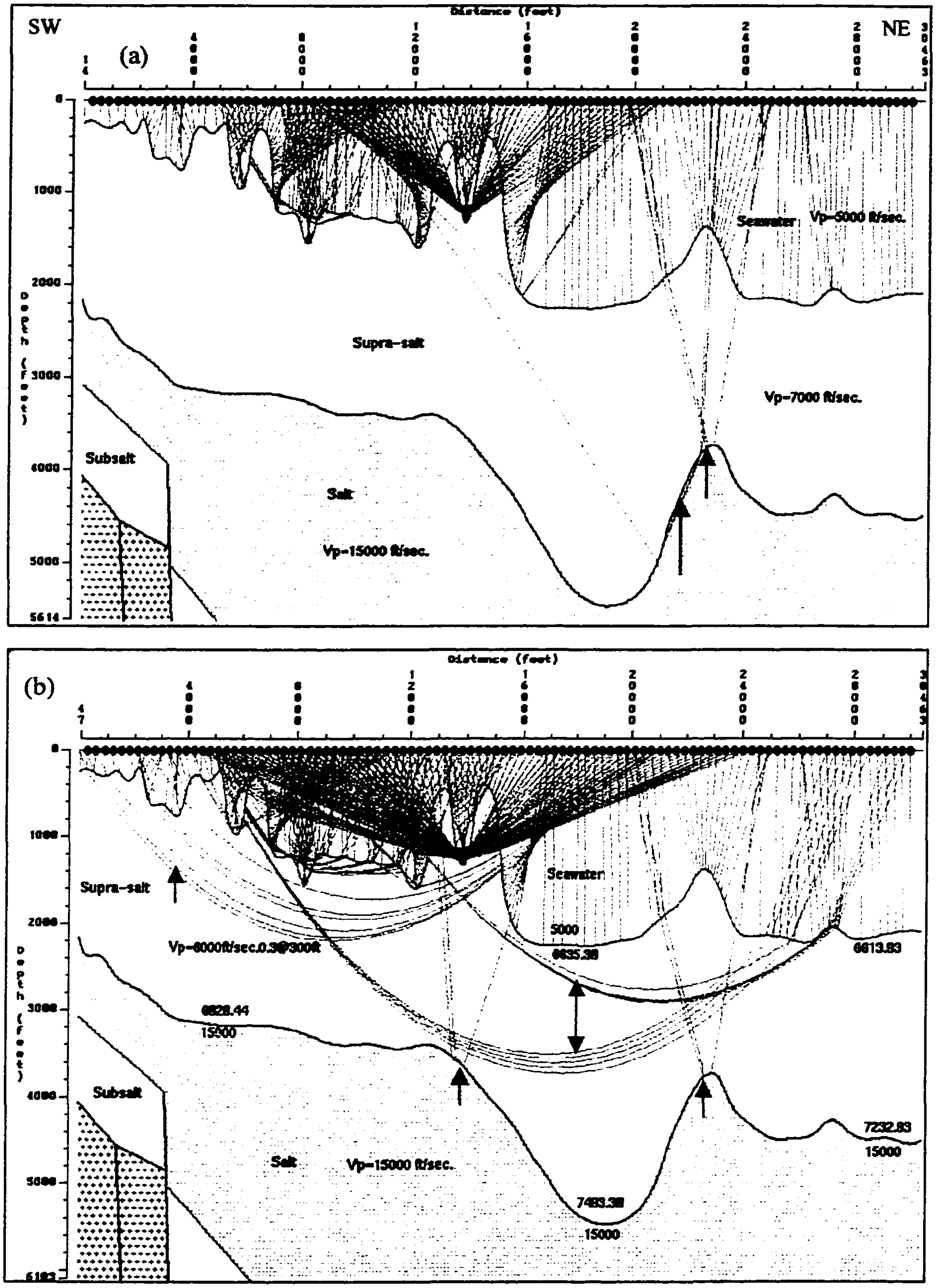

Figure 5.32. Zero offset raypaths for water-bottom of seismic line 16. Supra-salt layers have a constant (a) and variable velocity field (b).

refraction hence reduces the illumination of the underlying subsalt structures. Lateral velocity changes cause raypaths distortion and degrade the subsalt imaging quality.

V.2.3. Post-stack signal enhancement results:

Figure 5.33 shows a portion of line 16 before and after multiple suppression. It is obvious that very few multiple are removed from the shallower part of the section. Wave equation datuming, and F-X deconvolution are implemented to improve the continuity of primary reflections by reducing the deleterious effect of rugged seafloor on underlying events and removing random noise, respectively. Figures 5.34, 5.35, and 5.36 compare the southwest, middle, and northeast parts of line 16 before and after signal enhancement. The imaging distortions become more obvious after signal enhancement. On the southwest and middle parts of the section (Figs. 5.34, 5.35), the intensity of diffractions from faults and criss-crossing events due scattering from seafloor irregularities have obviously degraded the salt and subsalt reflection events. Due to intensive diffracrions in these areas, the improvement in salt and subsalt reflection continuity obtained by wave equation datuming and F-X deconvolution is hard to observe. However, a noticeable improvement in continuity is observed in areas that are not disrupted by diffractions, such as the shallower parts of the section. The result also indicates the subsalt seismic events, beneath high-velocity thick salt on the northeast part of the section, are weak and hard to observed. These observations are consistent with the 2-D modeling results discussed previously.

V.2.4. Post stack migration results:

V.2.4.1. Steep dip explicit finite difference time migration:

Figures 5.37, 5.38, and 5.39 compare the southwest, middle, and northeast part of line 16 before and after steep dip explicit finite difference time migration. It is clear from these Figures that the migration yields a reasonably accurate result. It collapses all the diffractions, removes the linear events, and improves the overall lateral resolution of the seismic section. This makes the definition of faults and picking of topsalt, basesalt, and top of basement reflectors a lot easier than before the migration. However, The curved events which appear to cross-cut the primary reflections still exist on the migrated section which suggests they are likely sideswipe. The processing sequence and the parameters used in post-stack signal enhancement processes and steep dip explicit finite difference time migration performed on line 16 are listed on pages 220 and 221. Figure 5.40 shows seismic line 16 after migration and interpretation.

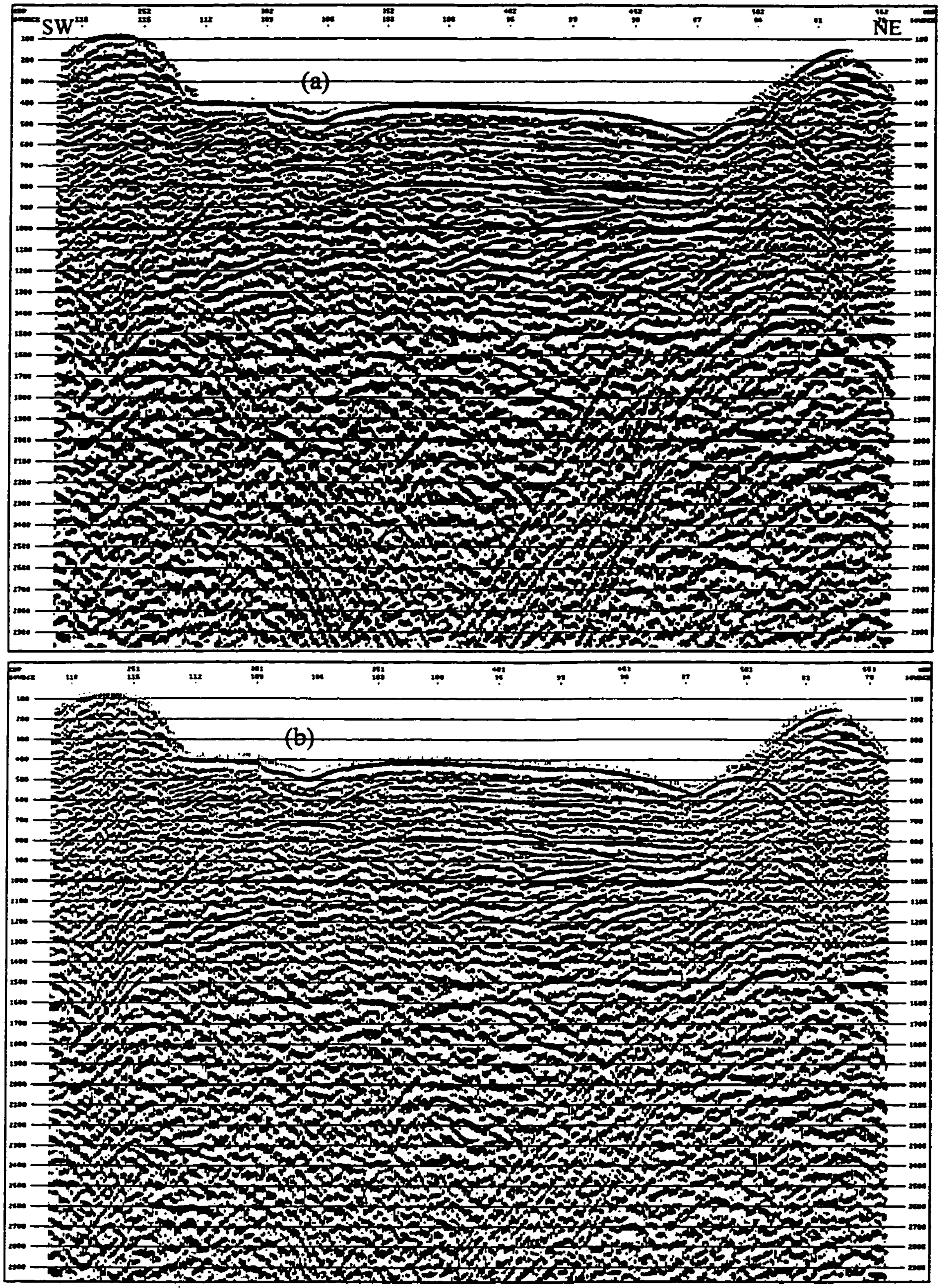

Figure 5.33. Seismic line 16 (SP: 118-78) before (a) and after (b) post-stack wave equation multiple rejection.

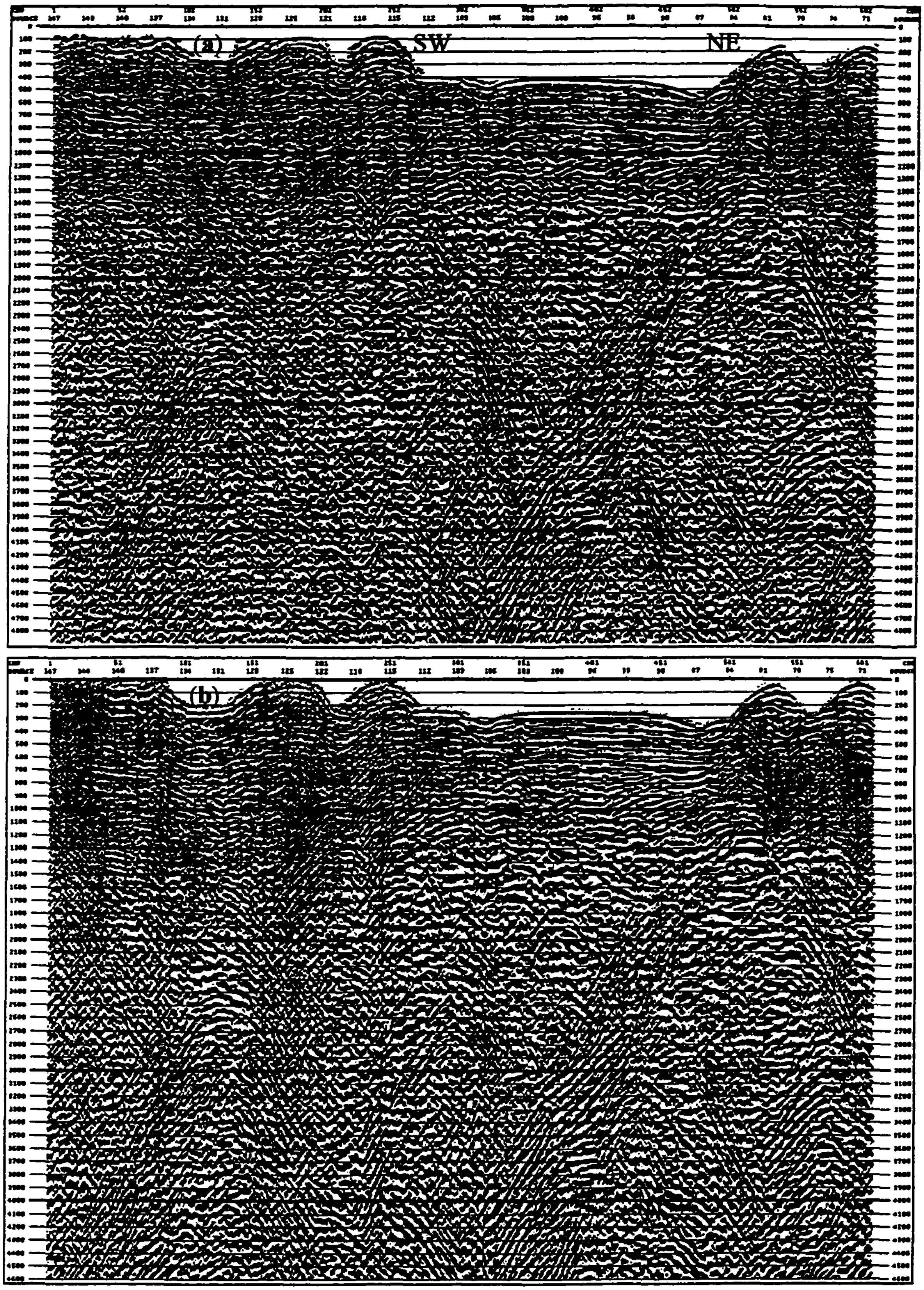

Figure 5.34. The southwest part of line16 before(a) and after (b) post-stack wave equation multiple rejection, wave equation datuming, and F-X deconvolution.

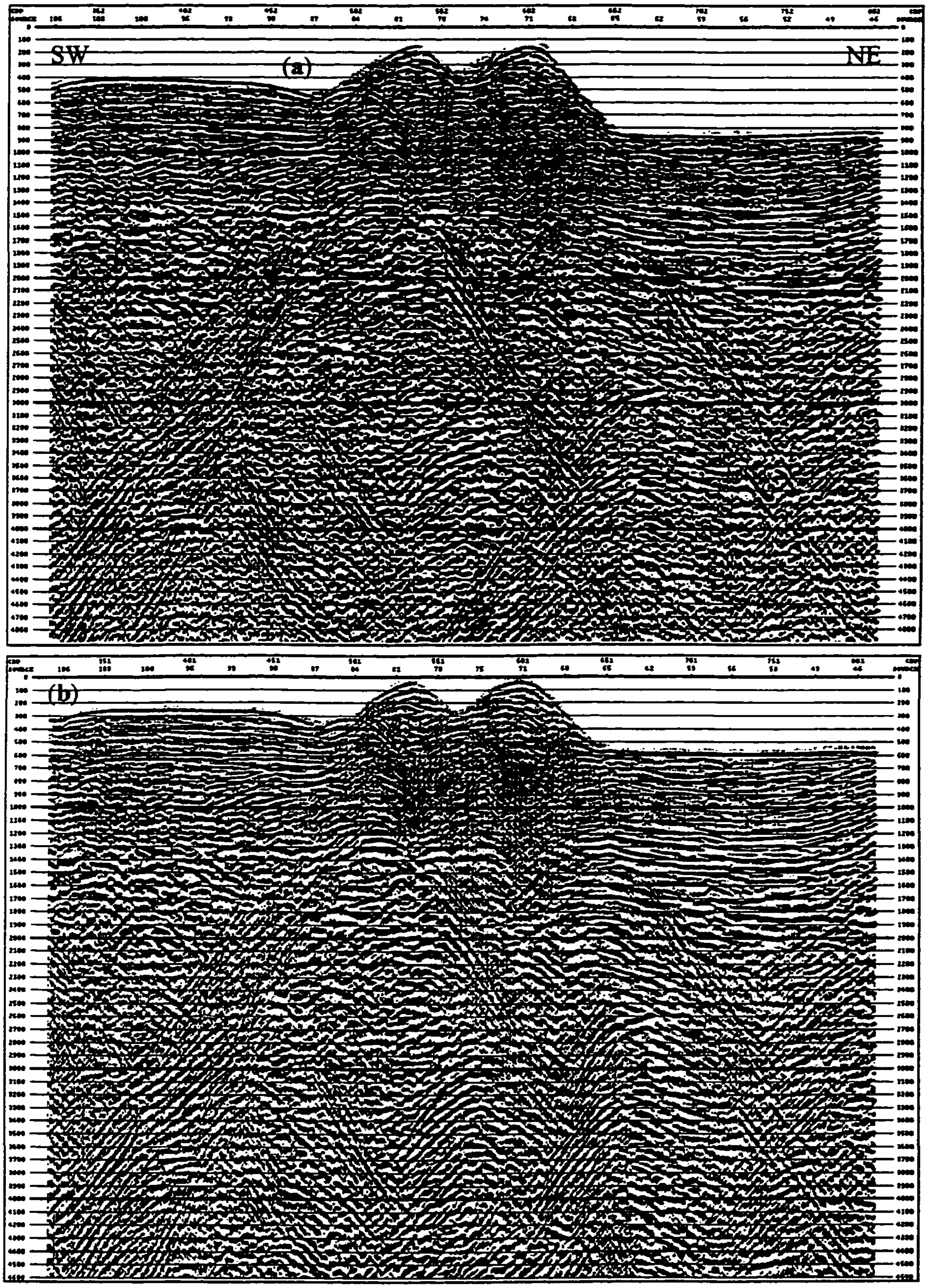

Figure5.35. The middle part of line16 before (a) and after (b) post-stack wave equation multiple rejection, wave equation datuming, and F-X deconvolution.

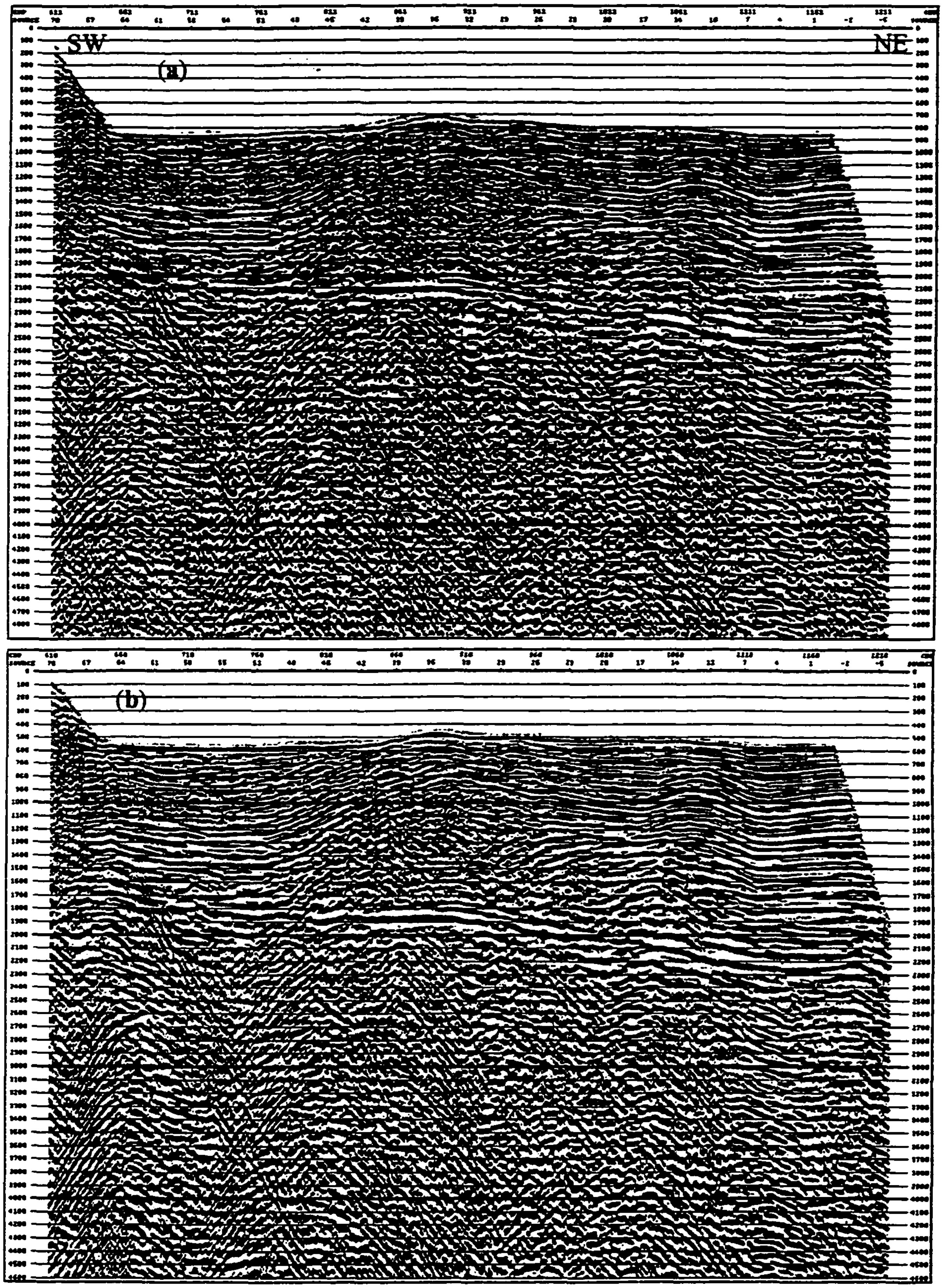

Figure 5.36. The northeast part of line16 before (a) and after (b) post-stack wave equation multiple rejection, wave equation datuming, and F-X deconvolution.

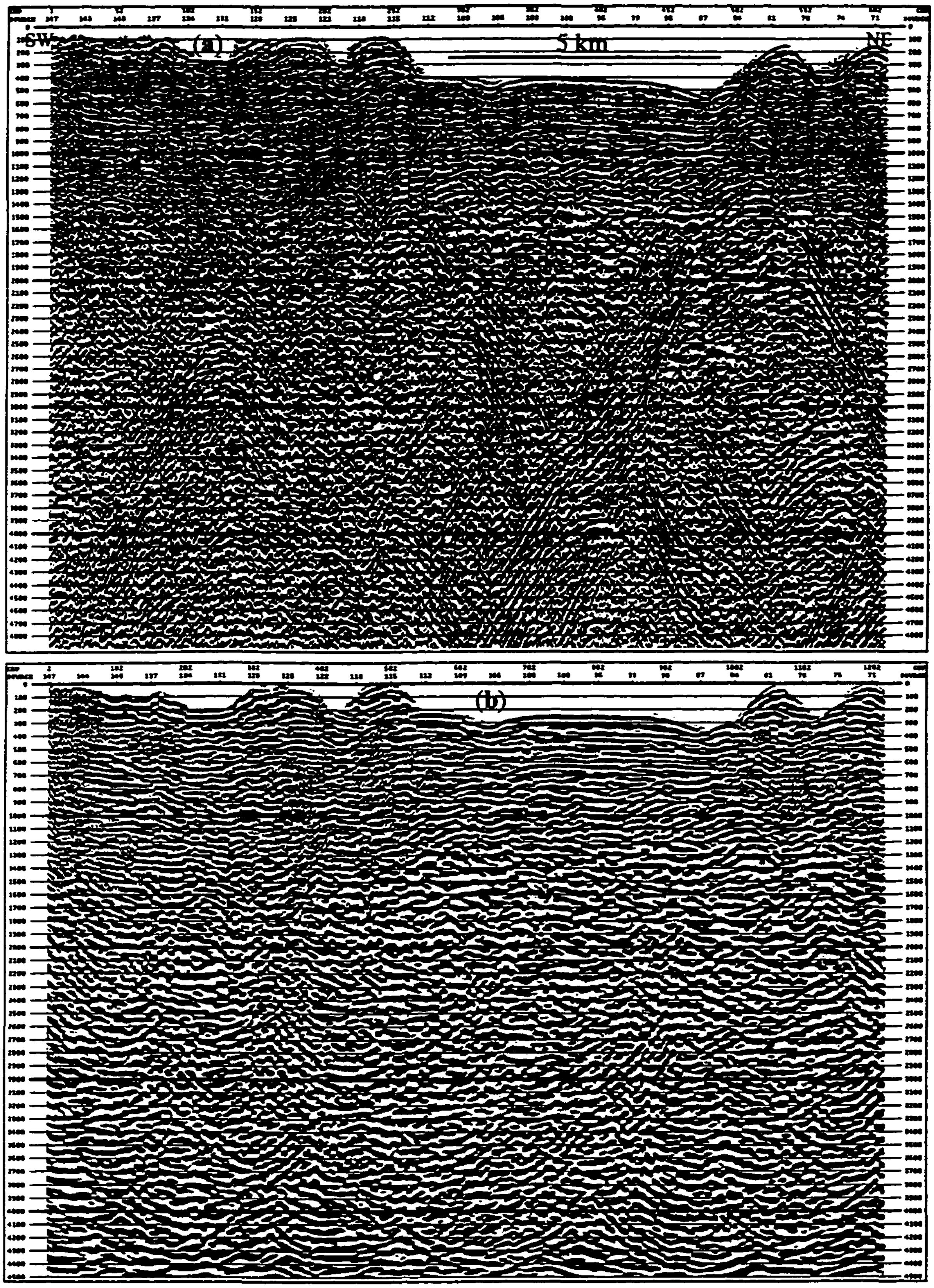

Figure 5.37. The southwest part of seismic line 16 (SP: 147-71) before (a) and after (b) signal enhancement and steep dip explicit finite difference time migration.

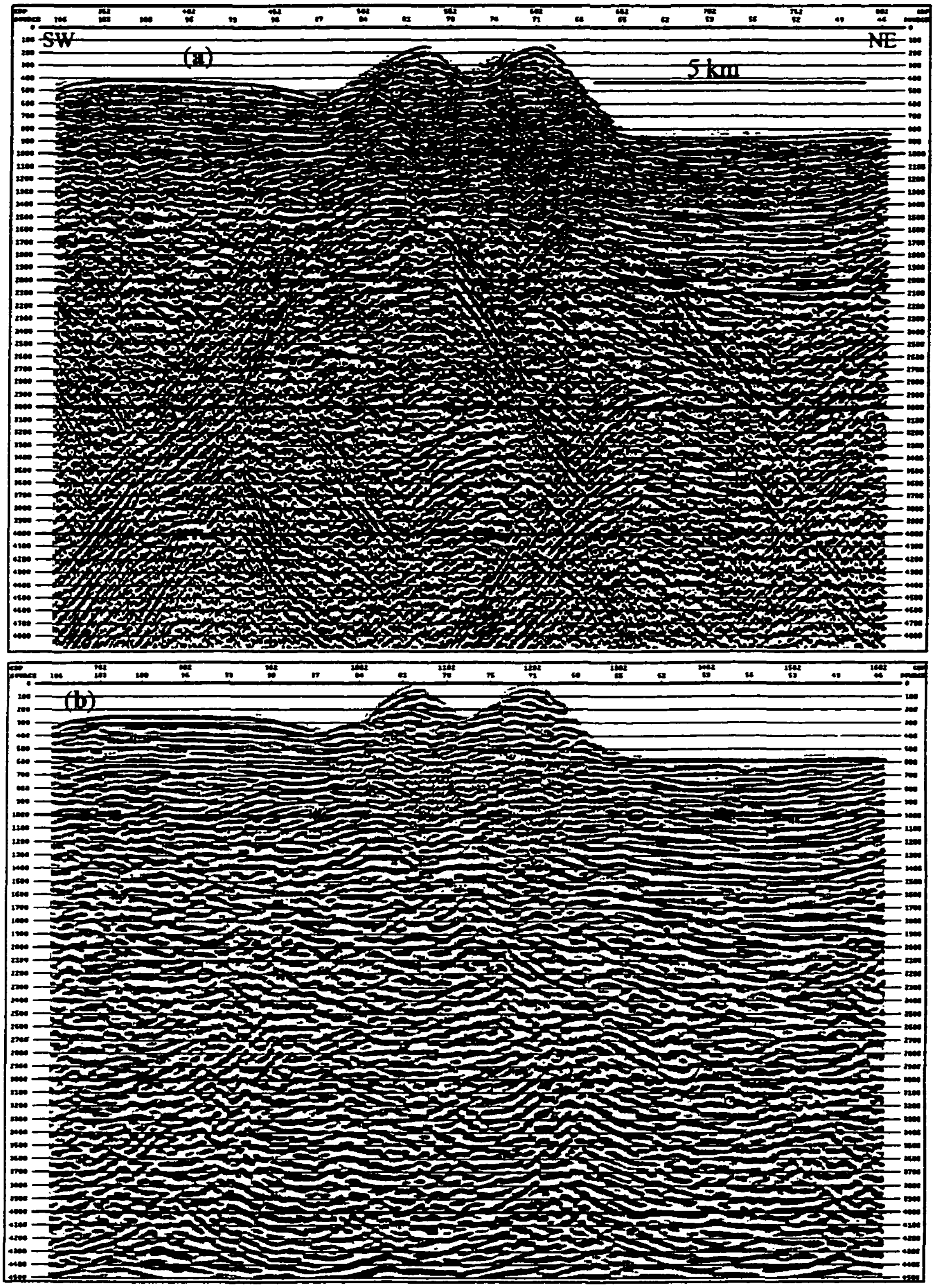

Figure 5.38. The middle part of seismic line 16 (SP: 106-46) before (a) and after (b) post-stack signal enhancement and steep dip explicit finite difference time migration.

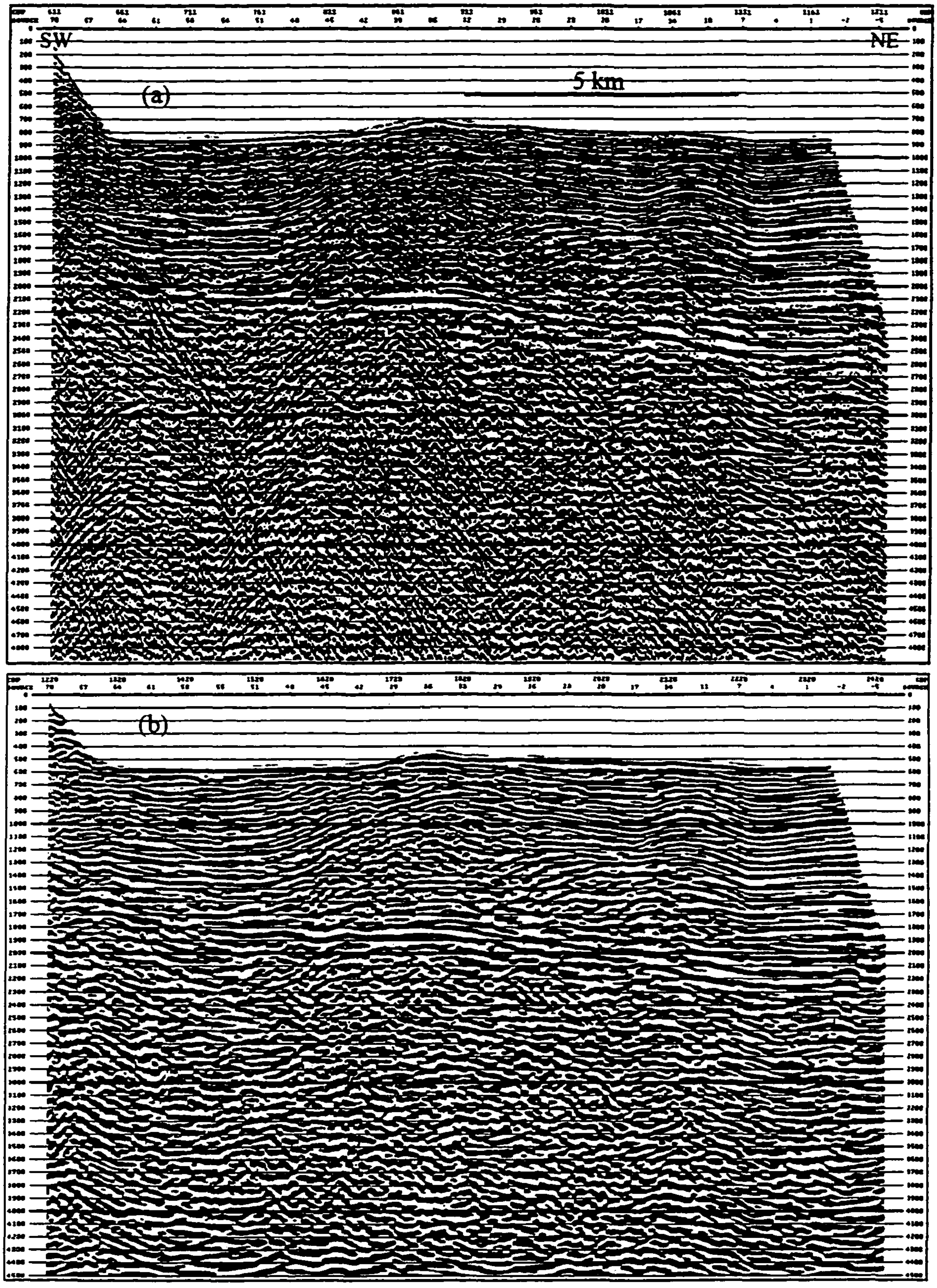

Figure 5.39. The northeast part of seismic line 16 (SP: 70- -5) before (a) and after (b) post-stack signal enhancement and steep dip explicit finite difference time migration.

```
★SEG-Y Input

FLOW - WAVEEq     Thu Jan  8 23:13:50 1998
  Output - RB16WDOUBLECDP Add 1217 Over 0
 Trace Header Math
  Select mode                                  Fixed equation mode
    DEFINE trace header equation
    CDP=CDP*2

FLOW - WAVEEq     Fri Jan  9 22:35:27 1998
  Output - DBHORIRNSFCDPTIME2 Add 1217 Over 0
 Database/Header Transfer
  Direction of transfer                        Load TO trace header FROM c
  First header entry                           REC_H2OD

FLOW - WAVEEq     Fri Jan  9 22:35:32 1998
  Output - DBHORTRNFRCDPTIME2 Add 1217 Over 0
 Trace Header Math
  Select mode                                  Fixed equation mode
    DEFINE trace header equation
    REC_H2OD=REC_H2OD*2.5

FLOW - WAVEEq     Fri Jan  9 22:42:13 1998
  Output - wemrcdptime2 Add 1217 Over 0
★Wave Eq. Multiple Rejection
  Pad and infill traces at missing             No
  offsets?
  MODE of operation                            Estimate and Remove Multipl
  F-K filter before multiple estimation?       Yes

FLOW - WAVEEq     Fri Jan  9 23:57:32 1998
★ Output - wemrcdptime2datum2300ftDN Add 1217 Over 0
 Post Stack Wave Eq. Datuming
  Maximum frequency (in Hz)                    50.
  Datumize through a constant velocity?        No
  Get interval velocities from database?       Yes
    Select interval vs. depth velocity         VintDIVEINTRPLTforwemrcdpti
  file

FLOW - WAVEEq     Mon Jan 12 23:59:58 1998
  Output - wemrdtm2300fdn7000fsUP Add 1217 Over 0
 Disk Data Input
  Read data from other lines/surveys?          No
  Select dataset                               wemrcdptime2datum2300ftDN
  Trace read option                            Get All
  Read the data multiple times?                No
  Process trace headers only?                  No
★ Override input data's sample interval?       No
★Post Stack Wave Eq. Datuming
  CDP spacing (feet or meters)                 82.
  Maximum frequency (in Hz)                    50.
  Depth step size for datuming                 0.
  Elevation to datumize to                     0.
  What maximum dip would you like to           50 degrees
  handle?
  Datumize through a constant velocity?        Yes
  Velocity to use for datuming                 7000.
  Change maximum memory usage?                 No
  Taper the edges?                             No
  Re-kill dead traces?                         Yes
 Disk Data Output
  Output Dataset Filename                      wemrdtm2300fdn7000fsUP
  New, or Existing, File?                      New
  Record length to output                      0.
  Trace sample format                          16 bit
  Skip primary disk storage?                   No

FLOW - WAVEEq     Tue Jan 13 00:02:13 1998
  Output - wemrdatum2300ftdn7000fsUP Add 1217 Over 0
 Trace Length
  New trace length                             4600.

FLOW - WAVEEq     Tue Jan 13 00:05:37 1998
★ Output - wemrdatum2300fdn7000fsmutUP Add 1217 Over 0
★Trace Muting
  Re-apply previous mutes                      No
  TYPE of mute                                 Top
    Starting ramp                              30.
    SELECT mute parameter file                 wemrcdp2datumfxdecon
```

Continue on next page

Post-stack processing sequence performed on seismic line 16.

```
FLOW - WAVEEq     Tue Jan 13 00:10:50 1998
  Output - wemrdtm2300fdn7000fsmutcdp/2up Add 1217 Over 0
 Trace Header Math
  Select mode                                      Fixed equation mode
    DEFINE trace header equation
    CDP = CDP/2
```

Continue from previous page

```
FLOW - WAVEEq     Wed Jan 14 01:13:38 1998
* Output - wemrdtm2300fdn7000fsupFXDECON Add 1217 Over 0
*F-X Decon
  TYPE of filter                                   Wiener Levinson
  Percentage of white noise                        0.
  Horizontal window length                         10
  Number of filter samples                         5
  Time window length                               300.
  Time window overlap                              30.
  F-X filter start frequency                       5.
  F-X filter end frequency                         50.

FLOW - WAVEEq     Wed Jan 14 03:02:41 1998
  Output - wemrdatumfxdeconbpfltmixSDFDTM Add 1217 Over 0
 Trace Header Math
  Select mode                                      Fixed equation mode
    DEFINE trace header equation
    cdp=cdp*2
*Bandpass Filter
  TYPE of filter                                   Single Filter
  Type of filter specification                     Ormsby bandpass
  PHASE of filter                                  Zero
  Apply a notch filter?                            No
  Ormsby filter frequency values                   5-10-40--50
*Trace Mixing
*Steep Dip Explicit FD Time Mig.
  Maximum frequency (in Hz)                        40.
  Get interval velocities from database?           Yes
    Select interval vs. time velocity              VImodtoCDPtime2wemrdtmfxdm
  file
  Re-apply trace mutes?                            No

FLOW - WAVEEq     Wed Jan 14 04:23:02 1998
  Output - wemrdtmfxdFLTmixFDTMfltAGCplt6 Add 1217 Over 0
 Trace Muting
  Re-apply previous mutes                          No
  TYPE of mute                                     Top
    Starting ramp                                  30.
    SELECT mute parameter file                     tpmutafterwemrdtmmixsdfdtm
 Trace Length
* New trace length                                 4500.
*Bandpass Filter
  TYPE of filter                                   Single Filter
  Type of filter specification                     Ormsby bandpass
  PHASE of filter                                  Zero
  Apply a notch filter?                            No
  Ormsby filter frequency values                   5-10-24-36
*Automatic Gain Control
  Application mode                                 APPLY
  Type of AGC scalar                               MEAN
  AGC operator length                              500.
  BASIS for scalar application                     Centered
  Robust Scaling?                                  No
*Trace Muting
  Re-apply previous mutes                          No
  TYPE of mute                                     Top
    Starting ramp                                  30.
    SELECT mute parameter file                     corner
```

Post-stack processing sequence performed on seismic line 16.

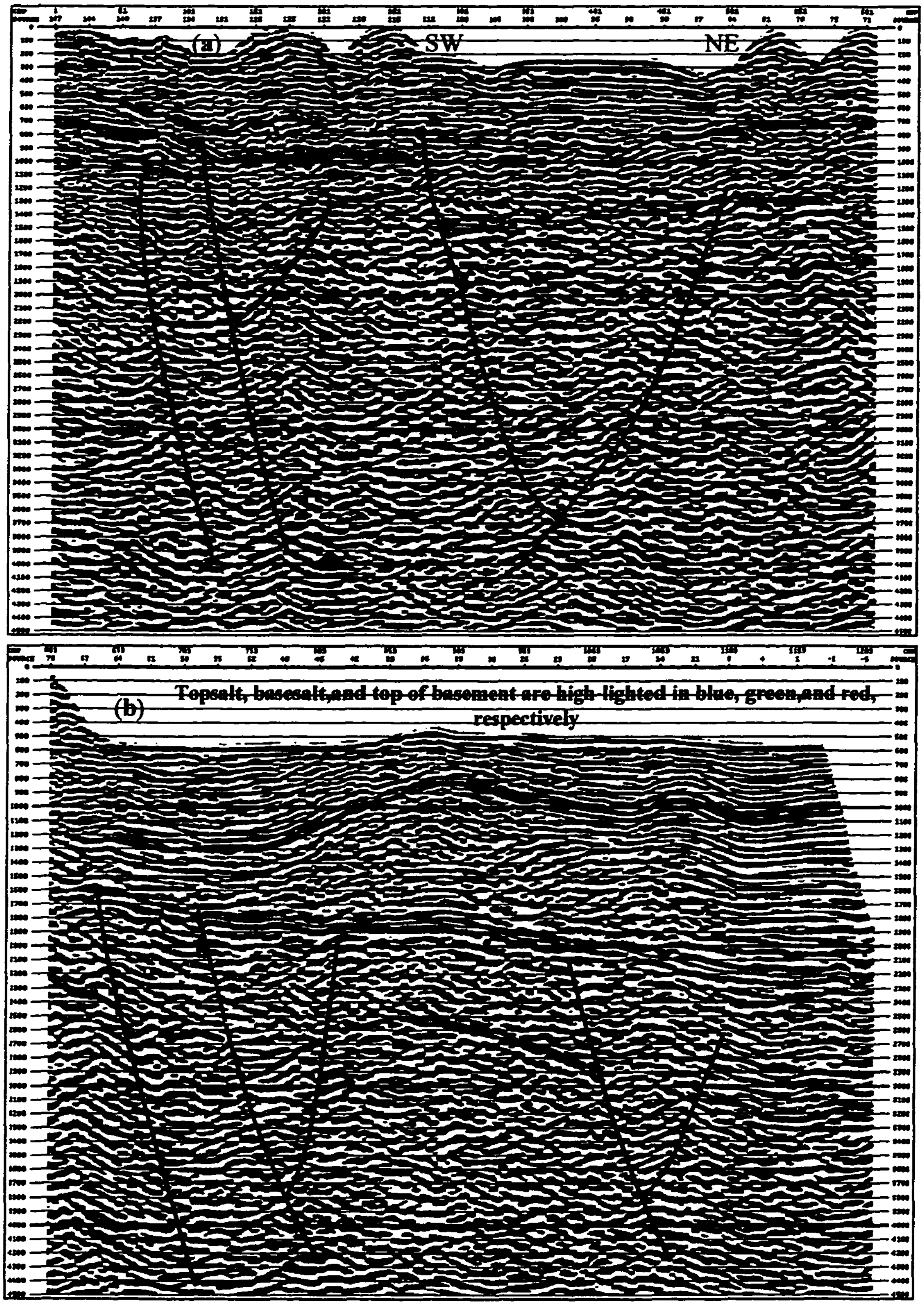

Figure 5.40. (a) The Southwestern (a) and northeastern (b) parts of seismic line 16 after Post-stack signal enhancement, steep dip explicit finite difference time migration, and interpretation.

V.3. **Seismic line 13**

Seismic line 13 is located 24 km north of line 16 and runs from southwest to northeast (Fig. 1.2). This line is chosen for this investigation because it has geological features that are very common in this area. This line begins 3.5 km east of the shoreline and extends 24-km seaward. The major carbonate reef, the shallow shelf area, and the intervening valley they created, produce a strong undulating seafloor on the southwest portion of the line (Fig 5.41). The bathymetry in this area varies from 188 to 1875 feet. The northeast part of the line exhibits mild seafloor topography with water depth ranging from 1575 to 2375 ft.

Initial interpretation.

The top and base of salt and top of basement reflectors defined on line 16, are extrapolated to line 13 through the strike lines 54N, and 55. The basement-involved normal faults divide the subsalt section into tilted fault blocks beneath the shelf and northeast of the reef buildup. The faulting results in a horst beneath the reef and a graben between the reef and the shelf area. A broad, gentle synclinal feature or depocenter exists within the northeast part of the section. The depocenter consists of thick subsalt section overlain by Middle Miocene salt. The salt exhibits gradual thinning towards southwest and pinches out beneath the carbonate reef.

V.3.1. Imaging problems:

The most obvious imaging problem is the definition of subsalt section on the southwest part of the seismic line 13 (southwest of shotpoint 93). In this area, topsalt, basesalt, and top of basement reflectors are considerably disrupted, particularly underneath the edges of the reefs, by what appears to be diffraction events (Fig. 5.42).

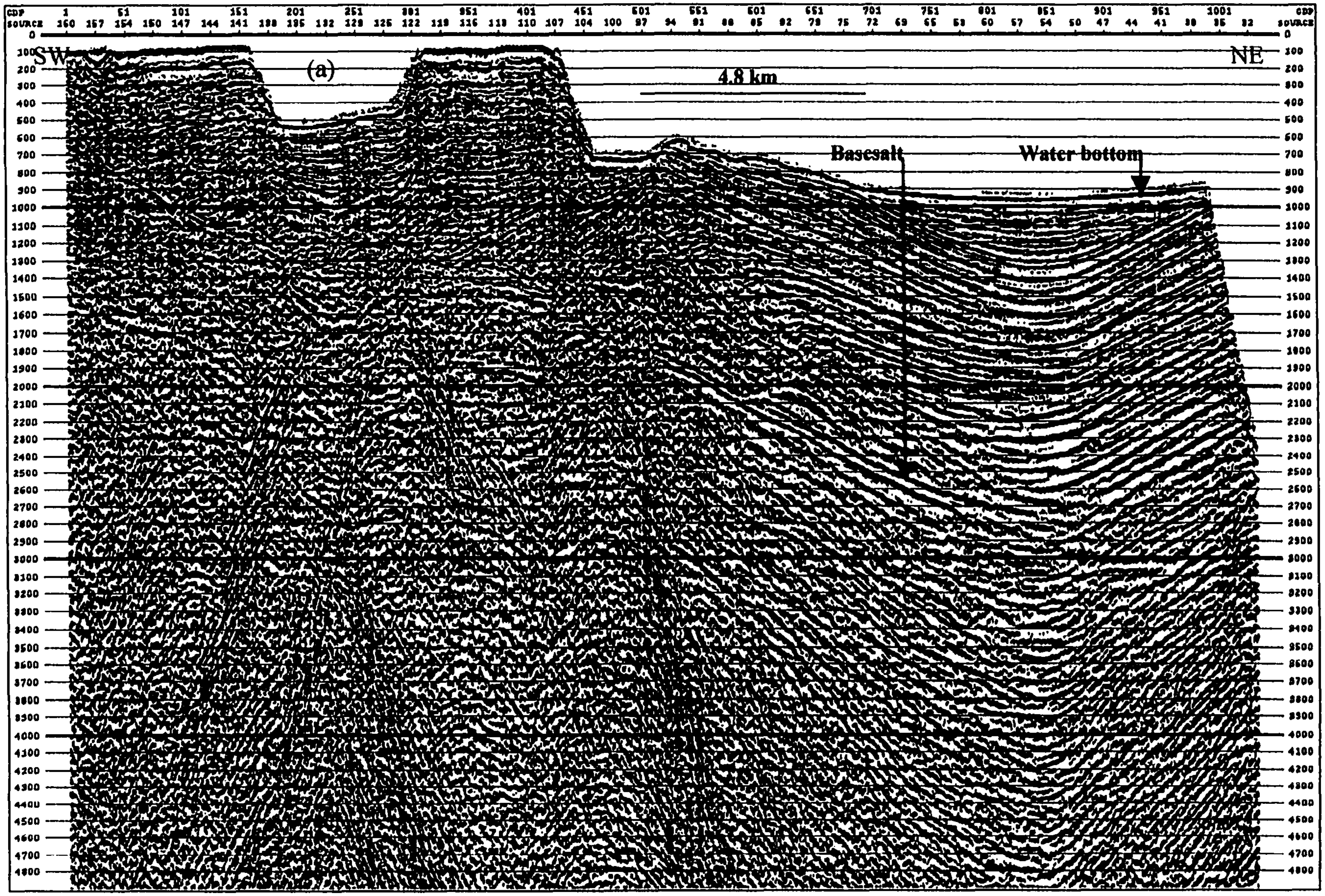

Figure 5.41. Seismic line 13 before signal enhancement and migration.

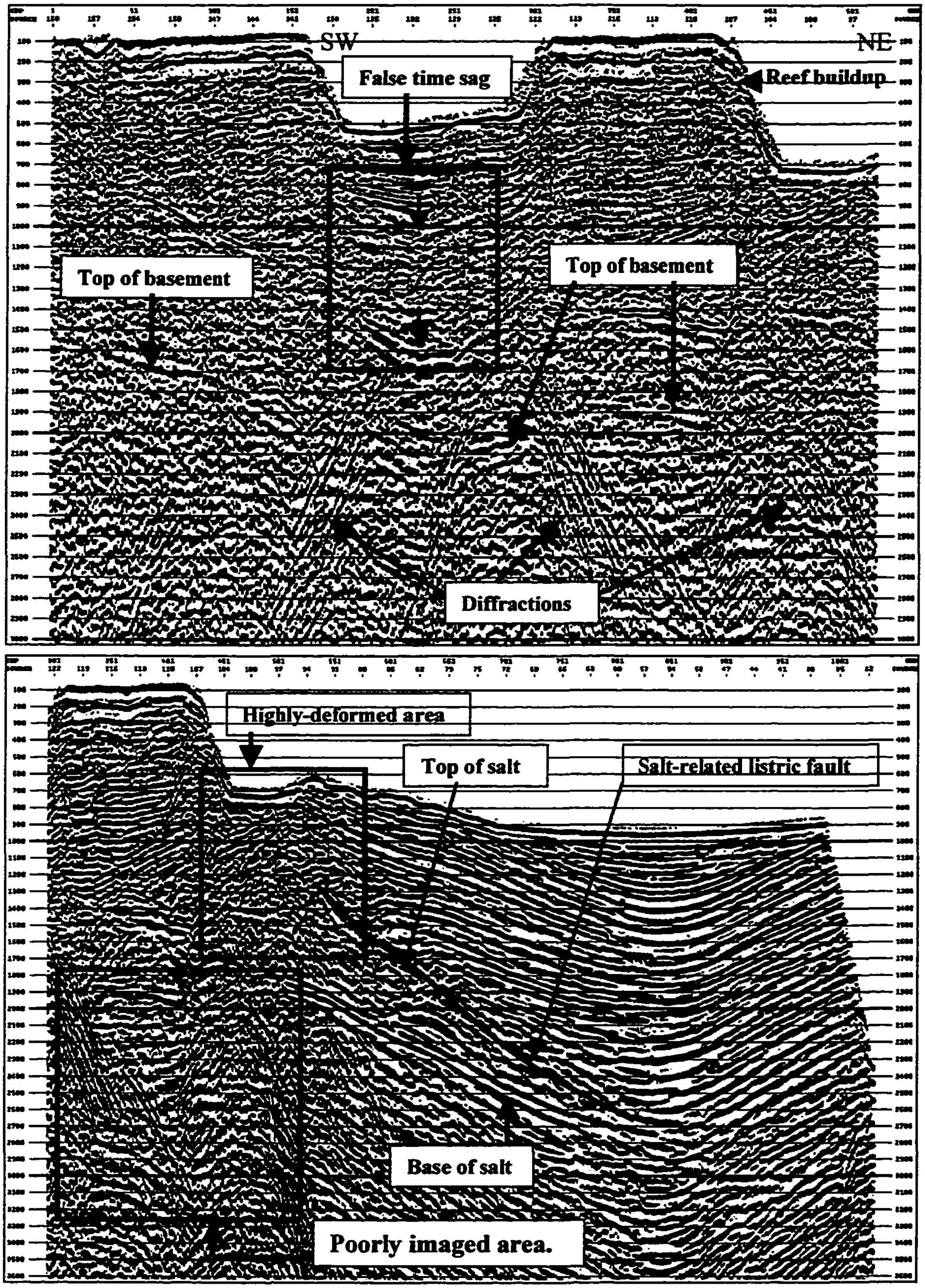

Figure 5.42. The image distortions observed on the southwest (a) and northeast (b) parts of line13. Note the severe distortions underneath the highly-deformed salt.

Also the top and base of salt in this area appear as impressed image of the overlying water bottom topography. Note how the false time sag of base of salt exaggerates the thickness of supra-salt section in the graben. The topsalt, basesalt, and top of basement are easy to pick on the northeast part of the section. However, the top of basement reflector is weak in the deeper part of the depocenter and the topsalt is significantly deformed northeast of shotpoint 86. What is unique about this line is that the thinning and pinching out of salt beneath the reef enable illumination of underlying subsalt section in the southwest part of the line. Note how the top of basement reflector is visible and easy to pick, at locations that are not disrupted by diffractions, such as beneath the shelf and the center of the reef.

V.3.2. 2-D seismic modeling Results:

The time model constructed from the initial seismic interpretation is shown in figure 5.43. The time model is then converted to depth using normal incidence ray process described previously. The initial depth model and the normal incidence synthetic trace it produces are displayed in Figure 4.44. Comparison of arrival times of topsalt, basesalt, and top of basement horizons of the synthetic with those of the real seismic section does produce a good match. After several iterations, a final velocity-depth is produced (Fig. 5.45). The modification of the depth model includes the geometry and thickness of salt and fault blocks. The thickness of supra-salt and subsalt layers and their velocities. The synthetic section generated by the final depth model provides a reasonably acceptable match, in arrival times, with the real seismic section (Fig. 4.46). The synthetic also simulates most of the features observed on the real line. It simulates the poorly imaged area beneath variable seafloor, the false time sag underneath the valley, and the broad syncline region.

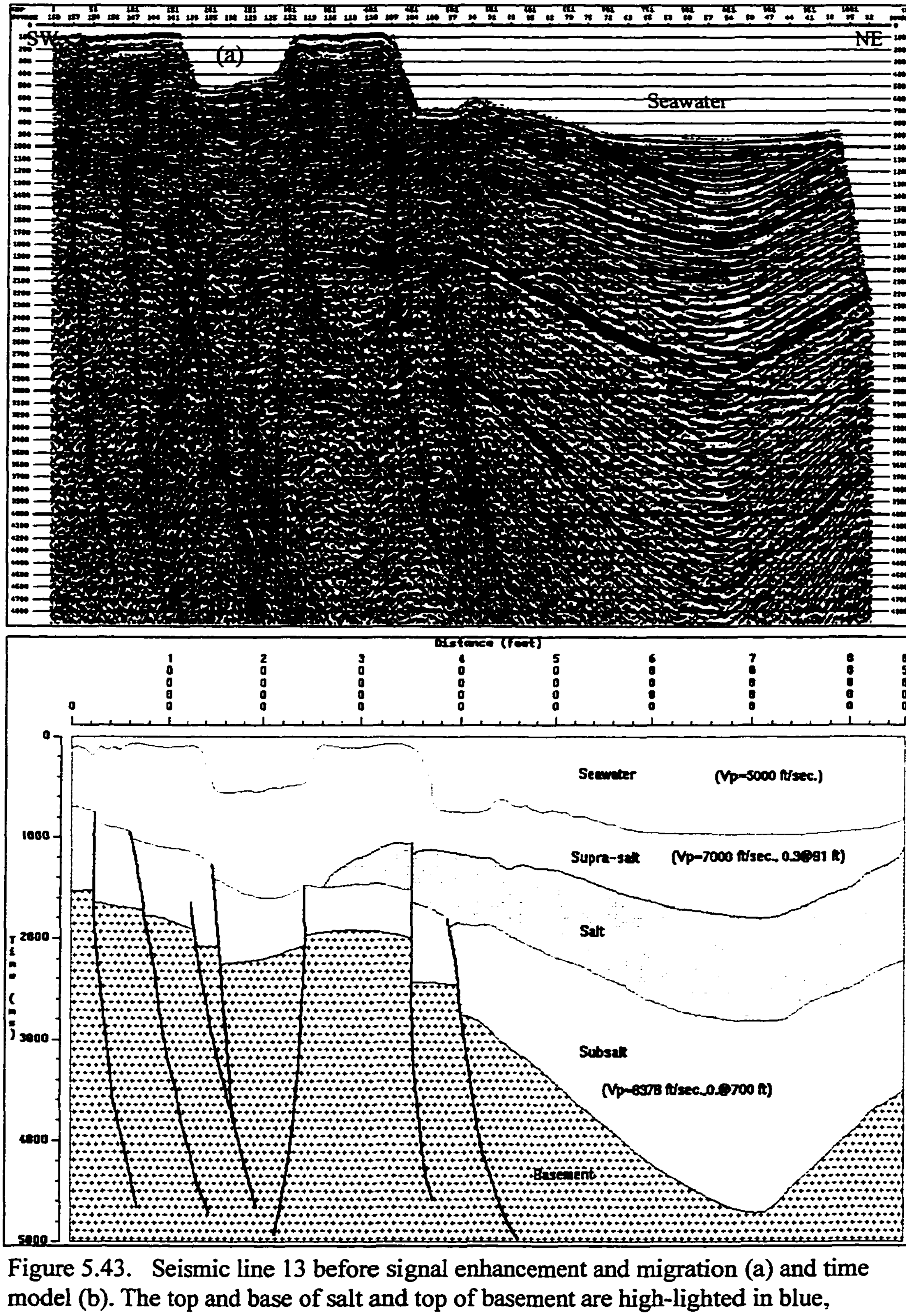

Figure 5.43. Seismic line 13 before signal enhancement and migration (a) and time model (b). The top and base of salt and top of basement are high-lighted in blue, green, and red ,respectively.

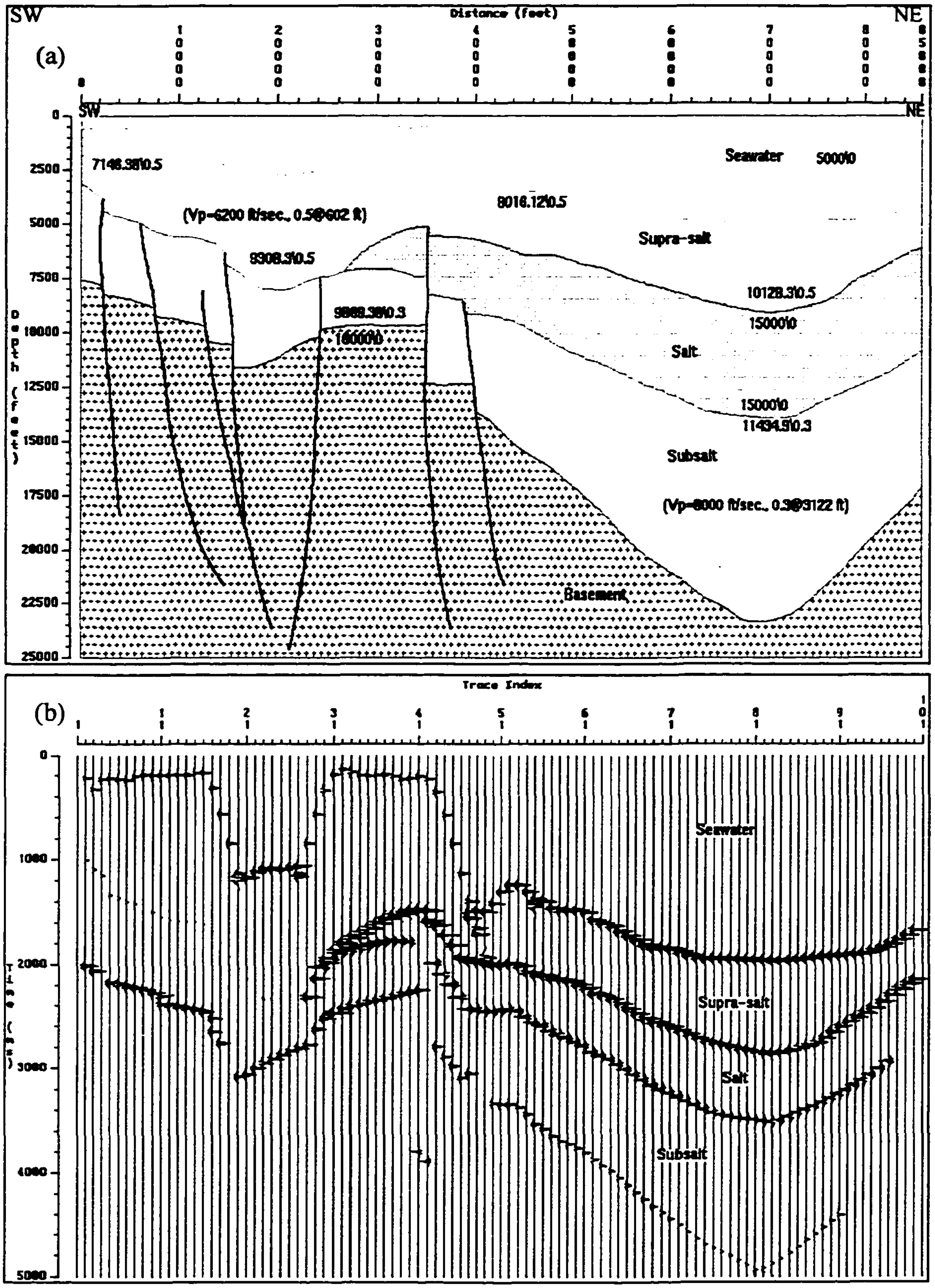

Figure 5.44. Initial velocity-depth model (a) and normal incidence synthetic section (b) of line 13.

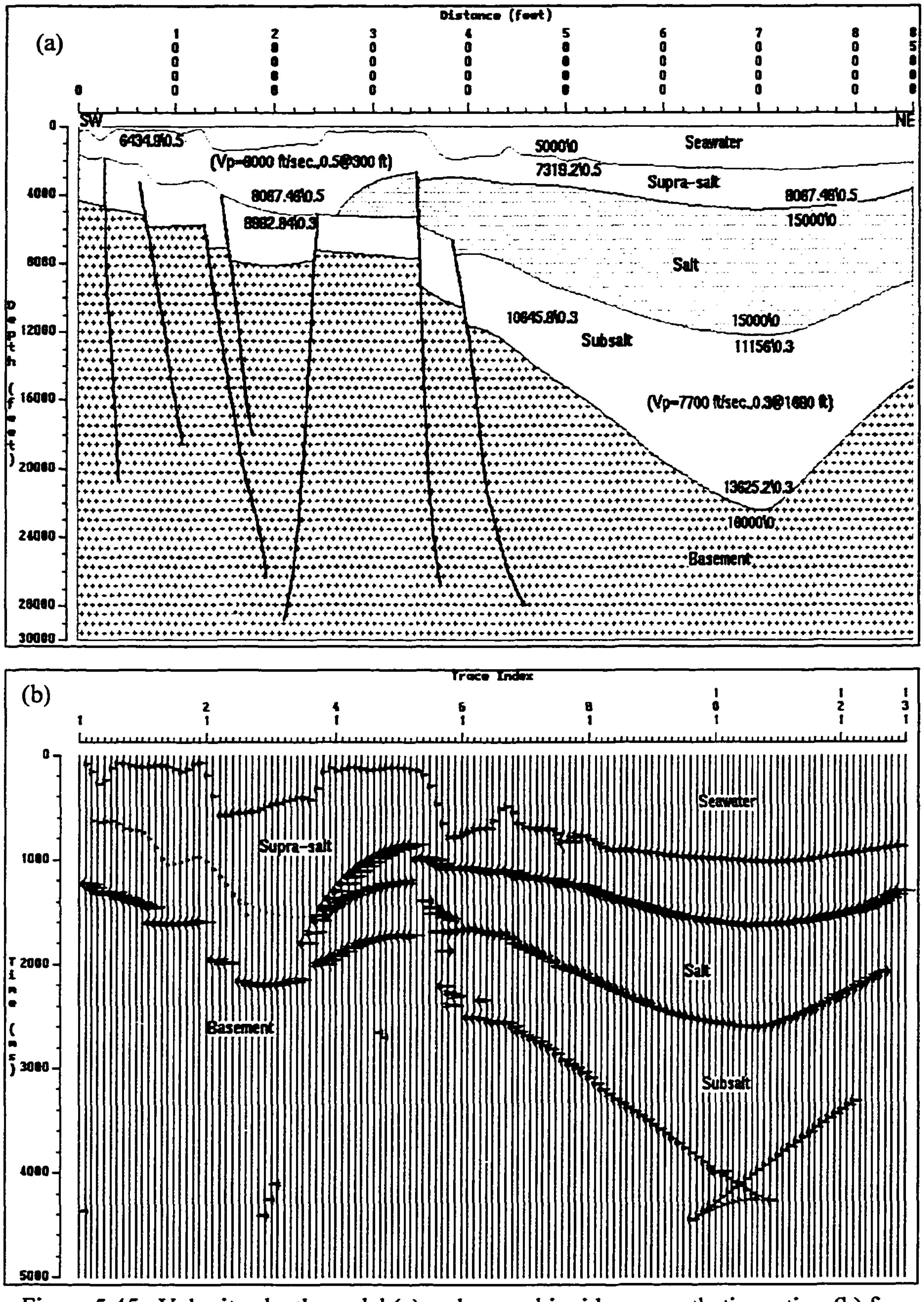

Figure 5.45. Velocity-depth model (a) and normal incidence synthetic section (b) for seismic line 13.

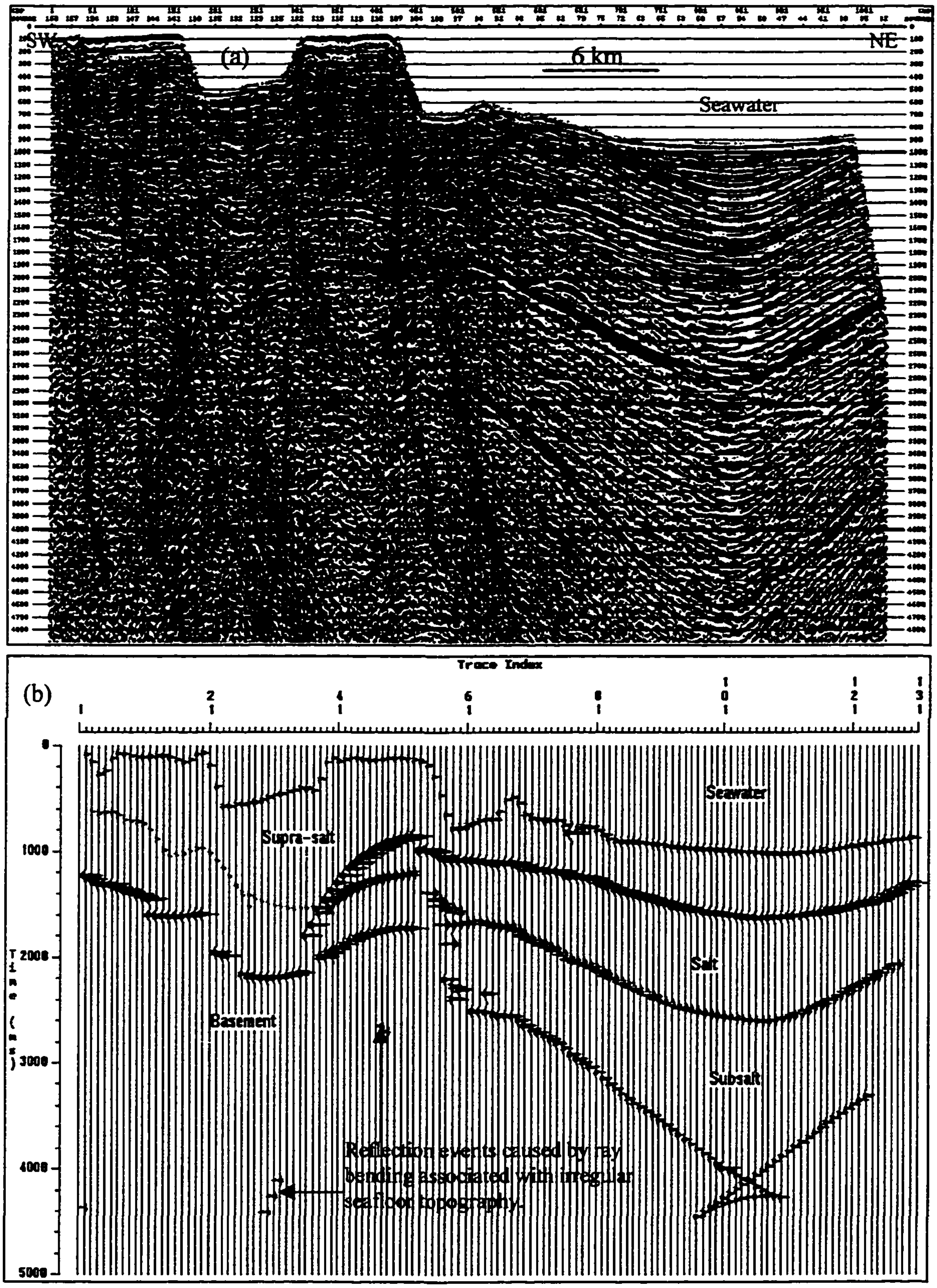

Figure 5.46. (a) Seismic line 13 before signal enhancement and migration. (b) Normal incidence synthetic trace displayed with arrival times. The top and base of salt and top of basement are high-lighted in blue, green, and red, respectively.

Raypath characteristics:

Zero offset ray-tracing is performed on the final depth model to investigate the effects of strongly variable water bottom, high-velocity salt, and basement-involved major normal faults on the imaging of the underlying subsalt section. Zero offset raypaths for water bottom reveals that the high velocity contrast at the steeply dipping reef and shelf edge walls cause both the reflected and transmitted rays to undergo significant bending (Fig. 5.47). The gradual deviation of the transmitted rays due to lateral velocity variations within supra-salt is also observed. Moreover, the down-doing rays refract at the top of salt. The refraction is due to the sharp velocity contrast at the steeply dipping salt boundary.

Figure 5.48 shows zero offset raypaths and synthetic section for diffraction from faulted block edges beneath varying seafloor. Each faulted block edge acts like a source and re-emits (diffracts) the incidence rays in all directions. The diffraction is manifested on the synthetic time section (Fig. 5.48) as strong hyperbolic events, known as diffraction curves, that masks the subsalt reflection structures. The strong ray bending of the upgoing rays at the top and base of the salt layer is due to high velocity contrast across the salt boundaries. The gradual deviation of upgoing rays within supra-salt layer is due to lateral velocity variations. The complex travel paths resulting from this ray bending distort the hyperbolic shape of the diffraction curves and displaced their apexes laterally from the underlying diffracting faulted block edges. This complicates the definition of faults and subsalt reflection structures.

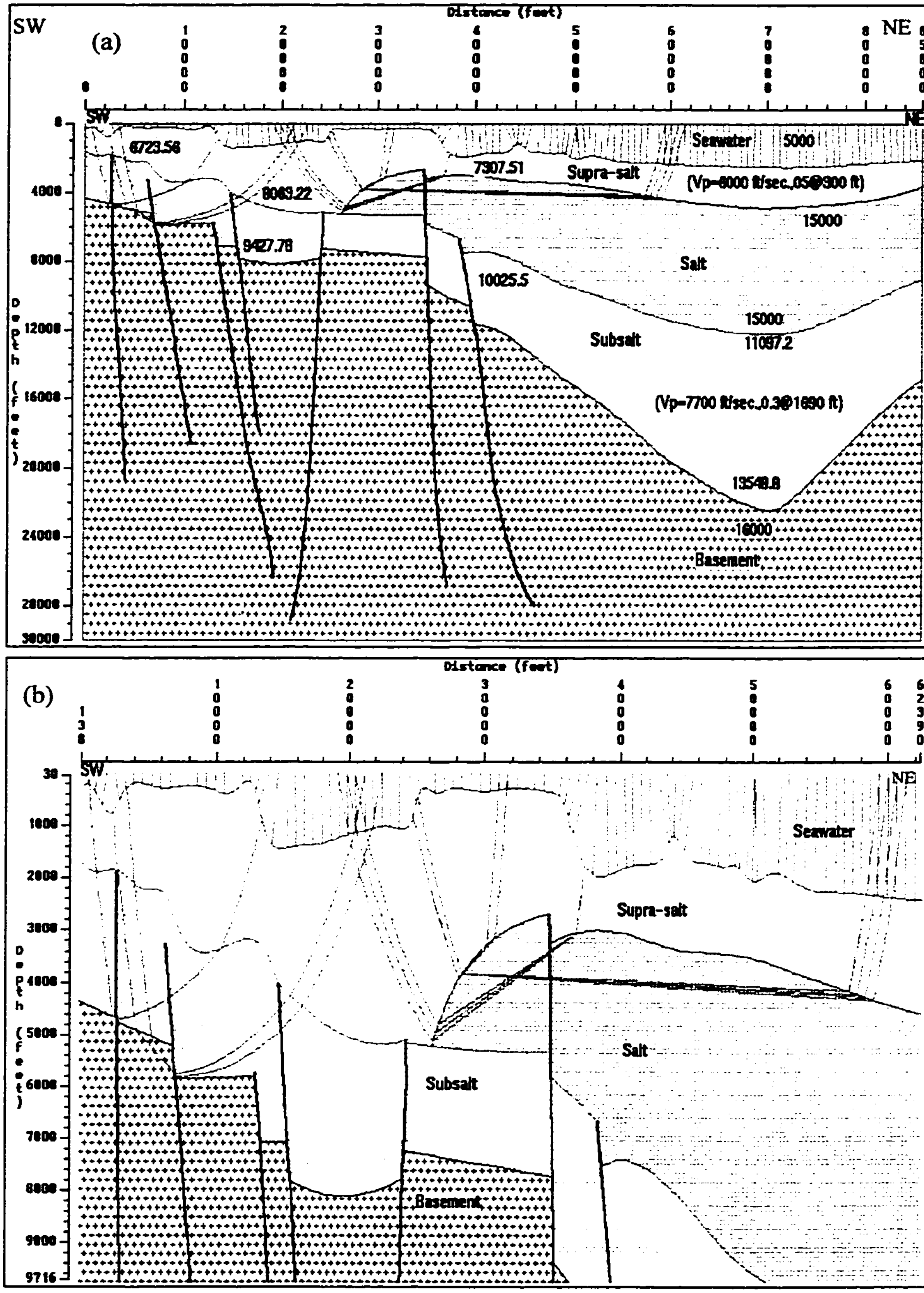

Figure 5.47. (a) Zero offset raypaths for water-bottom. (b) The raypaths after magnification.

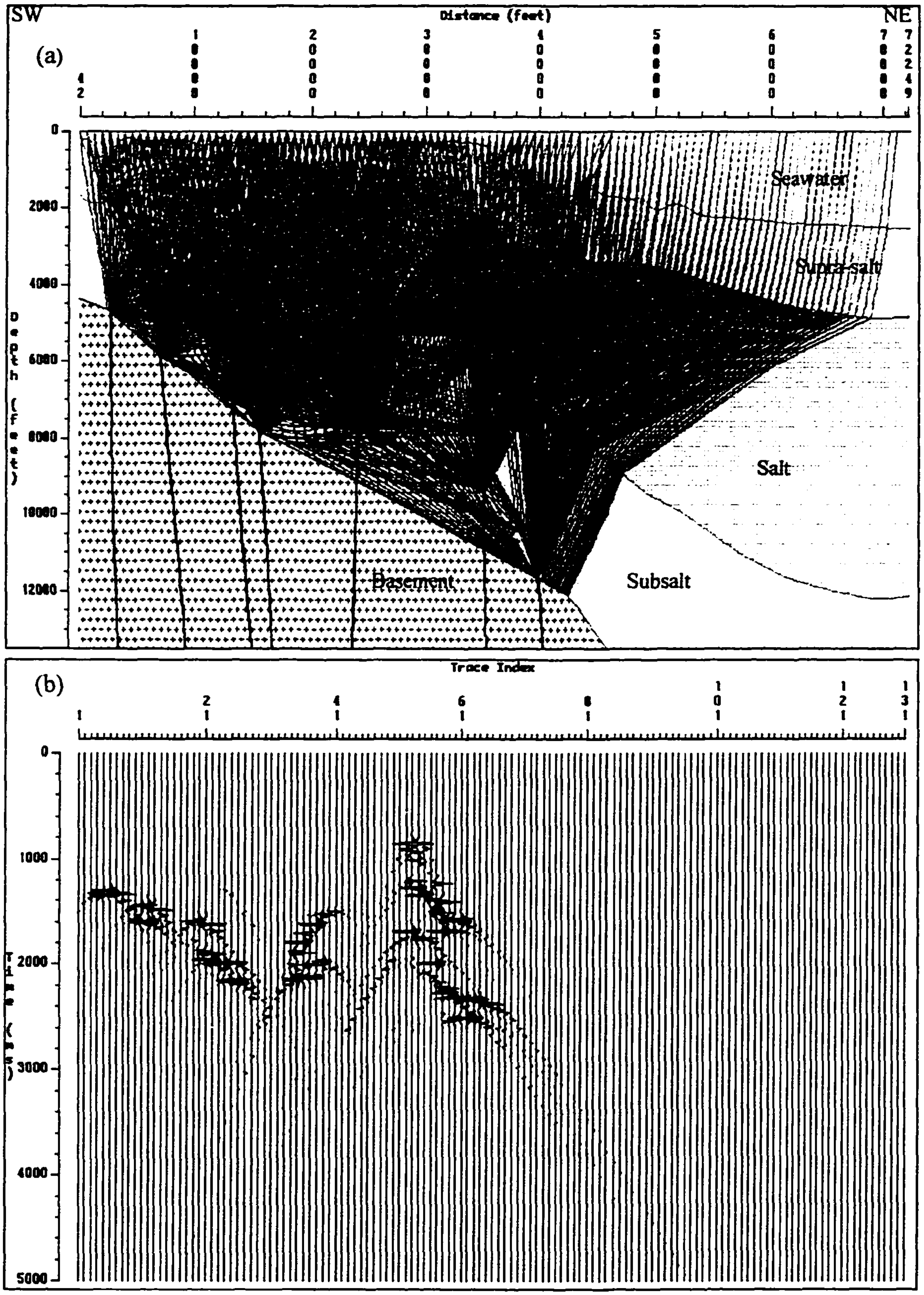

Figure 5.48. Zero offset raypaths (a) and synthetic section (b) for diffractions from faulted block edges (magnified). Raypaths colors indicate horizons.

V.3.3. Post-stack signal enhancement:

V.3.3.1. F-X deconvolution:

Figures 5.49 compares line 13 before and after F-X deconvolution. It is clear from this comparison that the continuity of reflections (in areas not seriously disrupted by diffractions) has improved and the complexity of the image distortions on this section becomes very clear. The deconvolution not only reveals the intensity of the diffractions and the velocity pull-up, but also the deformation and rupturing of salt just northeast of the reef and the seaward-dipping salt-related listric fault on the flank of dipocentre.

Wave equation multiple rejection:

This process is conducted on line 13 to suppress possible water bottom multiple particularly within the depocentre on the northeast part of the line. Comparison of the southwest and northeast parts of the section before and after multiple rejection (Figs. 5.50, 5.51) indicates that some water bottom multiples have been suppressed, specially on the northeast portion of the section and underneath the carbonate reefs.

V.3.4. Post stack migration results.

V.3.4.1. Steep dip explicit finite difference time migration. Steep dip explicit FD time migration, performed after signal enhancement, produces reasonably accurate subsurface image (Figs. 5.52, 5.53). The intensive diffractions and false time sags are completely removed. The continuity of subsalt reflecton events, the horst beneath the reef, and the graben structure to the southwest are much better imaged than before migration. The salt-related listric fault, the rollover, and the geometry of salt body can be easily observed on the migrated section as shown in Figure 5.54. Figure 5.55 shows the interpretation of the geometry of salt on the migrated seismic section.

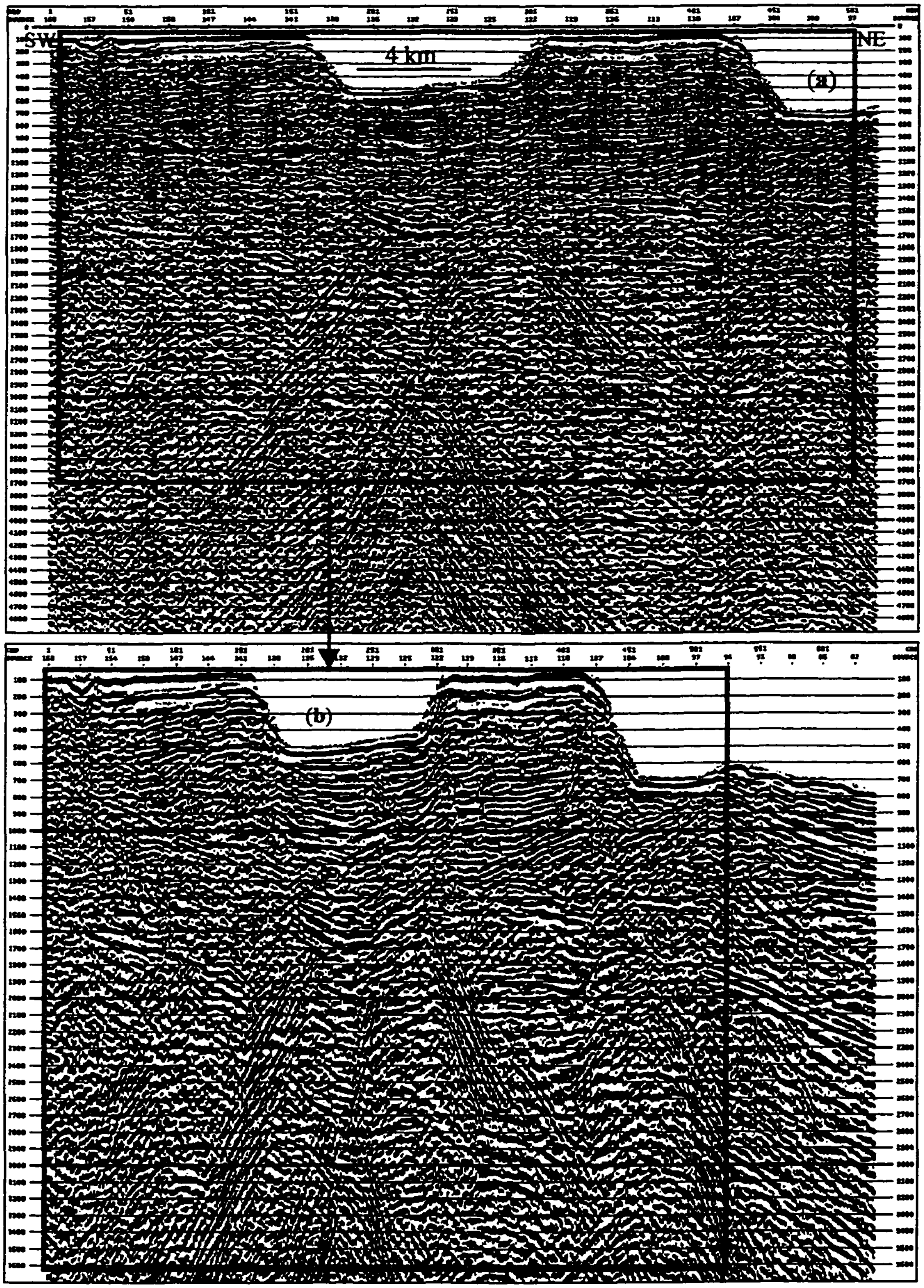

Figure 5.49. The southwest part of line 13 before (a) and after F-X deconvolution (b). The imaging distortions became very obvious after F-X deconvolution.

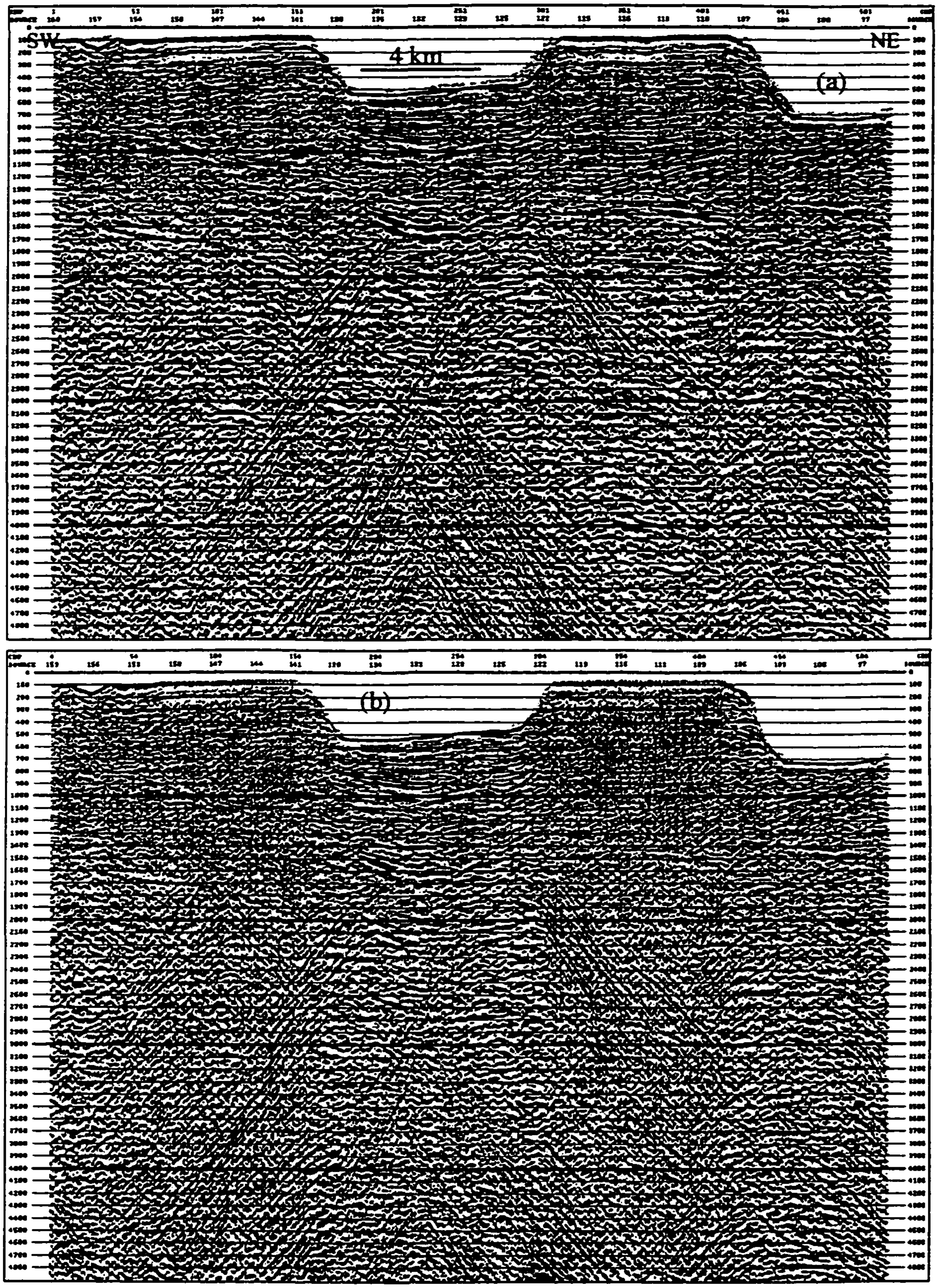

Figure 5.50. The southwestern part of line 13 before (a) and after wave equation multiple rejection (b).

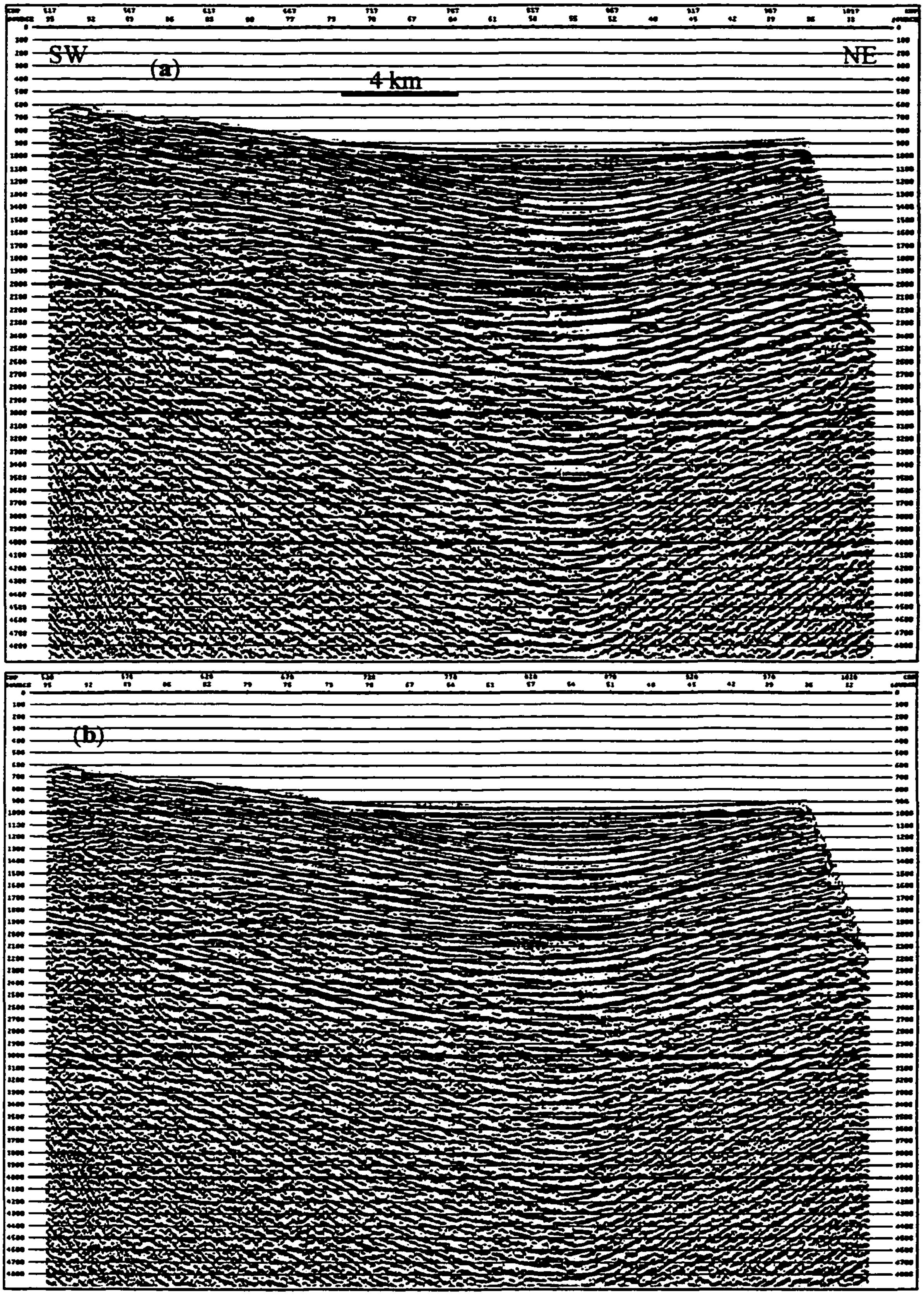

Figure 5.51. The northeastern part of line 13 before (a) and after (b) wave equation multiple rejection.

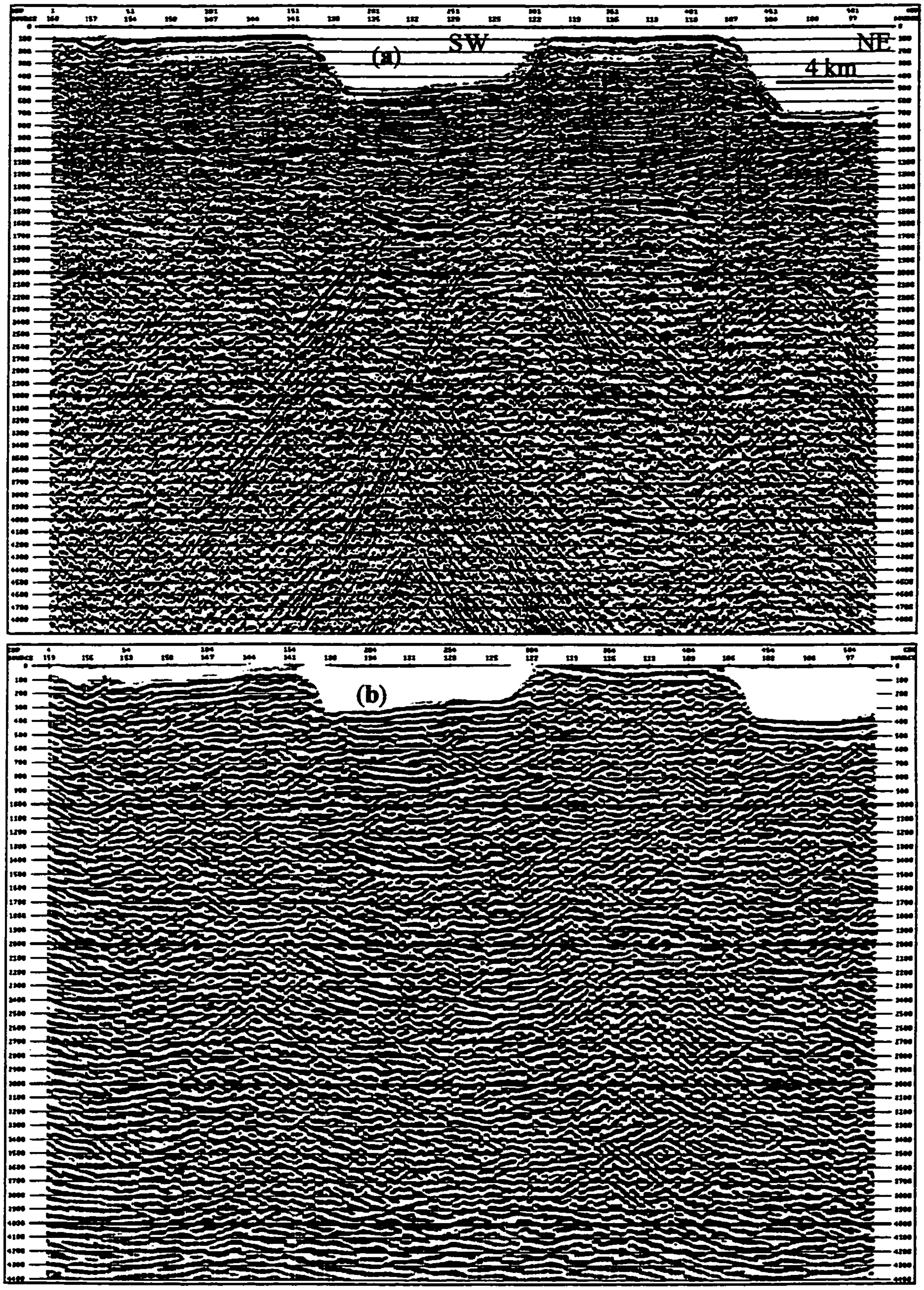

Figure 5.52. The southwest part of line13 before (a) and after (a) post-stack signal enhancement and steep dip explicit finite difference time migration.

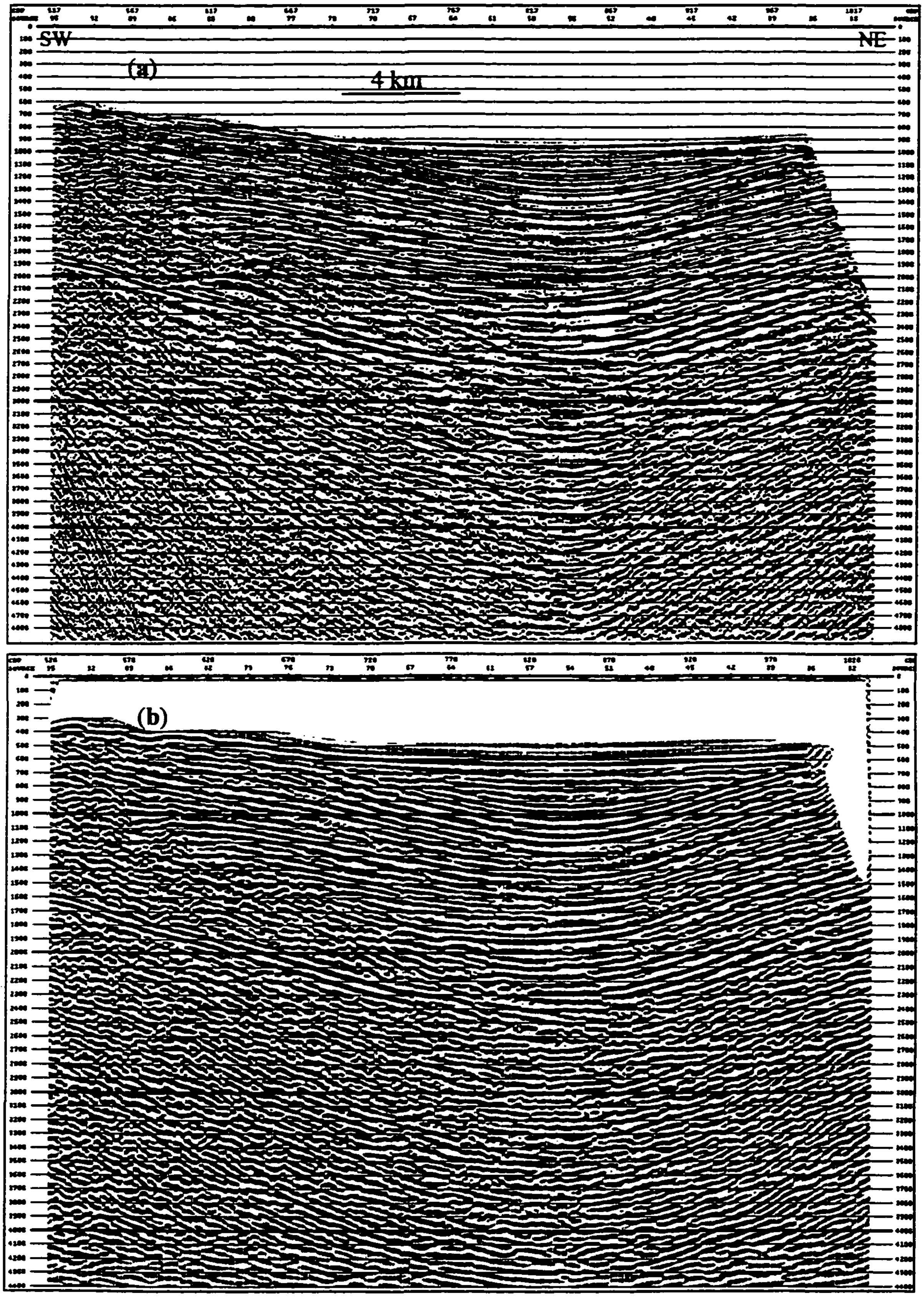

Figure 5.53. The northeast part of seismic line before (a) and after (b) post-stack signal enhancement and steep dip explicit finite difference time migration.

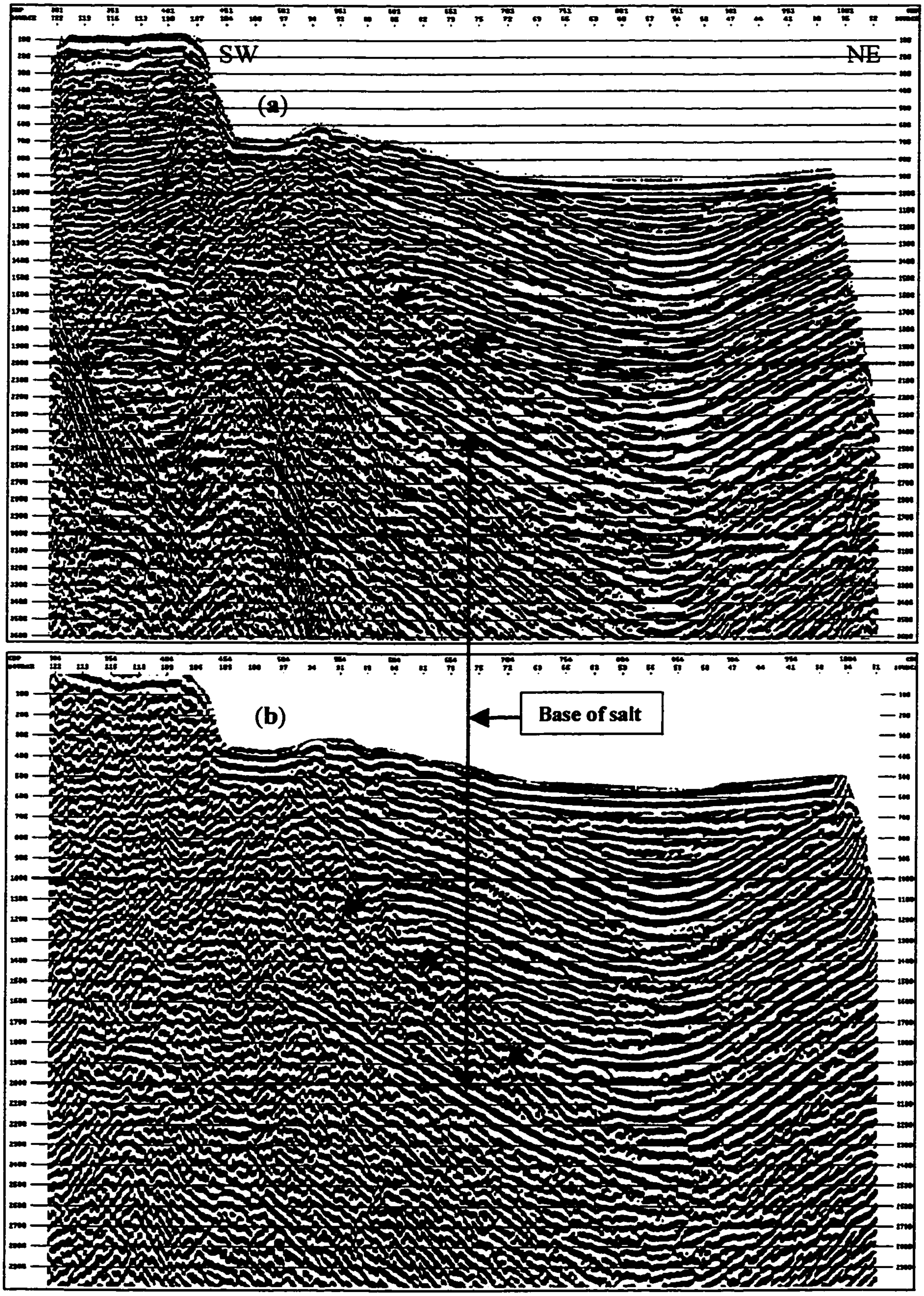

Figure 5.54. The northeast part of seismic line before (a) and after (b) post-stack signal enhancement and steep dip explicit finite difference time migration.Arrows indicated the salt-related fault plane.

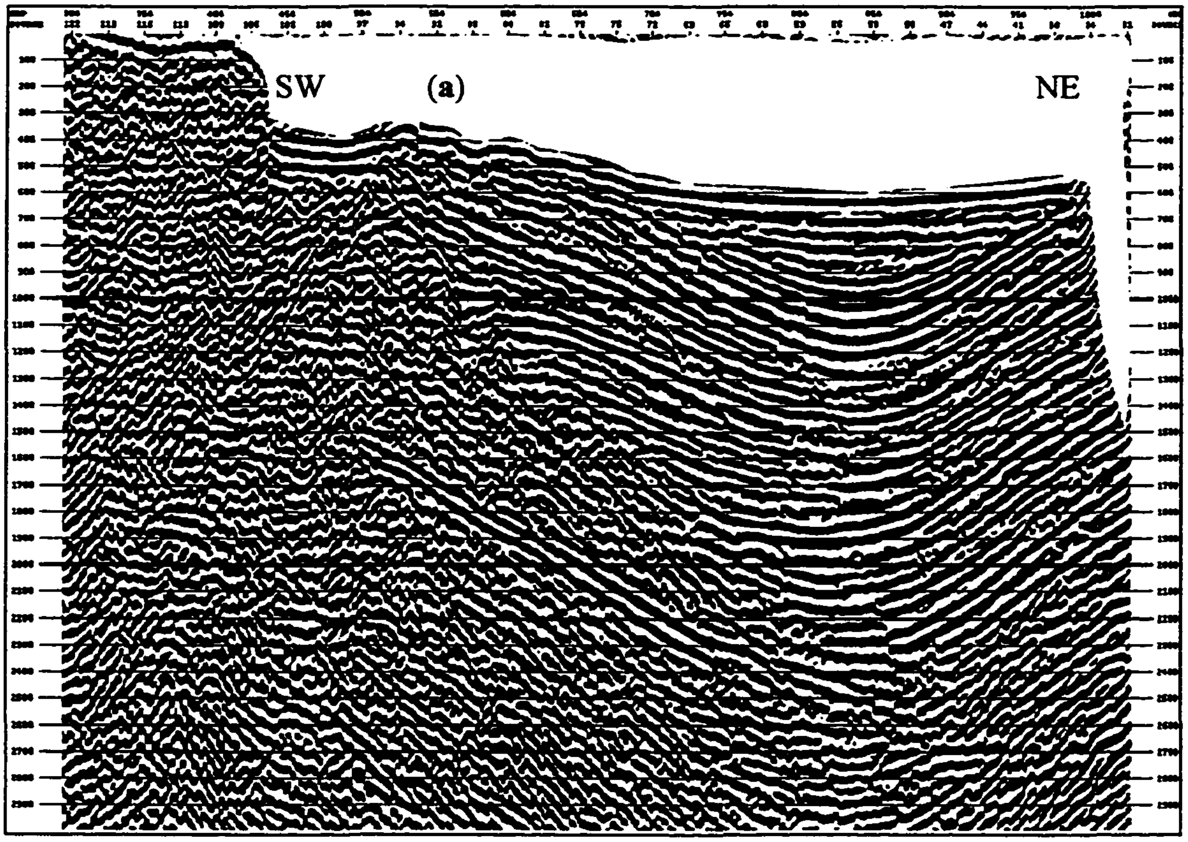

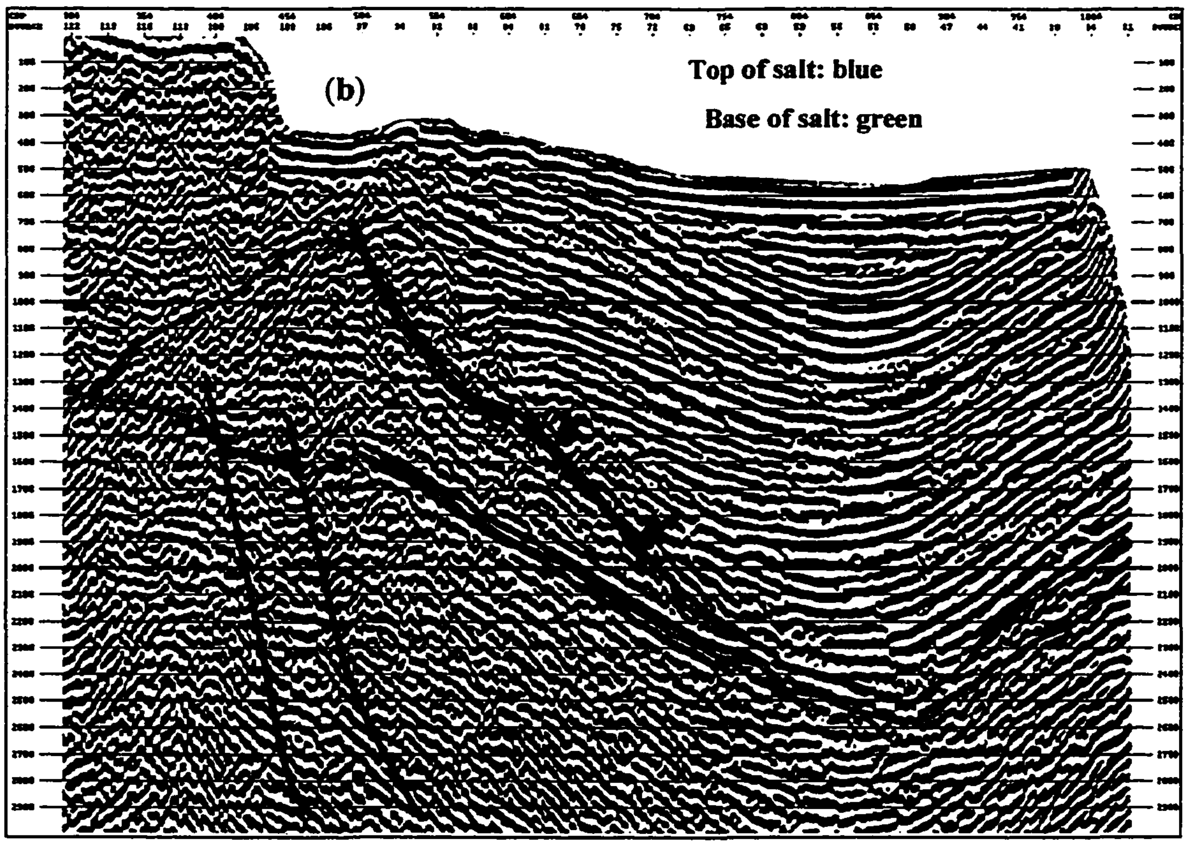

Figure. 5.55 (a) The northeast part of line 13 after post-stack signal enhancement and steep dip explicit finite difference time migration. (b) Same line after interpretation. Arrows indicated a salt-related fault.

V.4. **Seismic line 17-7**

Line 17-7 is located about 14 km south of line 16. It runs from southwest to northeast and intersects line 53-4 at shotpoint 7 (Fig. 1.2). This dip line begins 1 km east of the shoreline and extends 21.5-km seaward. The most obvious feature of the seafloor topography of this line is the carbonate reef close to the middle of the line (Fig. 5.56). The water depth on the reef buildup is 250 ft. It ranges from 1125 to 1750 feet and from 1938 to 2125 feet west and east of the reef, respectively.

<u>Initial interpretation</u>.

Line 17-7 is dominated by a multitude of diffraction events, especially in the areas to the east and west of the carbonate reef (Fig. 5.56). Although these diffractions cause severe image disruption, they are useful in defining the fault surfaces. The initial definition of major faults on this line is accomplished by tracing and joining successive diffraction apexes. Reflectors corresponding to the topsalt, basesalt, and top basement reflectors picked on line 16 to the north are tied to the strike line 53-4 (Fig. 5.57) and then carried to the dip line 17-7. The transfer of these reflectors to line 17-7 is rather difficult because the data quality at the intersection of lines 53-4 and 17-7 is very poor. Therefore, the strike line 55 is used to extrapolate the objective reflectors defined on line 16E to the eastern part of line 17-7. The poor imaging of top of basement reflector over the entire section and distortion of topsalt and basesalt reflectors beneath the edges of the buildup complicate extrapolation on line 17-7. The initial interpretation indicated several basement-involved major normal faults. The faults offset the subsalt section and terminate at the base of salt on the western part of the seismic section and cut through the entire sedimentary section on the eastern part. The salt exhibits variable geometry and irregular

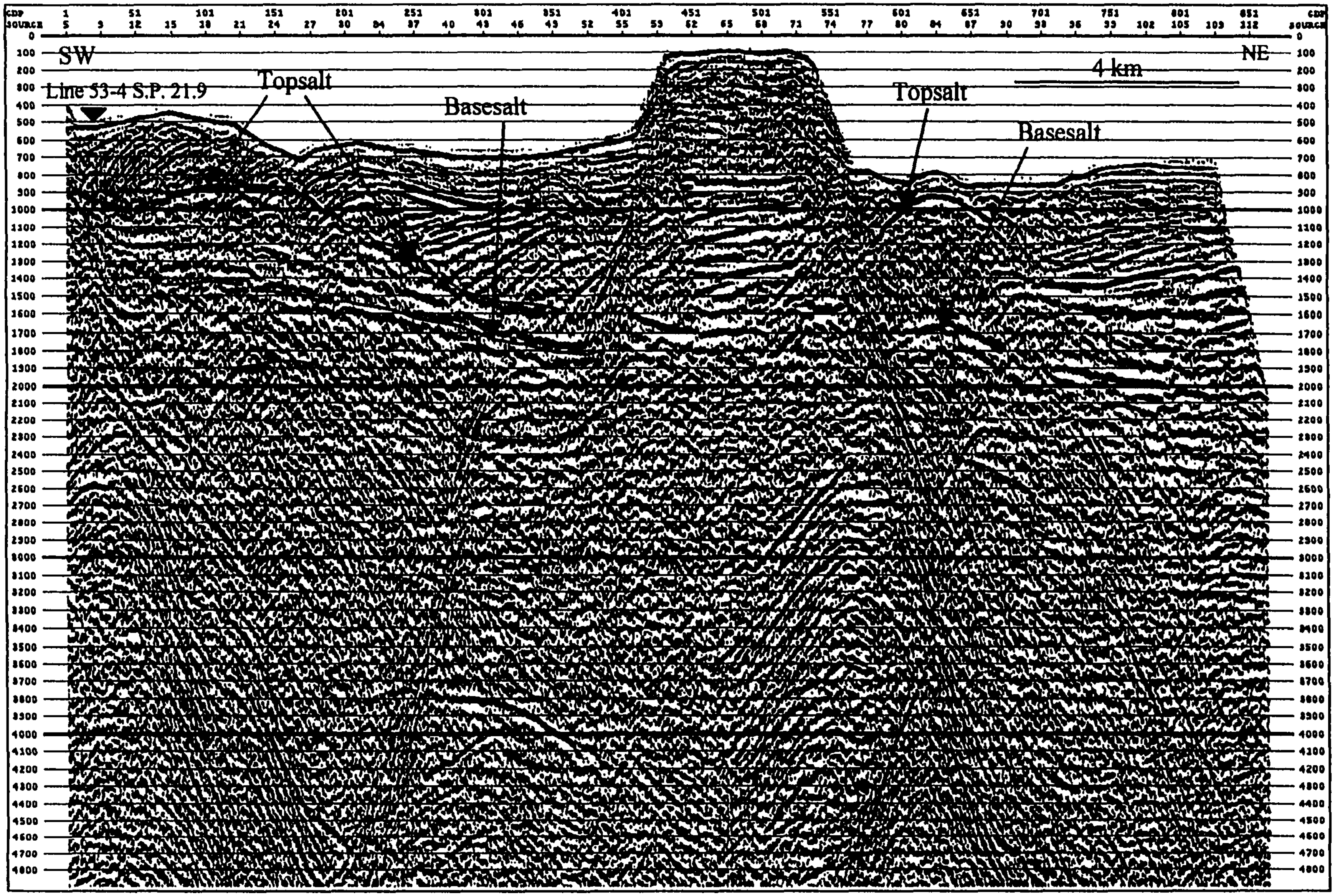

Figure 5.56. Seismic line 17-7 before signal enhancement and migration.

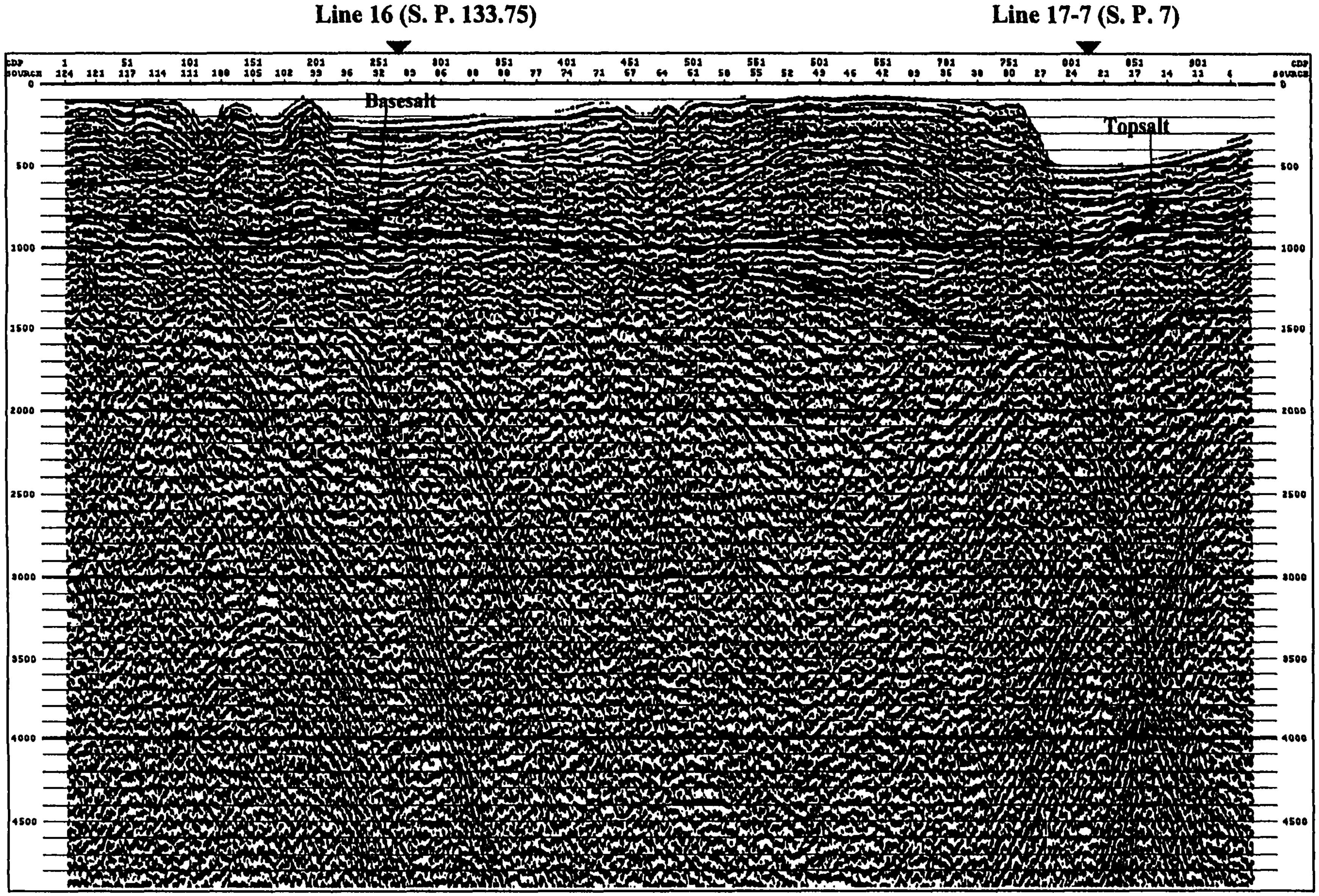

Figure 5.57. Seismic line 534 before signal enhancement and migration. This strike line intersects dip lines 16 and 17.7 at shotpoints 135 and 7, respectively.

upper boundary. The interpretation reveals a very thin salt layer overlain by thick supra-salt section below and east of the carbonate reef and relatively thick salt, with chaotic internal reflection pattern, on the rest of the line.

V.4.1. Imaging problems:

The imaging distortions observed on the western, middle, and eastern parts of line 71-7 are highlighted on Figures 5.58, 5.59. It very obvious, at first glance, that this line is dominated by diffraction events. These diffraction events crosscut one another and overlap with the primary reflections and hence degrade the subsalt and basement reflection structures. Steeply dipping, linear events, associated with abrupt change in seafloor topography, obscure the salt, subsalt events below the edges of the carbonate reef. The gentle hyperbolic events within the deeper part of the section are possibly sideswipe or diffractions from discontinuity deep below the bottom of the section. The basesalt is pulled up due to the high velocity of the overlying salt just east of the carbonate reef. The high amplitude events just below the reef buildup are likely to be water bottom multiple. These image distortions mask the top of basement reflector and subsalt section and obscure geometry of salt body beneath and west of the carbonate reef.

V.4.2. Post-stack signal enhancement

V.4.2.1. Wave equation multiple rejection:

Wave equation multiple rejection process is performed line on 17-7 to suppress possible water bottom multiple and peg-leg multiple. Figure 5.60 compares the seismic section before and after multiple rejection. It is clear the events with high amplitude just beneath the carbonate reef have been attenuated. However, the landward-dipping events above the salt weld just west of the carbonate reef have not been suppressed.

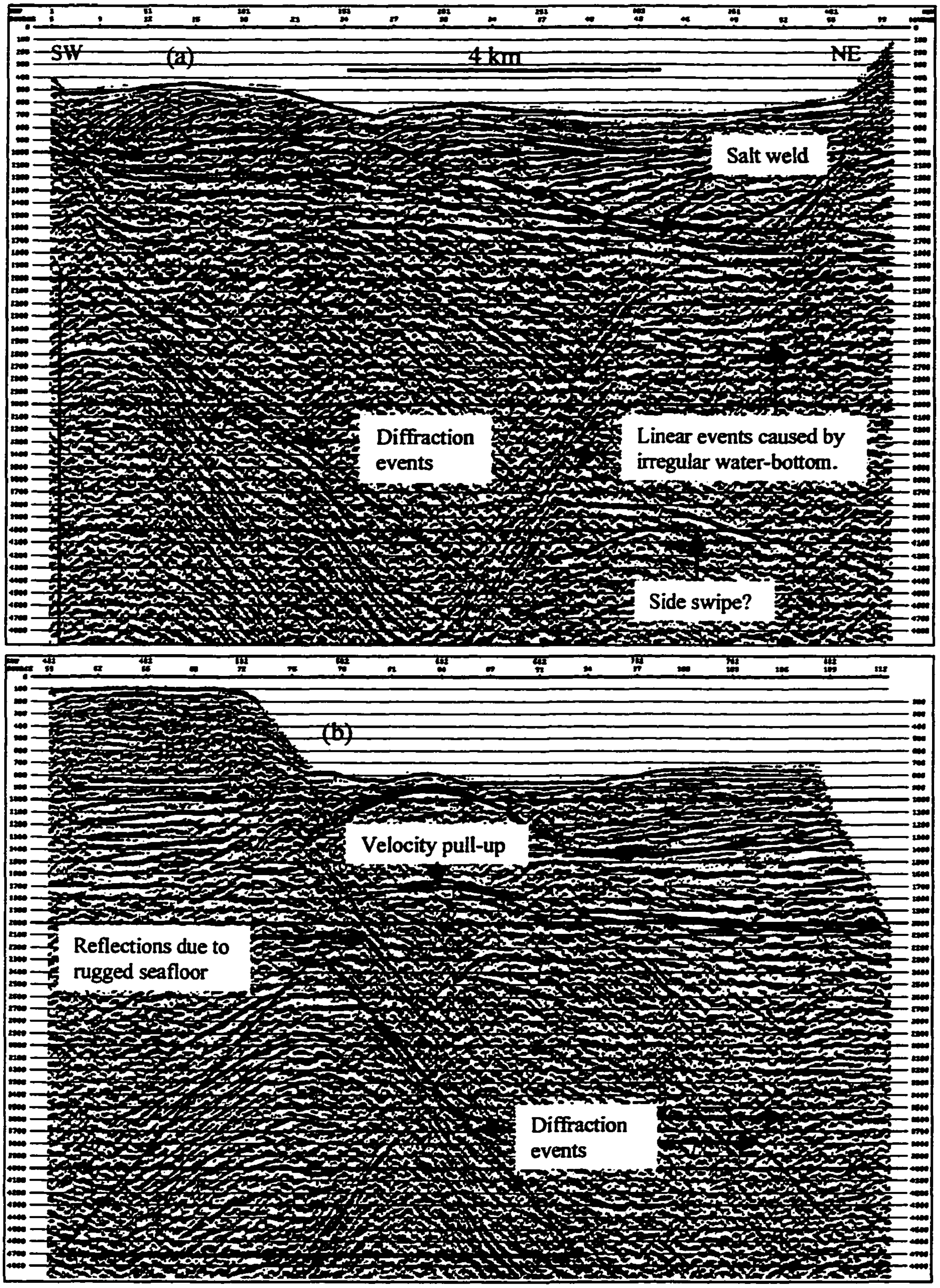

Figure 5.58. The southwestern (a) and northeastern (b) part of seismic line 17-7 before migration. Note the significant image distortion associated with faulting, variable seafloor and salt geometry. The top and base of salt are high-lighted in blue and green, respectively.

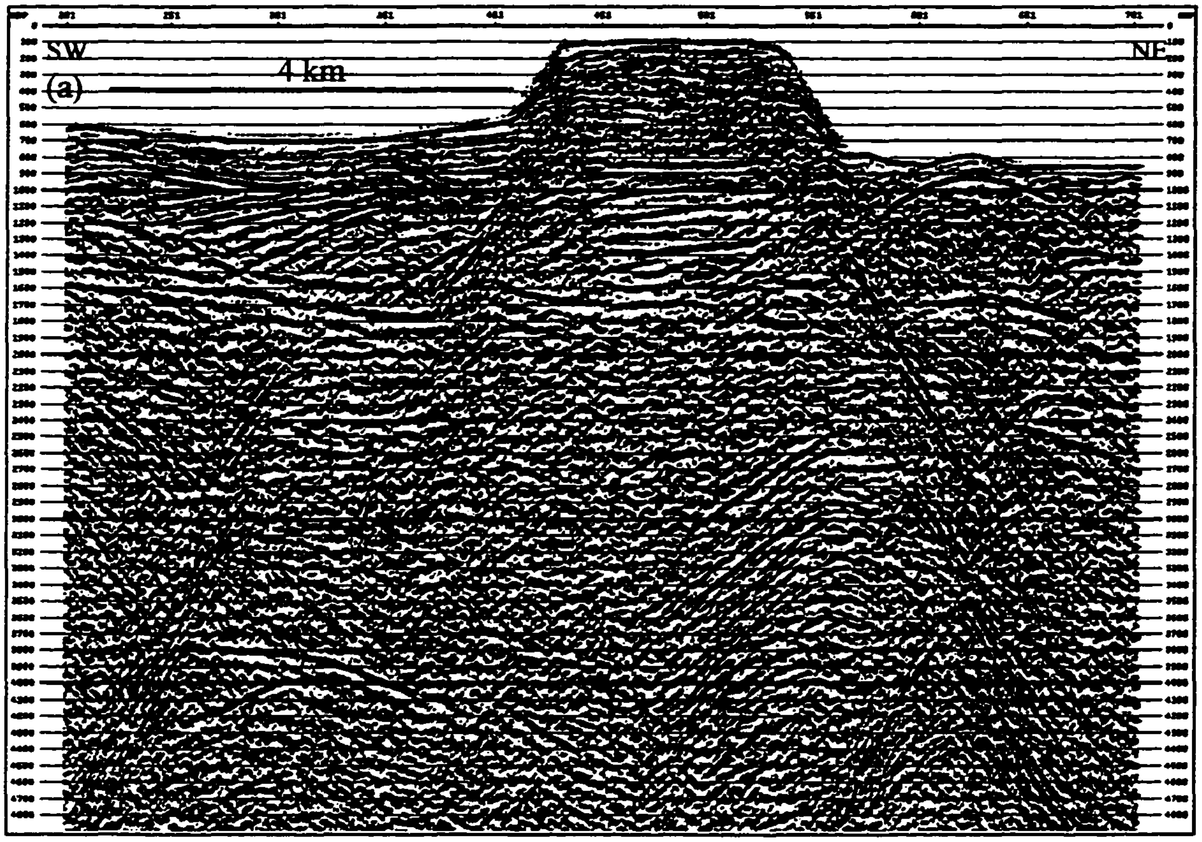

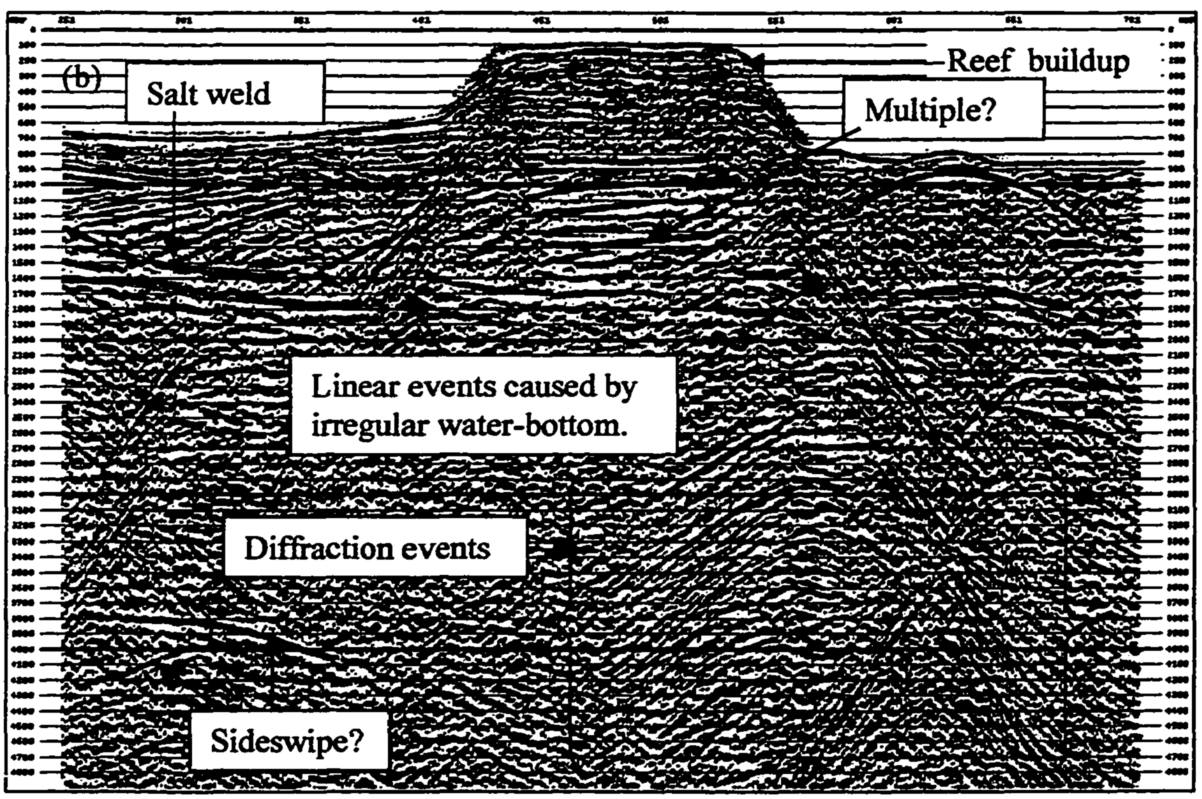

Figure 5.59. (a) The middle part of seismic line 17-7 before signal enhancement and migration. The top and base of salt are high-lighted in blue and green, respectively (b).

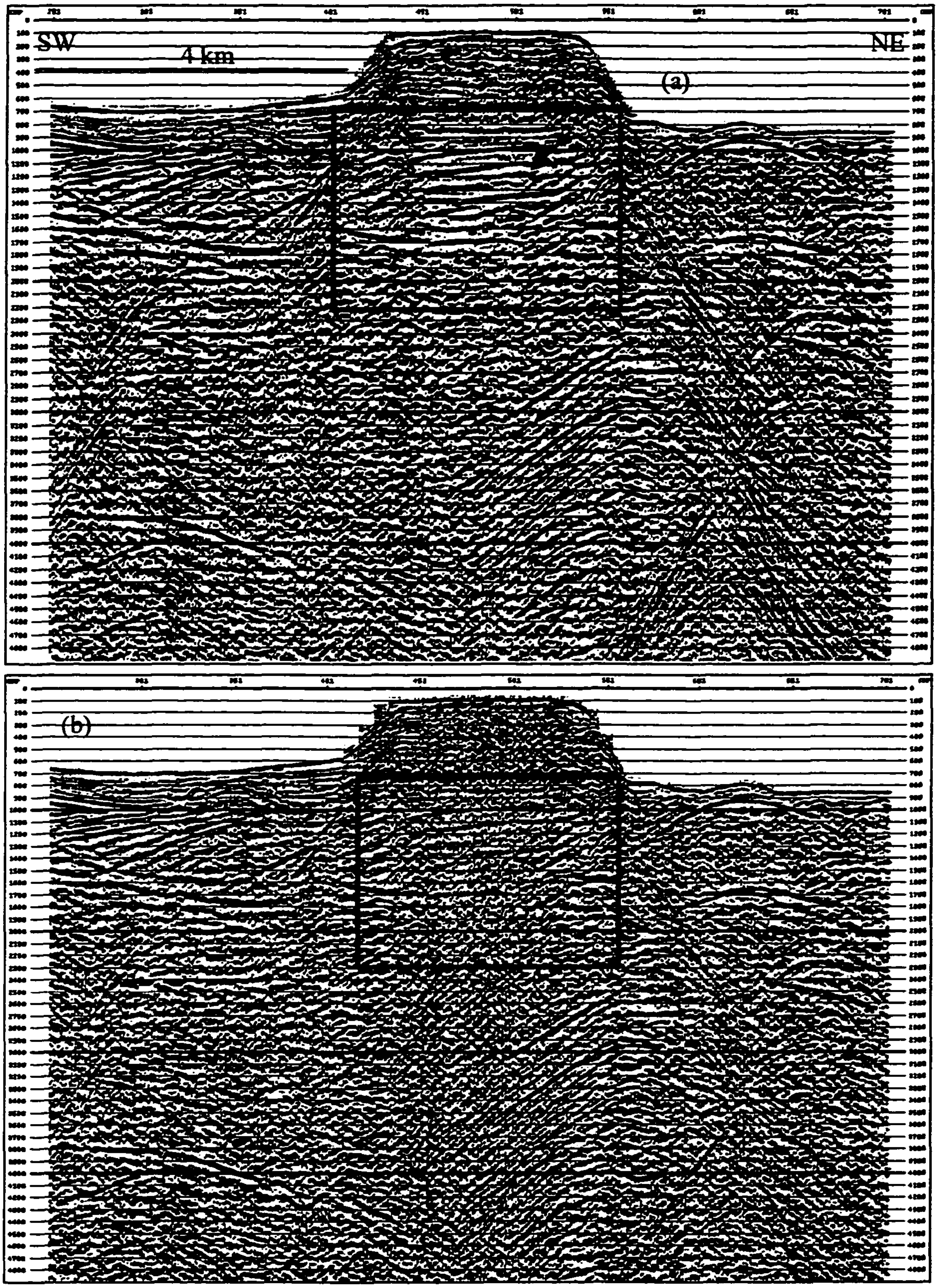

Figure 5.60. The middle part of line 17-7 before signal enhancement and migration (a) and after post-stack wave equation multiple rejection (b).

V.4.2. F-X deconvolution:

The F-X deconvolution, performed after wave equation multiple suppression, reduces the random noise considerably and reveals the severe damage associated with intensive diffractions. F-X deconvolution also reveals serious image distortions beneath the carbonate reef that have not been observed on the original line. Figure 5.61 compares the area underneath the reef buildup before and after wave equation multiple suppression and F-X deconvoltuon. The criss-cross events (indicated by a box) below the center of the reef contaminate the subsalt seismic and add to the confusion caused by diffractions.

V.4.4. Post stack migration results.

V.4.4.1. Steep dip explicit finite difference time migration.

This migration method have been performed after multiple suppression, F-X decon, and wave equation datuming. Figures 5.62, displays the southwest and northeast parts of line 17-7 before and after steep dip explicit finite difference time migration. It is evident from these Figures that the migration has collapsed almost all of the diffraction events. However, the section contains a considerable amount of migration artifacts, which obscure the continuity of the top of basement reflector particularly beneath the carbonate reef. After additional signal enhancement processes are included in the processing sequence, the steep dip explicit FD time migration produces a much better image as shown in Figures 5.63, 5.64, and 5.65. The diffractions, steeply dipping linear events and velocity pull-up are all removed. The hyperbolic events within the basement on the southwest part of the line still exist which suggest that they are from outside the 2-D plane of the section (sideswipe). Some distortions still exist within the basement beneath the reef buildup, which makes it difficult to define the nature of basement structure at this

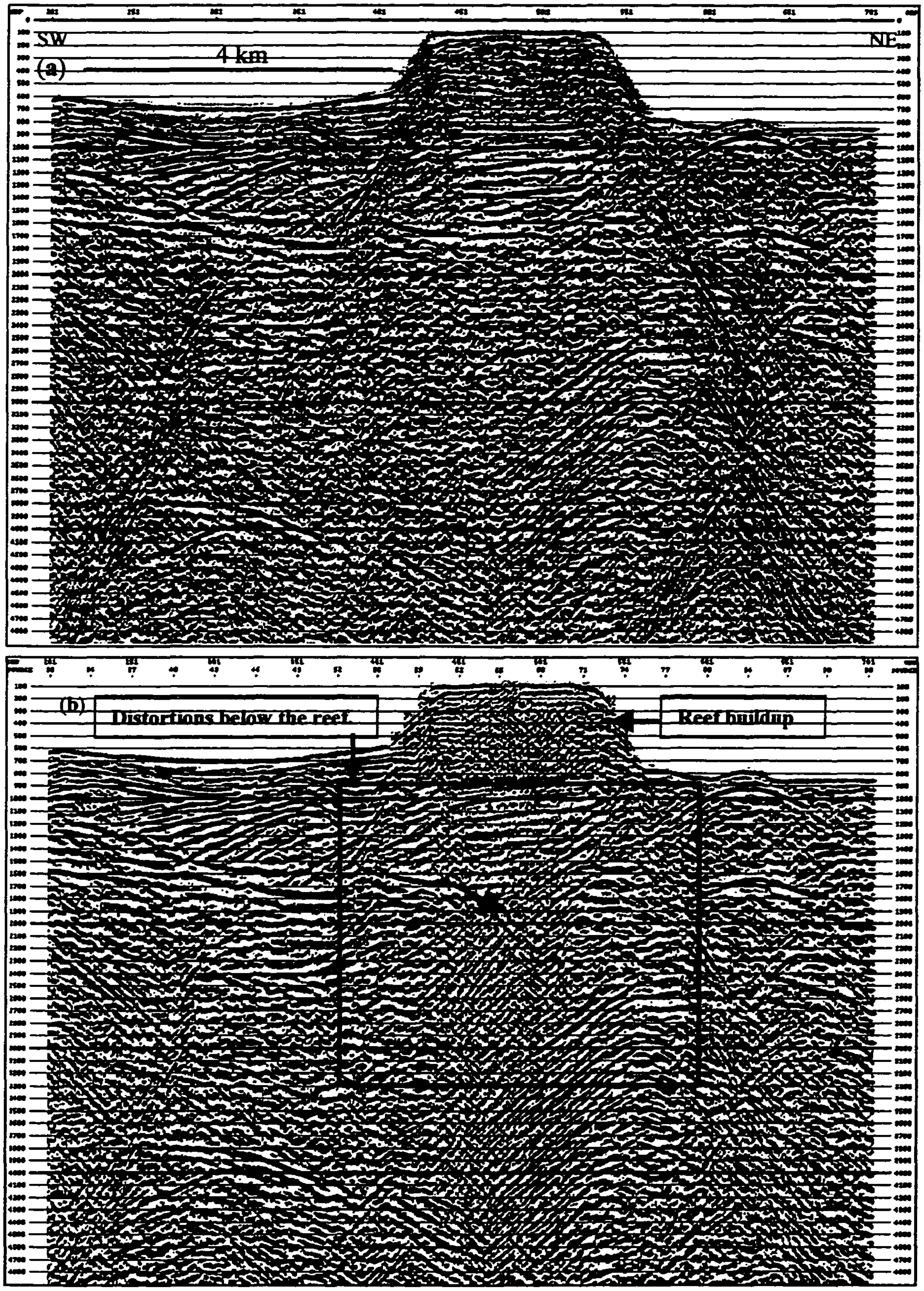

Figure 5.61. (a) The middle part of line 17-7 before (a) and after (b) post-stack wave equation rejection and F-X deconvolution. The distortions beneath the reef became very clear after F-X deconvolution.

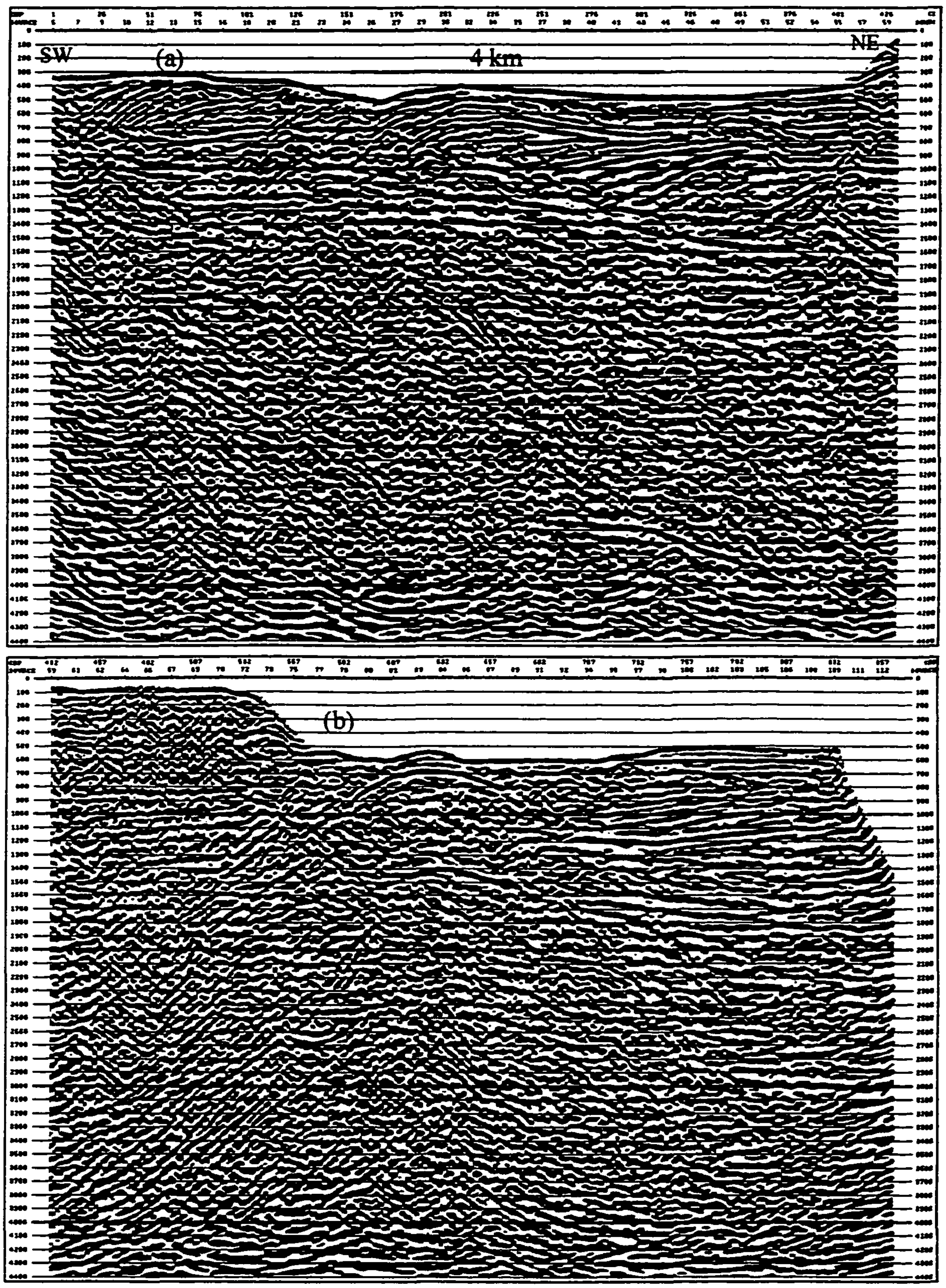

Figure 5.62. The southwestern (a) and northeastern (b) part of seismic line 17-7 after post-stack wave equation multiple rejection, wave equation datuming, F-X deconvolution, and steep dip explicit finite difference time migration.

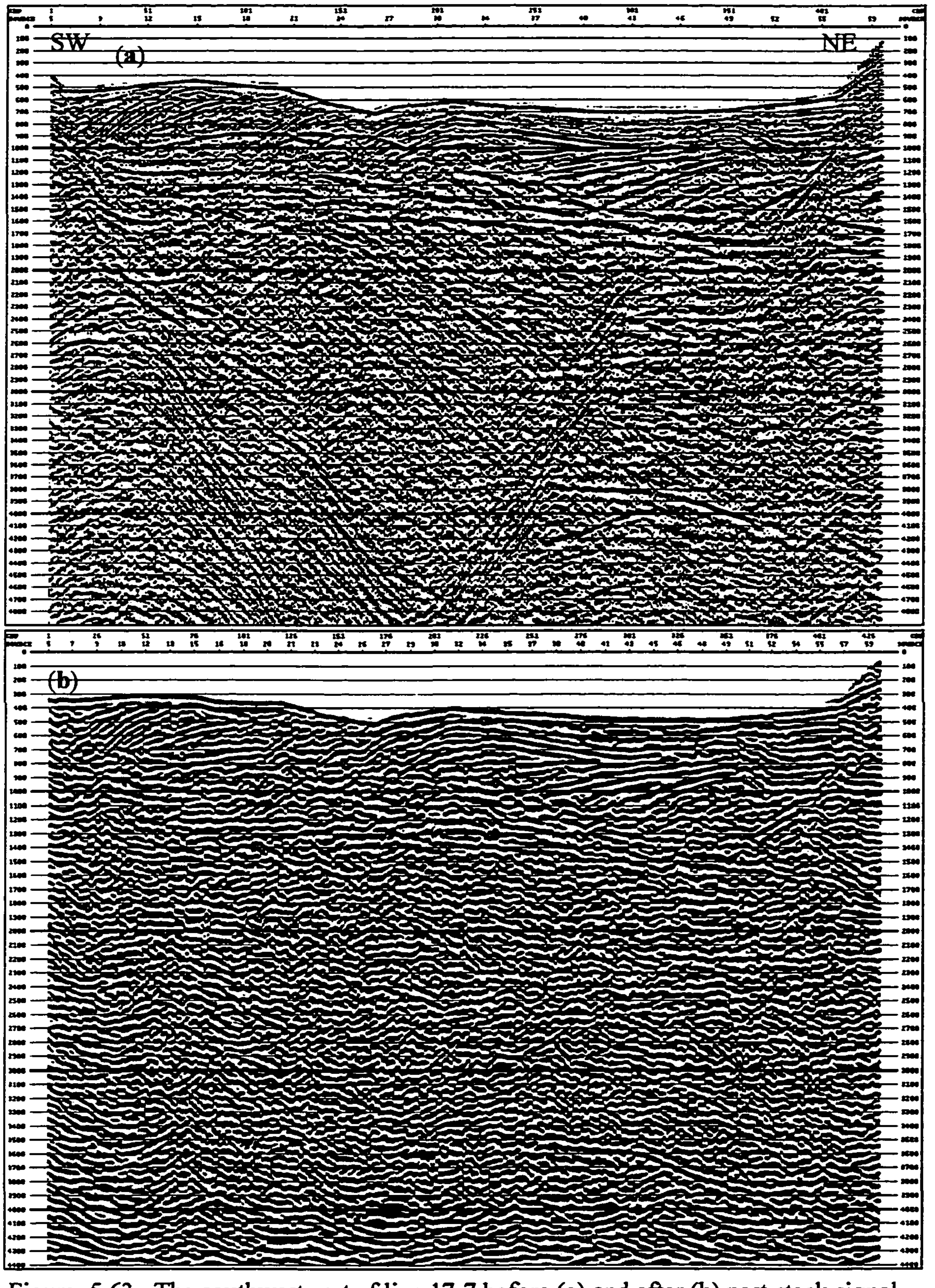

Figure 5.63. The southwest part of line 17-7 before (a) and after (b) post-stack signal enhancement and steep dip explicit finite difference time migration.

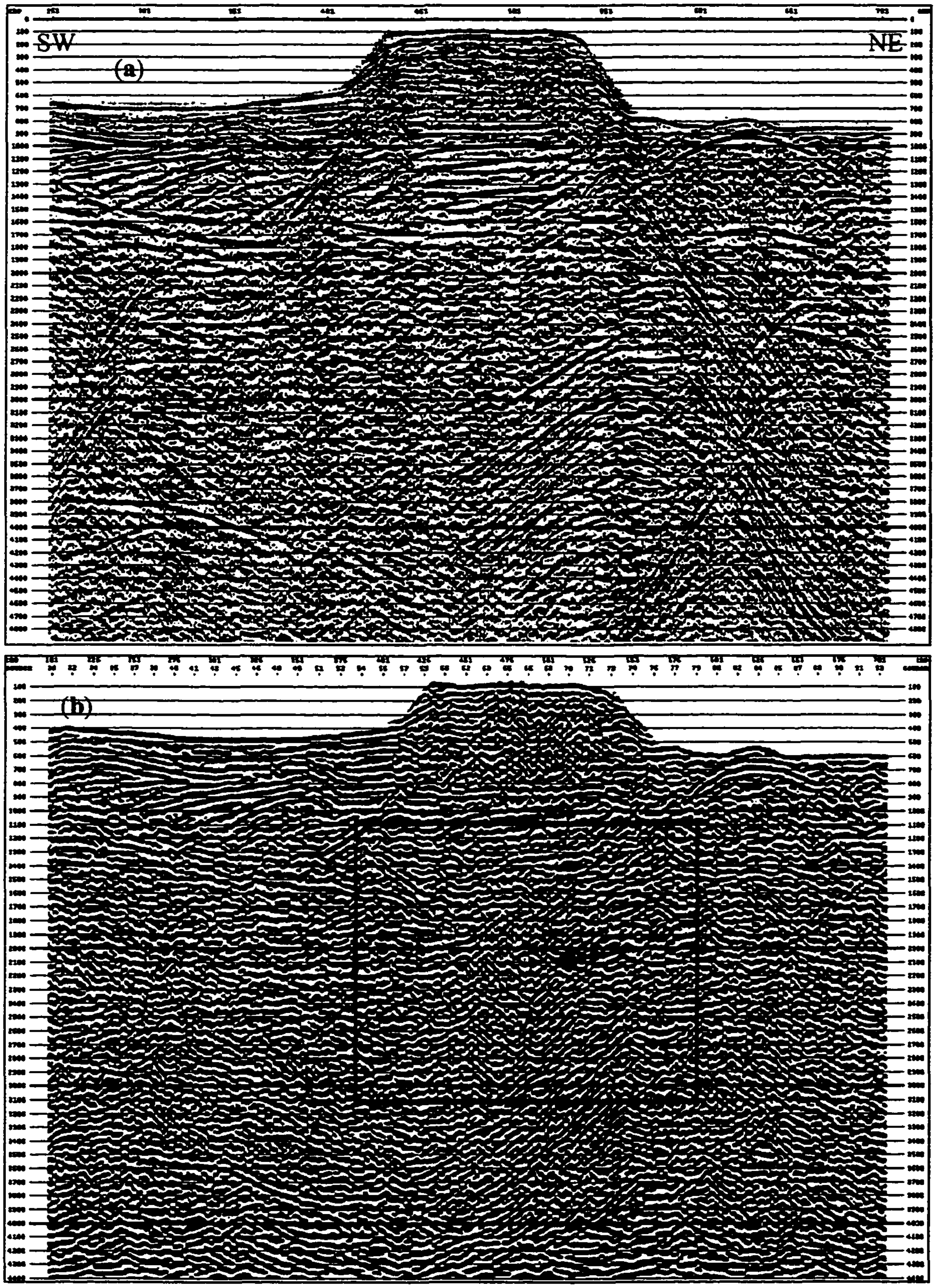

Figure 5.64. The middle part of line 17-7 before (a) and after (b) post-stack signal enhancement and steep dip explicit finite difference time migration.

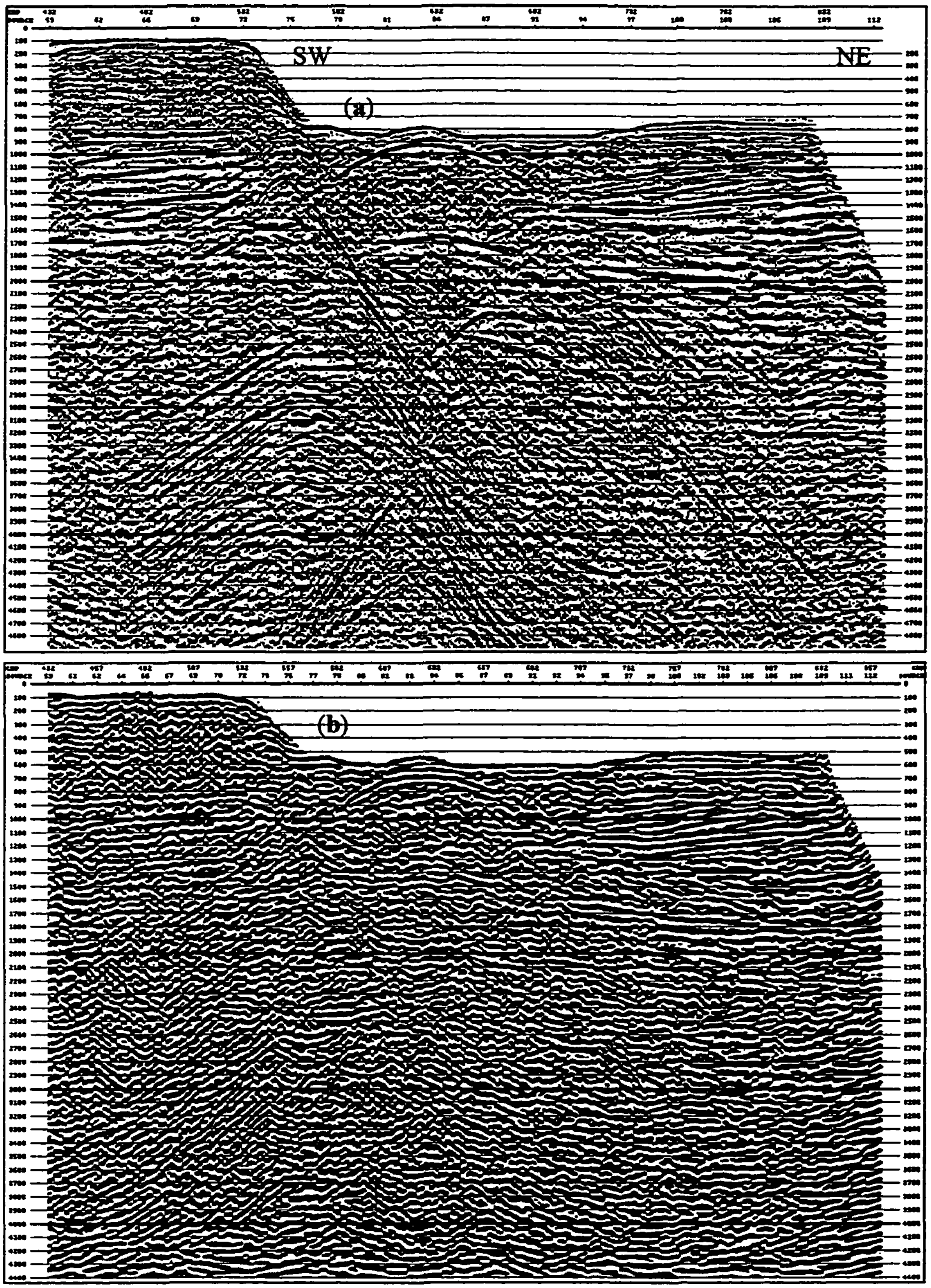

Figure5.65. The northeast part of line 17-7 before (a) and after (b) post-stack signal enhancement and steep dip explicit finite difference time migration.

location. Perhaps, and as discussed previously, the imaging problem underneath the reef is more complicated that steep dip explicit FD time migration can not handle. As already pointed out, finite difference time migration does not yield accurate results in the presence of strong lateral velocity variations.

<u>Steep dip finite difference depth migration:</u>

Steep dip finite difference depth migration improves the lateral resolution on the southwest and northeast parts of line 17-7. The area below the carbonate reef and the deeper part of the section appear to be over migrated as indicated by what seems to be migration smiles. To find out if this migration artifact is due to high migration velocity, the steep dip FD depth migration have been performed using 70 percent interval velocity. The results shown in Figures 5.66, 5.67,and 5.68 indicate that the migration smiles are corrected but the area below shotpoints 62 to 71 (on the carbonate reef) is not accurately imaged. This suggests that the distortion is more complex than can be handled by post-stack FD depth migration. The severe ray bending and amplitude distortions observed at this location can be attributed to the abrupt change in seafloor topography and equally abrupt changes in velocity.

The complex lateral velocity changes associated with the irregular geometry salt cause considerable raypath distortions and result in non-hyperbolic travel times, which degrade the stacked section at this location. Of course, the optimum-imaging tool to correct this problem is pre-stack depth migration. As pointed out previously, the field records required for the pre-stack depth migration are not available for this investigation.

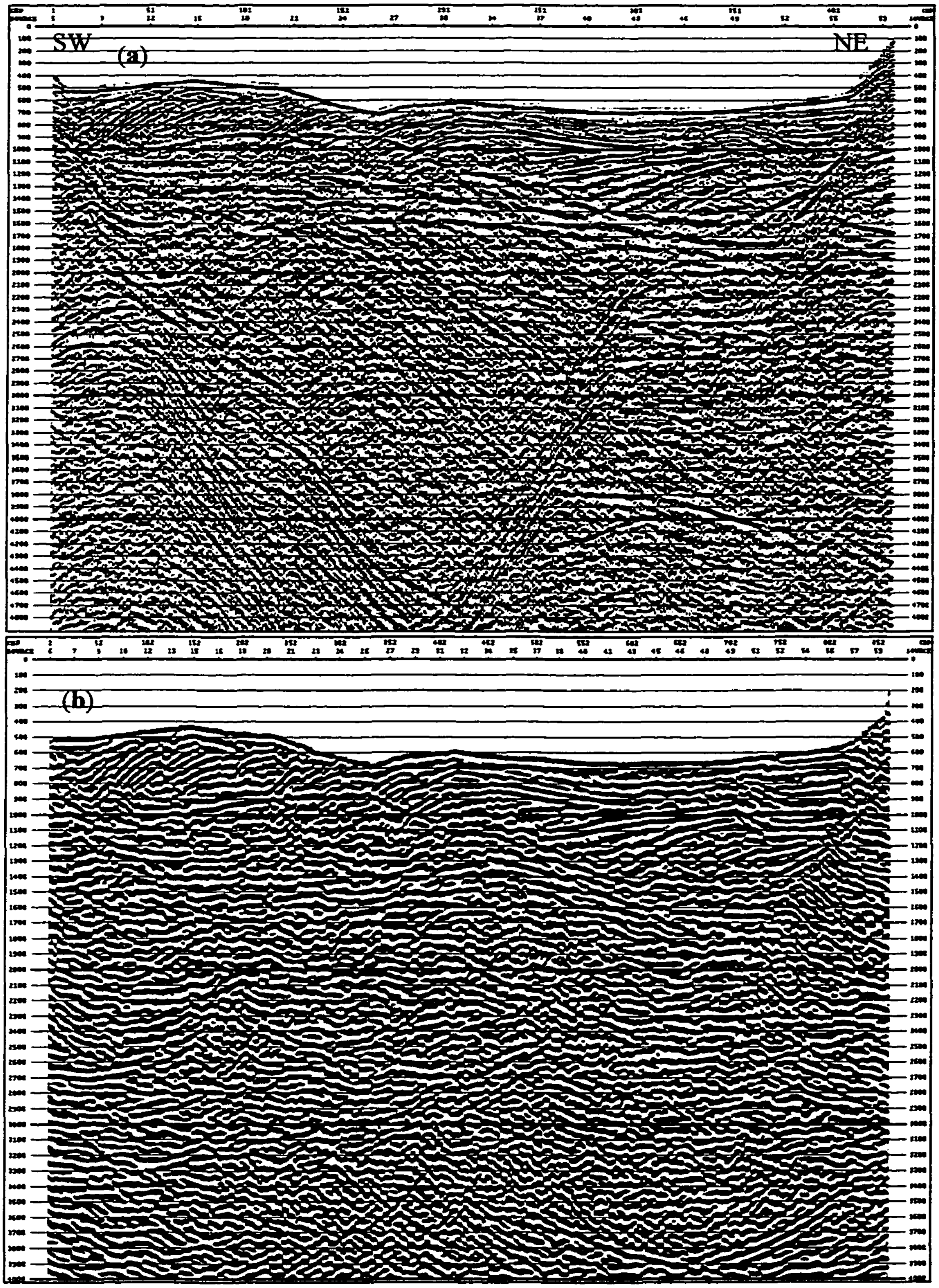

Figure 5.66. The southwest part of line 17-7 before (a) and after (b) post-stack signal enhancement and steep dip finite difference depth migration.

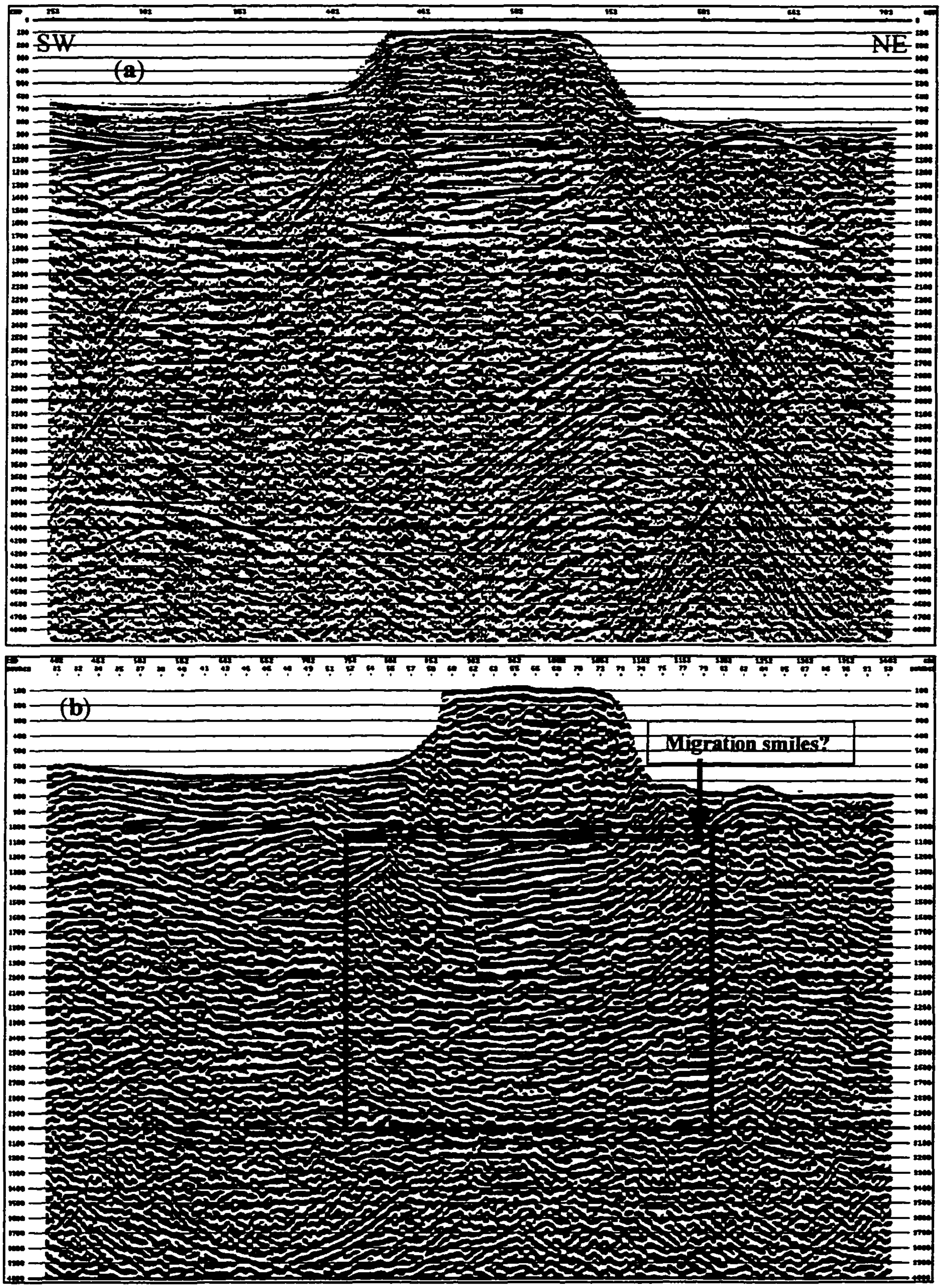

Figure 5.67. The middle part of line 17-7 before (a) and after (b) post-stack signal enhancement and steep dip finite difference depth migration.

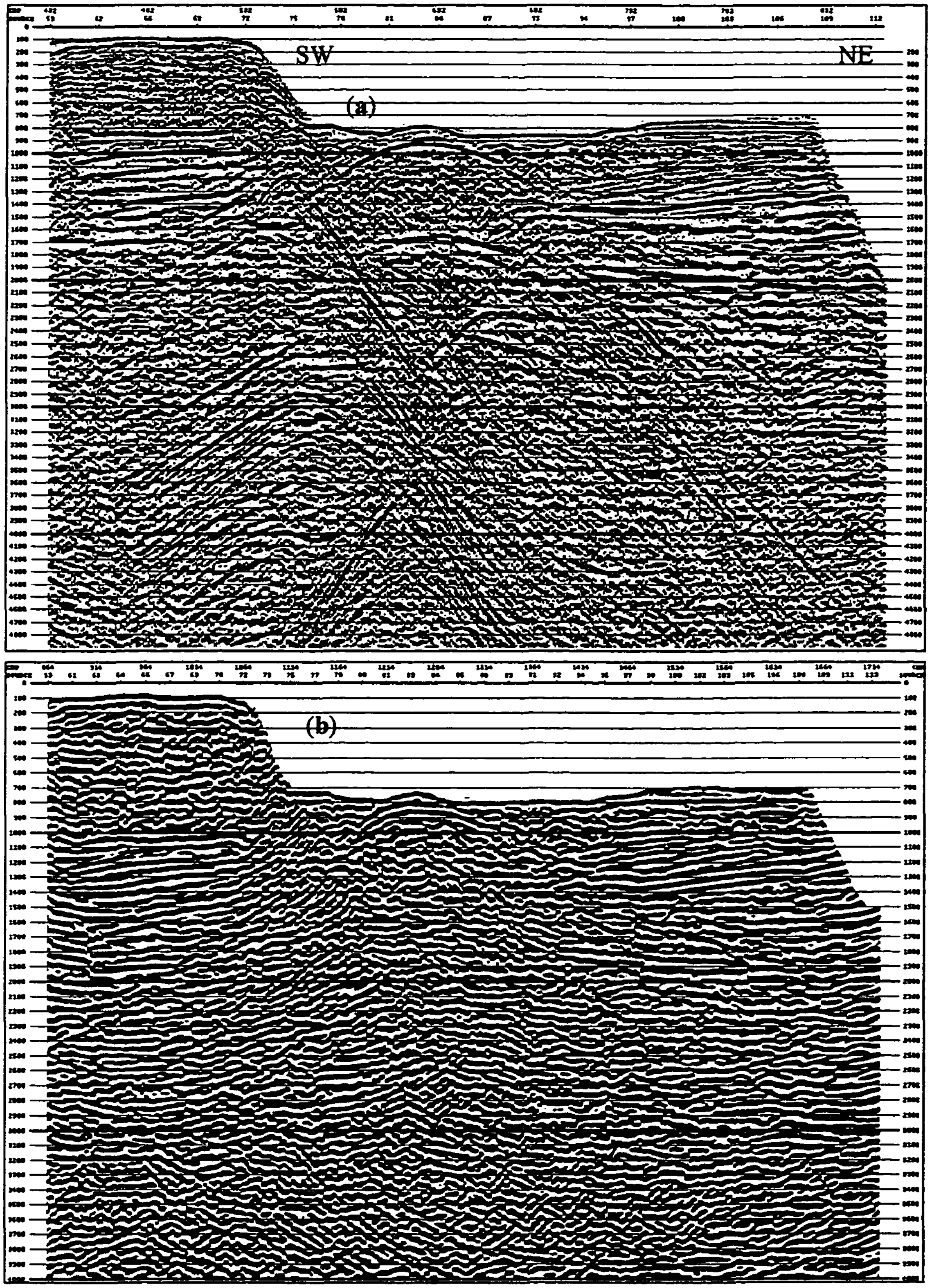

Figure 5.68. The northeast part of line 17-7 before (a) and after (b) post-stack signal enhancement and steep dip finite difference depth migration.

Final interpretation:

The final interpretation reveals a horst structure beneath the carbonate buildup and a graben below the residual salt just west of the reef. It reveals seaward-dipping, basement-related, major normal faults southeast of the graben and northeast of horst structures. The thick supra-salt section overlying the graben and carbonate reef above the horst reflect the influence of the geometry and size of basement structures on the overlying sedimentary section in this area. The most significant structural features of this line are, the presence of residual salt beneath thick supra-salt section just southwest of the carbonate reef, the thickening of salt to the southwest of the graben, above the horst, and just to the northeast of the reef buildup. Evidently, these features are developed in response to salt-sediment interaction in this part of the section. One obvious interpretation is that, the differential loading associated with the deposition of thick supra-salt in the structurally low area above the garben has mobilized and evacuated the underlying salt to structurally high areas to the southwest and on the horst. The thick salt ridge just northeast of the reef can be attributed to overburden weight caused by rapidly growing reef buildup. The significant thickening of salt at this location and the hyperbolic curvature of its upper boundary (which indicates shortening associated with salt tectonics) implies that this location has received salt from both underneath the reef to the southwest and from relatively high-pressure area down-dip to the northeast. Or it may be simply that the salt evacuated from underneath the reef to this location could not move down-dip (because of its low density) to the major normal fault hanging-wall, instead it deformed the overlying thin supra-salt section. The chaotic to reflection-free pattern of salt at this location further confirms salt-sediment interaction observed on this line.

Summary:

2-D seismic modeling results reveal that the severe ray bending and sharp refraction caused by the irregular geometry and complex boundaries of salt result in insufficient down-going energy for illuminating the subsalt reflection events. Post stack signal enhancement techniques improve the migration results and produce interpretable seismic sections. Steep dip Finite difference depth migration eliminates the distortions caused by the severe ray bending associated with irregular salt geometry and by rapid velocity changes at the complex salt boundaries. This migration method effectively improves the resolution and structural interpretation of subsalt seismic events.

CHAPTER VI
IMAGE DISTORTIONS ASSOCITED WITH INTENSIVE DIFFRACTIONS CASE HISTORIES: NORTHERN RAS BANAS AND SAFAGA AREAS

The basement-involved, major, normal faults, the tilted fault blocks, and salt-related faults produce intensive diffractions, which severely distort the desirable reflections and obscure the subsalt seismic events in these areas. Seismic lines 9 and 316 are examples of the image distortions caused by diffractions in northern Ras Banas and Safaga areas, respectively.

VI.1. **Seismic line 9**

Seismic line 9 is located in the southern part of the northern area (Fig. 1.2). It runs from southwest to northeast. It begins 7.8 km from the shoreline and extends 23.5 km offshore. The water bottom topography on this line is not as complex as observed on previous lines (Fig. 6.1). The variable portion of seafloor close to the middle of the line lies between shotpoint 61 and 27 with water depth ranging from 1875 to 2500 ft. Between shotpoint 119 and 95 on the first part of the line to the southwest, the water depth ranges from 500 to 2000ft. The rest of the line is almost flat.

Initial interpretation

The initial interpretation reveals a thick salt section with moderately undulating upper boundary on the northeast part of the line. The salt exhibits gradual thinning towards the southwest (Fig. 6.1). The upper part of the salt section appear be offset by a series of seaward and landward-dipping shallow normal faults. The supra-salt sequence is relatively thick on the southwest but exhibits significant thinning on the northeast part of

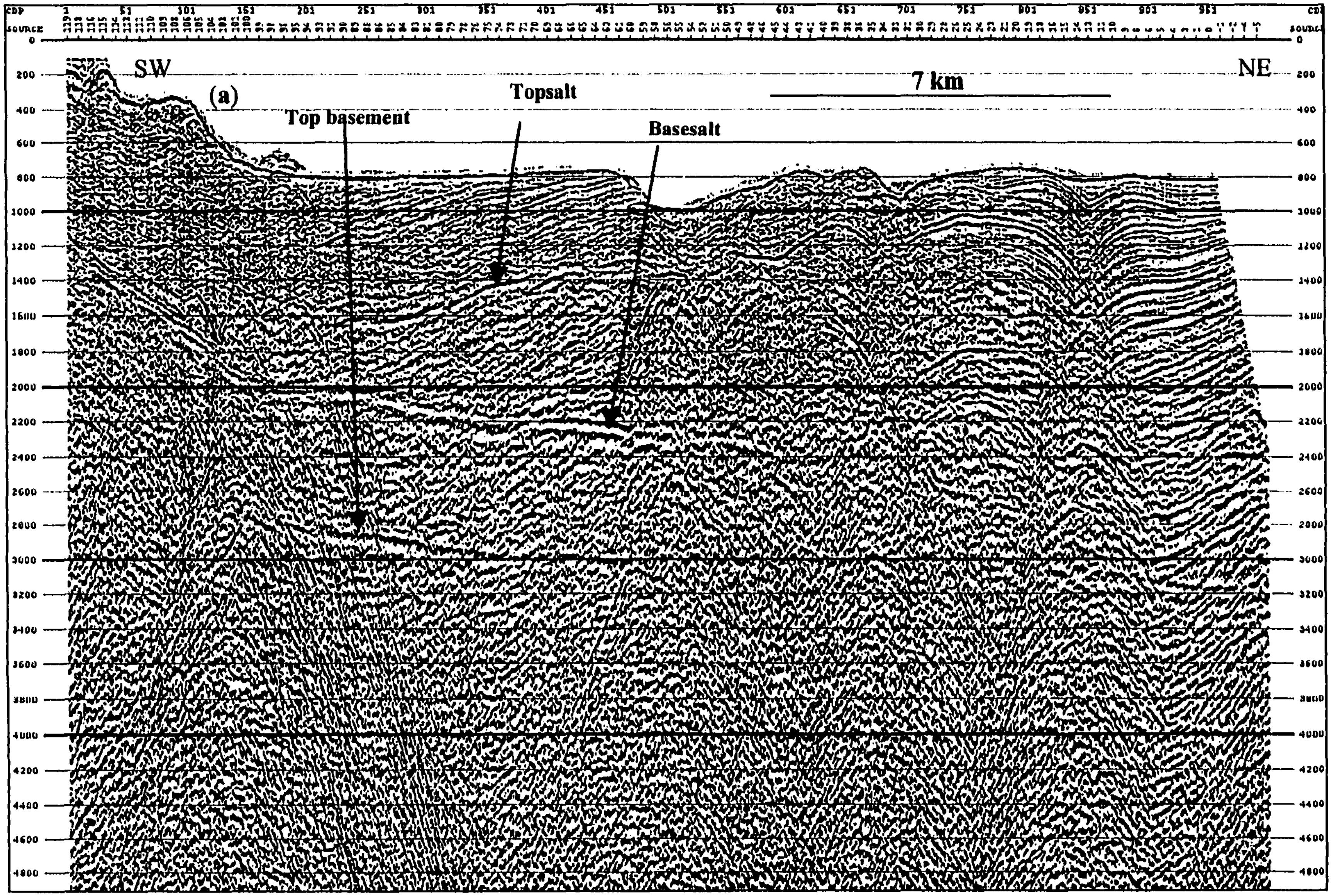

Figure 6.1. Seismic line 9 before signal enhancement and migration.

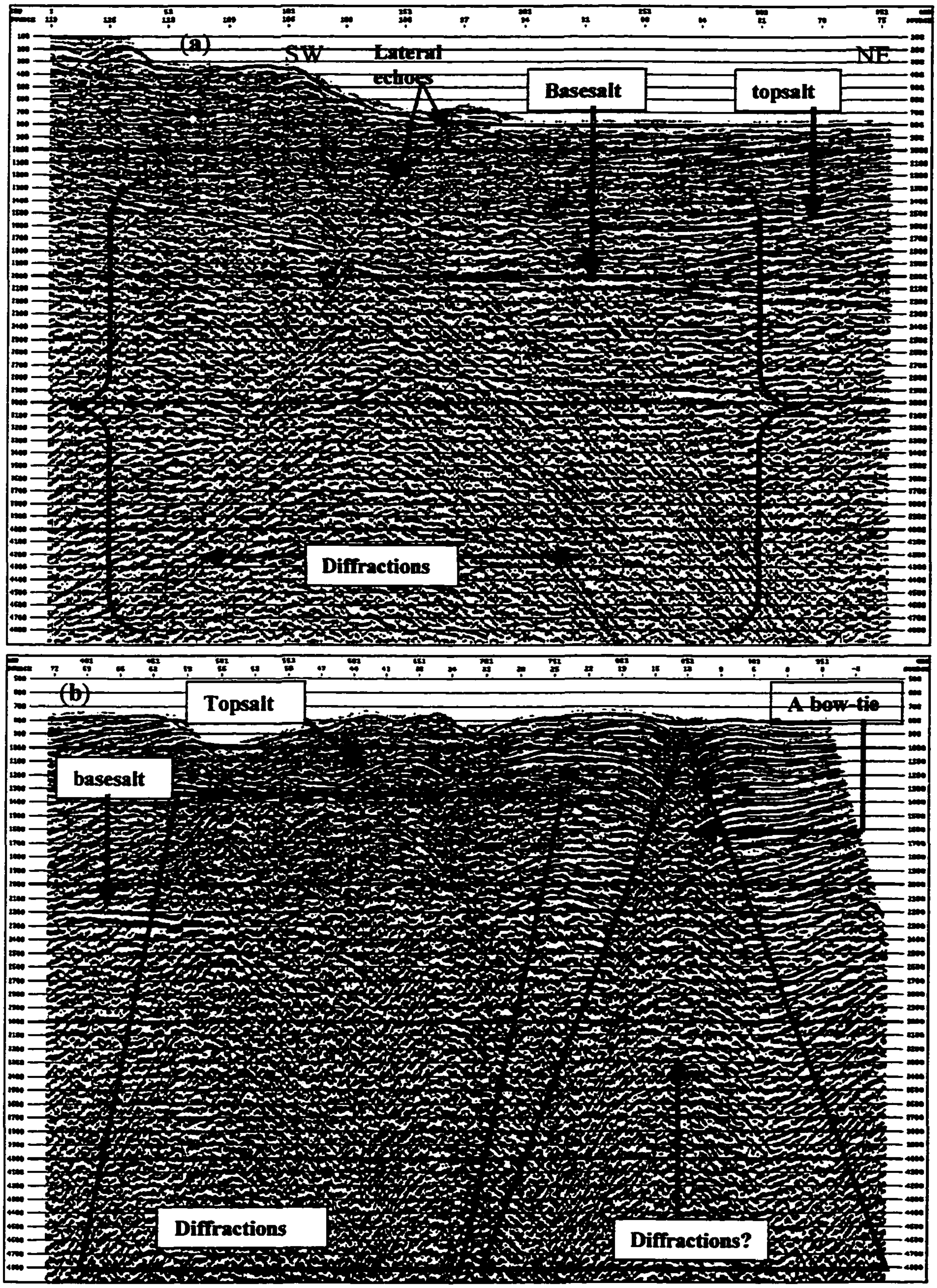

Figure 6.2. Image distortions observed on the southwest (a) and northeast (b) parts of seismic line 9 before signal enhancement and migration.

the line. The subsalt sequence is poorly imaged on most of the line but can be observed below shotpoints 90 to 62. The subsalt section within the northeast part and first portion of the line is offset by basement-involved normal faults. The most obvious features of this line are the elegant bow-tie and the underlying magnificent diffraction event.

VI.1.1. Image problems:

There are three areas on this line that have imaging problems. On the first portion of the line, between shotpoints 119 and 90, the tops of salt and basement reflectors are disrupted by diffraction events and what seem to be lateral echoes from outside the vertical plane of the seismic section (Fig. 6.2a). In the area between shotpoint 60 to 30, the top of basement is completely masked and the base of salt is hard to define (Fig. 6.2b). The overlying salt appears to be deformed and disrupted by shallow faults. The imaging distortions in this area are interpreted to be due to the considerable diffractions and relatively thick salt section. On the last portion of the line, between shotpoints 30 and 5, the top of basement is poorly imaged and the base of salt is seriously disrupted and difficult to pick. The thick salt, the major diffraction event, and the overlying bow-tie complicate the imaging in this part of the section.

VI.1.2. The result of 2-D seismic modeling:

Figure 6.3 shows seismic line 9 and the velocity-depth model derived from it. This depth model is produced after several iterations in which the geometry, the thickness, and velocity of supra-salt, salt, and subsalt sections are modified until acceptable match between the synthetic section and real seismic section is obtained. The subsalt, salt and supra-salt are given a velocity gradient to account for increase in velocity with depth.

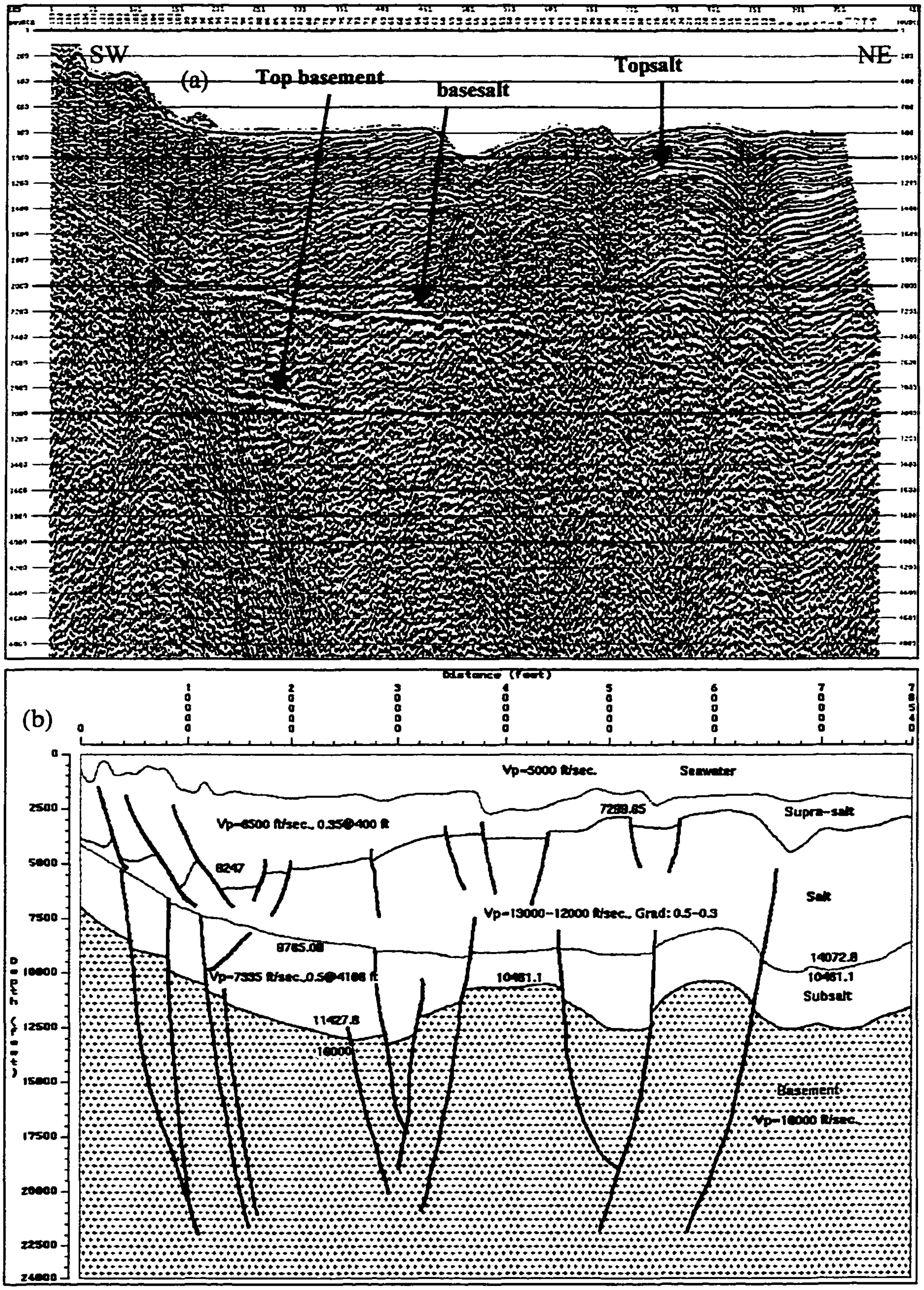

Figure 6.3. (a) Seismic line 9 before signal enhancement and migration. (b) velocity-depth model.

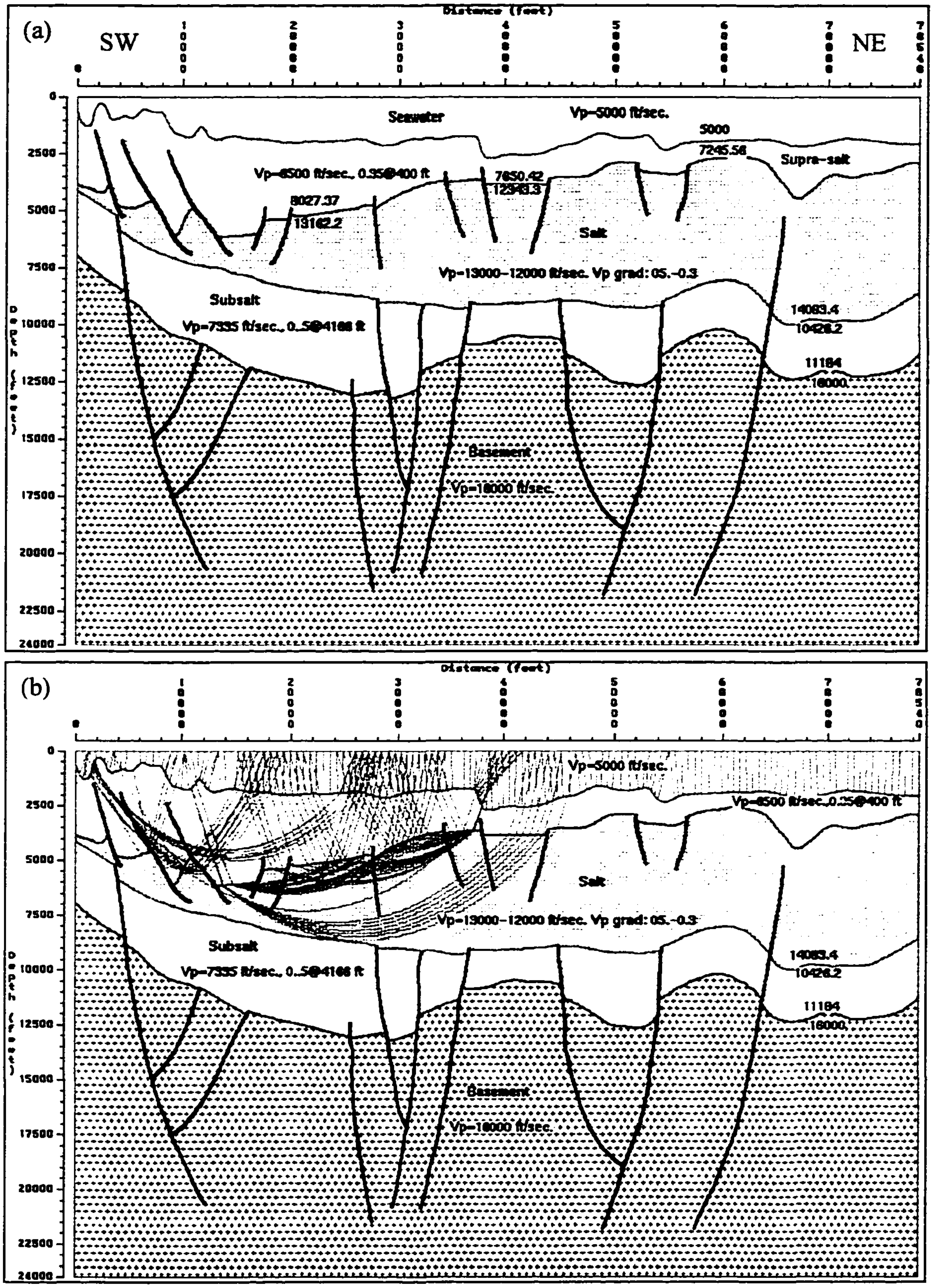

Figure 6.4. Line 9. (a) Velocity-depth model. (b) Zero offset reflection raypaths for water-bottom. Note the strong raypaths bending at the rugged seafloor.

Raypaths characteristics:

Velocity-depth model 1:

Figure 6.4 displays the depth model (after modification of faults geometry) and zero offset raypaths for water bottom. Both the downgoing and upgoing raypaths exhibit a very complicated behavior. They undergo sharp bending at the variable seafloor, and at the top of the salt. The significant deviation of rays within supra-salt and salt is due to lateral velocity changes within these layers. The key factors responsible for this complex raypaths are the high velocity contrast at the variable water bottom, irregular salt boundaries, and lateral velocity variations within supra-salt and subsalt layers. The serious raypath distortions result in considerable travel time errors and in drastic reduction of the amplitude of underlying reflections. Zero offset raypaths for topsalt, basesalt and top of basement are shown in Figures 6.5, 6.6. First and most importantly, the raypath distortions on these Figures simulate the poorly imaged areas observed on the real seismic section. Compare the complex raypaths bending on the southwest portion of the model, the deviated and missing rays on the middle part, and focussing and de-focussing of rays by the undulating boundaries of thick salt on the northeast part of the depth model to equivalent parts on the original seismic section. Again, the considerable raypaths bending is due to the high velocity contrast across the rugged seafloor and at irregular top of salt. Moreover, zero offset raypaths to the shallow faults (Fig. 6.6b) show severe raypaths distortion, which further complicated the imaging problem. The normal incidence synthetic section produced by the final depth model is shown in Figure 6.7. The synthetic section satisfactorily matches the real seismic line and recreates most of the features observed on it. It simulates the three poorly imaged areas observed on the first, middle and last

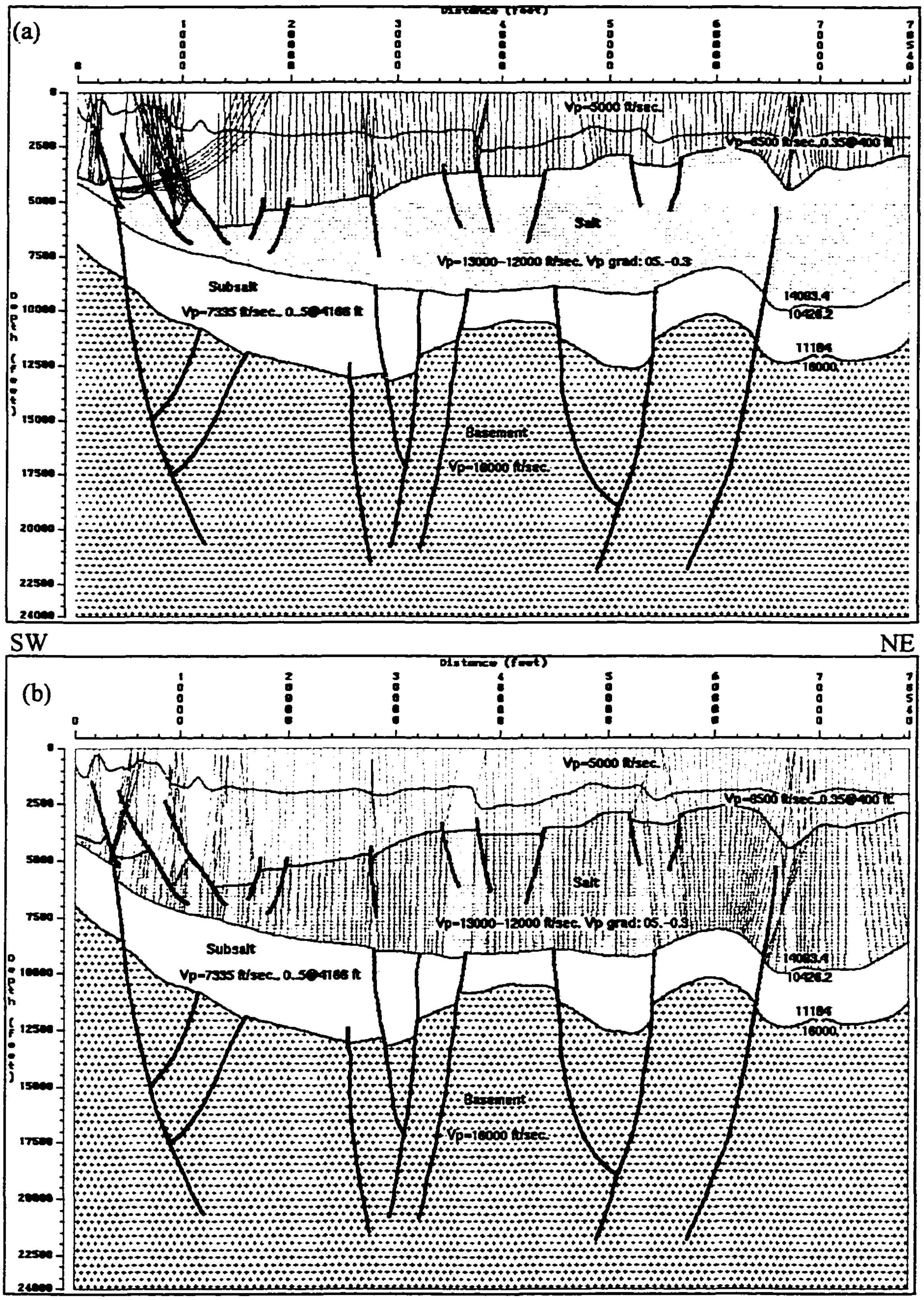

Figure 6.5 . Line 9. Zero offset raypaths for topsalt (a) and basesalt (b).

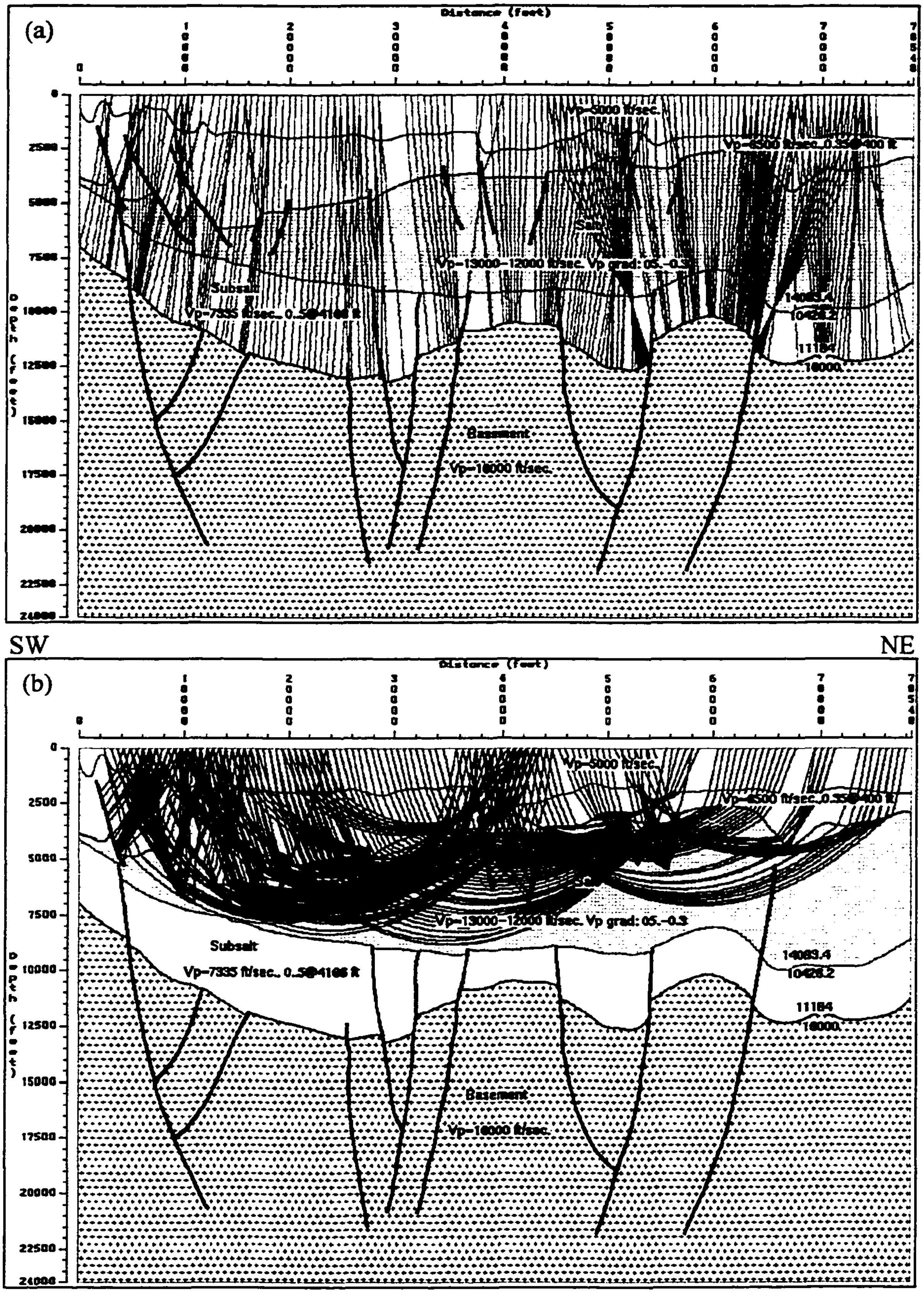

Figure 6.6. Line 9. Zero offset raypaths for top basement (a) and for shallow faults (b).

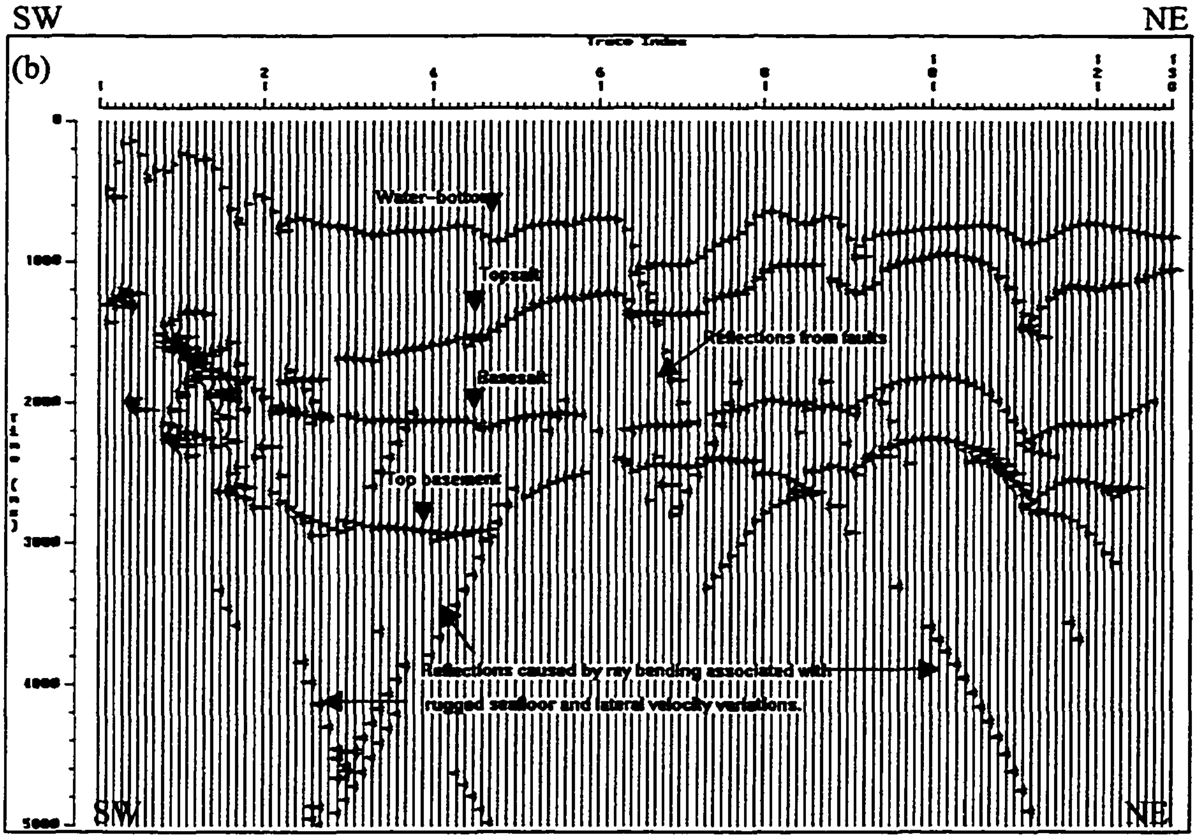

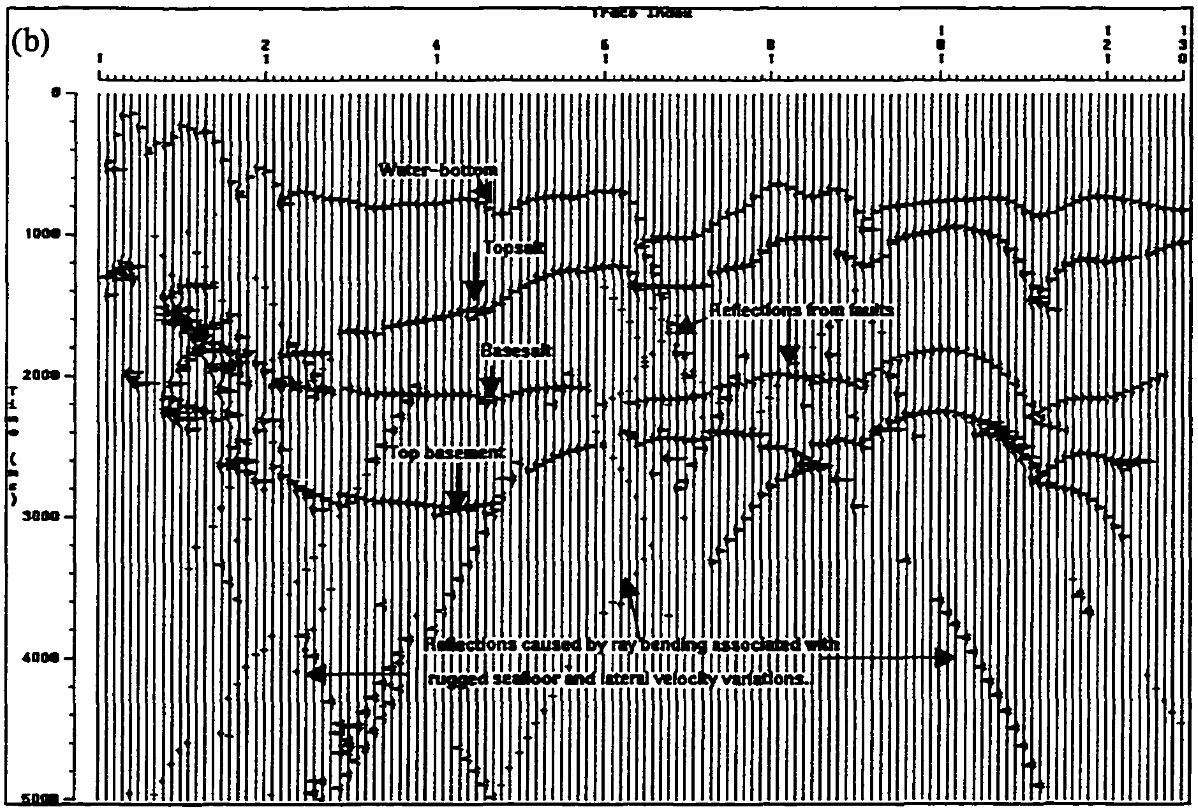

Figure 6.7. Line 9. (a) Normal incidence synthetic trace (b) Synthetic trace displayed with arrival times for all layers.

portions of the seismic section.

Velocity depth model 2:

In the depth model discussed above, the salt layer is given a velocity gradient (0.3 to 0.5). The salt is interpreted to be consisting mainly of halite and has a constant velocity of 15000 ft/sec. Figures 6.8, 6.9 show the zero offset rayapths for water bottom, topsalt, basesalt, and top of basement. It is obvious from Figure 6.8 that the rayapths for water bottom undergo less distortion than when the salt has varying velocity. Close inspection and comparison of the rayapths to the basesalt and top of basement of the two model depth models further confirm this. The point is, lateral velocity changes within the salt cause considerable ray bending, hence contribute to the image problem. The synthetic section produced by the constant velocity-salt depth model (Fig. 6.10) has relatively less distortion than the previous model. Figure 6.10b displays the synthetic section for reflection and diffraction events. Again, the distortions observed on the southwest, middle, and northeast portions of the synthetic section simulate the poorly imaged areas of the equivalent parts of the real seismic section as shown in Figures 6.11, 6.12, and 6.13.

VI.1.3. Post-stack signal enhancement results

Comparison of seismic line 9 before and after F-X trace interpolation, F-X deconvolution, and post-stack wave equation datuming indicate a moderate improvement in reflection continuity in areas that are not severely distorted. The distortions became more obvious after the signal enhancement.

VI.1.4. Post-stack migration results

VI.1.4.1. Residual time migration:

Residual migration (Stolt FK followed by steep dip explicit FD time migration)

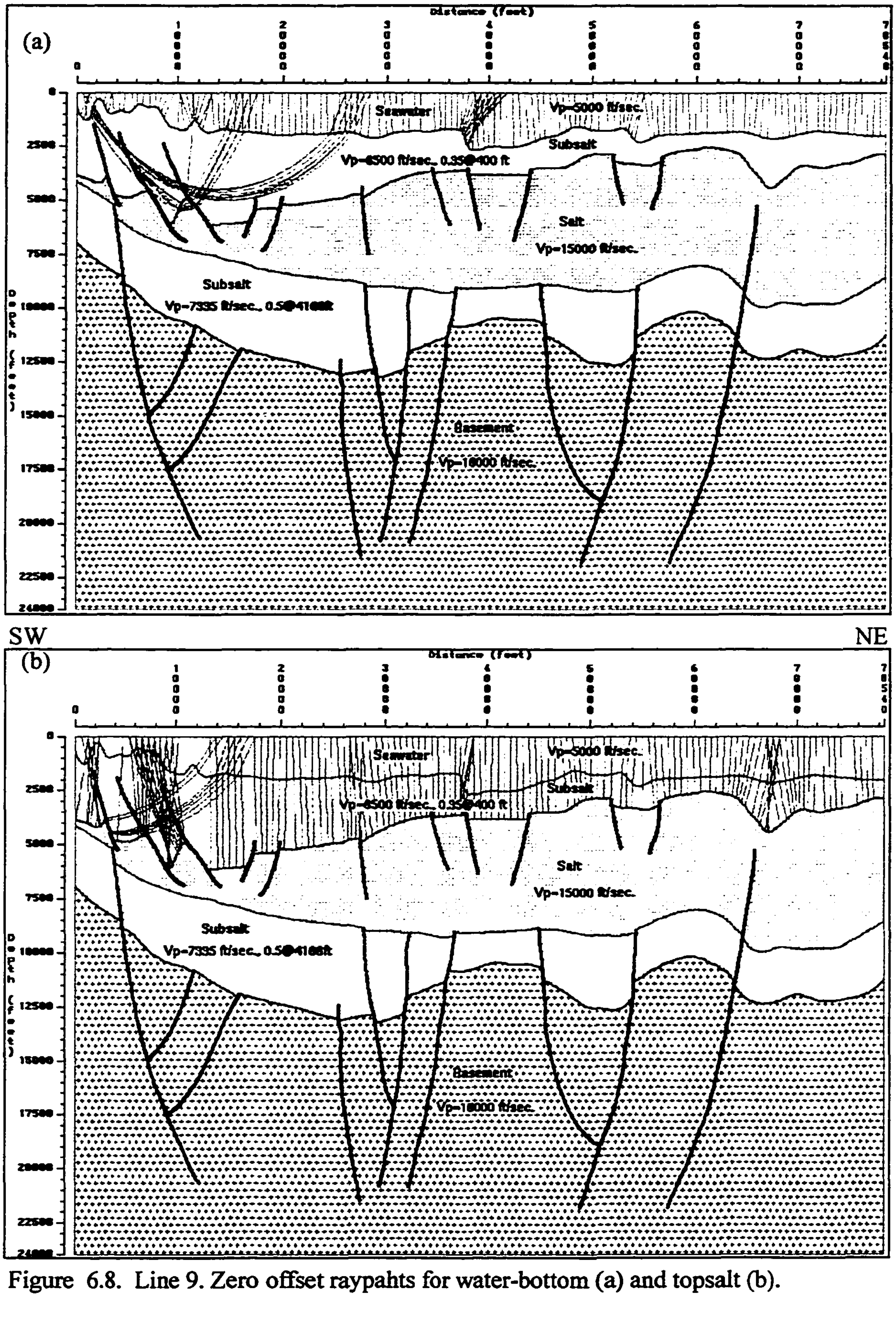

Figure 6.8. Line 9. Zero offset raypahts for water-bottom (a) and topsalt (b).

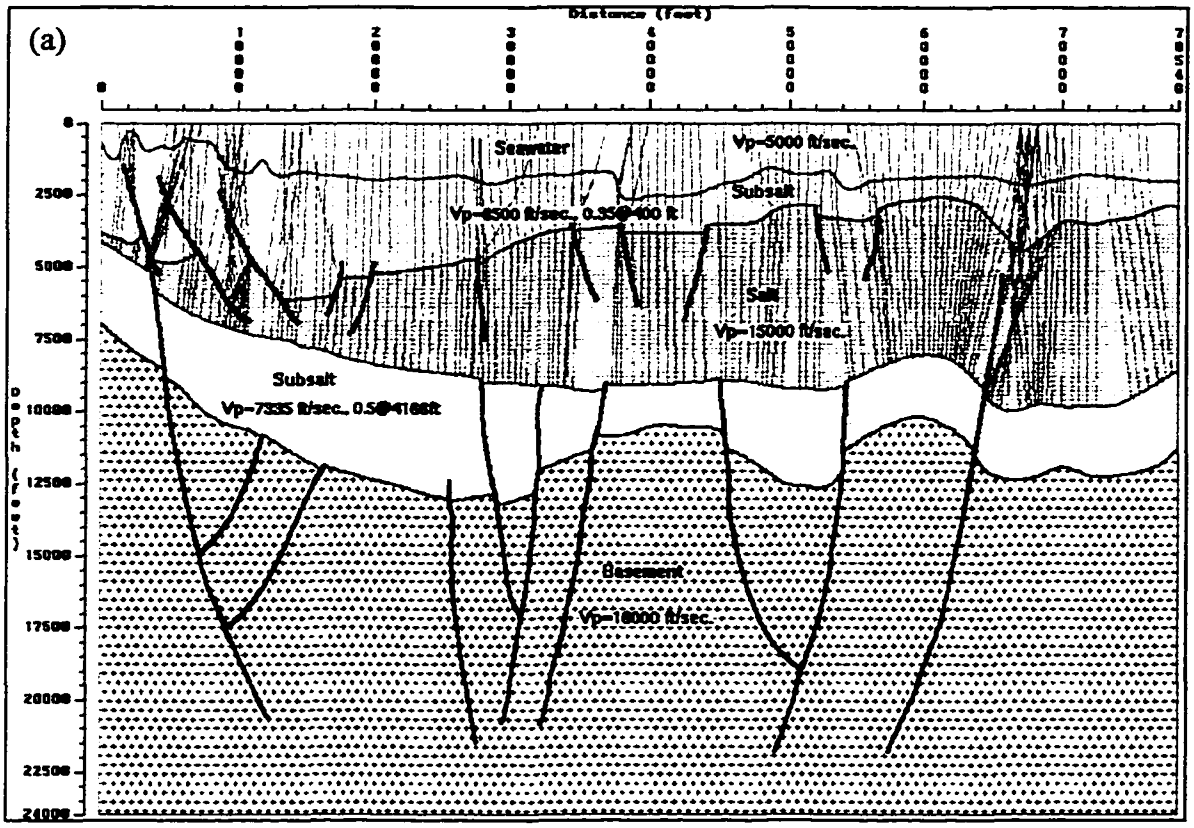

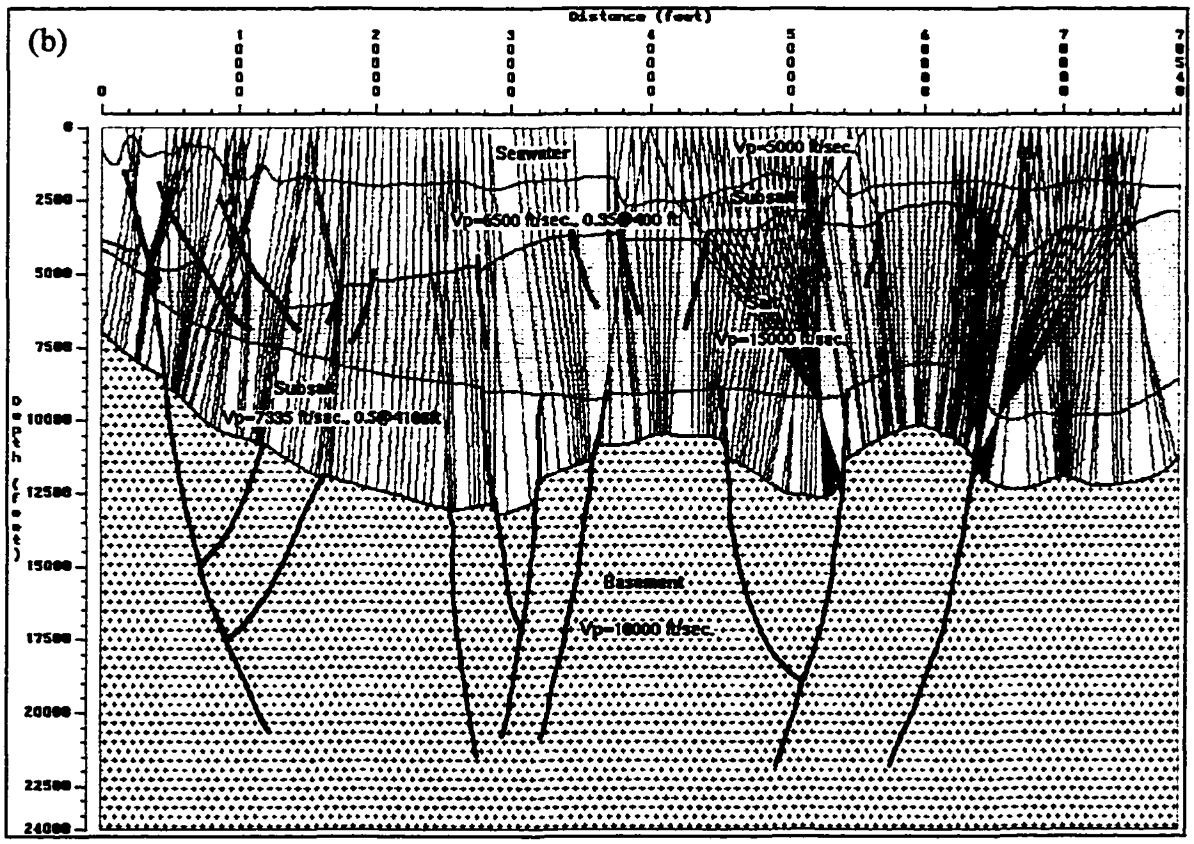

Figure 6.9. Line 9. Zero offset raypaths for basesalt (a) and top basement (b).

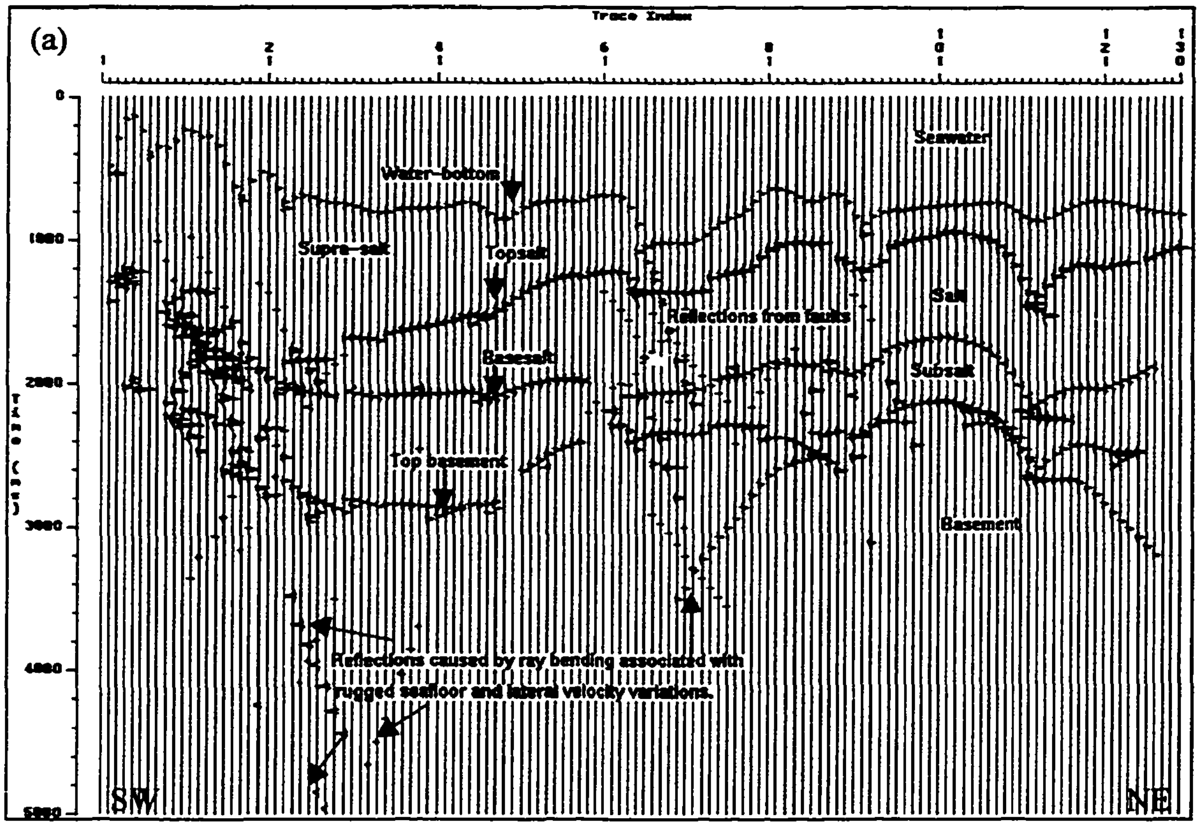

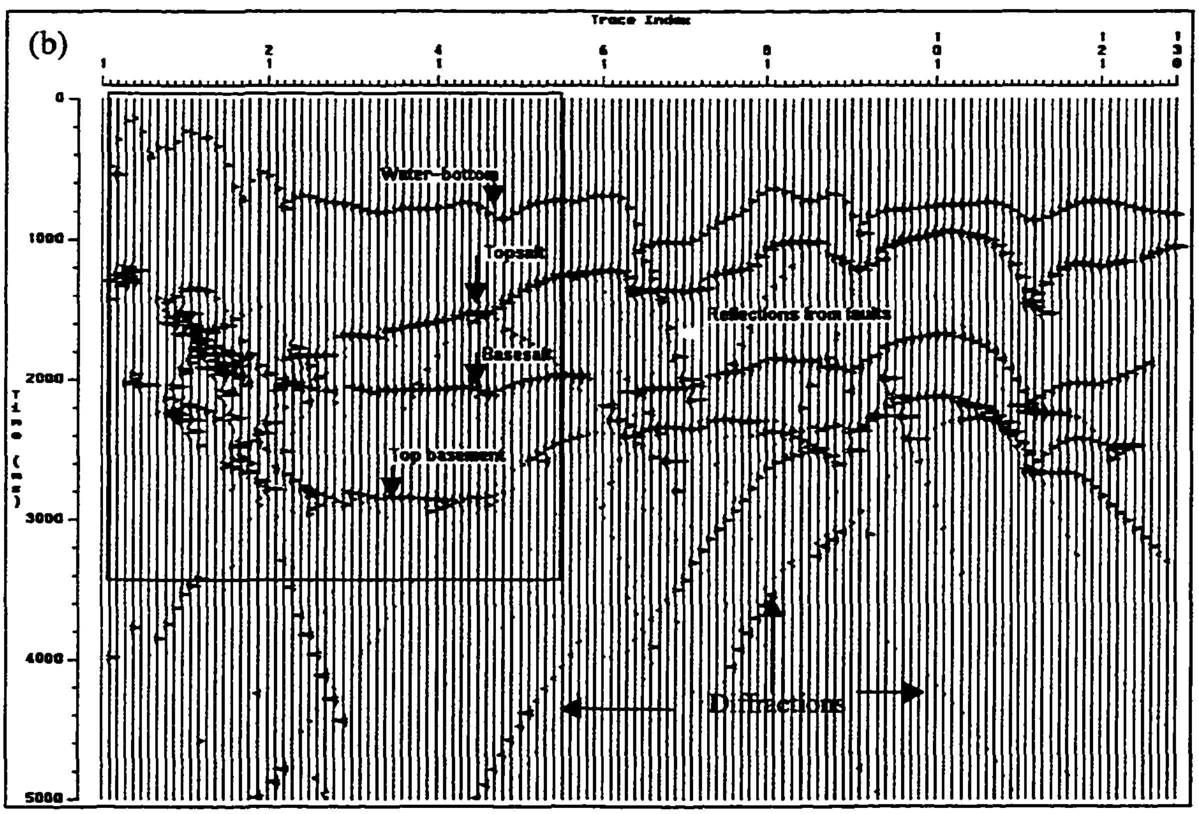

Figure 6.10. Line 9. (a) Normal incidence synthetic trace displayed with arrival times. (b) Normal incidence and diffractions from faults and faulted block edges.

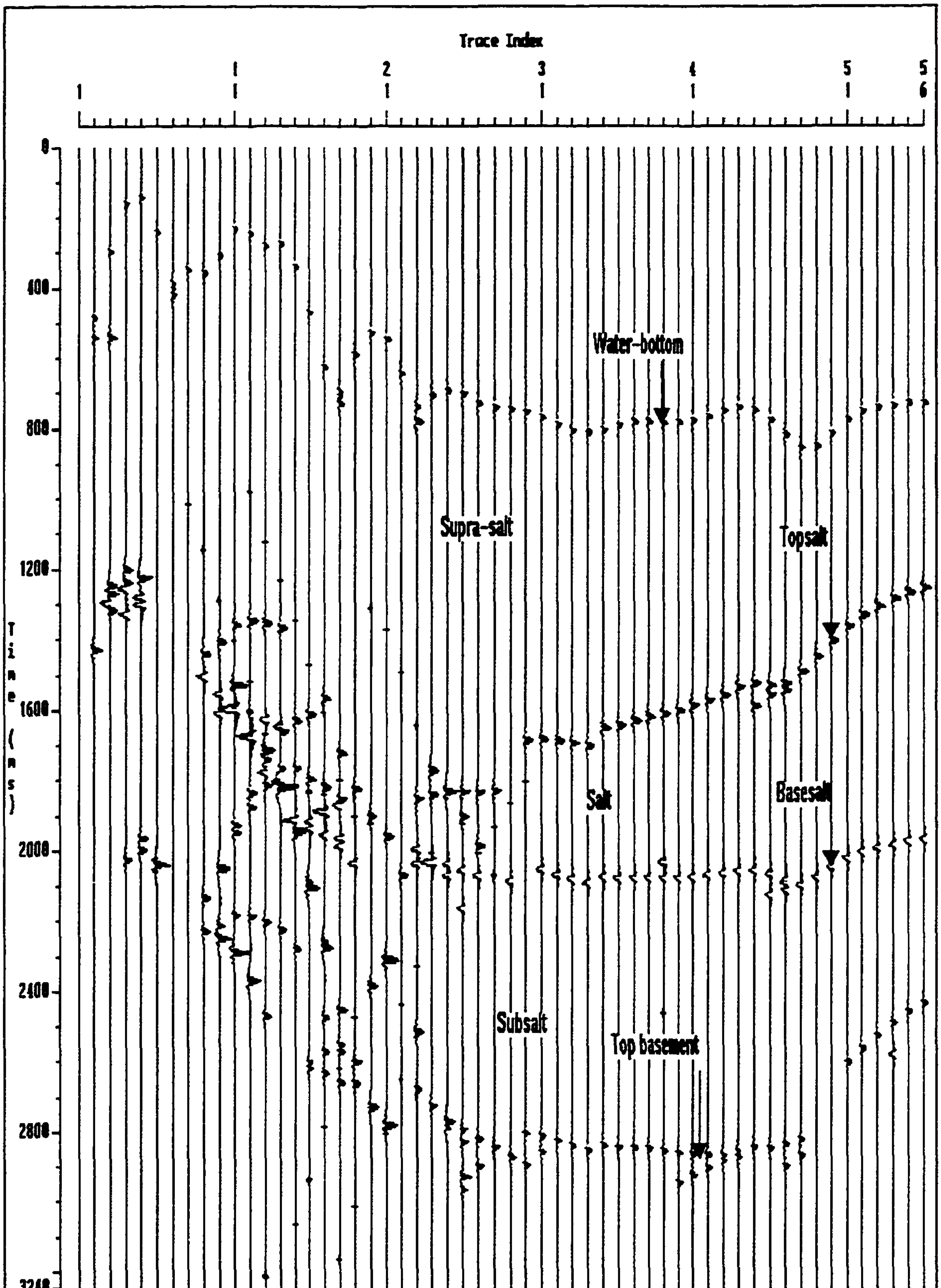

Figure 6.11. Normal incidence synthetic trace (magnified) for the western part of seismic line 9.

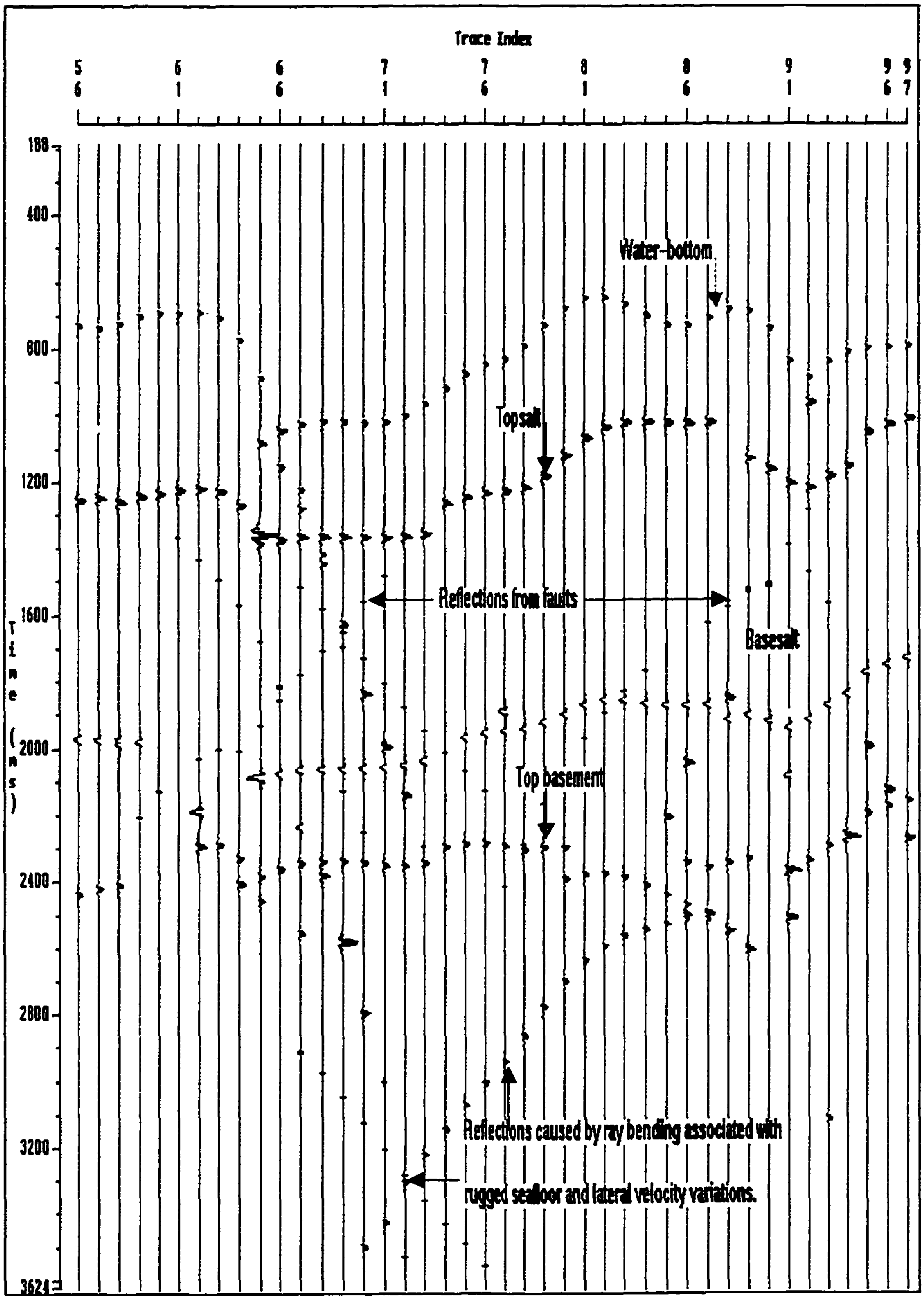

Figure 6.12. Normal incidence synthetic trace (magnified) for the middle part seismic line 9.

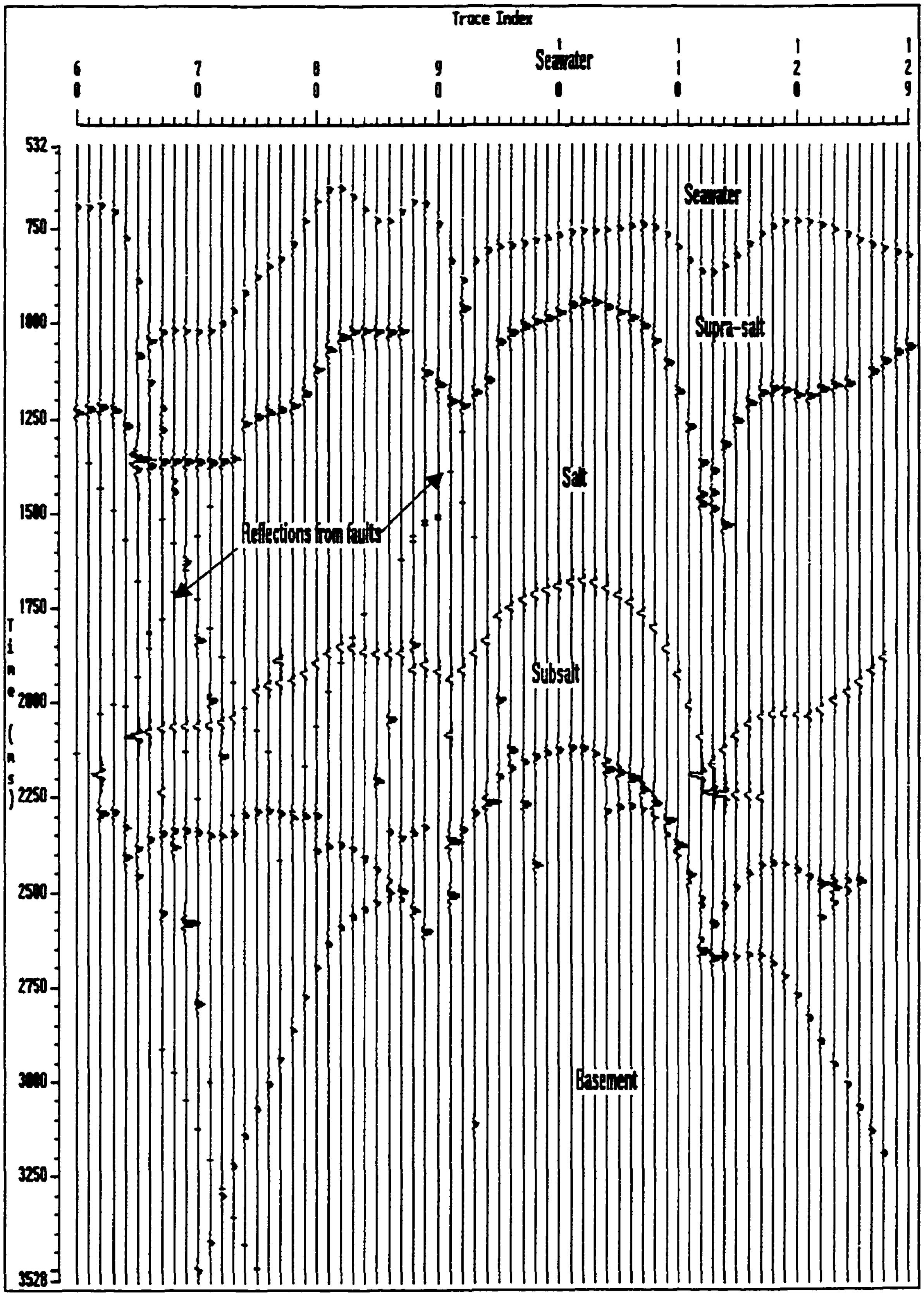

Figure 6.13. Normal incidence synthetic trace (magnified) for the western part of seismic line 9.

collapses the diffractions but does not make any significant improvement in the three poorly imaged areas and produces considerable migration artifacts.

VI.1.4.2. Steep dip finite difference depth migration:

Steep dip FD depth migration yields a relatively cleaner image than residual migration (Fig. 6.14). The migration collapses almost all of the diffraction. It unties the bow-tie and reveals what seems to be a very tight syncline or salt withdrawal feature. However, the basesalt and top of basement reflectors are still not visible in the poorly imaged parts of the section and fault planes are not well defined. The failure of FD depth migration to produce better result is possibly due to its high sensitivity to velocity errors.

VI.1.4.3. Steep dip explicit finite difference time migration:

Steep dip explicit FD time migration produces a fairly good result (Fig. 6.15). The base of salt and top basement reflectors (indicated by yellow and red arrows) is more visible in poorly imaged portions of the section. However the migrated section contains considerable amount of migration artifacts and the subsalt reflection events appear to be slightly overmigrated. Figures 6.16, 6.17, and 6.18 show the three poorly imaged areas before and after steep dip explicit FD time migration. The improvement is very obvious. The topsalt, basesalt, and top of basement are highlighted in blue, yellow, and red colors.

VI.1.4.4. Fast explicit finite difference time migration:

Fast explicit FD time migration yields a much better image than the previous methods. The diffractions are well focussed and the faults are easy to trace. Figure 6.19 compares the unmigrated and migrated sections. The comparison indicates that the continuity of basesalt and top of basement reflectors has improved significantly in poorly imaged areas. Figure 6.19 shows two possible interpretation of the migrated section.

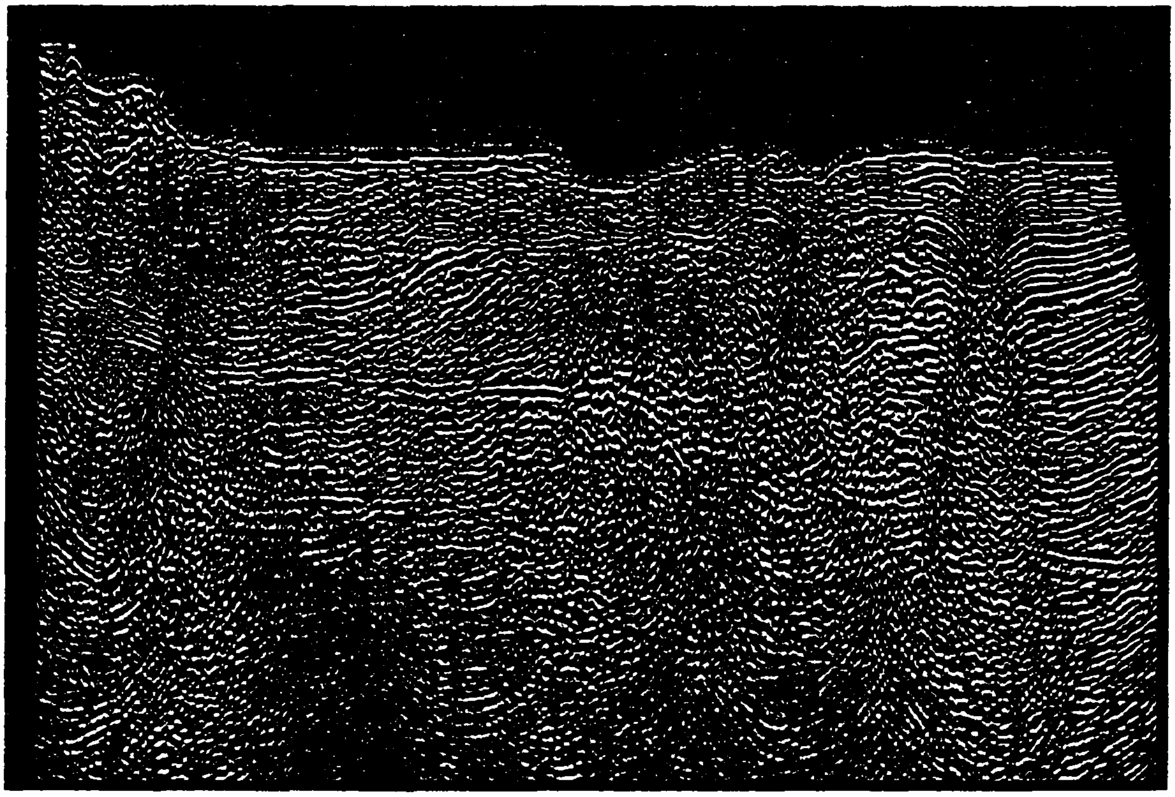

b

```
FLOW - 9datum     Fri Nov 28 10:53:00 1997
  Output - line9stack Add 999 Over 0
 SEG-Y Input

FLOW - 9datum     Mon Dec  8 23:26:32 1997
  Output - 9umdtmfxdecon30flt30SDFDDMIG Add 999 Over 0
 Dynamic S/N Filtering
  Horizontal window length                        20
  Time window length                              300.
  Time window overlap                             30.
  F-X filter start frequency                      10.
  F-X filter end frequency                        30.
 Bandpass Filter
  TYPE of filter                                  Single Filter
  Type of filter specification                    Butterworth bandpass
  PHASE of filter                                 Zero
  Apply a notch filter?                           No
  Butterworth filter freq-slope values            5-10-30-40
 Steep Dip FD Depth Migr.
  Maximum frequency vs depth to migrate
    0-30,10000-30,15000-30,20000-20/
  Get interval vs depth velocities from           Yes
  DATABASE?
    SELECT Interval vs depth Velocity             VintDfrmVintTposted
  File
  Percent velocity scale factor                   75.
  Defines the largest angle to properly           45
  migrate.
  Output the migration in Depth or Time?          TIME
  Re-kill dead traces ?                           No
```

Figure 6.14. (a) Seismic line 9 after steep dip finite difference depth migration. (b) Post-stack processing parameters.

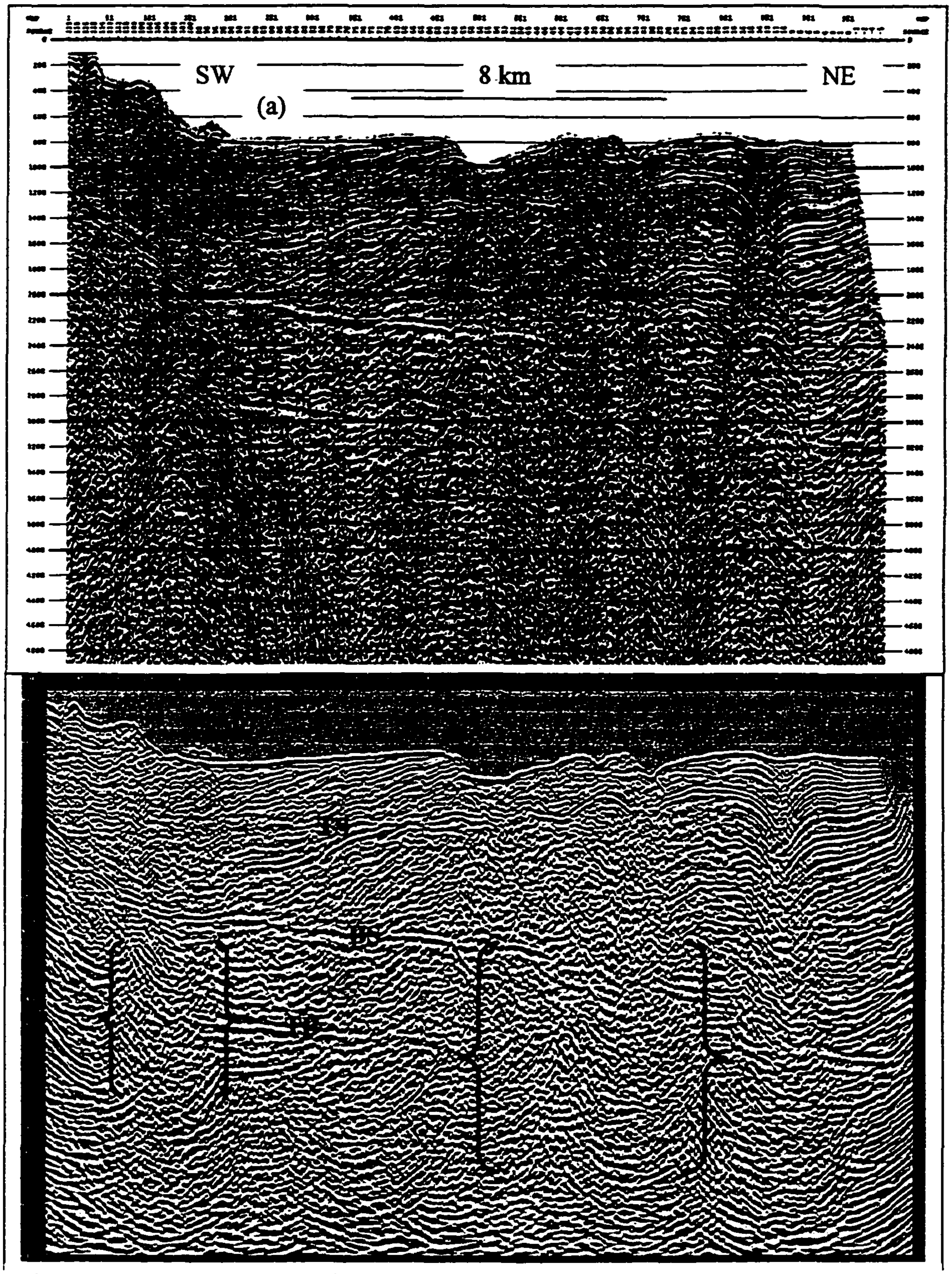

Figure 6.15. line 9 before (a) and after (a) signal enhancement and steep dip explicit finite difference time migration. TS, BS, and TB indicate topsalt, basesalt, and top of basement, respectively.

```
FLOW - 9datum     Fri Nov 28 10:53:00 1997
  Output - line9stack Add 999 Over 0
 SEG-Y Input

FLOW - 9datum     Mon Dec  8 00:40:51 1997
  Output - 9fxdecon30hzdatum2520ftDN Add 999 Over 0
 F-X Decon
  TYPE of filter                                   Wiener Levinson
  Percentage of white noise                        0.
  Horizontal window length                         10
  Number of filter samples                         5
  Time window length                               300.
  Time window overlap                              30.
  F-X filter start frequency                       10.
  F-X filter end frequency                         30.
 Post Stack Wave Eq. Datuming
  Maximum frequency (in Hz)                        30.
  Datumize through a constant velocity?            No
  Get interval velocities from database?           Yes
    Select interval vs. depth velocity             VintDfrmVintTposted
  file

FLOW - 9datum     Mon Dec  8 00:41:50 1997
  Output - 9fxd30hzdatm7000fsUP Add 999 Over 0
 Post Stack Wave Eq. Datuming
  Maximum frequency (in Hz)                        30.
  Datumize through a constant velocity?            Yes

FLOW - 9datum     Mon Dec  8 01:17:08 1997
  Output - 9fxd30hzdtm7000fsup Add 999 Over 0
 Trace Length
  New trace length                                 4600.

FLOW - 9datum     Wed Dec 10 23:21:20 1997
  Output - 9FXD30DTMbpfltSDEXFDTM Add 999 Over 0
 Bandpass Filter
  TYPE of filter                                   Single Filter
  Type of filter specification                     Butterworth bandpass
  PHASE of filter                                  Zero
  Apply a notch filter?                            No
  Butterworth filter freq-slope values             5-10-30-40

 Steep Dip Explicit FD Time Mig.
  Maximum frequency (in Hz)                        30.
  Get interval velocities from database?           Yes
    Select interval vs. time velocity              VintTmdotodtmcdp99980per
  file
  Re-apply trace mutes?                            No

FLOW - 9datum     Thu Dec 11 12:16:39 1997
  Output - 9fxd30hzdatmbpfltSDEXFDTMmut Add 999 Over 0
 Bandpass Filter
  TYPE of filter                                   Single Filter
  Type of filter specification                     Butterworth bandpass
  PHASE of filter                                  Zero
  Apply a notch filter?                            No
  Butterworth filter freq-slope values             5-10-30-40
 Automatic Gain Control
  Application mode                                 APPLY
  Type of AGC scalar                               MEAN
  AGC operator length                              500.
  BASIS for scalar application                     Centered
  Robust Scaling?                                  No
 Trace Muting
  Re-apply previous mutes                          No
  TYPE of mute                                     Top
    Starting ramp                                  30.
    SELECT mute parameter file                     tpmut9fxddatm30hzsdexfdtmic
 Trace Length
  New trace length                                 4400.
 Bandpass Filter
  TYPE of filter                                   Single Filter
  Type of filter specification                     Butterworth bandpass
  PHASE of filter                                  Zero
  Apply a notch filter?                            No
  Butterworth filter freq-slope values             5-10-30-40
```

Post-stack processing sequence performed on seismic line 9 of Figure 6.15.

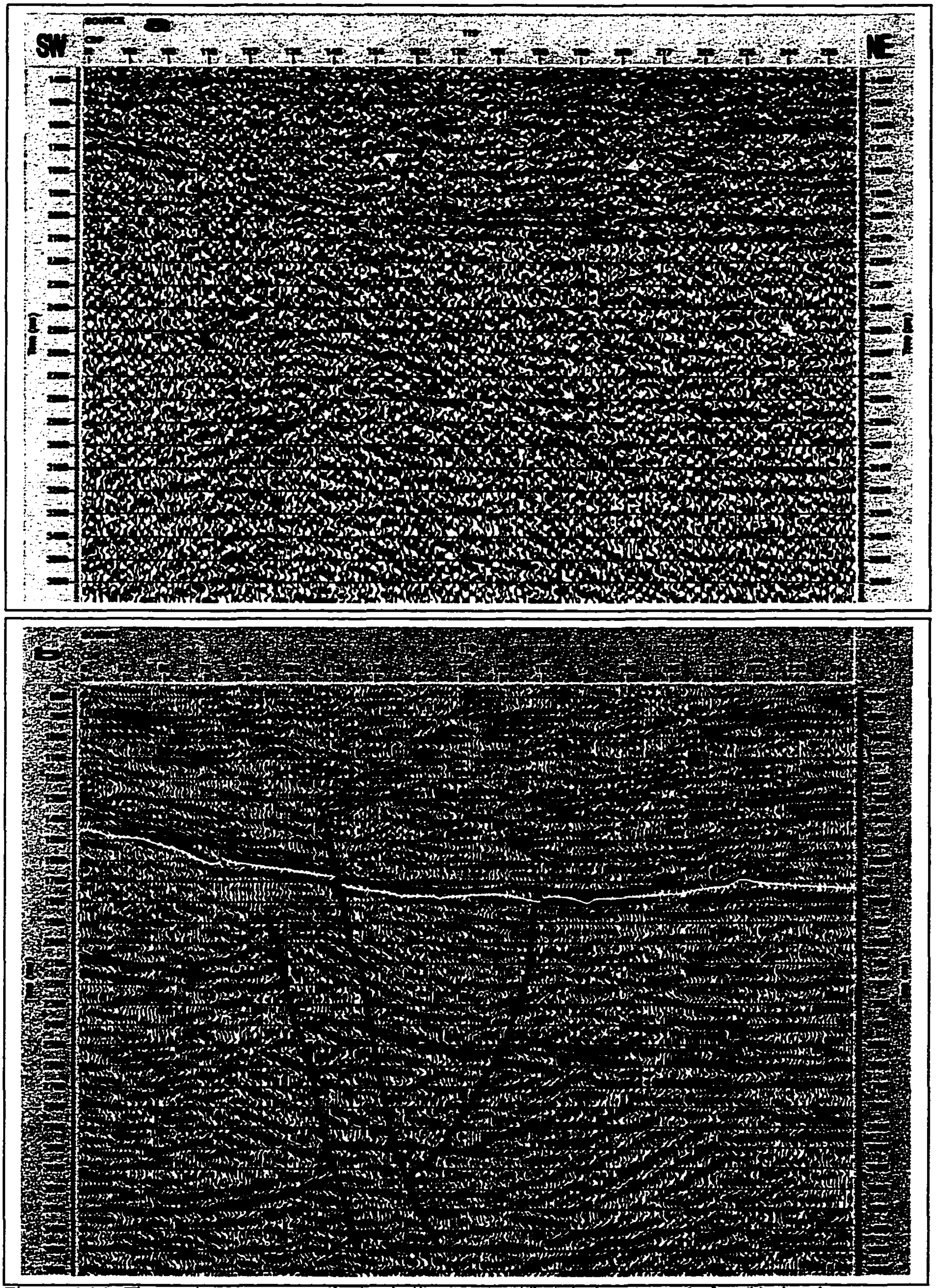

Figure 6.16. The southwestern part of seismic line 9 (magnified) before (a) and after (b) signal enhancement and steep dip explicit finite difference time migration. Basesalt (BS) and top basement (TB) .

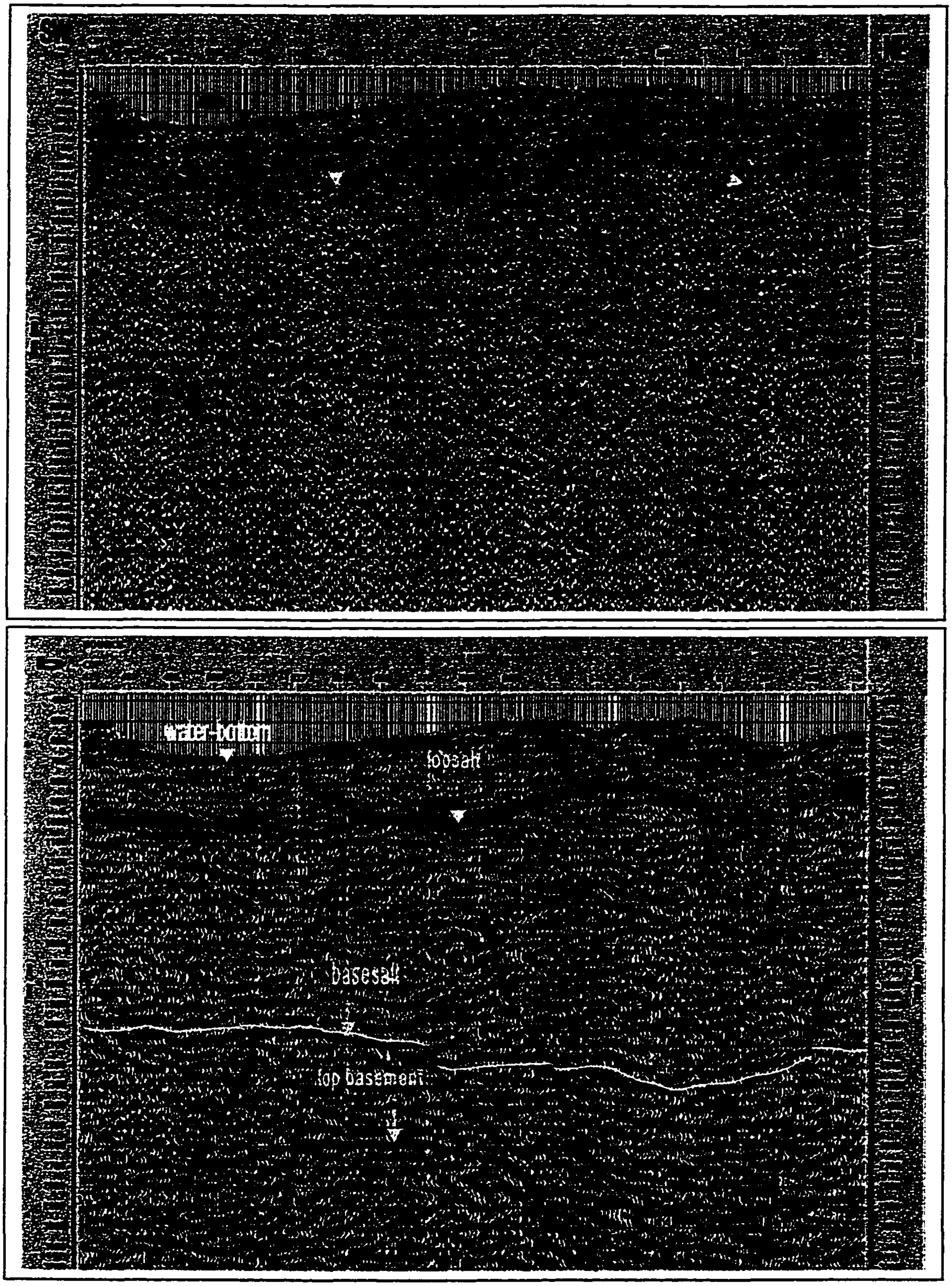

Figure 6.17. The middle part of seismic line 9 (magnified) before (a) and after (b) signal enhancement and steep dip explicit finite difference time migration.

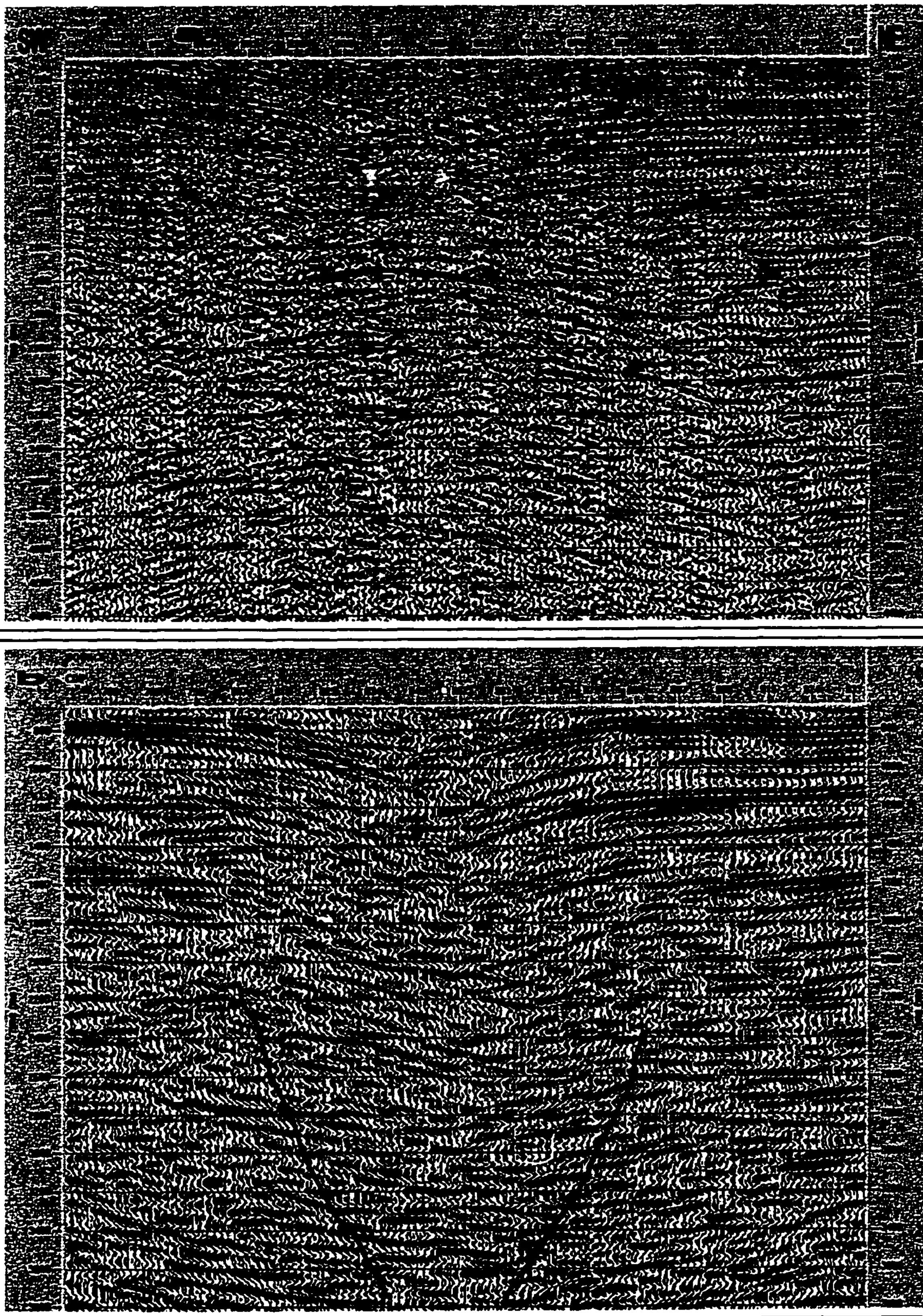

Figure 6.18. The northeastern part of seismic line 9 (magnified) before (a) and after (b) signal enhancement and steep dip explicit finite difference time migration.

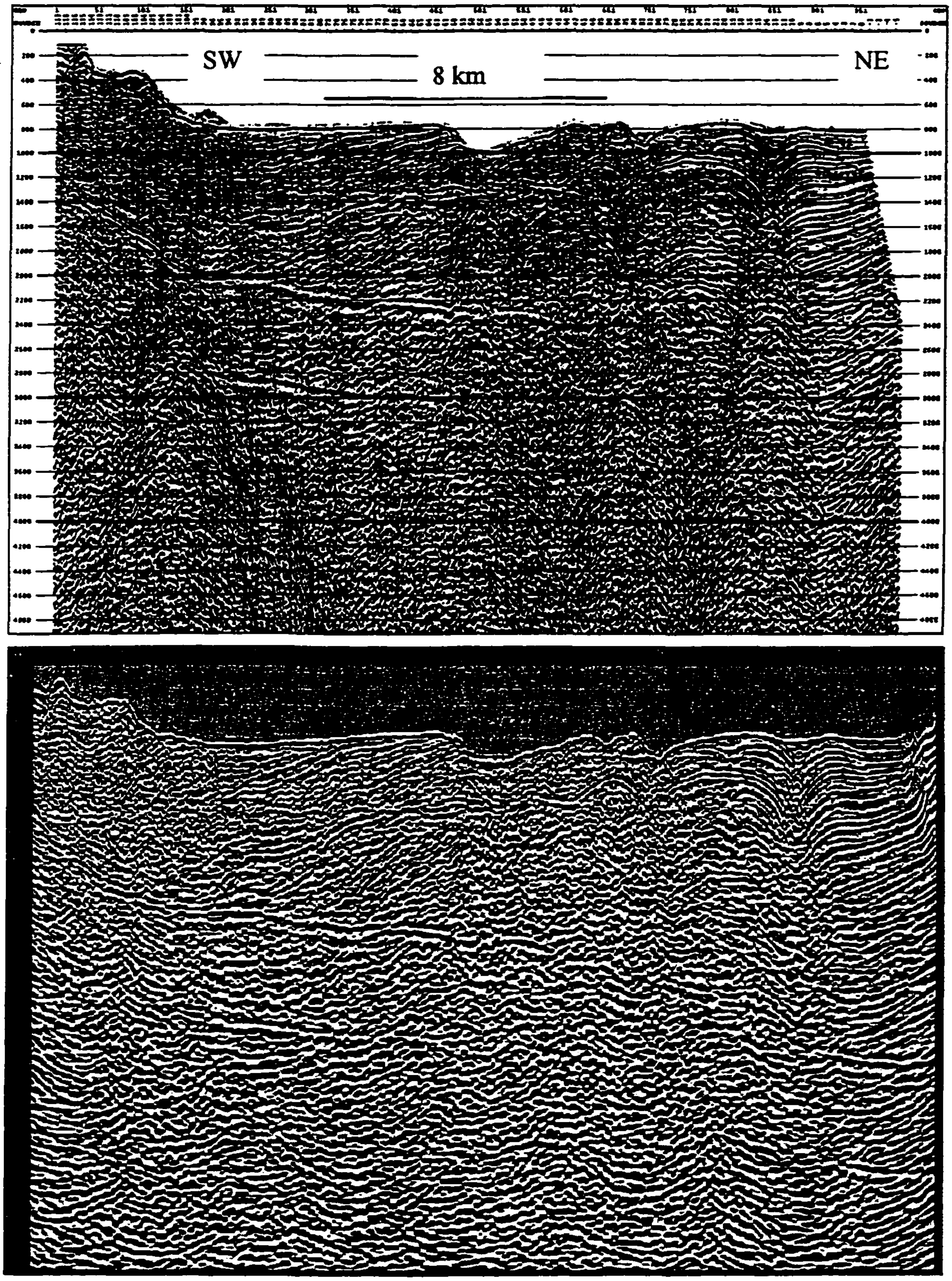

Figure 6.19. Seismic line 9. (a) Before signal enhancement and migration. (b) After signal enhancement and fast explicit finite difference time migration.

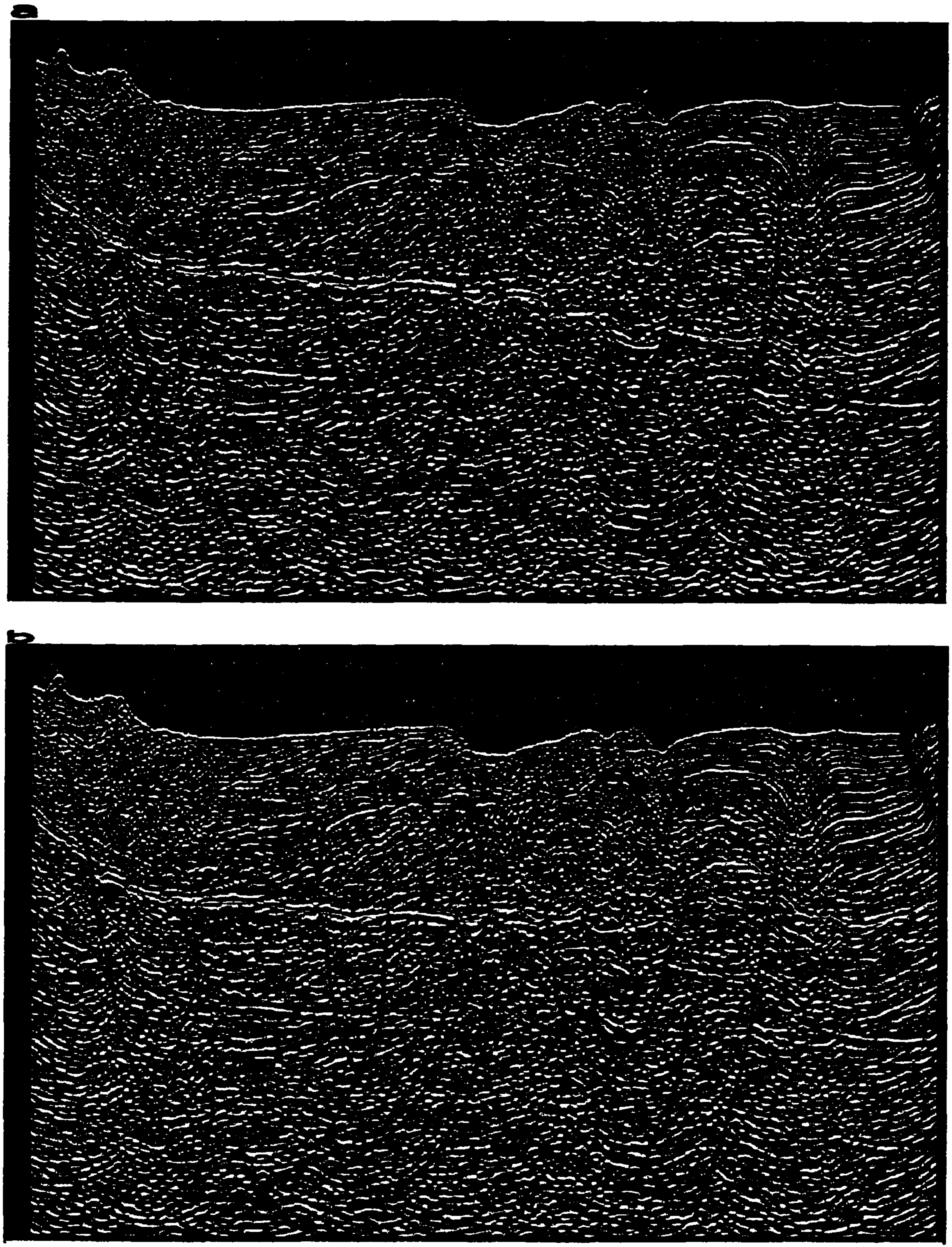

Figure 6.20. Migrated line 9 showing two possible interpretations. Topsalt, basesalt, and top basement are highlighted in blue, green, and red, respectively.

VI.2. SEIMIC LINE 316

Seismic line 316 is located offshore in the northern part of the safaga area (Fg.1). RSO-T 95-1 well located on the southwestern part of this line (Fig. 6.21) encountered the tops of salt, basesalt, and the top of basement at 4050, 4520, and 5574ft respectively, and bottomed in basement at total depth of 6401ft.

Lithological description:

The basement rocks encountered in this well (5574-6401 ft) consist of crystalline igneous rocks recorded as altered rhyolite and dacite of volcanic origin. The basement is overlain by Rudeis Formation (5000-5574 ft) which consists mostly of calcareous mudstone in the upper part and fine to medium grained sandstone at the base. Kareen Formation (4865-5000 ft) consists of very fine to coarse grained and locally pebbly sandstone, gravel and conglomerate interbedded with mudstone with rare anhydrite and thin interbeds of dolomite. Belayim Fm (4520-4865 ft) consists of anhydrite interbedded with argillaceous dolomite. South Gharib Formation (4050-4520ft) consists mainly halite with rare gypsum, anhydrite and mudstone. The overlying Zeit Formation (3202-4050 ft) consists of interbedded dolomite, anhydrite, mudstone and sandstone with rare halite.

VI.2.1. Imaging problem

Inspection of line 316 reveals a multitude of diffraction events, which overwhelm the entire seismic section and obscure the subsalt reflection events (Fig. 6.21). The distortions caused by the intensive diffractions make the extrapolation of topsalt, basesalt, and the top of basement reflectors (defined at the well location) to the northeast part of

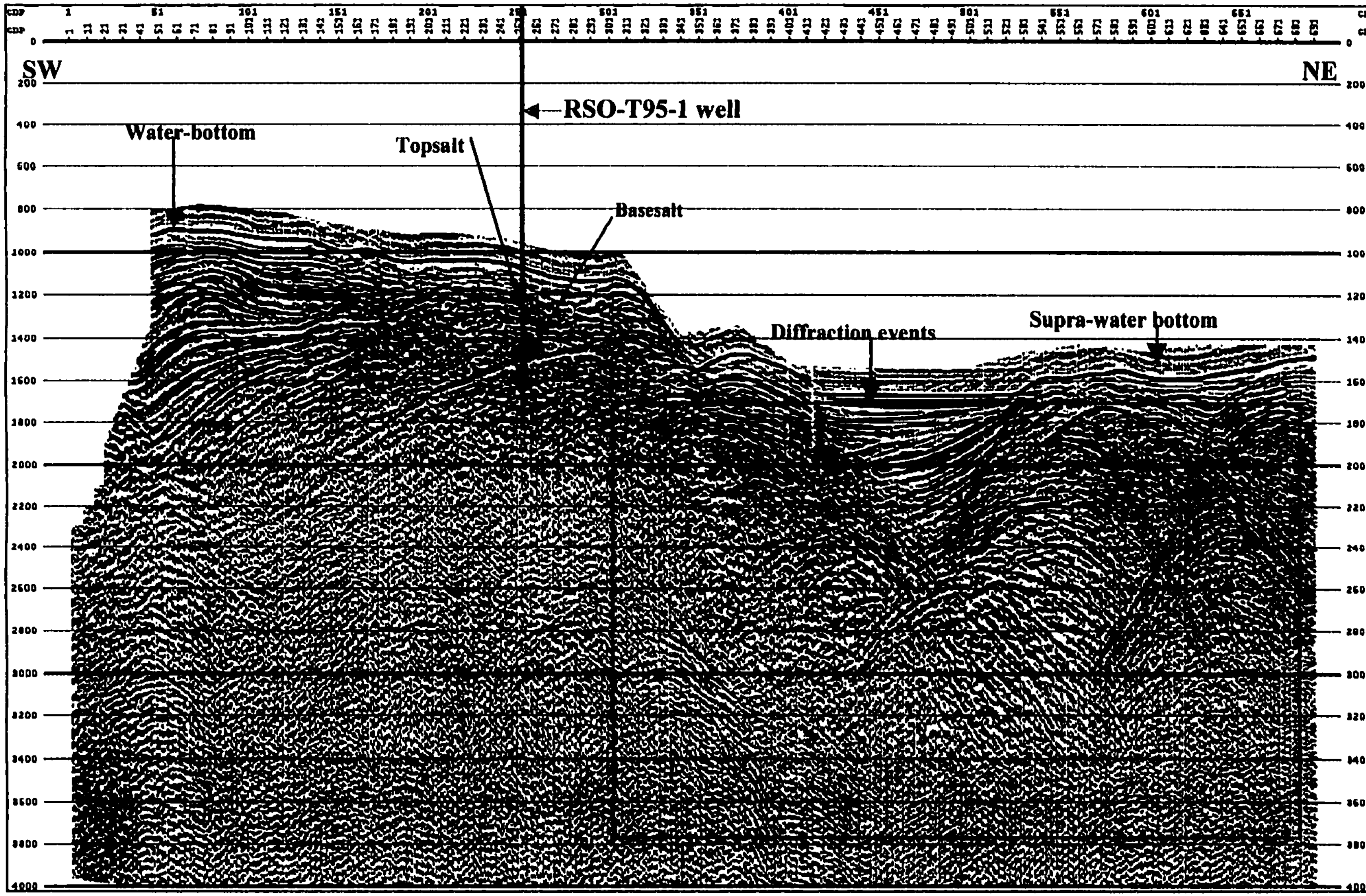

Figure 6.21. Seismic line316 before signal enhancement and migration. RSO-T95-1 well encountered the topsalt, basesalt, and the top of the basement at 4050, 4520, and 5574 ft, respectively, and bottomed in the basement at 6401 ft.

the section hard to accomplish. The seismic section exhibits a high amplitude reflection pattern in the shallow parts and a very low amplitude, discontinuous reflection within the southwest (below 1900 ms) and the northeast (below 3000 ms) parts of the line. The water bottom is overlain by what appears to be supra-water bottom events.

VI.2.2. The result of post-stack signal enhancement:

VI.2.2.a. F-X deconvolution

F-X deconvolution is used to remove the random noise and spurious events from line 316. The result of F-X deconvolution (Fig. 6.22) reveals a multitude of diffraction events which severely degrade and obscure the subsalt seismic reflections.

V.I.2.2.b. Wave equation datuming

The wave equation datuming is performed to reduce any possible deleterious effects caused by variable water depth. Figure 6.23 shows line 316 after wave equation datuming and dynamic S/N filtering. It is obvious from this Figure that the intensive diffractions which dominate the seismic section makes the improvement obtained by wave equation datuming hard to observe.

VI.2.2.c. Post-stack migration results.

The result of steep dip explicit finite difference time migration performed after post-stack signal enhancement is shown in Figure 6.24. It is clear from this Figure that the migration has collapsed all the diffractions and revealed several basement-related, major, normal faults.

VI.2.2.d. Final interpretation

Figure 6.25 shows seismic line 316 after signal enhancement, steep dip explicit finite difference migration and interpretation. The interpretation reveals a salt body varying

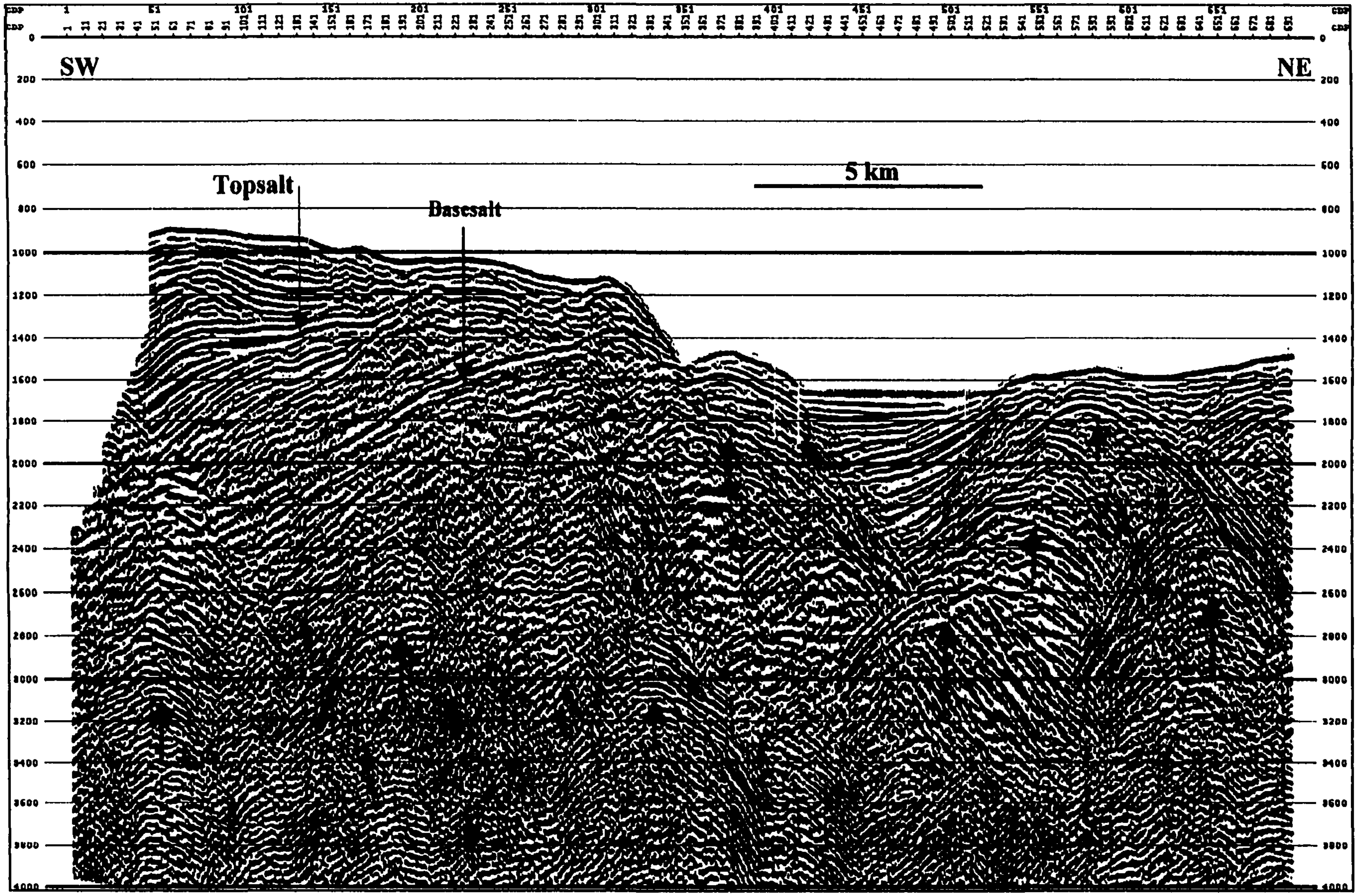

Figure 6.22 . Seismic line 316 after top mute, AGC, and F-X deconvolution. The F-X deconvolution reveals clearly that the seismic line is dominated by a multitude of diffractions (indicated by arrows) which severely distort and obscure the subsalt reflection events.

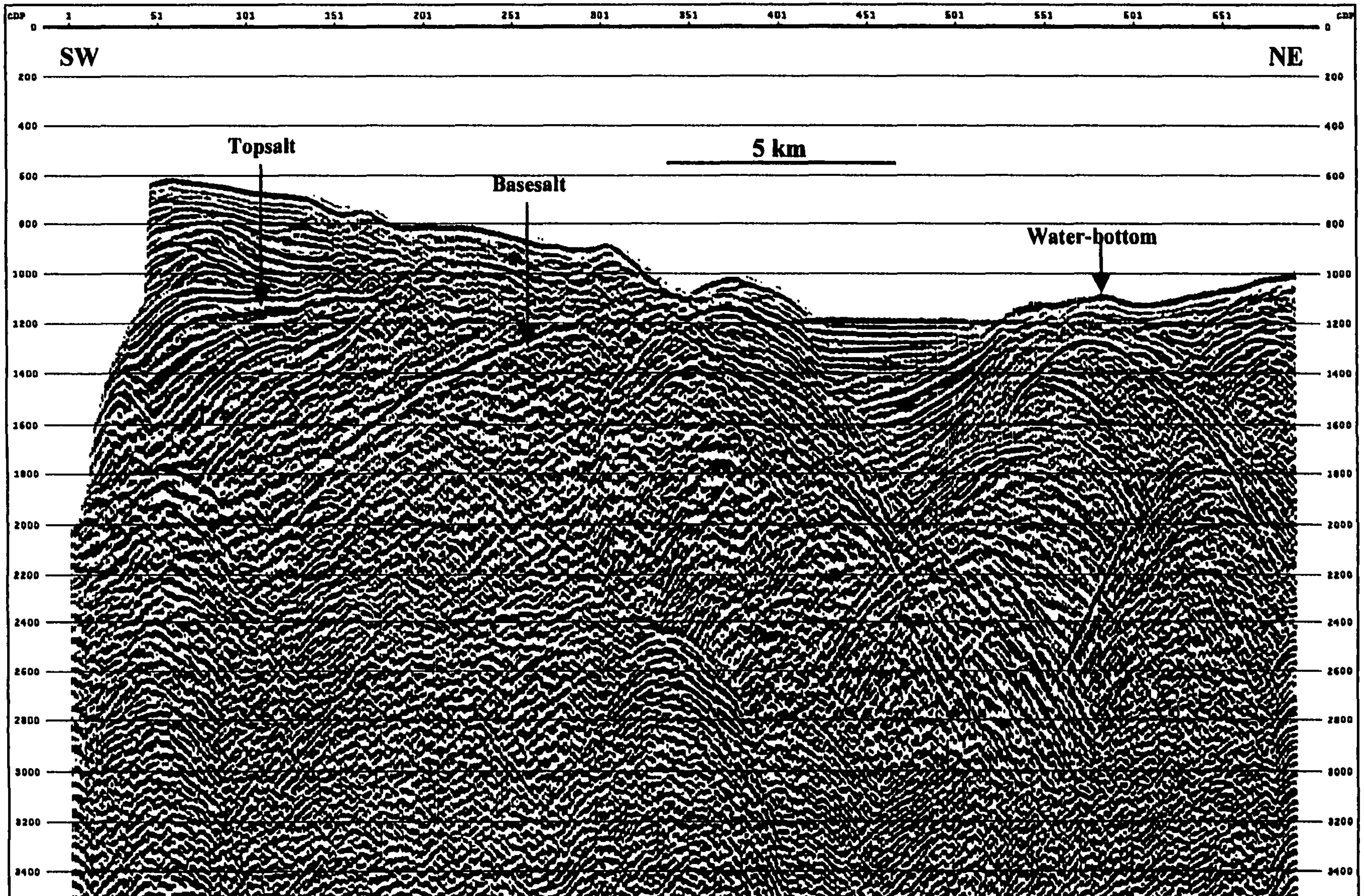

Figure 6.23. Seismic line 316 after top mute, AGC, wave equation datuming, and dynamic signal filtering. It very obvious that the entire seismic section is overwhelmed with intensive diffractions which obscure the salt and subsalt seismic events particularly on the northeast part of the section.

in thickness and lateral geometry and exhibiting complex boundaries within the northeast part of the section. On this part of the line, the salt shows significant thinning in the major half graben and a pronounce thickening in adjacent high areas. This suggests that the deformation of salt in this part of the section is due to the salt-sediments interaction. The salt exhibits a gradual thinning (from SW to NE) and less complex boundaries on the southwest portion of the line.

Summary:

The intensive diffractions from basement-involved normal faults, tilted fault blocks, and salt-related faults commingle with reflections and coherent noise and obscure the subsalt seismic events in these areas. Post-stack signal enhancement techniques remove the degrading effects caused by random noise, variable seafloor, and water bottom multiples. Steep dip explicit finite difference time migration performed after signal enhancement effectively collapsed the diffractions and improves the resolution of subsalt seismic events.

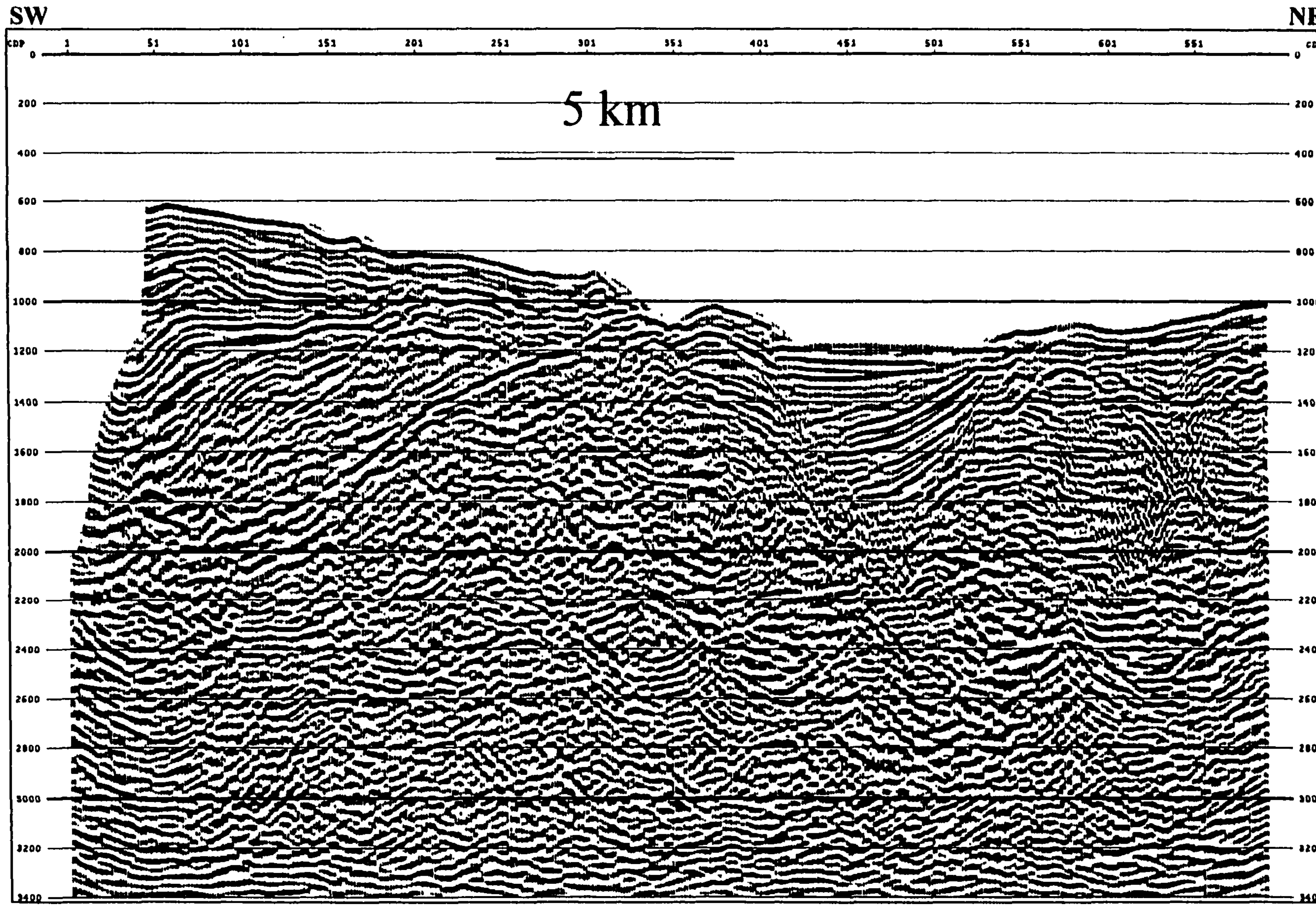

Figure 6 . 24. Seismic line 316 after post-stack signal enhancement and steep dip explicit FD time migration.

```
>  Disk Data Input   <- DTMDYS/NFLTAGCSDEXFDTM <
   Trace Length
   Trace Mixing
   Dynamic S/N Filtering
   Bandpass Filter
   Automatic Gain Control
>  Disk Data Output   -> DTMDYS/NAGCSEFDTMMIXDYS/NAGC <
```

(a)

```
FLOW - datum    Thu Mar  6 14:16:51 1997
 Output - 316SR4MS Add 691 Over 0
SEG-Y Input

FLOW - datum    Wed Mar 19 00:07:57 1997
 Output - 316DTMDN Add 691 Over 0
Post Stack Wave Eq. Datuming
 Maximum frequency (in Hz)                 48.
 Datumize through a constant velocity?     No
 Get interval velocities from database?    Yes
   Select interval vs. depth velocity      VintdlfrmRMS
 file

FLOW - datum    Wed Mar 19 23:17:59 1997
 Output - 316dtm7000fsUP Add 691 Over 0
Post Stack Wave Eq. Datuming
 Maximum frequency (in Hz)                 48.
 Datumize through a constant velocity?     Yes

FLOW - datum    Wed Mar 19 23:23:23 1997
 Output - 316dtm7000fsUPTRLGNgth Add 691 Over 0
Trace Length
 New trace length                          3700.

FLOW - datum    Thu Mar 20 00:08:59 1997
 Output - 316DTM7000fsUPMUTdyS/NFLTAGC Add 691 Over 0
Trace Muting
 Re-apply previous mutes                   No
 TYPE of mute                              Top
   Starting ramp                           30.
   SELECT mute parameter file              TPMUTAfterWEDTMUP7000fs
Dynamic S/N Filtering
 Horizontal window length                  20
 Time window length                        300.
 Time window overlap                       30.
 F-X filter start frequency                5.
 F-X filter end frequency                  40.
Automatic Gain Control
 Application mode                          APPLY
 Type of AGC scalar                        MEAN
 AGC operator length                       500.
```

(b)

```
 BASIS for scalar application              Centered
 Robust Scaling?                           No

FLOW - datum    Thu Mar 20 02:01:44 1997
 Output - DTMDYS/NFLTAGCSDEXFDTM Add 691 Over 0
Steep Dip Explicit FD Time Mig.
 Maximum frequency (in Hz)                 40.
 Get interval velocities from database?    Yes
   Select interval vs. time velocity       Vinttlsmth
 file
 Re-apply trace mutes?                     Yes

FLOW - datum    Sun Mar 23 16:21:09 1997
 Output - DTMDYS/NAGCSEFDTMMIXDYS/NAGC Add 691 Over 0
Trace Length
 New trace length                          3500.
Trace Mixing
Dynamic S/N Filtering
 Horizontal window length                  20
 Time window length                        300.
 Time window overlap                       30.
 F-X filter start frequency                12.5
 F-X filter end frequency                  36.
Bandpass Filter
 TYPE of filter                            Single Filter
 Type of filter specification              Ormsby bandpass
 PHASE of filter                           Zero
 Apply a notch filter?                     No
 Ormsby filter frequency values            8-12.5-30-36
Automatic Gain Control
 Application mode                          APPLY
 Type of AGC scalar                        MEAN
 AGC operator length                       500.
 BASIS for scalar application              Centered
 Robust Scaling?                           No
```

Processing parameters used in post-stack signal enhancement techniques and steep dip explicit finite difference time migration. The input to the processing is seismic line 316 of Figure 6.21. The output is line 316 of Figured 6.24.

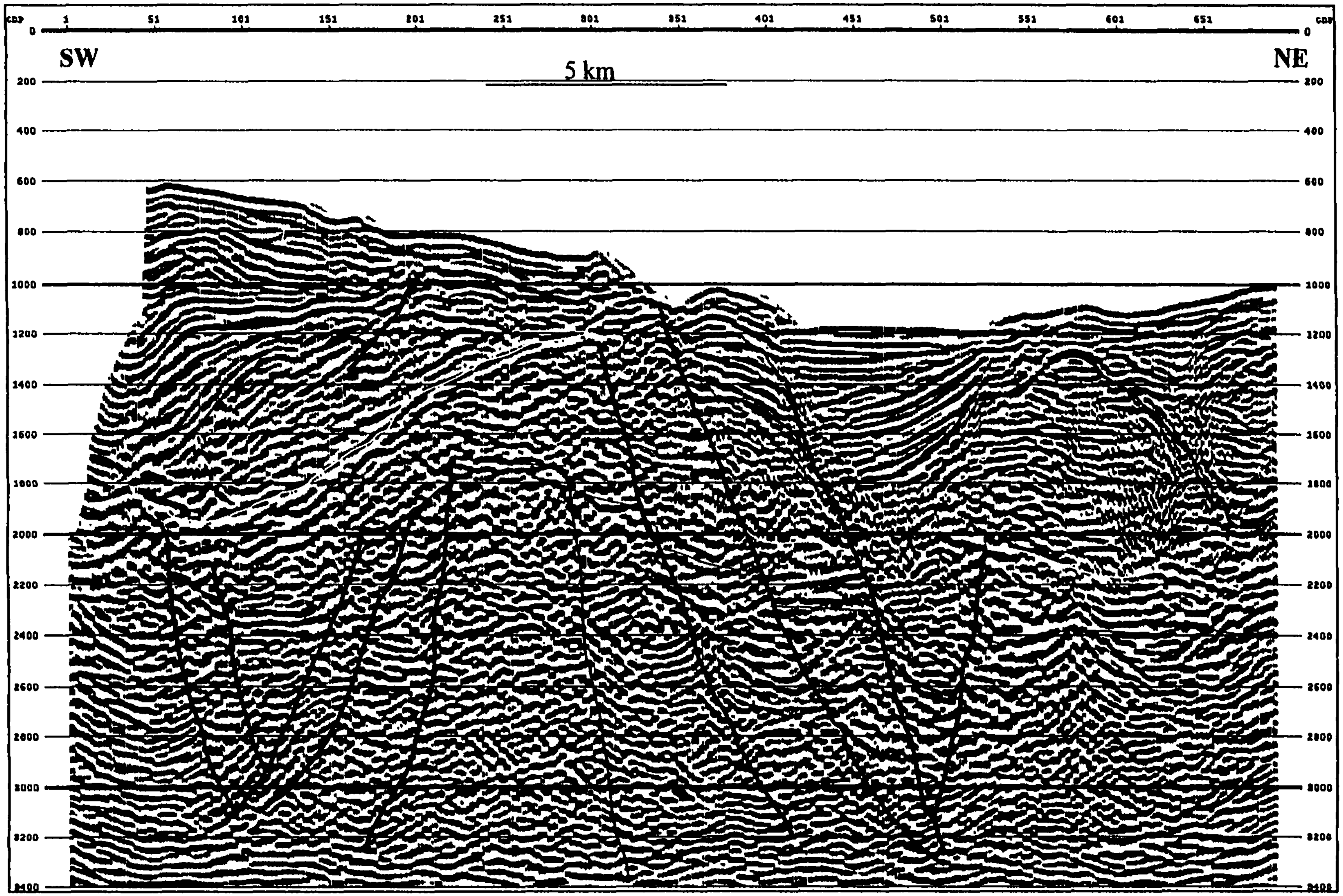

Figure 6.25. Seismic line 316 after post-stack signal enhancement and steep dip explicit FD time migration. Topsalt, basesalt, and top of basement are high-lighted in blue, yellow, and red, respectively.

CHAPTER VII

CONCLUSIONS

1. The origin of imaging problems and their likely effects must be understood in order to migrate and interpret the seismic data properly. 2-D seismic modeling is used in this study to investigate the causes and effects of imaging distortions observed on seismic lines from the study area. The modeling reveals five discrete causes: (a) rugged seafloor topography. The highly irregular water bottom topography (caused by organic reef buildups, complex halokinetic features, and localized tectonics) and the velocity contrast across the seafloor causes severe raypath bending, which induces disruption and distortion of reflections below. These distortions are: Coherent noise due to in-line and out-of-section scattering of reflections off the sides of sea floor irregularities, significant travel time errors, and drastic reduction of the amplitudes of the underlying reflections. (b) thick salt bodies varying in lateral geometry and exhibiting complex boundaries cause severe ray-bending and sharp refraction, resulting in insufficient downgoing energy for illuminating the underlying subsalt reflection events. (c) intensive diffractions, from basement-involved normal faults, tilted fault blocks, and salt-related faults, commingle with reflections and coherent noise and obscure the subsalt seismic events. (d) discrete lateral velocity anomalies from shallow reefal limestone and evaporite bodies lead to velocity pull-up of the underlying structures and degrade the subsalt image quality. (e) lateral velocity variation causes considerable ray bending and complicates the imaging problem. (f) water bottom related multiples and salt boundaries multiples further contaminate the subsalt images. These distortions mask the salt and subsalt reflections and create

uncertainty in structural interpretation and definition of hydrocarbon prospects in this area.

2. This investigation demonstrates the interpretive nature of post-stack seismic imaging. It shows how geologically constrained seismic migration can be achieved through joint-interpretation inversion approach. The iterative model-guided seismic imaging and interpretation performed in this study provide constraints in a form of raypath analyses, predict imaging problems, and narrowly constrain the range of acceptable interpretation. This integrated approach significantly minimizes the distortions and improves seismic imaging and structural interpretation of salt and subsalt seismic events.

Post stack signal enhancement techniques improve the migration results and produce interpretable seismic sections. F-X deconvolution removes random noise and improves the continuity of desirable reflections. Wave equation multiple rejection suppresses water-bottom multiples. Wave equation datuming reduces the damaging effects of variable seafloor on the underlying reflections. The improvement in reflectors continuity below variable water depth is the result of higher amplitude and increased coherence after wave equation datuming.

Time migrations performed after wave equation datuming produce results nearly identical to more costly full depth migration methods. Steep dip Finite difference depth migration eliminates the distortions caused by ray bending associated with irregular salt geometry and lateral velocity changes. It effectively collapses the diffractions, improves the resolution of subsalt seismic events, and removes the degrading effects caused by velocity pull-up.

REFERENCES

Bally, A. W., 1983, Seismic expression of structural styles: AAPG Studies in Geology N0. 15.

Bancroft, J. C., 1997, Apractical understanding of pre- and poststack migration Society of Exploration Geophysicists, Young, R. A., Eds. Course Notes Series, No. 7

Barton, D. C. 1993, Mechanics of formation of salt domes with special reference to Gulf Coast salt domes of Texas and Louisiana: AAPG Bulletin, v. 17, p. 1025-83.

Bayer, H. J., Hotzl, H., Jado, A. R., Ruscher, B., and Voggenreiter, W., 1988, Sedimentary and structural evolution of the northwest Arabian Red Sea margin: Tectonophysics, v. 153, p.137-151.

Beasley, C. and Lynn, W., 1992, The zero-velocity layer: Migration from irregular surfaces: Geophysics, 57, 1435-1443

Beasley, C. and Lynn, W., Migration from irregular surfaces: Geophysics, v. 57, p. 1435-1443.

Berkout, A. J., 1979, Steep dip finite-difference migration:Geophysical prospecting, v. 27, p. 196-213.

Berryhill, J. R., 1979, Wave-equation datuming: Geophysics, 44, 1329-1344.

--------, 1986 Submarine canyons: Velocity replacement by wave equation datuming before stack: Geophysics, 51, 1572-1579.

Bevc, D., 1997, Flooding the topography: wave equation datuming of land data with rugged topography: Geophysics, 2, 1558-1569.

Beydoun, Z. R., 1989, The hydrocarbon prospects of the Red Sea-Gulf of Aden: Jour. Petrol. Geol., 12, 125-144.

Beydoun, Z. R. and Sikander, A.H., 1992, The Red Sea-Gulf of Aden: regional assessment of hydrocarbon potential. Marine Petrol. Geol., 9, 474-485.

Bohannon, R. G., 1989, Style of extensional tectonism during rifting, Red Sea and Gulf of Aden, Jour. African Earth Sci., 8, 589-602.

Brewer, R. C. and Groshong, R. H. jr., 1989, Balancing and restoring cross-sections Of diaper-related structures: An example from the West Bay Field, Louisiana. GCSSEPM 10th Annual Conference program and Abstracts, p. 16-21.

Brooks, R. O., 1989, Horizontal component of Gulf of Mexico salt tectonics: GCSSEPM 10th Annual Research Conference Program and Abstracts, p. 22-24.

Canales, L. L., 1984, Random noise reduction: Presented at the 54th Annual SEG Meeting, Atlanta.

Chun, J. H. and Jacewitz, C. A., 1980, Fundamental of frequency domain migration: Geophysics, v. 46, p717-733.

Claerbout, J., F., 1976, Fundamental of geophysical data processing: New York, McGrraw-Hill Book Co., Inc.

Claerbout, J., F., 1985, Imaging the Earth's Iterior: Blackwell Science Publishers, Oxford, England.

Claerbout, J. F., and Doherty, S., 1972, Downward continuation of moveout-corrected seismograms: Geophysics, v. 37, p. 741-768.

Cochran, J. R. 1983, and A model for the development of the Red Sea: AAPG Bulletin, v. 67, p. 41-69.

Cochran, J. R., and Martinez, F., 1988 Evidence from the northern Red Sea on the transition from the continental to oceanic rifting, Tectonophysics, v. 153, p. 221-234.

Dent, B., 1983, Compensation of marine seismic data for the effects of highly variable water depth using ray-tracing modeling: A case history: Geophysics, 48, 910-933.

Dobrin, M. B., Savit, C. H., 1988, Introduction to geophysical prospecting: McGraw-Hill, New York.

Duval, B. C., CRamez, C. and Jackson, M. P. A.: 1992 Raft tectonic in the Kwanza basin, Angola, Marine and Petroleum Geology, Vol. 9, No4, 389-404.

Evan, B. J., 1997, A handbook for seismic data acquision in exploration, Geophysical Monogram Series no. 7. Society of Exploration Geophysicists, Tulsa Oklahoma.

Fagin, S. W., 9992, Seismic modeling of geologic structures: Application to Exploration Problems. Society of Exploration Geophysicists, Hoover, G. M., Eds. Geophysical Development series v. 2.

Girdler, R. W., and M. Underwood, 1985, The evolution of of the early oceanic lithosphere In the southern Red Sea: Tectonophysics, v. 116, p. 95-108.

Gulunay, Necati, 1986, F-X Decon and complex Weiner prediction filter for Radom noise reduction on stacked data, paper presented at the Society of Exploration Geophysicists 56th Annual International Meeting, Houston, TX.

Hatton, L., Larner, K., and Gibson, B., 1981, Migration of seismic data from inhomgeneous media: Geophysics, v. 46, p. 735-755.

Hood, P., 1987, Finite diference and wave number migration: Geophysical Prospecting, v. 26, p. 773-789.

Hubral, P., 1977, Time migration- Some ray theoretical aspects: Geophys. Prosp., v. 25, p. 738-745

Hughes, G. W., and Z. R. Beydoun, 1992, The Red Sea-Gulf of Aden: Biostratigraphy, lithostratigraphy, and palaeoenvironments: Journal of Petroleum Geology, v. 15, p. 135-156.

Hughes, G. W., Varol, O. and Beydoun, Z. R., 1991, Evidence for Middle Oligocene rifting of the Gulf of Aden and for late Oligocene rifting of the southern Red Sea. Marine Petrol. Geol. 8, 354-358.

Ibrahim, A. A. and Pigott, J. D., 1998, Post-stack model-guided seismic imaging and interpretation of salt and subsalt structures, Offshore Egyptian Red Sea: Society of Exploration Geophysicists, Africa/Middle East 2nd International Geophysical Conference & Exposition, Cairo, Egypt, Abstracts, p. 56-57.

Izzeldin, A. Y., 1987, Seismic, gravity and magnetic surveys in the central part of the Red Sea: Their interpretation and implication for structure and evolution of the Red Sea. Tectonophysics, 143, 269-306.

Judson D. R. Lin, J., Schultz, P. S., and Sherwood J. W. C., 1980, Depth migration after stack: Geophysics, v. 45, p. 361-375.

Larner, K., and Beasley, C., 1987, Cascaded Migration: Improving the accuracy of finite-difference migration: geophysics, v. 52, p.618-643.

Laner, K., Chambers, R., Yang, M., Lynn, W., and Wai, W., 1983, Coherent noise in marine seismic data: Geophysics, v. 48, p. 854-886.

Larner, K. L., Hatton, L., Gibson, B. S., and Hsu, I. C., 1985, Depth migration of imaged time sections: Society of Exploratron Geophysicists, Gerald H. F. Gardner, and Eds. P.Migration of seismic data Geophysics reprint series no. 4, p. 380-396.

Lynn, W., MacKay, S., and Beasley, C., 1990, Efficient migration through irregular water-bottom topography: 60th Ann. Internat. Mtg. Soc. Expl. Geophys., Expanded Abstracts, 1297-1300.

Loewenthal, D., Lu, L., Roberson, R., and Sherwood, J. W. C., 1976, The wave equation applied to migration: geophys. Prosp., v. 24, p. 380-399.

Lowell, J. D., and Genik, G. J., 1972, Sea-floor spreading and structural evolution of southern Red Sea. Bull. Am. Assoc. Petrol. Geol., 56, 247-259.

Makris, J., Henke, C. H., Eglof, F., and Akamaluk, T. 1991a, The gravity field of the Red Sea and East Africa, in J. Makris and Rihm, Eds. Red Sea –birth and early history of a new ocaenic basin: Tectonophysics, v. 198, p. 369-381.

Makris, J, and Henke, C. H., Pull-apart evolution of the Red Sea. Jour. Petrol. Geol. 15, 17-134.

Makris, J., and Rihm, R., 1991, Shear-controlled evolution of the Red Sea: Pull-apart model. Tectonophysics, 198, 441-466.

Marinez, F. and Cochran, J. R., 1988, Structure and tectonics of the northern Red Sea: Catching a continental margin between rifting and drifting. Tectonophysics, 150 \1-32.

Mitchell, D. J. W., R. B. Allen, W. Salama, and A. Abouzakm, 1992, Tectonostratigraphy framework and hydrocarbon potential of the Red Sea: Journal of Petroleum Geology, v. 15, p. 187-210.

Pigott, J. D. and Ibrahim, A. A., 1995, Salt basin seismic sequences as a signature of near to far field tectonics; Example: High Island, Northern Gulf of Mexico, AAPG Annual Convention Abstracts, p. 76A.

Robinson, E. A., 1983, Migration of seismic data: International Human resources Development Corporation, Boston, MA.

Rothman, D., Levin, S., and Rocca, F., 1985, Residual migration: applications and limitations: Geophysics, 50, 10-126.

Roure F., Brun J. P., Colleta B. and Van Den Driessche J., 1992: geometry and Kinematics of Extensional Structures in the Alpine Foreland Basin of Southern France. J. Struct. Geol., 14, pp. 503-519.

Roure F., Brun J. P., Colletta B. and Vially R., 1994: Multiphase Extensional Structures fault Reactivation and petroleum Plays in the Alpine Foreland Basin of Southern France. In: EAPG Memoir 4, A. Mascle (ed.), and Springer-Verlag.

Schneider, W.,1978, Integral formulation for migration in two and three dimensions: Geophysics, v. 43, p. 49-76.

Sherwood, J.W. C., Adams, H., Blum, C. Judson, D. R., Lin, J., and Meadours, B., 1976: Development in seismic data: Presented at the 46th Annual International SEG Meeting October 25, in Houston.

Shriff, R. E., 19911, Encyclopedic dictionary of exploration geophysics. Soc. Of Expl. Geophys. Tulsa, Oklahoma.

Spitz, S., 1991, Seismic trace interpolation in the F-X domain: geophysics, v.

Stolt, R, H., 1978, Migration by Fourier transform: Geophysics, v. 43, p. 23-48.

Sultan, M., R. Becker, R. E. Arvidson, P. Shore, R. J. Stern, Z. El Alfy, and Guinness, E.A.1992, Nature of the Red Sea crust: A controversy revisited: Geology, v. 20, p. 593-596.

Sultan, M., Becker, R., Arvidson, R. E., Shore, P., Stern, R. J., El Alfy, Z. and Attia, R. I., 1993, New constraints on the Red Sea Rifting from Correlation of Arabian and Nubian Neoproterozoic outcrops. Tectonics, 12, 1303-1319.

Taner, M.T., and Koehler, F.,1981, Surface-consistent corrections:Geophysics, 46,17-22 UNDP/World Bank Red Sea/Gulf of Aden Regional Hydrocarbon Study Project, 1990a, Petroleum Geology and Regional Hydrocarbon Evaluation, Egyptian Red Sea.

UNDP/World Bank Red Sea/Gulf of Aden Regional Hydrocarbon Study Project, 1990a, Petroleum Geology and Regional Hydrocarbon Evaluation, Sudanese Red Sea.

Voggenreiter, W., Hotzl, H., and Mechie, J., 1988, Low-angle detachment origin of the Red Sea Rift System. Tectonophysics, 150, 51-75.

Wiggins, J. W., 1984, Kirchhoff integral extrapolation and migration of nonplanar data: Geophysics, v. 49, p. 1239-1248.

Wiggins, J. W., 1988, Attenuation of complex water-bottom multiples by wave-equation based prediction and subtraction: geophysics, 53, 1527-1539.

Yilmaz, O., 1991, Seismic data processing: Soc. Of Expl. Geophys. Tulsa, Oklahoma.

IMAGE EVALUATION
TEST TARGET (QA-3)

150mm

6"

APPLIED IMAGE . Inc
1653 East Main Street
Rochester, NY 14609 USA
Phone: 716/482-0300
Fax: 716/288-5989